Mathematical Problems in Engineering

Applications of Mode Decomposition in Nonlinear and Nonstationary Signal Processing

Lead Guest Editor: Yuxing Li
Guest Editors: Neggaz Nabil and Xiao Chen

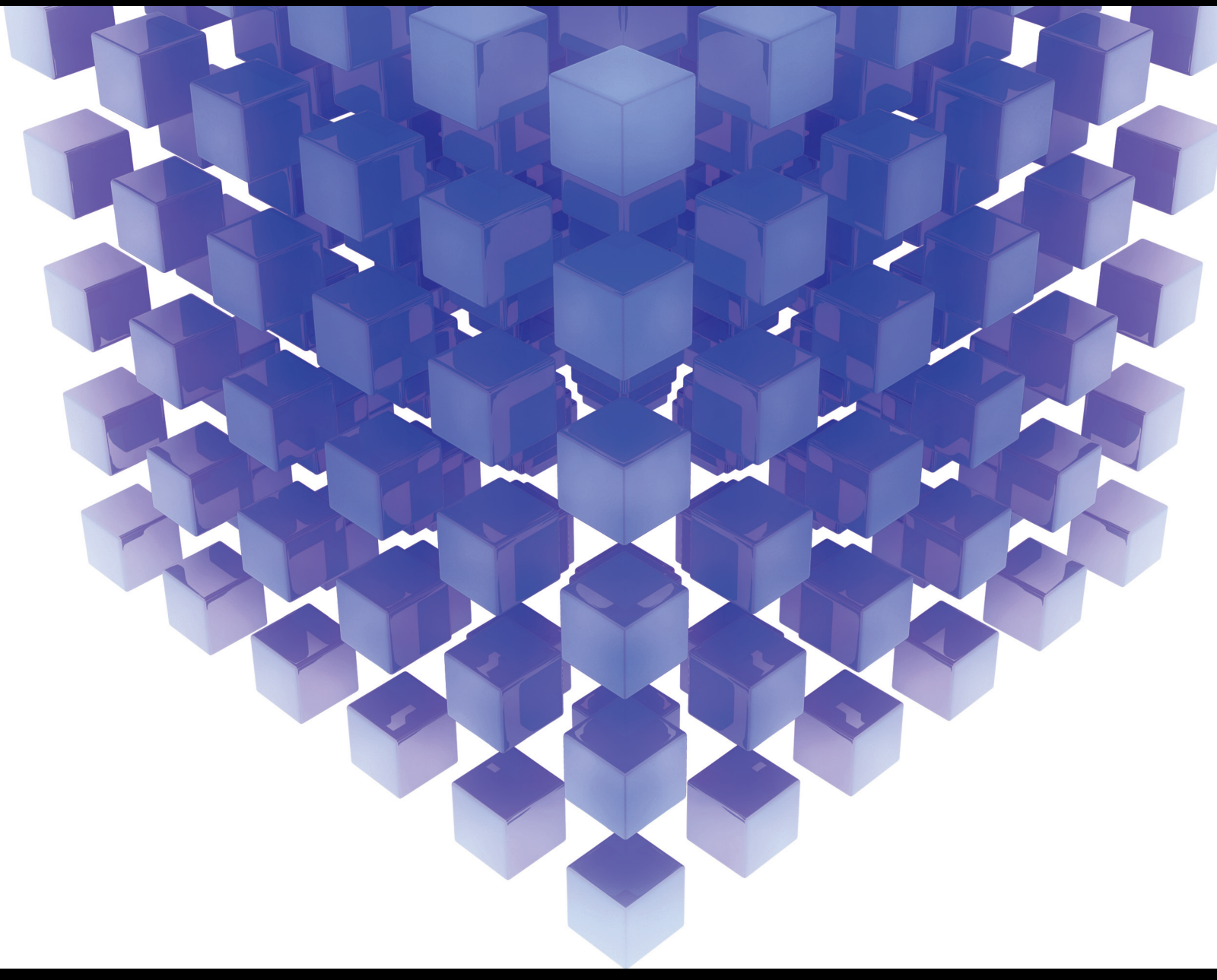

Applications of Mode Decomposition in Nonlinear and Nonstationary Signal Processing

Mathematical Problems in Engineering

Applications of Mode Decomposition in Nonlinear and Nonstationary Signal Processing

Lead Guest Editor: Yuxing Li
Guest Editors: Neggaz Nabil and Xiao Chen

Chief Editor

Academic Editors

Contents

Hindawi
Mathematical Problems in Engineering
Volume 2022, Article ID 2058258, 19 pages
https://doi.org/10.1155/2022/2058258

Research Article

Bearing Fault Feature Extraction Method Based on GA-VMD and Center Frequency

Yuxing Li,[1,2] **Bingzhao Tang**,[1] **Xinru Jiang**,[1] **and Yingmin Yi**[1,2]

[1]*School of Automation and Information Engineering, Xi'an University of Technology, Xi'an 710048, China*
[2]*Shaanxi Key Laboratory of Complex System Control and Intelligent Information Processing, Xi'an University of Technology, Xi'an 710048, China*

Correspondence should be addressed to Yingmin Yi; yiym@xaut.edu.cn

Received 14 September 2021; Revised 25 November 2021; Accepted 15 January 2022; Published 30 January 2022

Academic Editor: Jian G. Zhou

To promote the effect of variational mode decomposition (VMD) and further enhance the recognition performances of bearing fault signals, genetic algorithm (GA) is applied to optimize the combination of VMD parameters in this paper, and GA-VMD algorithm is put forward to improve the decomposition accuracy of VMD. In addition, combined with the center frequency, a feature extraction method based on GA-VMD and center frequency is proposed to ameliorate the difficulty of bearing fault feature extraction. Firstly, the bearing signal is decomposed into a series of intrinsic mode components (IMFs) by GA-VMD. Then, the Center Frequency of IMFs is extracted, and the recognition rate is calculated by k-nearest neighbor (KNN) algorithm. Simulation signal experiments state clearly that, compared with manual parameter setting-VMD algorithm and parameter optimization VMD algorithm based on particle swarm optimization (PSO), the decomposition result of GA-VMD has a smaller root mean square error and higher decomposition accuracy, which verifies the effectiveness of GA-VMD. The experimental results demonstrate that, by comparison with the feature extraction method based on envelope entropy, the feature extraction method based on center frequency has better inter class separability and higher mean recognition rate (the highest recognition rate of single feature is 94.5%, and in the case of multiple features, the recognition rate reaches 100% when four features are extracted) and can realize the accurate identification of different bearing fault signals.

1. Introduction

As an essential part of various mechanical equipment, bearings have been widely used in civil, industrial, and military applications [1, 2]. However, due to the arduous working conditions, bearings are extremely susceptible to damage [3], which can cause economic losses and even affect personal safety. Simultaneously, the bearing signal in the fault state will produce some periodic transients, which contains the status information of the bearing during operation [4]. Therefore, fault diagnosis of bearings is of great significance to ensure the safe, stable, and reliable operation of mechanical equipment [5, 6].

In recent years, many scholars have put forward their methods for fault diagnosis [7, 8]. Generally speaking, there are two key steps in bearing signal fault diagnosis; the first step is the extracted features. Recently, there are many methods that can be extracted as features and used for fault detection of various types of signals, such as the Lempel-Ziv complexity (LZC) [9], the correlation dimension [10], the Lyapunov exponent [11], and the entropy-based method [12, 13]. Among which, LZC and the entropy-based method can effectively reflect the complexity of the time series and have better robustness and simplicity compared with other features [14, 15]. However, only relying on the separability of the extracted features will be susceptible to interference from noise signals.

Another critical step of bearing signal fault diagnosis is the signal processing method. In 1998, Huang et al. first proposed empirical mode decomposition (EMD) and used it for adaptive decomposition of target signals [16], which has received extensive attention. In 2009, Wu et al. proposed an

ensemble empirical mode decomposition (EEMD) method on the basis of EMD, which can use the statistical properties of white noise to reduce modal aliasing [17, 18]. However, EEMD still belongs to recursive decomposition and is vulnerable to modal aliasing and endpoint effect, so there will be some decomposition errors [19, 20]. In order to solve these problems, Dragomiretskiy et al. proposed the variational modal decomposition (VMD) method in 2014 [21], which can achieve adaptive decomposition of the target signal by iteratively searching for the optimal solution of the variational model, so as to determine the center frequency and bandwidth of each mode. Compared with EMD and EEMD, VMD also has stronger robustness [22–24].

However, different from EMD and its improved algorithm, VMD is more dependent on the setting of parameters, including the number of decomposition layers and penalty factors. In recent years, many scholars have improved VMD [25–27]. Tang Guiji et al. used particle swarm optimization (PSO) algorithm to optimize combination parameters and established a fitness function based on minimum envelope entropy [28]; Mirjalili et al. proposed the whale optimization algorithm (WOA) algorithm in 2016 and proved that it has Strong local and global search ability [29]. In this paper, genetic algorithm (GA) [30, 31] is used as the optimization method, and envelope entropy is selected as the fitness function, and then combined with VMD for automatic optimization of parameters. Because the center frequency obtained by VMD does not need to be calculated like other features, a feature extraction method based on GA-VMD and center frequency is proposed and applied to bearing fault diagnosis. Compared with other methods, the method proposed in this paper has clear physical significance, and it is simpler and has higher recognition rate. After the feature extraction, we utilize K-Nearest Neighbor (KNN) [32] to classify all kinds of fault bearing signals, and both the simulated signal and the actual bearing signal experimental results show the effectiveness of the feature extraction method proposed in this paper.

The rest of this paper is structured as follows. Section 2 proposes GA-VMD algorithm and introduces the specific steps of GA-VMD algorithm. Section 3 introduces the main steps of the proposed fault feature extraction method. Section 4 carries out the simulation signal experiment and compares the GA-VMD algorithm and PSO-VMD algorithm. Section 5 carries out the experiments of bearing signal extraction and KNN classification based on center frequency and envelope entropy, respectively. Section 6 gives conclusion of this paper.

2. Basic Principles

2.1. Variational Mode Decomposition. Variational mode decomposition (VMD) is an adaptive signal decomposition algorithm. It can decompose a signal into multiple components, and its essence and core idea is the construction and solution of the variational problems. The solution process is as follows:

Firstly, set the variational model:

$$\max_{\{u_k\},\{\omega_k\}} \left\{ \sum_{k=1}^{K} \partial_t \left[\left(\delta(t) + \frac{j}{\pi t} \right) * u_k(t) \right] e_2^{-j\omega_k t 2} \right\}, \tag{1}$$

$$\text{s.t} \sum_{k=1}^{K} u_k = f, \tag{2}$$

where ∂_t is partial derivative operation, $\delta(t)$ is the Dirichlet distribution function, $*$ represents convolution, $\{u_k\} = \{u_1, u_2, u_3, \ldots, u_K\}$ represents K IMFs obtained by VMD, $\{\omega_k\} = \{\omega_1, \omega_2, \omega_3, \ldots, \omega_K\}$ represents the center frequency of each IMF, f represents the original signal, and K is the number of IMFs.

Then, (1) is transformed into an unconstrained problem by using penalty factor and multiplication operator; the augmented Lagrange function is obtained as follows:

$$L(\{u_k\}, \{\omega_k\}, \lambda) = \alpha \sum_{k=1}^{K} \delta_t \left[\left(\delta(t) + \frac{j}{\pi t} \right) * u_k(t) \right] e^{-j\omega_k t 2} + f(t) - \sum_{k=1}^{K} u_k(t) + \lambda(t), f(t) - \sum_{k=1}^{K} u_k(t), \tag{3}$$

where λ is the Lagrange constant, and α is the penalty factor.

Lastly, for the sake of solving the optimal solution of the variational problem, it is necessary to update variable by alternating direction multiplier of method (ADMM). Updated after $n+1$ cycles, update the formulas for $\widehat{u}_k^{n+1}$, ω_k^{n+1}, and $\widehat{\lambda}^{n+1}$ as follows:

$$\frac{\hat{f}(\omega) - \sum_{i<k} \hat{u}_i^{n+1}(\omega) - \sum_{i>k} \hat{u}_i^{n}(\omega) + x\widehat{\lambda}^{n}(\omega)/2}{1 + 2\alpha(\omega - \omega_k^n)^2} \longrightarrow \widehat{u}_k^{n+1}(\omega),$$

$$\frac{\int_0^\infty \omega \left| \widehat{u}_k^{n+1}(\omega) \right|^2 d\omega}{\int_0^\infty \left| \widehat{u}_k^{n+1}(\omega) \right|^2 d\omega} \longrightarrow \omega_k^{n+1},$$

$$\widehat{\lambda}^{n}(\omega) + \tau \left(\widehat{f}(\omega) - \sum_{k} \widehat{u}_k^{n+1}(\omega) \right) \longrightarrow \widehat{\lambda}^{n+1}(\omega), \tag{4}$$

where τ is the noise tolerance, and $\widehat{u}_i^{n+1}(\omega)$, $\widehat{u}_i^{n}(\omega)$, $\widehat{f}(\omega)$ and $\widehat{\lambda}^{n}(\omega)$ correspond to the Fourier transform of $u_i^{n+1}(\omega)$, $u_i^{n+1}(\omega)$, $f(\omega)$ and $\lambda^n(\omega)$, respectively.

The main iterative solution process of VMD algorithm is as follows:

(1) Initialize $\{\widehat{u}_k^1\}$, $\{\omega_k^1\}$, $\left\{\widehat{\lambda}^1\right\}$

(2) $n = n + 1$, enter the cycle, where n is the number of iterations

(3) Update u_k, ω_k, λ

(4) Repeat steps (2) through (5) until the iteration stop condition is satisfied:

$$\sum_k \frac{\left\|\hat{u}_k^{n+1} - \hat{u}_k^n\right\|_2^2}{\left\|\hat{u}_k^n\right\|_2^2} < \varepsilon, \tag{5}$$

where ε is a constant and $\varepsilon > 0$.

2.2. Optimization of VMD by Genetic Algorithm. As a signal decomposition algorithm, the variational modal decomposition (VMD) algorithm is greatly affected by the number of modal components and penalty factors, so it is necessary to use the optimization algorithm to optimize the parameters. Compared with the particle swarm optimization (PSO) algorithm, the genetic algorithm (GA) has higher global performance and a more mature convergence analysis method. The optimal parameters of VMD algorithm are searched by optimization algorithm. The algorithm steps of GA-VMD are shown in Figure 1, and the algorithm steps of GA-VMD are as follows:

(1) The parameters of GA algorithm are determined, and the optimization objective function can be expressed as

$$C = \min \sum_{i=1}^{K} \frac{E_i}{K}. \tag{6}$$

Constraints can be expressed as

$$\text{s.t.} \begin{cases} K_{\min} \le K_i \le K_{\max} \\ a_{\min} \le a_i \le a_{\max} \\ K \in N+,\ a \in N+ \end{cases}, \tag{7}$$

where K is the optimal number of IMFs, i is the IMF serial number ($i = 1,2,3, ...$) obtained from the decomposition of the original signal, E_i represents the envelope entropy of the i-th IMF, C is the objective function, a_i is the penalty factor of the i-th IMF, K_i is the optimal number of IMF for the i-th IMF, and N is natural number.

(2) Initialize the population, namely, VMD parameter [K, α].

(3) Input the population into VMD to obtain the IMFs, calculate the average envelope entropy of all IMFs as the fitness function, and save the minimum average envelope entropy and its corresponding VMD parameters [K, α], and the envelope entropy can be expressed as

$$\begin{cases} P_{i,j} = \dfrac{a_i(j)}{\sum_{j=1}^{N} a_i(j)} \\ \\ E_i = -\sum_{j=1}^{N} P_{i,j} lg p_{i,j} \end{cases}, \tag{8}$$

where $a_i(j)$ is the envelope signal obtained from the signal $\mathrm{IMF}_i(j)$ after Hilbert mediation, and $P_{i,j}$ is the normalized form of the signal $a_i(j)$.

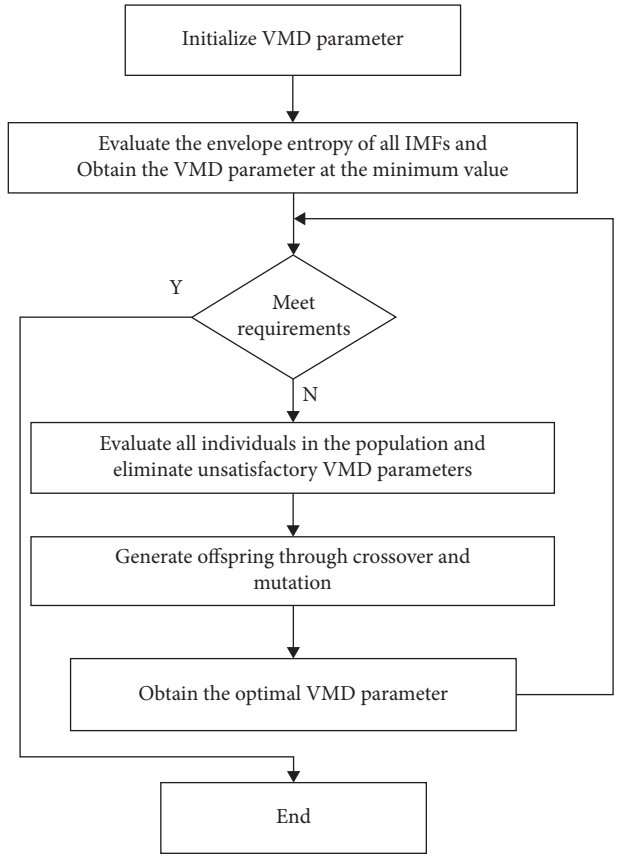

Figure 1: The algorithm steps of GA-VMD.

(4) Evaluate the fitness of all individuals in the population, that is, the parameter combination, and eliminate unsatisfactory individuals.

(5) According to the principle that the higher the fitness is, the greater the selection probability is, two individuals are selected from the population as the parent and mother, and the offspring are generated through binary crossover and mutation;

(6) Repeat steps (4) and (5) and update the population;

(7) Cycle steps (3) ~ (6) until the maximum number of iterations is completed;

(8) The minimum value of the local minimum average envelope entropy in each iteration obtained in step (7) is selected as the global minimum value of this optimization, and its corresponding parameter combination [K, α] is the best parameter combination obtained in this optimization.

3. Fault Feature Extraction Method

The bearing fault feature extraction flow chart is shown in Figure 2, and the specific steps are as follows.

(1) The bearing signals under four different states are obtained, including normal signal, inner ring fault signal, outer ring fault signal, and rolling element fault signal.

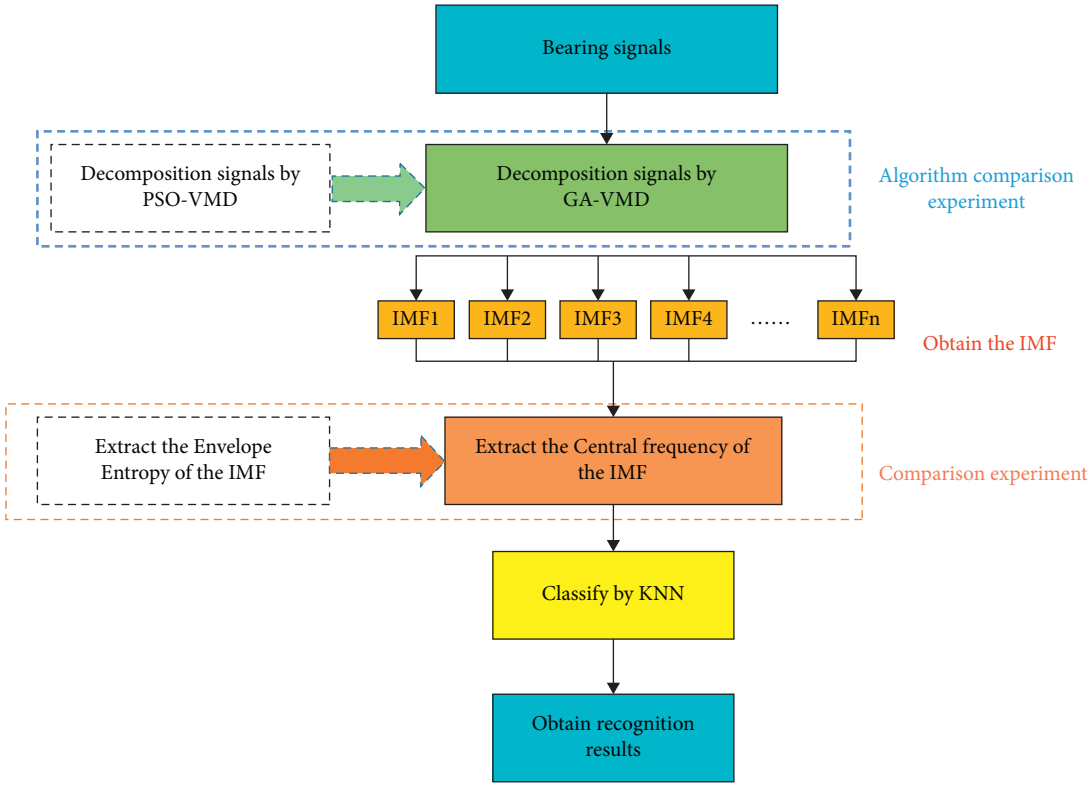

Figure 2: Bearing fault feature extraction flow chart.

(2) GA-VMD algorithm is used to carry out signal adaptive decomposition of the four types of bearing signals, and the IMF combinations are obtained. The effectiveness of GA-VMD algorithm is convinced through simulation signal analysis in Section 4.

(3) The central frequency of bearing signal IMF is extracted, and a comparison experiment with the envelope entropy is carried out.

(4) Recognition results of bearing signals are obtained through KNN.

4. Simulation Signal Analysis

In order to verify the effectiveness of GA-VMD algorithm, the VMD decomposition results based on particle swarm optimization algorithm are compared with the proposed method in this paper. Set up a set of simulation signals for analysis, and its specific expression is

$$X = x_1 + x_2 + x_3 + x_4,$$
$$\begin{cases} x_1 = 10\cos\left(2\pi f_1 t + 3.5\right) \\ x_2 = 10\cos\left(2\pi f_2 t + 2.0\right) \\ x_3 = 10\cos\left(2\pi f_3 t + 1.5\right) \\ x_4 = 10\cos\left(2\pi f_4 t + 1.0\right) \end{cases}, \quad (9)$$

where X is the original signal, x_1, x_2, x_3, x_4 are the subsignals, f_1, f_2, f_3, f_4 are the subfrequencies of x_1, x_2, x_3, x_4, and their values are, respectively, 170 Hz, 120 Hz, 50 Hz, and 10 Hz.

Set the number of analysis points N as 1024 and the sampling frequency f_s as 1024 kHz. Figure 3 shows the time-domain waveform of the simulation signal and its original component.

The root mean square error is used to calculate the amplitude difference between the original component signal and the decomposed component signal to verify the decomposition performance of the two algorithms. The root mean square error calculation formula is

$$\mathrm{RMSE} = \sqrt{\frac{\sum_{i=1}^{n}\left[\widehat{f}\left(t_i\right) - f\left(t_i\right)\right]^2}{n}}, \quad (10)$$

where n is the number of observations, $\widehat{f}\left(t_i\right)$ is the original component signal, and $f\left(t_i\right)$ is decomposed component signal. The root mean square error reflects the difference of signal amplitude between the decomposed signal and the original signal component. The smaller the RMSE value is, the better the decomposition effect is.

The VMD algorithm based on genetic algorithm (GA-VMD) and the parameter optimization VMD algorithm based on particle swarm optimization (PSO-VMD) are used to decompose the simulation signal. The genetic algorithm parameters are set as follows: the initial population is 20, the number of iterations is 100, the crossover probability is 0.8, and the mutation probability is 0.4. The specific parameters of Particle swarm optimization are as follows: the inertia weight W is 1, the acceleration factors C1 and C2 are 1.5, the maximum optimization speed of K value is 1, the minimum optimization speed is −1, and the optimization range is 3 to

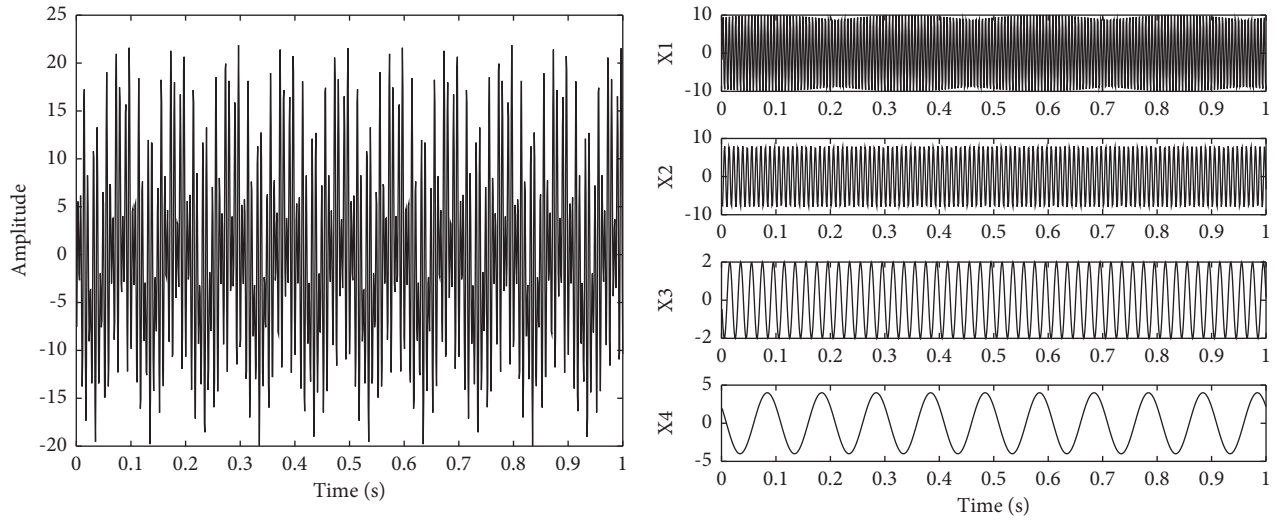

(a) (b)

Figure 3: The time-domain waveform of the simulation signal and its original component. (a) The simulation signal. (b) The original component.

5. The maximum optimization speed of α value is 2000, the minimum optimization speed is 200, and the optimization range is from 200 to 2000. The optimal input parameters obtained by GA-VMD and PSO-VMD search are $(K, a) = [4, 984]$ and $[4, 1264]$, respectively. GA-VMD and PSO-VMD decomposition results are shown in Figures 4 and 5.

According to Figures 4 and 5, IMF1 corresponds to the original signal component x_1, IMF2 to the original signal component x_2, IMF3 to the original signal component x_3, and IMF4 to the original signal component x_4. Since there are two parameters in the parameter combination, modal component K and penalty factor α, to prove the influence of the two parameters on the decomposition results, the values of K and α are changed, respectively, for VMD decomposition. The four groups of VMD parameter combinations determined manually are as follows: when the value of α change and the value of K remain unchanged, determine the parameter combination $(K, a) = [4, 500]$, $[4, 1029]$, *an d* $[4, 1500]$; when the value of K changes and the value of α remain unchanged, determine the parameter combination $(K, a) = [5, 984]$;

To further compare the effectiveness of the two algorithms and manual parameter setting-VMD, the root mean square error of the two optimization algorithms and manual parameter setting-VMD are shown in Table 1.

It can be seen from Table 1 that the root mean square error of the optimal result of GA-VMD is 0.002 lower than that of PSO-VMD, and the IMF decomposed by GA-VMD is closer to the original signal component. In addition, The root mean square error of GA-VMD is lower than that of Manual parameter setting-VMD. Therefore, GA-VMD is used to analyze the bearing fault signal in this paper.

5. Bearing Signal Feature Extraction

5.1. Bearing Signals. Bearing signal feature extraction experiment adopts bearing data provided by the laboratory of Case Western Reserve University [33]. The diameter of rolling bearing failure is 0.1778 mm, and the speed is 1730r/min. Normal signal and the sampling frequency of the signal, which include acceleration data of inner ring fault, outer ring fault, and rolling element fault obtained from the rolling bearing fault, are 12 kHz. There are 100 samples for each type of bearing signal, and each sample contains 1200 sampling points. The time-domain waveform of rolling bearing signals under four states (one sample) is shown in Figure 6.

5.2. Bearing Signal Decomposition. The optimal number of IMF components K of the four bearing signals decomposed by GA-VMD algorithm is 9, and the penalty factors α are 12040, 15480, 9880, and 15560, respectively. The decomposition results of the four bearing signals obtained are shown in Figure 7.

In order to further verify the effectiveness of GA-VMD algorithm, comparative experiments with PSO-VMD algorithm are carried out. The bearing signal is decomposed by PSO-VMD to obtain the corresponding IMF, and then the root mean square error of the measured signal by the two optimization algorithms is shown in Table 2.

It can be seen from Table 2 that, for each bearing signal, the root mean square error of the optimization result of GA-VMD is lower than that of PSO-VMD, especially normal signal and rolling element fault signal; for normal signal, the root mean square error of GA-VMD is about 0.01 lower than

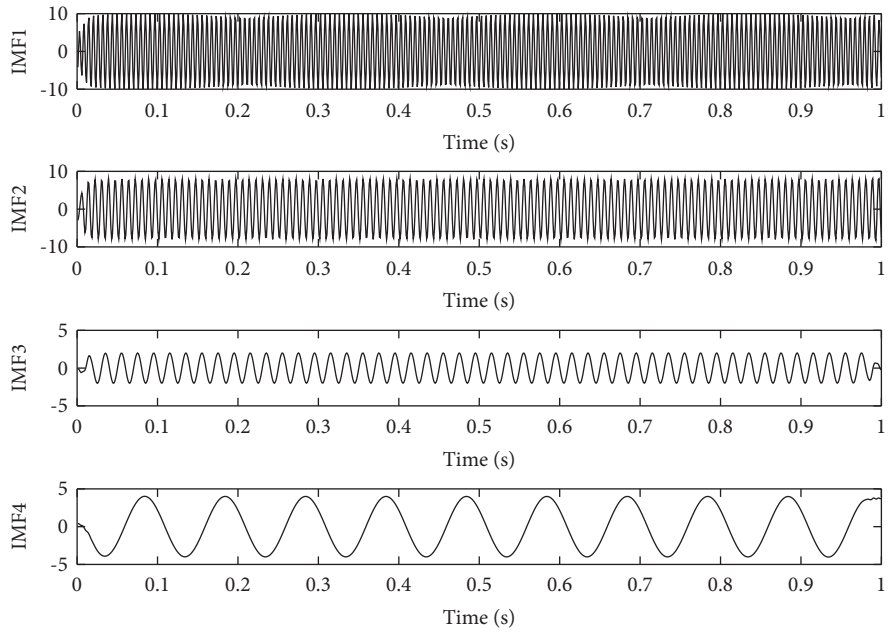

Figure 4: GA-VMD decomposition result.

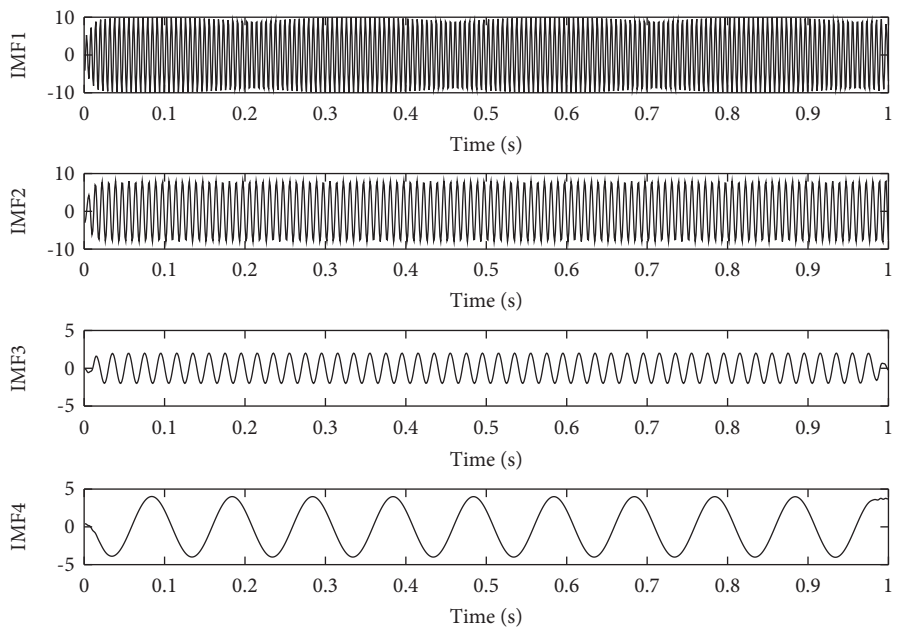

Figure 5: PSO-VMD decomposition result.

Table 1: The root mean square error of the two optimization algorithms and manual parameter setting-VMD.

	GA-VMD	PSO-VMD	Manual parameter setting-VMD			
$[K, \alpha]$	[4, 984]	[4, 1264]	[4, 500]	[4, 1185]	[4, 1500]	[5, 984]
RMSE	0.2104	0.2143	1.0001	0.2131	0.6326	0.2568

that of PSO-VMD; for rolling element fault signal, the root mean square error of GA-VMD is about 0.0176 lower than that of PSO-VMD. Therefore, compared with PSO-VMD, GA-VMD has better optimization results.

5.3. Feature Extraction of Bearing Signals. The characteristics of center frequency and envelope entropy of IMF of four kinds of bearing signals are extracted. The characteristic distribution of center frequency and envelope entropy of

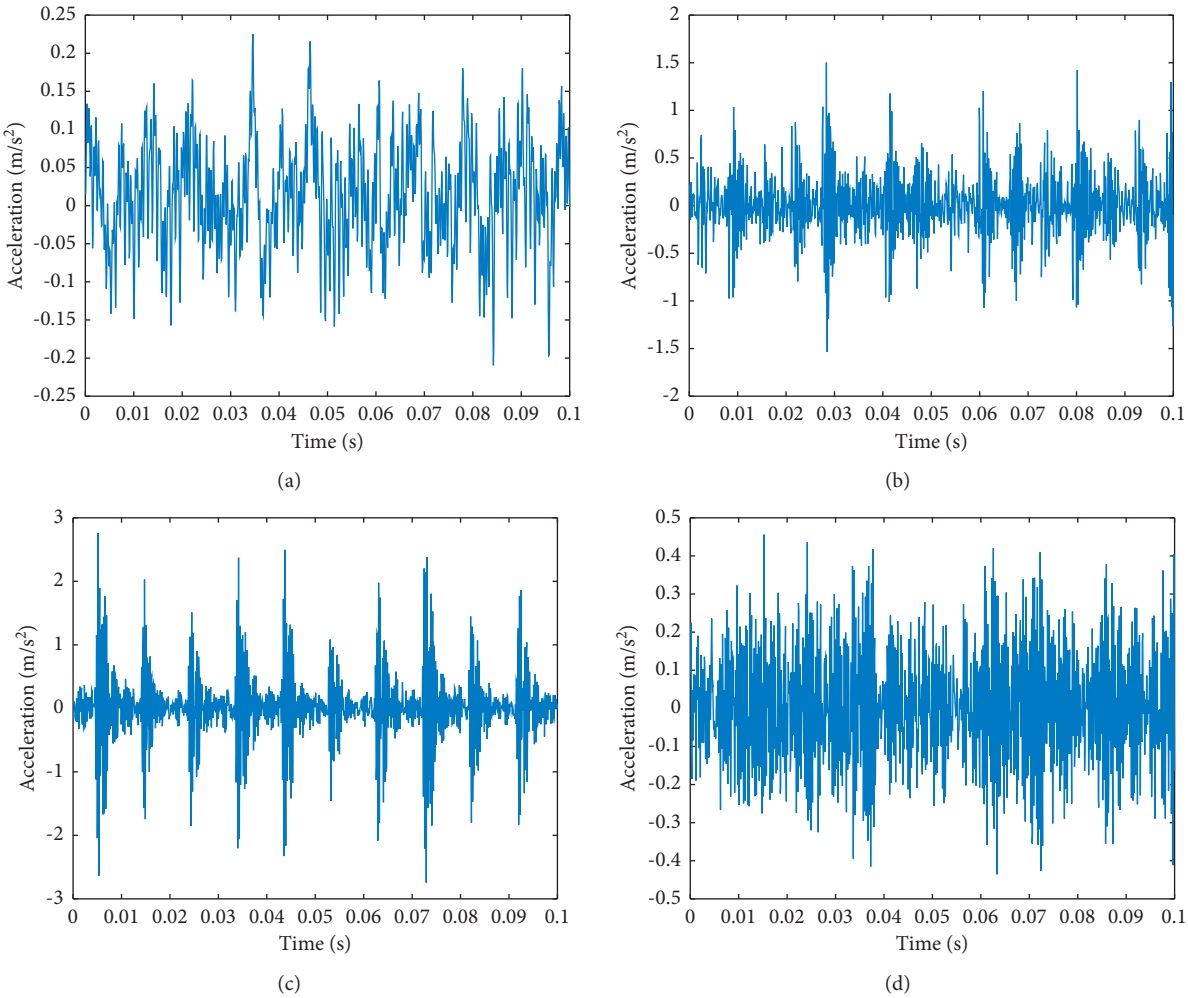

Figure 6: The time-domain waveform of rolling bearing signals under four states. (a) Normal. (b) Inner ring fault. (c) Outer ring fault. (d) Rolling element fault.

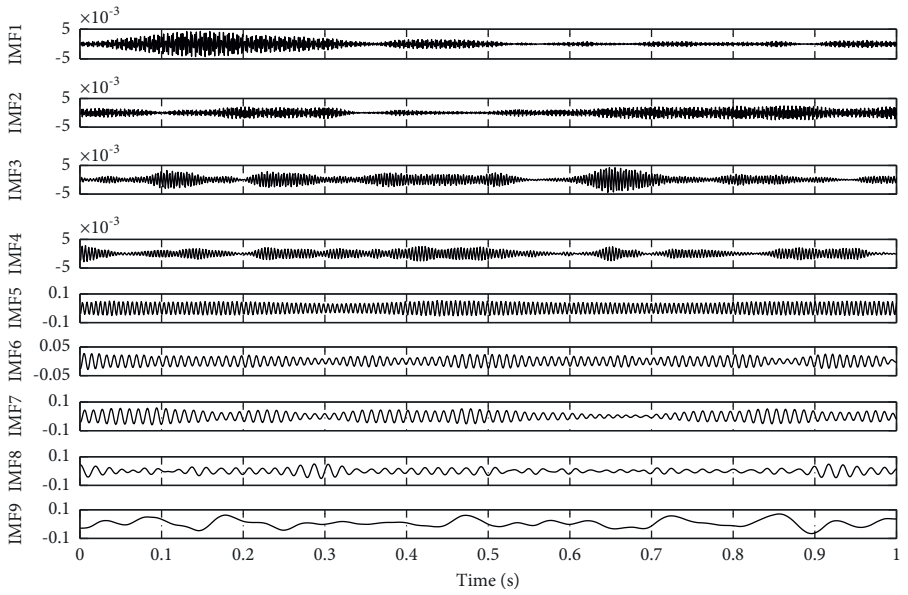

Figure 7: Continued.

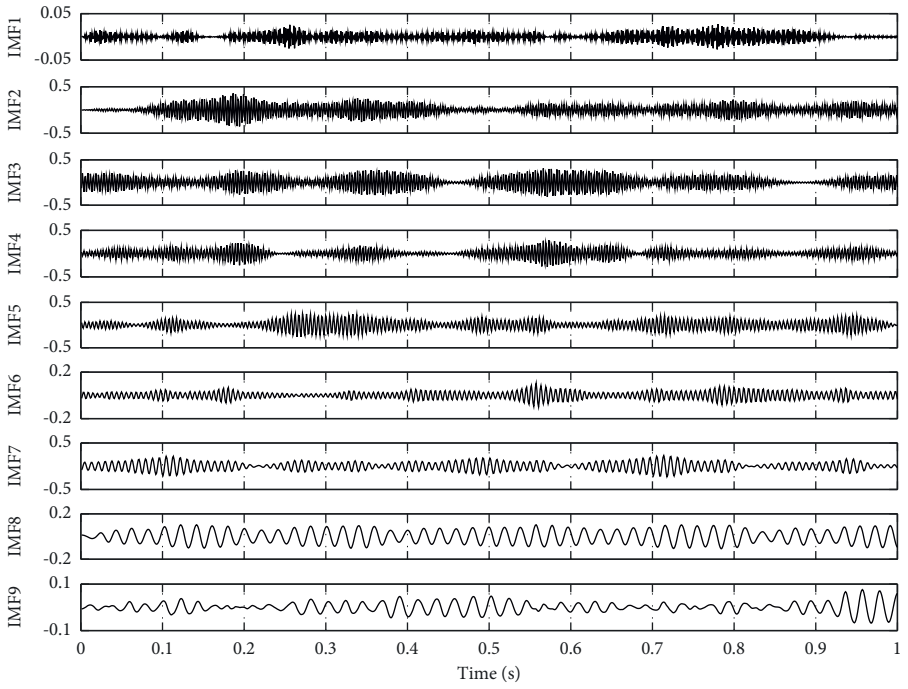

(b)

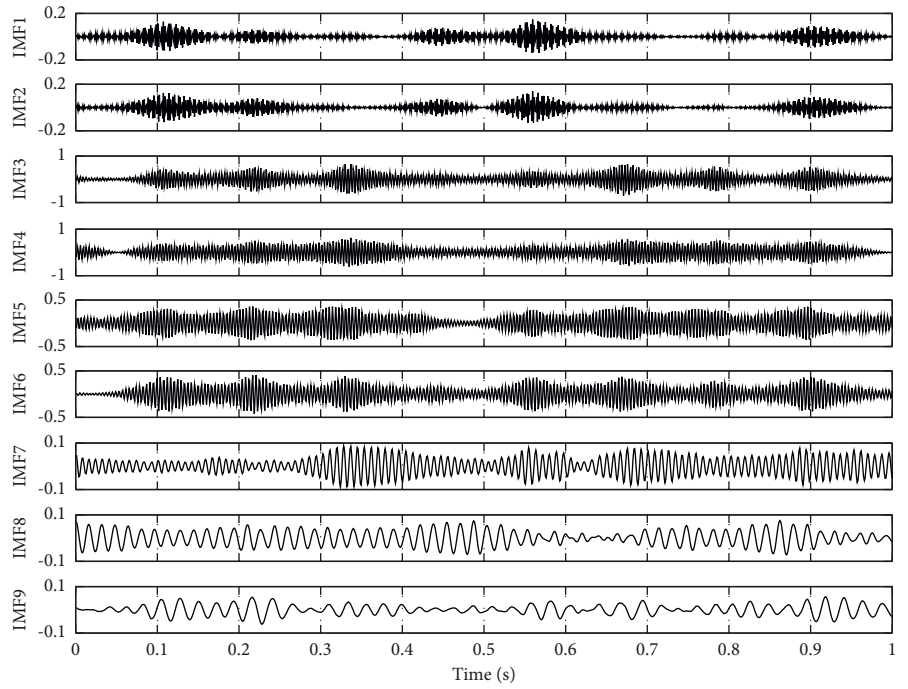

(c)

Figure 7: Continued.

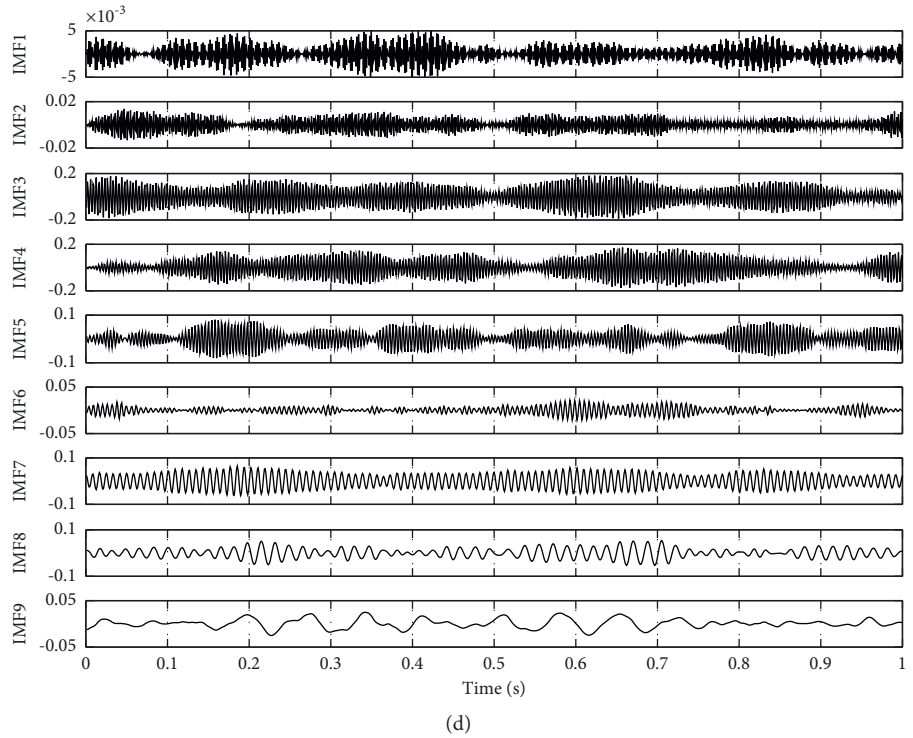

(d)

Figure 7: The decomposition results of the four bearing signals. (a) Normal. (b) Inner ring fault. (c) Outer ring fault. (d) Rolling element fault.

Table 2: The root mean square error of the measured signal by the two optimization algorithms.

Bearing signal	GA-VMD		PSO-VMD	
	$[K, \alpha]$	RMSE	$[K, \alpha]$	RMSE
Normal	[4, 12040]	0.2204	[4, 13500]	0.2303
Inner ring fault	[4, 15480]	0.1317	[4,18840]	0.1332
Outer ring fault	[4, 9880]	0.0694	[4,1274]	0.0821
Rolling element fault	[4, 15560]	0.1081	[4,1760]	0.1257

IMF of four kinds of bearing signals are shown in Figure 8 and 9.

It can be seen from Figures 8 and 9 that the envelope entropy distribution in each IMF of the four kinds of bearing signals is chaotic, and there are many overlaps, while the center frequency distribution of each mode of the four types of bearing signals is more regular, and the overlaps are significantly reduced; the center frequency values of inner ring fault signal, outer ring fault signal, and rolling element fault in IMF4 and IMF7 are very close, while there are obvious differences from the center frequency of normal signal; the envelope entropy of outer ring fault signals in IMF4 and IMF5 is lower than that of the other three kinds of signals; the center frequency of normal signals in IMF7 is almost at the same level, and the frequency range of the center frequency of other three types of bearing signals also has obvious differences; compared with enveloping entropy, extracting center frequency features is more beneficial to distinguish four kinds of bearing signals.

5.4. Classification of Bearing Signals

5.4.1. Single Feature Classification. For purpose of further identifying the features, KNN classifier is used to classify the signals. The center frequency and envelope entropy of a single IMF in 200 sample signals in each of the four states are classified as characteristic parameters.

KNN is one of the most basic and simplest machine learning algorithms. KNN is classified by measuring the distance between different eigenvalues. Its core idea is as follows: a sample is most similar to the K samples in the dataset. If most of the K samples belong to category A, the sample also belongs to category A. The method only determines the category of the samples to be divided according to the category of the nearest one or several samples.

In KNN, the number of neighbors K is 1. Besides, in this experiment, for each type of bearing signal, 200 samples are randomly selected; the first 50 sample signals are used as training samples, while the other 150 sample signals are used as test samples. The characteristic classification results of the

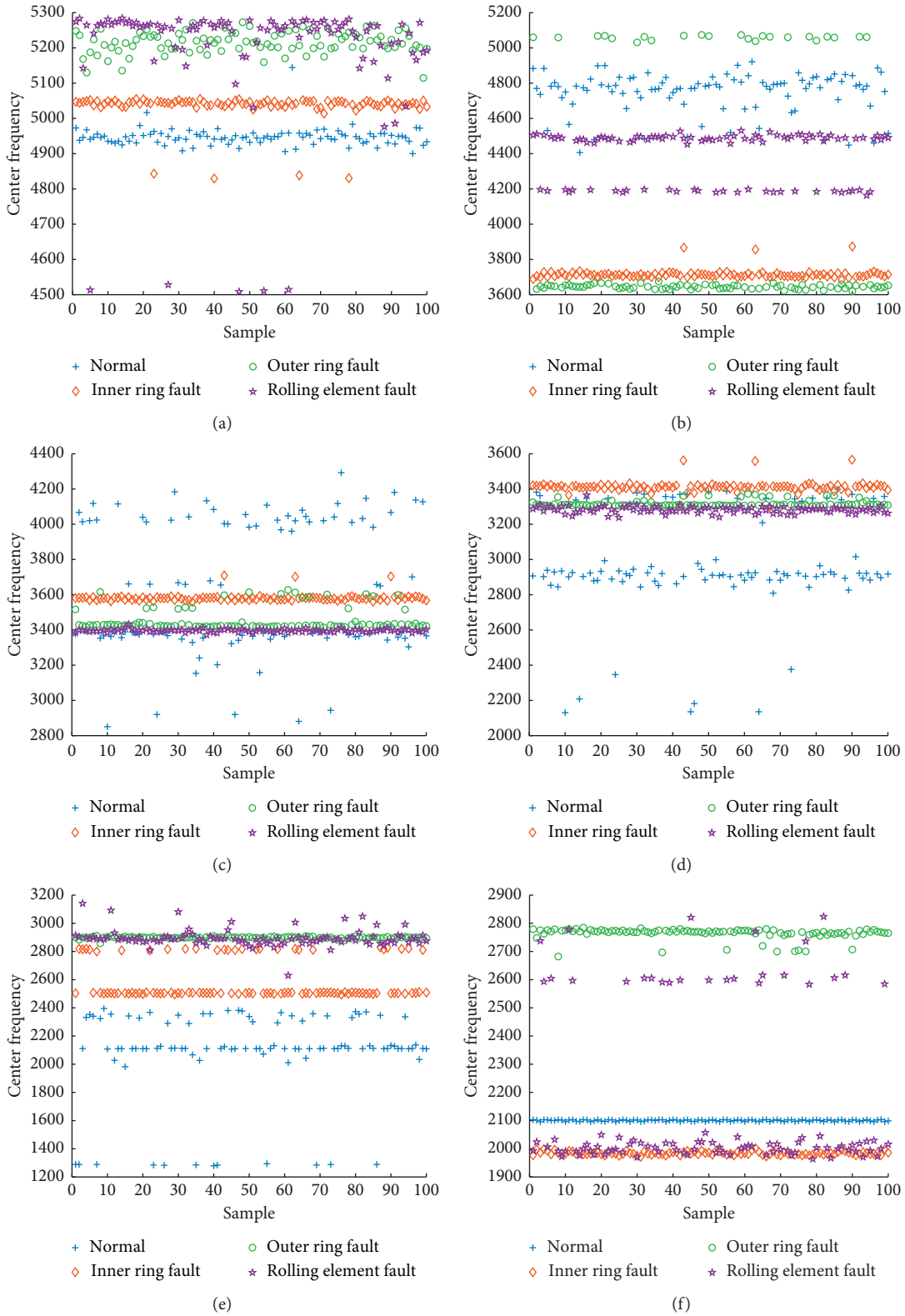

Figure 8: Continued.

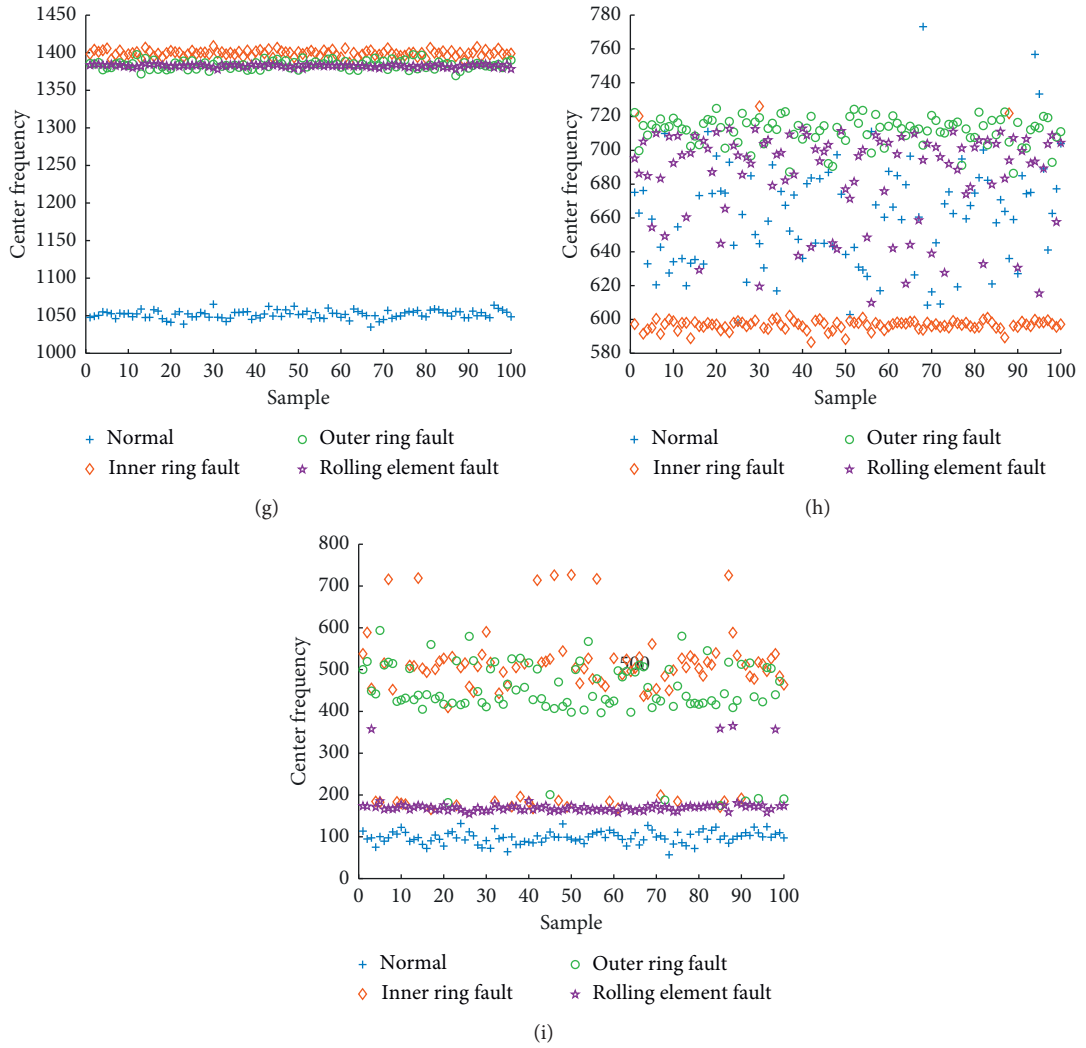

Figure 8: The characteristic distribution of center frequency of IMF of four kinds of bearing signals. (a) IMF1. (b) IMF2. (c) IMF3. (d) IMF4. (e) IMF5. (f) IMF6 (g). IMF7 (h). IMF8. (i) IMF9.

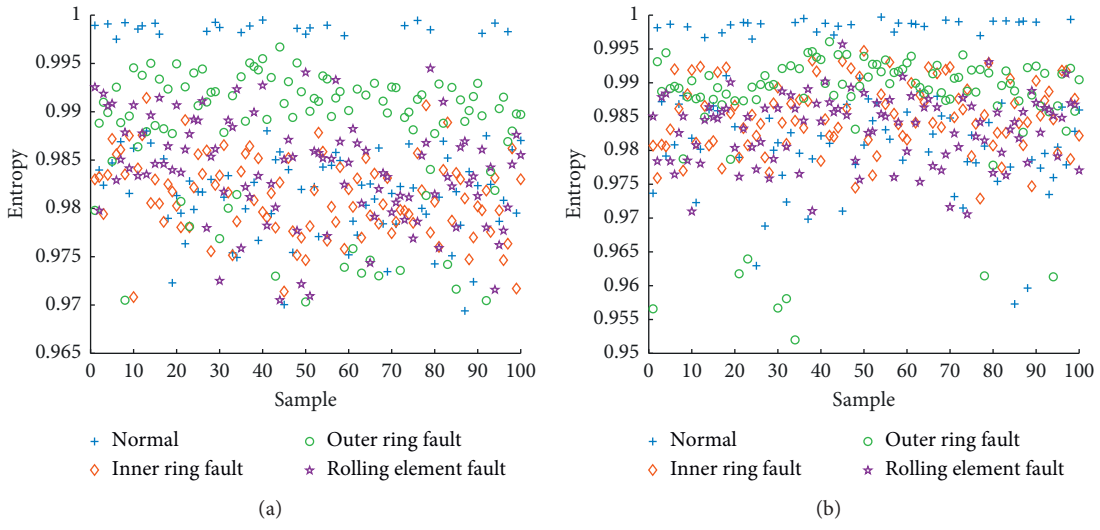

Figure 9: Continued.

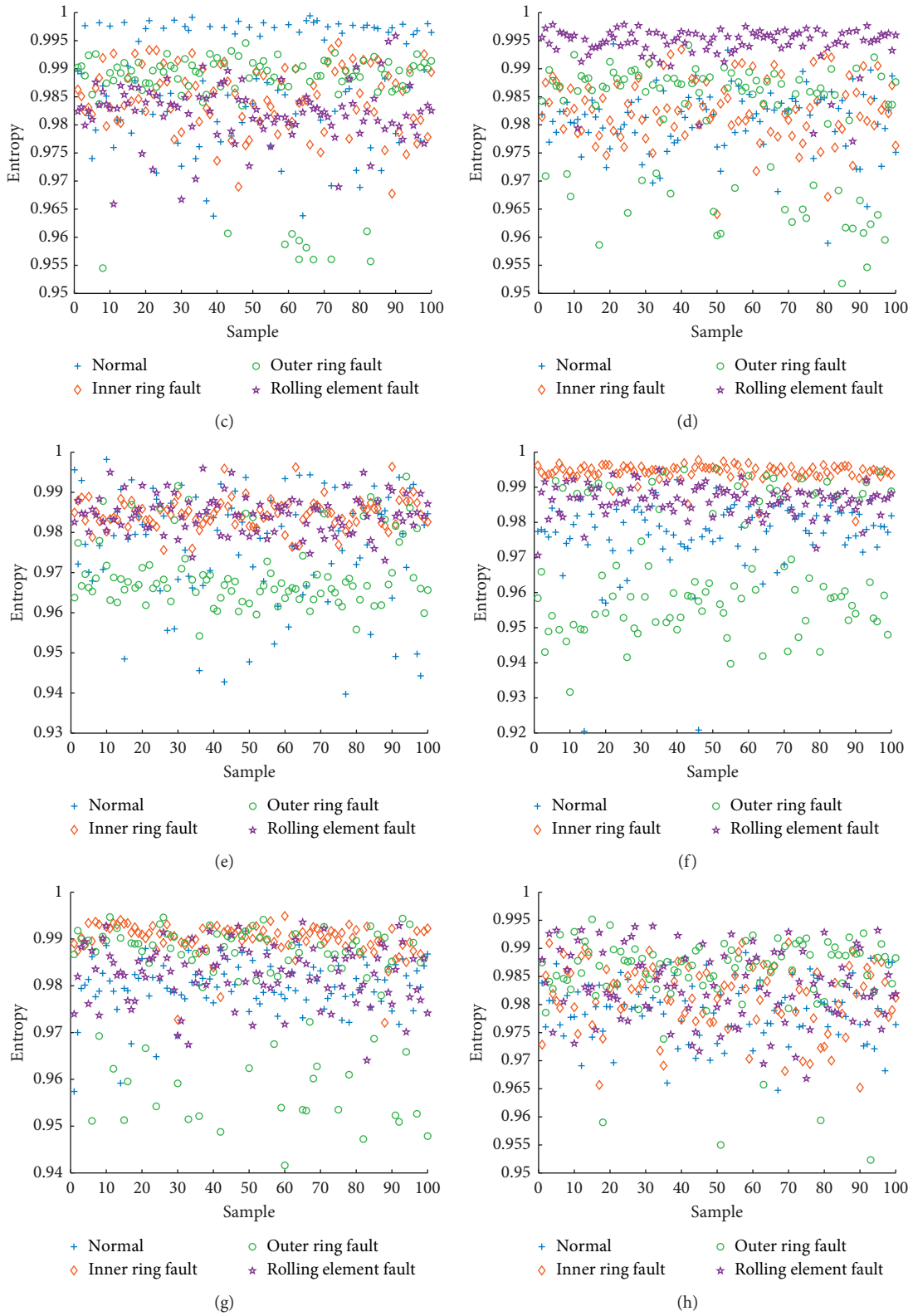

Figure 9: Continued.

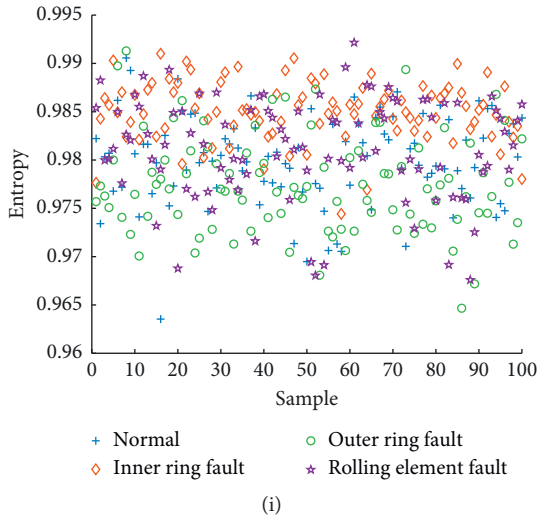

(i)

Figure 9: The characteristic distribution of envelope entropy of IMF of four kinds of bearing signals. (a) IMF1. (b) IMF2. (c) IMF3. (d) IMF4. (e) IMF5. (f) IMF6 (g). IMF7 (h). IMF8. (i) IMF9.

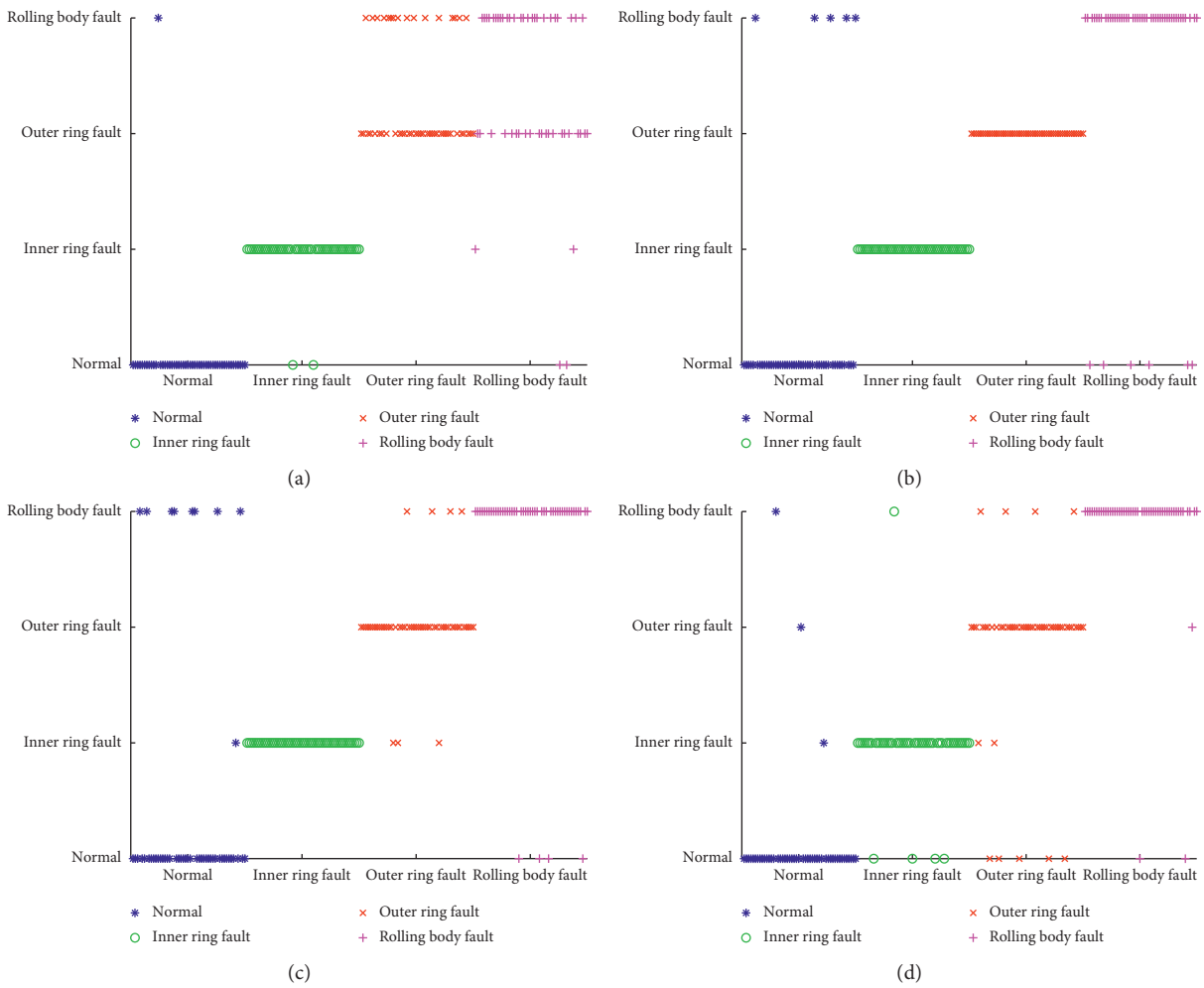

(a) (b)

(c) (d)

Figure 10: Continued.

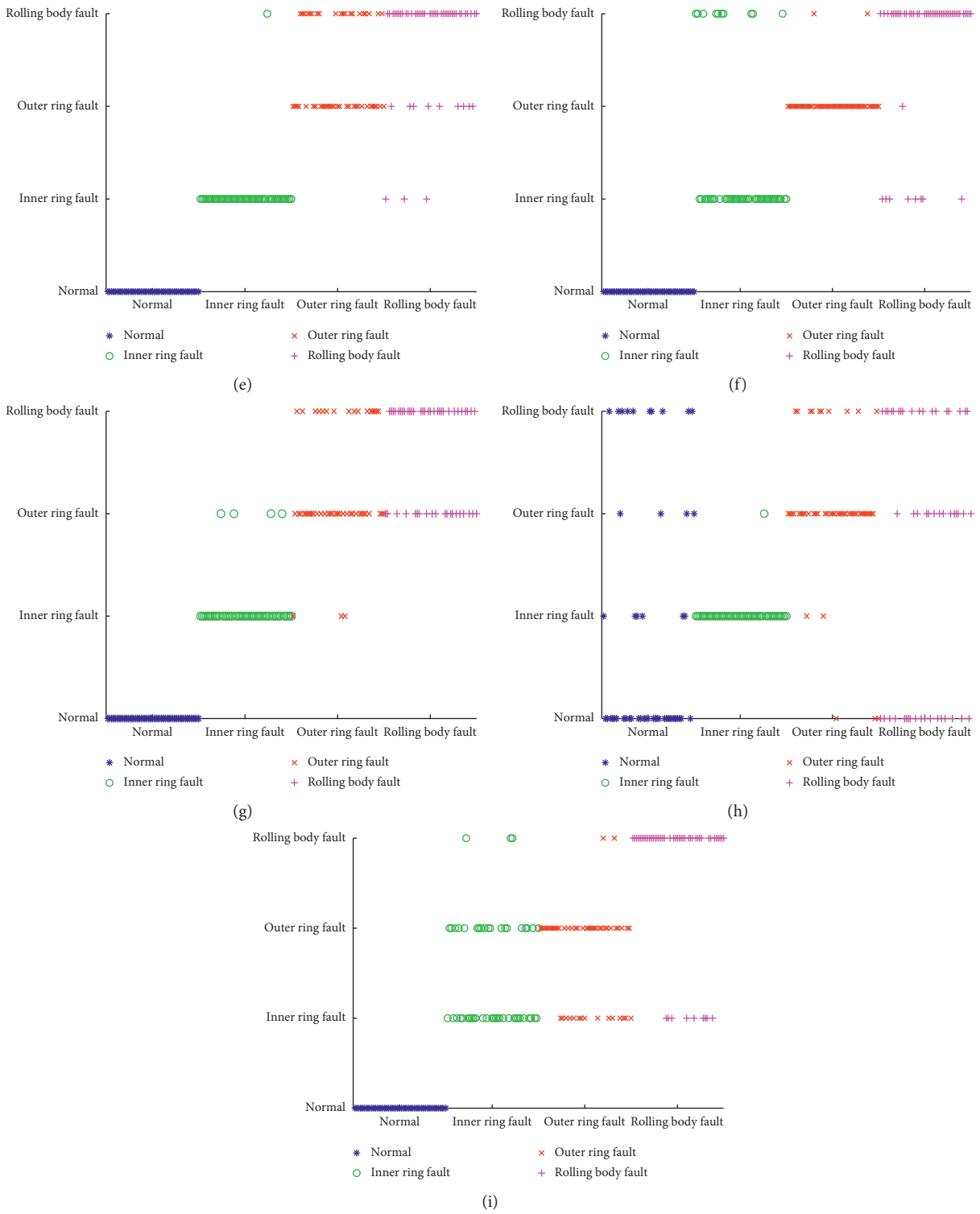

Figure 10: The characteristic classification results of the center frequency of each IMF. (a) IMF1. (b) IMF2. (c) IMF3. (d) IMF4. (e) IMF5. (f) IMF6 (g). IMF7 (h). IMF8. (i) IMF9.

Figure 11: Continued.

FIGURE 11: The characteristic classification results of the envelope entropy of each IMF. (a) IMF1. (b) IMF2. (c) IMF3. (d) IMF4. (e) IMF5. (f) IMF6 (g). IMF7 (h). IMF8. (i) IMF9.

center frequency and envelope entropy of each IMF are shown in Figures 10 and 11.

It can be seen from Figures 10 and 11 that, compared with the envelope entropy feature, under the same mode, fewer samples are identified incorrectly by using the method characterized by center frequency; for the center frequencies of different modes, IMF2 has the best result of feature classification. Classification recognition rates of single IMF component center frequency and envelope entropy are shown in Table 3 and 4 respectively.

It can be seen from Tables 3 and 4 that the center frequency feature extraction and recognition effect of a single IMF component is better than that of the single component feature extraction and recognition of IMF component envelope entropy; the average recognition rate of envelope entropy feature of single IMF component is generally lower than 60%, some even lower than 40%, and the maximum recognition rate is 61%; the recognition effect is poor, so it is impossible to identify and diagnose the four bearing signals; except for a few components, the accuracy of extraction and classification of central frequency features of most IMF components reached more than 75%, and the accuracy of IMF2 component even reached 94.5%; in the recognition of normal signals, the recognition accuracy of center frequency of IMF5, IMF6, IMF7, and IMF9 components all reached 100%; the recognition rate of IMF2 and IMF3 component center frequency in inner ring fault recognition is also 100%.

5.4.2. Multifeature Classification. Aiming to improve the signal recognition rate, a multicomponent feature recognition method is adopted, that is, the method of simultaneously recognizing the center frequency or envelope entropy of multiple IMF components, to classify and recognize the four bearing signals.

KNN classifier is used to extract and classify the component features of the center frequency and envelope entropy of the four kinds of bearing signals. Classification

Table 3: Classification recognition rates of single IMF component center frequency.

IMF	Classification and recognition accuracy (%)				
	Normal	Inner ring fault	Outer ring fault	Rolling element fault	Mean
IMF1	98	96	68	50	78
IMF2	90	100	100	88	94.5
IMF3	82	100	86	92	90
IMF4	94	90	78	94	89
IMF5	100	98	60	76	83.5
IMF6	100	80	96	82	89.5
IMF7	100	92	62	60	78.5
IMF8	60	98	70	36	66
IMF9	100	56	66	82	76

Table 4: **C**lassification recognition rates of single IMF component envelope entropy.

IMF	Classification and recognition accuracy (%)				
	Normal	Inner ring fault	Outer ring fault	Rolling element fault	Mean
IMF1	28	50	76	34	47
IMF2	44	44	98	40	56.5
IMF3	28	42	56	22	37
IMF4	32	40	60	42	43.5
IMF5	60	28	40	60	47
IMF6	90	54	36	64	61
IMF7	56	38	46	90	57.5
IMF8	40	70	38	44	48
IMF9	22	48	26	33	38

Table 5: Classification recognition rates of center frequency.

IMF	Classification and recognition accuracy (%)				
	Normal	Inner ring fault	Outer ring fault	Rolling element fault	Mean
$IMF_{1\sim2}$	100	100	100	94	98.5
$IMF_{1\sim3}$	100	100	100	94	98.5
$IMF_{1\sim4}$	100	100	100	100	100
$IMF_{1\sim5}$	100	100	100	100	100
$IMF_{1\sim6}$	100	100	100	100	100
$IMF_{1\sim7}$	100	100	100	100	100
$IMF_{1\sim8}$	100	100	100	100	100
$IMF_{1\sim9}$	100	100	100	100	100

Table 6: Classification recognition rates of envelope entropy.

IMF	Classification and recognition accuracy (%)				
	Normal	Inner ring fault	Outer ring fault	Rolling element fault	Mean
$IMF_{1\sim2}$	40	62	100	50	63.0
$IMF_{1\sim3}$	40	50	100	40	57.5
$IMF_{1\sim4}$	38	54	100	46	59.5
$IMF_{1\sim5}$	56	80	100	66	75.5
$IMF_{1\sim6}$	84	98	100	96	94.5
$IMF_{1\sim7}$	86	100	100	98	96.0
$IMF_{1\sim8}$	92	98	100	96	96.5
$IMF_{1\sim9}$	96	100	100	98	98.5

recognition rates of center frequency and envelope entropy are shown in Tables 5 and 6, where $IMF_{1\text{-}2}$ means to simultaneously identify the features of IMF component 1 and 2 signals, $IMF_{1\sim3}$ means to simultaneously identify the features of IMF component 1, 2 and 3 signals, and so on.

It can be seen from Tables 4 and 5 that, under the same number of components, the classification effect of multicomponent central frequency feature extraction is significantly better than that of multicomponent envelope entropy feature extraction; when the number of IMFs is greater than 2, the average recognition rate of envelope entropy feature extraction increases with the increase of the number of components, up to 98.5%; the average recognition rate of multicomponent center frequency feature extraction is not less than 98.5%, which is higher than the highest value of recognition rate of envelope entropy feature extraction; when the number of components is 9, the envelops entropy feature extraction effect is optimal, and the average recognition rate is 98.5%; when the number of components is 4, the recognition accuracy of multifeature center frequency extraction has reached 100%; therefore, compared with feature extraction based on envelope entropy, feature extraction based on center frequency can achieve higher recognition rate in the case of a small number of components and can realize effective recognition of bearing faults.

6. Conclusion

In this paper, a bearing fault feature extraction method based on GA-VMD and center frequency is proposed, and the feasibility of the proposed method is verified by feature extraction and classification recognition experiments on four kinds of measured bearing signals. The main conclusions are as follows:

(1) Compared with PSO-VMD algorithm, the root mean square error of GA-VMD algorithm is smaller, and the decomposed IMF is closer to the corresponding signal component

(2) For single feature extraction method, the highest recognition rate of feature extraction method based on center frequency is 94.5%, which is 33.5% higher than that of feature extraction method based on envelope entropy

(3) Compared with the single feature extraction method, the average recognition rate of multifeature extraction method is 17% (center frequency) and 32% (envelope entropy) higher than that of single feature extraction method; compared with the multifeature center frequency extraction method, the average recognition rate of multifeature center frequency feature extraction method is 19.5% higher than that of multifeature envelope entropy extraction method

Data Availability

Data are available upon request to the authors.

Conflicts of Interest

The authors declare that they have no conflicts of interest.

References

[1] L. Zhang, J. Lin, and R. Karim, "Adaptive kernel density-based anomaly detection for nonlinear systems," *Knowledge-Based Systems*, vol. 139, pp. 50–63, 2018.

[2] S. Haidong, C. Junsheng, J. Hongkai, Y. Yu, and W. Zhantao, "Enhanced deep gated recurrent unit and complex wavelet packet energy moment entropy for early fault prognosis of bearing," *Knowledge-Based Systems*, vol. 188, Article ID 105022, 2020.

[3] Y. Li, S. Wang, and Z. Deng, "Intelligent fault identification of rotary machinery using refined composite multi-scale Lempel-Ziv complexity," *Journal of Manufacturing Systems*, vol. 61, pp. 725–735, 2021.

[4] J. Zheng and H. Pan, "Use of generalized refined composite multiscale fractional dispersion entropy to diagnose the faults of rolling bearing," *Nonlinear Dynamics*, vol. 101, no. 2, pp. 1417–1440, 2020.

[5] B. Cai, H. Liu, and M. Xie, "A real-time fault diagnosis methodology of complex systems using object-oriented Bayesian networks," *Mechanical Systems and Signal Processing*, vol. 80, pp. 31–44, 2016.

[6] Y. Li, X. Wang, Z. Liu, X. Liang, and S. Si, "The entropy algorithm and its variants in the fault diagnosis of rotating machinery: a review," *IEEE Access*, vol. 6, Article ID 66723, 2018.

[7] T. Han, C. Liu, L. Wu, S. Sarkar, and D. Jiang, "An adaptive spatiotemporal feature learning approach for fault diagnosis in complex systems," *Mechanical Systems and Signal Processing*, vol. 117, pp. 170–187, 2019.

[8] T. Han, Y. Li, and M. Qian, "A hybrid generalization network for intelligent fault diagnosis of rotating machinery under unseen working conditions," *IEEE Transactions on Instrumentation and Measurement*, vol. 70, Article ID 3520011, 2021.

[9] A. Lempel and J. Ziv, "On the complexity of finite sequences," *IEEE Transactions on Information Theory*, vol. 22, no. 1, pp. 75–81, 1976.

[10] Z. Zhang, A. Verma, and A. Kusiak, "Fault analysis and condition monitoring of the wind turbine gearbox," *IEEE Transactions on Energy Conversion*, vol. 27, no. 2, pp. 526–535, 2012.

[11] A. Babloyantz and A. Destexhe, "Is the normal heart a periodic oscillator?" *Biological Cybernetics*, vol. 58, pp. 203–211, 1988.

[12] J. Zheng, J. Cheng, Y. Yang, and S. Luo, "A rolling bearing fault diagnosis method based on multi-scale fuzzy entropy and variable predictive model-based class discrimination," *Mechanism and Machine Theory*, vol. 78, pp. 187–200, 2014.

[13] Y. Li, X. Liang, Y. Wei, and X. Wang, "A method based on refined composite multi-scale symbolic dynamic entropy and ISVM-BT for rotating machinery fault diagnosis," *Neurocomputing*, vol. 315, pp. 246–260, 2018.

[14] Y. Li, S. Jiao, and X. Gao, "A novel signal feature extraction technology based on empirical wavelet transform and reverse dispersion entropy," *Defence Technology*, vol. 17, no. 5, pp. 1625–1635, 2021.

[15] S. Jiao, B. Geng, and Y. Li, "Fluctuation-based reverse dispersion entropy and its applications to signal classification," *Applied Acoustics*, vol. 175, no. 4, Article ID 107857, 2021.

[16] N. E. Huang, Z. Shen, S. R. Long et al., "The empirical mode decomposition and the Hilbert spectrum for nonlinear and non-stationary time series analysis," *Proceedings*

Mathematical Physical & Engineering Sciences, vol. 454, no. 1971, pp. 903–995, 1998.
[17] Z. Wu and N. Huang, "Ensemble empirical mode decomposition: a noise-assisted data analysis method," *Advances in Adaptive Data Analysis*, vol. 1, no. 1, pp. 1–41, 2009.
[18] Y. Li, Y. Li, and X. Chen, "Ships' radiated noise feature extraction based on EEMD," *Journal of Vibration and Shock*, vol. 36, no. 5, pp. 114–119, 2017.
[19] Y. Li, Y. Li, X. Chen, and J. Yu, "Denoising and feature extraction algorithms using NPE combined with VMD and their applications in ship-radiated noise," *Symmetry*, vol. 9, no. 11, p. 256, 2017.
[20] Y. Li, Y. Li, and X. Chen, "Feature extraction of ship-radiated noise based on VMD and center frequency," *Journal of Vibration and Shock*, vol. 37, no. 23, pp. 213–218, 2018.
[21] K. Dragomiretskiy and D. Zosso, "Variational mode decomposition," *IEEE Transactions on Signal*, vol. 62, no. 3, pp. 531–544, 2014.
[22] J. Xia, L. Zhao, Y. Bai, and M. Yu, "Feature extraction for rolling element bearing weak fault based on MCKD and VMD," *Journal of Vibration and Shock*, vol. 36, no. 20, pp. 78–83, 2017.
[23] W. Liu, S. Cao, Z. Wang, X. Kong, and Y. Chen, "Spectral decomposition for hydrocarbon detection based on VMD and teager–kaiser energy," *IEEE Geoscience and Remote Sensing Letters*, vol. 4, pp. 1–5, 2017.
[24] L. Xie, L. Luo, Y. Li, Y. Zhang, and Y. Cao, "A traveling wave-based fault location method employing VMD-TEO for distribution network," *IEEE Transactions on Power Delivery*, vol. 35, no. 4, pp. 1987–1998, 2020.
[25] L. Cheng, W. Cheng, W. Yun, and Y. J. Zhao, "Probabilistic analyses of structural dynamic response with modified Kriging-based moving extremum framework," *Engineering Failure Analysis*, vol. 125, Article ID 105398, 2021.
[26] W. Cheng, H. Liu, S. Li, H. Li, L. An, and C. Lu, "Dynamic parametric modeling-based model updating strategy of aeroengine casings," *Chinese Journal of Aeronautics*, vol. 34, no. 12, pp. 145–157, 2021.
[27] W. Cheng, H. Li, H. Liu et al., "Enhanced network learning model with intelligent operator for the motion reliability evaluation of flexible mechanism," *Aerospace Science and Technology*, vol. 107, Article ID 106342, 2020.
[28] G. Tang and X. Wang, "Application of parameter optimization variational mode decomposition method in early fault diagnosis of rolling bearing," *Journal of Xi'an Jiaotong University*, vol. 49, no. 5, pp. 73–81, 2015.
[29] S. Mirjalili and A. Lewis, "The whale optimization algorithm," *Advances in Engineering Software*, vol. 95, pp. 51–67, 2016.
[30] S. Zhang and Y. Zhang, "Harmonic detection method based on permutation entropy and variational modal decomposition optimized by genetic algorithm," *Review of Scientific Instruments*, vol. 92, no. 2, Article ID 25118, 2021.
[31] Z. Chao and Y. He, "Bault diagnosis method based on self-adaptive stochastic resonance of genetic algorithm and VMD," *Journal of Mechanical Transmission*, vol. 162, Article ID 108018, 2018.
[32] J. M. Keller, M. R. Gray, and J. A. Givens, "A fuzzy K-nearest neighbor algorithm," *IEEE Transactions on Systems Man & Cybernetics*, vol. 15, no. 4, pp. 580–585, 2012.
[33] W. A. Smith and R. B. Randall, "Rolling element bearing diagnostics using the case Western reserve University data: a benchmark study," *Mechanical Systems and Signal Processing*, vol. 64–65, pp. 100–131, 2015.

Hindawi
Mathematical Problems in Engineering
Volume 2022, Article ID 8092706, 12 pages
https://doi.org/10.1155/2022/8092706

Research Article

Feature Extraction of Ship Radiation Signals Based on Wavelet Packet Decomposition and Energy Entropy

Yuxing Li,[1,2] **Feiyue Ning**,[1] **Xinru Jiang**,[1] **and Yingmin Yi**[1,2]

[1]*School of Automation and Information Engineering, Xi'an University of Technology, Xi'an 710048, China*
[2]*Shaanxi Key Laboratory of Complex System Control and Intelligent Information Processing, Xi'an University of Technology, Xi'an 710048, China*

Correspondence should be addressed to Yingmin Yi; yiym@xaut.edu.cn

Received 12 September 2021; Revised 11 December 2021; Accepted 18 December 2021; Published 3 January 2022

Academic Editor: Akif Akgul

The analysis of ship radiation signals to identify ships is an important research content of underwater acoustic signal processing. The traditional fast Fourier transform (FFT) is not suitable for analyzing non-stationary, non-Gaussian, and nonlinear signal processing. In order to realize the feature extraction and accurate classification of ship radiation signals with higher accuracy, a feature extraction method of ship radiation signals based on wavelet packet decomposition and energy entropy is proposed in this paper. According to wavelet packet decomposition, the ship radiation signal is decomposed into different frequency bands, and its energy entropy feature is extracted. As for comparisons, the center frequency and permutation entropy are also used as features to be extracted, then the *k*-nearest neighbor is applied to classify and recognize the extracted results. Based on the comparisons of wavelet packet decomposition, the center frequency, permutation entropy, and the *k*-nearest neighbor are used for classification and recognition. The experimental results present that, when comparing with center frequency and permutation entropy, the method based on energy entropy has the best availability, with the highest average recognition rate for four types of ship radiation signals, up to 98%.

1. Introduction

In the development of science and technology, underwater acoustic signal processing plays an extremely important role in the human exploration of the ocean and plays a great role in military and marine life research [1, 2]. Since the radiated noise signal of a ship contains a lot of information about the ship's characteristics, it has become one of the important indicators to measure the ship's performance, and it is widely used as the information source of passive sonar for the detection, tracking, and classification of ship targets [3, 4], so the feature extraction of the ship radiated noise signal has always been an important research content in the field of underwater acoustic signal processing, which has important theoretical and practical significance [5–8].

In general, many nonlinear, dynamic, and statistical parameters can be extracted as features of ship's radiated noise and for signal classification, such as the Lempel Ziv complexity (LZC) [9, 10], Lyapunov exponent [11], correlation coefficient analysis [12], spectral kurtosis [13, 14], and the entropy-based complexity, among which the entropy-based complexity has attracted widespread attention. Entropy, as an indicator of the complexity of time series, can quantify the randomness of a time series, and greater entropy also represents greater irregularity [15, 16]. Some commonly used entropies include approximate entropy [17], sample entropy [18], and permutation entropy [15]. Compared with approximate entropy and sample entropy, the arrangement is not easily affected by the length of the time series, and the calculation time is relatively short, so it has been applied in many fields [19–21]. However, the PE only considers the order of amplitude values and ignores some information of amplitude values. Therefore, the traditional PE algorithm should be improved [22].

Since the late 1980s, many scholars have also applied spectrum analysis to underwater acoustic target feature

extraction, such as extracting the line spectrum and modulation spectrum of underwater target radiated noise by using acoustic power spectrum [23], Wigner-Ville distribution (WVD) [24], bispectrum and high-order spectrum analysis [25], empirical mode decomposition (EMD) [26], and wavelet or wavelet packet decomposition [27]. In particular, as a preprocessor, wavelet packet decomposition can divide the frequency space into various finite frequency bands to realize the time-frequency localization of the signal. It can decompose not only the low frequency but also the high frequency of the signal, and adaptively select the corresponding frequency band according to the analyzed signal, which has good time-frequency characteristics. Hence, wavelet packet decomposition is also widely used in signal feature extraction in various fields [28–30].

In this paper, we introduce the wavelet packet decomposition on the basis of energy entropy and calculate the corresponding PE value for each frequency band after decomposition and use it as a feature. Finally, the k-nearest neighbor (KNN) algorithm is introduced and used as a classifier to verify the validity of the extracted features. A large number of comparative experimental results also prove the effectiveness of the feature extraction method proposed in this paper.

The train of thought of this paper is given as follows: Section 2 gives an introduction to wavelet packet decomposition; Section 3 proposes a feature extraction method based on PE and wavelet packet decomposition; Section 4 verifies the effectiveness of the feature extraction method proposed in this paper through comparative experiments; Section 5 embraces main conclusions obtained.

2. Wavelet Packet Decomposition

Wavelet packet decomposition, also known as an optimal sub-band tree structure, is a further optimization of the wavelet transform. The main algorithm idea is on the basis of the wavelet transform, in each stage of signal decomposition, not only the low-frequency sub-band is further decomposed, but also the high-frequency sub-band is further decomposed. The original signal is decomposed by the optimal signal decomposition path, which was calculated by minimizing a cost function.

h_k and g_k is the filter coefficient of the scale function, $g_k = (-1)^k h_{1-k}$ The wavelet function is equivalent to high-pass filtering the signal to preserve the change details, while the scaling function is equivalent to low-pass filtering the signal to preserve the smooth shape. The basic function of the wavelet is actually formed by scaling and translating the scale function and the wavelet function. The size of the shift is related to the current scaling degree.

The scaling function $\psi(x)$ and wavelet function $\varphi(x)$ satisfy the following equations:

$$\begin{aligned} \phi(x) &= \sqrt{2}\sum_k h_k \phi(2x-k), \\ \psi(x) &= \sqrt{2}\sum_k g_k \phi(2x-k). \end{aligned} \tag{1}$$

The time-domain signal $\mu(x)$ can be decomposed recursively as

$$\begin{aligned} \mu_{j,2n}(x) &= \sum_k h_k \mu_{j-1,n}(2x-k), \\ \mu_{j,2n+1}(x) &= \sum_k g_k \mu_{j-1,n}(2x-k), \end{aligned} \tag{2}$$

where $n = 0, 1, ..., 2(j-1)-1$, g_k, h_k is low pass filter and high pass filter, respectively. When $n = 0$, $\mu_{0,0}(x) = \varphi(x)$ $\mu_{0,1}(x) = \psi(x)$, $\mu_{j,n}(x)$ denotes the wavelet coefficients at the j^{th} level, n^{th} frequency band. The recursive function set $\{\mu_n(x)\}_{n\in Z}$ defined in the abovementioned formula is the wavelet packet defined by the orthogonal scaling function. Figure 1 shows an example of a three-layer wavelet packet decomposition of signals.

From Figure 1, the wavelet packet of the signal is decomposed into three layers into eight frequency bands, and each layer is decomposed into two parts, high-frequency and low-frequency. The high-frequency and low-frequency coefficients of wavelet packet coefficients are decomposed again, unlike the wavelet decomposition, which only decomposes low-frequency coefficients.

3. Proposed Feature Extraction Method

Let $P = \{P_1, P_2, \ldots, P_n\}$ be a probability distribution, its information entropy $H(P)$ can be expressed as

$$H(P) = \sum_{i=1}^{n} P_i \ln P_i. \tag{3}$$

The difference of signal in time-frequency distribution can be expressed by the uncertainty of energy distribution in different frequency bands. Therefore, a feature extraction method of ship radiated signal based on wavelet packet decomposition and energy entropy is proposed in this paper. The wavelet packet is used to decompose ship signals to obtain different frequency bands. Energy entropy, as a feature, is used to estimate the uncertainty of ship signal frequency band energy distribution. The specific steps of the proposed feature extraction method are as follows:

(1) The ship signal is decomposed into M frequency bands by wavelet packet decomposition. In this paper, a three-layer wavelet packet decomposition is performed, where the M value is 8 The sum of the energy of the M frequency bands is equal to the total energy of the ship signal.

(2) The energy proportion of each frequency band signal is calculated by

$$C_i = \frac{E_i}{E}. \quad (4)$$

E_i is the energy of the i^{th} frequency band signal; E is the total energy of ship signal; C_i is the proportion of the i^{th} band signal to the total energy of the ship signal.

The total energy of the ship signal can be expressed as

$$E = \sum_{i=1}^{M} E_i. \quad (5)$$

M is the number of signals in different frequency bands obtained after wavelet packet decomposition.

(3) The energy entropy of the ship signal after wavelet packet decomposition is calculated by the definition of information entropy, which can be defined as

$$H(C) = -\sum_{i=1}^{M} C_i \ln C_i. \quad (6)$$

(4) To demonstrate the effectiveness of the proposed feature extraction method, the k-nearest neighbor algorithm is used in the classification of the energy entropy features of ship signals to obtain the identification results. Given a training data set, for a new input instance, K instances closest to the instance are found in the training data set. Most of the K instances belong to a class, and the input instance is classified into this class.

4. Feature Extraction of Ship Radiated Noise

4.1. Ship Radiation Signals. In this paper, feature extraction and classification identification are carried out for four types of measured ship radiation signals (SRS), named SRS1, SRS2, SRS3, and SRS4. The signal lengths of the first and second types are 1380000, the third type is 28282835, and the fourth type is 164160, and the sampling frequency is 44.1 kHz. Data points within 5001 to 1000000 of the four types of SRS are taken, Figure 2 presents four types of SRS after normalization.

4.2. Wavelet Packet Decomposition of Ship Radiation Signal. For the wavelet packet decomposition of four types of SRS, 100 samples are extracted from each type of SRS, each sample contains 5000 sampling points. One sample for each type of SRS is processed with the wavelet packet decomposition, using the DB2 wavelet basis function, each sample is decomposed into eight frequency bands (FB), named FB1, FB2, FB3, FB4, FB5, FB6, FB7, and FB8. The wavelet packet decomposition results of four types of SRS are shown in Figure 3 (1 sample). For the four types of SRS, the amplitudes in different FB have obvious differences, FB1 has the lowest frequency.

4.3. Feature Extraction Experiment. The energy entropy feature of each FB is extracted, center frequency (CF) and permutation entropy (PE) are used as comparative features.

4.3.1. Energy Entropy. Four types of SRS are extracted from the perspective of energy, the energy proportion is calculated for each FB. Figure 4 displays the energy distribution of four types of SRS (1 sample).

From Figure 4, for the four types of SRS, FB1 has the highest energy; the energy of SRS1 and SRS4 in FB2 is greater than that of SRS2 and SRS3; for FB2 of the four types of SRS, SRS4 has the most energy distribution, and similarly, for FB3 and FB4, SRS4 is also the highest; in the eight FB, the energy distributions of SRS2 are almost all concentrated in FB1, while those of SRS4 are more dispersed. Figure 5 exhibits the energy entropy of 100 samples for four types of ship signals.

In the light of Figure 5, there is a big difference in energy entropy among the four types of SRS; SRS2 has the smallest range of sample distribution, and has great stability; most samples of SRS1 are distributed between 0.4 and 0.7, while a small number of samples of SRS3 and SRS4 also appears in this range; there is a clear order of the energy entropy of the samples for the four kinds of SRS.

4.3.2. Center Frequency. The CF feature extraction is performed for each FB of the four types of SRS, and the CF of each FB for the four types of SRS is shown in Figure 6.

As presented in Figure 6, for the four types of SRS, the CF under the same FB is different; for SRS2, the CF of FB7 and 8 is very different from the other three types of SRS; the CF distribution of samples in FB4 and FB6 is similar, the CF of SRS1 and SRS2 are close, and so are SRS3 and SRS4, but there is an obvious gap between the two groups; the CF distribution of the samples for SRS1 and SRS3 are very dispersed in each FB.

4.3.3. Permutation Entropy. PE mainly includes three parameters: data length, embedding dimension, and delay time, which are 5000, 3, and 1, respectively, in this experiment. Figure 7 indicates the PE of each FB for the four types of SRS.

As exhibited in Figure 7, the PE for the four types of SRS in the same FB is very close; the PE of the SRS2 coincides less with the range of PE distributions from the other SRS in FB1 and 7; SRS3 has a difference in its PE from the other SRS in FB5; the distribution of PE of samples for each type of SRS in each FB is very scattered.

4.4. Analysis of Classification and Recognition Results

4.4.1. K-Nearest Neighbor. KNN is one of the machine learning methods that classify each record in a data collection. The principle is that if a majority of the K most similar samples in a feature space belong to a class, then that sample also belongs to that class. This method is simple and easy to understand and implement, and K is set to 5 in this

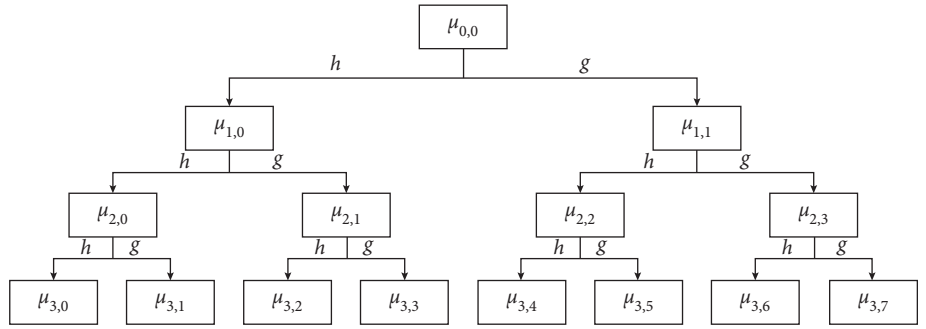

Figure 1: Three-layer wavelet packet decomposition.

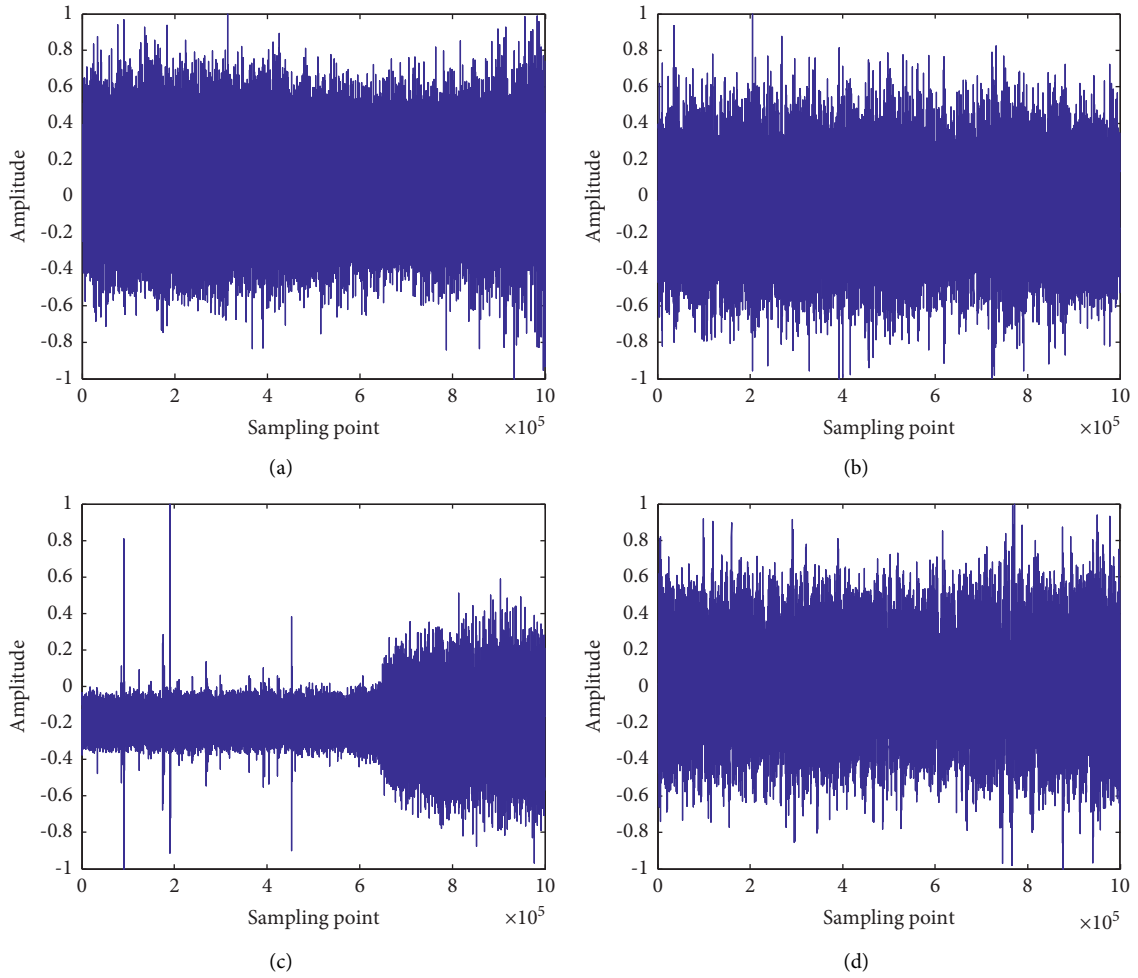

Figure 2: Four types of SRS after normalization. (a) SRS1. (b) SRS2. (c) SRS3. (d) SRS4.

paper. 50 samples of each type of SRS are selected as the training set and the remaining 50 as the test samples to classify and identify the four types of SRS. The recognition rate of each feature extraction method is obtained to compare and prove the effectiveness of the proposed method. The recognition rates of the energy entropy for four types of SRS are presented in Table 1.

According to Table 1, the recognition rate for each type of SRS is greater than 90%, the recognition rates of SRS1 and SRS2 are 100%; the average recognition rate is 98%; it is indicated that all the four types of SRS have good recognition results. The recognition rates of CF for four types of SRS are demonstrated in Table 2.

From Table 2, for the CF of each FB, the highest recognition rates of SRS1 and SRS4 is only 74%, the recognition rate of SRS2 reaches 100%; for SRS3, the recognition rates of each FB have a great difference; the highest average recognition rate of the four SRS is only 72%, which is difficult to

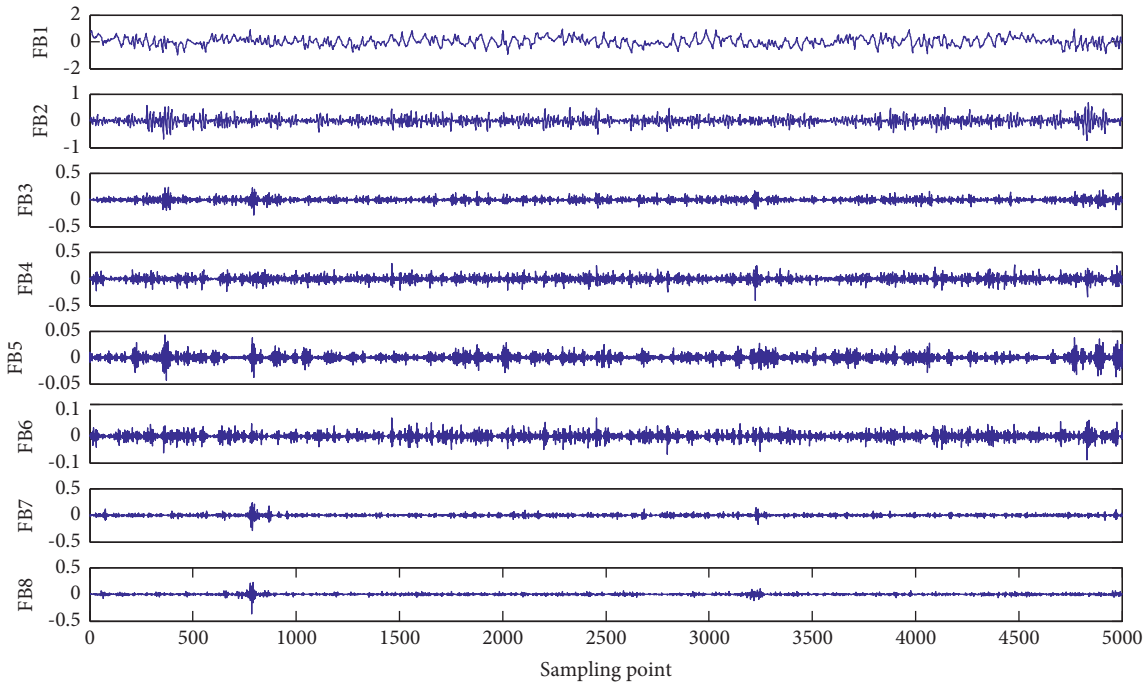

(a)

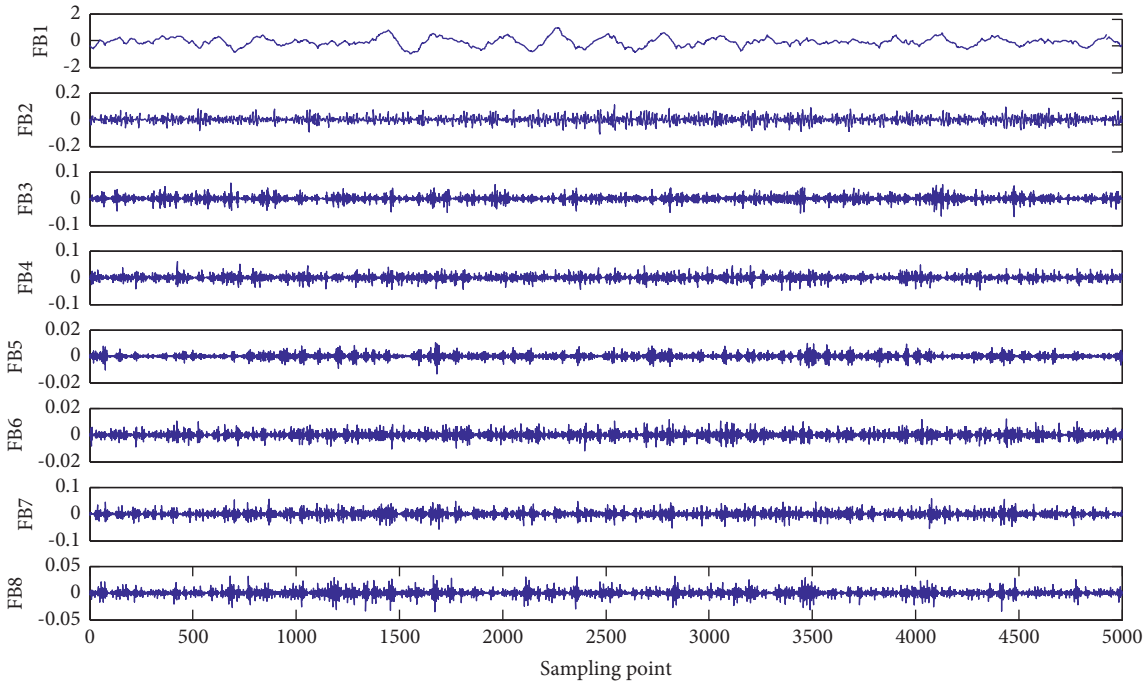

(b)

Figure 3: Continued.

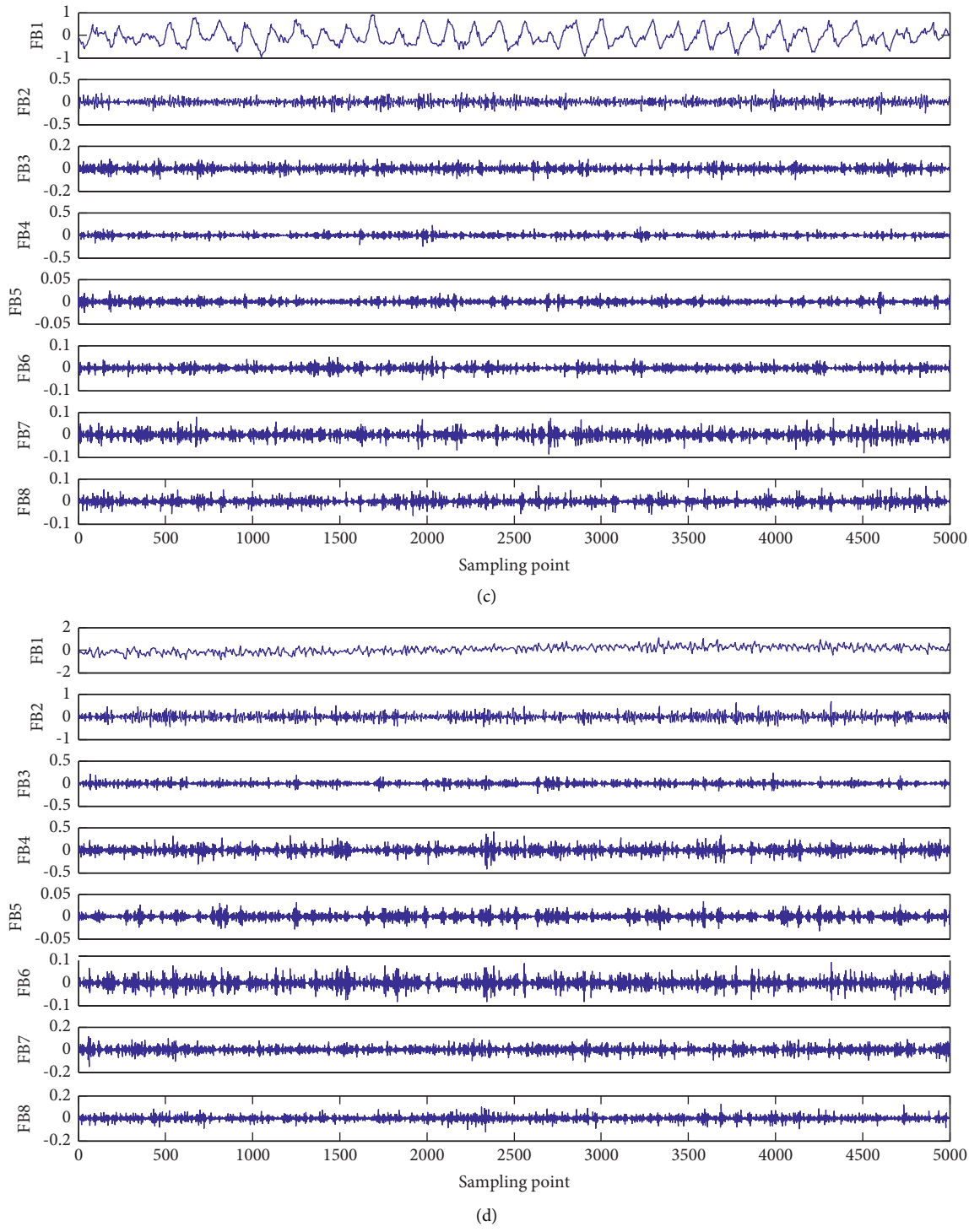

Figure 3: Wavelet packet decomposition results of four types of SRS (1 sample). (a) SRS1. (b) SRS2. (c) SRS3. (d) SRS4.

distinguish between the four SRS. The recognition rates of PE of four types of SRS are displayed in Table 3.

As can be seen from Table 3, overall, only FB6 had the highest average recognition rate of 52%, and the other FB average recognition rates are below 50%; the recognition rates of PE for SRS1 is less than 60%, for SRS3 and SRS4 is less than 70%; only the highest recognition rate of SRS2 is 86%; the recognition results make it hard to classify and

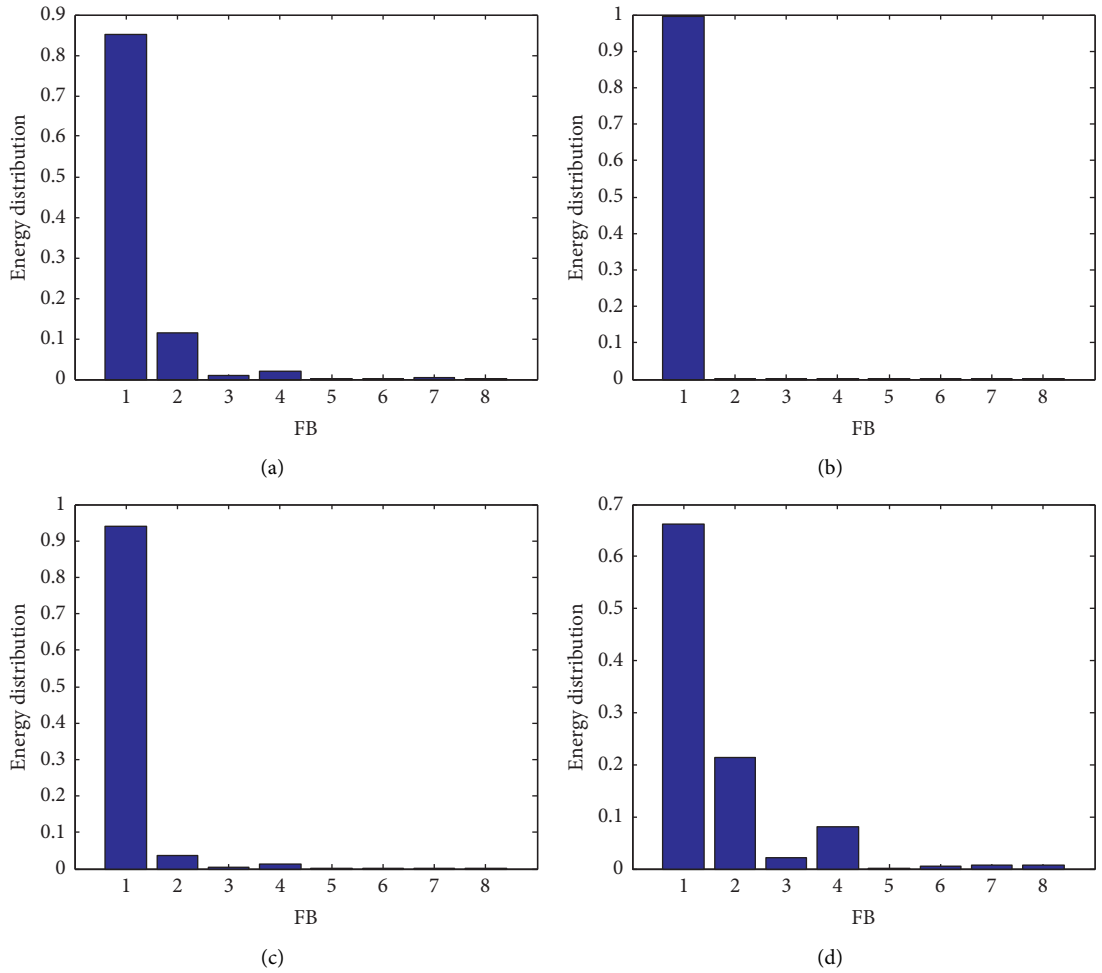

Figure 4: Energy distribution of four types of SRS (1 sample). (a) SRS1. (b) SRS2. (c) SRS3. (d) SRS4.

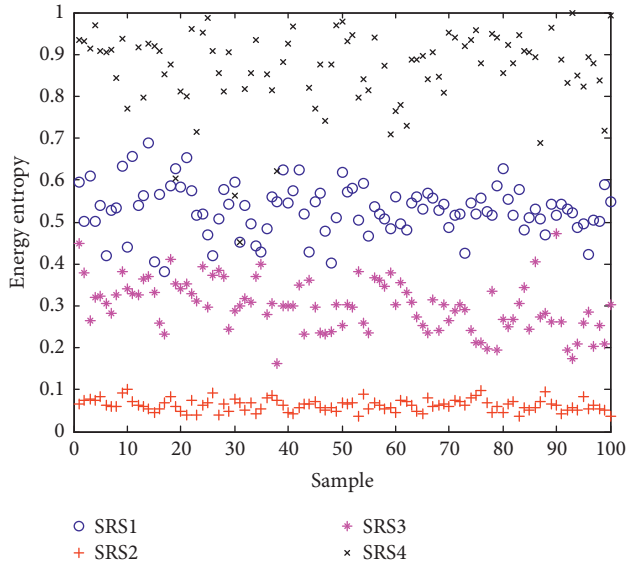

Figure 5: Energy entropy of 100 samples for four types of SRS.

recognize the four types of SRS as well. For comparison, the highest recognition rates of the three methods are displayed in Table 4.

It is known from Table 4 that the feature extraction based on wavelet packet decomposition and energy entropy can effectively identify four types of SRS with the highest recognition rate of 98%, much better than the other two.

4.4.2. Random Forest. In this subsection, the random forest (RF) method is introduced to compare with KNN, RF is a machine learning method that integrates multiple trees by the idea of ensemble learning. Its basic unit is the decision tree, and its essence is an important branch of machine learning— ensemble learning method and the number of trees in this paper is set to 25. As in Section 4.4.1, 50 training samples and 50 test samples for each type of SRS are taken. The recognition rates of the energy 7entropy for four types of SRS are presented in Table 5.

Table 5 shows that the recognition rates of both SRS1 and SRS2 reached 100%; for each type of SRS, the recognition

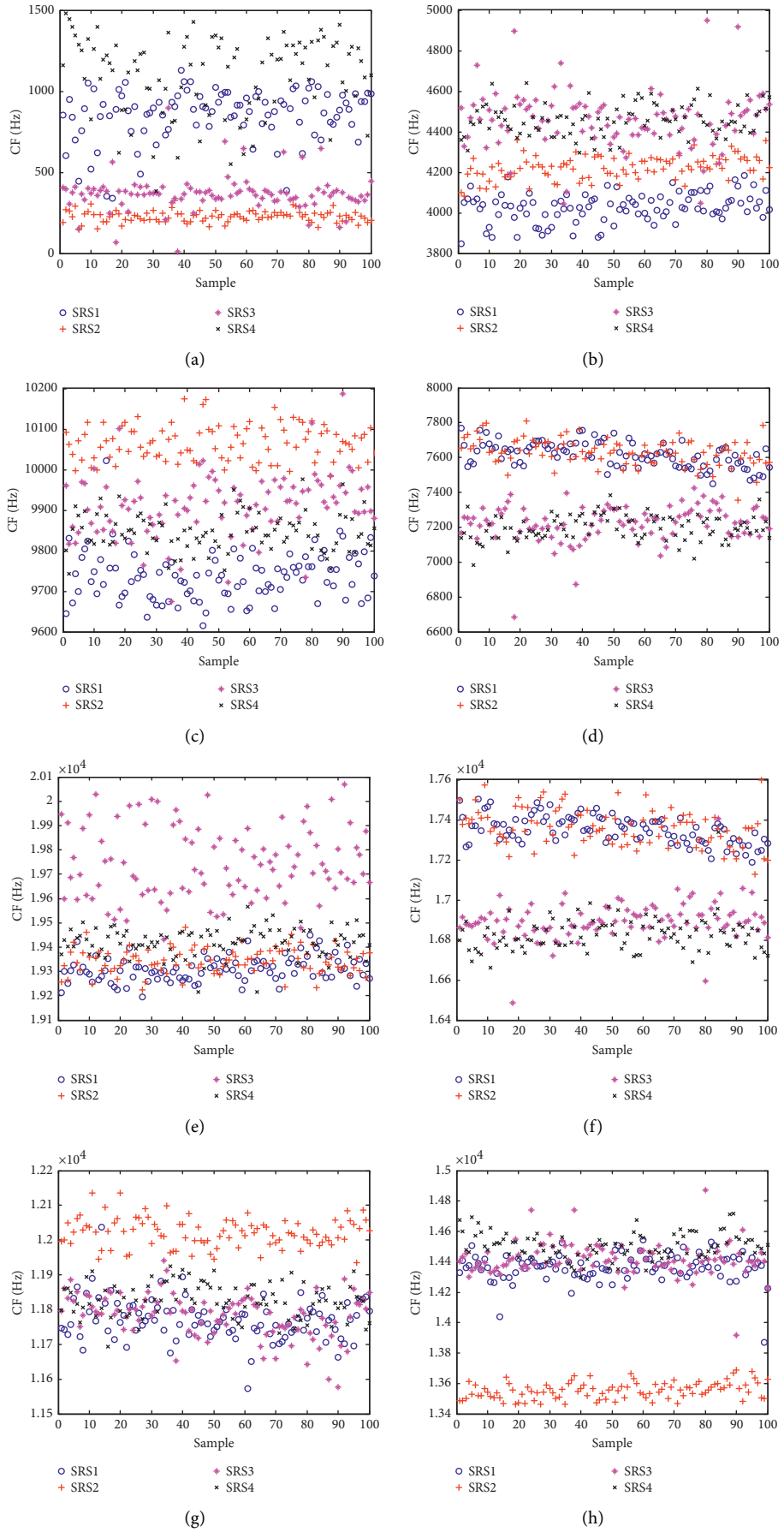

Figure 6: CF of each FB for the four types of SRS. (a) FB1. (b) FB2. (c) FB3. (d) FB4. (e) FB5. (f) FB6. (g) FB7. (h) FB8.

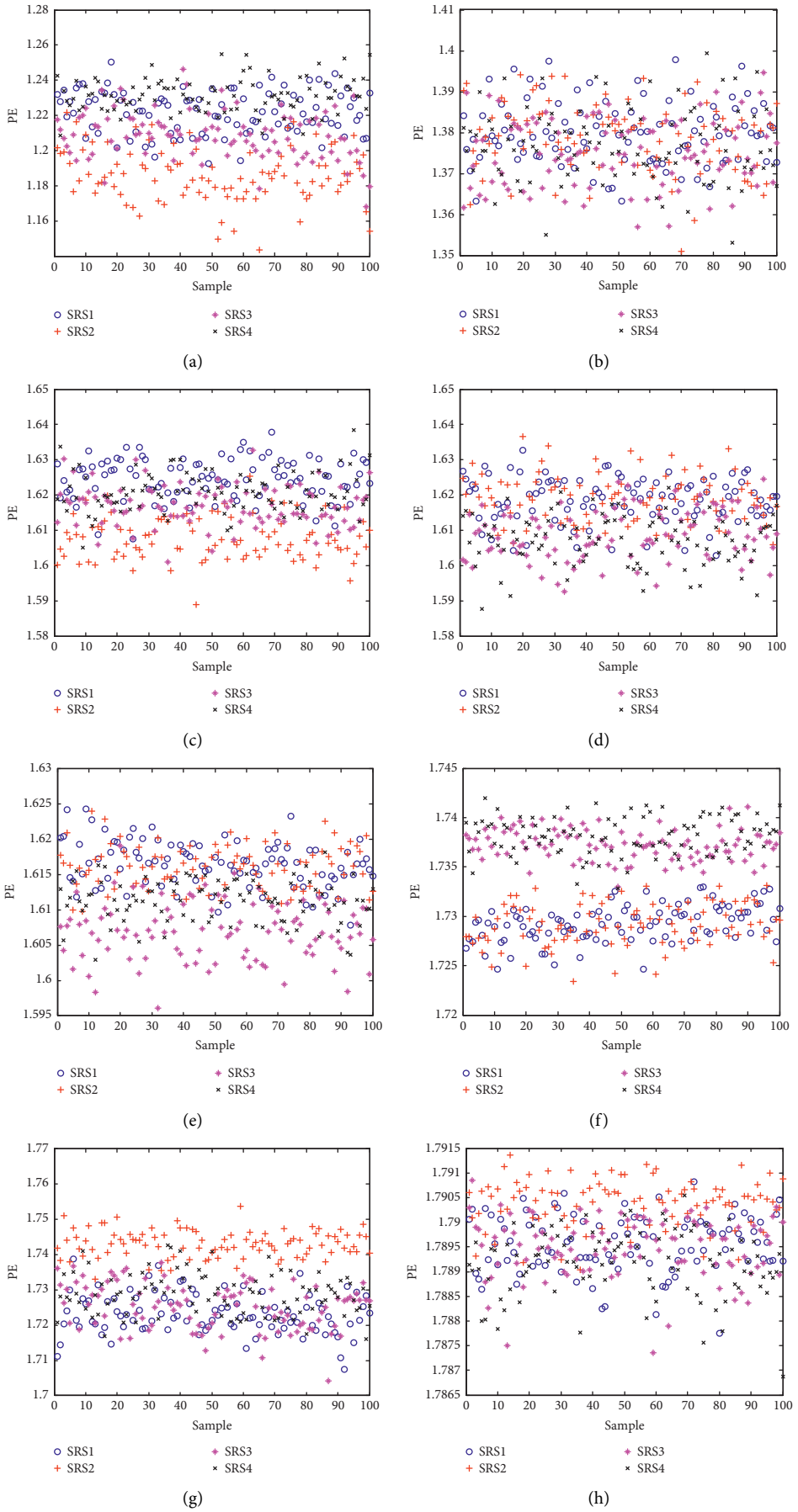

Figure 7: PE of each FB for the four types of SRS. (a) FB1. (b) FB2. (c) FB3. (d) FB4. (e) FB5. (f) FB6. (g) FB7. (h) FB8.

Table 1: The recognition rates of energy entropy for four types of SRS.

SRS1	SRS2	SRS3	SRS4	Average
100%	100%	94%	98%	98%

Table 2: The recognition rates of CF for four types of SRS.

	SRS1 (%)	SRS2 (%)	SRS3 (%)	SRS4 (%)	Average (%)
FB1	62	98	54	74	72
FB2	74	88	36	38	59
FB3	66	90	64	42	65.5
FB4	52	56	40	52	50
FB5	48	44	98	68	64.5
FB6	48	56	72	56	58
FB7	34	98	26	48	51.5
FB8	40	100	42	66	62

Table 3: The recognition rates of PE for four types of SRS.

	SRS1 (%)	SRS2 (%)	SRS3 (%)	SRS4 (%)	Average (%)
FB1	20	80	42	46	47
FB2	30	20	38	36	31
FB3	56	64	22	32	43.5
FB4	26	46	38	34	36
FB5	34	32	64	40	42.5
FB6	38	42	60	68	52
FB7	32	86	42	36	49
FB8	24	60	20	34	34.5

Table 4: The highest recognition rates of the three feature extraction methods.

Energy entropy	CF	PE
98%	72%	52%

Table 5: The recognition rates of energy entropy for four types of SRS (Random forests).

SRS1	SRS2	SRS3	SRS4	Average
100%	100%	94%	96%	97.5%

Table 6: The recognition rates of CF for four types of SRS (Random forests).

	SRS1 (%)	SRS2 (%)	SRS3 (%)	SRS4 (%)	Average (%)
FB1	72	98	42	76	72
FB2	74	88	36	32	57.5
FB3	72	92	68	36	67
FB4	58	46	56	48	52
FB5	50	40	98	60	62
FB6	54	52	84	38	57
FB7	46	98	16	50	52.5
FB8	50	100	38	52	60

rates were generally higher than 90%, and the average recognition rate reached 97.5%, which verified the effectiveness of the feature extraction method proposed in this paper.

The recognition rates of CF for four types of SRS are displayed in Table 6. From Table 6, it can be seen that the highest average recognition rate of the four SRSs is 72% and the lowest is only 52%; there is a significant difference in the recognition rate of each FB of SRS3; in FB7, the recognition rate of SRS2 is 98%, but the recognition rate of SRS3 is only 16%; these results imply that it is difficult to distinguish one SRS from another.

Table 7 shows the recognition rate of PE for the four types of SRSs, from Table 7, the recognition rate of PE is very low, none of the results has a recognition rate over 50%; the highest recognition rate for SRS3 is 48%; for SRS1 and SRS4, the recognition rate is below 40%; the highest average recognition rate is 38.5%, which indicates that the classification of the four types of SRSs by PE of random forest is very difficult.

The highest recognition rates of the three methods are shown in Table 8. As we can see from Table 8, with the recognition rate of 97.5%, the energy entropy can recognize the SRS better than the other two features. The above results show that the influence of the classifier is not dominant, and the energy entropy-based feature extraction method proposed in this paper still has the highest recognition rate compared with the CF and PE in the comparison experiments with RF as the classifier.

5. Discussion

In this paper, energy entropy, CF and PE are used to extract the features for each FB of SRS. Energy entropy has a very significant effect in identifying the SRS. The CF is presented as a method other than entropy. The PE can easily and accurately locate the time when the system changes abruptly, and it can amplify the small changes of the signal. PE and energy entropy are in the form of entropy, so the results of permutation entropy and energy entropy are compared in this paper to prove the effectiveness of energy entropy. From the comparison results of recognition rates, we can see that energy entropy has better separability as an extracted feature compared to PE.

In the classification comparison experiment, we calculate the recognition rate while introducing different classifiers for comparison. For energy entropy, the recognition result of KNN is 98%, while the recognition result of random forest is 97.5%. Both classifiers prove the effectiveness of the feature extraction method proposed in this paper, but the result of KNN is better than RF, while the recognition results of CF and PE also prove this point.

Finally, we introduce cross-validation to avoid overfitting. Different numbers of training samples are randomly selected from 100 samples, and the rest are used as test samples. To reduce randomness, the cycle is repeated 20 times to compare whether the standard deviations are close under different numbers of training samples. The classification results of the proposed feature extraction method using a different number of samples for training are shown in Table 9.

As can be seen from the table, the average recognition rate at the end is similar for different training sample numbers, and the standard deviation fluctuates just a little, indicating that there is no overfitting problem. We can also

Table 7: The recognition rates of PE for four types of SRS (Random forests).

	SRS1 (%)	SRS2 (%)	SRS3 (%)	SRS4 (%)	Average (%)
FB1	26	48	40	28	35.5
FB2	32	28	24	20	26
FB3	20	34	20	20	23.5
FB4	20	34	32	30	29
FB5	30	28	36	30	31
FB6	36	38	48	32	38.5
FB7	34	46	34	30	36
FB8	16	24	18	28	21.5

Table 8: The highest recognition rates of the three feature extraction methods (Random forests).

Energy entropy	CF	PE
97.5%	72%	38.5%

Table 9: The classification results of the proposed feature extraction method using a different number of samples for training.

Number of training samples	80	70	60	50	40	30
Average accuracy	95.125%	96.009%	95.000%	95.400%	95.625%	95.553%
Standard deviation	0.0205	0.01848	0.0163	0.0086	0.01025	0.00971

observe that when we select 50 training samples, the recognition rate reaches 95.4% with the standard deviation of 0.0086, which is the most stable group under each combination in Table 9. Considering the average recognition rate and standard deviation, we select 50 samples for training and the remaining 50 for testing, so as to verify the advantages of the feature extraction method proposed in this paper.

6. Conclusions

According to this paper, the wavelet packet decomposition is integrated with energy entropy to extract features of four types of SRS. By comparing with CE and PE, the effectiveness of EE is testified, and the major conclusions are summarized as follows:

(1) In view of the advantages of wavelet analysis theory in non-stationary signal analysis and processing, and based on this theory, this paper presents an analysis method of SRS by combining energy entropy.

(2) Observing the conditions of figures and contrasting the recognition rates, it can be found that, when compared with CF and PE, the energy entropy can reflect the energy distribution of each FB from a macro perspective, which is more valid.

(3) Compared with other feature extraction methods, the feature extraction method of wavelet packet decomposition and energy entropy proposed in this paper has the highest recognition rate of 98%, at least 26% higher. As a result, the availability of the new method can be fully confirmed.

Data Availability

The data used to support the findings of this study are available from the corresponding author upon request.

Conflicts of Interest

The authors declare that they have no conflicts of interest.

References

[1] Y. Li, Y. Li, X. Chen, and J. Yu, "A novel feature extraction method for ship-radiated noise based on variational mode decomposition and multi-scale permutation Entropy," *Entropy*, vol. 19, no. 7, 2017.

[2] X. Guo, Y. Li, and K. Yang, "On the dynamics of ocean ambient noise: two decades later," *Chaos*, vol. 25, Article ID 103117, 2015.

[3] S. Wang and X. Zeng, "Robust underwater noise targets classification using auditory inspired time-frequency analysis," *Applied Acoustics*, vol. 78, no. 4, pp. 68–76, 2014.

[4] S. Jiao, B. Geng, Y. Li, Q. Zhang, and Q. Wang, "Fluctuation-based reverse dispersion entropy and its applications to signal classification," *Applied Acoustics*, vol. 175, no. 4, Article ID 107857, 2021.

[5] Y. Li, S. Jiao, and B. Geng, "A comparative study of four multiscale entropies combined with grey relational degree in classification of ship-radiated noise," *Applied Acoustics*, vol. 176, no. 4, Article ID 107865, 2021.

[6] A. K. S. Jardine, D. Lin, and D. Banjevic, "A review on machinery diagnostics and prognostics implementing condition-based maintenance," *Mechanical Systems and Signal Processing*, vol. 20, no. 7, pp. 1483–1510, 2006.

[7] Y. Zhang, X. Li, L. Gao, L. Wang, and L. Wen, "Imbalanced data fault diagnosis of rotating machinery using synthetic oversampling and feature learning," *Journal of Manufacturing Systems*, vol. 48, pp. 34–50, 2018.

[8] Y. Li, X. Chen, J. Yu, X. Yang, and H. Yang, "The data-driven optimization method and its application in feature extraction of ship-radiated noise with sample entropy," *Energies*, vol. 12, no. 3, p. 359, 2019.

[9] A. Lempel and J. Ziv, "On the complexity of finite sequences," *IEEE Transactions on Information Theory*, vol. 22, no. 1, pp. 75–81, 1976.

[10] L. Cui, X. Gong, J. Zhang, and H. Wang, "Double-dictionary matching pursuit for fault extent evaluation of rolling bearing based on the Lempel-Ziv complexity," *Journal of Sound and Vibration*, vol. 385, pp. 372–388, 2016.

[11] A. Babloyantz and A. Destexhe, "Is the normal heart a periodic oscillator?" *Biological Cybernetics*, vol. 58, no. 3, pp. 203–211, 1988.

[12] Z. Zhang, A. Verma, and A. Kusiak, "Fault analysis and condition monitoring of the wind turbine gearbox," *IEEE Transactions on Energy Conversion*, vol. 27, no. 2, pp. 526–535, 2012.

[13] J. Antoni and R. B. Randall, "The spectral kurtosis: application to the vibratory surveillance and diagnostics of rotating machines," *Mechanical Systems and Signal Processing*, vol. 20, no. 2, pp. 308–331, 2006.

[14] N. Sawalhi, R. B. Randall, and H. Endo, "The enhancement of fault detection and diagnosis in rolling element bearings using minimum entropy deconvolution combined with spectral kurtosis," *Mechanical Systems and Signal Processing*, vol. 21, no. 6, pp. 2616–2633, 2007.

[15] C. Bandt and B. Pompe, "Permutation entropy: a natural complexity measure for time series," *Physical Review Letters*, vol. 88, Article ID 174102, 2012.

[16] C. Bandt, "Ordinal time series analysis," *Ecological Modelling*, vol. 182, no. 3-4, pp. 229–238, 2005.

[17] S. M. Pincus, "Approximate entropy as a measure of system complexity," *Proceedings of the National Academy of Sciences*, vol. 88, no. 6, pp. 2297–2301, 1991.

[18] J. S. Richman and J. R. Moorman, "Physiological time-series analysis using approximate entropy and sample entropy," *American Journal of Physiology - Heart and Circulatory Physiology*, vol. 278, no. 6, pp. H2039–H2049, 2000.

[19] R. Alcaraz and J. J. Rieta, "A review on sample entropy applications for the non-invasive analysis of atrial fibrillation electrocardiograms," *Biomedical Signal Processing and Control*, vol. 5, no. 1, pp. 1–14, 2010.

[20] E. Olofsen, J. W. Sleigh, and A. Dahan, "Permutation entropy of the electroencephalogram: a measure of anaesthetic drug effect," *British Journal of Anaesthesia*, vol. 101, no. 6, pp. 810–821, 2008.

[21] J. M. Yentes, N. Hunt, K. K. Schmid, J. P. Kaipust, D. McGrath, and N. Stergiou, "The appropriate use of approximate entropy and sample entropy with short data sets," *Annals of Biomedical Engineering*, vol. 41, no. 2, pp. 349–365, 2013.

[22] Y. Bai, Z. Liang, and X. Li, "A permutation lempel-ziv complexity measure for EEG analysis," *Biomedical Signal Processing and Control*, vol. 19, pp. 102–114, 2015.

[23] D. V. Ha, V. D. Nguyen, and Q. K. Nguyen, "Modeling of Doppler power spectrum for underwater acoustic channels," *Journal of Communications and Networks*, vol. 19, no. 3, pp. 270–281, 2017.

[24] E. Widjiati, E. B. Jatmiko, W. Wardhana et al., "Analysis of propeller cavitation-induced signal using neural network and wigner-ville distribution," in *Proceedings of the 2012 Oceans*, Yeosu, Korea (South), May 2012.

[25] J. Wang and Y. Pi, "SAR tomography imaging via higher-order spectrum analysis," *Journal of Systems Engineering and Electronics*, vol. 04, pp. 748–754, 2009.

[26] Y. Li, L. Wang, X. Li, and X. Yang, "A novel linear spectrum frequency feature extraction technique for warship radio noise based on complete ensemble empirical mode decomposition with adaptive noise, duffing chaotic oscillator, and weighted-permutation entropy," *Entropy*, vol. 21, no. 5, p. 507, 2019.

[27] I. Cohen, S. Raz, and D. Malah, "Orthonormal shift-invariant wavelet packet decomposition and representation," *Signal Processing*, vol. 57, no. 3, pp. 251–270, 1997.

[28] B.. Luk, Z. D. Jiang, K. P. Liu, and F. Tong, "Impact acoustic non-destructive evaluation in noisy environment based on wavelet packet decomposition," *Lecture Notes in Engineering and Computer Science*, vol. 2169, no. 1, pp. 1338–1341, 2008.

[29] I. Saha and R. V. Sagar, "Classification of the acoustic emissions generated during the tensile fracture process in steel fibre reinforced concrete using a waveform-based clustering method," *Construction and Building Materials*, vol. 294, Article ID 123541, 2021.

[30] R. P. J. Kumar, C. Akila, R. Mercy, and M. D. Lakshmi, "Texture classification using wavelet packet decomposition based on SGS & MISS algorithm," *Digital Image Processing*, vol. 36, no. 5, pp. 57–59, 2010.

Hindawi
Mathematical Problems in Engineering
Volume 2021, Article ID 7150921, 18 pages
https://doi.org/10.1155/2021/7150921

Research Article

RCMFRDE: Refined Composite Multiscale Fluctuation-Based Reverse Dispersion Entropy for Feature Extraction of Ship-Radiated Noise

Yuxing Li,[1,2] **Shangbin Jiao**,[1,2] **Bo Geng**,[1] **and Xinru Jiang**[1]

[1]*School of Automation and Information Engineering, Xi'an University of Technology, Xi'an 710048, China*
[2]*Shaanxi Key Laboratory of Complex System Control and Intelligent Information Processing, Xi'an University of Technology, Xi'an 710048, China*

Correspondence should be addressed to Shangbin Jiao; jiaoshangbin@xaut.edu.cn

Received 16 September 2021; Revised 11 November 2021; Accepted 2 December 2021; Published 16 December 2021

Academic Editor: Mohammad Yaghoub Abdollahzadeh Jamalabadi

Dispersion entropy (DE), as a newly proposed entropy, has achieved remarkable results in its application. In this paper, on the basis of DE, combined with coarse-grained processing, we introduce the fluctuation and distance information of signal and propose the refined composite multiscale fluctuation-based reverse dispersion entropy (RCMFRDE). As an emerging complexity analysis mode, RCMFRDE has been used for the first time for the feature extraction of ship-radiated noise signals to mitigate the loss caused by the misclassification of ships on the ocean. Meanwhile, a classification and recognition method combined with K-nearest neighbor (KNN) came into being, namely, RCMFRDE-KNN. The experimental results indicated that RCMFRDE has the highest recognition rate in the single feature case and up to 100% in the double feature case, far better than multiscale DE (MDE), multiscale fluctuation-based DE (MFDE), multiscale permutation entropy (MPE), and multiscale reverse dispersion entropy (MRDE), and all the experimental results show that the RCMFRDE proposed in this paper improves the separability of the commonly used entropy in the hydroacoustic domain.

1. Introduction

The ocean is one of the main battlefields of future high-tech warfare [1, 2]. With the increasing development of electronic countermeasure technology, people can use signal processing technology to extract features of ship-radiated noise signals to complete military tasks such as target detection and target recognition [3], and these signal processing methods include wavelet transform (WT) [4], empirical mode decomposition (EMD) [5], and variational mode decomposition (VMD) [6]. However, the key step in the ship-radiated noise classification is the extracted features [7, 8]. The stronger the separability of the extracted features, the better the classification effect of ship-radiated noise signals.

Most of the traditional feature extraction methods extract the characteristic parameters of the waveform structure, which can be directly extracted from the time domain, including the mean value, variance, and peak value [9]. The transformation from the time domain to the frequency domain also transforms complex waveforms in the time domain into relatively simple single frequency component distributions in the frequency domain [10, 11]. Therefore, the low line spectrum features and broadband spectrum features in the power spectrum can also become effective features for ship-radiated noise target detection and recognition and have achieved good results in signal classification. In addition, there are also many other kinds of features, such as chaos feature [12], time-frequency joint feature [13,14], correlation dimension [15, 16], and auditory feature [17].

Lempel–Ziv complexity (LZC) is a commonly used indicator to identify dynamics [18–20] and is increasingly used as a feature for signal classification in various fields and has found numerous applications in characterizing the randomness of biological and ship-radiated noise signals [21].

In a nutshell, the physical meaning of LZC is that it reflects the rate at which new patterns appear in a time series as the length increases. The higher the LZC value of a sequence, the more new changes occur in the sequence and the more disordered and uncertain the sequence is, while the lower the LZC value, the more regular the sequence is [22, 23]. In addition, more and more improved algorithms based on LZC are constantly being proposed, such as DLZC [24] and PLZC [25].

Another commonly used feature is entropy, which was first proposed by Shannon in 1948 [26]. It has been widely concerned and applied since the beginning of the 21st century because of its excellent performance of quickly and effectively quantifying the complexity of time series. In 2002, Bandt and Pompe first proposed Permutation Entropy (PE) [27], which was quickly applied to characterize the randomness of information in various fields, and many scholars improved it on this basis, such as weighted PE (WPE) [28] and multiscale PE (MPE) [29]; compared with PE, these improved PE-based measures have more substantial stability. However, PE only considers the order of amplitude values, ignores some information of amplitude values, and does not mention the influence of medium amplitude of each embedded vector. In some time series with large differences, the same PE value will be obtained, which will affect the stability of the extracted features [30].

To overcome the deficiencies of PE, Rostaghi and Azami proposed dispersion entropy (DE) in 2016 [31]. As an entropy has been proposed in recent years, DE has been proved to be more effective in measuring signal complexity than PE and improved PE-based measures. DE not only considers the order of amplitude values but also quantizes them through different mapping methods. The medium amplitude in the vector will also affect the DE value according to its size, and small changes will not change its corresponding class label in the vector. Compared with PE and improved PE-based measures, DE also has more vital noise anti-interference ability [32–34]. Because of the excellent ability of DE as a feature to characterizing the randomness of signals, many DE-based improved algorithms have appeared in just a few years, such as fluctuation-based DE (FDE) [35], reverse DE (RDE) [36], and the combination of the two, namely, fluctuation-based reverse DE (FRDE) [7]. However, the study in [7] did not consider various modes at different scales.

On the basis of FRDE, we first introduced the concept of multiscale, where the same sequence can obtain multiple subsequences by multiscale operation, and then improved the multiscale calculation by introducing the concept of refined composite, which can divide each subsequence into multiple sequences and average the final obtained entropy value, and finally obtained a new entropy called RCMFRDE. Combined with the clustering methods for classification recognition, the common clustering methods are K-nearest neighbor (KNN) [37], K-mean clustering [38], etc. In this paper, we choose the K-nearest neighbor as the classifier. In addition, we can further improve the final calculated entropy by introducing fractional order [34, 37], but this may lead to a lower separability of the final result out instead due to the effect of the backward scattering entropy. Experimental results show that the classification method based on RCMFRDE has stronger separability compared with several other commonly used entropy-based classification methods.

The train of thought of the paper is as follows: Section 2 reveals formulas of RCMFRDE; Section 3 proposes a feature extraction method that comes from RCMFRDE; Sections 4 and 5 extract four types of ship-radiated noise signals under single feature and double features; ultimately, Section 6 embraces main conclusions obtained.

2. RCMFRDE

Step 1: for a known time series $A(j) = \{a_j(j = 1, 2, \ldots, N)\}$, $x_k^{(s)}(k = 1, 2, \ldots, s)$ is the k^{th} coarse-grained time series of $A(j)$ as follows:

$$x_k^{(s)} = \frac{1}{s}\sum_{j=k+s(i-1)}^{is+k-1} a_j, \quad (i = 1, 2, \ldots, h),$$
$$h = \text{floor}\frac{N-(k-1)}{s}, \tag{1}$$

where s is the scale factor (SF), and floor is the downward rounding function. For $x_k^{(s)} = \{x_{k,i}^{(s)}(i = 1, 2, \ldots, h)\}$, $x_{k,i}^{(s)}$ is the i^{th} element in the k^{th} time series.

Step 2: to map $X = \{x_k^{(s)}(k = 1, 2, \ldots, s)\}$ to $Y = \{y_k^{(s)}(k = 1, 2, \ldots, s)\}$, normal cumulative distribution function is employed, which can be described as

$$y_k^{(s)} = \frac{1}{\sigma\sqrt{2\pi}}\int_{-\infty}^{x_k^{(s)}} e^{-((t-\mu)^2/2\sigma^2)}\mathrm{d}t, \tag{2}$$

where μ and σ^2 represent expectation and variance of $x_k^{(s)}$, respectively, and the range of $y_k^{(s)}$ distributes from 0 to 1.

Step 3: $y_{k,i}^{(s)}$ is mapped to $z_{k,i}^{(s)}$ by using linear transformation as follows:

$$z_{k,i}^{(s)} = \text{round}\left(c * y_{k,i}^{(s)} + 0.5\right), \tag{3}$$

where c is the number of categories, round is the integer function, and $z_{k,i}^{(s)}$ is an integer range from 1 to c. And, $z_{k,i}^{(s)}(i = 1, 2, \ldots, h)$ can form time series $z_k^{(s)}$, which can be expressed as $z_k^{(s)} = \{z_{k,i}^{(s)}(i = 1, 2, \ldots, h)\}$.

Step 4: phase space reconstruction of $z_k^{(s)}$ according to embedding dimension m and time delay τ, and embedding vectors $z_{k,n}^c, z_{k,n+\tau}^c, \ldots, z_{k,n+(m-1)\tau}^c$ is created as follows:

$$Z_k^{m,\tau} = \{z_{k,n}^c, z_{k,n+\tau}^c, \ldots, z_{k,n+(m-1)\tau}^c\},$$
$$(n = 1, 2, \ldots, h-(m-1)\tau). \tag{4}$$

Step 5: each embedding vector is mapped to fluctuation-based dispersion patterns $T_k^{m,\tau}$. After this, the total number of vectors is $V = h-(m-1)\tau$, with a maximum of $(2c-1)^{(m-1)}$ types of possible fluctuation-based dispersion patterns. There are $m-1$ values in

each vector, and each value ranges from $-c+1$ to $c-1$. Based on m, c, τ, $T_k^{m,\tau}$ can be expressed as

$$T_k^{m,\tau} = \left\{t_{k,n}^c, t_{k,n+\tau}^c, \ldots, t_{k,n+(m-1)\tau}^c\right\}, \quad (n = 1, 2, \ldots, h-(m-1)\tau). \tag{5}$$

All the vectors contained in the k^{th} matrix can be described as

$$\begin{bmatrix} \left\{t_{k,1}^c, t_{k,1+\tau}^c, \ldots, t_{k,1+(m-1)\tau}^c\right\} \\ \vdots \\ \left\{t_{k,j}^c, t_{k,j+\tau}^c, \ldots, t_{k,j+(m-1)\tau}^c\right\} \\ \vdots \\ \left\{t_{k,V}^c, t_{k,V+\tau}^c, \ldots, t_{k,V+(m-1)\tau}^c\right\} \end{bmatrix}. \tag{6}$$

Step 6: each $T_k^{m,\tau}$ corresponds to a fluctuation-based dispersion pattern $\pi_{v_0,v_1,\ldots,v_{m-2}}$ ($t_{k,n}^c = v_0, t_{k,n+\tau}^c = v_1, \ldots, t_{k,n+(m-1)\tau}^c = v_{m-2}$); then, the probability of each fluctuation-based dispersion pattern $P_k^{(s)}$ ($k = 1, 2, \ldots, s$) can be estimated by

$$P_k^{(s)} = \frac{\text{Num}\left\{i | i \le h-(m-1)\tau, \pi_{v_0,v_1,\ldots,v_{m-2}}\right\}}{h-(m-1)\tau}, \tag{7}$$

where $\text{Num}\left\{i | i \le h-(m-1)\tau, \pi_{v_0,v_1,\ldots,v_{m-2}}\right\}$ is the number of fluctuation-based dispersion pattern of $\pi_{v_0,v_1,\ldots,v_{m-2}}$ assigned to $Z_k^{m,\tau}$. Next, the final average dispersion pattern $\overline{P}(\pi_{v_0,v_1,\ldots,v_{m-2}})$ can be computed as

$$\overline{P}\left(\pi_{v_0,v_1,\ldots,v_{m-2}}\right) = \frac{1}{s}\sum_{k=1}^{s} P_k^{(s)}, \quad (k = 1, 2, \ldots, s). \tag{8}$$

Step 7: RCMFRDE(A, m, c, s) is expressed as

$$\text{RCMFRDE}(A, m, c, s) = \sum_{\pi=1}^{(2c-1)^{(m-1)}} \left(\overline{P}\left(\pi_{v_0,v_1,\ldots,v_{m-2}}\right) - \frac{1}{(2c-1)^{(m-1)}}\right)^2. \tag{9}$$

Step 8: the normalized RCMFRDE is defined as

$$\text{RCMFRDE} = \frac{\text{RCMFRDE}(A, m, c, s)}{1-\left(1/(2c-1)^{(m-1)}\right)}. \tag{10}$$

3. Feature Extraction Method

In this section, single feature extraction and double feature extraction are carried out, and Figure 1 shows the flowcharts of extracting features.

Detailed steps of extracting a single feature based on the method of RCMFRDE are as follows:

Step 1: four different types of S-NS are gathered for the comparison experiments of feature extraction.

Step 2: for each type of S-NS, 350 samples were randomly selected from them, and single feature extraction (from SF1 to SF5) was performed using RCMFRDE. To compare the various feature extraction methods, we performed the same operation for MDE, MFDE, MPE, and MRDE.

Step 3: KNN is used for classification. For each type of S-NS, the first 50 samples are considered as training samples, and the remaining 300 samples are considered as test samples.

Step 4: finally, the recognition rates of RCMFRDE (from SF1 to SF5) were obtained and compared with the other four feature extraction methods.

As shown in Figure 1(b), detailed steps of the double feature extraction method based on RCMFRDE are different from that of the single feature, especially in the number of features. There are four cases in which SF1 is combined with other scales for double feature extraction, including SF1 and SF2, SF1 and SF3, SF1 and SF4, and SF1 and SF5.

4. Single Feature Extraction of the Four Types of S-NS

4.1. Ship-Radiated Noise Signals. In this section, four types of S-NS are taken as the research object, called Ship I, Ship II, Ship III, and Ship IV, respectively. Each of the above S-NS lengths is 1.11×10^6, and the frequency of sample extraction is 44.1 kHz. The normalized results of each type of S-NS are represented in Figure 2.

4.2. Single Feature Extraction. In the experiment of single feature extraction, for each type of S-NS, 350 samples are selected, and each sample consists of 3,000 sampling points. Five kinds of entropies are employed to extract the complexity feature of each type of S-NS (from SF1 to SF5), including RCMFRDE, MDE, MFDE, MPE, and MRDE. Table 1 is the parameter settings of five kinds of entropies. For RCMFRDE, MDE, MFDE, MPE, and MRDE, time delay τ and embedding dimension m are 1 and 4, respectively. Except that MPE has no category number and mapping method, the category number and mapping method of other entropies are the same. Figures 3 to 7 demonstrate the distribution of five kinds of entropies for four types of S-NS for different scale factors.

From Figures 3 to 7, it can be demonstrated that the different entropy distributions of the four types of S-NS for different scale factors are at different levels; for MDE and MFDE, with the increase of scale, the coincidence of MDE and MFDE distributions of Ship I, Ship II, and Ship III becomes more and more obvious, especially for Ship I and Ship II; when the SF is 4 and 5, the MPE distributions of S-NS with 4 different scale factors are more independent and have less overlap; for RCMFRDE and MRDE, when the SF is 1, the distribution of S-NS for each type is at different levels for each scale factor, and the distribution of features for four types of S-NS is obviously different.

As evidenced by Table 2, the number of misidentified samples and the average recognition rate of the four S-NSs

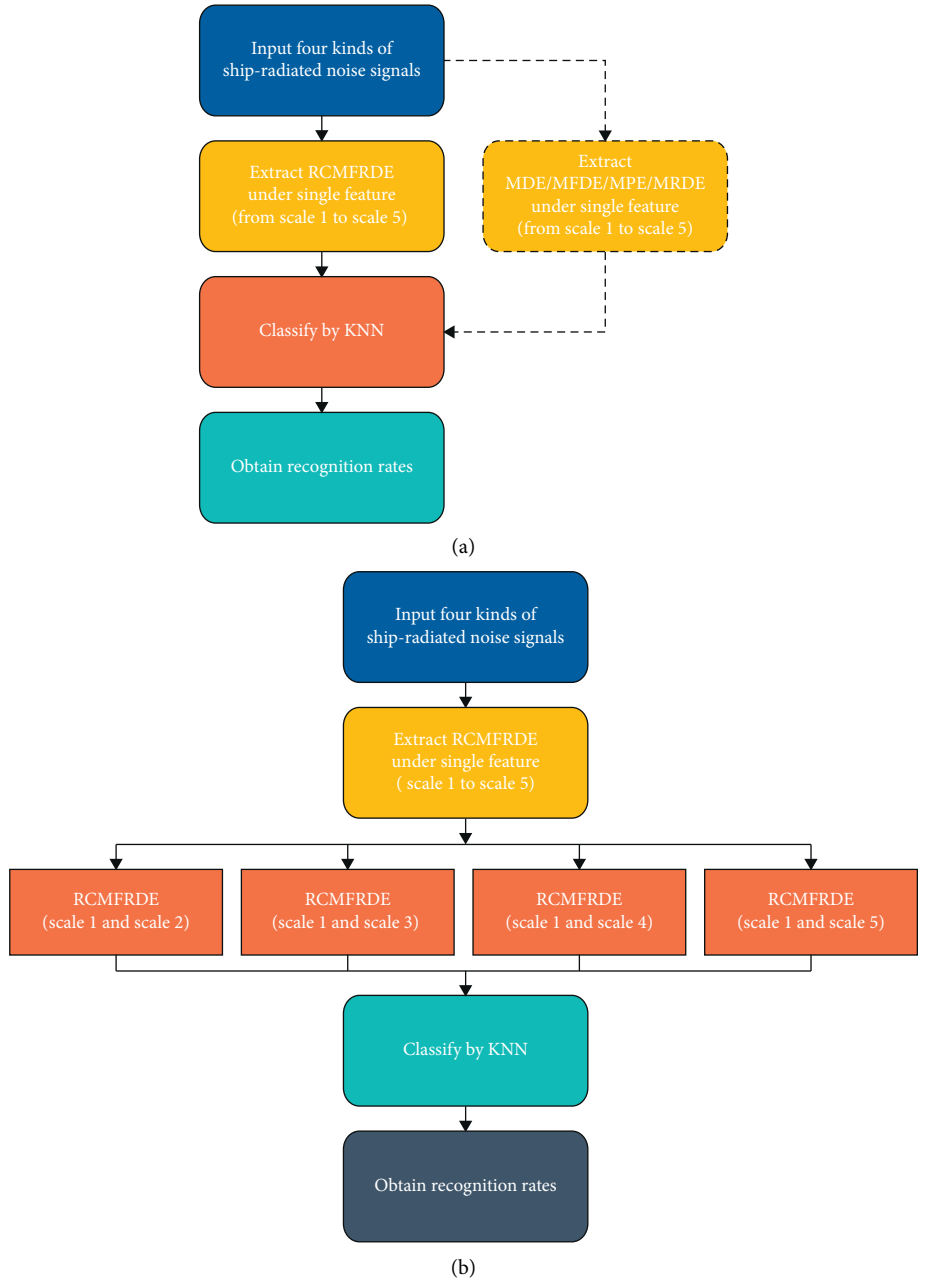

Figure 1: The flowcharts of extracting features. (a) Single feature. (b) Double feature.

under different entropies and different scale factors differ to different degrees; for RCMFRDE, three samples of ship IV are misidentified when the scale is 1; with the increase of scale, the number of misidentified samples of ship I, ship II, and ship III gradually increases, leading to a decrease in the average recognition rate of RCMFRDE; for MDE and MFDE, the three samples of ship IV are incorrectly recognized when SF is 1, while ship IV can be correctly recognized under other scale factors. We can conclude that the same feature extraction method has different recognition abilities for various types of S-NS under different scale factor conditions.

The experimental results proved that for all entropies, RCMFRDE has the highest recognition rate at scale 1, up to 99.75%, which is 10.19% higher than the other average recognition rates. However, while using only one feature, four types of S-NS cannot be fully recognized by RCMFRDE. For the sake of reducing the number of error samples and further improving the average recognition rate, the experiment of double feature extraction is carried out.

5. Double Feature Extraction of the Four Types of S-NS

5.1. Double Feature Extraction. The feature (SF1) with the highest average recognition rate of RCMFRDE is combined with other scale factors for double feature extraction. There are four cases, including SF1 and SF2, SF1 and SF3, SF1 and

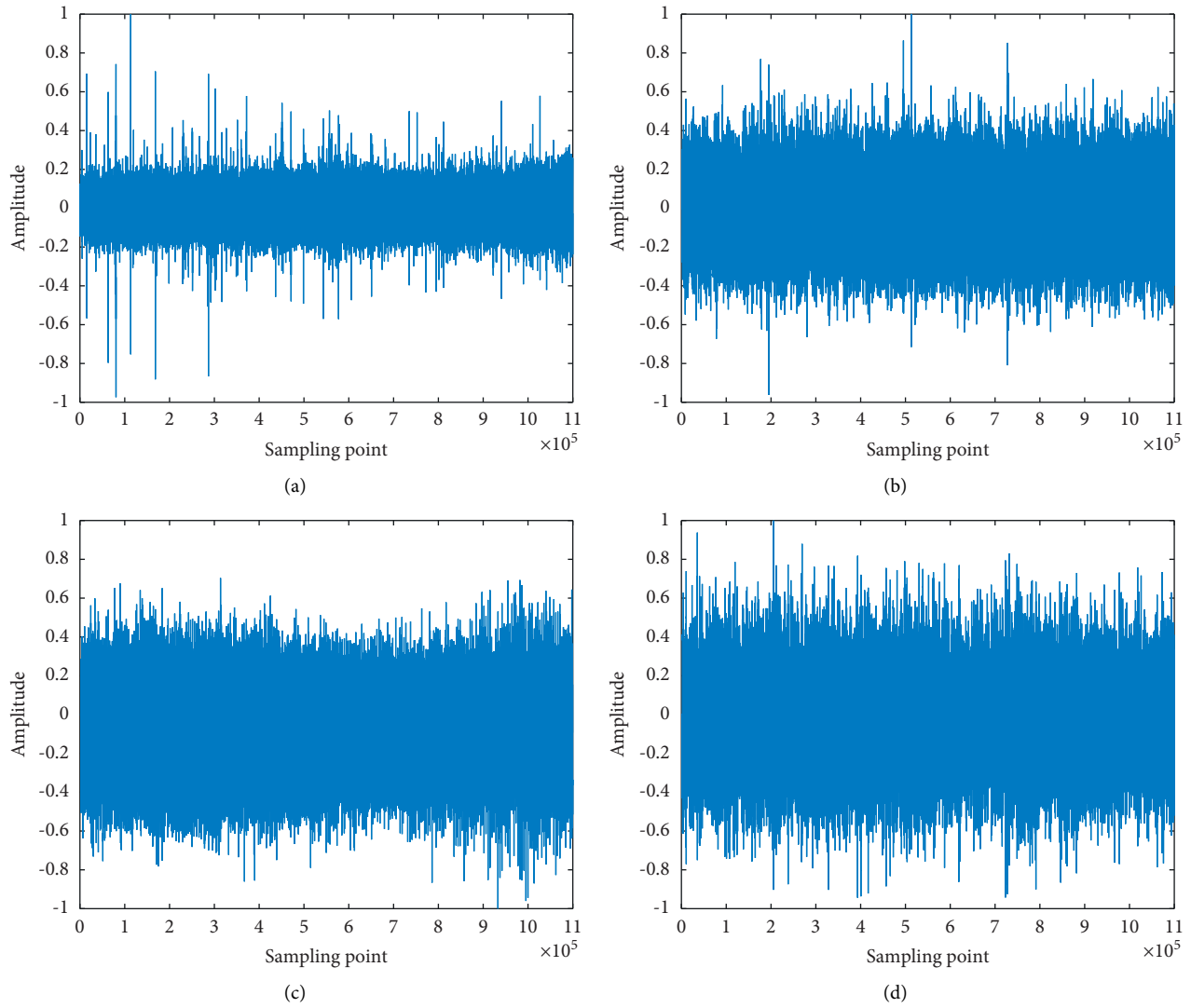

Figure 2: The normalized results of four types of S-NS. (a) Ship I. (b) Ship II. (c) Ship III. (d) Ship IV.

Table 1: Parameter settings of five kinds of entropies.

Entropy	Embedding dimension m	Time delay τ	Category number c	Mapping method	Scale s
RCMFRDE	4	1	5	NCDF	1,2,3,4,5
MDE	4	1	5	NCDF	1,2,3,4,5
MFDE	4	1	5	NCDF	1,2,3,4,5
MPE	4	1	-	—	1,2,3,4,5
MRDE	4	1	5	NCDF	1,2,3,4,5

SF4, and SF1 and SF5. Figures 8 to 12, respectively, express the distribution of five kinds of entropies for four types of S-NS under double features.

According to Figures 8 to 12, for the five kinds of entropies, Ship I and Ship IV are obviously different and easy to distinguish, while the difference between Ship II and Ship III is not obvious and difficult to distinguish; for Ship II and Ship III, RCMFRDE, MDE, and MFDE can distinguish them easily in all four cases, while other entropies cannot distinguish them completely.

5.2. Double Feature Classification and Recognition. For further comparing the double feature extraction effects of RCMFRDE, MDE, MFDE, MPE, and MRDE, KNN is applied to classify four types of S-NS, similar to feature classification and recognition, in which K value is selected as 1. Table 3 is the classification and recognition results of four types of S-NS under double features.

As shown in Table 3, only RCMFRDE can fully identify Ship III; all entropies except MRDE can fully identify Ship IV; among all combinations of entropies, the RCMFRDE-

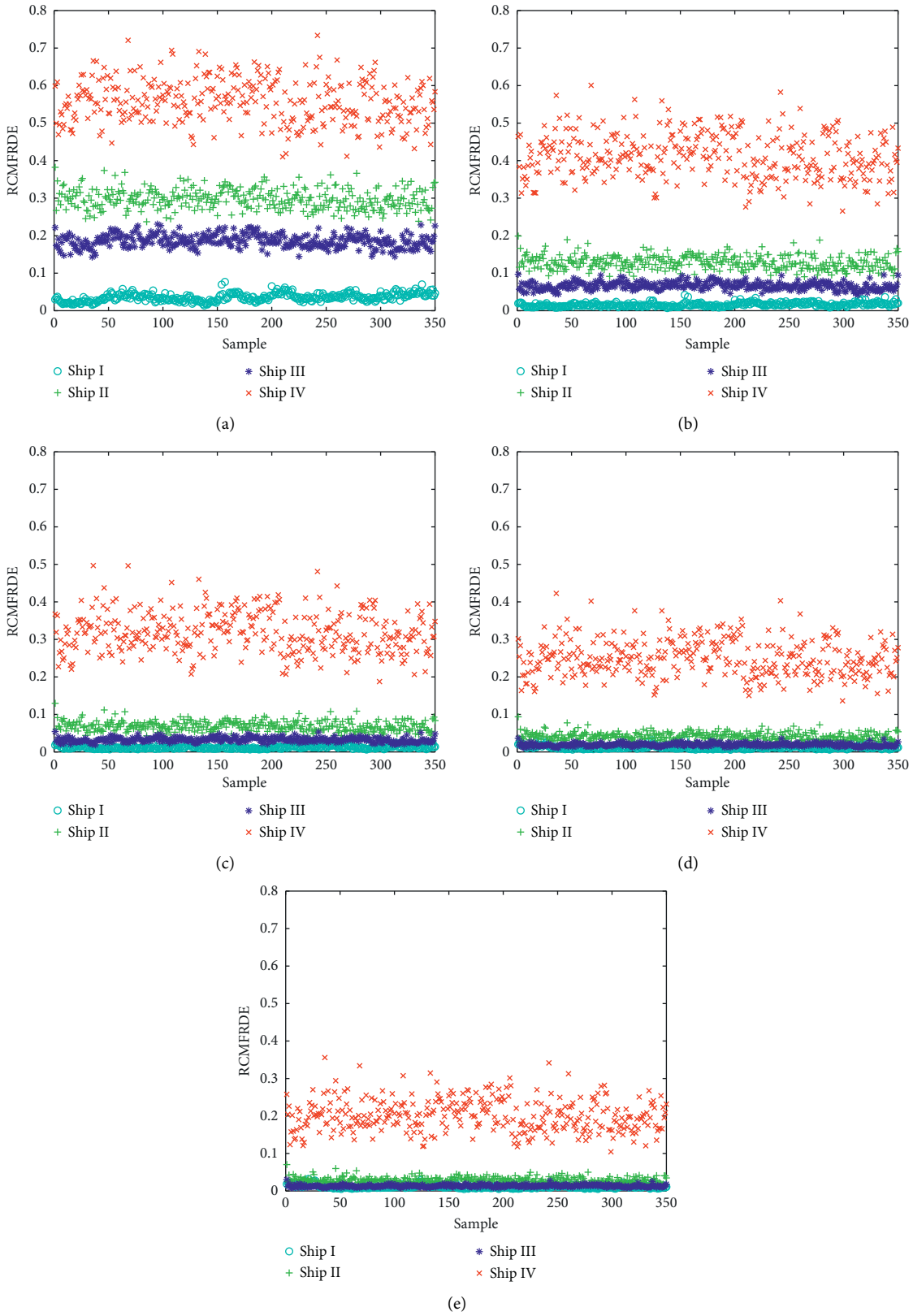

Figure 3: The distribution of RCMFRDE for four types of S-NS for different scale factors. (a) SF1. (b) SF2. (c) SF3. (d) SF4. (e) SF5.

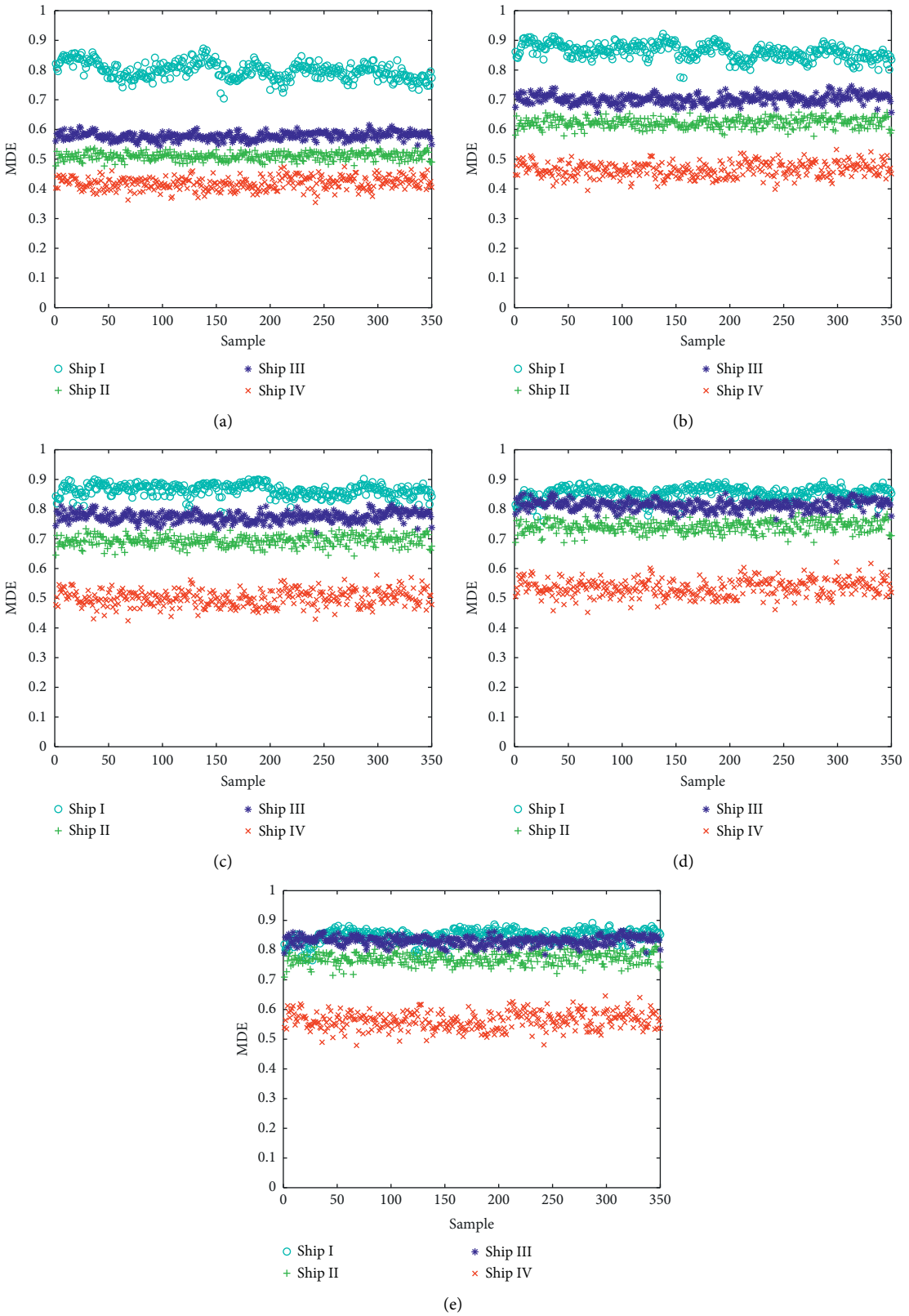

Figure 4: The distribution of MDE for four types of S-NS for different scale factors. (a) SF1. (b) SF2. (c) SF3. (d) SF4. (e) SF5.

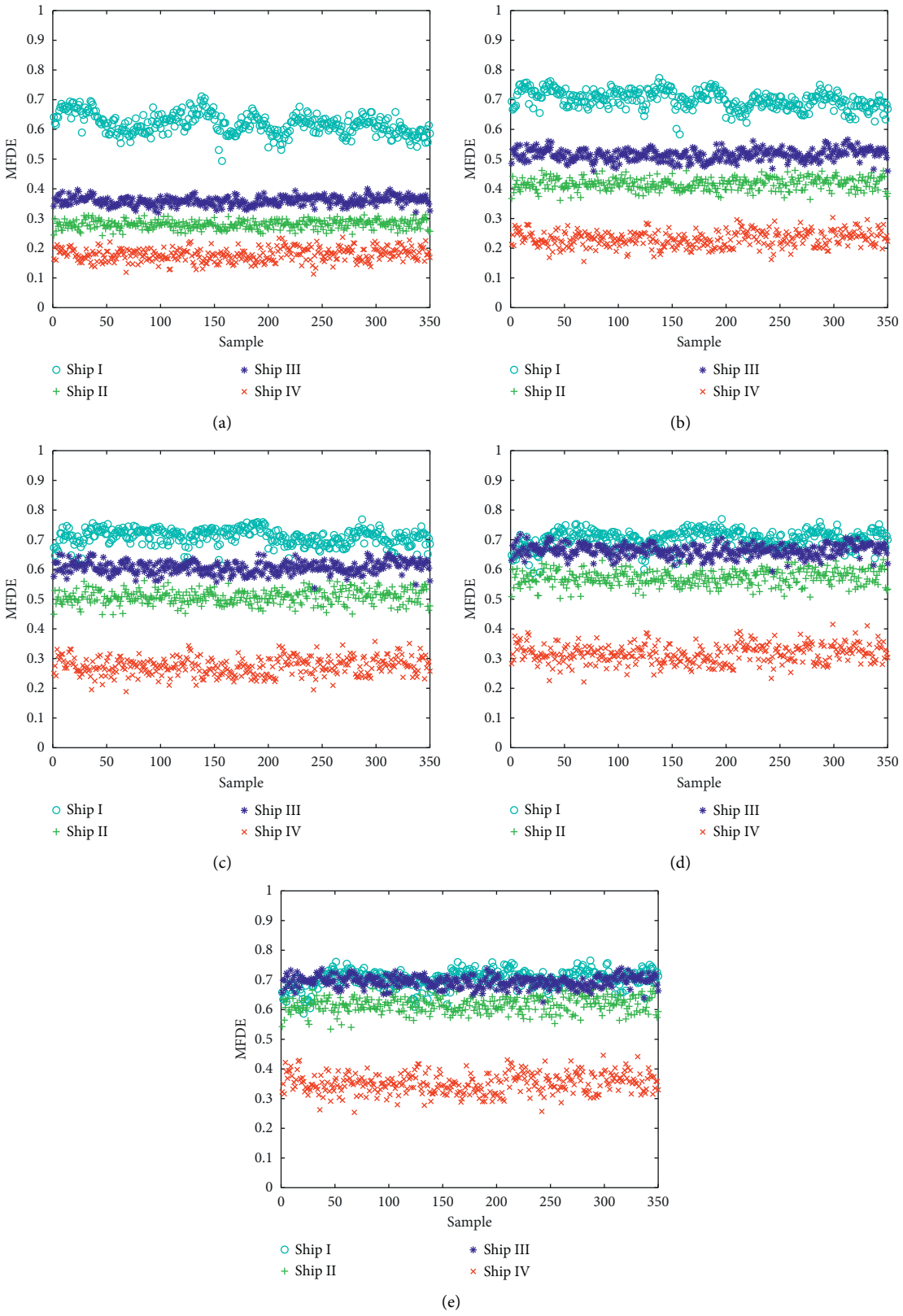

Figure 5: The distribution of MFDE for four types of S-NS for different scale factors. (a) SF1. (b) SF2. (c) SF3. (d) SF4. (e) SF5.

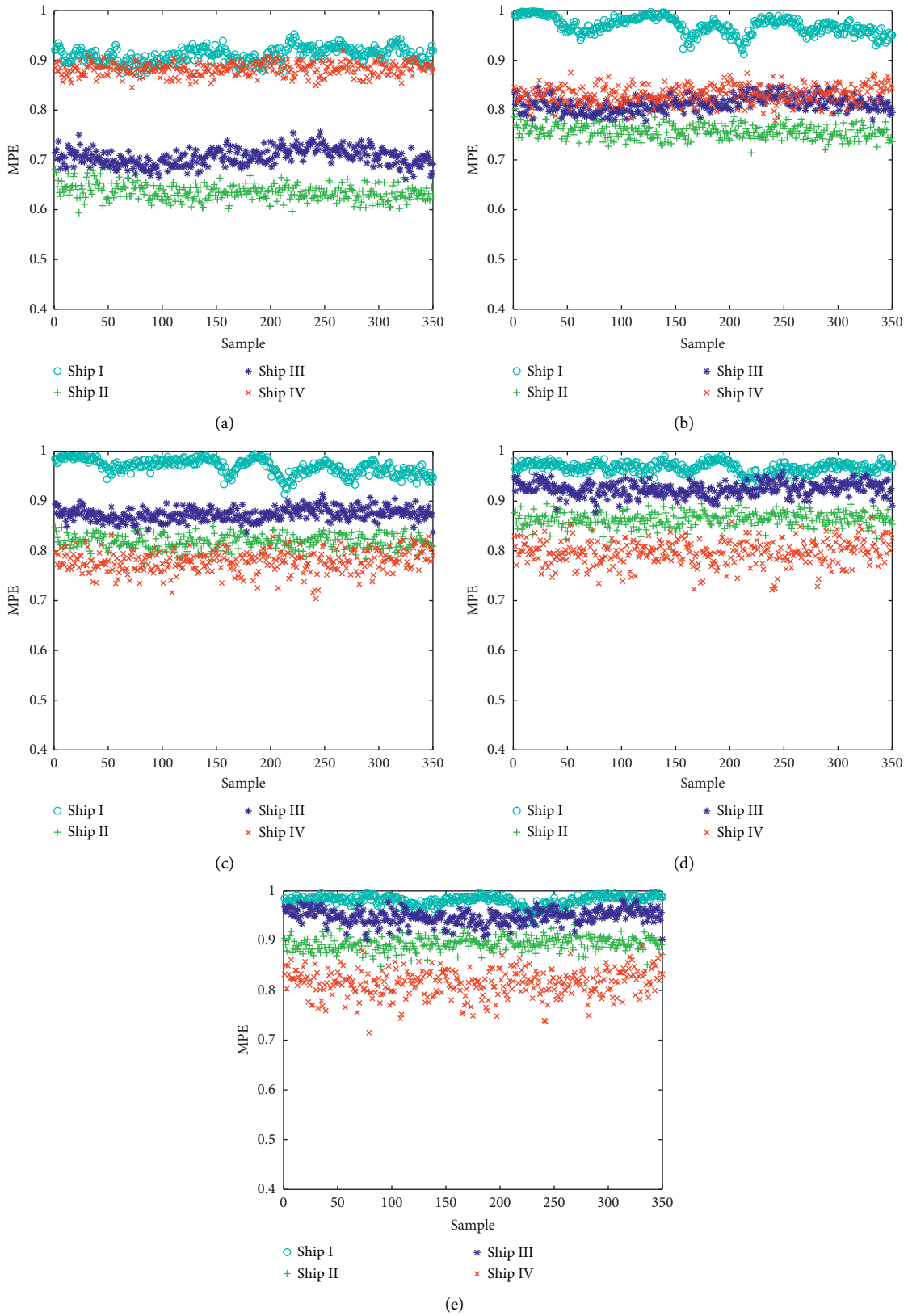

Figure 6: The distribution of MPE for four types of S-NS for different scale factors. (a) SF1. (b) SF2. (c) SF3. (d) SF4. (e) SF5.

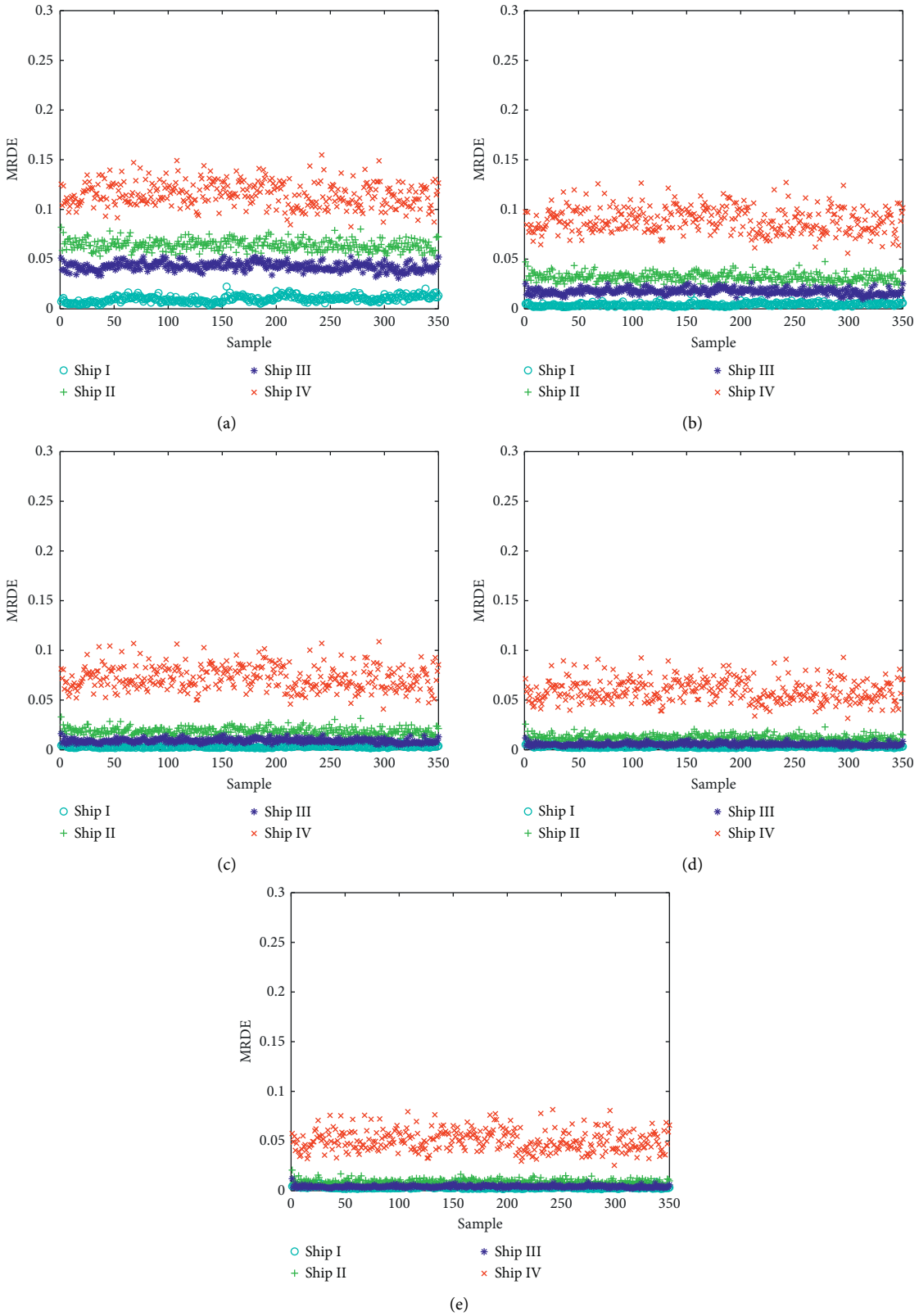

Figure 7: The distribution of MRDE for four types of S-NS for different scale factors. (a) SF1. (b) SF2. (c) SF3. (d) SF4. (e) SF5.

Table 2: The classification and recognition results of four types of S-NS under single feature.

Scale	Feature	Number of incorrectly identified samples				Average recognition rate (%)
		Ship I	Ship II	Ship III	Ship IV	
1	RCMFRDE	0	0	0	3	99.75
	MDE	0	0	2	3	99.58
	MFDE	0	0	5	3	99.33
	MPE	47	1	24	85	86.92
	MRDE	0	0	5	4	99.25
2	RCMFRDE	4	10	13	0	97.75
	MDE	2	0	2	0	99.67
	MFDE	2	0	7	0	99.25
	MPE	0	5	118	108	80.75
	MRDE	5	1	14	0	98.33
3	RCMFRDE	10	11	26	0	96.08
	MDE	5	0	8	0	98.92
	MFDE	8	0	28	0	97.00
	MPE	1	70	5	63	88.42
	MRDE	16	12	44	1	93.92
4	RCMFRDE	80	27	120	0	81.08
	MDE	67	14	104	0	84.58
	MFDE	94	17	120	0	80.75
	MPE	46	19	7	20	92.33
	MRDE	56	18	129	1	83.00
5	RCMFRDE	167	59	137	0	69.75
	MDE	120	42	129	0	75.75
	MFDE	153	62	147	0	69.83
	MPE	68	13	23	6	90.83
	MRDE	109	72	145	1	72.75

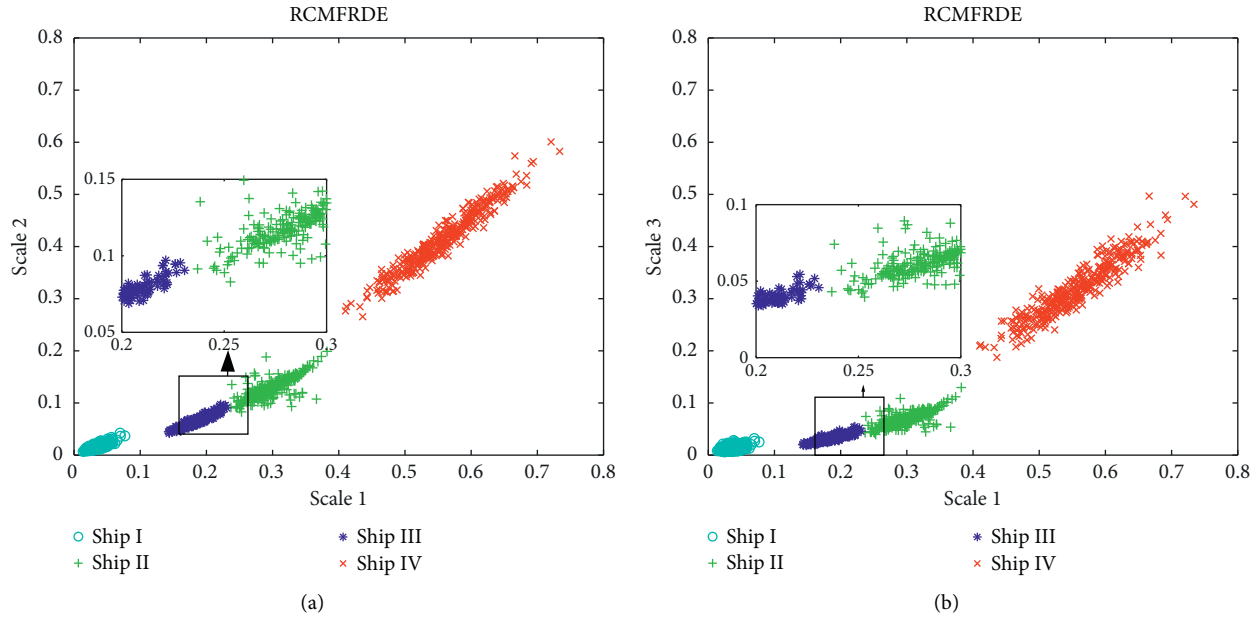

Figure 8: Continued.

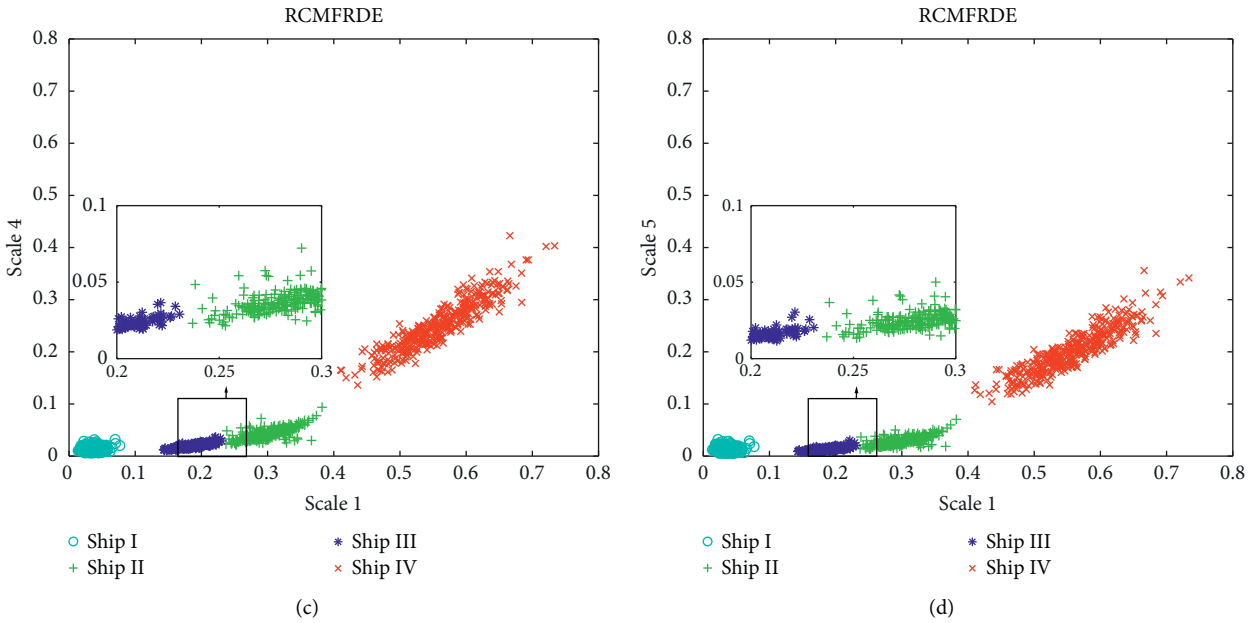

Figure 8: The distribution of RCMFRDE for four types of S-NS under double features. (a) SF1 and SF2. (b) SF1 and SF3. (c) SF1 and SF4. (d) SF1 and SF5.

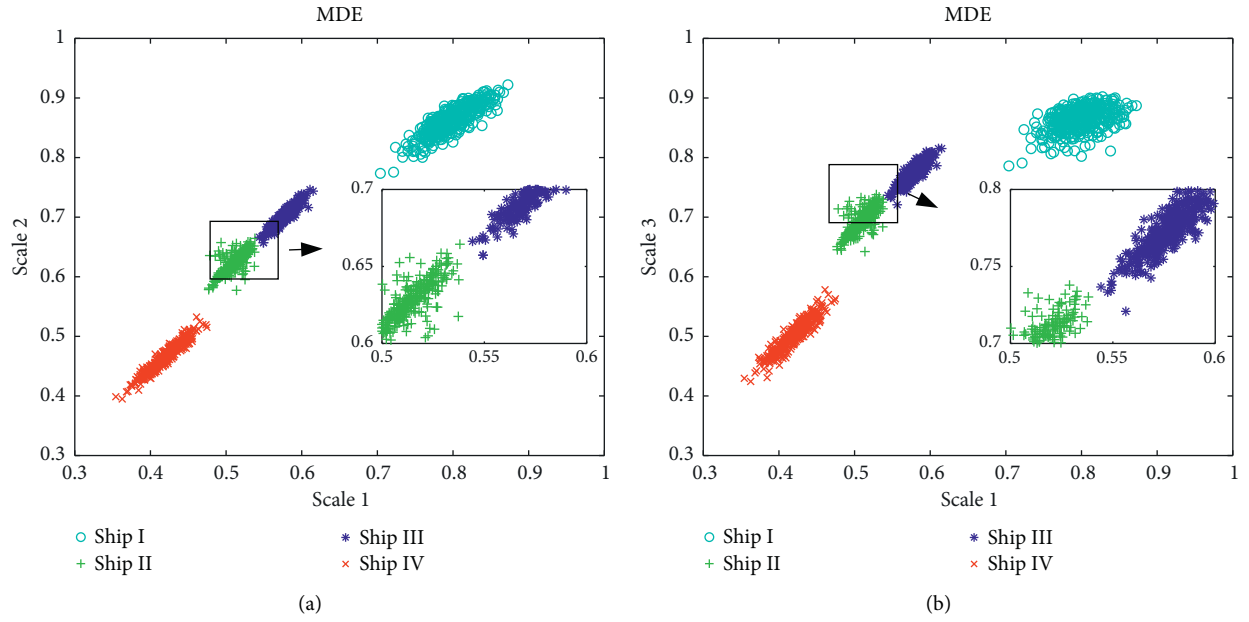

Figure 9: Continued.

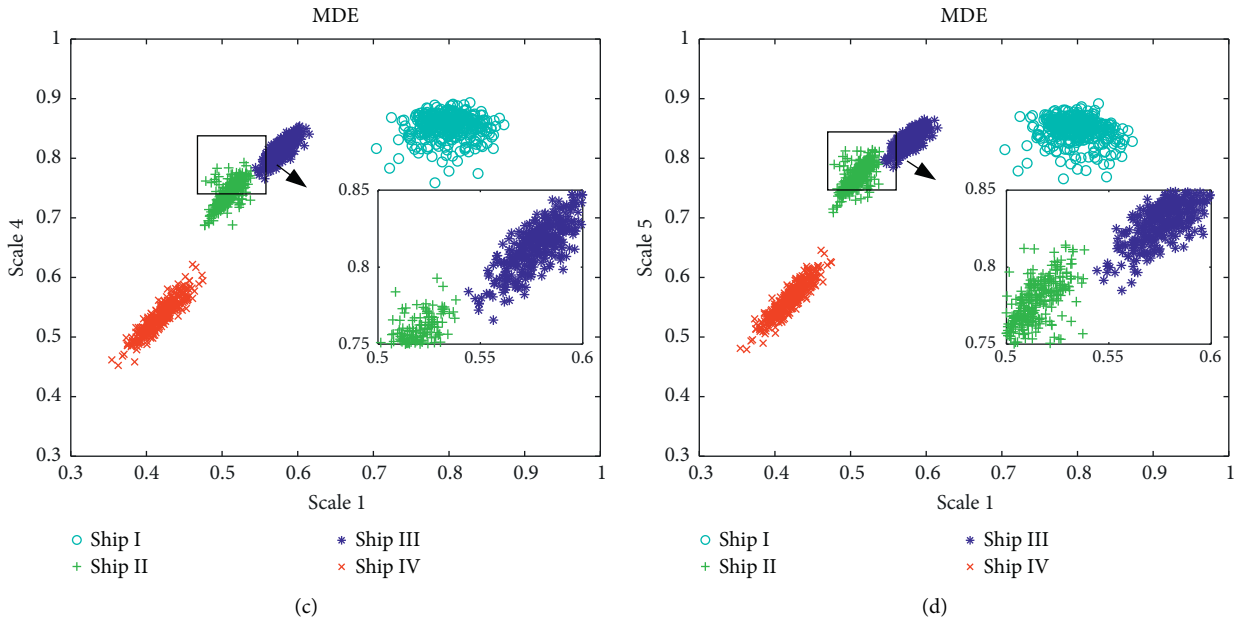

Figure 9: The distribution of MDE for four types of S-NS under double features. (a) SF1 and SF2. (b) SF1 and SF3. (c) SF1 and SF4. (d) SF1 and SF5.

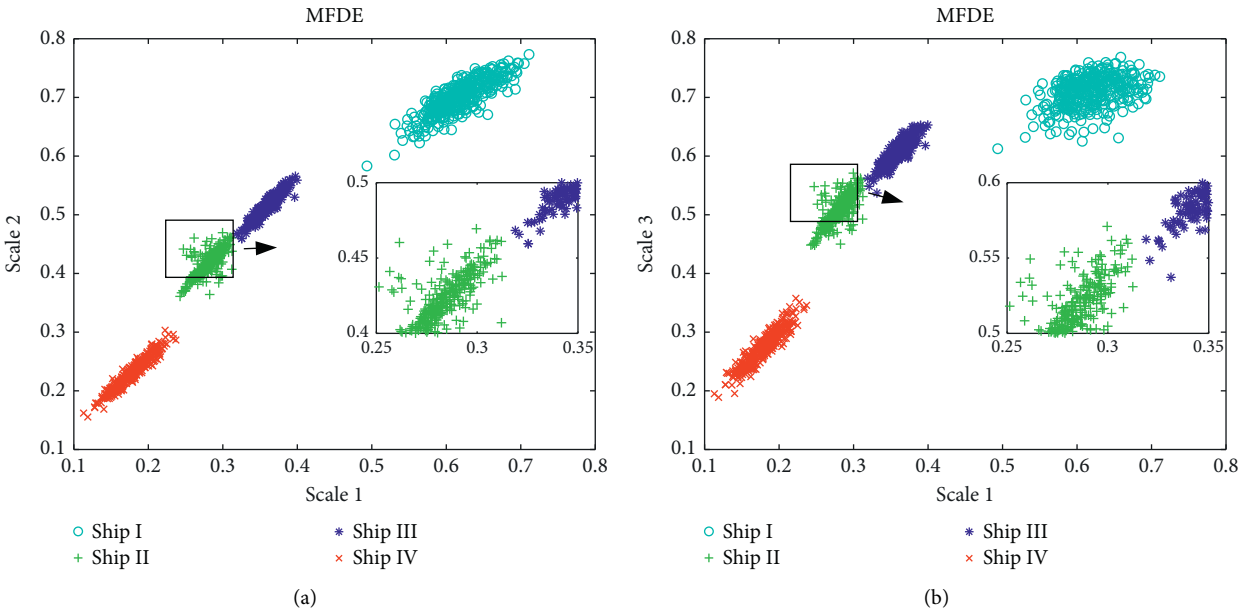

Figure 10: Continued.

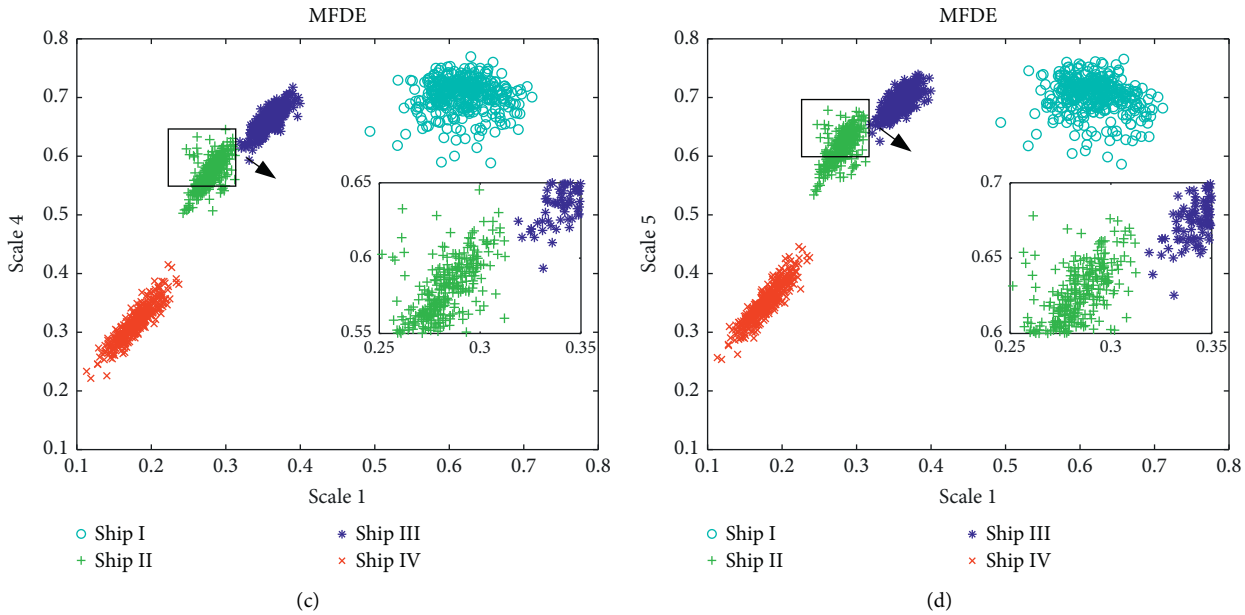

Figure 10: The distribution of MFDE for four types of S-NS under double features. (a) SF1 and SF2. (b) SF1 and SF3. (c) SF1 and SF4. (d) SF1 and SF5.

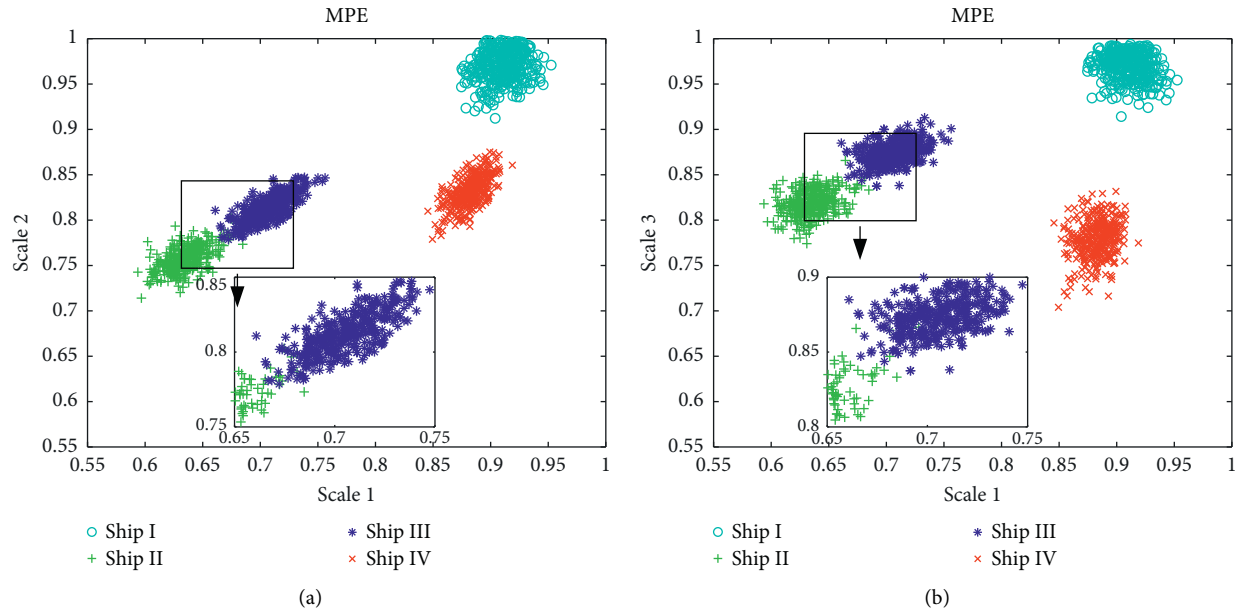

Figure 11: Continued.

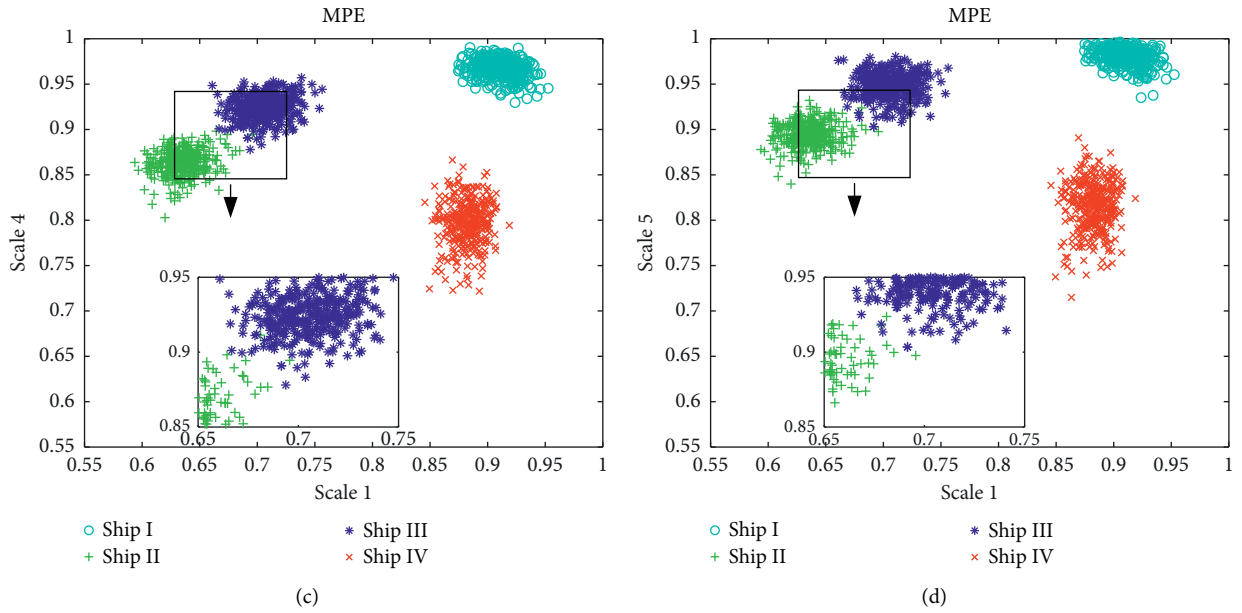

FIGURE 11: The distribution of MPE for four types of S-NS under double features. (a) SF1 and SF2. (b) SF1 and SF3. (c) SF1 and SF4. (d) SF1 and SF5.

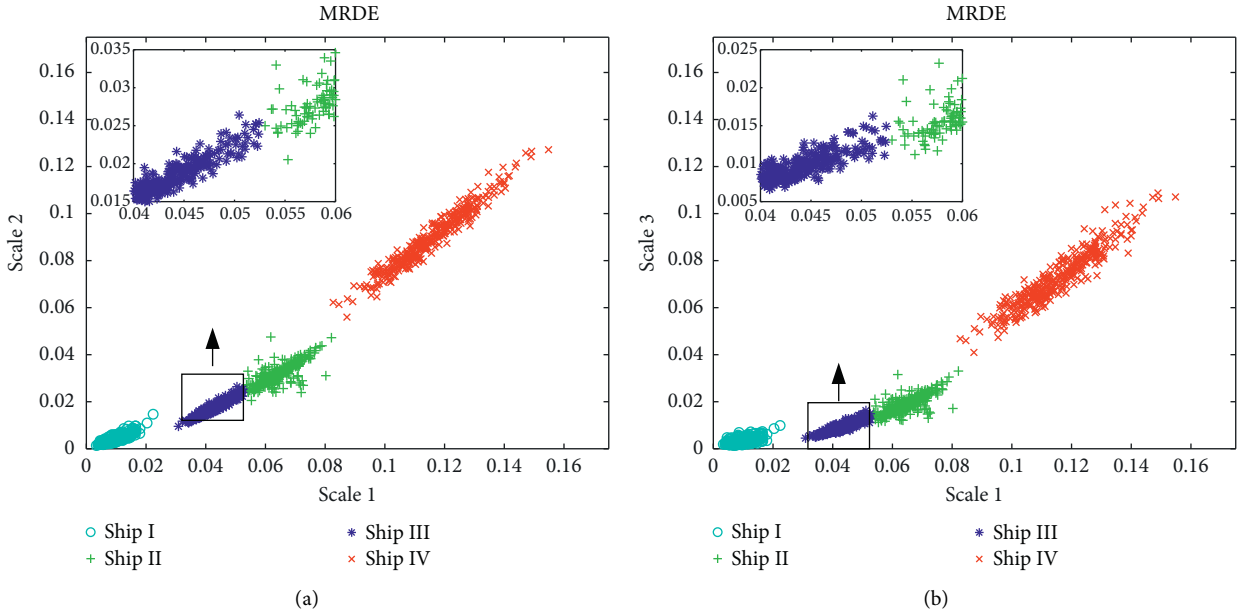

FIGURE 12: Continued.

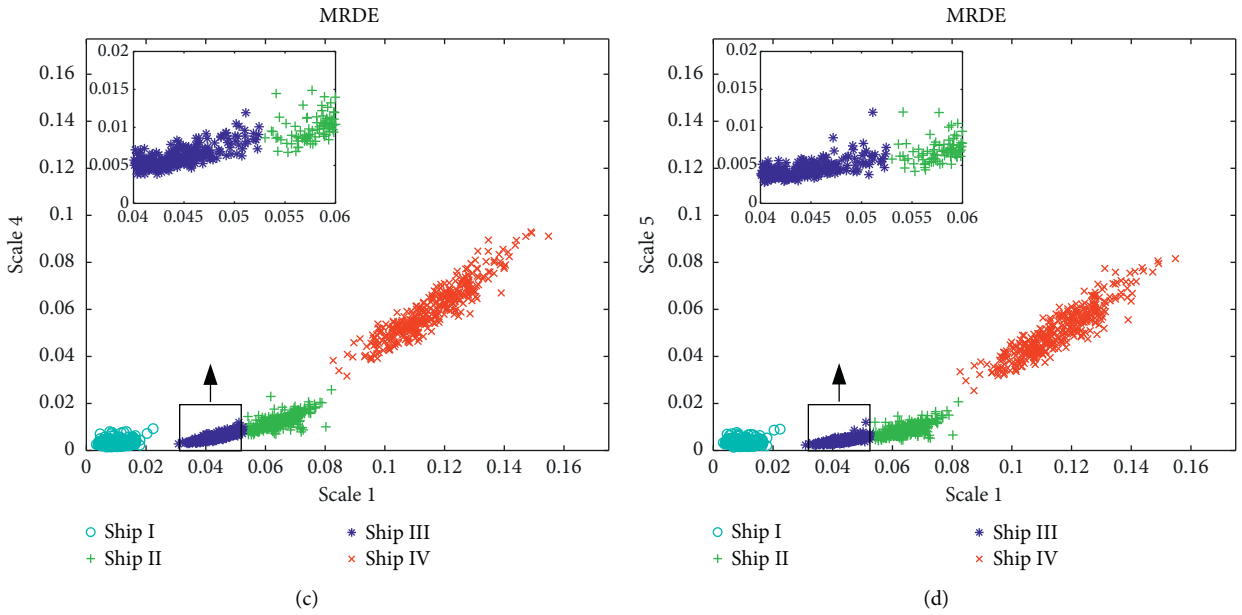

Figure 12: The distribution of MRDE for four types of S-NS under double features. (a) SF1 and SF2. (b) SF1 and SF3. (c) SF1 and SF4. (d) SF1 and SF5.

Table 3: The classification and recognition results of four types of S-NS under double features.

Scales	Feature	Number of incorrectly identified samples				Average recognition rate (%)
		Ship I	Ship II	Ship III	Ship IV	
1 and 2	RCMFRDE	0	0	0	0	100.00
	MDE	0	0	3	0	99.75
	MFDE	1	0	5	0	99.50
	MPE	0	1	20	0	98.25
	MRDE	1	0	6	1	99.33
1 and 3	RCMFRDE	0	0	0	0	100.00
	MDE	0	0	3	0	99.75
	MFDE	1	0	7	0	99.33
	MPE	0	3	7	0	99.17
	MRDE	1	1	14	1	98.58
1 and 4	RCMFRDE	0	0	0	0	100.00
	MDE	0	0	4	0	99.67
	MFDE	1	0	7	0	99.33
	MPE	0	2	6	0	99.33
	MRDE	0	1	16	2	98.42
1 and 5	RCMFRDE	0	0	0	0	100.00
	MDE	0	0	3	0	99.75
	MFDE	1	0	6	0	99.42
	MPE	0	0	5	0	99.58
	MRDE	0	1	18	1	98.33

based feature extraction method combined with two scales has the highest recognition rate of S-NS up to 100%.

In summary, compared with the single scale condition, the average recognition rate of RCMFRDE is improved, utilizing 13.05%. The double feature extraction method of RCMFRDE for S-NS can fully recognize four types of S-NS.

6. Conclusions

In this paper, RCMFRDE is proposed on the basis of FRDE and applied to S-NS feature extraction. The feasibility of the proposed method is verified through feature extraction and classification recognition experiments on four types of measured S-NS, and the main conclusions are drawn as follows:

(1) Based on the theory of DE, this paper introduces the operation of refined composite by combining the advantages of RDE and MFDE and proposes RCMFRDE for S-NS feature extraction.

(2) Compared with the other four single feature extraction methods, the recognition rate of the RCMFRDE-based single feature extraction method

proposed in this paper is the highest and reaches 99.75%, which is 10.19% higher than the other average recognition rates.

(3) The proposed double feature extraction method further improves the classification performance of the single feature extraction method. Compared with the other four double feature extraction methods, the RCMFRDE-based double feature extraction method has the best recognition of the four types of S-NS with a recognition rate of 100%.

Data Availability

The data used to support the findings of this study are available from the corresponding author upon request.

Conflicts of Interest

The authors declare that they have no conflicts of interest.

References

[1] J. D. Tucker and M. R. Azimi-Sadjadi, "Coherence-based underwater target detection from multiple disparate sonar platforms," *IEEE Journal of Oceanic Engineering*, vol. 36, no. 1, pp. 37–51, 2011.

[2] S. Siddagangaiah, Y. Li, X. Guo, and K. Yang, "On the dynamics of ocean ambient noise: two decades later," *Chaos: An Interdisciplinary Journal of Nonlinear Science*, vol. 25, no. 10, Article ID 103117, 2015.

[3] S. Wang and X. Zeng, "Robust underwater noise targets classification using auditory inspired time-frequency analysis," *Applied Acoustics*, vol. 78, no. 4, pp. 68–76, 2014.

[4] J. Guo, X. Liu, S. Li, and Z. Wang, "Bearing Intelligent fault diagnosis based on wavelet transform and convolutional neural network," *Shock and Vibration*, vol. 2020, no. 19, 14 pages, Article ID 6380486, 2020.

[5] S. D. Lu, H. W. Sian, M. H. Wang, and C. C. Kuo, "Fault diagnosis of power capacitors using a convolutional neural network combined with the chaotic synchronisation method and the empirical mode decomposition method," *IET Science, Measurement & Technology*, vol. 15, no. 7, pp. 551–561, 2021.

[6] Y. Zhang, Z. Lian, W. Fu, and X. Chen, "An ESR quasi-online identification method for the fractional-order capacitor of forward converters based on variational mode decomposition," *IEEE Transactions on Power Electronics*, p. 1, 2021.

[7] S. Jiao, B. Geng, Y. Li, Q. Zhang, and Q. Wang, "Fluctuation-based reverse dispersion entropy and its applications to signal classification," *Applied Acoustics*, vol. 175, no. 4, Article ID 107857, 2021.

[8] Y. Li, S. Jiao, and B. Geng, "A comparative study of four multi-scale entropies combined with grey relational degree in classification of ship-radiated noise," *Applied Acoustics*, vol. 176, no. 4, Article ID 107865, 2021.

[9] S. Tucker and G. J Brown, "Classification of transient sonar sounds using perceptually motivated features[J]," *IEEE Journal of Ocean Engineering*, vol. 30, no. 3, pp. 588–600, 2011.

[10] R. Pascoal and C. Guedes Soares, "Non-parametric wave spectral estimation using vessel motions," *Applied Ocean Research*, vol. 30, no. 1, pp. 46–53, 2008.

[11] Y. Guo, W. Rao, and Y. Han, "Extraction of higher-order coupling feature using three and one half dimension spectrum," *Applied Mathematics and Computation*, vol. 185, no. 2, pp. 798–809, 2007.

[12] Jović, A. Bogunović, and Nikola, "Feature extraction for ECG time-series mining based on chaos theory," in *Proceedings of the International Conference on Information Technology Interfaces*, no. 2, pp. 64–68, Article ID IEEE, Cavtat, Croatia, June 2007.

[13] C. Ioana, A. Quinquis, and Y. Stephan, "Feature extraction from underwater signals using time-frequency warping operators," *IEEE Journal of Oceanic Engineering*, vol. 31, no. 3, pp. 628–645, 2006.

[14] D. Bruzzone, C. Gironi, and A. Grasso, "Nonlinear effects on motions and loads using an iterative time-frequency solver," *International Journal of Naval Architecture and Ocean Engineering*, vol. 3, no. 1, pp. 20–26, 2011.

[15] B. Yu, Y. H. Li, and P. Zhang, "Application of correlation dimension and kolmogorov entropy in aeroengine fault diagnosis," *Journal of Aerospace Power*, vol. 21, no. 1, pp. 219–224, 2006.

[16] P. Grassberger and I. Procaccia, "Characterization of strange attractors," *Physical Review Letters*, vol. 50, no. 5, pp. 346–349, 1983.

[17] H. J. Shyu and R Hillson, "Integrating ocean acoustic propagation models and marine mammal auditory models," in *Proceedings of the Ocean's 2002 Conference and Exhibition, Marine Technology Society, IEEE, OES, Institute of Electrical and Electronics Engineers Inc.*, Jackson, MI, USA, October 2002.

[18] A. Lempel and J. Ziv, "On the complexity of finite sequences," *IEEE Transactions on Information Theory*, vol. 22, no. 1, pp. 75–81, 1976.

[19] L. Cui, X. Gong, J. Zhang, and H. Wang, "Double-dictionary matching pursuit for fault extent evaluation of rolling bearing based on the lempel-ziv complexity," *Journal of Sound and Vibration*, vol. 385, pp. 372–388, 2016.

[20] M. Kedadouche, T. Kidar, M. Thomas, A. Tahan, M El Badaoui, and R. Guilbault, "Combining EMD and lempel–ziv complexity for early detection of gear cracks," *Proceedings of the International Conference Surveillance*, vol. 7, pp. 100–10, 2013.

[21] D. Abásolo, R. Hornero, C. Gómez, M. García, and M. López, "Analysis of EEG background activity in alzheimer's disease patients with lempel-ziv complexity and central tendency measure," *Medical Engineering & Physics*, vol. 28, no. 4, pp. 315–322, 2006.

[22] M. Aboy, R. Hornero, D. Abasolo, and D. Alvarez, "Interpretation of the lempel-ziv complexity measure in the context of biomedical signal analysis," *IEEE Transactions on Biomedical Engineering*, vol. 53, no. 11, pp. 2282–2288, 2006.

[23] D. Z. Zhang, "Research on the correlation between the mutual information and lempel-ziv complexity of nonlinear time series," *Acta Physica Sinica -Chinese Edition*, vol. 56, no. 6, 2007.

[24] X. Mao, P. Shang, M. Xu, and C. K. Meng, "Measuring time series based on multiscale dispersion lempel–ziv complexity and dispersion entropy plane," *Chaos, Solitons & Fractals*, vol. 137, Article ID 109868, 2020.

[25] Y. Bai, Z. Liang, and X. Li, "A permutation lempel-ziv complexity measure for EEG analysis," *Biomedical Signal Processing and Control*, vol. 19, pp. 102–114, 2015.

[26] C. E. Shannon, "A mathematical theory of communication," *Bell System Technical Journal*, vol. 27, no. 4, pp. 623–656, 1948.

[27] C. Bandt and B. Pompe, "Permutation entropy: a natural complexity measure for time series," *Physical Review Letters*, vol. 88, no. 17, Article ID 174102, 2002.

[28] B. Fadlallah, B. Chen, A. Keil, and J. Principe, "Weighted-permutation entropy: a complexity measure for time series incorporating amplitude information," *Physical Review E Statistical Nonlinear & Soft Matter Physics*, vol. 87, no. 2, Article ID 022911, 2013.

[29] Y. Li, Y. Li, X. Chen, and Y. Jing, "A novel feature extraction method for ship-radiated noise based on variational mode decomposition and multi-scale permutation entropy," *Entropy*, vol. 19, no. 7, 2017.

[30] H. Azami and J. Escudero, "Amplitude-aware permutation entropy: illustration in spike detection and signal segmentation," *Computer Methods and Programs in Biomedicine*, vol. 128, pp. 40–51, 2016.

[31] M. Rostaghi and H. Azami, "Dispersion entropy: a measure for time-series analysis," *IEEE Signal Processing Letters*, vol. 23, no. 5, pp. 610–614, 2016.

[32] J. Zheng, H. Pan, Q. Liu, and K. Ding, "Refined time-shift multiscale normalised dispersion entropy and its application to fault diagnosis of rolling bearing," *Physica A: Statistical Mechanics and its Applications*, vol. 545, Article ID 123641, 2019.

[33] H. Azami, M. Rostaghi, D. Abásolo, and J. Escudero, "Refined composite multiscale dispersion entropy and its application to biomedical signals," *IEEE transactions on bio-medical engineering*, vol. 99, p. 1, 2017.

[34] J. Zheng and H. Pan, "Use of generalized refined composite multiscale fractional dispersion entropy to diagnose the faults of rolling bearing," *Nonlinear Dynamics*, vol. 101, no. 2, pp. 1417–1440, 2020.

[35] H. Azami and J. Escudero, "Amplitude- and fluctuation-based dispersion entropy," *Entropy*, vol. 20, no. 3, p. 210, 2018.

[36] Y. X. Li, S. B. Jiao, and X. Gao, "A novel signal feature extraction technology based on empirical wavelet transform and reverse dispersion entropy," *Defence Technology*, vol. 17, no. 5, pp. 1625–1635, 2021.

[37] L. Ma, M. Crawford, and J. Tian, "Local manifold learning-based k-nearest-neighbor for hyperspectral image classification," *IEEE Transactions on Geoscience & Remote Sensing*, vol. 48, no. 11, pp. 4099–4109, 2010.

[38] X. Ran, X. Zhou, M. Lei, W. Tepsan, and W. Deng, "A novel k-means clustering algorithm with a noise algorithm for capturing urban hotspots," *Applied Sciences*, vol. 11, no. 23, Article ID 11202, 2021.

Hindawi
Mathematical Problems in Engineering
Volume 2021, Article ID 6980715, 28 pages
https://doi.org/10.1155/2021/6980715

Research Article

Antidisturbance Control for Helicopter Stochastic Systems

Dongping Li[1] and Yankai Li[2]

[1]*School of Sciences, Xi'an Technological University, Xi'an 710021, China*
[2]*Institute of Automation and Information Engineering, Xi'an University of Technology, Xi'an 710048, China*

Correspondence should be addressed to Yankai Li; liyankai@xaut.edu.cn

Received 25 August 2021; Revised 6 October 2021; Accepted 15 October 2021; Published 16 November 2021

Academic Editor: Akif Akgul

In this paper, an antidisturbance controller is presented for helicopter stochastic systems under disturbances. To enhance the antidisturbance abilities, the nonlinear disturbance observer method is applied to reject the time-varying disturbances. Then, the antidisturbance nonlinear controller is designed by combining the backstepping control scheme. And the stochastic theory is used to guarantee that the closed-loop system is asymptotically bounded in mean square while the proposed control method is shown via some traditional nonlinear control techniques, which still show some common issues such as "dimension explosion" or others. The result of this paper can be regarded as a typical case of the nonlinear control method to help and promote the generation of advanced methods.

1. Introduction

For actual systems, the nonlinearities of the model are probably one of the most noticeable characteristics, which are issued from the physical laws, material science, mathematical derivation, and so on. Hence, nonlinear systems are typical research models in various control fields and can be used to describe the dynamics of the system states. In order to handle nonlinear control problems, many classical control methods were proposed based on the nonlinear control theory [1–3], such as the baskstepping control method, feedback linearization technique, and nonlinear disturbance observer-based control scheme. Based on these nonlinear control theories, a number of advanced control techniques were proposed for various control systems. In [4], a class of nonlinear systems was studied via the event-triggered robust adaptive fuzzy control method. In [5], the adaptive neural control scheme was adopted for the nonlinear multiple output systems under the time-varying output constraints. Combining the nonlinear disturbance observer control with sliding-mode fuzzy neural network methods, a new control scheme was presented to deal with the nonlinear systems with disturbances in [6]. In [7, 8], the issue of adaptive fuzzy tracking control was discussed for a class of strict-feedback nonlinear systems. In [9], the periodic event-triggered control method was used to design the controller for nonlinear networked control systems. In [10], the robust adaptive control problem was investigated for state-constrained nonlinear systems under the input saturation and unknown control direction. The observer-based H_∞ control was used for discrete-time T-S fuzzy systems in [11]. In [12], the switched-observer-based adaptive output-feedback control scheme was designed for pure-feedback switched nonlinear systems with unknown gains. The model-based adaptive event-triggered control method was discussed for nonlinear continuous-time systems in [13]. From the above discussion, the nonlinear control methods and theories are effective for disposing many troublesome nonlinear control problems. Therefore, the nonlinear control system theories are useful approaches to solve the issues of flight control for helicopters.

The flight control is a crucial issue of helicopters. An excellent flight controller guarantees the well flight performances of flying helicopters and prevents the crash, breakdown, and so on. In many books involving helicopters [14, 15], linear control methods were used for designing the helicopter flight controller and obtained expected control performances while, in fact, helicopter models are

complicated nonlinear systems, which are constructed according to the relationships of the components of helicopters. In some outstanding results, the helicopter flight controllers are designed by using the linear models, which are evolved from the nonlinear helicopter models under the linearization techniques. In [16], the tracking control issue was discussed for small-scale unmanned helicopter linear systems. In [17], the flight controller was designed for helicopters via the probabilistic robust linear parameter-varying control method using the iterative scenario approach. In [18], the model reference resilient control methods were designed for linear helicopter systems with time-varying disturbances. In [19], tracking control issues were discussed for the linear helicopter systems under time-varying disturbances and input stochastic perturbation. However, the dynamics of the helicopter states are complicated with many nonlinear characteristics. With development of the helicopter flight control techniques, the nonlinear flight controllers are designed for various helicopter systems. In [20], the adaptive trajectory tracking control approach was proposed for model-scaled nonlinear helicopter systems. The trajectory tracking control problems were discussed for small-scale nonlinear unmanned helicopters under model uncertainties in [21]. In [22], the composite block backstepping trajectory tracking control scheme was presented for disturbed nonlinear unmanned helicopter systems. In [23], the fixed-time autonomous shipboard landing control issues were studied for nonlinear helicopter systems under external disturbances. The finite-time control issue was discussed for small-scale nonlinear unmanned helicopter systems with disturbances in [24]. In [25], the sliding-mode control and extended disturbance observer methods were used to solve the tracking control issue of unmanned nonlinear helicopter systems. The dynamic decoupling control optimization methods were adopted for small-scale nonlinear unmanned helicopter systems in [26]. While helicopters fly in full noise surroundings, various random disturbances exist in helicopter control system models. In [27], the antidisturbance control was proposed for the attitude and altitude nonlinear helicopter systems under random disturbances. The random disturbances are considered for flight control, which improves the control performances and precision of flying helicopters.

In this paper, in order to enhance the control precision and robustness of the helicopter models, the random disturbances are considered to construct the fight controller. The helicopter stochastic systems are better to describe the flying dynamics states of the helicopter. While with the random disturbances introducing in the models, many advanced control methods, such as dynamic surface control, fuzzy control, and other intelligent control methods, cannot be used to design the flight controller directly because many control variables will lose some good characteristics, such as the continuity and derivability, under the random disturbances. Therefore, in this manuscript, the backstepping control method and nonlinear disturbance observer control scheme are used to establish the nonlinear flight controller. Due to the characteristics of underactuation, strong nonlinearity, and high-order of helicopter stochastic system models, the phenomenon of "dimension explosion" is inevitable for nonlinear controller designed, and the controller solved steps are presented in this paper. Our results present an approach to design the strong robust flight controller.

The organization of this paper is standard. The problem statement is stated in Section 2. The position loop control issues are discussed in Section 3. The attitude loop control problems are studied in Section 4. The stability analysis of the main result is given in Section 5. The conclusions are presented in Section 6.

2. Problem Statement

Consider the following helicopter dynamic system:

$$\begin{aligned} \mathrm{d}p &= v\,\mathrm{d}t, \\ \mathrm{d}v &= \left(-ge_3 + \frac{1}{m}Rf\right)\mathrm{d}t + \delta_1\mathrm{d}t + G_1\mathrm{d}\beta_1, \\ \mathrm{d}R &= Rw^{\times}\mathrm{d}t, \\ J\mathrm{d}w &= \left(-w^{\times}Jw + \tau\right)\mathrm{d}t + \delta_2\mathrm{d}t + G_2\mathrm{d}\beta_2, \end{aligned} \tag{1}$$

where p and v denote the position and velocity in inertial frame, respectively, g is the gravitational acceleration, $e_3 = \begin{pmatrix} 0 & 0 & 1 \end{pmatrix}^T$ is a unit vector, and R is the rotation matrix from body frame to inertial frame and defined by

$$\begin{aligned} R &= \begin{pmatrix} C\theta C\psi & S\theta S\phi C\psi - C\phi S\psi & C\phi S\theta C\psi + S\phi S\psi \\ C\theta S\psi & S\phi S\theta S\psi + C\phi C\psi & C\phi S\theta S\psi - S\phi C\psi \\ -S\theta & S\phi C\theta & C\phi C\theta \end{pmatrix} \\ &= \begin{pmatrix} R_{11} & R_{12} & R_{13} \\ R_{21} & R_{22} & R_{23} \\ R_{31} & R_{32} & R_{33} \end{pmatrix} = \begin{pmatrix} R_1 & R_2 & R_3 \end{pmatrix}, \end{aligned} \tag{2}$$

where $C\cdot$ and $S\cdot$ denote $\cos(\cdot)$ and $\sin(\cdot)$ with respective variables. $\phi(t)$, $\theta(t)$, and $\varphi(t)$ are roll, pitch, and yaw angles in body frame, respectively. $w = \begin{pmatrix} p(t) & q(t) & r(t) \end{pmatrix}$ is the angular velocity. p, q, and r are the roll, pitch, and yaw angular rates, respectively. J is the inertia matrix and denoted by $J = \mathrm{diag}\{J_{xx} \;\; J_{yy} \;\; J_{zz}\}$. f and τ are the sum of the external forces and moments. Consider the characteristics of these forces and moments, which are denoted as follows:

$$f = \begin{pmatrix} 0 & 0 & T_m \end{pmatrix}^T,$$
$$\tau_u = \begin{pmatrix} C_m + T_m L_z - H_z \\ C_m + T_m L_z 00 \\ -T_m L_y T_m L_x H_x \end{pmatrix} \begin{pmatrix} a \\ b \\ T_t \end{pmatrix} + \begin{pmatrix} -T_m L_y \\ -T_m L_x \\ -Q_m \end{pmatrix} = A(T_m)\rho + B(T_m), \tag{3}$$

with $Q_m = C_k T_m^{1.5} + D_k$. C_m, L_z, H_z, L_y, L_x, H_x, and D_k are known constants. β_1 and β_2 are independent one-dimensional standard Wiener processes, $(d\beta_1/dt) = \xi_1$ and $(d\beta_2/dt) = \xi_2$, where ξ_1 and ξ_2 are independent one-dimensional stochastic noises. $G_1\xi_1$ and $G_2\xi_2$ are the stochastic accelerated velocity and stochastic angular acceleration generated by the stochastic force and stochastic moment, G_1 and G_2 are known and bounded weight parameters, and δ_1 and δ_2 are disturbances with bounded derivatives, which are $\|\dot{\delta}_1\| \le \mu_1$ and $\|\dot{\delta}_2\| \le \mu_2$.

The following definitions and lemmas are crucial important to further analyze the main results of this paper. In order to state those definitions and lemmas, consider the following system:

$$dx = f(t,x)dt + g(t,x)d\beta, \tag{4}$$

where x is the system state, $f \in \mathscr{L}_1(\mathbb{R}_+; \mathbb{R}^n)$ and $g \in \mathscr{L}_2(\mathbb{R}_+; \mathbb{R}^{n\times m})$ are known functions, and β is the one-dimensional standard Wiener process.

For $V(t,x) \in \mathscr{C}^{2,1}(\mathbb{R}; \mathbb{R}^n \times \mathbb{R}_+)$, the infinitesimal generator along (4) is defined by

$$\mathscr{L}V(t,x) = V_t(t,x) + V_x(t,x)f(t,x) + \frac{1}{2}\mathrm{Tr}\left[g^T(t,x)V_{xx}(t,x)g(t,x)\right], \tag{5}$$

where Tr is the trace of a matrix, and

$$V_t(t,x) = \frac{\partial V(t,x)}{\partial t},$$
$$V_x(t,x) = \left(\frac{\partial V(t,x)}{\partial \vartheta_1}, \ldots, \frac{\partial V(t,x)}{\partial \vartheta_n}\right), \tag{6}$$
$$V_{xx}(t,x) = \left(\frac{\partial^2 V(t,x)}{\partial \vartheta_i \partial \vartheta_j}\right)_{n\times n}.$$

Definition 1 (see [28]). Let $p > 0$. System (4) is said to be asymptotically bounded in p-th moment if there is a positive constant H such that

$$\lim_{t\longrightarrow\infty} \sup E\left|x(t;x_0)\right|^p \le H, \tag{7}$$

for all $(t_0, x_0) \in \mathbb{R}_+ \times \mathbb{R}^n$. When $p = 2$, we say system (4) is asymptotically bounded in mean square.

Lemma 1. *For system (4), assume that there exists a function $V \in C^{2,1}(\mathbb{R}^n \times \mathbb{R}_+, \mathbb{R}_+)$, positive constants $k_i, k_i', p_i, p_i', c, d_c$, such that*

$$\sum_{i=1}^n k_i|x_i|^{p_i} \le V(x(t),t) \le \sum_{i=1}^n k_i'|x_i|^{p_i'}, \tag{8}$$

$$\mathscr{L}V(x(t),t) \le -\lambda V(x(t),t) + d_c. \tag{9}$$

Then, there exists a unique strong solution $x(t) = x(t;x_0,t_0)$ of system (4) for each $x(t_0) = x_0 \in \mathbb{R}^n$, and system (4) is p-th moment exponentially practically stable, where $p = \min\{p_1, \ldots, p_n\}$.

Lemma 2. *For any vectors $x, y \in \mathbb{R}^n$ and any scalars $\epsilon > 0, p > 1$, there holds $x^T y \le (\epsilon^p/p)|x|^p + (1/q\epsilon^q)|y|^q$, where $q = (p/(p-1))$.*

3. Position Loop Control

In this section, the DOBC method and backsetpping method are used to construct the flight controller for helicopters under stochastic disturbances. We first build disturbance observers to estimate the common disturbances δ_1 and δ_2.

3.1. Disturbance Observer Designed for Position Control. In what follows, the disturbance observer is designed to estimate the disturbance δ_1,

$$\hat{\delta}_1 = \sigma_1 + \rho_1(v),$$
$$d\sigma_1 = -\frac{\partial \rho_1(v)}{\partial v}\left(\left(-ge_3 + \frac{1}{m}Rf\right)dt + \hat{\delta}_1 dt\right) + \sigma_{11}dt, \tag{10}$$

where σ_1 is an auxiliary variable, σ_{11} is an auxiliary function to be designed, and $\rho_1(v)$ is a nonlinear function to be designed.

Estimate error is defined as $\tilde{\delta}_1 = \hat{\delta}_1 - \delta_1$. Then, the dynamic of the estimate error is given by

$$d\tilde{\delta}_1 = -\frac{\partial \rho_1(v)}{\partial v}\left(\tilde{\delta}_1 dt + G_1 d\beta_1\right) - \dot{\delta}_1 dt + \sigma_{11}dt. \tag{11}$$

The disturbance observer gain is selected as $(\partial\rho_1(v)/\partial v) = L_1$, with $L_1 = -\mathrm{diag}\{l_1 \ l_1 \ l_1\}$, where $l_1 > 0$.

Choose the Lyapunov function as follows:

$$V_{01} = \frac{1}{4}\left(\tilde{\delta}_1^T\tilde{\delta}_1\right)^2. \tag{12}$$

Then, the infinitesimal generator of V_{01} along with (11) is shown as follows:

$$\mathscr{L}V_{01} = -L_1\left(\tilde{\delta}_1^T\tilde{\delta}_1\right)^2 - \tilde{\delta}_1^T\tilde{\delta}_1\tilde{\delta}_1^T\dot{\delta}_1 + \tilde{\delta}_1^T\tilde{\delta}_1\tilde{\delta}_1^T\sigma_{11} + \frac{1}{2}\mathrm{Tr}\left(G_1^TL_1\left(2\tilde{\delta}_1\tilde{\delta}_1^T + \tilde{\delta}_1^T\tilde{\delta}_1 I\right)L_1G_1\right). \tag{13}$$

From Lemma 2, there exist parameters $\varepsilon_{01} > 0$ and $\varepsilon_{02} > 0$ such that

$$\begin{aligned} -\tilde{\delta}_1^T\tilde{\delta}_1\tilde{\delta}_1^T\dot{\delta}_1 &\le \frac{3\varepsilon_{01}^{(4/3)}}{4}\left(\tilde{\delta}_1^T\tilde{\delta}_1\right)^2 + \frac{1}{4\varepsilon_{01}^4}\left\|\dot{\delta}_1\right\|^4, \\ \frac{1}{2}\mathrm{Tr}\left(G_1^TL_1\left(2\tilde{\delta}_1\tilde{\delta}_1^T + \tilde{\delta}_1^T\tilde{\delta}_1 I\right)L_1G_1\right) &\le \frac{3}{2}\left\|\tilde{\delta}_1\right\|^2\left\|L_1G_1\right\|_F^2 \le \frac{3\varepsilon_{02}^2}{4}\left\|L_1G_1\right\|_F^4\left(\tilde{\delta}_1^T\tilde{\delta}_1\right)^2 + \frac{3}{4\varepsilon_{02}^2}. \end{aligned} \tag{14}$$

Design σ_{11} as

$$\sigma_{11} = -\left(\frac{3\varepsilon_{01}^{(4/3)}}{4} + \frac{3\varepsilon_{02}^2}{4}\left\|L_1G_1\right\|_F^4\right)\tilde{\delta}_1 + \sigma_{12}, \tag{15}$$

where σ_{12} is introduced in the following steps. Hence, from (15) and $\|\dot{\delta}_1\| \le \mu_1$, we have

$$\begin{aligned} \mathscr{L}V_{01} &\le -L_1\left(\tilde{\delta}_1^T\tilde{\delta}_1\right)^2 + \frac{1}{4\varepsilon_{01}^4}\left\|\mu_1\right\|^4 + \frac{3}{4\varepsilon_{02}^2} + \tilde{\delta}_1^T\tilde{\delta}_1\tilde{\delta}_1^T\sigma_{12} \\ &= -L_1\left(\tilde{\delta}_1^T\tilde{\delta}_1\right)^2 + \tilde{\delta}_1^T\tilde{\delta}_1\tilde{\delta}_1^T\sigma_{12} + H_{01}, \end{aligned} \tag{16}$$

where

$$H_{01} = \frac{1}{4\varepsilon_{01}^4}\left\|\mu_1\right\|^4 + \frac{3}{4\varepsilon_{02}^2}. \tag{17}$$

3.2. Position Loop Controller Designed. Consider the position loop system as follows:

$$\begin{aligned} \mathrm{d}p &= v\mathrm{d}t, \\ \mathrm{d}v &= \left(-ge_3 + \frac{1}{m}Rf\right)\mathrm{d}t + \delta_1\mathrm{d}t + G_1\mathrm{d}\beta_1. \end{aligned} \tag{18}$$

The predefined position is $p_r = (x_r, y_r, z_r)$, define the tracking error as $e_p = p - p_r$. The dynamic of the error system is given by

$$\begin{aligned} \mathrm{d}e_p &= v\mathrm{d}t - \mathrm{d}p_r = e_v\mathrm{d}t, \\ \mathrm{d}e_v &= \left(-ge_3 + \frac{T_m}{m}R_{3e} + \frac{T_m}{m}R_{3c} - \ddot{p}_r + \tilde{\delta}_1 + \hat{\delta}_1\right)\mathrm{d}t + G_1\mathrm{d}\beta_1. \end{aligned} \tag{19}$$

Define the controller $u_1 = (T_m/m)R_{3c}$ and $R_{3c} = \left(R_{13c}\ \ R_{23c}\ \ R_{33c}\right)^T$, and

$$u_1 = ge_3 + \ddot{p}_r - \hat{\delta}_1 - k_1\tanh\left(n_1e_p + n_2e_v\right) - k_2\tanh\left(n_2e_v\right), \tag{20}$$

where $k_1 > 0$, $k_2 > 0$, $n_1 > 0$, and $n_2 > 0$ are parameters to be designed. At this point, R_{3c} and T_m can be constructed as

$$\begin{aligned} R_{3c} &= \frac{m}{T_m}u_1, \\ T_m &= m\left\|ge_3 + \ddot{p}_r - \hat{\delta}_1 - k_1\tanh\left(n_1e_p + n_2e_v\right) - k_2\tanh\left(n_2e_v\right)\right\|. \end{aligned} \tag{21}$$

Then, the closed-loop position loop system is written as

$$\mathrm{d}e_p = e_v\mathrm{d}t, \tag{22}$$

$$\mathrm{d}e_v = \left(-k_1\tanh\left(n_1e_p + n_2e_v\right) - k_2\tanh\left(n_2e_v\right) + \frac{T_m}{m}R_{3e} + \tilde{\delta}_1\right)\mathrm{d}t + G_1\mathrm{d}\beta_1. \tag{23}$$

Remark 1. In fact, the helicopter should not be overturn under controller (21), for the continuity of $\cos\phi\cos\theta$. So that, we guarantee $\cos\phi\cos\theta > 0$ to ensure that the helicopter will not be overturn. Meanwhile, the defined signal R_{33c} should also satisfy $R_{33c} > 0$. Thus, the parameters k_1 and k_2 are designed to satisfy $g + \ddot{z}_r + \hat{\delta}_1 e - k_1 - k_2 > 0$. In fact, the acceleration of disturbance in z axis is far less than acceleration of gravity.

Consider $\|R_3\| = 1$, $R_{3e} = R_3 - R_{3c}$, $\overline{R}_3 = \begin{pmatrix} R_{13} \\ R_{23} \end{pmatrix}$, and $\overline{R}_{3c} = \begin{pmatrix} R_{13c} \\ R_{23c} \end{pmatrix}$. Thus,

$$
\begin{aligned}
R_3 &= \begin{pmatrix} R_{13} \\ R_{23} \\ R_{33} \end{pmatrix} = \begin{pmatrix} R_{13} \\ R_{23} \\ \sqrt{1 - R_{13}^2 - R_{23}^2} \end{pmatrix}, \\
R_{3e} &= \begin{pmatrix} R_{13} \\ R_{23} \\ R_{33} \end{pmatrix} - \begin{pmatrix} R_{13c} \\ R_{23c} \\ R_{33c} \end{pmatrix} = \begin{pmatrix} R_{13e} \\ R_{23e} \\ \sqrt{1 - R_{13}^2 - R_{23}^2} - \sqrt{1 - R_{13c}^2 - R_{23c}^2} \end{pmatrix}.
\end{aligned} \tag{24}
$$

Due to $R_{33} > 0$ and $R_{33c} > 0$, we have

$$
\sqrt{1 - R_{13}^2 - R_{23}^2} - \sqrt{1 - R_{13c}^2 - R_{23c}^2} = \frac{\alpha_1 \overline{R}_{3e}}{\sqrt{1 - R_{13}^2 - R_{23}^2} + \sqrt{1 - R_{13c}^2 - R_{23c}^2}}, \tag{25}
$$

where $\alpha_1 = -(R_{13} + R_{13c}, R_{23} + R_{23c})$. Hence,

$$
R_{3e} = \begin{pmatrix} \overline{R}_{3e} \\ \dfrac{\alpha_1 \overline{R}_{3e}}{\sqrt{1 - R_{13}^2 - R_{23}^2} + \sqrt{1 - R_{13c}^2 - R_{23c}^2}} \end{pmatrix} = \begin{pmatrix} I_2 \\ \dfrac{\alpha_1}{\sqrt{1 - R_{13}^2 - R_{23}^2} + \sqrt{1 - R_{13c}^2 - R_{23c}^2}} \end{pmatrix} \overline{R}_{3e} = \alpha \overline{R}_{3e} = \alpha(\overline{R}_3 - \overline{R}_{3c}), \tag{26}
$$

where $\alpha = \begin{pmatrix} I_2 \\ (\alpha_1 / (\sqrt{1 - R_{13}^2 - R_{23}^2} + \sqrt{1 - R_{13c}^2 - R_{23c}^2})) \end{pmatrix}$.

The velocity tracking error equation (23) can be rewritten as

$$
\mathrm{d}e_v = \left(-k_1 \tanh\left(n_1 e_p + n_2 e_v\right) - k_2 \tanh\left(n_2 e_v\right) + \frac{T_m}{m} \alpha \overline{R}_{3e} + \tilde{\delta}_1 \right) \mathrm{d}t + G_1 \mathrm{d}\beta_1. \tag{27}
$$

Choose Lyapunov function $V_{11}(t)$ as follows:

$$
V_{11}(t) = k_1 \int_0^{n_1 e_p + n_2 e_v} \tanh(\mu) \mathrm{d}\mu + k_2 \int_0^{n_2 e_v} \tanh(\mu) \mathrm{d}\mu + \frac{n_1}{2} e_v^T e_v. \tag{28}
$$

Then, the infinitesimal generator of V_{11} is represented as

$$\begin{aligned}\mathscr{L}V_{11}(t) = &-n_2\left(k_1\tanh\left(n_1e_p + n_2e_v\right) + k_2\tanh\left(n_2e_v\right)\right)^T \\ &\times\left(k_1\tanh\left(n_1e_p + n_2e_v\right) + k_2\tanh\left(n_2e_v\right)\right) - n_1k_2e_v^T\tanh\left(n_2e_v\right) \\ &+ F(t)^T\left(\frac{T_m}{m}\alpha\overline{R}_{3e} + \widetilde{\delta}_1\right) + \frac{1}{2}\mathrm{Tr}\left(\begin{pmatrix}0\\G_1\end{pmatrix}^T\begin{pmatrix}\dfrac{\partial^2V_{11}}{\partial e_p^2} & \dfrac{\partial^2V_{11}}{\partial e_p\partial e_v}\\ \dfrac{\partial^2V_{11}}{\partial e_p\partial e_v} & \dfrac{\partial^2V_{11}}{\partial e_v^2}\end{pmatrix}\begin{pmatrix}0\\G_1\end{pmatrix}\right),\end{aligned} \tag{29}$$

where

$$\begin{aligned}F(t) &= n_1e_v + n_2k_1\tanh\left(n_1e_p + n_2e_v\right) + n_2k_2\tanh\left(n_2e_v\right),\\ \frac{\partial^2V_{11}}{\partial e_p^2} &= \mathrm{diag}\left\{n_1^2k_1\left(1 + \tanh^2\left(n_1e_{p_1} + n_2e_{v_1}\right)\right), n_1^2k_1\left(1 + \tanh^2\left(n_1e_{p_2} + n_2e_{v_2}\right)\right), n_1^2k_1\left(1 + \tanh^2\left(n_1e_{p_3} + n_2e_{v_3}\right)\right)\right\},\\ \frac{\partial^2V_{11}}{\partial e_p\partial e_v} &= \mathrm{diag}\left\{n_1n_2k_1\left(1 + \tanh^2\left(n_1e_{p_1} + n_2e_{v_1}\right)\right), n_1n_2k_1\left(1 + \tanh^2\left(n_1e_{p_2} + n_2e_{v_2}\right)\right), n_1n_2k_1\left(1 + \tanh^2\left(n_1e_{p_3} + n_2e_{v_3}\right)\right)\right\},\\ \frac{\partial^2V_{11}}{\partial e_v^2} &= \mathrm{diag}\left\{n_2^2k_1\left(1 + \tanh^2\left(n_1e_{p_1} + n_2e_{v_1}\right)\right) + n_2^2k_2\left(1 + \tanh^2\left(n_2e_{v_1}\right)\right),\right.\\ &\quad n_2^2k_1\left(1 + \tanh^2\left(n_1e_{p_2} + n_2e_{v_2}\right)\right) + n_2^2k_2\left(1 + \tanh^2\left(n_2e_{v_2}\right)\right),\\ &\quad \left.n_2^2k_1\left(1 + \tanh^2\left(n_1e_{p_3} + n_2e_{v_3}\right)\right) + n_2^2k_2\left(1 + \tanh^2\left(n_2e_{v_3}\right)\right)\right\} + \mathrm{diag}\{1,1,1\}.\end{aligned} \tag{30}$$

For the function $\|\tanh(\cdot)\| \le 1$ and the bounded parameter G_1, there exists a parameter $H_{11} > 0$, such that

$$\frac{1}{2}\mathrm{Tr}\left(\begin{pmatrix}0\\G_1\end{pmatrix}^T\begin{pmatrix}\dfrac{\partial^2V_{11}}{\partial e_p^2} & \dfrac{\partial^2V_{11}}{\partial e_p\partial e_v}\\ \dfrac{\partial^2V_{11}}{\partial e_p\partial e_v} & \dfrac{\partial^2V_{11}}{\partial e_v^2}\end{pmatrix}\begin{pmatrix}0\\G_1\end{pmatrix}\right) \le H_{11}. \tag{31}$$

Notice that $-n_1k_2e_v^T\tanh(n_2e_v) \le -(n_1/n_2)k_2\tanh(n_2e_v)^T\tanh(n_2e_v)$. Then, we have

$$\begin{aligned}\mathscr{L}V_{11}(t) \le &-n_2\left(k_1\tanh\left(n_1e_p + n_2e_v\right) + k_2\tanh\left(n_2e_v\right)\right)^T\left(k_1\tanh\left(n_1e_p + n_2e_v\right) + k_2\tanh\left(n_2e_v\right)\right)\\ &-\frac{n_1}{n_2}k_2\tanh\left(n_2e_v\right)^T\tanh\left(n_2e_v\right) + F(t)^T\left(\frac{T_m}{m}\alpha\overline{R}_{3e} + \widetilde{\delta}_1\right) + H_{11}\\ = &-\begin{pmatrix}\tanh\left(n_1e_p + n_2e_v\right)\\ \tanh\left(n_2e_v\right)\end{pmatrix}\begin{pmatrix}n_2k_1^2 & n_2k_1k_2\\ n_2k_1k_2 & n_2k_2^2 + \dfrac{n_1}{n_2}k_2\end{pmatrix}\begin{pmatrix}\tanh\left(n_1e_p + n_2e_v\right)\\ \tanh\left(n_2e_v\right)\end{pmatrix}\\ &+F(t)^T\widetilde{\delta}_1 + F(t)^T\frac{T_m}{m}\alpha\overline{R}_{3e} + H_{11}.\end{aligned} \tag{32}$$

In fact, according to Lemma 2, there exist parameters $\varepsilon_{11} > 0$ and $\varepsilon_{12} > 0$, such that

$$\begin{aligned} F(t)^T\tilde{\delta}_1 &\le \frac{\varepsilon_{11}}{3}\tilde{\delta}_1^T\tilde{\delta}_1\tilde{\delta}_1^T\|F(t)\|^2F(t) + \frac{2}{3\varepsilon_{11}^{(1/2)}}, \\ F(t)^T\frac{T_m}{m}\alpha\overline{R}_{3e} &\le \frac{\varepsilon_{12}T_m^3\|\alpha\|^2\|F(t)\|^2}{3m^3}\overline{R}_{3e}^T\overline{R}_{3e}\overline{R}_{3e}^T\alpha^TF(t) + \frac{2}{3\varepsilon_{12}^{(1/2)}}. \end{aligned} \tag{33}$$

Let $k_3 = \min\left\{\mathrm{eig}\begin{pmatrix} n_2k_1^2 & n_2k_1k_2 \\ n_2k_1k_2 & n_2k_2^2 + (n_1/n_2)k_2 \end{pmatrix}\right\}$, we obtain

$$\begin{aligned} \mathscr{L}V_{11}(t) \le & -k_3\begin{pmatrix} \tanh\left(n_1e_p + n_2e_v\right) \\ \tanh\left(n_2e_v\right) \end{pmatrix}^T\begin{pmatrix} \tanh\left(n_1e_p + n_2e_v\right) \\ \tanh\left(n_2e_v\right) \end{pmatrix} + \frac{\varepsilon_{12}T_m^3\|\alpha\|^2\|F(t)\|^2}{3m^3}\overline{R}_{3e}^T\overline{R}_{3e}\overline{R}_{3e}^T\alpha^TF(t) \\ & + \frac{\varepsilon_{11}}{3}\tilde{\delta}_1^T\tilde{\delta}_1\tilde{\delta}_1^T\|F(t)\|^2F(t) + \frac{2}{3\varepsilon_{11}^{(1/2)}} + \frac{2}{3\varepsilon_{12}^{(1/2)}} + H_{11}. \end{aligned} \tag{34}$$

Since $h(x) = (\tanh(x)/x)$ is a continuous function, for any $\overline{x} > 0$, $0 \le x \le \overline{x}$, there exists a positive number $\beta(\overline{x})$ such that $\beta\|x\| \le \|\tanh(x)\| \le \|x\|$. Thus,

$$\begin{aligned} -\tanh\left(n_1e_p + n_2e_v\right)^T\tanh\left(n_1e_p + n_2e_v\right) &\le -\beta^2\left(n_1e_p + n_2e_v\right)^T\left(n_1e_p + n_2e_v\right), \\ -\tanh\left(n_2e_v\right)^T\tanh\left(n_2e_v\right) &\le -\beta^2n_2^2e_v^Te_v. \end{aligned} \tag{35}$$

Define Lyapunov function as follows:

$$V_1(t) = V_{01}(t) + V_{11}(t). \tag{36}$$

Based on (16) and (34), we obtain

$$\begin{aligned} \mathscr{L}V_1(t) \le & -k_3\beta^2\left(n_1e_p + n_2e_v\right)^T\left(n_1e_p + n_2e_v\right) - k_3\beta^2n_2^2e_v^Te_v \\ & + \frac{\varepsilon_{12}T_m^3\|\alpha\|^2\|F(t)\|^2}{3m^3}\overline{R}_{3e}^T\overline{R}_{3e}\overline{R}_{3e}^T\alpha^TF(t) + \frac{\varepsilon_{11}}{3}\tilde{\delta}_1^T\tilde{\delta}_1\tilde{\delta}_1^T\|F(t)\|^2F(t) \\ & + \frac{2}{3\varepsilon_{11}^{(1/2)}} + \frac{2}{3\varepsilon_{12}^{(1/2)}} + H_{11} - L_1\left(\tilde{\delta}_1^T\tilde{\delta}_1\right)^2 + \tilde{\delta}_1^T\tilde{\delta}_1\tilde{\delta}_1^T\sigma_{12} + H_{01}. \end{aligned} \tag{37}$$

Hence, σ_{12} is designed as

$$\sigma_{12} = -\frac{\varepsilon_{11}}{3}\|F(t)\|^2F(t). \tag{38}$$

Then,

$$\mathscr{L}V_1(t) \le -l_1\left(\widetilde{\delta}_1^T\widetilde{\delta}_1\right)^2 - k_4 e_p^T e_p - k_4 e_v^T e_v + \frac{\varepsilon_{12}T_m^3\|\alpha\|^2\|F(t)\|^2}{3m^3}\overline{R}_{3e}^T\overline{R}_{3e}\overline{R}_{3e}^T\alpha^T F(t) + H_1, \tag{39}$$

where $k_4 = \min\left\{\mathrm{eig}\left\{\begin{pmatrix} k_3\beta^2 n_1^2 & k_3\beta^2 n_1 n_2 \\ k_3\beta^2 n_1 n_2 & 2k_3\beta^2 n_2^2 \end{pmatrix}\right\}\right\} > 0$ and $H_1 = H_{11} + H_{01} + (2/3\varepsilon_{11}^{(1/2)}) + (2/3\varepsilon_{12}^{(1/2)})$.

Moreover, the error dynamic of disturbance $\widetilde{\delta}_1$ can be rewritten as

$$\mathrm{d}\widetilde{\delta}_1 = -\left(L_1 + \left(\frac{3\varepsilon_{01}^{(4/3)}}{4} + \frac{3\varepsilon_{02}^2}{4}\left\|L_1G_1\right\|_F^4\right)\right)\widetilde{\delta}_1\mathrm{d}t - L_1G_1\mathrm{d}\beta_1 - \dot{\delta}_1\mathrm{d}t - \frac{\varepsilon_{11}}{3}\|F(t)\|^2F(t)\mathrm{d}t. \tag{40}$$

4. Attitude Loop Control

In this section, the DOBC method and backsetpping method are used to construct the flight controller for helicopters under stochastic disturbances. We first build disturbance observers to estimate the common disturbances δ_1 and δ_2.

4.1. Disturbance Observer Designed for Attitude Control. In order to estimate the disturbance δ_2, we design the following disturbance observers:

$$\begin{aligned} \widehat{\delta}_2 &= \sigma_2 + J\rho_2(w), \\ \mathrm{d}\sigma_2 &= -\frac{\partial\rho_2(w)}{\partial w}\left((-w^{\times}Jw + \tau)\mathrm{d}t + \widehat{\delta}_2\mathrm{d}t\right) + \sigma_{02}\mathrm{d}t, \end{aligned} \tag{41}$$

where σ_2 is an auxiliary variable, σ_{02} is an auxiliary function to be designed, and $\rho_2(v)$ is a nonlinear function to be designed.

Define estimate error as $\widetilde{\delta}_2 = \widehat{\delta}_2 - \delta_2$. Then, the dynamic of the estimate error can be shown as

$$\mathrm{d}\widetilde{\delta}_2 = -\frac{\partial\rho_2(w)}{\partial w}\left(\widetilde{\delta}_2\mathrm{d}t + G_2\mathrm{d}\beta_2\right) - \dot{\delta}_2\mathrm{d}t + \sigma_{02}\mathrm{d}t. \tag{42}$$

The disturbance observer gain is selected as $(\partial\rho_2(w)/\partial w) = L_2$, with $L_2 = -\mathrm{diag}\{l_2\ \ l_2\ \ l_2\}$, where $l_2 > 0$.

Choose Lyapunov function as follows:

$$V_{02} = \frac{1}{4}\left(\widetilde{\delta}_2^T\widetilde{\delta}_2\right)^2. \tag{43}$$

Similarly with V_{01}, for V_{02}, there exist $\varepsilon_{03} > 0$ and $\varepsilon_{04} > 0$, such that

$$\mathscr{L}V_{02} \le -l_2\left(\widetilde{\delta}_2^T\widetilde{\delta}_2\right)^2 + H_{02}, \tag{44}$$

where

$$H_{02} = \frac{1}{4\varepsilon_{03}^4}\left\|\mu_2\right\|^4 + \frac{3}{4\varepsilon_{04}^2}. \tag{45}$$

Design the auxiliary variable σ_{02} as follows:

$$\sigma_{02} = -\left(\frac{3\varepsilon_{03}^{(4/3)}}{4} + \frac{3\varepsilon_{04}^2}{4}\left\|L_2G_2\right\|_F^4\right)\widetilde{\delta}_2. \tag{46}$$

The error dynamics of disturbance (42) can be rewritten as

$$\mathrm{d}\widetilde{\delta}_2 = -\left(l_2 + \frac{3\varepsilon_{03}^{(4/3)}}{4} + \frac{3\varepsilon_{04}^2}{4}\left\|L_2G_2\right\|_F^4\right)\widetilde{\delta}_2\mathrm{d}t - \dot{\delta}_2\mathrm{d}t - L_2G_2\mathrm{d}\beta_2. \tag{47}$$

4.2. Attitude Loop Controller Designed. The predefined tracking signals are position and yaw angle, which are denoted by p_r and ψ_r. After designing the position loop control, the reasonable attitude tracking signals are obtained, which are given as $\overline{R}_{3c}$ and ψ_r. Moreover, defining $\gamma_r = \begin{pmatrix} \overline{R}_3^T & \psi \end{pmatrix}$ and $\gamma = \begin{pmatrix} \theta & \phi & \psi \end{pmatrix}$, we can confirm that $\|\partial\gamma_r/\partial\gamma\| = \cos\theta \neq 0$, for $|\theta| < (\pi/2)$. Hence, the mapping that from γ to γ_r is a local topological homeomorphism, which means that the dynamic of γ_r can represent the dynamic of γ for $|\theta| < (\pi/2)$. The error dynamic of γ_r is given by

$$\mathrm{d}\overline{R}_{3e} = \widehat{R}_3 w_1\mathrm{d}t - \mathrm{d}\overline{R}_{3c}, \tag{48}$$

$$\mathrm{d}e_{\psi} = \left(\frac{\sin\phi}{\cos\theta}q + \frac{\cos\phi}{\cos\theta}r\right)\mathrm{d}t - \mathrm{d}\psi_r, \tag{49}$$

where $w_1 = \begin{pmatrix} p & q \end{pmatrix}^T$ and $\widehat{R}_3 = \begin{pmatrix} -R_{12} & R_{11} \\ -R_{22} & R_{21} \end{pmatrix}$.

For (48), $\mathrm{d}R_{3c}$ can be written as

$$\mathrm{d}R_{3c} = \mathrm{d}\left(\frac{u_1}{\sqrt{u_1^Tu_1}}\right) = \frac{1}{\sqrt{u_1^Tu_1}}\left(I_3 - \frac{u_1u_1^T}{u_1^Tu_1}\right)\mathrm{d}u_1. \tag{50}$$

For $\mathrm{d}u_1$, we have

$$\mathrm{d}u_1 = \mathrm{d}\ddot{p}_r - \mathrm{d}\widehat{\delta}_1 - k_1\mathrm{d}\tanh\left(n_1e_p + n_2e_v\right) - k_2\mathrm{d}\tanh\left(n_2e_v\right). \tag{51}$$

From (10), $\mathrm{d}\widehat{\delta}_1$ is written as follows:

$$\mathrm{d}\widehat{\delta}_1 = -\overline{l}_1\widetilde{\delta}_1\mathrm{d}t - L_1G_1\mathrm{d}\beta_1 - \frac{\varepsilon_{11}}{3}\|F(t)\|^2F(t)\mathrm{d}t, \tag{52}$$

where $\overline{l}_1 = l_1 + (3\varepsilon_{01}^{(4/3)}/4) + (3\varepsilon_{02}^2/4)\|L_1G_1\|_F^4$.

Hence, we get

$$\mathrm{d}u_1 = \Delta_{01}(t)\mathrm{d}t + \Delta_{02}(t)\widetilde{\delta}_1\mathrm{d}t + \Delta_{03}(t)\mathrm{d}\beta_1, \tag{53}$$

for $x = (x_1, x_2, x_3)$, $\mathrm{Tanh}^2(x) = \mathrm{diag}\{\tanh^2(x_1), \tanh^2(x_2)y, \tanh^2(x_3)\}$, where

$$\begin{aligned}
\Delta_{01}(t) &= \dddot{p}_r - k_1 n_1\left(I + \mathrm{Tanh}^2\left(n_1 e_p + n_2 e_v\right)\right)e_v - \left(\left(k_2 n_2\left(I + \mathrm{Tanh}^2\left(n_2 e_v\right)\right) + k_1 n_2\left(I + \mathrm{Tanh}^2\left(n_1 e_p + n_2 e_v\right)\right)\right)\right.\\
&\quad \left.\cdot\left(-k_1\tanh\left(n_1 e_p + n_2 e_v\right) - k_2\tanh\left(n_2 e_v\right) + \frac{T_m}{m}\alpha\overline{R}_{3e}\right) + \frac{\varepsilon_{11}}{3}\|F(t)\|^2 F(t),\right.\\
\Delta_{02}(t) &= \bar{l}_1 I - \left(k_2 n_2\left(I + \mathrm{Tanh}^2\left(n_2 e_v\right)\right) + k_1 n_2\left(I + \mathrm{Tanh}^2\left(n_1 e_p + n_2 e_v\right)\right)\right),\\
\Delta_{03}(t) &= L_1 G_1 - \left(k_2 n_2\left(I + \mathrm{Tanh}^2\left(n_2 e_v\right)\right) + k_1 n_2\left(I + \mathrm{Tanh}^2\left(n_1 e_p + n_2 e_v\right)\right)\right)G_1.
\end{aligned} \tag{54}$$

From (50),

$$\begin{aligned}
\mathrm{d}R_{3c} &= \frac{1}{\|u_1\|}\left(\Delta_{101}(t) + \Delta_{102}(t)e_v + \Delta_{103}(t)\Delta_{104}(t) + \frac{\varepsilon_{11}}{3}\|F(t)\|^2 F(t)\right)\mathrm{d}t\\
&\quad + \frac{1}{\|u_1\|}\Delta_{12}(t)\tilde{\delta}_1\mathrm{d}t + \frac{1}{\|u_1\|}\Delta_{13}(t)\mathrm{d}\beta_1,
\end{aligned} \tag{55}$$

where

$$\begin{aligned}
\Delta_{101}(t) &= \left(I_3 - \frac{u_1 u_1^T}{u_1^T u_1}\right)\dddot{p}_r,\\
\Delta_{102}(t) &= -k_2\left(I_3 - \frac{u_1 u_1^T}{u_1^T u_1}\right)\left(I + \mathrm{Tanh}^2(e_v)\right),\\
\Delta_{103}(t) &= -\left(I_3 - \frac{u_1 u_1^T}{u_1^T u_1}\right)\left(k_2\left(I + \mathrm{Tanh}^2(e_v)\right) + k_1\left(I + \mathrm{Tanh}^2\left(e_p + e_v\right)\right)\right),\\
\Delta_{104}(t) &= \left(-k_1\tanh\left(e_p + e_v\right) - k_2\tanh(e_v) + \frac{T_m}{m}\alpha\overline{R}_{3e}\right),\\
\Delta_{12}(t) &= \left(I_3 - \frac{u_1 u_1^T}{u_1^T u_1}\right)\left(\bar{l}_1 I - \left(k_2\left(I + \mathrm{Tanh}^2(e_v)\right) + k_1\left(I + \mathrm{Tanh}^2\left(e_p + e_v\right)\right)\right)\right),\\
\Delta_{13}(t) &= \left(I_3 - \frac{u_1 u_1^T}{u_1^T u_1}\right)\left(L_1 G_1 - \left(k_2\left(I + \mathrm{Tanh}^2(e_v)\right) + k_1\left(I + \mathrm{Tanh}^2\left(e_p + e_v\right)\right)\right)G_1\right).
\end{aligned} \tag{56}$$

For $\|u_1 u_1^T\|_F \le \|u_1\|_F \|u_1^T\|_F = \|u_1\|^2$, one has

$$\left\|\left(I_3 - \frac{u_1 u_1^T}{u_1^T u_1}\right)\right\|_F \le \|I_3\|_F + \frac{\|u_1 u_1^T\|_F}{\|u_1\|^2} \le \sqrt{3} + 1. \tag{57}$$

Then, we confirm that

$$\begin{aligned}
&\|\Delta_{101}(t)\| \le (\sqrt{3}+1)\|\dddot{p}_r\|,\\
&\|\Delta_{102}(t)\|_F \le k_2(\sqrt{3}+1)\|I + \mathrm{Tanh}^2(e_v)\|_F \le k_2(3\sqrt{2}+\sqrt{6}),\\
&\|\Delta_{103}(t)\|_F \le (\sqrt{3}+1)\left\|k_2\left(I + \mathrm{Tanh}^2(e_v)\right) + k_1\left(I + \mathrm{Tanh}^2\left(e_p + e_v\right)\right)\right\|_F \le (6+2\sqrt{3})(k_1+k_2),\\
&\|\Delta_{12}(t)\| \le (\sqrt{3}+1)\left(\bar{l}_1 + 2\sqrt{3}(k_1+k_2)\right),\\
&\|\Delta_{13}(t)\| \le (\sqrt{3}+1)\left(\|L_1 G_1\| + 2\sqrt{3}(k_1+k_2)\|G_1\|\right).
\end{aligned} \tag{58}$$

Thus, (48) can be rewritten as

$$\begin{aligned}
\mathrm{d}\overline{R}_{3e} = {}& \widehat{R}_3 e_{w_1}\mathrm{d}t + \widehat{R}_3 w_{1c}\mathrm{d}t - E_0\frac{1}{\|u_1\|}\left(\Delta_{101}(t) + \Delta_{102}(t)e_v + \Delta_{103}(t)\Delta_{104}(t) + \frac{\varepsilon_{11}}{3}\|F(t)\|^2 F(t)\right)\mathrm{d}t\\
&- E_0\frac{1}{\|u_1\|}\Delta_{12}(t)\widetilde{\delta}_1\mathrm{d}t - E_0\frac{1}{\|u_1\|}\Delta_{13}(t)\mathrm{d}\beta_1,
\end{aligned} \tag{59}$$

where $E_0 = \begin{pmatrix} 1 & 0 & 0\\ 0 & 1 & 0 \end{pmatrix}$.

Choose Lyapunov function $V_{21}(t)$ as

$$V_{21}(t) = \frac{1}{4}\left(\overline{R}_{3e}^T \overline{R}_{3e}\right)^2. \tag{60}$$

The infinitesimal generator of V_{21} along with (60) is shown as

$$\begin{aligned}
\mathscr{L}V_{21}(t) = {}& \overline{R}_{3e}^T\overline{R}_{3e}\overline{R}_{3e}^T\widehat{R}_3 e_{w_1} + \overline{R}_{3e}^T\overline{R}_{3e}\overline{R}_{3e}^T\widehat{R}_3 w_{1c} - \overline{R}_{3e}^T\overline{R}_{3e}\overline{R}_{3e}^T E_0\frac{1}{\|u_1\|}\Delta_{101}(t)\\
&- \overline{R}_{3e}^T\overline{R}_{3e}\overline{R}_{3e}^T E_0\frac{1}{\|u_1\|}\Delta_{102}(t)e_v - \overline{R}_{3e}^T\overline{R}_{3e}\overline{R}_{3e}^T E_0\frac{1}{\|u_1\|}\Delta_{103}(t)\Delta_{104}(t)\\
&- \frac{\varepsilon_{11}}{3}\overline{R}_{3e}^T\overline{R}_{3e}\overline{R}_{3e}^T E_0\frac{1}{\|u_1\|}\|F(t)\|^2 F(t) - \overline{R}_{3e}^T\overline{R}_{3e}\overline{R}_{3e}^T E_0\frac{1}{\|u_1\|}\Delta_{12}(t)\widetilde{\delta}_1\\
&+ \frac{1}{2\|u_1\|^2}\mathrm{Tr}\left(\Delta_{13}^T(t)E_0^T\left(2\overline{R}_{3e}\overline{R}_{3e}^T + \overline{R}_{3e}^T\overline{R}_{3e}I\right)E_0\Delta_{13}(t)\right).
\end{aligned} \tag{61}$$

From Lemma 2, there exist parameters $\varepsilon_{21} > 0$, $\varepsilon_{22} > 0$, $\varepsilon_{231} > 0$, $\varepsilon_{232} > 0$, $\varepsilon_{24} > 0$, and $\varepsilon_{25} > 0$, such that

$$\overline{R}_{3e}^{T}\overline{R}_{3e}\overline{R}_{3e}^{T}\widehat{R}_{3}e_{w_1}\le\frac{3}{4\varepsilon_{21}^{(1/3)}}\left(\overline{R}_{3e}^{T}\overline{R}_{3e}\right)^{2}+\frac{\varepsilon_{21}}{4}\left\|\widehat{R}_{3}\right\|^{4}\left(e_{w_1}^{T}e_{w_1}\right)^{2},$$

$$-\overline{R}_{3e}^{T}\overline{R}_{3e}\overline{R}_{3e}^{T}E_{0}\frac{1}{\left\|u_1\right\|}\Delta_{101}(t)\le\frac{3\varepsilon_{22}^{(1/3)}}{4\left\|u_1\right\|^{(4/3)}}\left(\overline{R}_{3e}^{T}\overline{R}_{3e}\right)^{2}+\frac{1}{4\varepsilon_{22}}\left\|E_0\right\|^{4}\left\|\Delta_{101}(t)\right\|^{4},$$

$$-\overline{R}_{3e}^{T}\overline{R}_{3e}\overline{R}_{3e}^{T}E_{0}\frac{1}{\left\|u_1\right\|}\Delta_{102}(t)e_{v}\le\frac{\varepsilon_{231}}{2}\left(\overline{R}_{3e}^{T}\overline{R}_{3e}\right)^{2}+\frac{\varepsilon_{232}}{2\left\|u_1\right\|^{4}}\left(\overline{R}_{3e}^{T}\overline{R}_{3e}\right)^{2}\left(e_{v}^{T}e_{v}\right)^{2}+\frac{\left\|E_0\right\|^{4}\left\|\Delta_{102}(t)\right\|^{4}}{8\varepsilon_{232}\varepsilon_{231}},\tag{62}$$

$$-\overline{R}_{3e}^{T}\overline{R}_{3e}\overline{R}_{3e}^{T}E_{0}\frac{1}{\left\|u_1\right\|}\Delta_{12}(t)\widetilde{\delta}_{1}\le\frac{3\varepsilon_{24}^{(1/3)}}{4\left\|u_1\right\|^{(4/3)}}\left(\overline{R}_{3e}^{T}\overline{R}_{3e}\right)^{2}+\frac{1}{4\varepsilon_{24}}\left\|E_0\right\|_{F}^{4}\left\|\Delta_{12}(t)\right\|^{4}\left(\widetilde{\delta}_{1}^{T}\widetilde{\delta}_{1}\right)^{2},$$

$$\frac{1}{2\left\|u_1\right\|^{2}}\mathrm{Tr}\left(\Delta_{13}^{T}(t)E_{0}^{T}\left(2\overline{R}_{3e}\overline{R}_{3e}^{T}+\overline{R}_{3e}^{T}\overline{R}_{3e}I\right)E_{0}\Delta_{13}(t)\right)\le\frac{3\varepsilon_{25}}{4\left\|u_1\right\|^{2}}\left(\overline{R}_{3e}^{T}\overline{R}_{3e}\right)^{2}+\frac{1}{2\varepsilon_{25}}\left\|E_0\Delta_{13}(t)\right\|_{F}^{4}.$$

Furthermore, for $T_m = m\|u_1\|$, there exist parameters $\varepsilon_{26}>0$ and $\varepsilon_{27}>0$, such that

$$\begin{aligned}&-\overline{R}_{3e}^{T}\overline{R}_{3e}\overline{R}_{3e}^{T}E_{0}\frac{1}{\left\|u_1\right\|}\Delta_{103}(t)\Delta_{104}(t)\\&\le\frac{3\varepsilon_{26}^{(1/3)}}{4\left\|u_1\right\|^{(4/3)}}\left(\overline{R}_{3e}^{T}\overline{R}_{3e}\right)^{2}+\frac{1}{4\varepsilon_{26}}\left\|E_0\right\|_{F}^{4}\left\|\Delta_{103}(t)\right\|^{4}\left(\left\|k_1\tanh\left(e_p+e_v\right)\right\|+k_2\left\|\tanh\left(e_v\right)\right\|\right)^{4}\\&+\frac{3\varepsilon_{27}^{(1/3)}}{4}\left\|E_0\right\|_{F}^{(4/3)}\left\|\Delta_{103}(t)\right\|_{F}^{(4/3)}\left(\overline{R}_{3e}^{T}\overline{R}_{3e}\right)^{2}+\frac{1}{4\varepsilon_{27}}\left\|\alpha\right\|_{F}^{4}\left(\overline{R}_{3e}^{T}\overline{R}_{3e}\right)^{2}.\end{aligned}\tag{63}$$

Then, $\mathscr{L}V_{21}(t)$ satisfies

$$\begin{aligned}\mathscr{L}V_{21}(t)\le&\left(H_{25}+\frac{H_{24}}{4\left\|u_1\right\|^{(4/3)}}+\frac{3\varepsilon_{25}}{4\left\|u_1\right\|^{2}}+\frac{1}{4\varepsilon_{27}}\left\|\alpha\right\|_{F}^{4}\right)\left(\overline{R}_{3e}^{T}\overline{R}_{3e}\right)^{2}+\overline{R}_{3e}^{T}\overline{R}_{3e}\overline{R}_{3e}^{T}\widehat{R}_{3}w_{1c}+H_{23}\left(\widetilde{\delta}_{1}^{T}\widetilde{\delta}_{1}\right)^{2}\\&-\frac{\varepsilon_{11}}{3}\overline{R}_{3e}^{T}\overline{R}_{3e}\overline{R}_{3e}^{T}E_{0}\frac{1}{\left\|u_1\right\|}\left\|F(t)\right\|^{2}F(t)+\frac{\varepsilon_{232}}{2\left\|u_1\right\|^{4}}\left(\overline{R}_{3e}^{T}\overline{R}_{3e}\right)^{2}\left(e_{v}^{T}e_{v}\right)^{2}+\frac{\varepsilon_{21}}{4}\left\|\widehat{R}_{3}\right\|^{4}\left(e_{w_1}^{T}e_{w_1}\right)^{2}+H_{21},\end{aligned}\tag{64}$$

where

$$
\begin{aligned}
H_{21} &= \frac{1}{2\varepsilon_{25}}\|E_0\|_F^4\left((\sqrt{3}+1)\left(\|L_1G_1\|+2\sqrt{3}\,(k_1+k_2)\|G_1\|\right)\right)_F^4+\frac{1}{4\varepsilon_{22}}\|E_0\|_F^4\|(\sqrt{3}+1)\|^4\left\|\dddot{p}_r\right\|^4\\
&\quad+\frac{1}{4\varepsilon_{26}}\|E_0\|_F^2(6+2\sqrt{3})(k_1+k_2)^4(k_1+k_2)^4+\frac{\|E_0\|^4\|k_2(3\sqrt{2}+\sqrt{6})\|^4}{8\varepsilon_{232}\varepsilon_{231}},\\
H_{22} &= \frac{1}{4\varepsilon_{23}}\|E_0\|_F^4\left(k_2(3\sqrt{2}+\sqrt{6})\right)^2,\\
H_{23} &= \frac{1}{4\varepsilon_{24}}\left((\sqrt{3}+1)\left(\|\bar{l}_1\|_F+2\sqrt{3}\,(k_1+k_2)\right)\right)^4,\\
H_{24} &= 3\varepsilon_{22}^{(1/3)}+3\varepsilon_{24}^{(1/3)}+3\varepsilon_{26}^{(1/3)},\\
H_{25} &= \frac{3}{4\varepsilon_{21}^{(1/3)}}+\frac{3\varepsilon_{27}^{(1/3)}}{4}\|E_0\|_F^{(4/3)}(6+2\sqrt{3})(k_1+k_2)^{(4/3)}+\frac{\varepsilon_{231}}{2}.
\end{aligned}
\tag{65}
$$

Define $V_2(t)=V_1+V_{21}$. Based on the above discussion and according to (39) and (64), we have

$$
\begin{aligned}
\mathscr{L}V_2(t) \le & -(l_1-H_{23})\left(\tilde{\delta}_1^T\tilde{\delta}_1\right)^2-k_4e_p^Te_p-k_4e_v^Te_v+\frac{\varepsilon_{21}}{4}\|\hat{R}_3\|^4\left(e_{w_1}^Te_{w_1}\right)^2+\overline{R}_{3e}^T\overline{R}_{3e}\overline{R}_{3e}^T\hat{R}_3w_{1c}\\
&+\left(H_{25}+\frac{H_{24}}{4\|u_1\|^{(4/3)}}+\frac{3\varepsilon_{25}}{4\|u_1\|^2}+\frac{1}{4\varepsilon_{27}}\|\alpha\|_F^4\right)\left(\overline{R}_{3e}^T\overline{R}_{3e}\right)^2+\frac{\varepsilon_{12}T_m^3\|\alpha\|^2\|F(t)\|^2}{3m^3}\overline{R}_{3e}^T\overline{R}_{3e}\overline{R}_{3e}^T\alpha^TF(t)\\
&+\frac{\varepsilon_{232}}{2\|u_1\|^4}\left(\overline{R}_{3e}^T\overline{R}_{3e}\right)^2\left(e_v^Te_v\right)^2-\frac{\varepsilon_{11}}{3}\overline{R}_{3e}^T\overline{R}_{3e}\overline{R}_{3e}^TE_0\frac{1}{\|u_1\|}\|F(t)\|^2F(t)+H_2,
\end{aligned}
\tag{66}
$$

where $H_2=H_1+H_{21}$. Hence, we design the virtual control law w_{1c} as

$$
\begin{aligned}
w_{1c} = & -\left(k_5+H_{25}+\frac{H_{24}}{4\|u_1\|^{(4/3)}}+\frac{3\varepsilon_{25}}{4\|u_1\|^2}+\frac{1}{4\varepsilon_{27}}\|\alpha\|_F^4\right)\hat{R}_3^{-1}\overline{R}_{3e}-\frac{\varepsilon_{12}T_m^3\|\alpha\|^2\|F(t)\|^2}{3m^3}\hat{R}_3^{-1}\alpha^TF(t)\\
&-\frac{\varepsilon_{232}}{2\|u_1\|^4}\left(e_v^Te_v\right)^2\hat{R}_3^{-1}\overline{R}_{3e}+\frac{\varepsilon_{11}\|F(t)\|^2}{3\|u_1\|}\hat{R}_3^{-1}E_0F(t),
\end{aligned}
\tag{67}
$$

where $k_5>0$. Then, we obtain

$$
\mathscr{L}V_2(t) \le -(L_1-H_{23})\left(\tilde{\delta}_1^T\tilde{\delta}_1\right)^2-k_4e_p^Te_p-k_4e_v^Te_v-k_5\left(\overline{R}_{3e}^T\overline{R}_{3e}\right)^2+\frac{\varepsilon_{21}}{4}\|\hat{R}_3\|^4\left(e_{w_1}^Te_{w_1}\right)^2+H_2. \tag{68}
$$

From (61), the dynamic of $\overline{R}_{3e}$ can be rewritten as

$$d\overline{R}_{3e} = \overline{R}_{3e1}(t)dt + \overline{R}_{3e2}(t)\widetilde{\delta}_1 dt + \overline{R}_{3e3}(t)d\beta_1, \tag{69}$$

where

$$\begin{aligned}\overline{R}_{3e1}(t) &= \widehat{R}_3 e_{w_1} - \left(k_5 + H_{25} + \frac{H_{24}}{4\|u_1\|^{(4/3)}} + \frac{3\varepsilon_{25}}{4\|u_1\|^2} + \frac{1}{4\varepsilon_{27}}\|\alpha\|_F^4\right)\overline{R}_{3e} - \frac{\varepsilon_{12}T_m^3\|\alpha\|^2\|F(t)\|^2}{3m^3}\widehat{R}_3^{-1}\alpha^T F(t) \\ &\quad - \frac{\varepsilon_{232}}{2\|u_1\|^4}\left(e_v^T e_v\right)^2\widehat{R}_3^{-1}\overline{R}_{3e} - \frac{E_0}{\|u_1\|}\left(\Delta_{101}(t) + \Delta_{102}(t)e_v + \Delta_{103}(t)\Delta_{104}(t)\right), \\ \overline{R}_{3e2}(t) &= \frac{E_0}{\|u_1\|}\Delta_{12}(t), \\ \overline{R}_{3e3}(t) &= -\frac{E_0}{\|u_1\|}\Delta_{13}(t).\end{aligned} \tag{70}$$

For (37), we have

$$de_\psi = \left(E_{11}w_1 + \frac{\cos\phi}{\cos\theta}e_r + \frac{\cos\phi}{\cos\theta}r_c - \dot{\psi}_r\right)dt, \tag{71}$$

where $E_{11} = \begin{pmatrix}0 & \sin\phi/\cos\theta\end{pmatrix}$ and r_c is the virtual control law to be designed.

Choose Lyapunov function V_{31} as

$$V_{31} = \frac{1}{4}e_\psi^4. \tag{72}$$

The derivative of $V_{31}(t)$ along with (71) is derived as follows:

$$\dot{V}_{31}(t) = e_\psi^3\left(E_{11}w_1 + \frac{\cos\phi}{\cos\theta}e_r + \frac{\cos\phi}{\cos\theta}r_c - \dot{\psi}_r\right). \tag{73}$$

Then, the virtual control law r_c is designed as

$$r_c = -\frac{\cos\theta}{\cos\phi}\left(E_{11}w_{1c} - \dot{\psi}_r + k_3 e_\psi\right). \tag{74}$$

At this point, the dynamic of e_ψ can be written as

$$de_\psi = \left(-k_6 e_\psi + E_{11}e_{w_1} + \frac{\cos\phi}{\cos\theta}e_r\right)dt = \left(-k_6 e_\psi + E_1 e_w\right)dt, \tag{75}$$

where $E_1 = \begin{pmatrix}0 & (\sin\phi/\cos\theta) & (\cos\phi/\cos\theta)\end{pmatrix}$ and $e_w = (p,q,r)^T - (p_c,q_c,r_c)^T$. Thus, based on Lemma 2, there exists $\varepsilon_{28} > 0$, such that

$$\dot{V}_{31}(t) = e_\psi^3\left(-k_6 e_\psi + E_1 e_w\right) = -k_6 e_\psi^4 + e_\psi^3 E_1 e_w \le -\left(k_6 - \frac{3\varepsilon_{28}^{(1/3)}}{4}\right)e_\psi^4 + \frac{1}{4\varepsilon_{28}}\|E_1\|^4\left(e_w^T e_w\right)^2. \tag{76}$$

Define $V_3(t) = V_2(t) + V_{31}(t)$; combining (68) and (76) yields

$$\begin{aligned}\mathscr{L}V_3(t) \le &-(l_1 - H_{23})\left(\widetilde{\delta}_1^T\widetilde{\delta}_1\right)^2 - k_4 e_p^T e_p - k_4 e_v^T e_v - k_5\left(\overline{R}_{3e}^T\overline{R}_{3e}\right) + \frac{\varepsilon_{21}}{4}\|\widehat{R}_3\|^4\|E_0\|^4\left(e_w^T e_w\right)^2 + H_2 \\ &-\left(k_6 - \frac{3\varepsilon_{28}^{(1/3)}}{4}\right)e_\psi^4 + \frac{1}{4\varepsilon_{28}}\|E_1\|^4\left(e_w^T e_w\right)^2.\end{aligned} \tag{77}$$

In what follows, consider the dynamic of angular velocity:

$$Jdw = \left(-w^\times Jw + A(T_m)\rho + B(T_m) + \delta_2\right)dt + G_2 d\beta_2. \tag{78}$$

Defining $\rho = A(T_m)^{-1}(u_2 - B(T_m) + w^{\times}Jw - \hat{\delta}_2)$, the error dynamic of e_w is

$$Jde_w = \left(u_2 + \tilde{\delta}_2\right)dt + G_2 d\beta_2 - dw_c, \tag{79}$$

where dw_c is obtained in Appendix. Then, according to (79),

$$Jde_w = \left(u_2 + \tilde{\delta}_2\right)dt + G_2 d\beta_2 - W_{c1}(t)dt - W_{c2}(t)\tilde{\delta}_1 dt - W_{c20}\left(t, \tilde{\delta}_1\right)dt - W_{c3}(t)d\beta_1, \tag{80}$$

which implies that

$$de_w = \left(J^{-1}u_2 - J^{-1}W_{c1}(t) - J^{-1}W_{c2}(t)\tilde{\delta}_1 - J^{-1}W_{c20}\left(t, \tilde{\delta}_1\right) + J^{-1}\tilde{\delta}_2\right)dt - J^{-1}W_{c3}(t)d\beta_1 + J^{-1}G_2 d\beta_2. \tag{81}$$

Choose Lyapunov function as follows:

$$V_{41}(t) = \frac{1}{4}\left(e_w^T e_w\right)^2. \tag{82}$$

The infinitesimal generator of V_{41} along with (81) is obtained as follows:

$$\begin{aligned}\mathscr{L}V_{41}(t) &= e_w^T e_w e_w^T J^{-1}u_2 - e_w^T e_w e_w^T J^{-1}W_{c1}(t) - e_w^T e_w e_w^T J^{-1}W_{c2}(t)\tilde{\delta}_1 - e_w^T e_w e_w^T J^{-1}W_{c20}\left(t, \tilde{\delta}_1\right)\\ &+ e_w^T e_w e_w^T J^{-1}\tilde{\delta}_2 + \frac{1}{2}\mathrm{Tr}\left(W_{c3}^T(t)J^{-T}\left(2e_w e_w^T + e_w^T e_w I\right)J^{-1}W_{c3}(t)\right)\\ &+ \frac{1}{2}\mathrm{Tr}\left(G_2^T J^{-T}\left(2e_w e_w^T + e_w^T e_w I\right)J^{-1}G_2\right).\end{aligned} \tag{83}$$

From Lemma 2, there exist parameters $\varepsilon_{31} > 0$, $\varepsilon_{32} > 0$, $\varepsilon_{33} > 0$, $\varepsilon_{34} > 0$, and $\varepsilon_{35} > 0$ such that

$$\begin{aligned}-e_w^T e_w e_w^T J^{-1}W_{c2}(t)\tilde{\delta}_1 &\le \frac{3}{4\varepsilon_{31}^{(1/3)}}\left\|J^{-1}\right\|_F^{(4/3)}\left\|W_{c2}(t)\right\|_F^{(4/3)}\left(e_w^T e_w\right)^2 + \frac{\varepsilon_{31}}{4}\left(\tilde{\delta}_1^T\tilde{\delta}_1\right)^2,\\ e_w^T e_w e_w^T J^{-1}\tilde{\delta}_2 &\le \frac{3}{4\varepsilon_{32}^{(1/3)}}\left\|J^{-1}\right\|_F^{(4/3)}\left(e_w^T e_w\right)^2 + \frac{\varepsilon_{32}}{4}\left(\tilde{\delta}_2^T\tilde{\delta}_2\right)^2,\\ \frac{1}{2}\mathrm{Tr}\left(W_{c3}^T(t)J^{-T}\left(2e_w e_w^T + e_w^T e_w I\right)J^{-1}W_{c3}(t)\right) &\le \frac{3\varepsilon_{33}}{4}\left\|J^{-1}\right\|_F^4\left\|W_{c3}(t)\right\|^4\left(e_w^T e_w\right)^2 + \frac{3}{4\varepsilon_{33}},\\ \frac{1}{2}\mathrm{Tr}\left(G_2^T J^{-T}\left(2e_w e_w^T + e_w^T e_w I\right)J^{-1}G_2\right) &\le \frac{3\varepsilon_{34}}{4}\left\|J^{-1}\right\|_F^4\left\|G_2\right\|^4\left(e_w^T e_w\right)^2 + \frac{3}{4\varepsilon_{34}},\\ -e_w^T e_w e_w^T J^{-1}W_{c20}\left(t, \tilde{\delta}_1\right) &\le \frac{3}{4\varepsilon_{35}^{(1/3)}}\Pi\left(e_w^T e_w\right)^2 + \frac{\varepsilon_{35}}{2}\left(\tilde{\delta}_1^T\tilde{\delta}_1\right)^2,\end{aligned} \tag{84}$$

where $\Pi = \|J^{-1}\|\|W_{c21}(t)\|^{(4/3)}\|\Delta_{502}(t)\|^{(4/3)}\|\alpha_{31}\|^{(4/3)}\|F(t)\|^{(4/3)} + \|J^{-1}\|\|W_{c21}(t)\|^{(4/3)}\|\Delta_{512}(t)\|^{(4/3)}\|\alpha_{32}\|^{(4/3)}\|F(t)\|^{(4/3)}$. Hence, based on (83), we get

$$\begin{aligned}\mathscr{L}V_{41}(t) \le\ & e_w^T e_w e_w^T J^{-1} u_2 - e_w^T e_w e_w^T J^{-1} W_{c1}(t) + \frac{3}{4\varepsilon_{31}^{(1/3)}}\left\|J^{-1}\right\|_F^{(4/3)}\left\|W_{c2}(t)\right\|_F^{(4/3)}\left(e_w^T e_w\right)^2 + \frac{\varepsilon_{31}}{4}\left(\tilde{\delta}_1^T\tilde{\delta}_1\right)^2 \\ & + \frac{3}{4\varepsilon_{32}^{(1/3)}}\left\|J^{-1}\right\|_F^{(4/3)}\left(e_w^T e_w\right)^2 + \frac{\varepsilon_{32}}{4}\left(\tilde{\delta}_2^T\tilde{\delta}_2\right)^2 + \frac{3\varepsilon_{33}}{4}\left\|J^{-1}\right\|_F^4\left\|W_{c3}(t)\right\|^4\left(e_w^T e_w\right)^2 + \frac{3}{4\varepsilon_{33}} \\ & + \frac{3\varepsilon_{34}}{4}\left\|J^{-1}\right\|_F^4\left\|G_2\right\|^4\left(e_w^T e_w\right)^2 + \frac{3}{4\varepsilon_{34}} + \frac{3}{4\varepsilon_{35}^{(1/3)}}\Pi\left(e_w^T e_w\right)^2 + \frac{\varepsilon_{35}}{4}\left(\tilde{\delta}_1^T\tilde{\delta}_1\right)^2.\end{aligned} \tag{85}$$

Design the controller u_2 as

$$\begin{aligned}u_2 = -\Bigg(& k_7 + \frac{3}{4\varepsilon_{31}^{(1/3)}}\left\|J^{-1}\right\|_F^{(4/3)}\left\|W_{c2}(t)\right\|_F^{(4/3)} + \frac{3}{4\varepsilon_{32}^{(1/3)}}\left\|J^{-1}\right\|_F^{(4/3)} + \frac{3\varepsilon_{33}}{4}\left\|J^{-1}\right\|_F^4\left\|W_{c3}(t)\right\|^4 \\ & + \frac{3\varepsilon_{34}}{4}\left\|J^{-1}\right\|_F^4\left\|G_2\right\|^4 + \frac{3}{4\varepsilon_{35}^{(1/3)}}\Pi\Bigg)e_w + W_{c1}(t) + u_3,\end{aligned} \tag{86}$$

where u_3 is designed in the following steps.

$\mathscr{L}V_{41}(t)$ can be written by

$$\mathscr{L}V_{41}(t) \le -k_7\left(e_w^T e_w\right)^2 + \left(\frac{\varepsilon_{31}}{4} + \frac{\varepsilon_{35}}{4}\right)\left(\tilde{\delta}_1^T\tilde{\delta}_1\right)^2 + \frac{\varepsilon_{32}}{4}\left(\tilde{\delta}_2^T\tilde{\delta}_2\right)^2 + e_w^T e_w e_w^T J^{-1} u_2 + \frac{3}{4\varepsilon_{33}} + \frac{3}{4\varepsilon_{34}}. \tag{87}$$

Define Lyapunov function as follows:

$$V(t) = V_{02}(t) + V_3(t) + V_{41}. \tag{88}$$

Combining (44), (77), and (87), the infinitesimal generator of (88) is represented as

$$\begin{aligned}\mathscr{L}V(t) \le\ & -\left(l_1 - H_{23} - \frac{\varepsilon_{31}}{4} - \frac{\varepsilon_{35}}{4}\right)\left(\tilde{\delta}_1^T\tilde{\delta}_1\right)^2 - \left(l_2 - \frac{\varepsilon_{32}}{4}\right)\left(\tilde{\delta}_2^T\tilde{\delta}_2\right)^2 - k_4 e_p^T e_p - k_4 e_\nu^T e_\nu \\ & - k_5\left(\overline{R}_{3e}^T\overline{R}_{3e}\right)^2 - \left(k_6 - \frac{3\varepsilon_{28}^{(1/3)}}{4}\right)e_\psi^4 - k_7\left(e_w^T e_w\right)^2 + e_w^T e_w e_w^T J^{-1} u_3 \\ & + \frac{\varepsilon_{21}}{4}\left\|\widehat{R}_3\right\|_F^4\left\|E_0\right\|^4\left(e_{w_1}^T e_{w_1}\right)^2 + \frac{1}{4\varepsilon_{28}}\left\|E_1\right\|^4\left(e_w^T e_w\right)^2 + H_3,\end{aligned} \tag{89}$$

where

$$H_3 = H_2 + \frac{3}{4\varepsilon_{33}} + \frac{3}{4\varepsilon_{34}} + H_{02}. \tag{90}$$

Recalling that $e_{w_1}^T e_{w_1} \le e_w^T e_w$, u_3 is designed as

$$u_3 = -\left(\frac{\varepsilon_{21}}{4}\left\|\widehat{R}_3\right\|_F^4\left\|E_0\right\|^4 + \frac{1}{4\varepsilon_{28}}\left\|E_1\right\|^4\right)Je_w. \tag{91}$$

Then, from (89),

$$\begin{aligned}\mathscr{L}V(t) \le\ & -\left(l_1 - H_{23} - \frac{\varepsilon_{31}}{4} - \frac{\varepsilon_{35}}{4}\right)\left(\tilde{\delta}_1^T\tilde{\delta}_1\right)^2 - \left(l_2 - \frac{\varepsilon_{32}}{4}\right)\left(\tilde{\delta}_2^T\tilde{\delta}_2\right)^2 - k_4 e_p^T e_p \\ & - k_4 e_\nu^T e_\nu - k_5\left(\overline{R}_{3e}^T\overline{R}_{3e}\right)^2 - \left(k_6 - \frac{3\varepsilon_{28}^{(1/3)}}{4}\right)e_\psi^4 - k_7\left(e_w^T e_w\right)^2 + H_3.\end{aligned} \tag{92}$$

Based on (86) and (91), (81) can be written as

$$\begin{aligned} J\mathrm{d}e_w = &-\left(k_7 + \frac{3}{4\varepsilon_{31}^{(1/3)}}\left\|J^{-1}\right\|_F^{(4/3)}\left\|W_{c2}(t)\right\|_F^{(4/3)} + \frac{3}{4\varepsilon_{32}^{(1/3)}}\left\|J^{-1}\right\|_F^{(4/3)} + \frac{3\varepsilon_{33}}{4}\left\|J^{-1}\right\|_F^4\left\|W_{c3}(t)\right\|^4 + \frac{3\varepsilon_{34}}{4}\left\|J^{-1}\right\|_F^4\left\|G_2\right\|^4\right. \\ &\left. + \frac{3}{4\varepsilon_{35}^{(1/3)}}\Pi\right)e_w\mathrm{d}t - \left(\frac{\varepsilon_{21}}{4}\left\|\widehat{R}_3\right\|_F^4\left\|E_0\right\|^4 + \frac{1}{4\varepsilon_{28}}\left\|E_1\right\|^4\right)Je_w\mathrm{d}t - W_{c20}\left(t,\widetilde{\delta}_1\right)\mathrm{d}t + \widetilde{\delta}_2\mathrm{d}t \\ &- W_{c3}(t)\mathrm{d}\beta_1 + G_2\mathrm{d}\beta_2. \end{aligned} \tag{93}$$

By using (40), (41), (22), (27), (68), (75), and (93), we get

$$\begin{aligned} \mathrm{d}\widetilde{\delta}_1 &= -\left(L_1 + \left(\frac{3\varepsilon_{01}^{(4/3)}}{4} + \frac{3\varepsilon_{02}^2}{4}\left\|L_1G_1\right\|_F^4\right)\right)\widetilde{\delta}_1\mathrm{d}t - L_1G_1\mathrm{d}\beta_1 - \dot{\delta}_1\mathrm{d}t - \frac{\varepsilon_{11}}{3}\|F(t)\|^2F(t)^T\mathrm{d}t, \\ \mathrm{d}\widetilde{\delta}_2 &= -\left(l_2 + \frac{3\varepsilon_{03}^{(4/3)}}{4} + \frac{3\varepsilon_{04}^2}{4}\left\|L_2G_2\right\|_F^4\right)\widetilde{\delta}_2\mathrm{d}t - \dot{\delta}_2\mathrm{d}t - L_2G_2\mathrm{d}\beta_2, \\ \mathrm{d}e_p &= e_v\mathrm{d}t, \\ \mathrm{d}e_v &= \left(-k_1\tanh\left(e_p + e_v\right) - k_2\tanh\left(e_v\right) + \frac{T_m}{m}\alpha\overline{R}_{3e} + \widetilde{\delta}_1\right)\mathrm{d}t + G_1\mathrm{d}\beta_1, \\ \mathrm{d}e_\psi &= \left(-k_6e_\psi + E_1e_w\right)\mathrm{d}t, \\ \mathrm{d}\overline{R}_{3e} &= \overline{R}_{3e1}(t)\mathrm{d}t + \overline{R}_{3e2}(t)\widetilde{\delta}_1 + \overline{R}_{3e3}(t)\mathrm{d}\beta_1, \\ J\mathrm{d}e_w &= -\left(k_7 + \frac{3}{4\varepsilon_{31}^{(1/3)}}\left\|J^{-1}\right\|_F^{(4/3)}\left\|W_{c2}(t)\right\|_F^{(4/3)} + \frac{3}{4\varepsilon_{32}^{(1/3)}}\left\|J^{-1}\right\|_F^{(4/3)} + \frac{3\varepsilon_{33}}{4}\left\|J^{-1}\right\|_F^4\left\|W_{c3}(t)\right\|^4 + \frac{3\varepsilon_{34}}{4}\left\|J^{-1}\right\|_F^4\left\|G_2\right\|^4\right. \\ &\quad\left. + \frac{3}{4\varepsilon_{35}^{(1/3)}}\Pi\right)e_w\mathrm{d}t - \left(\frac{\varepsilon_{21}}{4}\left\|\widehat{R}_3\right\|_F^4\left\|E_0\right\|^4 + \frac{1}{4\varepsilon_{28}}\left\|E_1\right\|^4\right)Je_w\mathrm{d}t - W_{c20}\left(t,\widetilde{\delta}_1\right)\mathrm{d}t + \widetilde{\delta}_2\mathrm{d}t \\ &\quad - W_{c3}(t)\mathrm{d}\beta_1 + G_2\mathrm{d}\beta_2. \end{aligned} \tag{94}$$

Remark 2. In this paper, the dynamics of helicopter are modeled as the stochastic systems due to the disturbances including the random disturbances. Many control variables of the helicopter stochastic systems are discontinuous. Hence, some advanced control methods cannot be used to design the flight controller, directly, such as the dynamic surface control, fuzzy control, and other control methods. In order to construct the antidisturbance flight controller for the helicopter stochastic systems, the disturbance observer method and backstepping control scheme are applied in our paper.

Remark 3. The control method proposed in this paper shows some weaknesses, such as the complicated controller structure and tedious mathematical derivation while the helicopter stochastic system models are first discussed in this paper and the nonlinear control method is feasible in theory. In the future, we will construct the more advanced antidisturbance flight controller with the simple structure based on the proposed control scheme of this paper.

Remark 4. The structure block diagram of the antidisturbance control scheme is shown in Figure 1. The noises from inside and outside of the helicopter are considered to construct the helicopter models and divided as to different parts: the random disturbances and other times-varying disturbances. Then, the stochastic control theory is applied to analyze the stability of the closed-loop systems. And the stochastic antidisturbance flight controller is constructed.

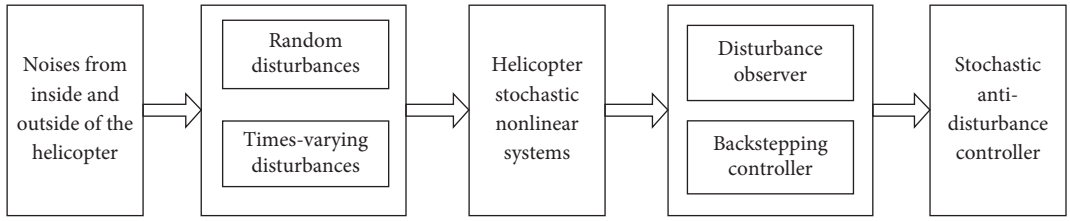

Figure 1: The structure block diagram of the antidisturbance control scheme.

5. Stability Analysis

In this section, the asymptotic boundedness in mean square of the composite closed-loop system (94) is guaranteed under the controllers u_1 and u_2.

Theorem 1. *Considering helicopter system (1) with disturbances, design the disturbance observers as (10) and (41) and the controllers as (20) and (86). The composite closed-loop system (94) is asymptotically bounded in mean square. If there exist parameters* $k_1 > 0,\ k_2 > 0,\ k_3 > 0, k_4 > 0,\ k_5 > 0,\ k_6 > 0,\ k_7 > 0,\ k_8 > 0,\ k_9 > 0,\ l_1 > 0,\ l_2 > 0,\ \varepsilon_{01} > 0,\ \varepsilon_{02} > 0,\ \varepsilon_{03} > 0,\ \varepsilon_{04} > 0, \varepsilon_{11} > 0, \varepsilon_{12} > 0, \varepsilon_{21} > 0, \varepsilon_{22} > 0, \varepsilon_{23} > 0, \varepsilon_{231} > 0, \varepsilon_{232} > 0, \varepsilon_{24} > 0,\ \varepsilon_{25} > 0,\ \varepsilon_{26} > 0,\ \varepsilon_{27} > 0,\ \varepsilon_{28} > 0, \varepsilon_{31} > 0, \varepsilon_{32} > 0, \varepsilon_{33} > 0, \varepsilon_{34} > 0,$ *and* $\varepsilon_{35} > 0,$ *such that* $l_1 - H_{23} - (\varepsilon_{31}/4) - (\varepsilon_{35}/4) > 0,\ l_2 - (\varepsilon_{32}/4) > 0,\ k_4 - H_{22} > 0,\ k_6 - (3\varepsilon_{28}^{(1/3)}/4) > 0$ *hold.*

Proof. Consider the Lyapunov function $V(t)$ as follows:

$$\begin{aligned} V(t) &= V_{02}(t) + V_3(t) + V_{41}(t) \\ &= \frac{1}{4}\left(\tilde{\delta}_1^T\tilde{\delta}_1\right)^2 + \frac{1}{4}\left(\tilde{\delta}_2^T\tilde{\delta}_2\right)^2 + k_1\int_0^{e_p+e_v}\tanh(\mu)\mathrm{d}\mu + k_2\int_0^{e_v}\tanh(\mu)\mathrm{d}\mu \\ &\quad + \frac{1}{2}e_v^Te_v + \frac{1}{4}\left(\overline{R}_{3e}^T\overline{R}_{3e}\right)^2 + \frac{1}{4}e_\psi^4 + \frac{1}{4}\left(e_w^Te_w\right)^2. \end{aligned} \tag{95}$$

Since $h(x) = (\tanh(x)/x)$ is a continuous function, for any $\overline{x} > 0$ and $0 \le x \le \overline{x}$, there exists a positive number $\beta_1 = \beta(\overline{x})$, such that $\beta_1\|x\| \le \|\tanh(x)\| \le \|x\|$. Hence, we have

$$k_1\int_0^{e_p+e_v}\tanh(\mu)\mathrm{d}\mu + k_2\int_0^{e_v}\tanh(\mu)\mathrm{d}\mu \ge k_8e_p^Te_p + k_8e_v^Te_v, \tag{96}$$

where $k_8 = \max\left\{\mathrm{eig}\left\{\begin{pmatrix} (1/2)k_1\beta_1 & (1/2)k_1\beta_1 \\ (1/2)k_1\beta_1 & (1/2)k_1\beta_1 + (1/2)k_2\beta_1 \end{pmatrix}\right\}\right\} > 0$. Moreover,

$$k_1\int_0^{e_p+e_v}\tanh(\mu)\mathrm{d}\mu + k_2\int_0^{e_v}\tanh(\mu)\mathrm{d}\mu \le k_9e_p^Te_p + k_9e_v^Te_v, \tag{97}$$

where $k_9 = \min\left\{\mathrm{eig}\left\{\begin{pmatrix} (1/2)k_1 & (1/2)k_1 \\ (1/2)k_1 & (1/2)k_1 + (1/2)k_2 \end{pmatrix}\right\}\right\} > 0.$

Then, we confirm that

$$\begin{aligned} &\frac{1}{4}\left(\tilde{\delta}_1^T\tilde{\delta}_1\right)^2 + \frac{1}{4}\left(\tilde{\delta}_2^T\tilde{\delta}_2\right)^2 + k_8e_p^Te_p + \left(k_8 + \frac{1}{2}\right)e_v^Te_v + \frac{1}{4}\left(\overline{R}_{3e}^T\overline{R}_{3e}\right)^2 + \frac{1}{4}e_\psi^4 + \frac{1}{4}\left(e_w^Te_w\right)^2 \\ &\le V(t) \le \frac{1}{4}\left(\tilde{\delta}_1^T\tilde{\delta}_1\right)^2 + \frac{1}{4}\left(\tilde{\delta}_2^T\tilde{\delta}_2\right)^2 + k_9e_p^Te_p + \left(k_9 + \frac{1}{2}\right)e_v^Te_v + \frac{1}{4}\left(\overline{R}_{3e}^T\overline{R}_{3e}\right)^2 + \frac{1}{4}e_\psi^4 + \frac{1}{4}\left(e_w^Te_w\right)^2, \end{aligned} \tag{98}$$

which satisfies (8) in Lemma 1 with $p = 2$.

From the discussion in Sections 3 and 4, we have

$$\begin{aligned} \mathscr{L}V(t) \le &-\left(l_1 - H_{23} - \frac{\varepsilon_{31}}{4} - \frac{\varepsilon_{35}}{4}\right)\left(\tilde{\delta}_1^T\tilde{\delta}_1\right)^2 - \left(l_2 - \frac{\varepsilon_{32}}{4}\right)\left(\tilde{\delta}_2^T\tilde{\delta}_2\right)^2 - k_4e_p^Te_p \\ &- k_4e_v^Te_v - k_5\left(\overline{R}_{3e}^T\overline{R}_{3e}\right)^2 - \left(k_6 - \frac{3\varepsilon_{28}^{(1/3)}}{4}\right)e_\psi^4 - k_7\left(e_w^Te_w\right)^2 + H_3 \le -\lambda V(t) + H_3, \end{aligned} \tag{99}$$

where

$$\lambda = \min\left\{4\left(l_1 - H_{23} - \frac{\varepsilon_{31}}{4} - \frac{\varepsilon_{35}}{4}\right), 4\left(l_2 - \frac{\varepsilon_{32}}{4}\right), \frac{k_4}{k_9}, \frac{k_4}{k_9 + (1/2)}, 4k_5, 4\left(k_6 - \frac{3\varepsilon_{28}^{(1/3)}}{4}\right), 4k_7\right\}, \tag{100}$$

which implies that $V(t)$ satisfies (9) in Lemma 1 with $p = 2$.

Consequently, based on the discussion above, the composite closed-loop system (94) is asymptotically bounded in mean square. □

6. Conclusion

This paper studies the tracking control issue for nonlinear helicopter systems under stochastic disturbances and time-varying disturbances. These disturbances are attenuated and rejected via the nonlinear disturbance observer control method and stochastic control theory, and the backstepping control approach is adopted for nonlinear helicopter systems. The problems of "dimension explosion" are analyzed for complicated nonlinear control systems.

Since the helicopter systems are modeled as the stochastic systems, many advanced nonlinear control methods can be directly used. The phenomenon of "dimension explosion" is inevitable in nonlinear controller constructing process. In the future, we will combine some advanced nonlinear control methods and stochastic control theory and propose the more advanced antidisturbance flight control scheme with simple structure.

Appendix

From (67), $\mathrm{d}w_{1c}$ can be written by

$$\begin{aligned}
\mathrm{d}w_{1c} = &-\mathrm{d}\left(\left(k_5 + H_{25} + \frac{H_{24}}{4\|u_1\|^{(4/3)}} + \frac{3\varepsilon_{25}}{4\|u_1\|^2} + \frac{1}{4\varepsilon_{27}}\|\alpha\|_F^4\right)\widehat{R}_3^{-1}\overline{R}_{3e}\right) \\
&- \mathrm{d}\left(\frac{\varepsilon_{12}\|u_1\|^3\|\alpha\|^2\|F(t)\|^2}{3}\widehat{R}_3^{-1}\alpha^T F(t)\right) \\
&- \mathrm{d}\left(\frac{\varepsilon_{232}}{2\|u_1\|^4}\left(e_v^T e_v\right)^2\widehat{R}_3^{-1}\overline{R}_{3e}\right) + d\left(\frac{\varepsilon_{11}\|F(t)\|^2}{3\|u_1\|}\widehat{R}_3^{-1}E_0F(t)\right).
\end{aligned} \tag{A.1}$$

A. The Calculation of $\mathrm{d}((k_5 + H_{25} + (H_{24}/4\|u_1\|^{(4/3)}) + (3\varepsilon_{25}/4\|u_1\|^2) + (1/4\varepsilon_{27})\|u_1\|_F^4)\widehat{R}_3^{-1}\overline{R}_{3e})$

Consider

$$\begin{aligned}
&\mathrm{d}\left(\left(k_5 + H_{25} + \frac{H_{24}}{4\|u_1\|^{(4/3)}} + \frac{3\varepsilon_{25}}{4\|u_1\|^2} + \frac{1}{4\varepsilon_{27}}\|\alpha\|_F^4\right)\widehat{R}_3^{-1}\overline{R}_{3e}\right) \\
&= \mathrm{d}\left(k_5 + H_{25} + \frac{H_{24}}{4\|u_1\|^{(4/3)}} + \frac{3\varepsilon_{25}}{4\|u_1\|^2} + \frac{1}{4\varepsilon_{27}}\|\alpha\|_F^4\right)\widehat{R}_3^{-1}\overline{R}_{3e} \\
&\left(k_5 + H_{25} + \frac{H_{24}}{4\|u_1\|^{(4/3)}} + \frac{3\varepsilon_{25}}{4\|u_1\|^2} + \frac{1}{4\varepsilon_{27}}\|\alpha\|_F^4\right)\mathrm{d}\widehat{R}_3^{-1}\overline{R}_{3e} \\
&\left(k_5 + H_{25} + \frac{H_{24}}{4\|u_1\|^{(4/3)}} + \frac{3\varepsilon_{25}}{4\|u_1\|^2} + \frac{1}{4\varepsilon_{27}}\|\alpha\|_F^4\right)\widehat{R}_3^{-1}\mathrm{d}\overline{R}_{3e}.
\end{aligned} \tag{A.2}$$

For $\mathrm{d}u_1$, we deduce

$$\mathrm{d}\left\|u_1\right\| = -\frac{\mathrm{d}u_1^T \cdot u_1 + u_1^T \mathrm{d}u_1}{2\sqrt{u_1^T u_1}} = -\frac{u_1^T}{\left\|u_1\right\|}\left(\Delta_{01}(t)\mathrm{d}t + \Delta_{02}(t)\widetilde{\delta}_1 \mathrm{d}t + \Delta_{03}(t)\mathrm{d}\beta_1\right), \tag{A.3}$$

which means that

$$\begin{aligned}
\mathrm{d}\frac{H_{24}}{4\left\|u_1\right\|^{(4/3)}} &= -\frac{H_{24}}{3\left\|u_1\right\|^{(7/3)}}\mathrm{d}\left\|u_1\right\| = \frac{H_{24}u_1^T}{3\left\|u_1\right\|^{(10/3)}}\left(\Delta_{01}(t)\mathrm{d}t + \Delta_{02}(t)\widetilde{\delta}_1 \mathrm{d}t + \Delta_{03}(t)\mathrm{d}\beta_1\right), \\
\mathrm{d}\frac{3\varepsilon_{25}}{4\left\|u_1\right\|^2} &= -\frac{3\varepsilon_{25}}{2\left\|u_1\right\|^3}\mathrm{d}\left\|u_1\right\| = \frac{3\varepsilon_{25}u_1^T}{2\left\|u_1\right\|^4}\left(\Delta_{01}(t)\mathrm{d}t + \Delta_{02}(t)\widetilde{\delta}_1 \mathrm{d}t + \Delta_{03}(t)\mathrm{d}\beta_1\right).
\end{aligned} \tag{A.4}$$

For $\|\alpha\|_F$, one has

$$\alpha^T\alpha = \begin{pmatrix} 1 & 0 & \dfrac{-R_{13}-R_{13c}}{R_{33}+R_{33c}} \\ 0 & 1 & \dfrac{-R_{23}-R_{23c}}{R_{33}+R_{33c}} \end{pmatrix}\begin{pmatrix} 1 & 0 \\ 0 & 1 \\ \dfrac{-R_{13}-R_{13c}}{R_{33}+R_{33c}} & \dfrac{-R_{23}-R_{23c}}{R_{33}+R_{33c}} \end{pmatrix} = \begin{pmatrix} 1+\left(\dfrac{R_{13}+R_{13c}}{R_{33}+R_{33c}}\right)^2 & \dfrac{(R_{13}+R_{13c})(R_{23}+R_{23c})}{(R_{33}+R_{33c})^2} \\ \dfrac{(R_{13}+R_{13c})(R_{23}+R_{23c})}{(R_{33}+R_{33c})^2} & 1+\left(\dfrac{R_{23}+R_{23c}}{R_{33}+R_{33c}}\right)^2 \end{pmatrix}. \tag{A.5}$$

Hence,

$$\begin{aligned}
\|\alpha\|_F &= \left(\mathrm{Tr}\left(\alpha\alpha^T\right)\right)^{(1/2)} = \left(\mathrm{Tr}\left(\alpha^T\alpha\right)\right)^{(1/2)} = 2 + \frac{(R_{13}+R_{13c})^2 + (R_{23}+R_{23c})^2}{(R_{33}+R_{33c})^2}, \\
d\|\alpha\|_F &= \Delta_{21}(t)\mathrm{d}R_3 + \Delta_{21}(t)\frac{1}{\sqrt{u_1^T u_1}}\left(I_3 - \frac{u_1u_1^T}{u_1^T u_1}\right)\Delta_{01}(t)\mathrm{d}t + \Delta_{21}(t)\frac{1}{\sqrt{u_1^T u_1}}\left(I_3 - \frac{u_1u_1^T}{u_1^T u_1}\right)\Delta_{02}(t)\widetilde{\delta}_1\mathrm{d}t \\
&\quad + \Delta_{21}(t)\frac{1}{\sqrt{u_1^T u_1}}\left(I_3 - \frac{u_1u_1^T}{u_1^T u_1}\right)\Delta_{03}(t)\mathrm{d}\beta_1,
\end{aligned} \tag{A.6}$$

where

$$\Delta_{21}(t) = \begin{pmatrix} \dfrac{2(R_{13}+R_{13c})}{(R_{33}+R_{33c})^2} & \dfrac{2(R_{23}+R_{23c})}{(R_{33}+R_{33c})^2} & \dfrac{2(R_{13}+R_{13c})^2 + (R_{23}+R_{23c})^2}{(R_{33}+R_{33c})^2} \end{pmatrix}. \tag{A.7}$$

From the above discussion,

$$\mathrm{d}\left(k_5 + H_{25} + \frac{H_{24}}{4\left\|u_1\right\|^{(4/3)}} + \frac{3\varepsilon_{25}}{4\left\|u_1\right\|^2} + \frac{1}{4\varepsilon_{27}}\|\alpha\|_F^4\right) = \Delta_{31}(t)\mathrm{d}t + \Delta_{32}(t)\widetilde{\delta}_1\mathrm{d}t + \Delta_{33}(t)\mathrm{d}\beta_1, \tag{A.8}$$

where

$$\Delta_{31}(t) = \frac{H_{24}u_1^T}{3\|u_1\|^{(10/3)}}\Delta_{01}(t) + \frac{3\varepsilon_{25}u_1^T}{2\|u_1\|^4}\Delta_{01}(t) + \frac{1}{\varepsilon_{27}}\|\alpha\|_F^3\Delta_{22}(t),$$
$$\Delta_{32}(t) = \frac{H_{24}u_1^T}{3\|u_1\|^{(10/3)}}\Delta_{02}(t) + \frac{3\varepsilon_{25}u_1^T}{2\|u_1\|^4}\Delta_{02}(t) + \frac{1}{\varepsilon_{27}}\|\alpha\|_F^3\Delta_{23}(t), \tag{A.9}$$
$$\Delta_{33}(t) = \frac{H_{24}u_1^T}{3\|u_1\|^{(10/3)}}\Delta_{03}(t) + \frac{3\varepsilon_{25}u_1^T}{2\|u_1\|^4}\Delta_{03}(t) + \frac{1}{\varepsilon_{27}}\|\alpha\|_F^3\Delta_{24}(t).$$

Note that

$$\widehat{R}_3^{-1} = \frac{1}{\|\widehat{R}_3\|}\begin{pmatrix} R_{22} & -R_{11} \\ R_{21} & -R_{12} \end{pmatrix} = \frac{1}{\cos\phi\cos\theta}\begin{pmatrix} R_{22} & -R_{11} \\ R_{21} & -R_{12} \end{pmatrix} = \frac{1}{R_{33}}\begin{pmatrix} R_{22} & -R_{11} \\ R_{21} & -R_{12} \end{pmatrix}, \tag{A.10}$$

then we have

$$\mathrm{d}\widehat{R}_3^{-1} = \frac{-\mathrm{d}R_{33}}{R_{33}^2}\begin{pmatrix} R_{22} & -R_{11} \\ R_{21} & -R_{12} \end{pmatrix} + \frac{1}{R_{33}}\begin{pmatrix} \mathrm{d}R_{22} & -\mathrm{d}R_{11} \\ \mathrm{d}R_{21} & -\mathrm{d}R_{12} \end{pmatrix}. \tag{A.11}$$

In fact, $\mathrm{d}R = R \times w\mathrm{d}t$, which is

$$\begin{pmatrix} \mathrm{d}R_{11} & \mathrm{d}R_{12} & \mathrm{d}R_{13} \\ \mathrm{d}R_{21} & \mathrm{d}R_{22} & \mathrm{d}R_{23} \\ \mathrm{d}R_{31} & \mathrm{d}R_{32} & \mathrm{d}R_{33} \end{pmatrix} = \begin{pmatrix} R_{11} & R_{12} & R_{13} \\ R_{21} & R_{22} & R_{23} \\ R_{31} & R_{32} & R_{33} \end{pmatrix}\begin{pmatrix} 0 & -r & q \\ r & 0 & -p \\ -q & p & 0 \end{pmatrix}. \tag{A.12}$$

Thus, $\mathrm{d}\widehat{R}_3^{-1}$ can be obtained for the controller u_2. Moreover, we can easily get that

$$\mathrm{d}\left(\left(k_5 + H_{25} + \frac{H_{24}}{4\|u_1\|^{(4/3)}} + \frac{3\varepsilon_{25}}{4\|u_1\|^2} + \frac{1}{4\varepsilon_{27}}\|\alpha\|_F^4\right)\widehat{R}_3^{-1}\overline{R}_{3e}\right) = \Delta_{41}(t)\mathrm{d}t + \Delta_{42}(t)\widetilde{\delta}_1\mathrm{d}t + \Delta_{43}(t)\mathrm{d}\beta_1, \tag{A.13}$$

where

$$\begin{aligned}\Delta_{41}(t) &= \widehat{R}_3^{-1}\overline{R}_{3e}\Delta_{31}(t) + \left(k_5 + H_{25} + \frac{H_{24}}{4\|u_1\|^{(4/3)}} + \frac{3\varepsilon_{25}}{4\|u_1\|^2} + \frac{1}{4\varepsilon_{27}}\|\alpha\|_F^4\right)\mathrm{d}\widehat{R}_3^{-1}\overline{R}_{3e} \\ &\quad + \left(k_5 + H_{25} + \frac{H_{24}}{4\|u_1\|^{(4/3)}} + \frac{3\varepsilon_{25}}{4\|u_1\|^2} + \frac{1}{4\varepsilon_{27}}\|\alpha\|_F^4\right)\widehat{R}_3^{-1}\overline{R}_{3e1}(t), \\ \Delta_{42}(t) &= \widehat{R}_3^{-1}\overline{R}_{3e}\Delta_{32}(t) + \left(k_5 + H_{25} + \frac{H_{24}}{4\|u_1\|^{(4/3)}} + \frac{3\varepsilon_{25}}{4\|u_1\|^2} + \frac{1}{4\varepsilon_{27}}\|\alpha\|_F^4\right)\widehat{R}_3^{-1}\overline{R}_{3e2}(t), \\ \Delta_{43}(t) &= \widehat{R}_3^{-1}\overline{R}_{3e}\Delta_{33}(t) + \left(k_5 + H_{25} + \frac{H_{24}}{4\|u_1\|^{(4/3)}} + \frac{3\varepsilon_{25}}{4\|u_1\|^2} + \frac{1}{4\varepsilon_{27}}\|\alpha\|_F^4\right)\widehat{R}_3^{-1}\overline{R}_{3e3}(t).\end{aligned} \tag{A.14}$$

B. The Calculation of $\mathrm{d}((\varepsilon_{12}\|u_1\|^3\|\alpha\|^2\|F(t)\|^2/3)\widehat{R}_3^{-1}\alpha^T F(t))$

Consider

$$\begin{aligned}
&\mathrm{d}\left(\frac{\varepsilon_{12}\|u_1\|^3\|\alpha\|^2\|F(t)\|^2}{3}\widehat{R}_3^{-1}\alpha^T F(t)\right)\\
&=\varepsilon_{12}\|u_1\|^2\mathrm{d}\|u_1\|\|\alpha\|^2\|F(t)\|^2\widehat{R}_3^{-1}\alpha^T F(t)+\frac{2\varepsilon_{12}}{3}\|u_1\|^3\|\alpha\|\mathrm{d}\|\alpha\|\|F(t)\|^2\widehat{R}_3^{-1}\alpha^T F(t)\\
&\quad+\frac{2\varepsilon_{12}}{3}\|u_1\|\|\alpha\|^2\|F(t)\|\mathrm{d}\|F(t)\|\widehat{R}_3^{-1}\alpha^T F(t)+\frac{\varepsilon_{12}}{3}\|u_1\|^3\|\alpha\|^2\|F(t)\|^2\mathrm{d}\widehat{R}_3^{-1}\alpha^T F(t)\\
&\quad+\frac{\varepsilon_{12}}{3}\|u_1\|^3\|\alpha\|^2\|F(t)\|^2\widehat{R}_3^{-1}\mathrm{d}\alpha^T F(t)+\frac{\varepsilon_{12}}{3}\|u_1\|^3\|\alpha\|^2\|F(t)\|^2\widehat{R}_3^{-1}\alpha^T\mathrm{d}F(t).
\end{aligned}\tag{B.1}$$

Hence,

$$\begin{aligned}
&\varepsilon_{12}\|u_1\|^2\mathrm{d}\|u_1\|\|\alpha\|^2\|F(t)\|^2\widehat{R}_3^{-1}\alpha^T F(t)\\
&=\frac{2\varepsilon_{12}}{3}\|u_1\|^3\|\alpha\|\|F(t)\|^2\widehat{R}_3^{-1}\alpha^T F(t)\Big\|\left(\Delta_{22}(t)\mathrm{d}t+\Delta_{23}(t)\widetilde{\delta}_1\mathrm{d}t+\Delta_{24}(t)\mathrm{d}\beta_1\right).
\end{aligned}\tag{B.2}$$

For $(2\varepsilon_{12}/3)\|u_1\|^3\|\alpha\|^2\|F(t)\|\mathrm{d}\|F(t)\|\widehat{R}_3^{-1}\alpha^T F(t)$, we first calculate the $\mathrm{d}F(t)$:

$$\mathrm{d}F(t)=\Delta_{401}(t)\mathrm{d}t+\Delta_{402}(t)\widetilde{\delta}_1\mathrm{d}t+\Delta_{403}(t)\mathrm{d}\beta_1,\tag{B.3}$$

where

$$\begin{aligned}
\Delta_{401}(t)&=\left((k_1+k_2+1)I+k_1\mathrm{Tanh}^2\left(e_p+e_v\right)+k_2\left(\mathrm{Tanh}^2(e_v)\right)\right)\left(-k_1\tanh\left(e_p+e_v\right)-k_2\tanh(e_v)+\frac{T_m}{m}\alpha\overline{R}_{3e}\right)\\
&\quad+k_1\left(I+\mathrm{Tanh}^2\left(e_p+e_v\right)\right)e_v,\\
\Delta_{402}(t)&=\left((k_1+k_2+1)I+k_1\mathrm{Tanh}^2\left(e_p+e_v\right)+k_2\left(\mathrm{Tanh}^2(e_v)\right)\right),\\
\Delta_{403}(t)&=\left((k_1+k_2+1)I+k_1\mathrm{Tanh}^2\left(e_p+e_v\right)+k_2\left(\mathrm{Tanh}^2(e_v)\right)\right)G_1.
\end{aligned}\tag{B.4}$$

Thus, we obtain

$$\mathrm{d}\|F(t)\|=-\frac{\mathrm{d}F(t)^T\cdot F(t)+F(t)^T\mathrm{d}F(t)}{2\sqrt{F(t)^TF(t)}}=-\frac{F(t)^T}{\|F(t)\|}\left(\Delta_{401}(t)\mathrm{d}t+\Delta_{402}(t)\widetilde{\delta}_1\mathrm{d}t+\Delta_{403}(t)\mathrm{d}\beta_1\right).\tag{B.5}$$

Then, we drive

$$\begin{aligned}&\frac{2\varepsilon_{12}}{3}\left\|u_1\right\|^3\|\alpha\|^2\|F(t)\|\mathrm{d}\|F(t)\|\widehat{R}_3^{-1}\alpha^T F(t)\\&=-\frac{2\varepsilon_{12}}{3}\left\|u_1\right\|^3\|\alpha\|^2\|F(t)\|\widehat{R}_3^{-1}\alpha^T F(t)\left(\frac{F(t)^T}{\|F(t)\|}\left(\Delta_{401}(t)\mathrm{d}t+\Delta_{402}(t)\widetilde{\delta}_1\mathrm{d}t+\Delta_{403}(t)\mathrm{d}\beta_1\right)\right).\end{aligned}\tag{B.6}$$

In order to calculate $(\varepsilon_{12}/3)\|u_1\|^3\|\alpha\|^2\|F(t)\|^2\widehat{R}_3^{-1}\mathrm{d}\alpha^T F(t)$, we first give the derivative of $\mathrm{d}\alpha$ as follows:

$$\begin{aligned}\mathrm{d}\alpha=&\begin{pmatrix}0&0\\0&0\\\dfrac{-(R_{33}+R_{33c})\mathrm{d}R_{13}+(R_{13}+R_{13c})\mathrm{d}R_{33}}{(R_{33}+R_{33c})^2}&\dfrac{-(R_{33}+R_{33c})\mathrm{d}R_{23}+(R_{23}+R_{23c})\mathrm{d}R_{33}}{(R_{33}+R_{33c})^2}\end{pmatrix}\\&+\begin{pmatrix}0&0\\0&0\\\dfrac{-(R_{33}+R_{33c})\mathrm{d}R_{13c}+(R_{13}+R_{13c})\mathrm{d}R_{33c}}{(R_{33}+R_{33c})^2}&\dfrac{-(R_{33}+R_{33c})\mathrm{d}R_{23c}+(R_{23}+R_{23c})\mathrm{d}R_{33c}}{(R_{33}+R_{33c})^2}\end{pmatrix}.\end{aligned}\tag{B.7}$$

Due to

$$\begin{aligned}\frac{-(R_{33}+R_{33c})\mathrm{d}R_{13c}+(R_{13}+R_{13c})\mathrm{d}R_{33c}}{(R_{33}+R_{33c})^2}&=\Delta_{501}(t)+\Delta_{502}(t)\widetilde{\delta}_1+\Delta_{503}(t)\mathrm{d}\beta_1,\\\frac{-(R_{33}+R_{33c})\mathrm{d}R_{23c}+(R_{23}+R_{23c})\mathrm{d}R_{33c}}{(R_{33}+R_{33c})^2}&=\Delta_{511}(t)+\Delta_{512}(t)\widetilde{\delta}_1+\Delta_{513}(t)\mathrm{d}\beta_1,\end{aligned}\tag{B.8}$$

where

$$\begin{aligned}\Delta_{501}(t)&=\frac{1}{(R_{33}+R_{33c})^2}\begin{pmatrix}R_{33}+R_{33c}&0&-(R_{13}+R_{13c})\end{pmatrix}\Delta_{01}(t),\\\Delta_{502}(t)&=\frac{1}{(R_{33}+R_{33c})^2}\begin{pmatrix}R_{33}+R_{33c}&0&-(R_{13}+R_{13c})\end{pmatrix}\Delta_{02}(t),\\\Delta_{503}(t)&=\frac{1}{(R_{33}+R_{33c})^2}\begin{pmatrix}R_{33}+R_{33c}&0&-(R_{13}+R_{13c})\end{pmatrix}\Delta_{03}(t),\\\Delta_{511}(t)&=\frac{1}{(R_{33}+R_{33c})^2}\begin{pmatrix}R_{33}+R_{33c}&0&-(R_{23}+R_{23c})\end{pmatrix}\Delta_{01}(t),\\\Delta_{512}(t)&=\frac{1}{(R_{33}+R_{33c})^2}\begin{pmatrix}R_{33}+R_{33c}&0&-(R_{23}+R_{23c})\end{pmatrix}\Delta_{02}(t),\\\Delta_{513}(t)&=\frac{1}{(R_{33}+R_{33c})^2}\begin{pmatrix}R_{33}+R_{33c}&0&-(R_{23}+R_{23c})\end{pmatrix}\Delta_{03}(t).\end{aligned}\tag{B.9}$$

Then, $d\alpha$ is represented as

$$d\alpha = \Delta_{51}(t) + \Delta_{52}\left(t, \widetilde{\delta}_1\right) + \Delta_{53}(t)d\beta_1, \tag{B.10}$$

where

$$\alpha_2 = \begin{pmatrix} 0 & 0 \\ 0 & 0 \\ \dfrac{-(R_{33}+R_{33c})dR_{13} + (R_{13}+R_{13c})dR_{33}}{(R_{33}+R_{33c})^2} & \dfrac{-(R_{33}+R_{33c})dR_{23} + (R_{23}+R_{23c})dR_{33}}{(R_{33}+R_{33c})^2} \end{pmatrix},$$

$$\alpha_{31} = \begin{pmatrix} 0 & 0 \\ 0 & 0 \\ 1 & 0 \end{pmatrix},$$

$$\alpha_{32} = \begin{pmatrix} 0 & 0 \\ 0 & 0 \\ 0 & 1 \end{pmatrix},$$

$$\Delta_{51} = \alpha_2 + \alpha_{31}\Delta_{501}(t) + \alpha_{32}\Delta_{511}(t),$$

$$\Delta_{52}\left(t, \widetilde{\delta}_1\right) = \Delta_{502}(t)\widetilde{\delta}_1\alpha_{31} + \Delta_{512}(t)\widetilde{\delta}_1\alpha_{32},$$

$$\Delta_{53} = \alpha_{31}\Delta_{503}(t) + \alpha_{32}\Delta_{513}(t). \tag{B.11}$$

Hence, we can obtain that

$$\frac{\varepsilon_{12}}{3}\|u_1\|^3\|\alpha\|^2\|F(t)\|^2\widehat{R}_3^{-1}d\alpha^T F(t) = \frac{\varepsilon_{12}}{3}\|u_1\|^3\|\alpha\|^2\|F(t)\|^2\widehat{R}_3^{-1}\left(\Delta_{51}(t) + \Delta_{52}\left(t, \widetilde{\delta}_1\right) + \Delta_{53}(t)d\beta_1\right)^T F(t). \tag{B.12}$$

For the part of $(\varepsilon_{12}/3)\|u_1\|^3\|\alpha\|^2\|F(t)\|^2\widehat{R}_3^{-1}\alpha^T dF(t)$, we have

$$\frac{\varepsilon_{12}}{3}\|u_1\|^3\|\alpha\|^2\|F(t)\|^2\widehat{R}_3^{-1}\alpha^T dF(t) = \frac{\varepsilon_{12}}{3}\|u_1\|^3\|\alpha\|^2\|F(t)\|^2\widehat{R}_3^{-1}\alpha^T\left(\Delta_{401}(t)dt + \Delta_{402}(t)\widetilde{\delta}_1 dt + \Delta_{403}(t)d\beta_1\right). \tag{B.13}$$

Hence,

$$d\left(\frac{\varepsilon_{12}\|u_1\|^3\|\alpha\|^2\|F(t)\|^2}{3}\widehat{R}_3^{-1}\alpha^T F(t)\right) = \Delta_{61}(t)dt + \Delta_{621}(t)\widetilde{\delta}_1 dt + \Delta_{622}\left(t, \widetilde{\delta}_1\right)dt + \Delta_{63}(t)d\beta_1, \tag{B.14}$$

where

$$\begin{aligned}
\Delta_{61}(t) &= -\varepsilon_{12}\|u_1\|\|\alpha\|^2\|F(t)\|^2\widehat{R}_3^{-1}\alpha^T F(t)u_1^T\Delta_{01}(t) + \frac{2\varepsilon_{12}}{3}\|u_1\|^3\|\alpha\|\|F(t)\|^2\widehat{R}_3^{-1}\alpha^T F(t)\Delta_{22}(t)\\
&\quad - \frac{2\varepsilon_{12}}{3}\|u_1\|^3\|\alpha\|^2\widehat{R}_3^{-1}\alpha^T F(t)F(t)^T\Delta_{401}(t) + \frac{\varepsilon_{12}}{3}\|u_1\|^3\|\alpha\|^2\|F(t)\|^2\mathrm{d}\widehat{R}_3^{-1}\alpha^T F(t)\\
&\quad + \frac{\varepsilon_{12}}{3}\|u_1\|^3\|\alpha\|^2\|F(t)\|^2\widehat{R}_3^{-1}\Delta_{51}(t)^T F(t) + \frac{\varepsilon_{12}}{3}\|u_1\|^3\|\alpha\|^2\|F(t)\|^2\widehat{R}_3^{-1}\alpha^T\Delta_{401}(t),\\
\Delta_{621}(t) &= -\varepsilon_{12}\|u_1\|\|\alpha\|^2\|F(t)\|^2\widehat{R}_3^{-1}\alpha^T F(t)u_1^T\Delta_{02}(t) + \frac{2\varepsilon_{12}}{3}\|u_1\|^3\|\alpha\|\|F(t)\|^2\widehat{R}_3^{-1}\alpha^T F(t)\Delta_{23}(t)\\
&\quad - \frac{2\varepsilon_{12}}{3}\|u_1\|^3\|\alpha\|^2\widehat{R}_3^{-1}\alpha^T F(t)F(t)^T\Delta_{402}(t),\\
\Delta_{63}(t) &= -\varepsilon_{12}\|u_1\|\|\alpha\|^2\|F(t)\|^2\widehat{R}_3^{-1}\alpha^T F(t)u_1^T\Delta_{03}(t) + \frac{2\varepsilon_{12}}{3}\|u_1\|^3\|\alpha\|\|F(t)\|^2\widehat{R}_3^{-1}\alpha^T F(t)\Delta_{24}(t)\\
&\quad - \frac{2\varepsilon_{12}}{3}\|u_1\|^3\|\alpha\|^2\widehat{R}_3^{-1}\alpha^T F(t)F(t)^T\Delta_{403}(t) + \frac{\varepsilon_{12}}{3}\|u_1\|^3\|\alpha\|^2\|F(t)\|^2\widehat{R}_3^{-1}\Delta_{53}(t)^T F(t)\\
&\quad + \frac{\varepsilon_{12}}{3}\|u_1\|^3\|\alpha\|^2\|F(t)\|^2\widehat{R}_3^{-1}\alpha^T\Delta_{403}(t),\\
\Delta_{622}\left(t,\widetilde{\delta}_1\right) &= \frac{\varepsilon_{12}}{3}\|u_1\|^3\|\alpha\|^2\|F(t)\|^2\widehat{R}_3^{-1}\Delta_{52}\left(t,\widetilde{\delta}_1\right)^T F(t).
\end{aligned} \tag{B.15}$$

C. The Calculation of $\mathrm{d}\left(\left(\varepsilon_{232}/2\|u_1\|^4\right)\left(e_v^T e_v\right)^2 \widehat{R}_3^{-1}\overline{R}_{3e}\right)$

Consider

$$\begin{aligned}
\mathrm{d}\left(\frac{\varepsilon_{232}}{2\|u_1\|^4}\left(e_v^T e_v\right)^2\widehat{R}_3^{-1}\overline{R}_{3e}\right) &= \mathrm{d}\frac{\varepsilon_{232}}{2\|u_1\|^4}\left(e_v^T e_v\right)^2\widehat{R}_3^{-1}\overline{R}_{3e} + \frac{\varepsilon_{232}}{2\|u_1\|^4}\mathrm{d}\left(e_v^T e_v\right)^2\widehat{R}_3^{-1}\overline{R}_{3e}\\
&\quad + \frac{\varepsilon_{232}}{2\|u_1\|^4}\left(e_v^T e_v\right)^2\mathrm{d}\widehat{R}_3^{-1}\overline{R}_{3e} + \frac{\varepsilon_{232}}{2\|u_1\|^4}\left(e_v^T e_v\right)^2\widehat{R}_3^{-1}\mathrm{d}\overline{R}_{3e}.
\end{aligned} \tag{C.1}$$

For the derivatives of those teams, we have

$$\begin{aligned}
\mathrm{d}\frac{\varepsilon_{232}}{2\|u_1\|^4}\left(e_v^T e_v\right)^2\widehat{R}_3^{-1}\overline{R}_{3e} &= \frac{4\varepsilon_{232}}{2\|u_1\|^6}\left(e_v^T e_v\right)^2\widehat{R}_3^{-1}\overline{R}_{3e}u_1^T\left(\Delta_{01}(t)\mathrm{d}t + \Delta_{02}(t)\widetilde{\delta}_1\mathrm{d}t + \Delta_{03}(t)\mathrm{d}\beta_1\right),\\
\frac{\varepsilon_{232}}{2\|u_1\|^4}\mathrm{d}\left(e_v^T e_v\right)^2\widehat{R}_3^{-1}\overline{R}_{3e} &= \frac{4\varepsilon_{232}}{2\|u_1\|^4}\widehat{R}_3^{-1}\overline{R}_{3e}e_v^T e_v e_v^T\left(-k_1\tanh\left(e_p + e_v\right) - k_2\tanh\left(e_v\right)\right.\\
&\quad \left. + \frac{T_m}{m}\alpha\overline{R}_{3e} + \widetilde{\delta}_1 + G_1\mathrm{d}\beta_1\right),\\
\frac{\varepsilon_{232}}{2\|u_1\|^4}\left(e_v^T e_v\right)^2\widehat{R}_3^{-1}\mathrm{d}\overline{R}_{3e} &= \frac{\varepsilon_{232}}{2\|u_1\|^4}\left(e_v^T e_v\right)^2\widehat{R}_3^{-1}\left(\overline{R}_{3e1}(t)\mathrm{d}t + \overline{R}_{3e2}(t)\widetilde{\delta}_1\mathrm{d}t + \overline{R}_{3e3}(t)\mathrm{d}\beta_1\right).
\end{aligned} \tag{C.2}$$

Therefore, one has

$$\mathrm{d}\left(\frac{\varepsilon_{232}}{2\left\|u_1\right\|^4}\left(e_v^T e_v\right)^2 \widehat{R}_3^{-1}\overline{R}_{3e}\right) = \Delta_{71}(t)\mathrm{d}t + \Delta_{72}(t)\widetilde{\delta}_1\mathrm{d}t + \Delta_{73}(t)\mathrm{d}\beta_1, \tag{C.3}$$

where

$$\begin{aligned}
\Delta_{71}(t) &= \frac{4\varepsilon_{232}}{2\left\|u_1\right\|^6}\left(e_v^T e_v\right)^2 \widehat{R}_3^{-1}\overline{R}_{3e}u_1^T\Delta_{01}(t) + \frac{4\varepsilon_{232}}{2\left\|u_1\right\|^4}\widehat{R}_3^{-1}\overline{R}_{3e}e_v^T e_v e_v^T\left(-k_1\tanh\left(e_p + e_v\right) - k_2\tanh\left(e_v\right)\right) \\
&\quad + \frac{T_m}{m}\alpha\overline{R}_{3e} + \frac{\varepsilon_{232}}{2\left\|u_1\right\|^4}\left(e_v^T e_v\right)^2 \mathrm{d}\widehat{R}_3^{-1}\overline{R}_{3e} + \frac{\varepsilon_{232}}{2\left\|u_1\right\|^4}\left(e_v^T e_v\right)^2 \widehat{R}_3^{-1}\overline{R}_{3e1}(t), \\
\Delta_{72}(t) &= \frac{4\varepsilon_{232}}{2\left\|u_1\right\|^6}\left(e_v^T e_v\right)^2 \widehat{R}_3^{-1}\overline{R}_{3e}u_1^T\Delta_{02}(t) + \frac{4\varepsilon_{232}}{2\left\|u_1\right\|^4}\widehat{R}_3^{-1}\overline{R}_{3e}e_v^T e_v e_v^T + \frac{\varepsilon_{232}}{2\left\|u_1\right\|^4}\left(e_v^T e_v\right)^2 \widehat{R}_3^{-1}\overline{R}_{3e2}(t), \\
\Delta_{73}(t) &= \frac{4\varepsilon_{232}}{2\left\|u_1\right\|^6}\left(e_v^T e_v\right)^2 \widehat{R}_3^{-1}\overline{R}_{3e}u_1^T\Delta_{03}(t) + \frac{4\varepsilon_{232}}{2\left\|u_1\right\|^4}\widehat{R}_3^{-1}\overline{R}_{3e}e_v^T e_v e_v^T G_1 + \frac{\varepsilon_{232}}{2\left\|u_1\right\|^4}\left(e_v^T e_v\right)^2 \widehat{R}_3^{-1}\overline{R}_{3e3}(t).
\end{aligned} \tag{C.4}$$

D. The Calculation of $\mathrm{d}\left(\left(\varepsilon_{11}\|F(t)\|^2/3\ \|u_1\|\right)\widehat{R}_3^{-1}E_0F(t)\right)$

Consider

$$\begin{aligned}
\mathrm{d}\left(\frac{\varepsilon_{11}\|F(t)\|^2}{3\left\|u_1\right\|}\widehat{R}_3^{-1}E_0F(t)\right) &= \mathrm{d}\frac{\varepsilon_{11}}{3\left\|u_1\right\|}\|F(t)\|^2\widehat{R}_3^{-1}E_0F(t) + \frac{\varepsilon_{11}}{3\left\|u_1\right\|}\mathrm{d}\|F(t)\|^2\widehat{R}_3^{-1}E_0F(t) \\
&\quad + \frac{\varepsilon_{11}}{3\left\|u_1\right\|}\|F(t)\|^2\mathrm{d}\widehat{R}_3^{-1}E_0F(t) + \frac{\varepsilon_{11}}{3\left\|u_1\right\|}\|F(t)\|^2\widehat{R}_3^{-1}E_0\mathrm{d}F(t).
\end{aligned} \tag{D.1}$$

For the derivatives of those teams, we have

$$\begin{aligned}
\mathrm{d}\frac{\varepsilon_{11}}{3\left\|u_1\right\|}\|F(t)\|^2\widehat{R}_3^{-1}E_0F(t) &= \frac{\varepsilon_{11}}{3\left\|u_1\right\|^3}\|F(t)\|^2\widehat{R}_3^{-1}E_0F(t)u_1^T\left(\Delta_{01}(t)\mathrm{d}t + \Delta_{02}(t)\widetilde{\delta}_1\mathrm{d}t + \Delta_{03}(t)\mathrm{d}\beta_1\right) \\
\frac{\varepsilon_{11}}{3\left\|u_1\right\|}\mathrm{d}\|F(t)\|^2\widehat{R}_3^{-1}E_0F(t) &= \frac{2\varepsilon_{11}}{3\left\|u_1\right\|}\|F(t)\|\widehat{R}_3^{-1}E_0F(t)\mathrm{d}\|F(t)\|, \\
&= -\frac{2\varepsilon_{11}}{3\left\|u_1\right\|}\|F(t)\|\widehat{R}_3^{-1}E_0F(t)\frac{F(t)^T}{\|F(t)\|}\left(\Delta_{401}(t)\mathrm{d}t + \Delta_{402}(t)\widetilde{\delta}_1 dt + \Delta_{403}(t)\mathrm{d}\beta_1\right), \\
\frac{\varepsilon_{11}}{3\left\|u_1\right\|}\|F(t)\|^2\widehat{R}_3^{-1}E_0\mathrm{d}F(t) &= \frac{\varepsilon_{11}}{3\left\|u_1\right\|}\|F(t)\|^2\widehat{R}_3^{-1}E_0\left(\Delta_{401}(t)\mathrm{d}t + \Delta_{402}(t)\widetilde{\delta}_1\mathrm{d}t + \Delta_{403}(t)\mathrm{d}\beta_1\right).
\end{aligned} \tag{D.2}$$

Hence, we deduce

$$\mathrm{d}\left(\frac{\varepsilon_{11}\|F(t)\|^2}{3\left\|u_1\right\|}\widehat{R}_3^{-1}E_0F(t)\right) = \Delta_{81}(t)\mathrm{d}t + \Delta_{82}(t)\widetilde{\delta}_1\mathrm{d}t + \Delta_{83}(t)\mathrm{d}\beta_1, \tag{D.3}$$

where

$$\begin{aligned}\Delta_{81}(t) &= \frac{\varepsilon_{11}}{3\|u_1\|^3}\|F(t)\|^2\widehat{R}_3^{-1}E_0F(t)u_1^T\Delta_{01}(t) - \frac{2\varepsilon_{11}}{3\|u_1\|}\widehat{R}_3^{-1}E_0F(t)F(t)^T\Delta_{401}(t)\\ &\quad + \frac{\varepsilon_{11}}{3\|u_1\|}\|F(t)\|^2\mathrm{d}\widehat{R}_3^{-1}E_0F(t) + \frac{\varepsilon_{11}}{3\|u_1\|}\|F(t)\|^2\widehat{R}_3^{-1}E_0\Delta_{401}(t)\\ \Delta_{82}(t) &= \frac{\varepsilon_{11}}{3\|u_1\|}\|F(t)\|^2\widehat{R}_3^{-1}E_0F(t)u_1^T\Delta_{02}(t) - \frac{2\varepsilon_{11}}{3\|u_1\|}\widehat{R}_3^{-1}E_0F(t)F(t)^T\Delta_{402}(t) + \frac{\varepsilon_{11}}{3\|u_1\|^3}\|F(t)\|^2\widehat{R}_3^{-1}E_0\Delta_{402}(t),\\ \Delta_{83}(t) &= \frac{\varepsilon_{11}}{3\|u_1\|}\|F(t)\|^2\widehat{R}_3^{-1}E_0F(t)u_1^T\Delta_{03}(t) - \frac{2\varepsilon_{11}}{3\|u_1\|}\widehat{R}_3^{-1}E_0F(t)F(t)^T\Delta_{403}(t) + \frac{\varepsilon_{11}}{3\|u_1\|^3}\|F(t)\|^2\widehat{R}_3^{-1}E_0\Delta_{403}(t).\end{aligned} \tag{D.4}$$

E. The Calculation of $\mathrm{d}w_{1c}$

$\mathrm{d}w_{1c}$ can be obtained as

$$\mathrm{d}w_{1c} = W_{1c1}(t)\mathrm{d}t + W_{1c2}(t)\widetilde{\delta}_1\mathrm{d}t + \Delta_{622}\left(t,\widetilde{\delta}_1\right)\mathrm{d}t + W_{1c3}(t)\mathrm{d}\beta_1, \tag{E.1}$$

where

$$\begin{aligned}W_{1c1}(t) &= \Delta_{41}(t) + \Delta_{61}(t) + \Delta_{71}(t) + \Delta_{81}(t),\\ W_{1c2}(t) &= \Delta_{42}(t) + \Delta_{621}(t) + \Delta_{72}(t) + \Delta_{82}(t),\\ W_{1c3}(t) &= \Delta_{43}(t) + \Delta_{63}(t) + \Delta_{73}(t) + \Delta_{83}(t).\end{aligned} \tag{E.2}$$

F. The Calculation of $\mathrm{d}r_c$

For r_c, we have

$$r_c = -\frac{\cos\theta}{\cos\phi}\left(\frac{\sin\phi}{\cos\theta}w_{1c} - \mathrm{d}\psi_r + k_3e_\psi\right) = -\tan\phi\left(E_2q_c - \mathrm{d}\psi_r + k_3e_\psi\right), \tag{F.1}$$

where $E_2 = \begin{pmatrix}0 & 1\end{pmatrix}$. Define $\Omega = \begin{pmatrix}\phi & \theta & \psi\end{pmatrix}$, then the derivative of Ω is

$$\dot{\Omega} = \begin{pmatrix}1 & S\phi T\theta & C\phi T\theta\\ 0 & C\phi & -S\phi\\ 0 & \dfrac{S\phi}{C\theta} & \dfrac{C\phi}{C\theta}\end{pmatrix}\begin{pmatrix}p\\ q\\ r\end{pmatrix}, \tag{F.2}$$

which means that $\mathrm{d}\psi$ is available for control designed. Then, $\mathrm{d}r_c$ can be denoted by

$$\mathrm{d}r_c = W_{rc1}(t)\mathrm{d}t + W_{rc2}(t)\widetilde{\delta}_1\mathrm{d}t + W_{rc20}\left(t,\widetilde{\delta}_1\right)\mathrm{d}t + W_{rc3}(t)\mathrm{d}\beta_1, \tag{F.3}$$

where

$$\begin{aligned}W_{rc1}(t) &= -\left(E_2w_{1c} - \mathrm{d}\psi_r + k_3e_\psi\right)\left(1 + \tan^2\phi\right)\mathrm{d}\phi\\ &\quad - \tan\phi E_2W_{1c1}(t)\mathrm{d}t + \tan\phi\,d\dot{\psi}_r\\ &\quad - \tan\phi k_6\left(-k_6e_\psi + E_1e_w\right),\\ W_{rc2}(t) &= -\tan\phi E_2W_{1c2}(t),\\ W_{rc20}\left(t,\widetilde{\delta}_1\right) &= -\tan\phi E_2\Delta_{622}\left(t,\widetilde{\delta}_1\right),\\ W_{rc3}(t) &= -\tan\phi E_2W_{1c3}.\end{aligned} \tag{F.4}$$

G. The Calculation of $\mathrm{d}w_c$

The derivative of w_c is obtained as follows:

$$\mathrm{d}w_c = \begin{pmatrix} \mathrm{d}w_{1c} \\ \mathrm{d}r_c \end{pmatrix} = W_{c1}(t)\mathrm{d}t + W_{c2}(t)\widetilde{\delta}_1 + W_{c20}\left(t, \widetilde{\delta}_1\right) + W_{c3}(t)\mathrm{d}\beta_1. \tag{G.1}$$

Notice that

$$W_{c20}\left(t, \widetilde{\delta}_1\right) = \begin{pmatrix} \Delta_{622}\left(t, \widetilde{\delta}_1\right) \\ W_{rc20}\left(t, \widetilde{\delta}_1\right) \end{pmatrix} = W_{c21}(t)\left(\Delta_{502}(t)\widetilde{\delta}_1\alpha_{31} + \Delta_{512}(t)\widetilde{\delta}_1\alpha_{32}\right)^T F(t), \tag{G.2}$$

with

$$W_{c21}(t) = \begin{pmatrix} 1 \\ -\tan\phi E_2 \end{pmatrix} \frac{\varepsilon_{12}}{3}\left\|u_1\right\|^3\|\alpha\|^2\|F(t)\|^2\widehat{R}_3^{-1}, \tag{G.3}$$

which implies that

$$\left\|W_{c20}\left(t, \widetilde{\delta}_1\right)\right\| \le \left\|W_{c21}(t)\right\|\left\|\Delta_{502}(t)\right\|\left\|\widetilde{\delta}_1\right\|\left\|\alpha_{31}\right\|\|F(t)\| + \left\|W_{c21}(t)\right\|\left\|\Delta_{502}(t)\right\|\left\|\widetilde{\delta}_1\right\|\left\|\alpha_{31}\right\|\|F(t)\|. \tag{G.4}$$

Data Availability

No data were used to support this study.

Conflicts of Interest

The authors declare that they have no conflicts of interest.

Acknowledgments

This work was supported by the National Natural Science Foundation of China (Grant nos. 12101481 and 62103327).

References

[1] A. Isidori, *Nonlinear Control Systems II*, Springer, London, UK, 1999.

[2] H. K. Khalil, *Nonlinear Systems*, Prentice-Hall, Hoboken, NJ, USA, Third edition, 2002.

[3] D. Comminiello and J. C. Príncipe, *Adaptive Learning Methods for Nonlinear System Modeling*, Butterworth-Heinemann, Oxford, UK, 2018.

[4] A. Wang, L. Liu, J. Qiu, and G. Feng, "Event-triggered robust adaptive fuzzy control for a class of nonlinear systems," *IEEE Transactions on Fuzzy Systems*, vol. 27, no. 8, pp. 1648–1658, 2019.

[5] W. Meng, Q. Yang, and Y. Sun, "Adaptive neural control of nonlinear MIMO systems with time-varying output constraints," *IEEE Transactions on Neural Networks and Learning Systems*, vol. 26, no. 5, pp. 1074–1085, 2015.

[6] Z. Zeng Lian Liu and J. Svoboda, "A new control scheme for nonlinear systems with disturbances," *IEEE Transactions on Control Systems Technology*, vol. 14, no. 1, pp. 176–181, 2006.

[7] T. Wang, J. Wu, Y. Wang, and M. Ma, "Adaptive fuzzy tracking control for a class of strict-feedback nonlinear systems with time-varying input delay and full state constraints," *IEEE Transactions on Fuzzy Systems*, vol. 28, no. 12, pp. 3432–3441, 2020.

[8] P. Zhou, L. Zhang, S. Zhang, and A. F. Alkhateeb, "Observer-based adaptive fuzzy finite-time control design with prescribed performance for switched pure-feedback nonlinear systems," *IEEE Access*, vol. 9, pp. 69481–69491, 2021.

[9] W. Wang, R. Postoyan, D. Nesic, and W. P. M. H. Heemels, "Periodic event-triggered control for nonlinear networked control systems," *IEEE Transactions on Automatic Control*, vol. 65, no. 2, pp. 620–635, 2020.

[10] Y. Wu and X.-J. Xie, "Robust adaptive control for state-constrained nonlinear systems with input saturation and unknown control direction," *IEEE Transactions on Systems, Man, and Cybernetics: Systems*, vol. 51, no. 2, pp. 1192–1202, 2021.

[11] X.-H. Chang, G.-H. Yang, and H. Wang, "Observer-based H∞-control for discrete-time T-S fuzzy systems," *International Journal of Systems Science*, vol. 42, no. 10, pp. 1801–1809, 2011.

[12] Y. Chang, P. Zhou, B. Niu et al., "Switched-observer-based adaptive output-feedback control design with unknown gain for pure-feedback switched nonlinear systems via average dwell time," *International Journal of Systems Science*, vol. 52, no. 9, pp. 1731–1745, 2021.

[13] Z. Chen, B. Niu, X. Zhao, L. Zhang, and N. Xu, "Model-Based adaptive event-Triggered control of nonlinear continuous-

time systems," *Applied Mathematics and Computation*, vol. 408, p. 126330, 2021.

[14] Y. Yang, *Helicopter Flight Control*, National Defense Industry Press, Beijing, China, 3rd edition, 2015.

[15] G. Padfield, *Helicopter Flight Dynamics: The Theory and Application of Flying Qualities and Simulation Modelling*, Blackwell, Oxford, UK, 2007.

[16] I. A. Raptis, K. P. Valavanis, and G. J. Vachtsevanos, "Linear tracking control for small-scale unmanned helicopters," *IEEE Transactions on Control Systems Technology*, vol. 20, no. 4, pp. 995–1010, 2012.

[17] Z. Fang, H. Tian, and P. Li, "Probabilistic robust linear parameter-varying control of a small helicopter using iterative scenario approach," *IEEE/CAA Journal of Automatica Sinica*, vol. 2, no. 1, pp. 85–93, 2015.

[18] M. Chen and Y. Li, "Model reference resilient control for the helicopter with time-varying disturbance," *International Journal of Robust and Nonlinear Control*, vol. 29, no. 15, pp. 5095–5117, 2019.

[19] Y. Li, M. Chen, T. Li, and H. Wang, "Tracking control for the helicopter with time-varying disturbance and input stochastic perturbation," *Proceedings of the Institution of Mechanical Engineers - Part G: Journal of Aerospace Engineering*, vol. 234, no. 4, pp. 961–976, 2020.

[20] Y. Zou, "Adaptive trajectory tracking control approach for a model-scaled helicopter," *Nonlinear Dynamics*, vol. 83, no. 4, pp. 2171–2181, 2016.

[21] P. Marantos, C. P. Bechlioulis, and K. J. Kyriakopoulos, "Robust trajectory tracking control for small-scale unmanned helicopters with model uncertainties," *IEEE Transactions on Control Systems Technology*, vol. 25, no. 6, pp. 2010–2021, 2017.

[22] X. Wang, X. Yu, S. Li, and J. Liu, "Composite block backstepping trajectory tracking control for disturbed unmanned helicopters," *Aerospace Science and Technology*, vol. 85, pp. 386–398, 2019.

[23] Y. Huang, M. Zhu, Z. Zheng, and M. Feroskhan, "Fixed-time autonomous shipboard landing control of a helicopter with external disturbances," *Aerospace Science and Technology*, vol. 84, pp. 18–30, 2019.

[24] T. Jiang, D. Lin, and T. Song, "Finite-time control for small-scale unmanned helicopter with disturbances," *Nonlinear Dynamics*, vol. 96, no. 3, pp. 1747–1763, 2019.

[25] I. Ullah and H. Pei, "Sliding mode tracking control for unmanned helicopter using extended disturbance observer," *Archives of Control Sciences*, vol. 29, no. 1, pp. 169–199, 2019.

[26] R. Ma, L. Ding, and H. Wu, "Dynamic decoupling control optimization for a small-scale unmanned helicopter," *Journal of Robotics*, vol. 2018, Article ID 9897684, 12 pages, 2018.

[27] Y. Li, M. Chen, S. S. Ge, and D. Li, "Anti-disturbance control for attitude and altitude systems of the helicopter under random disturbances," *Aerospace Science and Technology*, vol. 96, p. 105561, 2020.

[28] X. Mao and C. Yuan, *Stochastic Differential Equations with Markovian Switching*, Imperial College Press, London, UK, 2006.

Hindawi
Mathematical Problems in Engineering
Volume 2021, Article ID 8049516, 12 pages
https://doi.org/10.1155/2021/8049516

Research Article

Application of Adaptive Local Iterative Filtering and Permutation Entropy in Gear Fault Recognition

Wenbin Zhang,[1] **Yun Wang**,[1] **Yushuo Tan**,[2] **Dewei Guo**,[1] **and Yasong Pu**[1]

[1]*College of Engineering, Honghe University, Key Laboratory of Mechanical Performance Analysis and Optimization of Plateau in Yunnan Province, Mengzi, China*
[2]*Shijiazhuang Post and Telecommunications Technical College, Shijiazhuang, China*

Correspondence should be addressed to Wenbin Zhang; 190322507@qq.com

Received 4 June 2021; Revised 16 September 2021; Accepted 17 September 2021; Published 11 October 2021

Academic Editor: Yuxing Li

In this paper, a fault identification method combining adaptive local iterative filtering and permutation entropy is proposed. The adaptive local iterative filtering can decompose the nonstationary signal into a finite number of stationary intrinsic mode functions. And the experiment gear fault data are decomposed into several intrinsic mode functions by this method. Then, using the permutation entropy to calculate each intrinsic mode function, it is found that the permutation entropy of the first several intrinsic mode functions can represent the characteristics of different fault types, and the permutation entropy of the intrinsic mode function corresponding to the rotating frequency signal of the gear system could be the boundary. Finally, the fault type of gear is identified by calculating the gray correlation degree of permutation entropy of essential mode function of vibration signal decomposition under different working conditions. The example analysis results show that the proposed method can be effectively applied to the fault diagnosis of the gear system.

1. Introduction

Gearbox is the main part of mechanical equipment for motion and power transmission. In gear transmission, machine failure caused by gear failure will cause equipment shutdown or even damage. Therefore, how to extract the gear fault feature parameters effectively has been a research hot spot of many scholars [1, 2]. Since Huang et al. [3] proposed empirical mode decomposition, the empirical mode decomposition method has attracted the attention of many scholars. It extends from the traditional orthogonal basis function expansion to the data-driven signal representation with adaptive ability for any complex signal. However, the empirical mode decomposition (EMD) method has some problems, such as mode confusion caused by singular points in the signal and instability under noise interference. Inspired by the idea of empirical mode decomposition, some scholars have proposed a new adaptive mode decomposition method, among which adaptive local iterative filtering [4] is a representative one. Based on the idea of the empirical mode decomposition (EMD) method, the adaptive local iterative filtering method adopts the Fokker–Planck equation to design the filter, which can effectively avoid false components in the decomposition process and is more suitable for the analysis of nonlinear and nonstationary signals. Deyou et al. [5] applied the adaptive local iterative filtering method to feature extraction of nonstationary signals in the power system and achieved good results. Baojia et al. [6] applied this method to fault feature extraction of rolling bearing. However, in the fault feature extraction of the gear system, the research of the adaptive local iterative filtering method is still less. The results show that the gear fault signal has typical nonstationary and nonlinear characteristics. Therefore, how to effectively extract the fault features reflecting different working conditions of gears is extremely important [7].

Entropy is a powerful tool for the analysis of time series as it allows describing the probability distributions of the possible state of a system and therefore the information encoded in it. Entropy is a basic quantity with multiple field-

specific interpretations; for instance, it has been associated with disorder, state-space volume, or lack of information. When dealing with information content, the Shannon entropy is often considered as the foundational and most natural one. Nevertheless, important information may be codified also in the temporal dynamics, an aspect which is not usually taken into account. The idea of calculating entropy based on permutation patterns (that is, permutations defined by the order relations among values of a time series) has received a lot of attention in the last years. Permutation entropy is an information entropy for studying the complexity of nonlinear time series. Compared with the commonly used nonlinear dynamic methods, such as Lyapunov index, fractal dimension, and sample entropy, permutation entropy has good antinoise performance. Moreover, the time series required is short, the calculation is simple, and the operation speed is fast [8–11].

In this paper, adaptive local iterative filter decomposition, combined with permutation entropy and gray correlation degree, is used to classify and identify different fault types of the gear system. Firstly, the normal, mild wear, moderate wear, and broken teeth are simulated on the gearbox simulation experimental platform. Then, adaptive local iterative filtering is used to decompose the sampled signal adaptively. Then, the permutation entropy of each intrinsic mode function component is calculated. Finally, the fault recognition and classification are carried out by calculating the gray correlation degree between the samples to be identified and the standard failure modes. The results of case analysis show that the method can be used to identify different fault types of the gear system effectively.

2. Principle of Adaptive Local Iterative Filtering Technique

In empirical mode decomposition, the instantaneous mean is defined as the mean function of the upper and lower envelopes. Because the cubic spline which is sensitive to singular points is used to connect the local maximum and local minimum to fit the upper and lower envelopes, the instantaneous mean is unstable under disturbance. In order to overcome this defect, Lin et al. [12] proposed an iterative filtering algorithm in 2009. The algorithm follows the same framework as empirical mode decomposition (EMD), but the instantaneous mean is obtained by low-pass filtering. In order to ensure the stability and convergence under disturbance, the uniform double length average filter is used in iterative filtering. However, the filter is not smooth enough and may cause false fluctuations in the intrinsic mode function. In order to overcome this defect, Cicone et al. [4] proposed an adaptive local iterative filtering algorithm in 2016. This method extends the iterative filtering algorithm by using the nonuniform filter. The filter is designed as the Fokker–Planck equation, as shown in equation (1), so that the filter has compact support in the time domain and the length is flexible, which can avoid false fluctuations in the iterative filtering process.

$$\frac{\partial}{\partial t} g(x,t) = -\alpha \frac{\partial}{\partial x} [p(x,t) g(x,t)] + \beta \frac{\partial^2}{\partial x^2} \left[q^2(x,t) g(x,t) \right]. \tag{1}$$

In the formula [4], the value range of α and β is between (0, 1).

The implementation process of the adaptive local iterative filtering algorithm is as follows [13]:

(1) Initialization: let the iteration number $i = 1$ and the residual signal is $r_0(t) = x(t)$.

(2) The ith intrinsic mode function is extracted.

(2.1) Let the screening number $j = 0$ and the prototype intrinsic mode function is $h_{ij}(t) = r_{i-1}(t)$.

(2.2) The adaptive local Fokker–Planck filter $g_{ij}(t, \tau)$ is designed to determine the corresponding time-varying filter length $l_{ij}(t)$.

(2.3) Calculate the instantaneous mean value.

$$m_{ij}(t) = \int_{-l_{ij}(t)}^{l_{ij}(t)} h_{ij}(t+\tau) g_{ij}(t,\tau)\, \mathrm{d}\tau. \tag{2}$$

(2.4) Update the prototype intrinsic mode function.

$$h_{ij}(t) = h_{ij}(t) - m_{ij}(t). \tag{3}$$

(2.5) If the prototype intrinsic mode function $h_{ij}(t)$ satisfies the condition requirements of the intrinsic mode function, then let the i^{th} IMF intrinsic mode function be

$$c_i(t) = h_{ij}(t). \tag{4}$$

Otherwise, let the screening times be $j = j + 1$ and return to step (2.2).

(3) Update residual signal.

$$r_i(t) = r_{i-1}(t) - c_i(t). \tag{5}$$

(4) If the residual signal $r_i(t)$ satisfies the termination criterion of the algorithm, that is, only one extreme point becomes the trend term, the adaptive local iterative filtering decomposition is terminated. Otherwise, let the iteration number $i = i + 1$ and return to step (2).

3. Definition of Permutation Entropy

Let the sampling sequence be $[x(n)] = x(1), x(2), \ldots, x(N)$. The sequence permutation entropy [8–11] is calculated as follows:

(1) By reconstructing the phase space of the sampling sequence, the following results can be obtained:

$$X(i) = [x(i), x(i+\tau), \ldots, x(i+(m-1)\tau)]. \tag{6}$$

In formula, m and τ are embedding dimension and delay time, respectively.

(2) M data of $X(i)$ are arranged in ascending order:

$$x(i+(j_1-1)\tau) \le x(i+(j_2-1)\tau) \le \ldots \le x(i+(j_m-1)\tau). \quad (7)$$

In the formula, $j_1, j_2, \ldots, j_m$ is the location index of the elements after $X(i)$ reordering.

(3) If two elements of equal size exist in $X(i)$, that is,

$$x(i+(j_1-1)\tau) = x(i+(j_2-1)\tau), \quad (8)$$

they are sorted by the size of the location index value. If $j_1 < j_2$, then

$$x(i+(j_1-1)\tau) < x(i+(j_2-1)\tau). \quad (9)$$

(4) For any reconstructed signal $X(i)$, a group of sequences in ascending order can be obtained:

$$s(g) = (j_1, j_2, \ldots, j_m). \quad (10)$$

In the formula, $g = 1, 2, \ldots, k$, and $k \le m!$ Therefore, m-dimensional phase space reconstruction of different sequences total is $m!$ Sequence $s(g)$ is one of the permutations.

(5) Calculate the probability of occurrence of each sequence, then

$$P_i = \frac{l}{k}. \quad (11)$$

In the formula, l is the frequency of $s(g)$, and l does not change with g.

(6) In the form of Shannon entropy, the permutation entropy can be defined as

$$H_p(m,\tau) - \sum_{j=1}^{k} P_i \mathrm{In} P_i. \quad (12)$$

(7) After normalization of $H_P(m, \tau)$, the following results can be obtained [11]:

$$H_p = \frac{H_p(m,\tau)}{\mathrm{In}(m!)}. \quad (13)$$

According to the definition of permutation entropy, the value range of H_P is [0, 1]. The random degree of signal can be expressed by the size of permutation entropy. The smaller the permutation entropy is, the more regular the signal is; otherwise, the more complex it is. The permutation entropy of the sampled signal can be obtained, and the local subtle change of the signal can be detected by the change of its value.

4. Theory of Gear Fault Recognition Based on Adaptive Local Iterative Filtering and Permutation Entropy

The principle of gear fault identification is shown in Figure 1. In the gear test system, the fault states of normal gear, slight wear of tooth surface, moderate wear of tooth surface, and broken tooth are simulated. When the gray correlation degree is used for fault type identification, the standard fault mode with the largest gray correlation degree with the sample to be identified is considered as the fault type of the sample to be identified [14]. The detailed process of gray correlation degree identification can be seen in the author's previous research results [15].

5. Case Analysis

In order to verify the recognition effect of the proposed method for gear fault, we use the experiment platform to acquire the gear fault data. The experimental platform is shown in Figure 2. The gear rotation frequency is $f_r = 23.6$ Hz, the meshing frequency is $f_z = 686$ Hz, and the vibration signal sampling frequency is 16384 Hz. Due to the limited experiment condition, we only have four common gear working conditions, such as normal gear, slight wear of tooth surface, moderate wear of tooth surface, and broken tooth which are tested on the gear system test platform. Four kinds of gear working conditions are sampled, respectively, 20 samples are taken for each, and the adaptive local iterative filter is used to decompose the sampling signal adaptively. Now, we select one data of each working condition to decompose by adaptive local iterative filtering, and we can see that the decomposition results obtain 8 IMF components and 1 residual component, as shown in Figures 3–6.

It can be seen from the figures that the nonstationary gear fault signal is decomposed into several stationary IMF components by adaptive local iterative filtering. In IMF8 component, the obvious periodic component can be seen. After calculating the frequency of this component, it can be seen that this component corresponds to the gear frequency signal. Limited to space, Figure 7 shows the result of adaptive decomposition of the medium-worn signal by the EEMD method for comparison. In EEMD decomposition, although noise is added in the decomposition process to reduce the degree of modal aliasing, compared with the adaptive local iterative filter decomposition, the mode aliasing phenomenon is more obvious. Moreover, in the decomposition result of EEMD, the rotational frequency component of gear cannot be seen. It also shows that the adaptive iterative filter can effectively suppress the mode aliasing due to the introduction of the Fokker–Planck equation.

In order to further highlight the adaptive decomposition ability of the adaptive local iterative filter, the results of EMD decomposition of the same signal are shown in Figure 8. Compared with Figures 5, 7, and 8, it can be seen that 12 IMF components and 1 residual component are obtained by EMD decomposition. EEMD decomposition results in 11 IMF components and 1 residual component. However, eight IMF components and one residual component are obtained by adaptive local iterative filter decomposition. From the point of view of the degree of mode aliasing of the decomposed signal, the EEMD method reduces the degree of modal aliasing to a certain extent by adding white noise in

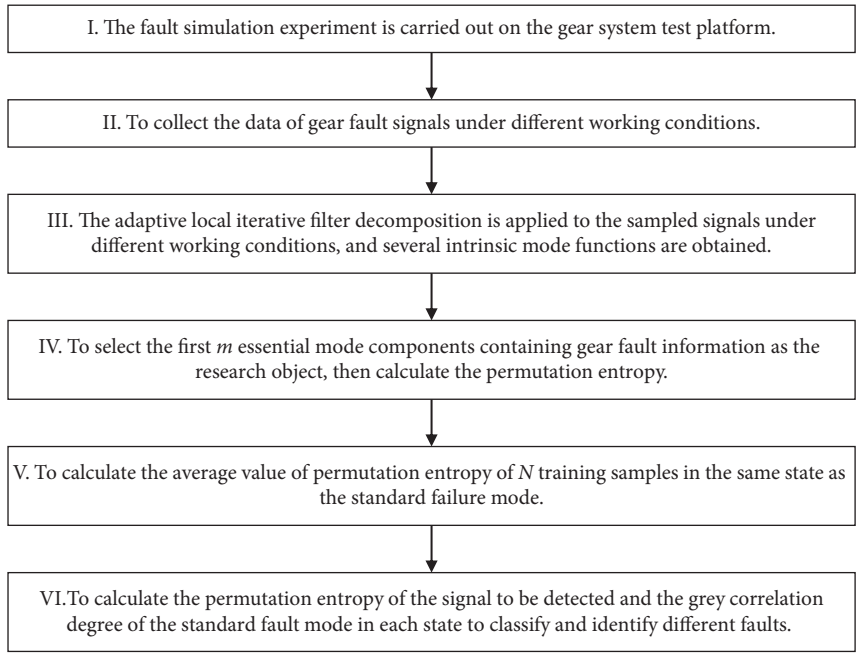

Figure 1: Gear fault recognition principle based on adaptive local iterative filter decomposition.

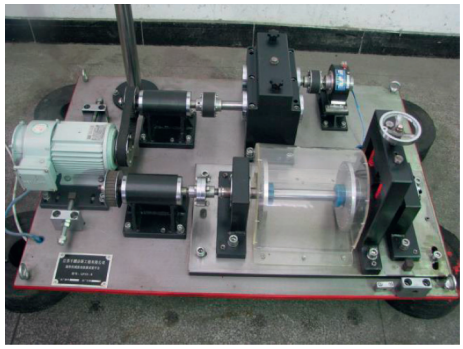

Figure 2: Gearbox simulation experiment platform.

the decomposition process on the basis of EMD decomposition. In the signal obtained by adaptive local iterative filtering, the degree of mode aliasing is effectively improved, which is more conducive to the fault feature extraction of the gear system.

Now, 10 samples of each state are randomly selected as training samples. According to the principle steps of fault identification shown in Figure 1, the permutation entropy of 8 intrinsic mode functions obtained by decomposition of each state is calculated, as shown in Figure 9. The value in the figure is the average value of permutation entropy of 10 training samples. It can be seen from the figure that the shape of permutation entropy curve under four conditions is relatively similar. Since the size of permutation entropy reflects the randomness of signals, it can be seen that with the continuous decomposition of signals, the components contained in the components tend to be simple, so the permutation entropy tends to decrease gradually. Since IMF8 corresponds to gear rotation frequency, it can be considered that the first seven IMF contain gear fault information, which shows that the permutation entropy can effectively represent the change of gear fault characteristics. The permutation entropy of the first seven IMF components is taken as the fault feature. Since the permutation entropy curves of the first seven IMF components are similar under the four working conditions, it is very important to select an appropriate identification method to effectively distinguish different fault types in subsequent fault classification and identification.

Due to the space limitation, 5 samples are randomly selected from the remaining 10 samples of each state as the samples to be tested. Table 1 shows the permutation entropy of the samples to be tested.

Finally, the gray correlation degree between the permutation entropy of the sample to be tested and the average value of the permutation entropy of the training sample in each state is calculated by using the gray correlation degree method. According to the value of correlation degree, the fault modes of the gear system are classified and identified. The results are shown in Table 2.

It can be seen from Table 2 that the method of gray correlation degree has achieved ideal results for the fault pattern recognition of the gear system. There is a big difference between the gray correlation degree of corresponding fault types and that of other fault types. In the permutation entropy curve of Figure 6, the shape of permutation entropy curve under four working conditions is similar. Through the method of gray correlation degree, four different fault types can be effectively classified, which shows that the gray correlation degree can accurately classify the problem of small sample fault identification. The correct classification results can also be obtained by identifying the remaining fault samples.

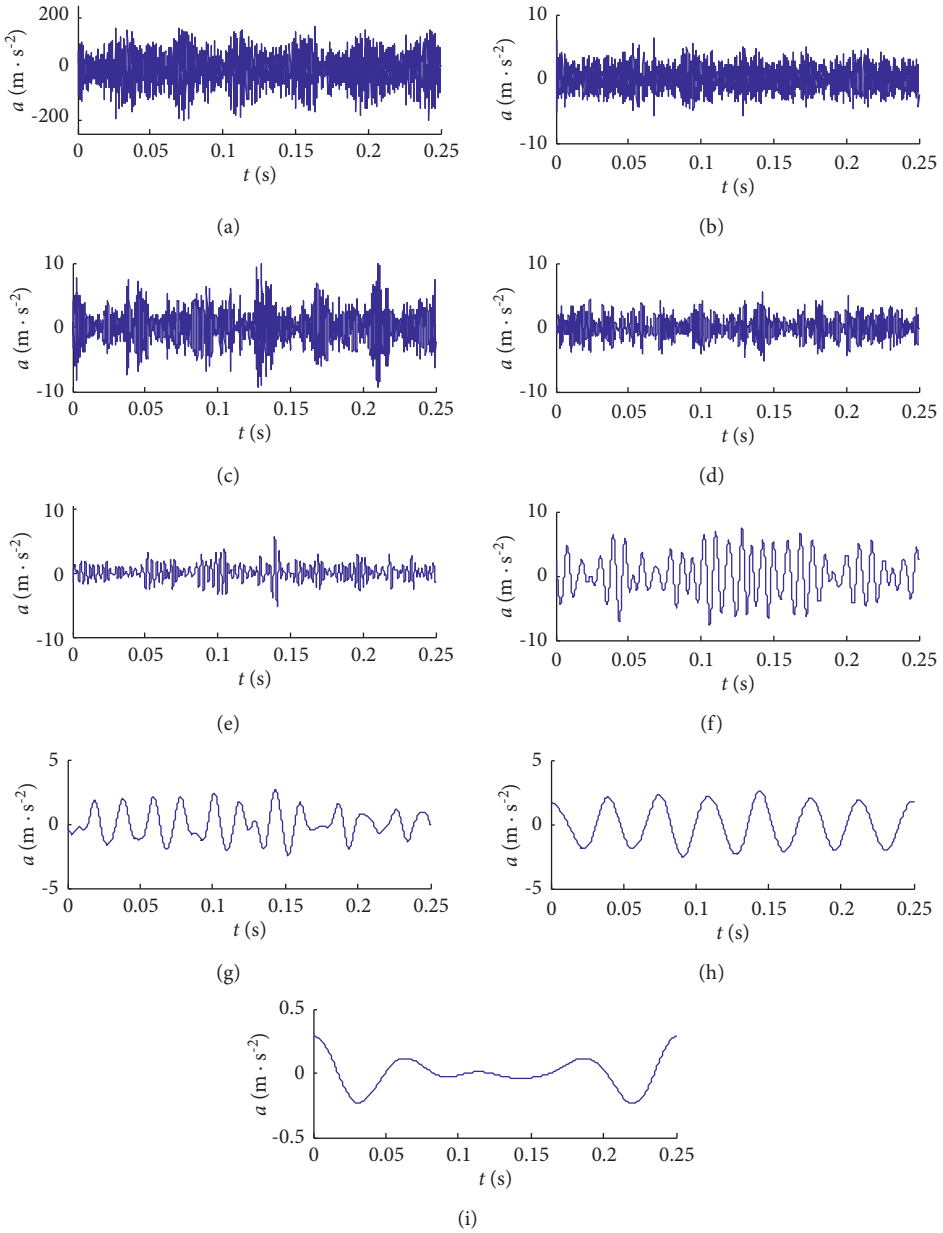

Figure 3: Decomposition results of normal signal by adaptive local iterative filtering: (a) IMF1; (b) IMF2; (c) IMF3; (d) IMF4; (e) IMF5; (f) IMF6; (g) IMF7; (h) IMF8; (i) Ra.

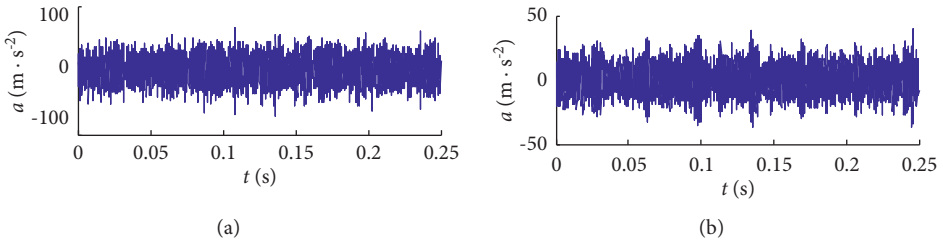

Figure 4: Continued.

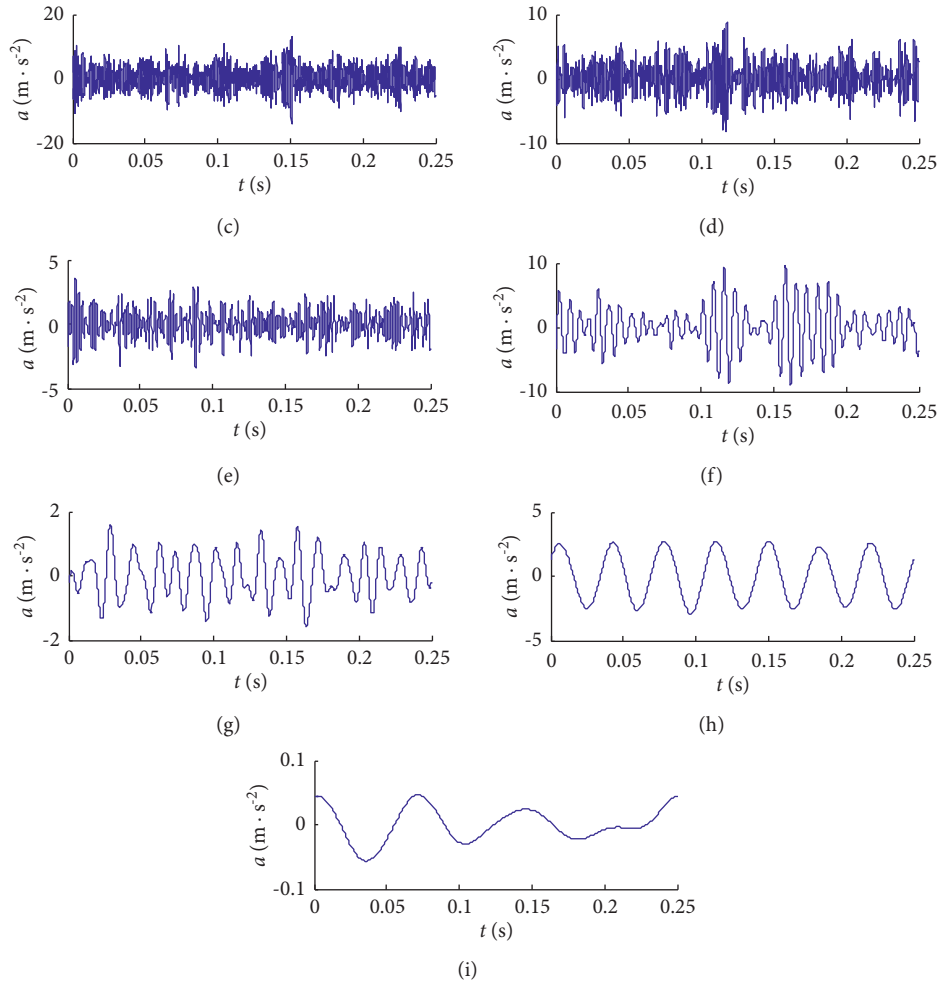

Figure 4: Decomposition results of slight-worn signal by adaptive local iterative filtering: (a) IMF1; (b) IMF2; (c) IMF3; (d) IMF4; (e) IMF5; (f) IMF6; (g) IMF7; (h) IMF8; (i) Ra.

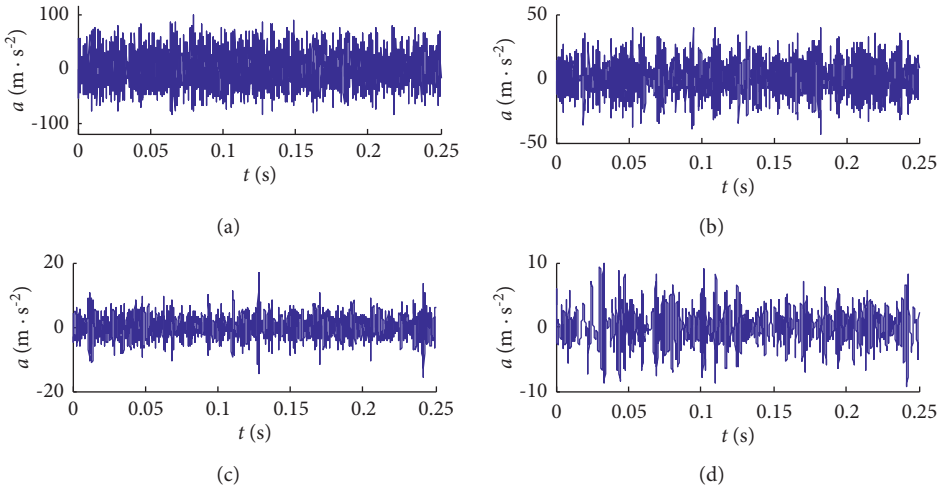

Figure 5: Continued.

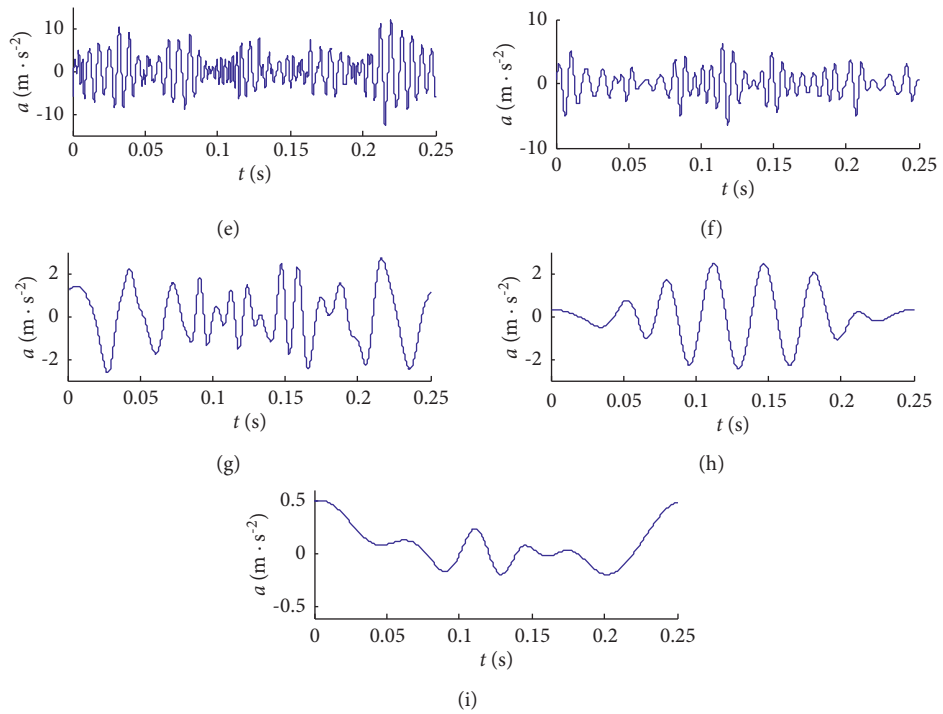

Figure 5: Decomposition results of medium-worn signal by adaptive local iterative filtering: (a) IMF1; (b) IMF2; (c) IMF3; (d) IMF4; (e) IMF5; (f) IMF6; (g) IMF7; (h) IMF8; (i) Ra.

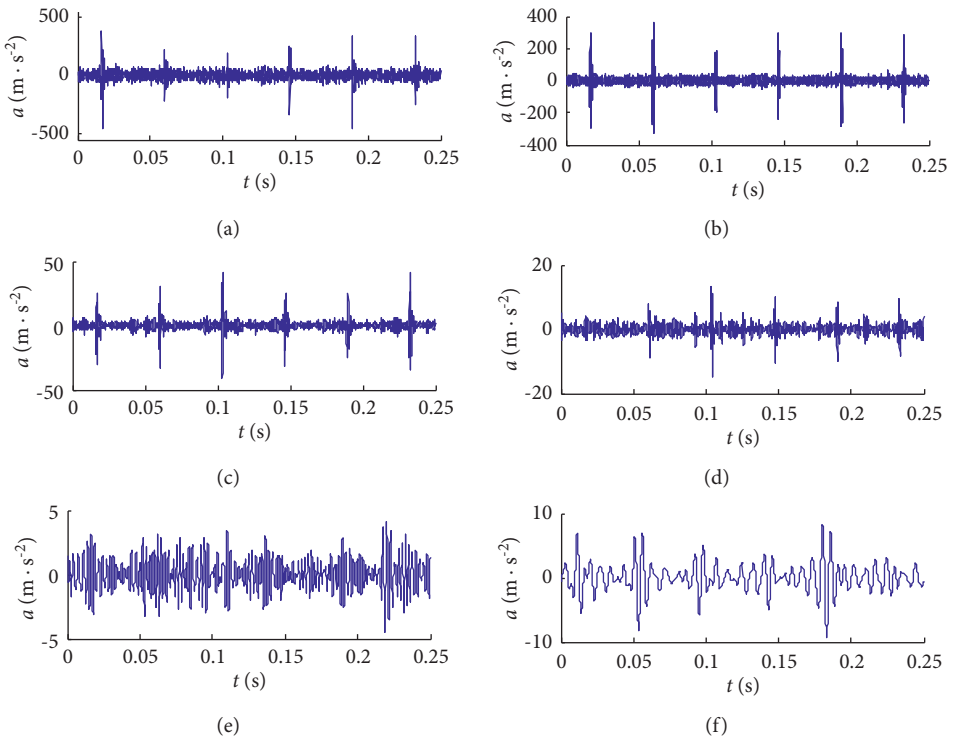

Figure 6: Continued.

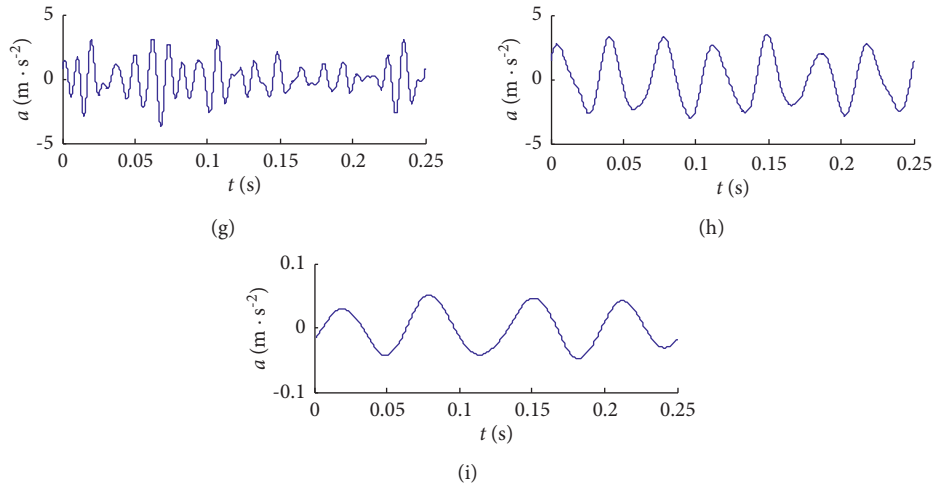

Figure 6: Decomposition results of broken-tooth signal by adaptive local iterative filtering: (a) IMF1; (b) IMF2; (c) IMF3; (d) IMF4; (e) IMF5; (f) IMF6; (g) IMF7; (h) IMF8; (i) Ra.

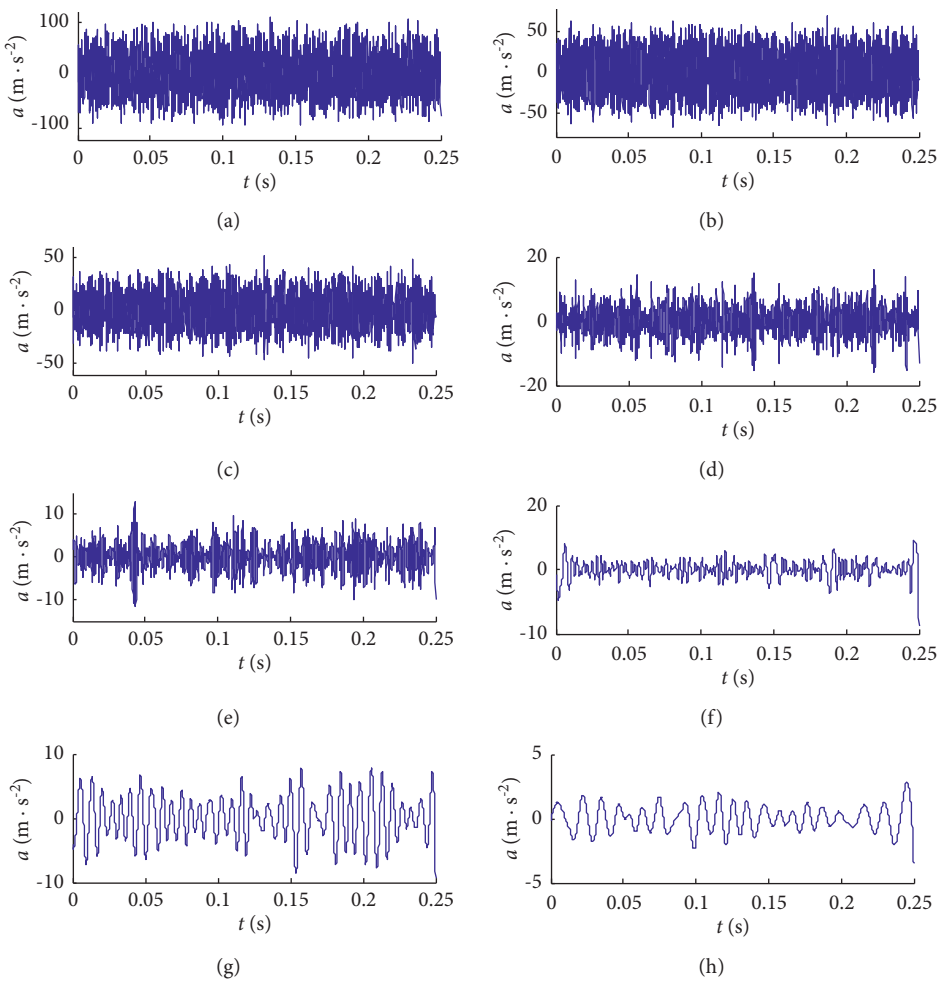

Figure 7: Continued.

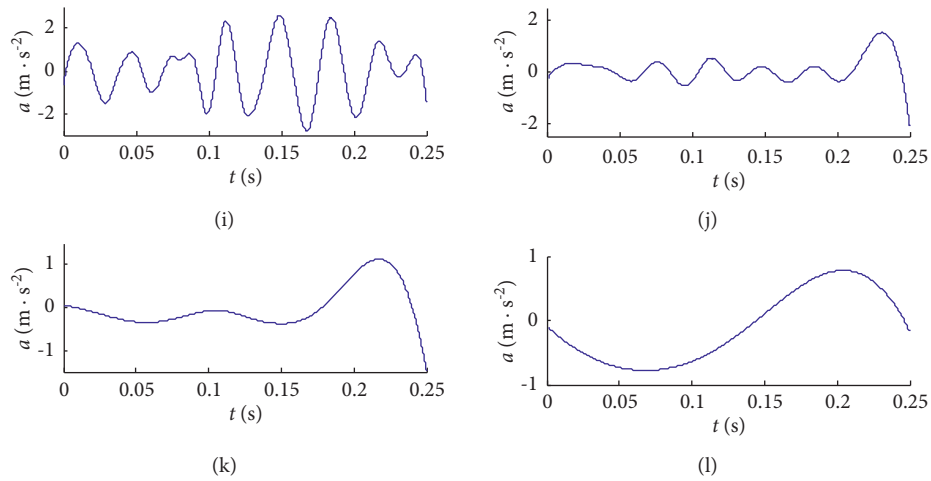

Figure 7: Decomposition results of medium-worn signal by EEMD: (a) IMF1; (b) IMF2; (c) IMF3; (d) IMF4; (e) IMF5; (f) IMF6; (g) IMF7; (h) IMF8; (i) IMF9; (j) IMF10; (k) IMF11; (l) Ra.

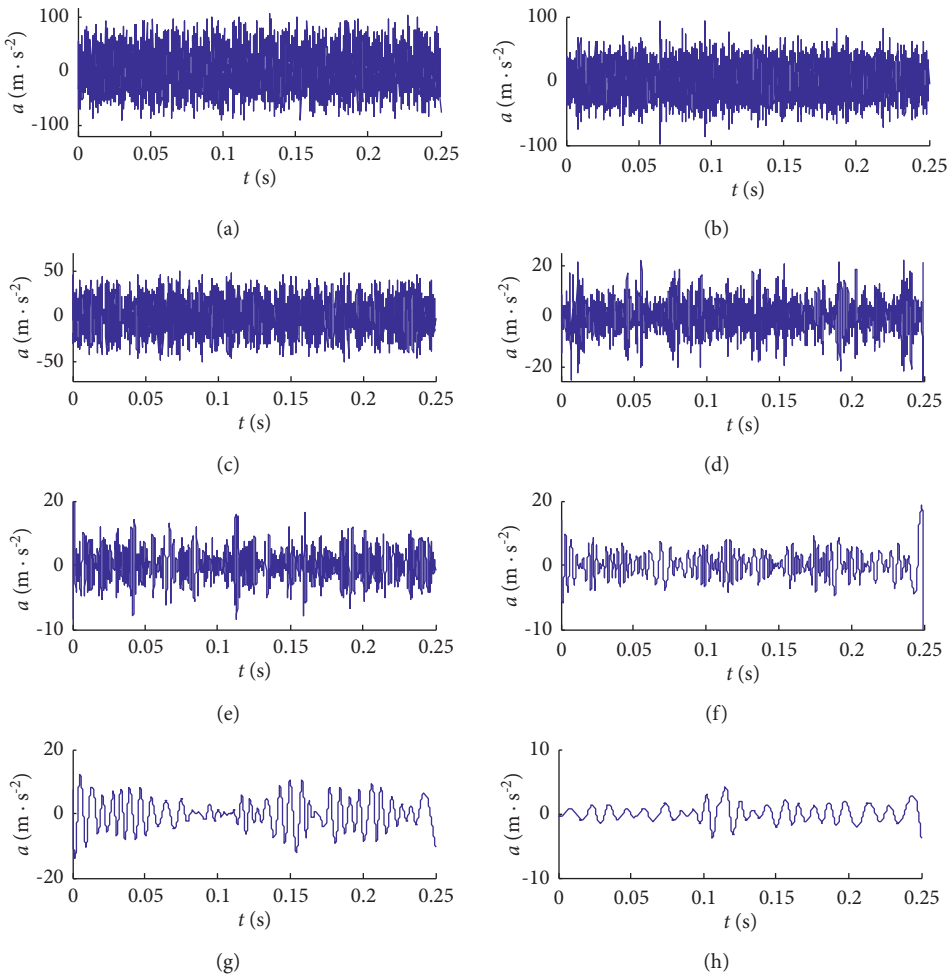

Figure 8: Continued.

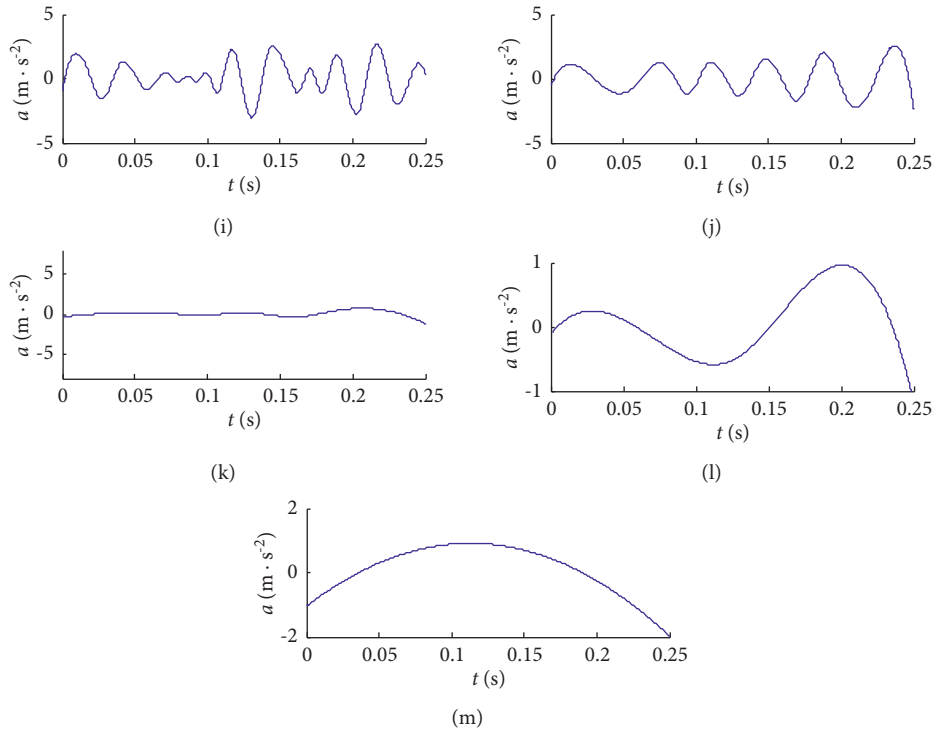

Figure 8: Decomposition results of medium-worn signal by EMD: (a) IMF1; (b) IMF2; (c) IMF3; (d) IMF4; (e) IMF5; (f) IMF6; (g) IMF7; (h) IMF8; (i) IMF9; (j) IMF10; (k) IMF11; (l) IMF12; (m) Ra.

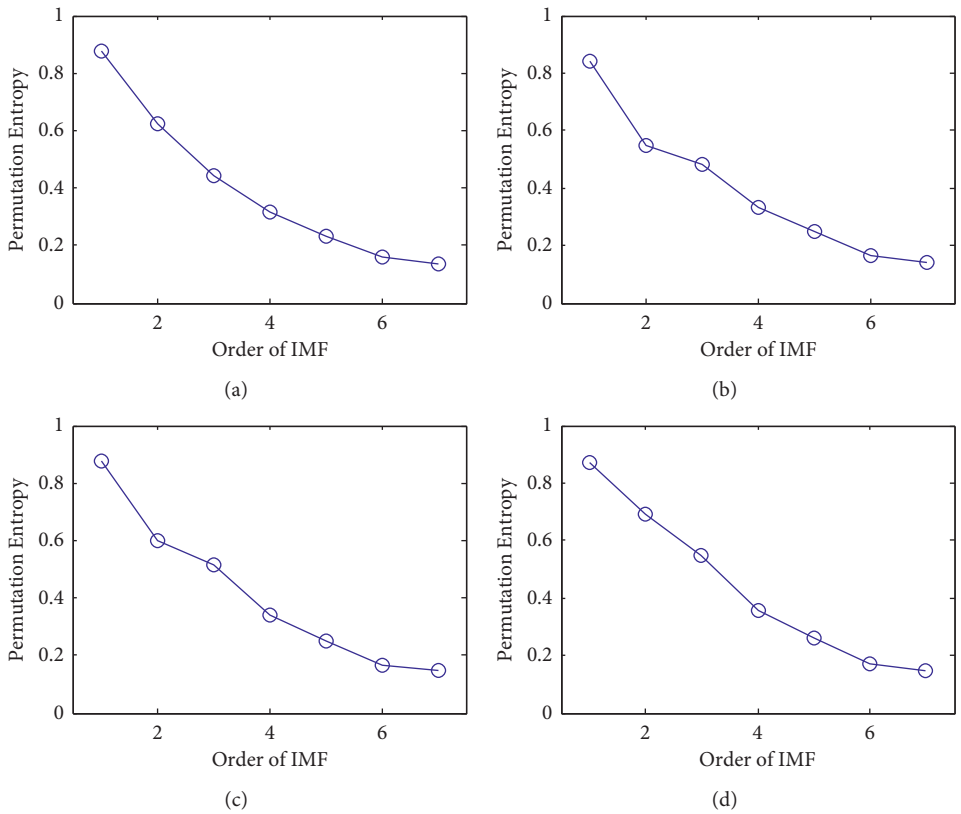

Figure 9: Permutation entropy curve of the gear system under different working conditions: (a) normal gear; (b) slight wear of tooth surface; (c) moderate wear of tooth surface; (d) broken tooth.

Table 1: Permutation entropy of the gear system under different working conditions.

Working condition	Sample	H_{p1}	H_{p2}	H_{p3}	H_{p4}	H_{p5}	H_{p6}	H_{p7}
Normal gear	1	0.8710	0.6331	0.4395	0.3143	0.2395	0.1663	0.1394
	2	0.8727	0.6264	0.4423	0.3177	0.2316	0.1593	0.1344
	3	0.8709	0.6321	0.4481	0.3197	0.2384	0.1596	0.1364
	4	0.8780	0.6259	0.4400	0.3240	0.2362	0.1593	0.1363
	5	0.8711	0.6224	0.4375	0.3090	0.2342	0.1592	0.1379
Slight wear of tooth surface	1	0.8379	0.5444	0.4829	0.3301	0.2479	0.1650	0.1392
	2	0.8371	0.5577	0.4796	0.3295	0.2550	0.1616	0.1373
	3	0.8328	0.5488	0.4765	0.3258	0.2456	0.1613	0.1377
	4	0.8408	0.5419	0.4766	0.3305	0.2552	0.1687	0.1448
	5	0.8390	0.5453	0.4842	0.3243	0.2482	0.1665	0.1413
Moderate wear of tooth surface	1	0.8748	0.5980	0.5124	0.3345	0.2511	0.1700	0.1478
	2	0.8795	0.5994	0.5079	0.3340	0.2478	0.1697	0.1478
	3	0.8752	0.6008	0.5151	0.3461	0.2479	0.1664	0.1473
	4	0.8826	0.6015	0.5177	0.3284	0.2486	0.1691	0.1474
	5	0.8786	0.5948	0.5121	0.3380	0.2531	0.1681	0.1441
Broken tooth	1	0.8633	0.6903	0.5470	0.3574	0.2586	0.1754	0.1520
	2	0.8693	0.6883	0.5446	0.3543	0.2581	0.1668	0.1459
	3	0.8705	0.6939	0.5497	0.3486	0.2576	0.1681	0.1461
	4	0.8734	0.6822	0.5510	0.3561	0.2548	0.1682	0.1449
	5	0.8651	0.6909	0.5452	0.3480	0.2597	0.1683	0.1442

Table 2: Gray relation degree between tested samples and standard fault patterns.

Sample	Normal gear	Slight wear of tooth surface	Moderate wear of tooth surface	Broken tooth	Result
1	0.9047	0.7927	0.7750	0.6951	Normal gear
2	0.9431	0.7684	0.7340	0.6716	Normal gear
3	0.9339	0.7670	0.7457	0.6694	Normal gear
4	0.9419	0.7727	0.7575	0.6635	Normal gear
5	0.9420	0.7578	0.7408	0.6617	Normal gear
6	0.7802	0.9670	0.8051	0.7081	Slight wear of tooth surface
7	0.7937	0.9022	0.7762	0.6853	Slight wear of tooth surface
8	0.8176	0.9244	0.7708	0.6818	Slight wear of tooth surface
9	0.7438	0.9102	0.8227	0.7550	Slight wear of tooth surface
10	0.7523	0.9309	0.7914	0.6914	Slight wear of tooth surface
11	0.6626	0.7026	0.9144	0.7109	Moderate wear of tooth surface
12	0.7060	0.7819	0.9149	0.7286	Moderate wear of tooth surface
13	0.6856	0.7524	0.9017	0.7252	Moderate wear of tooth surface
14	0.6893	0.7353	0.8994	0.7096	Moderate wear of tooth surface
15	0.6952	0.7404	0.9298	0.7140	Moderate wear of tooth surface
16	0.6694	0.7064	0.7616	0.9286	Broken tooth
17	0.7115	0.7489	0.8161	0.9384	Broken tooth
18	0.7194	0.7572	0.8340	0.9360	Broken tooth
19	0.7180	0.7534	0.8204	0.9161	Broken tooth
20	0.7006	0.7465	0.8002	0.9256	Broken tooth

6. Conclusion

In this paper, the adaptive local iterative filtering method is used to decompose the gear fault data. The method can decompose the nonstationary gear signal into a finite number of stationary intrinsic mode functions. The EEMD and EMD methods are used to process the same data. Comparison results show that the adaptive local iterative filtering can get the gear rotation frequency and avoid the false fluctuation in the iterative filtering process. Then, the permutation entropy is used to calculate the first several intrinsic mode functions of decomposition results. And the method of gray correlation degree is used to identify the different gear fault types. Results show that permutation entropy can really represent the characteristics of different fault types.

Data Availability

The data used to support the findings of this study are available from the corresponding author upon request.

Conflicts of Interest

The authors declare that they have no conflicts of interest to this work. The authors declare that they do not have any

commercial or associative interest that represents conflicts of interest in connection with the work submitted.

Acknowledgments

This research was supported by the National Natural Science Foundation of China (51769007), Yunnan Local Undergraduate Universities Basic Research Joint Special Key Project (202001BA070001-002), Yunnan Application Basis Research Youth Project (2018FD089), and Yunnan Provincial Key Laboratory Construction Program (2018ZD022).

References

[1] W. Xiyang, K. Zhigao, D. Hai, and G. Tingkai, "Autoregressive model-based gear shaft fault diagnosis," *Chinese Journal of Mechanical Engineering*, vol. 45, no. 4, pp. 265–272, 2009.

[2] P. Fuqiang, Y. Dejie, and W. Chunyan, "Am-fm signal extraction method by the sparse signal decomposition based on multi-scale chirplet and its application to gear fault diagnosis," *Chinese Journal of Mechanical Engineering*, vol. 46, no. 12, pp. 1–7, 2010.

[3] N. E. Huang, Z. Shen, S. R. Long et al., "The empirical mode decomposition and the Hilbert spectrum for nonlinear and non-stationary time series analysis," *Proceedings of the Royal Society of London. Series A: Mathematical, Physical and Engineering Sciences*, vol. 454, no. 1971, pp. 903–995, 1998.

[4] A. Cicone, J. Liu, and H. Zhou, "Adaptive local iterative filtering for signal decomposition and instantaneous frequency analysis," *Applied and Computational Harmonic Analysis*, vol. 41, no. 2, pp. 384–411, 2016.

[5] Y. Deyou, W. Bo, and C. Guowei, "Extracting oscillation modes from nonstationary signals for power system using adaptive local iterative filter," *Proceedings of the CSEE*, vol. 36, no. 20, pp. 5431–5439, 2016.

[6] C. Baojia, W. Xinbo, Z. Chunhua, C. Fafa, Q. Guangyin, and T. Hongliang, "Fault feature extraction of rolling bearing based on ALIF and energy operator demodulation," *Journal of Nanjing University of Science and Technology*, vol. 42, no. 4, pp. 445–452, 2018.

[7] L. Bing, Z. Peilin, R. Guoquan, L. Dongsheng, and M. Shuangshan, "Gear fault diagnosis using empirical mode decomposition, genetic algorithm and support vector machine," *Journal of Vibration, Measurement & Diagnosis*, vol. 29, no. 4, pp. 445–448, 2009.

[8] L. Tao, M. Zhuanxia, and D. Nan, "Application of multi-scale permutation entropy to fault diagnosis of scroll compressor," *Journal of Lanzhou University of Technology*, vol. 44, no. 1, pp. 42–46, 2018.

[9] L. Li, J. Rong, L. Taotao, Y. Jielin, M. Xiping, and G. Zewei, "Vibration fault diagnosis of wind turbine's gearbox based on multidimensional permutation entropy and SVM," *Power System and Clean Energy*, vol. 33, no. 5, pp. 87–91, 2017.

[10] W. Yukui, L. Hongru, and Y. Peng, "Fault identification of hydraulic pump based on multi-scale permutation entropy," *China Mechanical Engineering*, vol. 26, no. 4, pp. 518–523, 2015.

[11] Z. Massimiliano, Z. Luciano, and A. R. Osvaldo, "Permutation entropy and its main biomedical and econophysics applications: a review," *Entropy*, vol. 14, no. 8, pp. 1553–1577, 2012.

[12] L. Lin, Y. Wang, and H. Zhou, "Iterative filtering as an alternative algorithm for empirical mode decomposition," *Advances in Adaptive Data Analysis*, vol. 1, no. 4, pp. 543–560, 2009.

[13] F. Zhipeng, C. Fulv, and Z. Mingjian, *Principle and Fault Diagnosis of Complex Nonstationary Signal Analysis Method for Mechanical System*, Science Press, Beijing, China, 2018.

[14] Z. Wenbin, J. Jie, Y. Libin, G. Dewei, M. Jie, and P. Yasong, "Application of complementary ensemble empirical mode decomposition and singular value energy spectrum in wind power gear fault identification," *Acta Energiae Solaris Sinica*, vol. 41, no. 2, pp. 137–143, 2020.

[15] Z. Wenbin, G. Dewei, P. Yasong, T. Ruijing, W. Peng, and S. Yanping, "Harmonic window decomposition sample entropy and grey relation degree in rotor fault recognition," *Proceedings of the CSEE*, vol. 33, no. 21, pp. 132–137, 2013.

Hindawi
Mathematical Problems in Engineering
Volume 2021, Article ID 6032325, 24 pages
https://doi.org/10.1155/2021/6032325

Research Article

Determinants of Commodity Futures Prices: Decomposition Approach

Emmanuel Antwi,[1] **Emmanuel N. Gyamfi**,[2] **Kwabena Kyei**,[1] **Ryan Gill**,[3] **and Anokye M. Adam**[4]

[1]*University of Venda, Thohoyandou, South Africa*
[2]*School of Business, Ghana Institute of Management and Public Administration, Accra, Ghana*
[3]*University of Louisville, Louisville, USA*
[4]*School of Business, University of Cape Coast, Cape Coast, Ghana*

Correspondence should be addressed to Emmanuel N. Gyamfi; engyamfi@gimpa.edu.gh

Received 22 July 2021; Accepted 3 September 2021; Published 4 October 2021

Academic Editor: Yuxing Li

Developing models to analyze time series is a very sophisticated, time-consuming, but interesting experience for researchers. Commodity price component determination is challenging due to remarkable price volatility, uncertainty, and complexity in the futures market. This study aims to determine the components that drive the market price of commodity futures. This study utilized the decomposition methods, empirical mode decomposition (EMD), and variational mode decomposition (VMD), to analyze three commodity futures prices data: corn from agricultural products, crude oil from energy, and gold from industrial metal. We applied these techniques to decompose the daily data of each commodity price from different periods and frequencies into individual intrinsic mode functions for EMD and modes for VMD. We used the hierarchical clustering method and Euclidean distance approach to classify the IMFs and modes into high-frequency, low-frequency, and trend. Next, applying statistical measures, particularly, the Pearson product-moment correlation coefficient, Kendall rank correlation, and Spearman rank correlation coefficient, we observed that the trend and low-frequency parts of the market price are the main drivers of commodity futures markets' price fluctuations. The low-frequencies are caused by special events. In a nutshell, commodity futures prices are affected by economic development rather than short-lived market variations caused by ordinary disequilibrium of supply-demand.

1. Introduction

Globally, crude oil, corn, and gold futures prices have great influence on worldwide economy. These commodities are prone to price fluctuations and have decisive impact on international economic activities as well as both consumers and producers [1], [2]. Price fluctuation is a primary concern as investors are anticipated to make satisfactory profit from their commodity futures market exchange, and the price studies of crude oil, corn, and gold can supply macroeconomic information to investors to minimize risks of loss and maximize profit. The futures market price determinants of these commodities are not affected by demand-supply only but also influenced by several components such as financial policies, growing economy, exacerbation of market speculation, and special events (eruption of war, outbreak of pandemic, 911 gruesome attacks, and 2008 and 2012 global debt crisis) [3]. The remarkable price volatility in the futures market of crude oil, corn, and gold makes it difficult to develop models to analyze the price movements of the aforementioned commodities. Prudent economic and investment decision-making, which can assist investors and policymakers to reduce the danger posed by price swinging, therefore, can only be achieved by accurately analyzing the futures market.

The United States is the leading consumer of corn in the world. In 2019/2020, the United States consumed about 12.30 billion bushels of corn, followed by China. China consumed about 10.98 billion bushels of corn in the same year. The European Union is the third largest consumers of corn globally [4]. These countries are regarded as the world leading economies, which imply that this agricultural commodity plays significant role in the daily planning of the economy of these three countries. According to the International Energy Agency (IEA) 2019 report, United States and China are the leading consumers of crude oil worldwide, which consumed about 19.4 million barrels per day and 14 million barrels per day, respectively. Gold as a precious metal is used as an indicator to hedge against inflation and measure wealth in the world. It is a metal which is fascinated by everyone and has maintained its value over centuries. Unlike crude oil, gold price is not determined by any organization, but mostly depends on the cost of extraction and how much people are willing to pay for it. Gold is expensive due to the high cost associated with its production and also exceeding popularity and can maintain constant weight all the time, which makes it price rise more often. As stated by the futures price discovery mechanism, these commodities are extremely affected by macroeconomic policies; therefore, they are useful in providing price information to spot markets. Hence, discovering the drivers of these commodities is expected not only to minimize the unreliability and decrease the danger in commodity markets but can also help to make strategic and reliable blueprints for government.

Crude oil, corn, and gold were chosen across the commodity price market to conduct this study, which aimed at identifying the underlying components that drive the futures prices' fluctuations in energy, agriculture, and industrial metal because these commodities are regarded as the most volatile, interactive, and complex in the commodity price market and very sensitive to macroeconomic policies [4]. These commodities play a vital role in the world economy; hence, the futures prices of these commodities market price data are very important for any future development plan since there is strong mutual relationship between price, supply, and demand.

Inspired by the aforementioned reasons, we proposed an enhanced signal detector and EMD and VMD techniques, to decompose price series of crude oil, corn, and gold to establish the components that drive commodity futures spot markets' prices. This paper utilizes EMD and VMD to analyze the components of futures prices of corn (from agricultural commodities section), crude oil (from energies section), and gold (from industrial metals' section). By investigating the components that drive commodity futures prices of these selected items, this research contributes to the existing literature as follows:

(1) We demonstrate that the EMD and VMD can reveal the underlying factors that causes corn, crude oil, and gold markets price fluctuations.

(2) Using Hierarchical Clustering and Euclidean Distance Techniques, the IMFs and modes were grouped into their respective frequencies—high-frequency, low-frequency, and trend components.

(3) Subsequently, different statistical measures were used to evaluate the contribution of each frequency to the net variance of the volatility of crude oil, corn, and gold markets' price fluctuations.

(4) The economic interpretations of these components were categorized as near-term fluctuations, as a result of ordinary disequilibrium of supply-demand, unpredictable special events, and a long-term trend. It can, thus, be concluded that commodity futures prices are driven by economic development since low-frequency and trend are dominant components of commodity prices' series. From these processes, some strategic forecasting approaches are discussed in the conclusion.

The remainder of the paper is divided as follows: in Section 2, we review the relevant studies; we detail the data and introduce the EMD and VMD algorithms in Section 3; we discuss the empirical results in Section 4, where also the derived intrinsic modes by EMD and VMD are presented; Section 5 discusses and concludes our findings, where we also provide some possible explanations for the results and future developments.

2. Related Studies

Globally, energy, agricultural, and industrial metal products markets are complex, uncertain, volatile, and interdependent. As a result, crude oil, corn, and gold time series are nonlinear and nonstationary [5]. Therefore, determining the drivers of these commodities are demanding task [6]. Much research has been conducted into the analysis of commodity prices, and the usual methods used can be classified into two groups: data-driven approaches and structure-modeling techniques. Data-driven strategies consist of linear regression models such as autoregressive moving average (ARMA) and autoregressive conditional heteroscedasticity- (ARCH-) type models [7], [8] and nonlinear models such as back-propagation neural network (BPNN) and radial basis function neural network (RBFNN) [9]. The structure approach models profile commodity market prices and then uses schedule supply-demand equilibrium to examine the price volatility [10].

The mechanism of commodity price investigation and the factors that influence it can be modeled using structure models; however, the structure method is strenuous to apply due to the distinctive features of the commodity futures market. For instance, oil supplying is difficult to model because it is dispensed by two independent bodies, namely, the non-OPEC and OPEC nations. The non-OPEC countries have no control over oil prices, while the OPEC ones determine the production levels, using several factors, other than reserved capacity [11], Furthermore, the difficulty in modeling commodity futures prices is also due to the unsteady international market environment. The data-driven approaches have proven to be quite versatile for short-term predictions but do not have meaningful economic

interpretations, as they cannot justify the inherent forces that cause commodity price movement.

Several studies have cropped up in the literature trying to develop models to study the price fluctuations of commodity futures spot market prices. Studies such as those by Zhu et al. [12], Wang et al. [13], Miao et al. [14], Boubaker and Raza [15], and Wang and Li [16] used singular spectrum analysis (SSA) and wavelet and combined with neural network models such as backpropagation neural network, radial basis function, and wavelet neural network to predict commodity futures prices. They used SSA and wavelet to decompose crude oil, corn, and gold prices series. The experimental results revealed that the neural network models combined with SAA perform better than the benchmark models.

Boubaker and Raza [15] employed the wavelet method to analyze mean and volatility spillovers between oil price and BRICS stock markets at different time intervals. They developed a combined model, VARM-GARCH-cDCC, to examine the effects of spillover on mean and variances of level prices at different time scales. Evidence from the investigation indicates that the information within the oil industry and volatilities have strong influence on oil price and stock market prices but have no effects on the volatilities of other prices. The results also revealed that the proposed VARM-GARCH-cDCC combined with wavelet decomposition predicts the oil price accurately. However, using SAA and wavelet as a data preprocess tool has some drawbacks. SSA and wavelet decompositions extract false cycles forming part of the series since choosing the function basis, and the decomposition levels are subjective. Wavelet is nonadaptive in nature.

An objective data analysis approach, such as empirical mode decomposition (EMD), proposed by Huang et al. [17], and variational mode decomposition (VMD), suggested by Dragomiretskiy and Zosso [18], can be used to address the challenges in modeling and in the absence of meaningful economic interpretations in market price of commodity futures.

EMD is empirical in nature; it is instinctive, straight, and robust data pretreatment technique developed, particularly, for nonlinear and nonstationary data preprocessing. The work of EMD is to break down the data into a discrete number of intrinsic mode functions (IMFs) in such a manner that the data is near periodic based on peculiar characteristics, called the "extrema," which is the length between two sequential local extrema; thus, based on the scale, the meaning of each IMF and the interpretations can be established; for instance, an intrinsic mode associated with financial time series with a scale of three months is considered as a special event or seasonal event. Exploring data's intrinsic modes is very important to understand economic interpretation since data is the only relationship we have with real life.

Researchers have applied EMD in studies on economic and financial data. It has been applied, for example, in modeling agricultural products (Wang et al. [13]; Abadan and Shabri [19]), electricity price (Xiong et al. [20]; An et al. [21]; Crosato et al. [22]), on exchange rates (Lin et al. [23]; Premanode and Toumazou [24]; Plakandaras et al. [25]), gold prices (Jian-Hui and Wei [26]; Hua and Jiang [27]; Owusu Junior et al.[28]), crude oil prices (Meng et al. [29]; Chen et al. [30]; Yu et al. [31]; Zhang et al. [32]; Wu and Huang [33], and on carbon prices (Zhu et al. [12]). Premanode and Toumazou [24] used differential empirical mode decomposition (DEMD) for improving forecasting of exchange rates using the support of vector regression (SVR). The simulation report showed that when DEMD integrated with the SVR model, it was more robust than the state-of-art Markov switching generalized autoregressive conditional heteroskedasticity (MS-GARCH) and Markov switching regressive (MSR) models.

Korotin et al. [34] used EMD and combined with the Hurst exponent to assess the effects of economic sanctions on ruble exchange rate in Ukraine. They based their argument on the theory of an effective market and reported that there was no direct impact of sanctions on the ruble exchange rate and concluded that the foreign exchange market has a long memory.

Zhu et al. [35] proposed EMD and combined with the counterfactual analysis to estimate the effects of China's export policy on the price of tin. They used four different kinds of decompositions in their analysis and selected the EMD method as the best decomposition technique. The empirical results revealed that China's export policy has no effect on tin price, but the abolition of export policy brought about an increase in supply of global tin market, such that there was downward trend in the tin prices in the long run, which resulted in the short-term fluctuation in the international tin market, and that market policy and price are effective response of trade policy.

Zhu et al. [36] proposed the EMD method to study the spillover effects between carbon market and electricity market. EMD was applied to decompose carbon and electricity prices into several modes with different frequencies and used conditional value at risk was used to detect the spillover effects between carbon market and electricity market. The experimental results indicate that the spillover effects of carbon market affect electricity market positively, while spillover effects of electricity market affect carbon market negatively. It further revealed that, for high and low frequency modes, the spillover effects of carbon market affect electricity market positive, and vice versa. For the case of intermediate frequency, there exist a negative bidirectional spillover effect between the two markets.

Dragomiretskiy and Zosso [18] introduced the VMD model to improve EMD and EEMD by reducing endpoints' effect and mode mixing. VMD is a nonrecursive and bandwidth-limited optimization signal decomposition method, using the Wiener filtering and Hilbert transform; it can decompose nonlinear and nonstationary time series data. VMD assumes that each mode has a limited bandwidth of center frequency and minimizes the sum of estimated bandwidth of each mode and the sum of each is equal to the observed data; moreover, it is robust to noisy data.

VMD is developed to decompose nonlinear and nonstationary data and has, increasingly, attracted research attention in many fields. For instance, Lahmiri [37] employed VMD as a data preprocessing tool to predict

intraday stock prices at different frequencies. The study revealed that the VMD combined with other models forecast stock better than single models.

Aneesh et al. [38] studied performance analysis of VMD over empirical wavelet transform (EWT) using six different categories of power for recognition of power quality disturbances. The report on the identification indicated that VMD was superior to EWT in terms of the trait extraction process and identification accuracy. Seo et al. [39] employed VMD to model daily rainfall-runoff, and they reported that VMD models were robust regarding efficiency and effectiveness.

Niu et al. [40] used VMD-LSTM to forecast the stock price index. VMD was proposed to decompose the actual series of stock price into different number of modes, and the result was compared to EMD-based hybrid models. They reported that the VMD-LSTM model improves the forecasting of the stock price index. The combined model outperforms the single models, and predicting precision of VMD-based models was better than the EMD-based models using complexity-invariant distance (CID) as a statistical measure in rating the predictability of the models.

Zhu et al. [5] analyzed the price series and volatility of natural rubber's market using VMD as data preprocessing to decompose the rubber futures series from Shanghai Future Exchange into different modes. A hybrid VMD-BiGRU model was formulated to forecast the short-term rubber futures on the Shanghai Future Exchange. The empirical results revealed that the VMD approach emerged as a robust technique for analyzing natural rubber's market and can detect the hidden factors associated with rubber market price fluctuations. Similarly, Huang and Deng [41] employed VMD to predict the crude oil prices series. VMD was combined with long short-term memory (LSTM) and moving window to form a hybrid model, VMD-LSTM-MW, to forecast monthly and daily crude oil price. They reported that the VMD-LSTM-MW model was superior to a single-energy based (SE). Jianwei et al. [42] predicted the movement of gold price futures fluctuations by utilizing VMD technique to decompose the original gold price series into different modes. A hybrid model was formulated based on independent component analysis (ICA) and gate recurrent unit neural network (GRUNN) approach, called VMD-ICA-GRUNN. The empirical results indicate that the combined method, VMD-ICA-GRUNN, predicts gold price accurately as compared to single benchmark models, such ARIMA, radial basis function neural network (RBFNN), long short-term memory neural network (LSTM), GRUNN, and ICA-LSTM. He et al. [43] proposed forecasting models, combined with VMD quantile regression neural network (QRNN), to predict three crude oil markets, the West Taxes Intermediate (WTI), the Brent, and the OPEC markets, and reported that the proposed hybridization approach to forecast oil price volatility market accurately and increasing forecasting ability of QRNN.

It is clear evidence that EMD and VMD framework have been used recently as data processing in predicting commodity market prices. However, none of the studies analyzed the underlying components that drive commodity futures prices, and as a result, this current study proposes two decompositions, EMD and VMD techniques, as a data pretreatment method to identify the underlying factors that causes fluctuations in crude oil, corn, and gold markets. This paper introduces a new signal decomposition technique, VMD and EMD, to decompose crude oil, corn, and gold prices series into several modes and use statistical measures, hierarchical clustering method and Euclidean distance approach, to group the IMFs and the modes into high frequency, low frequency, and trend. The contribution of each component to the volatility of three commodity markets is analyzed. The contribution of each IMF or mode to the total variance of the volatility of crude oil, corn, and gold markets price fluctuations can be established using the Pearson product-moment correlation coefficient, Kendall rank correlation, and Spearman rank correlation coefficient.

3. Data and Descriptive Statistics

This part of the study presents the data selection, descriptive statistics of the data, data pretreatment, and experimental procedure. As mentioned in the Section 1, to analyze the drivers of commodity futures prices, this study chose three commodities' prices across the stock market, namely, corn from agricultural products, crude oil from energy, and gold from industrial metal, to conduct this empirical research. Table 1 shows the descriptive statistics of the three commodities, and Figures 1–3 represents the time series plots of corn, crude oil, and gold, respectively.

Daily closing spot market prices from Bloomberg Commodities Index were used in this empirical exercise. Bloomberg Commodities Index, which is considered the standard price for global commodity markets, was used to analyze futures prices of crude oil, corn, and gold in this experiment. We used 1277 observations for the price series of each commodity from May 2016 to April 2021. The data were obtained from http://www.bloomberg.com.

The corn and gold had positive skewness. This suggests the distribution of the two commodities spot market prices has a right tail. The crude oil had negative skewness, which indicates that the spot prices of crude oil have a left tail, as shown in Table 1. The results are confirmed by the minimum and the maximum and the time series plots of the commodity futures prices in Figures 1–3. Kurtosis of 11.98, 4.05, and 2.59, respectively, indicate that the distribution of daily spot market prices was leptokurtic. The high Jarque–Bera test statistics suggest that the commodity futures prices did not follow a normal distribution. These confirmed the nonnormality and positive skewness of corn and gold and negative skewness of crude oil daily spot market prices of commodity futures prices as revealed by time series plots in Figures 1–3, respectively.

4. Methods

4.1. Empirical Mode Decomposition (EMD) Algorithm. The empirical mode decomposition technique was introduced by Huang et al. [17] as a nonlinear and nonstationary historical dataset pretreatment tool. It is a robust and

Table 1: Period, sample size, and descriptive statistics of the three commodities' future price series of the three commodities.

Commodity	Period	Sample size	Mean	Std. dev.	Skewedness	Kurtosis	Jarque–Bera	Minimum	Maximum
Corn	2016–2021	1277	3.80	0.58	2.69	11.98	5830.30	3.02	7.53
Crude oil	2014–2021	1277	52.80	10.62	−0.61	4.05	137.17	10.01	76.41
Gold	2016–2021	1277	1429	232.89	0.99	2.59	215.66	1128	2069

Figure 1: Futures prices series of corn (May 2016–April 2021).

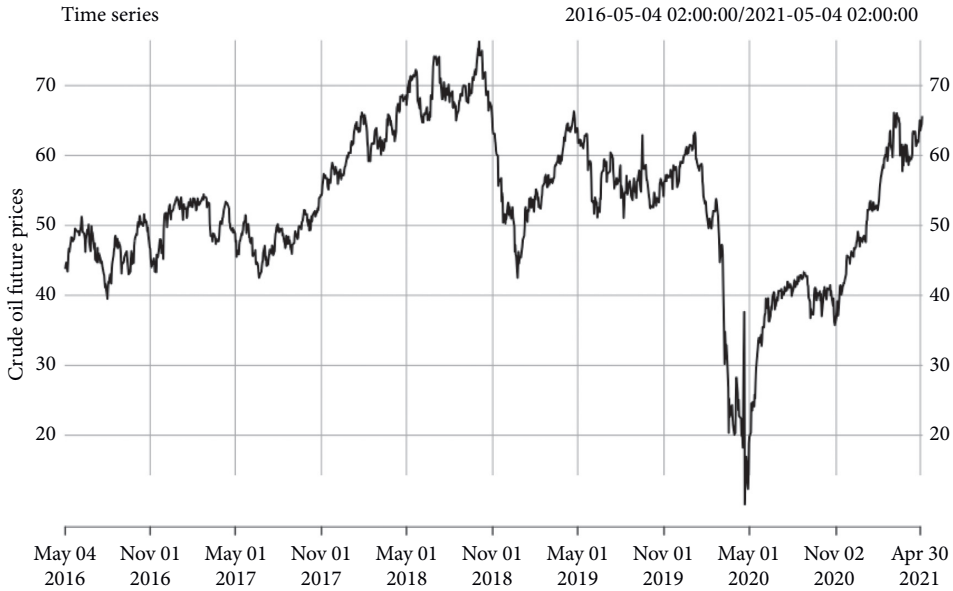

Figure 2: Futures prices series of crude oil (May 2016–April 2021).

systematic decomposition technique used in analyzing nonlinear and nonstationary time series. The EMD addresses full frequency content that cannot be explained by a single Hilbert transform. In analyzing commodity price series within its time domain, some important features may not be uncovered. EMD presumes that analyzing data in its bulk state may have several hidden modes swinging simultaneously. EMD, as a data processing tool, can bring out inherent modes from the actual series, derived from the distinct features of the actual data. EMD can present each inherent mode as an intrinsic mode function (IMF).

We follow Zhu et al. [12] in presenting the EMD algorithm. The EMD approach is operated on the following presumptions:

Figure 3: Futures prices series of gold (May 2016–April 2021).

(i) There must be at least one maximum and one minimum in the actual signal

(ii) There must be characteristics' time scale between the extrema

(iii) If there is no extremum in the data but have an inflexion point, then the data can be differentiated once or several times to bring out the extrema

The above assumptions make sure that there is harmony in the IMF and approaching periodic function and put the mean to zero. The following parameters, amplitude, frequency, and mean must be zero to certify that an IMF is a harmonic function. In practice, the act of extracting the IMFs from the data is called the "sifting" process. The EMD method can convert the time series data into a bounded and compact figure of intrinsic functions (IMFs).

The EMD process is as follows:

(a) All the maxima and minima of the commodity prices series were identified and denoted by $v(x)$

(b) Next, we used cubic spline interpolation to produce the upper and lower envelopes, $e_{\min(x)}$ and $e_{\max(x)}$

(c) The point-by-point mean represented by $h(x)$ were estimated from upper and lower envelopes using the following formula:

$$h(x) = \frac{e_{\min(x)} + e_{\max(x)}}{2}. \tag{1}$$

(d) The mean was obtained from the series, $v(x)$, and defined the difference of $v(x)$ and $h(x)$ by $d(x)$:

$$d(x) = v(x) - h(x). \tag{2}$$

(e) We checked the characteristics of $d(x)$

(i) If $d(x)$ is an IMF, we denoted $d(x)$ as ith IMF and replaced $v(x)$ with residual:

$$r(x) = v(x) - d(x). \tag{3}$$

The ith IMF is denoted by $c_i(x)$, and $c_i(x)$ is called its index

(ii) If $d(t)$ was not IMF, it replaced $v(x)$ with $d(x)$

(f) We repeated Steps (a)–(e) till the residuals met some stopping criteria. For details about stopping criteria, see the work of Zhu et al. [12].

Hence, the commodity futures prices $v(x)$ can be written as the sum of IMFs and a residue, mathematically as follows:

$$v(x) = \sum_{i=1}^{n} c_i(x) + r_n(x), \tag{4}$$

where n is the number of IMFs, $r_n(x)$ is the final residue, and $c_i(x)$ is the ith IMF.

In the extraction of IMFs, c_1 is the first extracted component and holds the IMF with the first-class scale of the commodity price series. After the extraction, c_1 is the residue and identified as the element with a longer period variation; thus, EMD filters and groups the IMFs into high-frequency and low-frequency modes. Practically, the grouping of IMFs is based on the algorithm called "fin-to-coarse reconstruction." This study uses the Euclidean distance and hierarchical clustering approaches to classify the IMFs into high and low frequencies.

In general, EMD has the following advantages over other decomposition methods:

(1) EMD can break down any sample size data into simple independent intrinsic mode function

(2) It differs from the wavelet approach because the decomposition depends on the distinct characteristic time scale of the data and allows only extrema in the sifting process; therefore, it is robust, highly efficient, and distinct [44]

(3) The extracted IMFs through EMD have an instantaneous frequency based on deriving the phase functions such that we can apply the Hilbert transformation to the IMFs

4.2. Variational Mode Decomposition (VMD) Algorithm. Empirical mode decomposition (EMD) has drawbacks, such as mode mixing, noise sensitivity, and sampling. VMD is more robust than EMD in terms of signal decomposition [18]. To overcome the difficulties with EMD, attempts were made at replacing local mean estimation and envelope in EMD [45]. Synchro-squeezed transform (SST) [46], empirical wavelet transforms (EWT) [47], and VMD are different classes of data-driven approaches that aim to extract EMD-like decomposition. VMD is a nonrepeating signal processing method; it is employed to disintegrate real-valued signals into several independent number of band-limited subsignals, called modes y_k, with specific sparsity characteristics. The extracted modes can be reduced to one center known as "pulsation" ω_t, accompanied by the decomposition process. In estimating the bandwidth, we follow the process below:

(1) Apply Hilbert transform to each extracted mode y_k, to calculate the center frequency spectrum

(2) The calculated center frequency is mixed with the exponential tuned to adjust the mode's frequency spectrum to baseband

(3) Estimate the bandwidth of each mode y_k, by using the H^1 Gaussian smoothness of the demodulated signal

Mathematically, a constrained variational problem is formulated as follows:

Let $v(t)$ be the actual signal of the series and y_k be the kth of the actual signal; then,

$$v(t) = \sum_{k=1}^{m} y_k. \tag{5}$$

The constrained variation can be minimized as follows:

$$\mathrm{Min}\{y_k\},\{\omega_k\}\left\{\sum_{k=1}^{m}\left\|\partial_t\left[\left(\delta_t|\delta(t)+\frac{j}{\lambda t}\right)\otimes y_k(t)\right]e^{-j\omega_k t}\right\|_2^2\right\}, \tag{6}$$

where $v(t)$ is the actual signal, y_k is the kth element of the actual signal, ω_k is the center frequency of y_k, $\delta(t)$ is Dirac distribution, $\otimes$ is convolution operator, m is the number of modes, and t is time script. Considering both penalty term and Lagrangian multiplier, λ, the above constrain problem can be changed to an unconstrained one as

$$L(\{y_k\},\{\omega_k\},\lambda) = \propto \sum_{k=1}^{m}\left\|\partial_t\left[\left(\delta(t)+\frac{1}{\pi t}\right)\otimes y_k(t)\right]e^{-j\omega_k t}\right\|_2^2 + \left\|v(t)-\sum_{k=1}^{m} y_k(t)\right\|_2^2 + \langle\lambda(t), v(t)-\sum_{k=1}^{m} y_k(t)\rangle, \tag{7}$$

where $\propto$ is the constraint-stabilizing parameter of the data and L is the augmented Lagrangian.

The augmented Lagrangian L can be estimated in equation (7), and it is the associated minimax point in the iterative series. Suboptimization of L and its minimax point can be obtained using the alternate direction method of multipliers (ADMM). The ADMM optimization method presumes that updating the actual signal, y_k, and center frequency, ω_k, in two different directions help to achieve better VMD analysis results. See [18] for a detailed algorithm of ADMM.

The solution for y_k and ω_k is mathematically illustrated as follows:

$$\begin{aligned}\widehat{y}_k^{n+1} &= \frac{\widehat{f}(\omega)-\sum_{i=k}\widehat{y}_i(\omega)+(\widehat{\lambda}(\omega)/2)}{1+2\propto(\omega-\omega_k)^2},\\ \omega_t^{n+1} &= \frac{\int_0^{\infty}\omega\left|y_k^{n+1}(\omega)\right|^2 d\omega}{\int_0^{\infty}\left|\widehat{y}_t^{n+1}(\omega)\right|^2 d\omega},\end{aligned} \tag{8}$$

where $\widehat{f}(\omega), \widehat{y}_i(\omega), \widehat{\lambda}(\omega)$, and $\widehat{y}_k^{n+1}$ are the Fourier transforms of $v(t), y_i(t), \lambda(t)$, and $y_k^{n+1}(t)$, respectively.

5. Empirical Results

This section concentrates on the detailed description of the empirical results and analysis of IMFs derived from EMD and VMD, respectively.

One of the significant contributions of this study is using two decomposition methods to establish the components of commodity futures prices. We applied EMD and VMD techniques to preprocess each sample data to establish commodity futures price units. The observed data of each commodity futures prices is disintegrated into many IMFs and a residue, RES, using the EMD approach. The IMFs generated by EMD is fixed for any sample data; thus, in the EMD technique, the decomposition components for a given data cannot be changed manually. The EMD approach is illustrated in Figure 4.

Unlike EMD, with the VMD technique, the number of modes can be changed to suit the experimental needs. In this research, many tests were carried out to select the optimal number of decompositions for each price series. Figure 5 illustrates the VMD process.

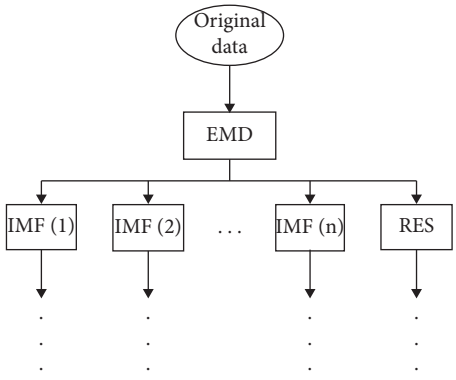

Figure 4: EMD decomposition process.

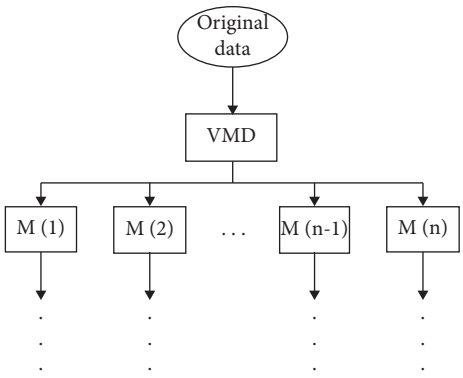

Figure 5: VMD decomposition process.

5.1. Decomposition Results and Analysis. This section presents the decomposition results of corn, crude oil, and gold using the EMD and VMD processes.

5.1.1. Decomposition Results of Corn. For corn futures using the EMD method, the sifting processes automatically produced 7 IMFs and one residue, defined as IMF1, IMF2, . . ., IMF7. Figure 6 illustrates all the IMFs and the residue of corn futures. The IMFs arranged itself automatically from high frequency to low frequency, and the last one represents the residue in each case. In other words, the IMFs were arranged in order of magnitude. These decompositions represent the price swinging known as a "trend" and market fluctuations, caused by demand-supply and random events, respectively.

Similarly, we applied the VMD technique to decompose the corn price series into eight bind-limit signals, called modes; the decomposition results are shown in Figure 7. The modes were arranged in order of amplitude, thus, the from low-frequency mode to high-frequency mode. We compared eight different decomposition modes, namely, M1, M2, . . ., M8, respectively.

5.1.2. Statistics of IMF of Corn Derived through EMD Method. The IMFs were analyzed using the following measures: the mean period of each extracted IMF, the correlation between each IMF and the actual price, the variance, and the variance percentage of each IMF. The statistical values of the IMFs and modes of the two decomposition methods of the price data series are presented in Tables 2 and 3, respectively.

The mean period is obtained by dividing the overall data points by the extrema for each decomposed IMF since the frequency and the amplitude of an IMF keep on changing as time goes by; hence, the periods are not static. We used the three correlation coefficients, namely, the Pearson product-moment correlation coefficient, Kendall rank correlation coefficient, and the Spearman correlation coefficient, to estimate the correlation between the IMFs and the actual price. The contribution of each IMF to the total variance of the actual price can be explained by summing up the variances and finding the percentage of the variance since these IMFs do not become dependent on each other. According to Peel et al. [48], the observed variance, the variances of IMFs, and the residue may differ when added up; this is a result of rounding-off during calculations, the irregularity in the actual data series, and the introduction of variance. It can be observed that there are a positive 57.245% and a negative 28.157% differences, as seen in Tables 2 and 4, respectively.

For the decomposition of corn futures prices' series, the original data series, the leading mode was not any IMF but the residue with the mean period of 425.667 and contributed more than 41% of the total variability of corn futures prices. It had the highest correlation coefficient with the observed price of 0.61478, 0.10777, and 0.16794, respectively, and is known for the long-term deterministic trend [17]. The next significant mode was IMF7, which contributed more than 32% of the total variation of the corn futures prices, with a correlation coefficient between the observed price of 0.54986, 0.36244, and 0.51175 for Pearson, Kendall, and Spearman in that order.

The combined variance of the residue and IMF7 accounted for more than 73% of the total variance of corn future price volatility. The third important mode was the IMF6, with a correlation coefficient between the observed price of 0.06365, 0.02319, and 0.03523 for Pearson, Kendall, and Spearman, respectively, as shown in Table 2, with a variance contribution of more than 18% of the future price of corn. The IMF5 accounted for 3.823% of the variability of corn future price. The IMF4 and IMF3 contributed 2.23% and 1.076% of the total variance of corn future price, respectively. The IMF1 and IMF2 accounted for less than 1% of the variance of the corn future price series.

5.1.3. Statistics of Mode of Corn Derived through VMD Method. Similarly, the decomposition of corn future price series data using VMD produced eight modes, as shown in Figure 7. The aggregate represents the signal of the observed data. It can be deduced from Table 4 that the leading mode of the actual price was M2, which contributed 50.56% overall variance of corn future price. Next was M1, with a mean period of 13.165, which accounted for more than 40% of the net variability of the actual price data. Besides M1 and M2,

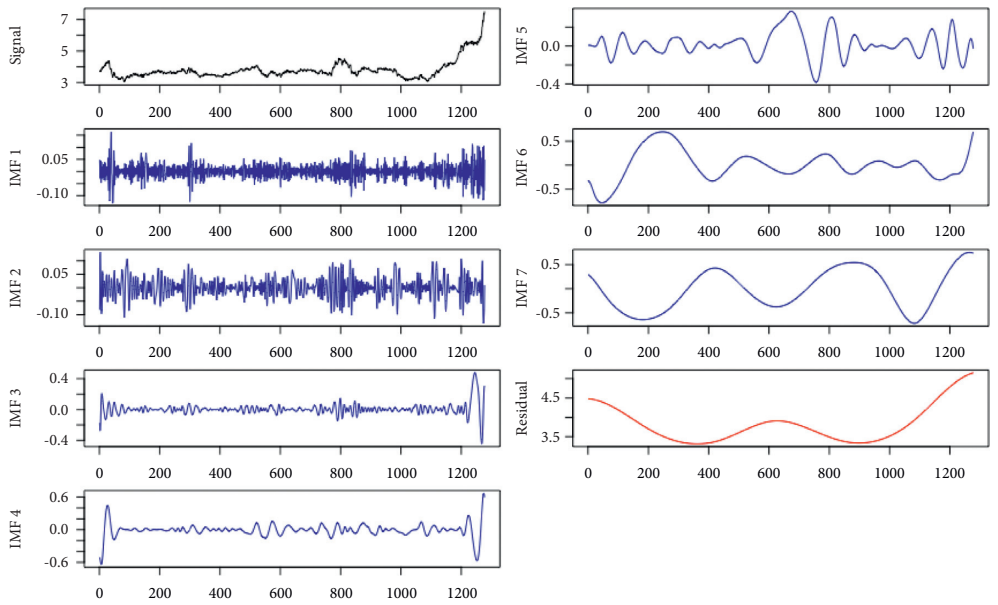

Figure 6: Empirical mode decomposition (EMD) curves for daily corn price series (May 2016–April 2021).

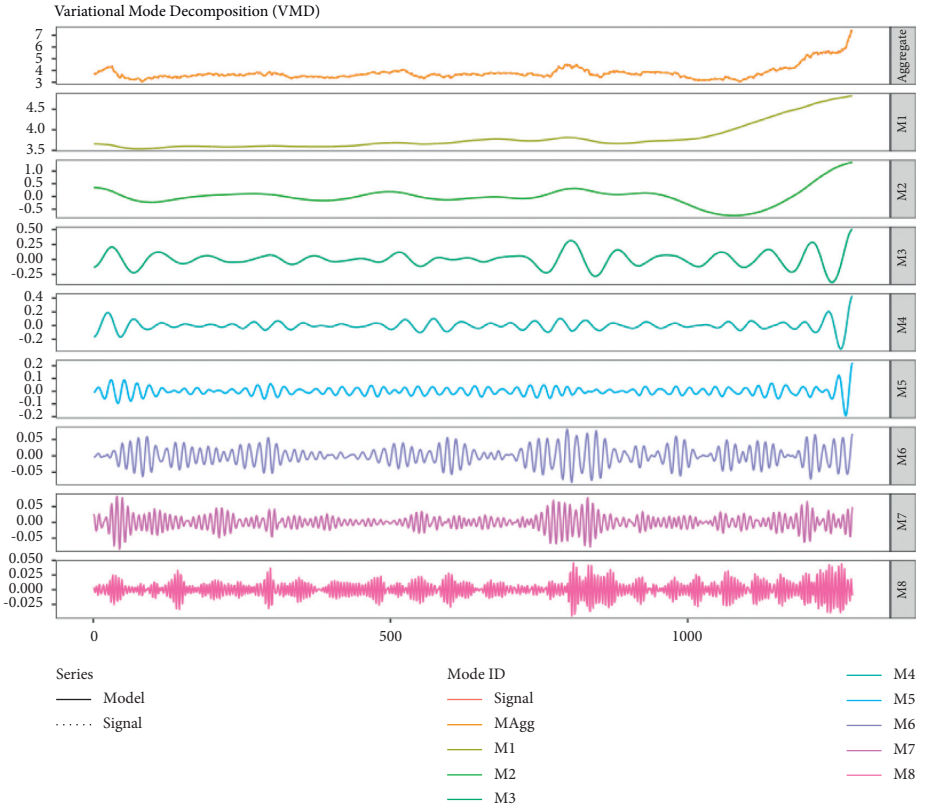

Figure 7: Variational mode decomposition (VMD) curves for daily corn price series (May 2016–April 2021).

M3, with a mean period of 38.697, contributed more than 5% of the variability of corn future price. For M4, M5, M6, M7, and M8, the values of correlation coefficients were very low. These modes (M4–M8) contributed 1.765%, 0.436%, 0.286%, 0.187%, and 0.066%, respectively, of the variability of the observed data.

5.1.4. Constitution of Corn Futures Prices. In addition, following Zhu et al. [12], we used Euclidean distance between pairs of any two IMFs or modes or between an IMF or mode and the residue and hierarchical clustering approach to group the IMFs and the modes into three components. The clustering results are presented in Figure 8. An IMF was

Table 2: Measures of IMFs and residue obtained through EMD of daily price series of corn (May 2016–April 2021): correlation is significant at the level of 0.05 (2-tailed).

	Mean period	Pearson correlation	Kendall correlation	Spearman correlation	Variance	Variance as of observed (%)	Variance as % of ∑IMFs + residual (%)
Observed series	2.02377				0.33526		
IMF1	1.65415	0.03033	0.05804	0.08160	0.00103	0.30722	0.19538
IMF2	3.85801	0.01557	0.05546	0.08244	0.00132	0.39372	0.25039
IMF3	8.03145	0.18821	0.08422	0.11590	0.00567	1.69122	1.07553
IMF4	17.98592	0.13127	0.16079	0.22557	0.01488	4.43835	2.82257
IMF5	38.69697	0.10200	0.19915	0.28984	0.01821	5.43161	3.45423
IMF6	116.09091	0.06365	0.02319	0.03523	0.09837	29.34141	18.65966
IMF7	212.83333	0.54986	0.36244	0.51175	0.16983	50.65621	32.21480
Residue	425.66667	0.61478	0.10777	0.16794	0.21787	64.98538	41.32744
Sum						157.245	100

Table 3: Correlation and variance of components obtained from the IMFs of EMD for daily price series of corn (May 2016–April 2021): correlation is significant at the level of 0.05 (2-tailed).

	Mean period	Pearson correlation	Kendall correlation	Spearman correlation	Variance	Variance as of observed (%)	Variance as % of ∑IMFs + residual (%)
Observed series	2.02377				0.33526		
High frequency	55.52174	0.56739	0.39879	0.54449	0.21369	63.73859	45.58662
Low frequency	32.74359	0.15351	0.26932	0.37196	0.03763	11.22412	8.02763
Trend	425.66667	0.61478	0.10777	0.16794	0.21787	64.98538	46.47834
Sum						139.94809	100

Table 4: Correlation and variance of components obtained from modes of VMD for daily price series of corn (May 2016–April 2021): correlation is significant at the level of 0.05 (2-tailed).

	Mean period	Pearson correlation	Kendall correlation	Spearman correlation	Variance	Variance as of observed (%)	Variance as % of ∑IMFs + residual (%)
Observed series	2.02377				0.33526		
M1	13.16495	0.7698	0.34161	0.44076	0.09867	29.43089	40.96571
M2	51.08000	0.81506	0.56521	0.72165	0.12177	36.32106	50.55634
M3	38.69697	0.27415	0.25665	0.33405	0.01382	4.12217	5.73777
M4	22.40351	0.17083	0.14986	0.20856	0.00425	1.26767	1.76451
M5	10.91453	0.09350	0.08122	0.11630	0.00105	0.31319	0.43594
M6	7.38150	0.07210	0.07910	0.11401	0.00069	0.20581	0.28647
M7	4.72963	0.05670	0.06294	0.08949	0.00045	0.13422	0.18683
M8	2.63299	0.03922	0.04783	0.06865	0.00016	0.04772	0.06643
Sum						71.843	100

classified as a high-frequency component when the Euclidean distance was less than 10. An IMF was categorized as a low-frequency component when the Euclidean distance was between 10 and 20. The Euclidean distance of more than 20 was considered a trend component. Table 3 and Figure9 presented the three components and their statistical measures as derived from EMD.

Following the above definition, IMF1, IMF2, IMF3, IMF6, and IMF7 formed the high-frequency components of EMD decomposition, while IMF4 and IMF5 correspond to the low-frequency part of the corn futures price series. Each component has a unique feature and economic interpretation—the low-frequency and the high-frequency components represent special events and short-term market price fluctuations, respectively. The residue changes gradually around the long-term mean, as mentioned in Section 2, and corresponds to the long-term corn futures price trend.

For VMD, unlike EMD, the decompositions are arranged from the low-frequency mode to high-frequency mode. M6–M8, with a short amplitude, represents the high-frequency component of corn price series and accounts for short-term market fluctuations. M2–M5 constitutes the low-frequency part of corn future price from May 4, 2016, to April 30, 2021, and represents the special events under study,

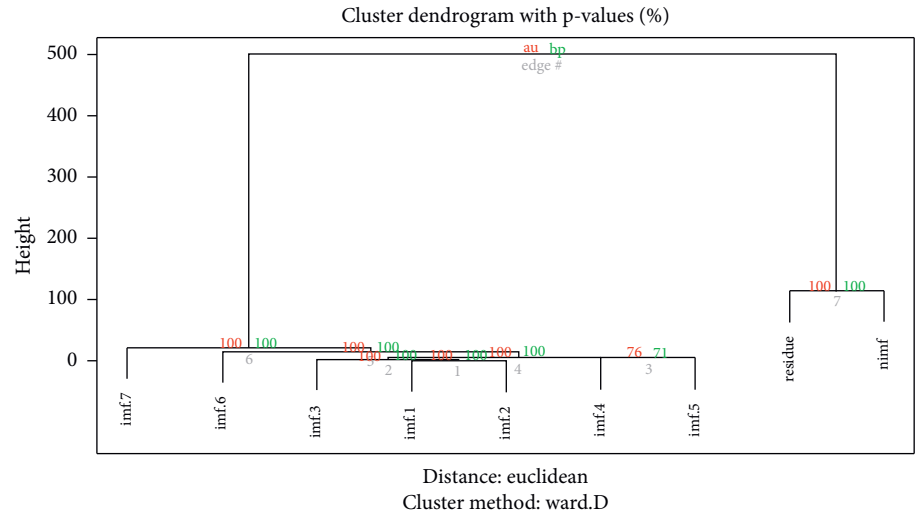

Figure 8: Hierarchical clustering diagram obtained for the IMFs and residue through EMD.

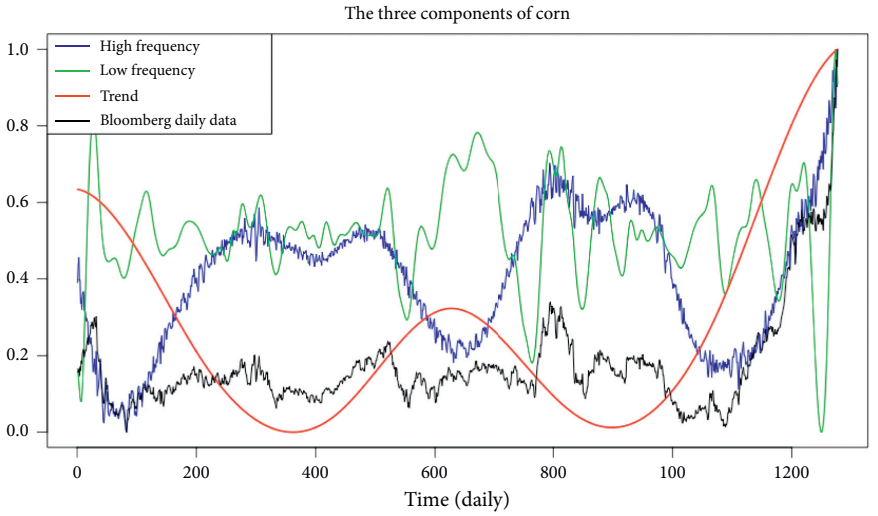

Figure 9: The three components of the Bloomberg daily data of corn (May 2016–April 2021) through EMD.

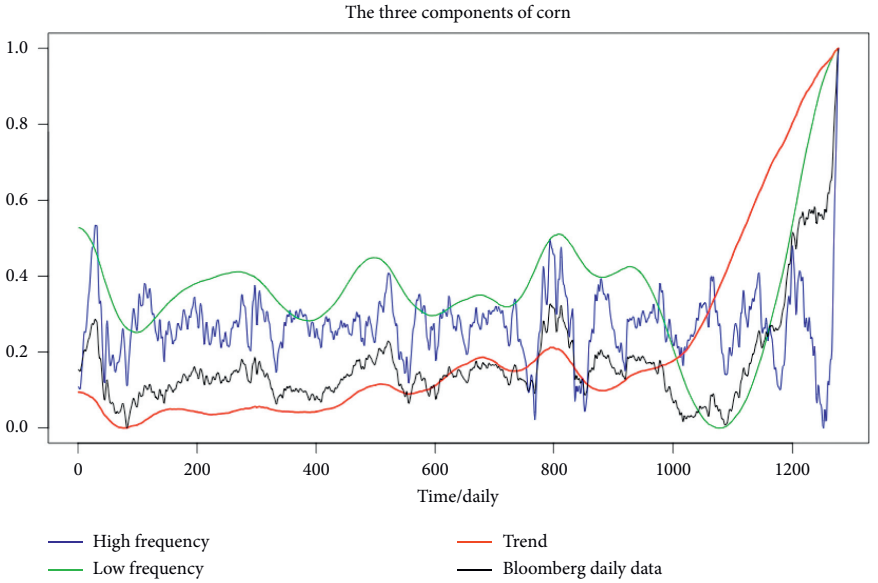

Figure 10: The three components of the Bloomberg daily data of corn (May 2016–April 2021) through VMD.

Table 5: Correlation and variance of components obtained from modes of VMD for daily price series of corn (May 2016–April 2021): correlation is significant at the level of 0.05 (2-tailed).

	Mean period	Pearson correlation	Kendall correlation	Spearman correlation	Variance	Variance as of observed (%)	Variance as % of ∑Ms + residual (%)
Observed series	2.02377				0.33526		
High frequency	4.76493	0.09428	0.10471	0.15044	0.00145	0.43250	0.58086
Low frequency	63.85000	0.85557	0.66760	0.78770	0.14951	44.5952	59.89264
Trend	13.16495	0.76976	0.34161	0.44076	0.09867	29.43089	39.52650
Sum						74.45863	100.000

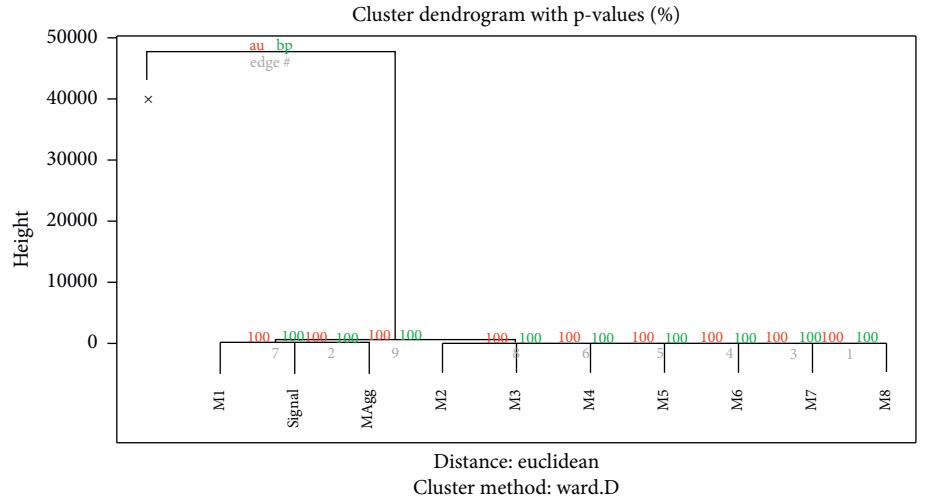

Figure 11: Hierarchical clustering obtained for the modes and residue through VMD.

while M1 represents the long-term trend of the corn future price. A plot of the extracted components and their statistical measures through VMD are presented in Figure 10 and Table 5. The classification of the modes using Euclidean distance is presented in Figure 11.

5.1.5. Trend of Corn Futures Prices. Trend accounted for 46.478% and 39.527% of the total variability of corn future price in terms of EMD and VMD, respectively. It had the highest correlation coefficient with the observed price of 0.244, 0.306, and 0.410 and 0.703, 0.616, and 0.819 in terms of Pearson, Kendall, and Spearman, respectively, for EMD and VMD. This indicates that trend is an inevitable factor in determining corn future price eventually, as shown in Tables 3 and 5. The persisting increase in the price of corn is due to worldwide economic evolution; therefore, by comparing the trend with the actual series of corn, it can be deduced that, occasionally, corn future price fluctuates due to unpredictable special events, such pest invasion, adverse weather conditions, and diseases, but reverse to the trend after the factor that triggered the event is controlled.

5.1.6. Effects of Special Events on Corn Price. The IMF6 and M2 from EMD and VMD represent the low-frequency components of corn futures prices, respectively, as shown in Figures 8 and 11. It can be seen from Figures 6 and 7 that the low frequencies are nonlinear and long-term trend. The low frequency contributed 8.028% and 59.893% of the total variance of corn futures prices in terms of EMD and VMD, respectively, as presented in Tables 3 and 5. These low frequencies correspond to significant events, such as bad weather, diseases, and pest invasion, which have significant impact on corn price. Based on the mean period of these modes, the shortest impact period is more than one month for the case of EMD and more than 2 months for VMD. It implies that it takes the market some time to eradicate these special events, and the duration may last for a while, looking at the mean period of these special events.

Furthermore, the amplitudes of some of the data points were more than $5, which suggests that some special events have a severe consequence on corn futures market prices. Large price fluctuations in corn futures occur in the medium term, due to such significant events. The normal market fluctuation takes place at a high frequency, and the trend changes gradually. We can measure the effectiveness of every significant event as low frequency and separate from the main price; hence, these results can be used in predicting any significant impact from the upcoming event of the same nature.

5.1.7. Effects of Ordinary Market Disequilibrium on Corn Price. Apart from the trend and the effect of significant events, corn futures prices are also affected by speculation. High frequency occurs as a result of random events, such as speculations within commodity market, financial policies, trade wars, and great events, such as outbreak of pandemic. The effect of these speculations can be classified as high frequency and accounted for more than 45.587% and 0.581% of the total variance of corn price in terms of EMD and VMD, respectively. The effects of ordinary market speculation are sometimes called "market disequilibrium" and consist of events with short-term impact on corn futures prices. The word, short term, is used to describe these effects since the data used in this research is daily. The disequilibrium of supply-demand as a normal market fluctuation has a serious impact on corn price as when these events persistently occur, they become one of the main drivers for pushing corn prices up. We can ignore the normal market fluctuations in the long-term trend forecasting; however, they are very crucial for short prediction. Thus, $386.75/ton of corn in April 2021 can be explicitly explained as a $106.81 trend price, $242.56 special event price, and an ordinary market fluctuation price of $37.38 through the VMD method.

5.1.8. Crude Oil Decomposition Results. Similarly, the price series of crude oil was decomposed using EMD and VMD methods, and the decomposition curves are shown in Figures 12 and 13, respectively. The EMD method decomposed the crude oil data into eight IMFs, called IMF1–IMF8, and one residue, defined as RES, as shown in Figure 12. The VMD approach produced eight modes, and the decomposition result is illustrated in Figure 13.

5.1.9. Statistics of IMF of Crude Oil Derived through EMD Method. In analyzing the IMFs derived from EMD of crude oil price series, we again followed Zhang et al. [32] by using the same parameters as that of corn to estimate each IMF contribution to the variability of crude oil price series. The mode which accounted most for the variance of the observed data was IMF8. It contributed more than 37% of the total variability with the mean period of 319.250 and the correlation coefficients between the observed data was 0.615, 0.426, and 0.604 in terms of Pearson, Kendall, and Spearman, respectively, as shown in Table 6. The IMF7 contributed more than 32% of the observed data's variability, and the correlation coefficients between the observed data was 0.498, 0.315, and 0.471 for Pearson, Kendall, and Spearman. The two most important IMFs—IMF8 and IMF7—contributed more than 69% of the crude oil price variance. The IMF5 and IMF6 accounted for 6.079% and 8.647% of the variance of crude oil price series, respectively. The remaining IMFs did not contribute much to the original price series variance, indicating that the effect of these IMFs on the crude oil price is minimal.

5.1.10. Statistics of Mode of Crude Oil Derived through VMD Method. Once more, we based our analysis of the modes derived from VMD on the following parameters: a mean period of each mode, the correlation between each mode and the observed data, the variance, and the variance percentage of each mode. Table7 presents the statistics of the modes produced by the VMD method.

The M1 emerged as the dominant mode, with correlation coefficients of 0.731, 0.607, and 0.778 between the mode and the observed data regarding the Pearson, Kendall, and Spearman correlation coefficients, and contributed more than 42% of the entire variance of the actual prices data. The M1 also exhibits a long cycle and continuously increased the trend, and the observed price series also followed the same pattern. The next important mode was M2 which caused more than 39% of the crude oil price volatility. The combined impact of M1 and M2 constituted 81.44% of the overall variance of the crude oil price series. The M3 and M4 contributed 15.42% and 1.72%, respectively, of the variance of crude oil price. On the contrary, the M5–M8 exhibited small correlation coefficients with the actual data and accounted for less than 2% of the net variability of crude oil price, suggesting that their impact on the futures prices of crude oil is insignificant.

5.1.11. Constitution of Crude Oil Price Series. Similarly, we grouped the IMFs of crude oil price series into their respective components using hierarchical clustering and the Euclidean distance techniques. The IMF1–IMF4 were classified as a high-frequency component of EMD decomposition, while IMF5–IMF8 represented the low-frequency component of the crude oil price, as shown in Figure 14. These components have unique features and economic meaning—the residue with long-term mean is classified as the trend component of crude oil futures prices, while the low-frequency part represents the effect of significant events. The high-frequency component is identified by its short amplitudes and constitutes shocks caused by short-lived market fluctuations.

For the VMD approach, M4–M8 form the high-frequency part of the oil price series and constitute short-term market fluctuations. The M2 and M3 correspond to the low-frequency component of the oil series from 2016 to 2021, representing the significant events of the period under consideration. The M1 represents the long-term trend of the crude oil futures prices, as shown in Table 8 and Figure 15.

5.1.12. The Trend of Crude Oil Futures Prices. The second deterministic factor of crude oil prices is the trend; it accounted for more than 10% of the variability of crude oil future price volatility through EMD, as shown in Table 9. This was confirmed by the VMD process, and the trend was still the second determinant of the crude oil price fluctuations, contributed more than 27% of the total variability of crude oil futures, and holds a correlation coefficient of 0.731, 0.607, and 0.778 between the original price series for Pearson, Kendall, and Spearman, suggesting that the trend

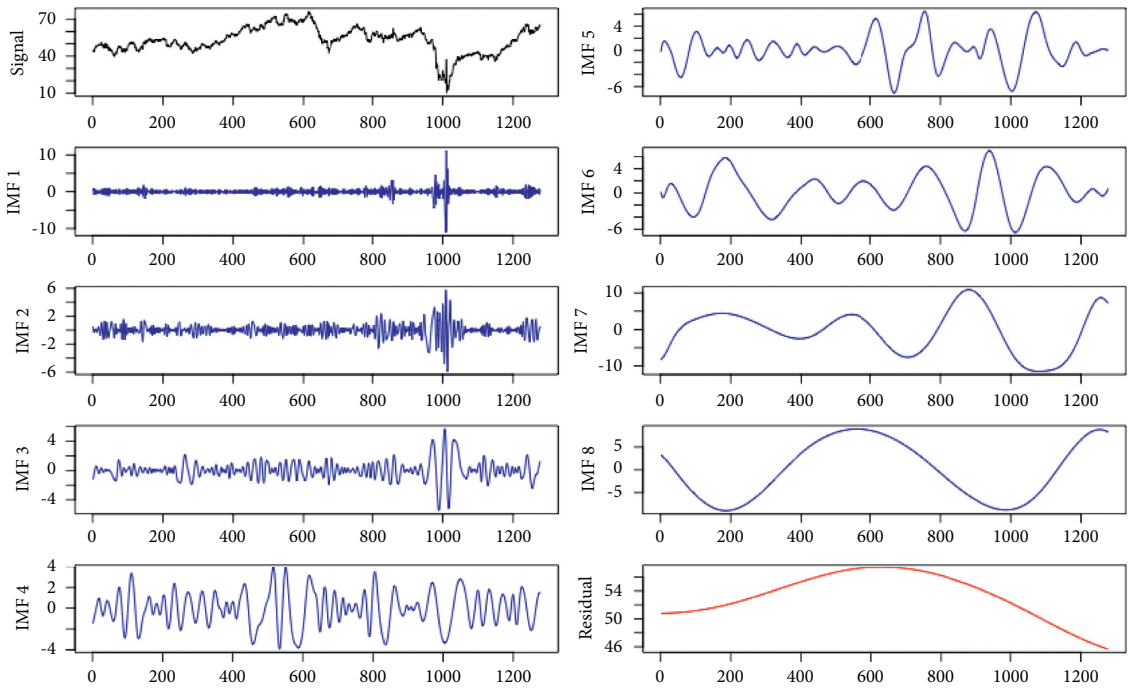

Figure 12: Empirical mode decomposition curves of daily crude oil price series (May 2016–April 2021).

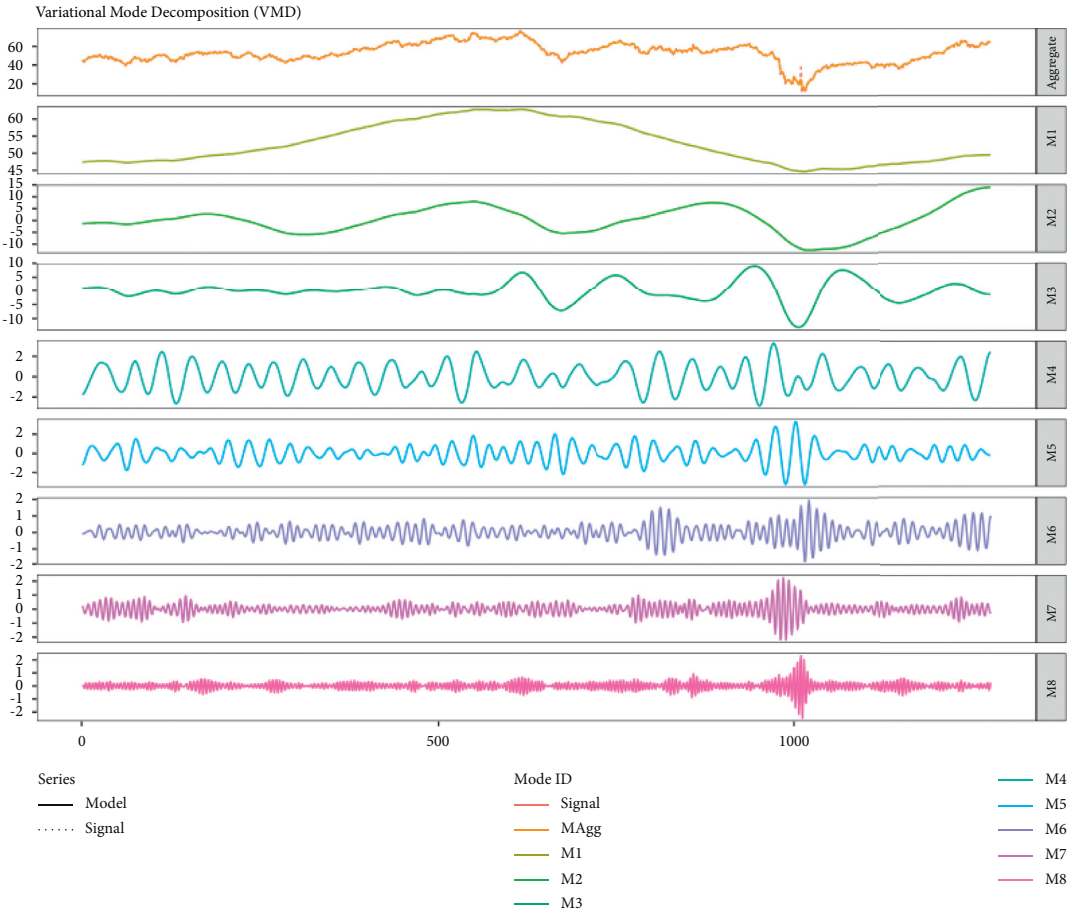

Figure 13: Variational mode decomposition curves of daily crude oil price (May 2016–April 2021).

Table 6: Measures of IMFs and residue derived through EMD for Bloomberg daily price series of crude oil (May 2016–April 2021): correlation is significant at the level of 0.05 (2-tailed).

	Mean period	Pearson correlation	Kendall correlation	Spearman correlation	Variance	Variance as of observed (%)	Variance as % of IMFs + residual (%)
Observed series	2.00786				113.1117		
IMF1	1.60025	0.12294	0.03922	0.05714	0.94290	0.83360	0.89788
IMF2	3.50824	0.04399	0.02738	0.03939	0.78348	0.69266	0.74607
IMF3	7.73939	0.05329	0.04523	0.06311	1.45815	1.28912	1.38853
IMF4	17.98592	0.16402	0.07260	0.10231	2.62998	2.32512	2.50442
IMF5	37.55882	0.34412	0.15764	0.22653	6.38402	5.64400	6.07923
IMF6	70.94444	0.31680	0.17563	0.26406	9.08070	8.02808	8.64716
IMF7	182.42857	0.49828	0.31549	0.47116	33.62158	29.72423	32.01638
IMF8	319.25000	0.61497	0.42600	0.60394	39.58971	35.00054	37.69957
Residue		0.48211	0.46130	0.61337	10.52316	9.30333	10.02075
Sum						92.84068	100.00

Table 7: Measures of modes and residue obtained through VMD for Bloomberg daily price series of crude oil (May 2016–April 2021): correlation is significant at the level of 0.05 (2-tailed).

	Mean period	Pearson correlation	Kendall correlation	Spearman correlation	Variance	Variance as of observed (%)	Variance as % of ∑IMFs + residual
Observed series	2.008				113.1117		
M1	21.283	0.731	0.607	0.778	34.704	30.68	42.03
M2	49.115	0.746	0.547	0.745	32.542	28.77	39.41
M3	55.523	0.447	0.226	0.299	12.728	11.25	15.42
M4	21.644	0.184	0.118	0.174	1.417	1.25	1.72
M5	13.302	0.129	0.066	0.097	0.733	0.65	0.89
M6	5.940	0.069	0.042	0.061	0.190	0.17	0.23
M7	3.835	0.057	0.035	0.051	0.157	0.14	0.19
M8	2.484	0.049	0.029	0.041	0.096	0.08	0.12
Sum						72.99	100

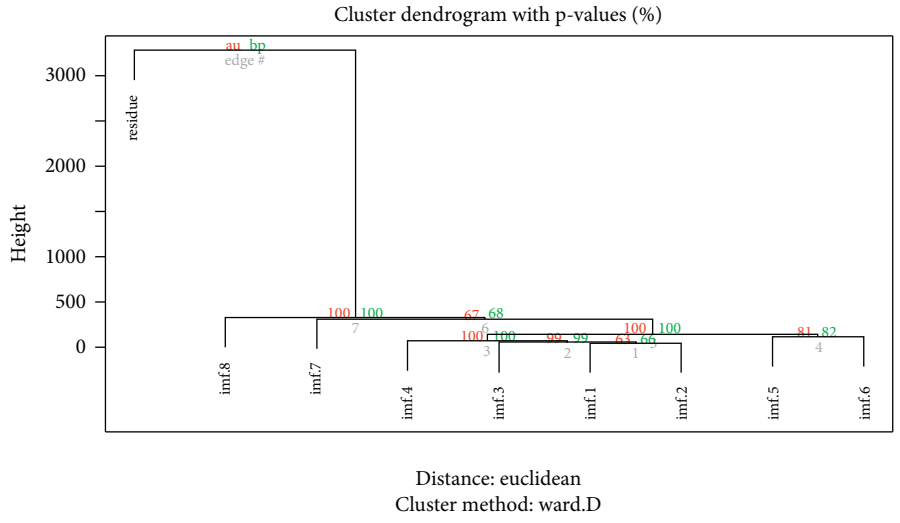

Figure 14: Hierarchical clustering diagram obtained for the IMFs and residue through EMD decomposition.

cannot be downplayed in discovering prices of crude oil in the long run, as presented in Table 8. Indeed, the continuing rise in the price of crude oil is in line with worldwide economic growth, and by comparing the trend with the original price series, we can deduce that crude oil prices could fluctuate due to momentous events. The price, however, reverts to trend after the effect of the special event is ended.

Table 8: Correlation and variance of components for Bloomberg daily data of crude oil (May 2016–April 2021) derived through VMD: Correlation is significant at 0.05 level (2-tailed).

	Mean period	Pearson correlation	Kendall correlation	Spearman correlation	Variance	Variance as of observed (%)	Variance as % of ∑Ms + residual
Observed series					113.1117		
High frequency	6.353	0.203	0.086	0.117	5.802	5.129	4.608
Low frequency	55.522	0.929	0.765	0.928	85.413	75.512	67.832
Trend	21.283	0.731	0.607	0.778	34.704	30.681	27.561
Sum						111.322	100

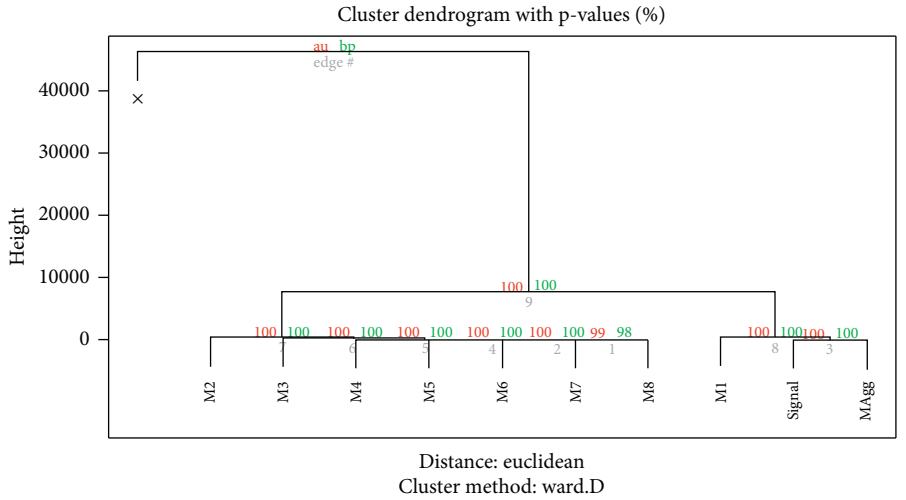

Figure 15: Hierarchical clustering diagram obtained from the modes through VMD decomposition.

Table 9: Correlation and variance of components obtained from IMFs of EMD for daily price series of crude oil: correlation is significant at 0.05 level (2-tailed).

	Mean period	Pearson correlation	Kendall correlation	Spearman correlation	Variance	Variance as of observed (%)	Variance as % of ∑IMFs + residual (%)
Observed series	2.00786				113.1117		
High frequency	6.35323	0.20288	0.08595	0.11719	5.80187	5.12933	5.70277
Low frequency	55.52174	0.92868	0.76549	0.92792	85.41266	75.51178	83.95380
Trend	1277.00000	0.4821122	0.46130	0.61337	10.52316	9.30333	10.34342
Sum						89.94444	100

5.1.13. Effects of Special Events on Crude Oil Price. Besides the trend, special events are the major contributor of the crude oil price fluctuations. The IMF5–IMF8 and M2 and M3 represent the low-frequency components of decomposition of futures prices of crude oil by EMD and VMD. From EMD, the special events contributed more than 83% and hold a high correlation coefficient of 0.929, 0.765, and 0.928 between the original price series in terms of Pearson, Kendall, and Spearman, respectively. The low frequency accounted for more than 67% through VMD of the variance of crude oil price, indicating that the special events were the major component of the wide price swings of crude oil. Interestingly, both EMD and VMD have the same mean period of 55.522 of the low-frequency components, respectively, as presented in Tables 7 and 9, indicate that the period of special events may persist for a more extended period. Examining the mean period of the IMFs and the modes, it takes an average of almost two months for the market to adjust itself to these special events.

Furthermore, the amplitude of some data points could reach a high level of $15, indicating that some special events have a remarkable effect on crude oil price determination.

The medium-term crude oil price fluctuation occurs through special events due to the gradual changes in trend and ordinary market fluctuation that take place at a high frequency. In forecasting, we can estimate every special event, and the results can be used to predict incoming special events of the same nature by isolating special events from the overall price series. Our study conformed to a similar investigation conducted by Zhang et al. [32] on crude oil price analysis using EMD and EEMD methods.

5.1.14. Effects of Ordinary Market Disequilibrium on Crude Oil Price. In addition to special events and trends, crude oil prices are also affected by the political situation, atmospheric conditions, inventory exhaustion, and strike actions. The combined effects of these factors constitute the high-frequency component of the crude oil futures price series since their effects are often short. The effect of the ordinary market disequilibrium on the crude oil price is not serious because it takes place at high frequency; thus, considering the amplitudes of the IMFs and modes, their duration is very short. We regarded this element as the consequences of ordinary market disequilibrium and considered it a set of events with near term influence on the crude oil price; we used, short-term or near term, to describe these effects because the data used in this research is daily. The disequilibrium of supply-demand from ordinary market fluctuation has no serious effect on the crude oil price. These events have frequently occurred and have become one of the major drivers that raise crude oil prices. The ordinary market fluctuations, thus, can be eliminated from the overall series in long-term trend forecasting but they are very crucial for near term prediction; for instance, through the VMD technique, the price of $64.81 per barrel in April 2021 can be explicitly explained as a trend price of $17.86, a special event price of $43.96, and an ordinary market fluctuation of $2.99. The three components derived from EMD and VMD methods are presented in Figures 16 and 17, respectively.

5.1.15. Decomposition Results of Gold through EMD and VMD Methods. Likewise, the EMD and VMD techniques were used to break up gold price data into their respective IMFs and modes in this section. The decomposition curves obtained are illustrated in Figures 18 and 19, respectively. The EMD method generated eight decomposed IMFs of gold futures price series, defined as IMF1, IMF2, . . ., IMF8, and one residue, as shown in Figure 18, while the VMD approach decomposed the gold series into eight modes. The decomposition result is presented in Figure 19.

5.1.16. Statistics of IMF of Gold Derived through EMD. The residue contributed most to the overall variability of the price series of gold and accounted for over 34% of the net variance. The correlation coefficients between the residue and the actual price of gold were 0.962, 0.559, and 0.743 in terms of Pearson, Kendall, and Spearman, respectively, as indicated in Table 10. The next significant contributor was IMF7 and accounted for more than 27% of the observed data variance. The IMF8 contributed more than 13% of the variance of the observed data with correlation coefficients of 0.285, 0.186, and 0.259 for Pearson, Kendall, and Spearman, in that order. The IMF5, IMF6, and IMF4 accounted for more than 11%, 5%, and 4%, respectively, of the total variance of gold price series. These IMFs, IMF4, IMF5, IMF6, IMF7, and IMF8, and residue contributed more than 96% of the overall variance of the gold futures series. The rest of the IMFs did not contribute much to the total variance of the gold price series, suggesting that the influence of these IMFs on gold price is insignificant.

5.1.17. Statistics of Mode of Gold through VMD. Similarly, the VMD method decomposed the price series of gold into eight modes, M1, M2, . . ., M8, as shown in Figure 19. The dominant mode was M1, which contributed more than 93% of the total variability of the gold price volatility, with correlation coefficients between the gold price series and the modes of 0.966, 0.731, and 0.902 in terms of Pearson, Kendall, and Spearman, respectively, as presented in Table 11. The next significant contributor to the variability in the gold price was M2, which accounted for 5.420% of the total variance of the gold futures price series. The correlation coefficients between the observed data and M2 were 0.417, 0.327, and 0.427 for Pearson, Kendall, and Spearman, respectively. The M1 and the M2 were considered the two most significant modes, which contributed over 98% of the entire variability of the volatility of the gold futures series. The contribution of the remaining modes, M3–M8, was less than 2% of the gold price variance. These modes also showed low correlations' coefficients with the price series of gold, suggesting that their impact on gold price determination is insignificant.

5.1.18. Constitution of Gold Price Series. In this section, we discuss the composition of the gold price in terms of the IMFs and modes' contributions separately. Using the hierarchical clustering and the Euclidean distance between pairs of any two IMFs or modes, the IMFs and the modes were categorized as low frequency, high frequency, and trend. The IMF1–IMF6 formed the high-frequency components of EMD, while IMF7-IMF8 were grouped as the low-frequency components of the gold price series, as shown in Figure 20. These two grouped IMFs and the residue have economic interpretations and provide vital information on gold futures prices. The gradual change of the mean of the residue corresponds to the long-lasting trend of the gold price. The low-frequency component is classified as special events. The effects of short-lived market fluctuations are represented by the high-frequency parts, which can be identified by their shorter amplitudes, as represented in Table 12 and Figure 18.

For VMD, M3–M8 correspond to the high-frequency components of the gold price series and constitute the short-term effects of normal market fluctuations. M2 represents the low-frequency part of gold futures prices from May 2016 to April 2021 and shows the significant events under study.

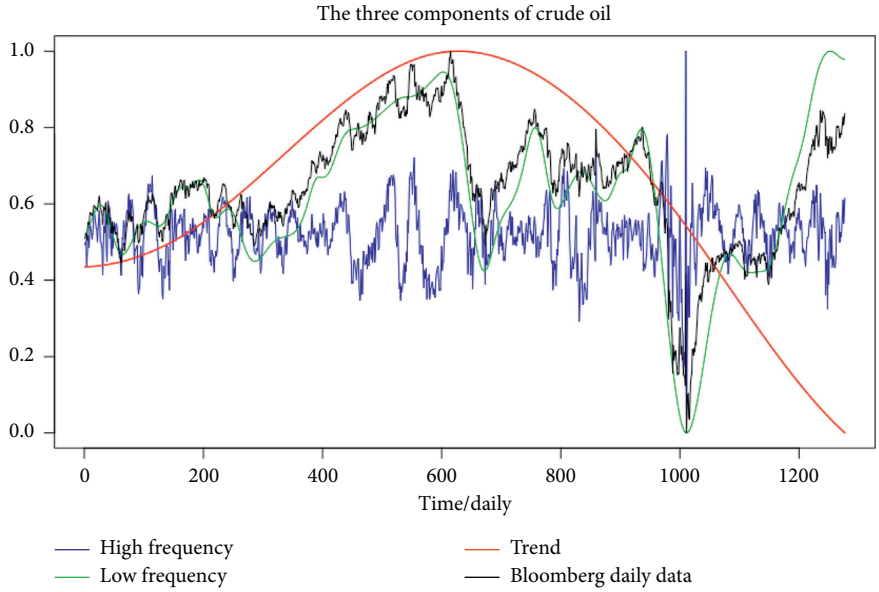

Figure 16: The three components derive from the Bloomberg daily data (May 2016–April 2021) through EMD.

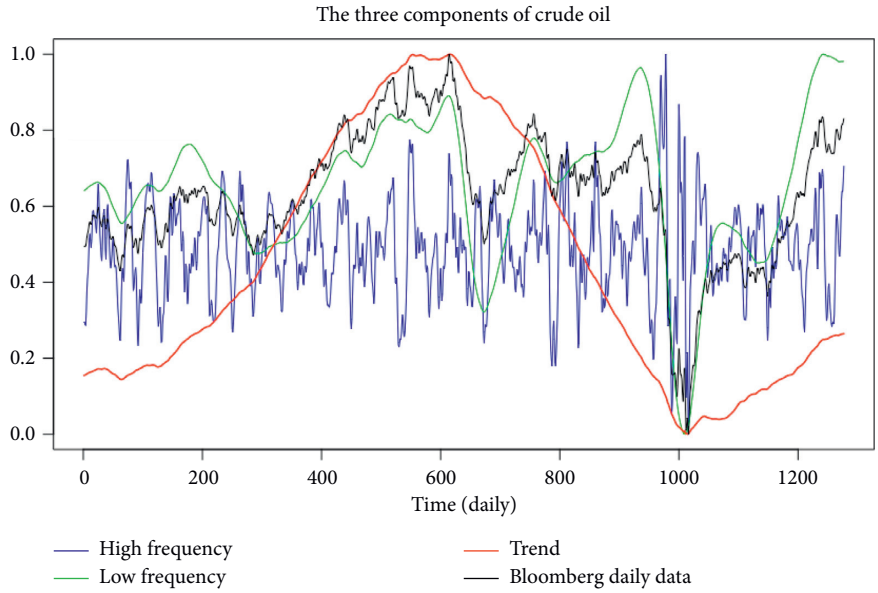

Figure 17: The three components derive from the Bloomberg daily data (May 2016–April 2021) through VMD.

The long-term trend of the gold futures prices corresponds to M1, as illustrated in Table 13 and Figure 21.

5.1.19. The Trend of Gold Price Series. Trend contributed more than 91% and 93% of the total gold price series variance in EMD and VMD, respectively. It holds the highest correlation coefficient with the observed data, indicating that it is the main force behind the long-term fluctuations of the gold price, as shown in Tables 12 and 13. By comparing the trend with the price series of gold, it demonstrates that, although, gold prices can fluctuate due to special events, but they come back to the trend after the special event is over. Figures 22 and 23 represent the three components of gold futures prices through EMD and VMD, respectively.

5.1.20. Effects of Special Events. The IMF7-IMF8 and M2 represent the low-frequency components of decomposition of futures prices of gold by EMD and VMD, respectively. Low frequency contributed more than 7% and 5% of the total variance of the price series of gold for EMD and VMD, while the low frequency constitutes the shock caused by special events of gold price. Based on the average period of the IMFs that constituted the low frequencies, the duration of the shocks takes a minimum of two months for EMD and a minimum of one month and two weeks for VMD; this means

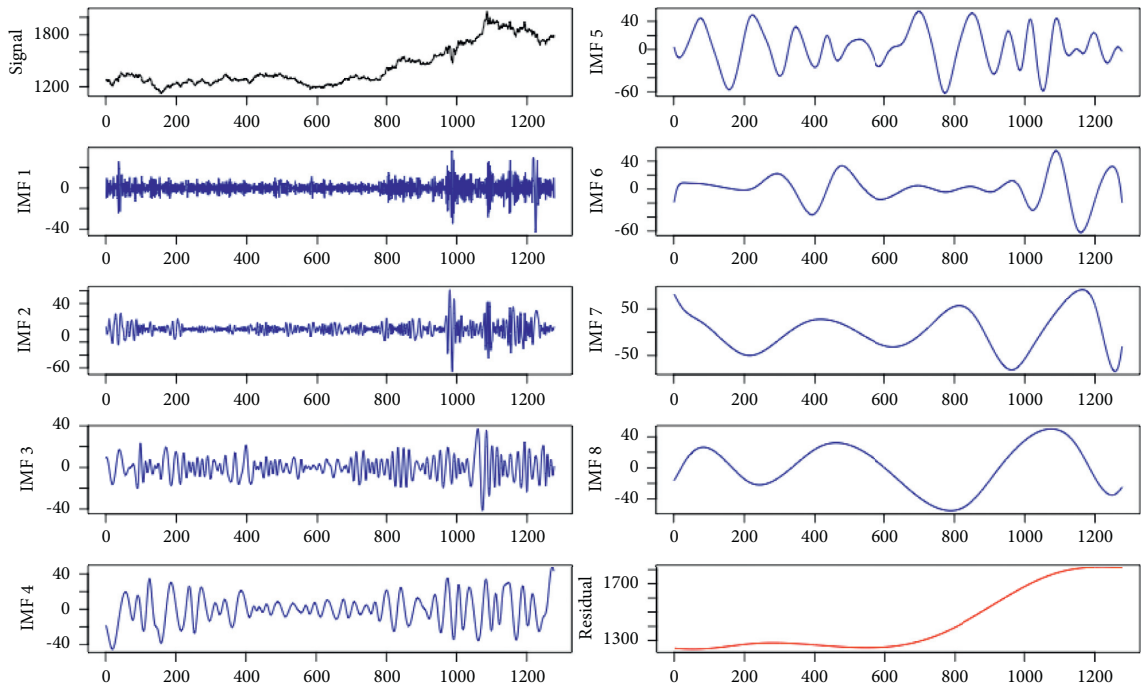

Figure 18: Empirical mode decomposition (EMD) curves for the daily gold price series (2008–2019).

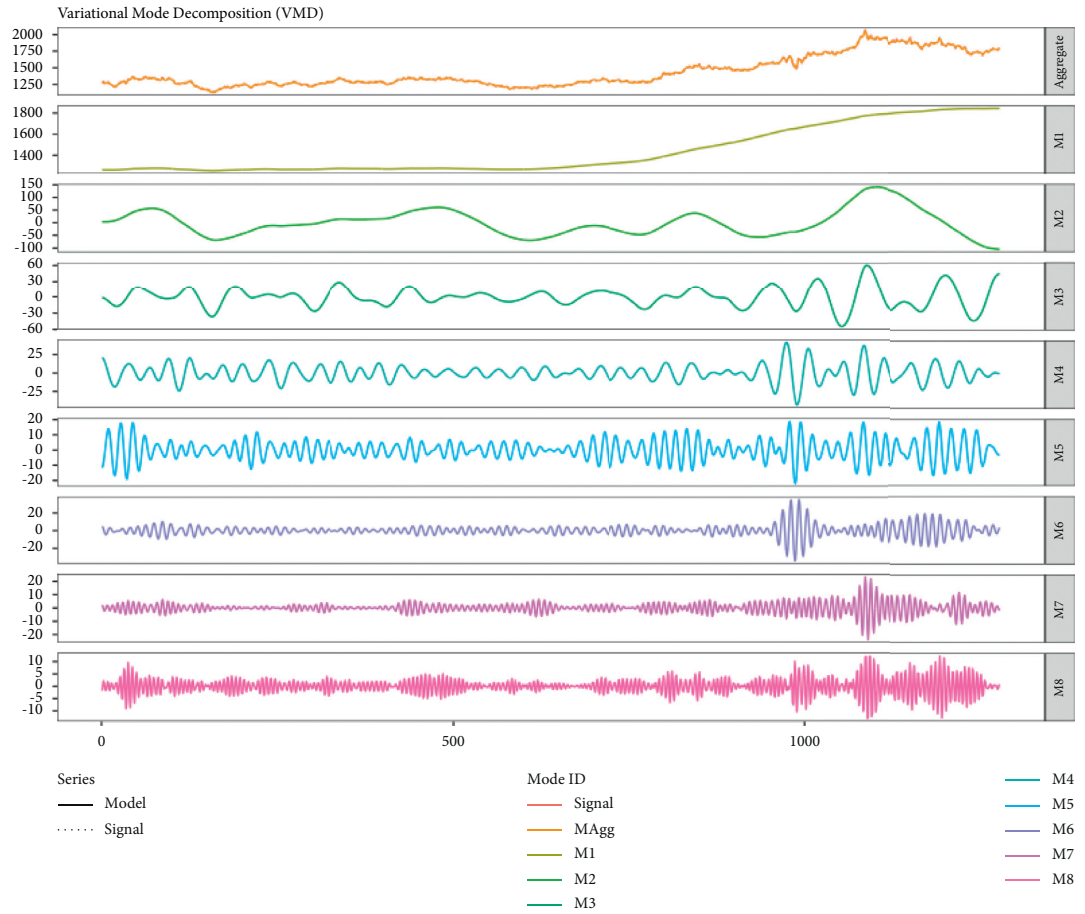

Figure 19: Variational mode decomposition (VMD) curves for the daily gold price series (May 2016–April 2021).

Table 10: Measures of IMFs and residue derived through EMD for Bloomberg daily price series of gold (May 2016–April 2021): correlation is significant at the level of 0.05 (2-tailed).

	Mean period	Pearson correlation	Kendall correlation	Spearman correlation	Variance	Variance as of observed (%)	Variance as % of IMFs + residual
Observed	1.912				54236.22		
IMF1	1.561	0.032	0.035	0.048	52.556	0.097	0.792
IMF2	3.966	0.070	0.041	0.060	108.516	0.200	1.636
IMF3	8.513	0.057	0.052	0.072	101.769	0.188	1.534
IMF4	19.060	0.158	0.125	0.173	267.592	0.493	4.034
IMF5	47.296	0.092	0.127	0.182	736.343	1.358	11.101
IMF6	79.813	−0.030	0.087	0.113	387.337	0.714	5.834
IMF7	182.429	0.249	0.239	0.310	1794.455	3.309	27.053
IMF8	212.833	0.285	0.186	0.259	876.000	1.615	13.206
Residue	319.250	0.962	0.559	0.743	2308.628	4.257	34.804
Sum						12.231	100.00

Table 11: Measures of modes and residue derived through VMD for Bloomberg daily price series of gold (May 2016–April 2019): correlation is significant at the level of 0.05 (2-tailed).

	Mean period	Pearson correlation	Kendall correlation	Spearman correlation	Variance	Variance as of observed (%)	Variance as % of ∑ IMFs + residual
Observed	1.912				54236.22		
M1	18.779	0.966	0.731	0.902	45806.270	84.457	93.458
M2	44.034	0.417	0.327	0.427	2656.298	4.898	5.420
M3	29.698	0.142	0.123	0.152	322.526	0.595	0.658
M4	15.202	0.075	0.080	0.113	122.172	0.225	0.249
M5	8.457	0.059	0.038	0.054	43.413	0.080	0.089
M6	5.626	0.047	0.040	0.051	37.134	0.068	0.076
M7	3.917	0.029	0.025	0.033	15.249	0.028	0.031
M8	2.929	0.024	0.021	0.029	9.602	0.018	0.020
Sum						92.196	100.00

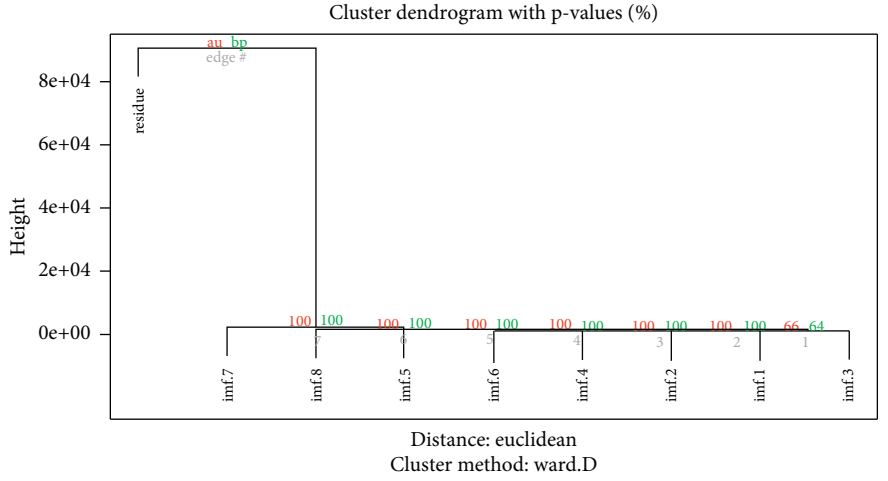

Figure 20: Hierarchical clustering diagram obtained for the IMFs and residue of gold through EMD.

that it is difficult for the market to adjust itself to the effects of these special events. The time frame of the effects of special events was longer, which suggests that most special events have a serious impact on the gold price; hence, intermittent fluctuations in gold prices arise through special events.

5.1.21. Effects of Ordinary Market Disequilibrium. Apart from special events and trends, the price of gold is also influenced by political situations, bad weather conditions, industrial action, and inventory depletion. The combined effects of these conditions are classified as high frequency. The effect has a short-term impact on gold price because the time frames of some of these conditions are very short, which suggest that the market disequilibrium has no serious impact on the price of gold. The disequilibrium of supply-demand as a normal market fluctuation, thus, has no serious impact on the gold price. On the one hand, if these events are

Table 12: Correlation and variance of components for Bloomberg daily data of gold from May 2016–April 2021 derived through EMD: correlation is significant at 0.05 level (2-tailed).

	Mean period	Pearson correlation	Kendall correlation	Spearman correlation	Variance	Variance as of observed (%)	Variance as % of ∑ IMFs + residual
Observed	1.912				54236.22		
High frequency	4.080	0.095	0.064	0.089	264.376	0.487	0.520
Low frequency	67.211	0.375	0.334	0.423	3913.372	7.215	7.690
Trend	319.250	0.962	0.559	0.743	46709.450	86.122	91.790
Sum						93.824	100

Table 13: Correlation and variance of constituents for daily series of gold (May 2016–April 2021) derived through VMD: correlation is significant at 0.05 level (2-tailed).

	Mean period	Pearson correlation	Kendall correlation	Spearman correlation	Variance	Variance as of observed (%)	Variance as % of ∑ Ms + residual
Observed	1.912				54236.22		
High frequency	5.149	0.161	0.165	0.217	649.378	1.197	1.322
Low frequency	44.034	0.417	0.327	0.427	2656.298	4.898	5.409
Trend	18.779	0.966	0.731	0.902	45806.270	84.457	93.269
Sum						90.552	100.00

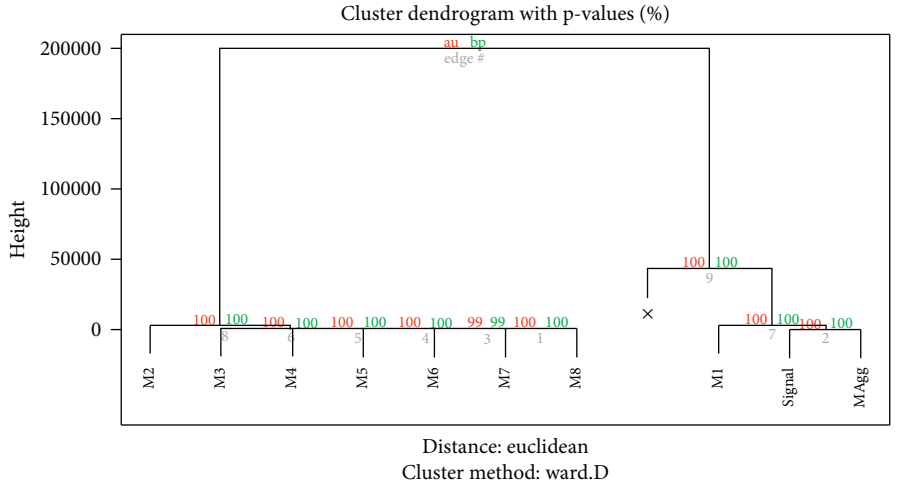

Figure 21: Hierarchical clustering diagram obtained for the modes and residue through VMD.

not checked for a long period, they become one of the major drivers for increasing gold prices. In long-range trend forecasting, the ordinary market fluctuations can be set aside, but crucial for short period prediction.

In a nutshell, gold price composes of the trend (which contributes most of gold price variations in the long period), the special events (which were the leading causes of sporadic price increases of gold in the medium term), and the ordinary market fluxes (with short-lived effects on the gold price). Using the VMD approach, the price of $1254.23 per ounce during April 2021 can be analyzed as a trend price of $1169.81, a special event price of $67.84, and a normal market fluctuation $16.58, as shown in Figure 23.

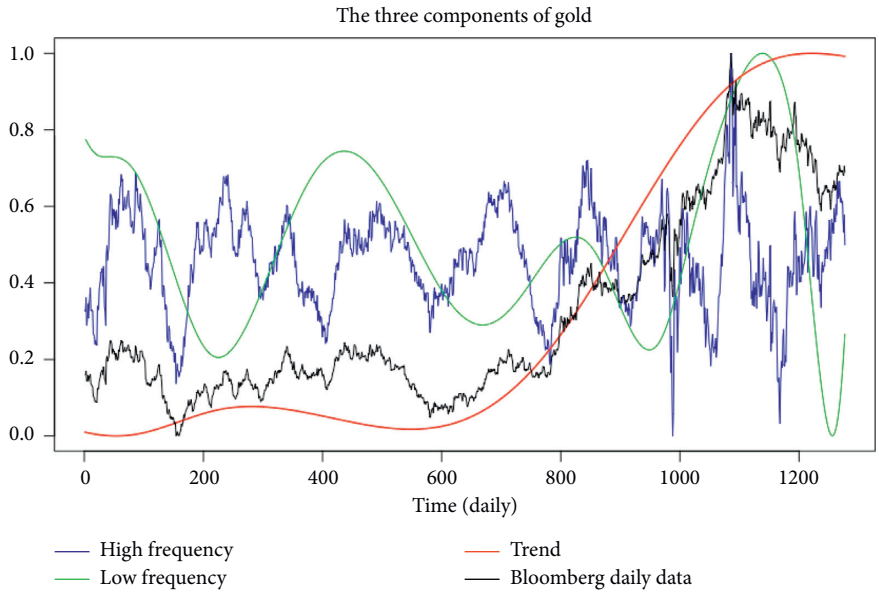

Figure 22: The three components of the Bloomberg daily data (May 2016–April 2021) through EMD.

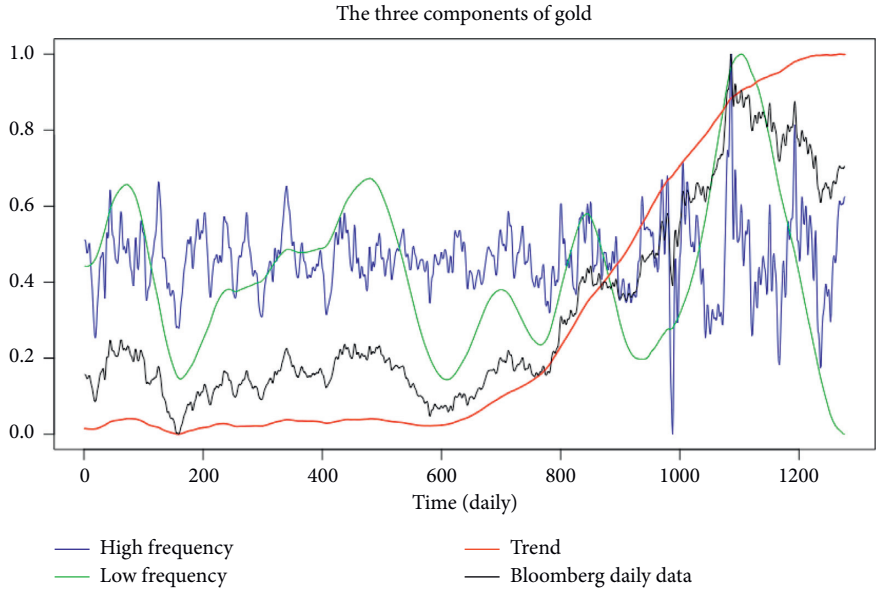

Figure 23: The three components of the Bloomberg daily data (May 2016–April 2021) through VMD.

6. Conclusion

A new model is proposed to study the underlying factors that causes crude oil, corn, and gold markets price fluctuations based on EMD and VMD techniques. EMD and VMD methods are used to decompose daily closing prices of corn, crude, and gold obtained from Bloomberg Commodity Index from May 2016 to April 2021 into their respective IMFs or modes and a residue to determine the components that derived commodity futures market prices.

Using the Pearson product-moment correlation coefficient, Kendall rank correlation, and Spearman rank correlation as statistical measures enabled us to evaluate each IMF's effects or mode on the commodity futures prices. Subsequently, we used hierarchical clustering and the Euclidean distance approach to classify the IMFs, residue, and modes into high frequency, low frequency, and trend components, with the trend and low-frequency components being the main drivers of commodity futures prices. The three commodities' prices could be analyzed as a combination of long-term trend, special events, and near term fluctuations resulting from usual market activities, such as imbalance of supply-demand. In general, the three commodities prices are driven by trends and special events. The effects from the trend deviates gradually and changes around the long-term mean. The unpredictable special events are responsible for irregular commodity price movements, and the effect could last for several years; this shows that the

short-term commodity price changes are mainly triggered by normal market activities, and the effects have a very short duration; hence, their impact on commodity price is not serious.

Essentially, in using the decomposition approach in analyzing components of commodity prices' data series explicitly, several forecasting techniques can be considered: firstly, depending on the characteristics of each IMF or mode, an appropriate forecasting method can be chosen to predict every IMF or mode; for instance, a polynomial function can be used to estimate the residue and Fourier analysis to predict low-frequency IMFs' modes, using a nonlinear method to stimulate high-frequency IMFs or modes and summing them up to obtain the final results. Secondly, the IMFs or modes can be categorized as linear and nonlinear components which can be forecasted separately and then integrating the individual parts to obtain the final predicted results; for instance, the trend can be dealt with using curve fitting, using nonlinear forecasting techniques such as the backpropagation neural network to forecast short-term fluctuations. Special events are difficult to predict since they are influenced by several elements, such as trade wars, outbreak of pandemic, atmospheric conditions, financial policies, and many other sophisticated factors.

Finally, we suggest that a new framework or integrated forecasting method should be developed to handle special events' effects on prices since no one knows when and where they will happen.

Data Availability

Data can be found at http://www.bloomberg.com.

Additional Points

Highlights. (i) We investigate futures prices of the following commodities: crude oil, corn, and gold. (ii) We propose a novel price determinant for these commodities: crude oil, corn, and gold. (iii) Empirical mode decomposition and variational mode decomposition are used to decompose crude oil, corn, and gold prices into different components. (iv) We examine the effects of each component on the market price fluctuations. (v) We indicate that empirical mode decomposition and variational mode decomposition can bring out the underlying factors of commodity market price volatility.

Conflicts of Interest

The authors declare that they have no conflicts of interest.

References

[1] D. Zhang, G. Zang, J. Li, K. Ma, and H. Liu, "Prediction of soybean price in China using QR-RBF neural network model," *Computers and Electronics in Agriculture*, vol. 154, pp. 10–17, 2018.

[2] W. Wang and L. Wei, "Impacts of agricultural price support policy on price variability and welfare: evidence from China's soybean market," *Agricultural Economics*, vol. 52, no. 1, pp. 3–17, 2021.

[3] L. Zhao, X. Zhang, S. Wang, and S. Xu, "The effects of oil price shocks on output and inflation in China," *Energy Economics*, vol. 53, pp. 101–110, 2016.

[4] H. F. Zou, G. P. Xia, F. T. Yang, and H. Y. Wang, "An investigation and comparison of artificial neural network and time series models for Chinese food grain price forecasting," *Neurocomputing*, vol. 70, no. 16–18, pp. 2913–292, 2007.

[5] Q. Zhu, F. Zhang, S. Liu, Y. Wu, and L. Wang, "A hybrid VMD-BiGRU model for rubber futures time series forecasting," *Applied Soft Computing*, vol. 84, Article ID 105739, 2019.

[6] T. Jin, H. Ding, B. Li, H. Xia, and C. Xue, "Valuation of interest rate ceiling and floor based on the uncertain fractional differential equation in Caputo sense," *Journal of Intelligent & Fuzzy Systems*, vol. 40, no. 3, pp. 5197–5206, 2021.

[7] P. Sadorsky, "Time-varying risk premiums in petroleum futures prices," *Energy Economics*, vol. 24, no. 6, pp. 539–556, 2002.

[8] C. Morana, "A semiparametric approach to short-term oil price forecasting," *Energy Economics*, vol. 23, no. 3, pp. 325–338, 2001.

[9] S. Mirmirani and H. C. Li, "A comparison of VAR and neural networks with genetic algorithm in forecasting price of oil," *Advances in Econometrics*, vol. 19, pp. 203–223, 2004.

[10] R. Bacon, "Modelling the price of oil," *Oxford Review of Economic Policy*, vol. 7, no. 2, pp. 17–34, 1991.

[11] S. Dées, P. Karadeloglou, R. K. Kaufmann, and M. Sánchez, "Modelling the world oil market: assessment of a quarterly econometric model," *Energy Policy*, vol. 35, no. 1, pp. 178–191, 2007.

[12] B. Zhu, P. Wang, J. Chevallier, and Y. Wei, "Carbon price analysis using empirical mode decomposition," *Computational Economics*, vol. 45, no. 2, pp. 195–206, 2015.

[13] D. Wang, C. Yue, S. Wei, and J. Lv, "Performance analysis of four decomposition-ensemble models for one-day-ahead agricultural commodity futures price forecasting," *Algorithms*, vol. 10, no. 3, p. 108, 2017.

[14] H. Miao, S. Ramchander, T. Wang, and D. Yang, "Influential factors in crude oil price forecasting," *Energy Economics*, vol. 68, pp. 77–88, 2017.

[15] H. Boubaker and S. A. Raza, "A wavelet analysis of mean and volatility spillovers between oil and BRICS stock markets," *Energy Economics*, vol. 64, pp. 105–117, 2017.

[16] J. Wang and X. Li, "A combined neural network model for commodity price forecasting with SSA," *Soft Computing*, vol. 22, no. 16, pp. 5323–5333, 2018.

[17] N. E. Huang, Z. Shen, S. R. Long et al., "The empirical mode decomposition and the Hilbert spectrum for nonlinear and non-stationary time series analysis," *Proceedings of the Royal Society of London. Series A: Mathematical, Physical and Engineering Sciences*, vol. 454, no. 1971, pp. 903–995, 1998.

[18] K. Dragomiretskiy and D. Zosso, "Variational mode decomposition," *IEEE Transactions on Signal Processing*, vol. 62, no. 3, pp. 531–544, 2014.

[19] S. Abadan and A. Shabri, "Hybrid empirical mode decomposition-ARIMA for forecasting price of rice," *Applied Mathematical Sciences*, vol. 8, no. 63, pp. 3133–3143, 2014.

[20] T. Xiong, C. Li, Y. Bao, Z. Hu, and L. Zhang, "A combination method for interval forecasting of agricultural commodity

futures prices," *Knowledge-Based Systems*, vol. 77, pp. 92–102, 2015.

[21] N. An, W. Zhao, J. Wang, D. Shang, and E. Zhao, "Using multi-output feedforward neural network with empirical mode decomposition based signal filtering for electricity demand forecasting," *Energy*, vol. 49, pp. 279–288, 2013.

[22] L. Crosato, L. Grossi, and F. Nan, "Forecasting the volatility of electricity prices by robust estimation: an application to the Italian market," in *Mathematical and Statistical Methods for Actuarial Sciences and Finance*, pp. 279–283, Springer, Cham, Switzerland, 2018.

[23] C.-S. Lin, S.-H. Chiu, and T.-Y. Lin, "Empirical mode decomposition-based least squares support vector regression for foreign exchange rate forecasting," *Economic Modelling*, vol. 29, no. 6, pp. 2583–2590, 2012.

[24] B. Premanode and C. Toumazou, "Improving prediction of exchange rates using differential EMD," *Expert Systems with Applications*, vol. 40, no. 1, pp. 377–384, 2013.

[25] V. Plakandaras, T. Papadimitriou, and P. Gogas, "Forecasting daily and monthly exchange rates with machine learning techniques," *Journal of Forecasting*, vol. 34, no. 7, pp. 560–573, 2015.

[26] Y. Jian-Hui and D. Wei, "Prediction of gold price based on WT-SVR and EMD-SVR model," in *Proceedings of the 2012 8th International Conference on Computational Intelligence and Security*, Guangzhou, China, 2012.

[27] Q. Hua and T. Jiang, "The prediction for London gold price: improved empirical mode decomposition," *Applied Economics Letters*, vol. 22, no. 17, pp. 1404–1408, 2015.

[28] P. Owusu Junior, A. M. Adam, and G. Tweneboah, "Connectedness of cryptocurrencies and gold returns: evidence from frequency-dependent quantile regressions," *Cogent Economics & Finance*, vol. 8, no. 1, Article ID 1804037, 2020.

[29] J. Meng, H. Nie, B. Mo, and Y. Jiang, "Risk spillover effects from global crude oil market to China's commodity sectors," *Energy*, vol. 202, Article ID 117208, 2020.

[30] H. Chen, H. Liao, B.-J. Tang, and Y.-M. Wei, "Impacts of OPEC's political risk on the international crude oil prices: an empirical analysis based on the SVAR models," *Energy Economics*, vol. 57, pp. 42–49, 2016.

[31] L. Yu, S. Wang, and K. K. Lai, "Forecasting crude oil price with an EMD-based neural network ensemble learning paradigm," *Energy Economics*, vol. 30, no. 5, pp. 2623–2635, 2008.

[32] X. Zhang, K. K. Lai, and S.-Y. Wang, "A new approach for crude oil price analysis based on empirical mode decomposition," *Energy Economics*, vol. 30, no. 3, pp. 905–918, 2008.

[33] Z. Wu and N. E. Huang, "Ensemble empirical mode decomposition: a noise-assisted data analysis method," *Advances in Adaptive Data Analysis*, vol. 1, no. 1, pp. 1–41, 2009.

[34] V. Korotin, M. Dolgonosov, V. Popov, O. Korotina, and I. Korolkova, "The Ukrainian crisis, economic sanctions, oil shock and commodity currency: analysis based on EMD approach," *Research in International Business and Finance*, vol. 48, pp. 156–168, 2019.

[35] Y. Zhu, D. Xu, J. Cheng, and S. H. Ali, "Estimating the impact of China's export policy on tin prices: a mode decomposition counterfactual analysis method," *Resources Policy*, vol. 59, pp. 250–264, 2018.

[36] B. Zhu, L. Huang, L. Yuan, S. Ye, and P. Wang, "Exploring the risk spillover effects between carbon market and electricity market: a bidimensional empirical mode decomposition based conditional value at risk approach," *International Review of Economics & Finance*, vol. 67, pp. 163–175, 2020.

[37] S. Lahmiri, "A variational mode decomposition approach for analysis and forecasting of economic and financial time series," *Expert Systems with Applications*, vol. 55, pp. 268–273, 2016.

[38] C. Aneesh, S. Kumar, P. M. Hisham, and K. P. Soman, "Performance comparison of variational mode decomposition over empirical wavelet transform for the classification of power quality disturbances using support vector machine," *Procedia Computer Science*, vol. 46, pp. 372–380, 2015.

[39] Y. Seo, S. Kim, and V. Singh, "Machine learning models coupled with variational mode decomposition: a new approach for modeling daily rainfall-runoff," *Atmosphere*, vol. 9, no. 7, p. 251, 2018.

[40] H. Niu, K. Xu, and W. Wang, "A hybrid stock price index forecasting model based on variational mode decomposition and LSTM network," *Applied Intelligence*, vol. 50, no. 12, pp. 4296–4309, 2020.

[41] Y. Huang and Y. Deng, "A new crude oil price forecasting model based on variational mode decomposition," *Knowledge-Based Systems*, vol. 213, Article ID 106669, 2021.

[42] E. Jianwei, J. Ye, and H. Jin, "A novel hybrid model on the prediction of time series and its application for the gold price analysis and forecasting," *Physica A: Statistical Mechanics and Its Applications*, vol. 527, Article ID 121454, 2019.

[43] K. He, G. K. F. Tso, Y. Zou, and J. Liu, "Crude oil risk forecasting: new evidence from multiscale analysis approach," *Energy Economics*, vol. 76, pp. 574–583, 2018.

[44] I. Daubechies, *Ten Lectures on Wavelets*, Society for Industrial and Applied Mathematics, Philadelphia, PA, USA, 1992.

[45] N. Pustelnik, P. Borgnat, and P. Flandrin, "Empirical mode decomposition revisited by multicomponent non-smooth convex optimization," *Signal Processing*, vol. 102, pp. 313–331, 2014.

[46] I. Daubechies, J. Lu, and H.-T. Wu, "Synchrosqueezed wavelet transforms: an empirical mode decomposition-like tool," *Applied and Computational Harmonic Analysis*, vol. 30, no. 2, pp. 243–261, 2011.

[47] J. Gilles, "Empirical wavelet transform," *IEEE Transactions on Signal Processing*, vol. 61, no. 16, pp. 3999–4010, 2013.

[48] M. C. Peel, G. E. Amirthanathan, G. G. S. Pegram, T. A. McMahon, and F. H. S. Chiew, "Issues with the application of empirical mode decomposition," in *Proceedings of the 2005 International Congress on Modelling and Simulation*, Melbourne, Australia, 2005.

Hindawi
Mathematical Problems in Engineering
Volume 2021, Article ID 5462965, 14 pages
https://doi.org/10.1155/2021/5462965

Research Article

Wavelet Analysis of Red Noise and Its Application in Climate Diagnosis

Zhihua Zhang

Climate Modeling Laboratory, School of Mathematics, Shandong University, Jinan 250100, China

Correspondence should be addressed to Zhihua Zhang; zhangzhihua@sdu.edu.cn

Received 21 May 2021; Revised 19 July 2021; Accepted 4 September 2021; Published 27 September 2021

Academic Editor: Neggaz Nabil

Signals are often destroyed by various kinds of noises. A common way to statistically assess the significance of a broad spectral peak in signals and the synchronization between signals is to compare with simple noise processes. At present, wavelet analysis of red noise is studied limitedly and there is no general formula on the distribution of the wavelet power spectrum of red noise. Moreover, the distribution of the wavelet phase of red noise is also unknown. In this paper, for any given real/analytic wavelet, we will use a rigorous statistical framework to obtain the distribution of the wavelet power spectrum and wavelet phase of red noise and apply these formulas in climate diagnosis.

1. Introduction

Signals are often destroyed by various kinds of noises during the process of generation, transportation, and processing [1, 2]. A common way to statistically assess the significance of a broad Fourier/wavelet spectral peak in signals [3, 4] and the synchronization between signals is to compare with a white/red noise process [4, 5]. White noise has zero mean, has constant variance, and is uncorrelated in time. As its name suggests, white noise has a power spectrum which is uniformly spread across all allowable frequencies. Different from white noise, red noise has a power spectrum weighted toward low frequencies and is serially correlated in time. Red noise can describe climatic background noise with relatively enhanced low-frequency fluctuations arising from the interaction of white noise forcing with the slow-response components in the earth system (e.g., the thermal inertia of the oceans provides memory, effectively integrating atmospheric "weather" forcing [6]). In practice, the red noise model has always provided a reasonable description of the noise spectra for a variety of climatic and hydrological time series [5–9]. The red noise is also an important noise model in outputs of the feedback system [4], the neural network coupled with genetic algorithm [10], the optimization system in random scenarios [11, 12], and the big data processing system [5, 13].

Wavelet analysis is a very popular analysis tool for a wide range of applications, including time-frequency analysis, feature extraction, statistical estimation, and denoising. A wavelet is a waveform-like function which has zero mean and is localized in both time and frequency space. The wavelet transform is the set of inner products of all dilated and translated wavelets with a signal; in detail, the wavelet transform of a discrete signal $X = \{x_k\}_{k=0,\ldots,N-1}$ with time step δt is defined as follows [14, 15]:

$$W_n(s) = \sum_{m=0}^{N-1} x_m \overline{\psi}\left(\frac{(m-n)\delta t}{s}\right), \tag{1}$$

where $\overline{\psi}$ is the conjugate of ψ. $|W_n(s)|^2$ is called the wavelet power spectrum, and $\mathrm{Arg}(W_n(s))$ is called the wavelet phase. Due to time and frequency localization of the wavelet, the wavelet transform can extract localized intermittent periodicity of any signal very well.

Wavelet analysis of white noise has been widely studied (e.g., [16–19]), while wavelet analysis of red noise is studied limitedly, only using some specific wavelets (Morlet/Paul/DOG wavelets [15] and modulated Haar wavelet [20]). Since 1980s, a large family of wavelets with nice properties has been constructed [14]. However, there is no general formula on the distribution of the wavelet power spectrum of red noise. On the other hand, the wavelet phase can be used to test the

synchronization between signals, but the distribution of the wavelet phase of red noise is also unknown. In this paper, for any given real/analytic wavelet, we will use a rigorous statistical framework to derive a general formula for the distribution of the wavelet power spectrum and wavelet phase of red noise.

2. Background

The simplest red noise model is the lag-1 autoregressive (AR (1)) red noise process [1, 4–6, 15]: Let $X = \{x_k\}_{k=0,1,\ldots,N-1}$ with time step δt be an AR (1) red noise with parameters $\lambda\,(0 \le \lambda < 1)$ and σ^2; then,

$$\begin{aligned} x_0 &= 0, \\ x_k &= \lambda x_{k-1} + Z_k, \quad k \in \mathbb{Z}_+, \end{aligned} \tag{2}$$

where $\{Z_k\}_{k\in\mathbb{Z}_+}$ is a Gaussian white noise with mean 0 and variance σ^2 and $E[Z_k Z_l] = 0\,(k \ne l)$. The discrete Fourier transform of an AR (1) red noise is

$$\widehat{x}_k = \frac{1}{N}\sum_{n=0}^{N-1} x_n e^{-in\theta_k}, \quad k = 0, 1, \ldots, N-1, \tag{3}$$

where $\theta_k = (2\pi k/N)$. Again, by equation (1), the wavelet transform of an AR (1) red noise can be expressed as [15]

$$W_n(s) = \sum_{k=0}^{N-1} \widehat{x}_k \overline{\widehat{\psi}}(s\omega_k) e^{in\theta_k}, \tag{4}$$

where $\omega_k = (\theta_k/\delta t), k \le (N/2)$, and $\omega_k = -(\theta_{N-k}/\delta t), k > (N/2)$ (here, we have fixed some typos according to Torrence and Compo's Matlab codes [15]).

Torrence and Compo [15] gave an empirical distribution of the Morlet wavelet power spectrum of an AR (1) red noise:

$$|W_n(s)|^2 \text{ is distributed as } \frac{\left(1-\lambda^2\right)\widetilde{\sigma}^2}{2\left(1-2\lambda\cos\left(2\pi k/N\right)+\lambda^2\right)}\chi_2^2, \tag{5}$$

where χ_2^2 is the chi-square distribution with two degrees of freedom and $\widetilde{\sigma}^2$ is the variance of the AR (1) red noise $(\widetilde{\sigma}^2 \approx \sigma^2/(1-\lambda^2))$. For Paul/DOG wavelet power spectrum of an AR (1) red noise, Torrence and Compo [15] empirically gave the following:

$$|W_n(s)|^2 \text{ is distributed as } \frac{\left(1-\lambda^2\right)\widetilde{\sigma}^2}{1-2\lambda\cos\left(2\pi k/N\right)+\lambda^2}\chi_1^2. \tag{6}$$

Formulas (5) and (6) are empirically obtained by assuming that "the wavelet spectrum of a red noise is distributed as its Fourier spectrum" [15].

Zhang and Jorgensen [20] showed that under the rigorous statistical framework, the modulated Haar wavelet power spectra of AR (1) red noise is distributed as

$$\frac{2\sigma^2}{s\left(1-\alpha^2\right)}\left(\sigma_R^2\chi_1^2 + \sigma_I^2\chi_2^2\right), \tag{7}$$

where χ_1 and χ_2 are two independent standard Gaussian distributions. Also, $P_k(\lambda) = (1-\lambda^2)/(1-2\lambda\cos(4k\pi/s)+\lambda^2)$ and

$$\begin{aligned} \sigma_R^2 &= \frac{s}{2}P_k(\lambda) + \frac{4\lambda\left(1-\lambda^{(s/2)}\right)}{\left(1-\lambda^2\right)}\left(\lambda-\cos\frac{4k\pi}{s}\right)\left(1-\lambda\cos\frac{2k\pi}{s^*}\right)P_k^2(\lambda) - \frac{2\lambda^2\left(1-\lambda^{s/2}\right)^2}{\left(1-\lambda^2\right)}\left(\lambda-\cos\frac{4k\pi}{s}\right)^2 P_k^2(\lambda), \\ \sigma_I^2 &= \frac{s}{2}P_k(\lambda) + P_k^2(\lambda)\frac{4\lambda^2\left(1-\lambda^{s/2}\right)}{\left(1-\lambda^2\right)^2}\sin^2\frac{4k\pi}{s} - P_k^2(\lambda)\frac{2\lambda^2\left(1-\lambda^{s/2}\right)^2}{\left(1-\lambda^2\right)^2}\sin^2\frac{4k\pi}{s}. \end{aligned} \tag{8}$$

Until now, wavelet analysis of red noise is studied limitedly, only using some specific wavelets. There is no general formula on the distribution of the wavelet power spectrum and wavelet phase of an AR (1) red noise.

3. Main Results

We will use a rigorous statistical framework to establish the distribution of the wavelet power spectrum and wavelet phase of an AR (1) red noise with time step δt, length N, and parameters λ and σ^2. Here, we assume a very weak condition: $\lambda^N \approx 0$ and $(1/N^2) \approx 0$. In practice, all climatic background noises satisfy this condition, e.g., if $\lambda = 0.5$ and $N = 50$, then $\lambda^N \approx 10^{-8}$ and $(1/N^2) = 0.0004$.

A wavelet is real if it is a real-valued function. All of spline wavelets and most of compactly supported wavelets are real wavelets.

Theorem 1. *For any real wavelet, the wavelet power spectrum $|W_n(s)|^2$ of an AR (1) red noise is distributed as*

$$\left(\frac{2\sigma^2}{N}\sum_{k=0}^{[N/2]}\frac{\left|\widehat{\psi}(s\omega_k)\right|^2}{1-2\lambda\cos\,\theta_k+\lambda^2}\right)\chi_1^2. \tag{9}$$

A wavelet ψ is said to be analytic if its Fourier transform satisfies $\widehat{\psi}(\omega) = 0, \omega < 0$. Different from real wavelets, analytic wavelets can extract not only spectral information but also phase information from any given signal.

Theorem 2. *For any analytic wavelet, the wavelet power spectrum of an AR (1) red noise is distributed as*

$$\left(\frac{\sigma^2}{2N}\sum_{k=0}^{[N/2]}\frac{\left|\widehat{\psi}(s\omega_k)\right|^2}{1-2\lambda\cos\,\theta_k+\lambda^2}\right)\chi_2^2. \tag{10}$$

Theorem 3. *For any analytic wavelet, the wavelet phase of an AR (1) red noise is distributed uniformly on* $[0, 2\pi]$.

4. Proofs

The AR (1) red noise with parameters λ, $|\lambda| < 1$ and σ^2 can be expressed as

$$x_k = \sum_{\nu=1}^{k} \lambda^{k-\nu} Z_\nu, \quad k \in \mathbb{Z}_+. \tag{11}$$

By $E[Z_\nu] = 0$,

$$E[x_k] = \sum_{\nu=1}^{k} \lambda^{k-\nu} E[Z_\nu] = 0, \tag{12}$$

and so the real part of the wavelet transform is

$$\mathrm{Re}(W_n(s)) = \sum_{m=0}^{N-1} x_m \mathrm{Re}\left(\psi\left(\frac{(m-n)\delta t}{s}\right)\right). \tag{13}$$

Since $\mathrm{Re}(W_n(s))$ is a linear combination of $\{x_m\}$, $\mathrm{Re}(W_n(s))$ is a Gaussian random variable and

$$\begin{aligned} &E[\mathrm{Re}(W_n(s))] = 0, \\ &\mathrm{Var}(\mathrm{Re}(W_n(s))) = E\left[(\mathrm{Re}(W_n(s)))^2\right]. \end{aligned} \tag{14}$$

Similarly, $\mathrm{Im}(W_n(s))$ is a Gaussian random variable and

$$\begin{aligned} &E[\mathrm{Im}(W_n(s))] = 0, \\ &\mathrm{Var}(\mathrm{Im}(W_n(s))) = E\left[(\mathrm{Im}(W_n(s)))^2\right]. \end{aligned} \tag{15}$$

Denote $\mathrm{Arg}(\overline{\widehat{\psi}}(s\omega_k)) = \varphi_k$. Then, $\overline{\widehat{\psi}}(s\omega_k)e^{in\theta_k} = |\widehat{\psi}(s\omega_k)|e^{i\eta_{n,k}}$, where $\eta_{n,k} = \varphi_k + n\theta_k$. By equation (4), we have

$$\begin{aligned} \mathrm{Re}(W_n(s)) &= \sum_{k=0}^{N-1} \left|\widehat{\psi}(s\omega_k)\right| \mathrm{Re}\left(\widehat{x}_k e^{i\eta_{n,k}}\right) = \sum_{k=0}^{N-1} \left|\widehat{\psi}(s\omega_k)\right| \left(\mathrm{Re}(\widehat{x}_k)\cos\eta_{n,k} - \mathrm{Im}(\widehat{x}_k)\sin\eta_{n,k}\right), \\ \mathrm{Im}(W_n(s)) &= \sum_{k=0}^{N-1} \left|\widehat{\psi}(s\omega_k)\right| \left(\mathrm{Re}(\widehat{x}_k)\sin\eta_{n,k} + \mathrm{Im}(\widehat{x}_k)\cos\eta_{n,k}\right). \end{aligned} \tag{16}$$

Let

$$\begin{aligned} \alpha_{k,j} &= E\left[\mathrm{Re}(\widehat{x}_k)\mathrm{Re}\left(\widehat{x}_j\right)\right], \\ \beta_{k,j} &= E\left[\mathrm{Re}(\widehat{x}_k)\mathrm{Im}\left(\widehat{x}_j\right)\right], \\ \gamma_{k,j} &= E\left[\mathrm{Im}(\widehat{x}_k)\mathrm{Im}\left(\widehat{x}_j\right)\right]. \end{aligned} \tag{17}$$

Then, the variances of $\mathrm{Re}(W_n(s))$ and $\mathrm{Im}(W_n(s))$ and their correlation are

$$\begin{aligned} &\mathrm{Var}(\mathrm{Re}(W_n(s))) \\ &= \sum_{k,j=0}^{N-1} \left|\widehat{\psi}(s\omega_j)\widehat{\psi}(s\omega_j)\right| \left(\alpha_{k,j}\cos\eta_{n,k}\cos\eta_{n,j} - \beta_{k,j}\sin\eta_{n,k}\cos\eta_{n,j} - \beta_{j,k}\cos\eta_{n,k}\sin\eta_{n,j} + \gamma_{k,j}\sin\eta_{n,k}\sin\eta_{n,j}\right), \\ &\mathrm{Var}(\mathrm{Im}(W_n(s))) \\ &= \sum_{k,j=0}^{N-1} \left|\widehat{\psi}(s\omega_j)\widehat{\psi}(s\omega_j)\right| \left(\alpha_{k,j}\sin\eta_{n,k}\sin\eta_{n,j} + \beta_{k,j}\cos\eta_{n,k}\sin\eta_{n,j} + \beta_{j,k}\sin\eta_{n,k}\sin\eta_{n,j} + \gamma_{k,j}\cos\eta_{n,k}\cos\eta_{n,j}\right), \\ &E[\mathrm{Re}(W_n(s))\mathrm{Im}(W_n(s))] \\ &= \sum_{k,j=0}^{N-1} \left|\widehat{\psi}(s\omega_k)\widehat{\psi}(s\omega_j)\right| \left(\alpha_{k,j}\cos\eta_{n,k}\sin\eta_{n,j} + \beta_{k,j}\sin\eta_{n,k}\sin\eta_{n,j} - \beta_{j,k}\cos\eta_{n,k}\cos\eta_{n,j} - \gamma_{k,j}\sin\eta_{n,k}\cos\eta_{n,j}\right). \end{aligned} \tag{18}$$

From these, we see that the computations of variances and the correlation of $\mathrm{Re}(W_n(s))$ and $\mathrm{Im}(W_n(s))$ are reduced to the computations of $\alpha_{k,j}$, $\beta_{k,j}$, and $\gamma_{k,j}$.

4.1. Computation of $\alpha_{k,j}$. By equation (3), we have

$$\mathrm{Re}(\widehat{x}_k) = \frac{1}{N} \sum_{n=0}^{N-1} x_n \cos(n\theta_k), \tag{19}$$

where $\theta_k = (2\pi k/N)$. Furthermore,

$$E\left[\mathrm{Re}\left(\widehat{x}_j\right)\mathrm{Re}\left(\widehat{x}_k\right)\right] = \frac{1}{N^2}\sum_{l,p=1}^{N-1} E\left[x_l x_p\right]\cos\left(l\theta_j\right)\cos\left(p\theta_k\right). \tag{20}$$

By equation (11), it follows that

$$x_l x_p = \left(\sum_{\nu=1}^{l}\lambda^{l-\nu}Z_\nu\right)\left(\sum_{m=1}^{p}\lambda^{p-m}Z_m\right) = \sum_{\nu=1}^{l}\sum_{m=1}^{p}\lambda^{l+p-\nu-m}Z_\nu Z_m, \tag{21}$$

where

$$E\left[Z_\nu Z_m\right] = \begin{cases} 0, & nu \neq m, \\ \sigma^2, & nu = m. \end{cases} \tag{22}$$

Hence, we have for $l > p$,

$$E\left[x_l x_p\right] = \sum_{\nu=1}^{p}\sum_{m=1}^{p}\lambda^{l+p-\nu-m}E\left[Z_\nu Z_m\right] = \sigma^2\sum_{\nu=1}^{p}\lambda^{l+p-2\nu} = \sigma^2\frac{\lambda^{l+p}-\lambda^{l-p}}{\lambda^2-1}. \tag{23}$$

Similarly, for $l \le p$,

$$E\left[x_l x_p\right] = \sigma^2\frac{\lambda^{l+p}-\lambda^{p-l}}{\lambda^2-1}. \tag{24}$$

From these, we obtain

$$N^2\left(\frac{\lambda^2-1}{\sigma^2}\right)E\left[\mathrm{Re}\left(\widehat{x}_k\right)\mathrm{Re}\left(\widehat{x}_j\right)\right] = \Sigma_1 + \Sigma_2, \tag{25}$$

where

$$\begin{aligned} \Sigma_1 &= \sum_{l=1}^{N-1}\lambda^l\cos\left(l\theta_j\right)\sum_{p=1}^{l-1}\left(\lambda^p-\lambda^{-p}\right)\cos\left(p\theta_k\right), \\ \Sigma_2 &= \sum_{l=1}^{N-1}\left(\lambda^l-\lambda^{-l}\right)\cos\left(l\theta_j\right)\sum_{p=l}^{N-1}\lambda^p\cos\left(p\theta_k\right). \end{aligned} \tag{26}$$

We first compute Σ_1. By using Euler formula $\cos(p\theta_k) = \mathrm{Re}(e^{ip\theta_k})$, the inner summation becomes

$$\sum_{p=1}^{l-1}\left(\lambda^p-\lambda^{-p}\right)\cos\left(p\theta_k\right) = P_k(\lambda) + \mu_l^1 + \mu_l^2, \tag{27}$$

where $P_k(\lambda) = (1-\lambda^2)/(1-2\lambda\cos\theta_k+\lambda^2)$ and

$$\begin{aligned} \mu_l^1 &= -\frac{\lambda^l}{1-\lambda^2}P_k(\lambda)\left(\cos\left(l\theta_k\right)-\lambda\cos(l-1)\theta_k\right), \\ \mu_l^2 &= \frac{\lambda^{-l+1}}{1-\lambda^2}P_k(\lambda)\left(\lambda\cos\left(l\theta_k\right)-\cos(l-1)\theta_k\right). \end{aligned} \tag{28}$$

From this and equation (25), we obtain

$$\Sigma_1 = P_k(\lambda)\sum_{l=1}^{N-1}\lambda^l\cos\left(l\theta_j\right) + \sum_{l=1}^{N-1}\lambda^l\cos\left(l\theta_j\right)\mu_l^1 + \sum_{l=1}^{N-1}\lambda^l\cos\left(l\theta_j\right)\mu_l^2 =: \Sigma_{11} + \Sigma_{12} + \Sigma_{13}. \tag{29}$$

For Σ_{11}, when $\lambda^N \approx 0$,

$$\Sigma_{11} = P_k(\lambda)\frac{\lambda\cos\theta_j-\lambda^2}{1-2\lambda\cos\theta_j+\lambda^2}. \tag{30}$$

For Σ_{13}, we have

$$\Sigma_{13} = \frac{\lambda^2}{1-2\lambda\cos\theta_k+\lambda^2}\sum_{l=1}^{N-1}\left(\cos\left(l\theta_k\right)-\lambda^{-1}\cos(l-1)\theta_k\right)\cos\left(l\theta_j\right) = \frac{A(\lambda)}{2\left(1-2\lambda\cos\theta_k+\lambda^2\right)}, \tag{31}$$

where

$$A(\lambda) = \lambda^2 \sum_{l=1}^{N-1} \left[\cos\left(l\theta_{k+j}\right) + \cos\left(l\theta_{k-j}\right) - \lambda^{-1}\left(\cos\left(l\theta_{k+j} - \theta_k\right) + \cos\left(l\theta_{k-j} - \theta_k\right)\right)\right]. \tag{32}$$

Noticing that $\theta_k = (2\pi k/N)$, we consider four cases to compute $A(\lambda)$ and then estimate Σ_{13}:

(i) For $k \neq j$ and $k + j \neq N$, by $\theta_k = (2\pi k/N)$ and $\sum_{l=0}^{N-1} \cos(l\theta_k) = \mathrm{Re}(\sum_{l=0}^{N-1} e^{il\theta_k}) = 0$, we have

$$A(\lambda) = -2\lambda^2 + 2\lambda \cos\,\theta_k, \tag{33}$$

and then $\Sigma_{13} = (-\lambda^2 + \lambda \cos\,\theta_k)/(1 - 2\lambda \cos\,\theta_k + \lambda^2)$.

(ii) For $k = j \neq (N/2)$, we obtain

$$A(\lambda) = \lambda^2 \sum_{l=1}^{N-1} \left(\cos(2l\theta_k) + 1 - \lambda^{-1}\left(\cos(2l\theta_k - \theta_k) + \cos\,\theta_k\right)\right), \tag{34}$$

and then

$$A(\lambda) = (N-2)\left(\lambda^2 - \lambda \cos\,\theta_k\right). \tag{35}$$

Therefore,

$$\Sigma_{13} = \frac{(N-2)\left(\lambda^2 - \lambda \cos\,\theta_k\right)}{2\left(1 - 2\lambda \cos\,\theta_k + \lambda^2\right)}. \tag{36}$$

(iii) For $k + j = N$ and $k \neq j$, we obtain

$$A(\lambda) = \lambda^2 \sum_{l=1}^{N-1} \left(1 + \cos\left(l\theta_{k-j}\right) - \lambda^{-1}\left(\cos\,\theta_k + \cos\left(l\theta_{k-j} - \theta_k\right)\right)\right) = (N-2)\left(\lambda^2 - \lambda \cos\,\theta_k\right). \tag{37}$$

Therefore,

$$\Sigma_{13} = \frac{(N-2)\left(\lambda^2 - \lambda \cos\,\theta_k\right)}{2\left(1 - 2\lambda \cos\,\theta_k + \lambda^2\right)}. \tag{38}$$

(iv) For $k = j = (N/2)$, we obtain

$$A(\lambda) = \lambda^2 \sum_{l=1}^{N-1} \left(2 - \frac{2\cos\,\theta_k}{\lambda}\right) = 2(N-1)\left(\lambda^2 - \lambda \cos\,\theta_k\right), \tag{39}$$

and so

$$\Sigma_{13} = \frac{(N-1)\left(\lambda^2 - \lambda \cos\,\theta_k\right)}{1 - 2\lambda \cos\,\theta_k + \lambda^2}. \tag{40}$$

Now, we compute Σ_2 in equation (25). When $\lambda^N \approx 0$, it follows that

$$\sum_{p=l}^{N-1} \lambda^p \cos(p\theta_k) = \frac{\lambda^l \cos(l\theta_k) - \lambda^{l+1} \cos(l-1)\theta_k}{1 - 2\lambda \cos\,\theta_k + \lambda^2}. \tag{41}$$

By equation (25), we obtain

$$\Sigma_2 = \sum_{l=1}^{N-1} \left(\lambda^l - \lambda^{-l}\right) \cos\left(l\theta_j\right) \left(\lambda \frac{\cos(l\theta_k) - \lambda \cos(l-1)\theta_k}{1 - 2\lambda \cos\,\theta_k + \lambda^2}\right) = \Sigma_{21} + \Sigma_{22}, \tag{42}$$

where

$$\begin{aligned} \Sigma_{21} &= \frac{1}{1 - 2\lambda \cos\,\theta_k + \lambda^2} \sum_{l=1}^{N-1} \lambda^{2l} \cos\left(l\theta_j\right) \left(\cos(l\theta_k) - \lambda \cos(l-1)\theta_k\right), \\ \Sigma_{22} &= -\frac{1}{1 - 2\lambda \cos\,\theta_k + \lambda^2} \sum_{l=1}^{N-1} \cos\left(l\theta_j\right) \left(\cos(l\theta_k) - \lambda \cos(l-1)\theta_k\right). \end{aligned} \tag{43}$$

Furthermore,

$$\Sigma_{22} = -\frac{1}{2\left(1 - 2\lambda\cos\ \theta_k + \lambda^2\right)} \sum_{l=1}^{N-1} \left(\left(\cos\left(l\theta_{k+j}\right) + \cos\left(l\theta_{k-j}\right)\right) - \lambda\left(\cos\left(l\theta_{k+j} - \theta_k\right) + \cos\left(l\theta_{k-j} - \theta_k\right)\right)\right). \tag{44}$$

Similar to the estimation process of Σ_{13}, we have

$$\begin{aligned}
\Sigma_{22} &= \frac{2 - 2\lambda\cos\ \theta_k}{2\left(1 - 2\lambda\cos\ \theta_k + \lambda^2\right)}, \quad k \neq j\ \&, k + j \neq N, \\
\Sigma_{22} &= -\frac{(N-2)\left(1 - \lambda\cos\ \theta_k\right)}{2\left(1 - 2\lambda\cos\ \theta_k + \lambda^2\right)}, \quad k = j \neq \frac{N}{2}, \\
\Sigma_{22} &= -\frac{(N-2)\left(1 - \lambda\cos\ \theta_k\right)}{2\left(1 - 2\lambda\cos\ \theta_k + \lambda^2\right)}, \quad k + j = N\ \&, k \neq j, \\
\Sigma_{22} &= -\frac{(N-1)\left(1 - \lambda\cos\ \theta_k\right)}{1 - 2\lambda\cos\ \theta_k + \lambda^2}, \quad k = j = \frac{N}{2}.
\end{aligned} \tag{45}$$

Combining this and equations (29)–(42), noticing that $\Sigma_{12} + \Sigma_{21} = 0$, it follows that

$$\begin{aligned}
\Sigma_1 + \Sigma_2 &= P_k(\lambda)P_j(\lambda), \quad k \neq j\ \&, k + j \neq N, \\
\Sigma_1 + \Sigma_2 &= -\frac{N\left(1 - \lambda^2\right)}{2\left(1 - 2\lambda\cos\ \theta_k + \lambda^2\right)} + P_k(\lambda)\left(\frac{\lambda\cos\ \theta_j - \lambda^2}{1 - 2\lambda\cos\ \theta_j + \lambda^2} - 1\right), \quad k = j \neq \frac{N}{2}, \\
\Sigma_1 + \Sigma_2 &= -\frac{N\left(1 - \lambda^2\right)}{2\left(1 - 2\lambda\cos\ \theta_k + \lambda^2\right)} + P_k(\lambda)\left(\frac{\lambda\cos\ \theta_j - \lambda^2}{1 - 2\lambda\cos\ \theta_j + \lambda^2} - 1\right), \quad k + j = N\ \&, k \neq j, \\
\Sigma_1 + \Sigma_2 &= -\frac{N\left(1 - \lambda^2\right)}{1 - 2\lambda\cos\ \theta_k + \lambda^2} + P_k(\lambda)\left(\frac{\lambda\cos\ \theta_j - \lambda^2}{1 - 2\lambda\cos\ \theta_j + \lambda^2} - 1\right), \quad k = j = \frac{N}{2}.
\end{aligned} \tag{46}$$

Noticing $|\lambda| < 1$ and $1 - 2\lambda\cos\ \theta_k + \lambda^2 > (1 - |\lambda|)^2$, we have

$$\left|P_k(\lambda)P_j(\lambda)\right| < \frac{4}{(1-|\lambda|)^4},$$
$$\left|P_k(\lambda)\left(\frac{\lambda\cos\theta_j - \lambda^2}{1-2\lambda\cos\theta_j+\lambda^2}-1\right)\right| < \frac{12}{(1-|\lambda|)^4}. \tag{47}$$

Again, by equation (25), we obtain

$$\begin{aligned}
\left|E\left[\mathrm{Re}(\widehat{x}_k)\mathrm{Re}(\widehat{x}_j)\right]\right| &\le \frac{C}{N^2}, \quad k\neq j \,\&\, k+j\neq N,\\
\left|E\left[\mathrm{Re}(\widehat{x}_k)\mathrm{Re}(\widehat{x}_j)\right] - \frac{\sigma^2}{2N\left(1-2\lambda\cos\theta_k+\lambda^2\right)}\right| &\le \frac{C}{N^2}, \quad k=j\neq\frac{N}{2} \text{ or } k+j=N \,\&\, k\neq j,\\
\left|E\left[\mathrm{Re}(\widehat{x}_k)\mathrm{Re}(\widehat{x}_j)\right] - \frac{\sigma^2}{N\left(1-2\lambda\cos\theta_k+\lambda^2\right)}\right| &\le \frac{C}{N^2}, \quad k=j=\frac{N}{2},
\end{aligned} \tag{48}$$

where $C = 12\sigma^2/(1-|\lambda|^2)(1-|\lambda|)^4$ is a constant.

Finally, we obtain the following.

Lemma 1. *When* $\lambda^N \approx 0$ *and* $(1/N^2)\approx 0$, *the series* $\{\mathrm{Re}(\widehat{x}_k)\}_{k=0,\ldots,N-1}$ *satisfy*

$$\alpha_{k,j} = E\left[\mathrm{Re}(\widehat{x}_k)\mathrm{Re}(\widehat{x}_j)\right] = \begin{cases} 0, & k\neq j \text{ and } k+j\neq N,\\ \dfrac{\sigma^2}{2N\left(1-2\lambda\cos\theta_k+\lambda^2\right)}, & k=j\neq\dfrac{N}{2} \text{ or } k+j=N \,\&\, k\neq j,\\ \dfrac{\sigma^2}{N\left(1-2\lambda\cos\theta_k+\lambda^2\right)}, & k=j=\dfrac{N}{2}. \end{cases} \tag{49}$$

4.2. Computation of $\gamma_{k,j}$. By equation (3), we have

$$E\left[\mathrm{Im}(\widehat{x}_j)\mathrm{Im}(\widehat{x}_k)\right] = \frac{1}{N^2}\sum_{l,p=1}^{N-1} E\left[x_l x_p\right]\sin(l\theta_j)\sin(p\theta_k). \tag{50}$$

Similar to the deducing process of equation (25), we have

$$\begin{aligned}
&N^2\left(\frac{\lambda^2-1}{\sigma^2}\right)E\left[\mathrm{Im}(\widehat{x}_j)\mathrm{Im}(\widehat{x}_k)\right]\\
&= \sum_{l=1}^{N-1}\lambda^l\sin(l\theta_j)\sum_{p=1}^{l-1}\left(\lambda^p-\lambda^{-p}\right)\sin(p\theta_k) + \sum_{l=1}^{N-1}\left(\lambda^l-\lambda^{-l}\right)\sin(l\theta_j)\sum_{p=l}^{N-1}\lambda^p\sin(p\theta_k)\\
&=: \widetilde{\Sigma}_1 + \widetilde{\Sigma}_2.
\end{aligned} \tag{51}$$

Noticing that

$$\sum_{p=1}^{l-1}\lambda^p \sin\left(p\theta_k\right) = \frac{-\lambda^l \sin\left(l\theta_k\right) + \lambda \sin\ \theta_k + \lambda^{l+1}\sin\left(l-1\right)\theta_k}{1-2\lambda\cos\ \theta_k + \lambda^2}, \tag{52}$$

we obtain

$$\sum_{p=1}^{l-1}\left(\lambda^p - \lambda^{-p}\right)\sin\left(p\theta_k\right) = \widetilde{\mu}_l^1 + \widetilde{\mu}_l^2, \tag{53}$$

where

$$\begin{aligned}\widetilde{\mu}_l^1 &= -\lambda^l \frac{\sin\left(l\theta_k\right) - \lambda\sin\left(l-1\right)\theta_k}{1-2\lambda\cos\ \theta_k + \lambda^2},\\ \widetilde{\mu}_l^2 &= \lambda^{-l+2}\frac{\sin\left(l\theta_k\right) - \lambda^{-1}\sin\left(l-1\right)\theta_k}{1-2\lambda\cos\ \theta_k + \lambda^2}.\end{aligned} \tag{54}$$

We estimate $\widetilde{\Sigma}_1$ in equation (51):

$$\widetilde{\Sigma}_1 = \sum_{l=1}^{N-1}\lambda^l\widetilde{\mu}_l^1 \sin\left(l\theta_j\right) + \sum_{l=1}^{N-1}\lambda^l\widetilde{\mu}_l^2 \sin\left(l\theta_j\right) =: \widetilde{\Sigma}_{11} + \widetilde{\Sigma}_{12}. \tag{55}$$

Notice that

$$\widetilde{\Sigma}_{12} = \frac{\lambda^2}{2\left(1-2\lambda\cos\ \theta_k + \lambda^2\right)}\sum_{l=1}^{N-1}\left(\left(-\cos\left(l\theta_{k+j}\right) + \cos\left(l\theta_{k-j}\right)\right) + \frac{1}{\lambda}\left(\cos\left(l\theta_{k+j} - \theta_k\right) - \cos\left(l\theta_{k-j} - \theta_k\right)\right)\right). \tag{56}$$

For $k \neq j$ and $k + j \neq N$, we have

$$\sum_{l=0}^{N-1}\cos\left(l\theta_{k+j}\right) = \sum_{l=0}^{N-1}\cos\left(l\theta_{k-j}\right) = \sum_{l=0}^{N-1}\cos\left(l\theta_{k+j} - \theta_k\right) = \sum_{l=0}^{N-1}\cos\left(l\theta_{k-j} - \theta_k\right) = 0, \tag{57}$$

and so $\widetilde{\Sigma}_{12} = 0$.

For $k = j \neq (N/2)$, we have

$$\widetilde{\Sigma}_{12} = \frac{N\left(\lambda^2 - \lambda\cos\ \theta_k\right)}{2\left(1-2\lambda\cos\ \theta_k + \lambda^2\right)}. \tag{58}$$

For $k + j = N$ and $k \neq (N/2)$, we have

$$\widetilde{\Sigma}_{12} = -\frac{N\left(\lambda^2 - \lambda\cos\ \theta_k\right)}{2\left(1-2\lambda\cos\ \theta_k + \lambda^2\right)}. \tag{59}$$

For $k = j = (N/2)$, $\widetilde{\Sigma}_{12} = 0$.

We estimate $\widetilde{\Sigma}_2$ in equation (51). Since $\lambda^N \approx 0$, it follows that

$$\sum_{p=l}^{N-1}\lambda^p \sin\left(p\theta_k\right) = \lambda^l \frac{\sin\left(l\theta_k\right) - \lambda\sin\left(l-1\right)\theta_k}{1-2\lambda\cos\ \theta_k + \lambda^2}. \tag{60}$$

Furthermore,

$$\begin{aligned}\widetilde{\Sigma}_2 &= \frac{1}{1-2\lambda\cos\ \theta_k + \lambda^2}\sum_{l=1}^{N-1}\lambda^{2l}\sin\left(l\theta_j\right)\left(\sin\left(l\theta_k\right) - \lambda\ \sin\left(l-1\right)\theta_k\right)\\ &\quad - \frac{1}{1-2\lambda\cos\ \theta_k + \lambda^2}\sum_{l=1}^{N-1}\sin\left(l\theta_j\right)\left(\sin\left(l\theta_k\right) - \lambda\ \sin\left(l-1\right)\theta_k\right)\\ &=: \widetilde{\Sigma}_{21} + \widetilde{\Sigma}_{22}.\end{aligned} \tag{61}$$

By equation (55), it follows that $\widetilde{\Sigma}_{11} + \widetilde{\Sigma}_{12} = 0$.

For $\widetilde{\Sigma}_{22}$,

$$\widetilde{\Sigma}_{22} = \frac{1}{2\left(1-2\lambda\cos\,\theta_k+\lambda^2\right)}\sum_{l=1}^{N-1}\left(\cos\left(l\theta_{k+j}\right)-\cos\left(l\theta_{k-j}\right)\right)-\lambda\left(\cos\left(l\theta_{k+j}-\theta_k\right)-\cos\left(l\theta_{k-j}-\theta_k\right)\right)$$

$$\begin{cases} 0, & k\neq j\,\&\,k+j\neq N \text{ or } k=j=\dfrac{N}{2}, \\ -\dfrac{N\left(1-\lambda\cos\,\theta_k\right)}{2\left(1-2\lambda\cos\left(2\pi k/N\right)+\lambda^2\right)}, & k=j\neq\dfrac{N}{2}, \\ \dfrac{N\left(1-\lambda\cos\,\theta_k\right)}{2\left(1-2\lambda\cos\,\theta_k+\lambda^2\right)}, & k+j=N\,\&\,k\neq\dfrac{N}{2}. \end{cases} \tag{62}$$

From all of the above, it follows that

$$\widetilde{\Sigma}_1+\widetilde{\Sigma}_2=\begin{cases} 0, & k\neq j\,\&,k+j\neq N \text{ or } k=j=\dfrac{N}{2}, \\ \dfrac{N\left(\lambda^2-1\right)}{2\left(1-2\lambda\cos\left(2\pi k/N\right)+\lambda^2\right)}, & k=j\neq\dfrac{N}{2}, \\ \dfrac{N\left(1-\lambda^2\right)}{2\left(1-2\lambda\cos\,\theta_k+\lambda^2\right)}, & k+j=N\,\&,k\neq\dfrac{N}{2}. \end{cases} \tag{63}$$

Therefore, we have the following.

Lemma 2. *When $\lambda^N \approx 0$, the series $\{\mathrm{Im}(\widehat{x}_k)\}_{k=0,\ldots,N-1}$ satisfy*

$$\gamma_{k,j}=E\left[\mathrm{Im}\left(\widehat{x}_k\right)\mathrm{Im}\left(\widehat{x}_j\right)\right]=\begin{cases} 0, & k\neq j\,\&\,k+j\neq N \text{ or } k=j=\dfrac{N}{2}, \\ \dfrac{\sigma^2}{2N\left(1-2\lambda\cos\,\theta_k+\lambda^2\right)}, & k=j\neq\dfrac{N}{2}, \\ -\dfrac{\sigma^2}{2N\left(1-2\lambda\cos\,\theta_k+\lambda^2\right)} & k+j=N,\,\&\,k\neq\dfrac{N}{2}. \end{cases} \tag{64}$$

4.3. Computation of $\beta_{k,j}$. By equation (3), we have

$$E\left[\mathrm{Re}\left(\hat{x}_j\right)\mathrm{Im}\left(\hat{x}_k\right)\right] = -\frac{1}{N^2}\sum_{l,p=1}^{N-1} E\left[x_l x_p\right]\cos\left(l\theta_j\right)\sin\left(p\theta_k\right). \tag{65}$$

Similar to the deducing process of equation (25), we obtain

$$\begin{aligned} &N^2\left(\frac{1-\lambda^2}{\sigma^2}\right)E\left[\mathrm{Re}\left(\hat{x}_j\right)\mathrm{Im}\left(\hat{x}_k\right)\right] \\ &= \sum_{l=1}^{N-1}\lambda^l\cos\left(l\theta_j\right)\sum_{p=1}^{l-1}\left(\lambda^p-\lambda^{-p}\right)\sin\left(s\theta_k\right) + \sum_{l=1}^{N-1}\left(\lambda^l-\lambda^{-l}\right)\cos\left(l\theta_j\right)\sum_{p=l}^{N-1}\lambda^p\sin\left(p\theta_k\right) \\ &=: \overline{\Sigma}_1 + \overline{\Sigma}_2. \end{aligned} \tag{66}$$

Since

$$\sum_{p=1}^{l-1}\left(\lambda^p-\lambda^{-p}\right)\sin\left(p\theta_k\right) = \overline{\mu}_l^1 + \overline{\mu}_l^2, \tag{67}$$

where

$$\begin{aligned} \overline{\mu}_l^1 &= -\lambda^l\frac{\sin\left(l\theta_k\right)-\lambda\,\sin\left(l-1\right)\theta_k}{1-2\lambda\cos\,\theta_k+\lambda^2}, \\ \overline{\mu}_l^2 &= \lambda^{-l+2}\frac{\sin\left(l\theta_k\right)-\lambda^{-1}\sin\left(l-1\right)\theta_k}{1-2\lambda\cos\,\theta_k+\lambda^2}, \end{aligned} \tag{68}$$

we have

$$\begin{aligned} \overline{\Sigma}_1 &= -\frac{1}{1-2\lambda\cos\,\theta_k+\lambda^2}\sum_{l=1}^{N-1}\lambda^{2l}\cos\left(l\theta_j\right)\left(\sin\left(l\theta_k\right)-\lambda\,\sin\left(l-1\right)\theta_k\right) \\ &\quad + \frac{\lambda^2}{1-2\lambda\cos\,\theta_k+\lambda^2}\sum_{l=1}^{N-1}\cos\left(l\theta_j\right)\left(\sin\left(l\theta_k\right)-\lambda^{-1}\sin\left(l-1\right)\theta_k\right) =: \overline{\Sigma}_{11} + \overline{\Sigma}_{12}. \end{aligned} \tag{69}$$

Furthermore,

$$\overline{\Sigma}_{12} = \frac{\lambda^2}{2\left(1-2\lambda\cos\,\theta_k+\lambda^2\right)}\sum_{l=1}^{N-1}\left(\sin\left(l\theta_{k+j}\right)+\sin\left(l\theta_{k-j}\right)-\lambda^{-1}\left(\sin\left(l\theta_{k+j}-\theta_k\right)+\sin\left(l\theta_{k-j}-\theta_k\right)\right)\right). \tag{70}$$

Noticing that $\sum_{l=1}^{N-1}\sin\left(l\theta_{k+j}\right) = \sum_{l=1}^{N-1}\sin\left(l\theta_{k-j}\right) = 0$, we obtain

$$\overline{\Sigma}_{12} = -\frac{\lambda}{2\left(1-2\lambda\cos\,\theta_k+\lambda^2\right)}\sum_{l=1}^{N-1}\left(\sin\left(l\theta_{k+j}-\theta_k\right)+\sin\left(l\theta_{k-j}-\theta_k\right)\right). \tag{71}$$

For $\overline{\Sigma}_2$, we obtain

$$\begin{aligned}\overline{\Sigma}_2 &= \frac{1}{1-2\lambda\cos\ \theta_k+\lambda^2}\sum_{l=1}^{N-1}\lambda^{2l}\cos\left(l\theta_j\right)\left(\sin\left(l\theta_k\right)-\lambda\sin\left(l-1\right)\theta_k\right)\\ &\quad-\frac{1}{1-2\lambda\cos\ \theta_k+\lambda^2}\sum_{l=1}^{N-1}\cos\left(l\theta_j\right)\left(\sin\left(l\theta_k\right)-\lambda\sin\left(l-1\right)\theta_k\right)=:\overline{\Sigma}_{21}+\overline{\Sigma}_{22},\end{aligned} \tag{72}$$

where

$$\begin{aligned}\overline{\Sigma}_{22} &= -\frac{1}{2\left(1-2\lambda\cos\ \theta_k+\lambda^2\right)}\sum_{l=1}^{N-1}\left(\sin\left(l\theta_{k+j}\right)+\sin\left(l\theta_{k-j}\right)-\lambda\left(\sin\left(l\theta_{k+j}-\theta_k\right)+\sin\left(l\theta_{k-j}-\theta_k\right)\right)\right)\\ &= \frac{\lambda}{2\left(1-2\lambda\cos\ \theta_k+\lambda^2\right)}\sum_{l=1}^{N-1}\left(\sin\left(l\theta_{k+j}-\theta_k\right)+\sin\left(l\theta_{k-j}-\theta_k\right)\right).\end{aligned} \tag{73}$$

Since

$$\begin{aligned}\overline{\Sigma}_{11}+\overline{\Sigma}_{21}&=0,\\ \overline{\Sigma}_{12}+\overline{\Sigma}_{22}&=0,\end{aligned} \tag{74}$$

we have the following.

Lemma 3. *When $\lambda^N \approx 0$, the series $E[\{\mathrm{Re}(\widehat{x}_k), \mathrm{Im}(\widehat{x}_j)\}]_{k,j=0,\ldots,N-1}$ satisfy*

$$\beta_{k,j} = E\left[\mathrm{Re}\left(\widehat{x}_k\right)\mathrm{Im}\left(\widehat{x}_j\right)\right]=0,\quad k,j=0,\ldots,N-1. \tag{75}$$

4.4. Proof of Theorem 1. Without loss of generalization, we assume that N is an odd number. By equation (4), we obtain

$$\begin{aligned}\mathrm{Re}\left(W_n(s)\right) &= \left(\sum_{k=0}^{[N/2]}+\sum_{k=[N/2]+1}^{N-1}\right)r_k\left(\mathrm{Re}\left(\widehat{x}_k\right)\cos\ \eta_{n,k}-\mathrm{Im}\left(\widehat{x}_k\right)\sin\ \eta_{n,k}\right)\\ &= I_1+I_2,\end{aligned} \tag{76}$$

where

$$\begin{aligned}\eta_{n,k}&=\varphi_k+n\theta_k,\\ \varphi_k&=\mathrm{Arg}\left(\overline{\widehat{\psi}}\left(s\omega_k\right)\right),\\ r_k&=\left|\widehat{\psi}\left(s\omega_k\right)\right|.\end{aligned} \tag{77}$$

Since $\widehat{x}_k$ is real, we have $\overline{\widehat{x}}_k=\widehat{x}_{N-k}$. This implies that

$$\begin{aligned}\mathrm{Re}\left(\widehat{x}_{N-k}\right)&=\mathrm{Re}\left(\widehat{x}_k\right),\\ \mathrm{Im}\left(\widehat{x}_{N-k}\right)&=-\mathrm{Im}\left(\widehat{x}_k\right).\end{aligned} \tag{78}$$

Since ψ is real-valued, $\widehat{\psi}(\xi)=\overline{\widehat{\psi}}(-\xi)$; by $\omega_k=(\theta_k/\delta t)$, $k\le(N/2)$, and $\omega_k=-(\theta_{N-k}/\delta t), k>(N/2)$, we obtain

$$\widehat{\psi}\left(s\omega_{N-k}\right)=\widehat{\psi}\left(-s\omega_k\right)=\overline{\widehat{\psi}}\left(s\omega_k\right). \tag{79}$$

Therefore, by equation (77),

$$\begin{aligned}r_{N-k}&=\left|\widehat{\psi}\left(s\omega_{N-k}\right)\right|=\left|\widehat{\psi}\left(s\omega_k\right)\right|=r_k,\\ \varphi_{N-k}&=\mathrm{Arg}\left(\overline{\widehat{\psi}}\left(s\omega_{N-k}\right)\right)=\mathrm{Arg}\left(\overline{\widehat{\psi}}\left(s\omega_k\right)\right)=-\mathrm{Arg}\left(\widehat{\psi}\left(s\omega_k\right)\right)=-\varphi_k.\end{aligned} \tag{80}$$

Hence, $\eta_{n,N-k}=\varphi_{N-k}+n\theta_{N-k}=-\varphi_k-n\theta_k=-\eta_{n,k}$. From this, $\widehat{\psi}(0)=0$, and equation (76), it follows that

$$\begin{aligned} I_2 &= \sum_{k=[N/2]+1}^{N-1} r_k\left(\mathrm{Re}\left(\widehat{x}_k\right)\cos\,\eta_{n,k} - \mathrm{Im}\left(\widehat{x}_k\right)\sin\,\eta_{n,k}\right) \\ &= \sum_{k=1}^{[N/2]} r_{N-k}\left(\mathrm{Re}\left(\widehat{x}_{N-k}\right)\cos\,\eta_{n,N-k} - \mathrm{Im}\left(\widehat{x}_{N-k}\right)\sin\,\eta_{n,N-k}\right) \\ &= I_1, \\ \left(W_n(s)\right)^2 &= 4\sum_{k,j=0}^{[N/2]} r_k r_j\left(\mathrm{Re}\left(\widehat{x}_k\right)\cos\,\eta_{n,k} - \mathrm{Im}\left(\widehat{x}_k\right)\sin\,\eta_{n,k}\right)\left(\mathrm{Re}\left(\widehat{x}_j\right)\cos\,\eta_{n,j} - \mathrm{Im}\left(\widehat{x}_j\right)\sin\,\eta_{n,j}\right). \end{aligned} \tag{81}$$

By Lemmas 1–3, we obtain

$$\begin{aligned} E\left[\left(W_n(s)\right)^2\right] &= 4\sum_{k=0}^{[N/2]} r_k^2\left(\left(E\left[\mathrm{Re}\left(\widehat{x}_k\right)\right]\right)^2\cos^2\eta_{n,k} + \left(E\left[\mathrm{Im}\left(\widehat{x}_k\right)\right]\right)^2\sin^2\eta_{n,k}\right) \\ &= 4\sum_{k=0}^{[N/2]} r_k^2\left(\mathrm{Re}\left(\widehat{x}_k\right)\right)^2\left(\cos^2\eta_{n,k} + \sin^2\eta_{n,k}\right) \\ &= 4\sum_{k=0}^{[N/2]} r_k^2\left(\mathrm{Re}\left(\widehat{x}_k\right)\right)^2 \\ &= \frac{2\sigma^2}{N}\sum_{k=0}^{[N/2]}\frac{\left|\widehat{\psi}\left(s\omega_k\right)\right|^2}{1-2\lambda\cos\,\theta_k+\lambda^2}. \end{aligned} \tag{82}$$

Since $W_n(s) = \mathrm{Re}(W_n(s))$ is a Gaussian random variable with mean 0, we obtain Theorem 1.

4.5. Proof of Theorems 2 and 3. Without loss of generalization, we assume that N is an old number. By equation (4), for $n = 0, \ldots, N-1$, we have

$$W_n(s) = \sum_{k=0}^{[N/2]} \widehat{x}_k\overline{\widehat{\psi}}\left(s\omega_k\right)e^{in\theta_k} + \sum_{k=[N/2]+1}^{N-1} \widehat{x}_k\overline{\widehat{\psi}}\left(s\omega_k\right)e^{in\theta_k}. \tag{83}$$

Since ψ is an analytic wavelet, $\widehat{\psi}(\omega) = 0, \omega < 0$. Notice that $\omega_k < 0, k > (N/2)$. The second term on the right-hand side of equation (83) is vanishing. Therefore,

$$W_n(s) = \sum_{k=0}^{[N/2]} \widehat{x}_k\overline{\widehat{\psi}}\left(s\omega_k\right)e^{in\theta_k}. \tag{84}$$

Furthermore,

$$E\left[\left(\mathrm{Re}\left(W_n(s)\right)\right)^2\right] = \sum_{k,j=0}^{[N/2]} r_k r_j E\left[\mathrm{Re}\left(\widehat{x}_k e^{i\eta_{n,k}}\right)\mathrm{Re}\left(\widehat{x}_j e^{i\eta_{n,j}}\right)\right]. \tag{85}$$

However, by Lemma 3 and equation (77), it follows that

$$E\left[\left(\mathrm{Re}\left(W_n(s)\right)\right)^2\right] = \sum_{k,j=0}^{[N/2]} r_k r_j\left(E\left[\mathrm{Re}\left(\widehat{x}_k\right)\mathrm{Re}\left(\widehat{x}_j\right)\right]\cos\,\eta_{n,k}\cos\,\eta_{n,j} + E\left[\mathrm{Im}\left(\widehat{x}_k\right)\mathrm{Im}\left(\widehat{x}_j\right)\right]\sin\,\eta_{n,k}\sin\,\eta_{n,j}\right). \tag{86}$$

By Lemmas 1 and 2, $E[(\mathrm{Re}(\widehat{x}_k))^2] = E[(\mathrm{Im}(\widehat{x}_k))^2]$, $0 \le k \le [N/2]$, and so

$$\begin{aligned} &E\left[\left(\mathrm{Re}\left(W_n(s)\right)\right)^2\right] \\ &= \sum_{k=0}^{[N/2]} r_k^2\left(E\left[\left(\mathrm{Re}\left(\widehat{x}_k\right)\right)^2\right]\cos^2\eta_{n,k} + E\left[\left(\mathrm{Im}\left(\widehat{x}_k\right)\right)^2\right]\sin^2\eta_{n,k}\right) \\ &= \sum_{k=0}^{[N/2]} r_k^2 E\left[\left(\mathrm{Re}\left(\widehat{x}_k\right)\right)^2\right]\left(\cos^2\eta_{n,k} + \sin^2\eta_{n,k}\right) = \sum_{k=0}^{[N/2]} r_k^2 E\left[\left(\mathrm{Re}\left(\widehat{x}_k\right)\right)^2\right]. \end{aligned} \tag{87}$$

Similarly, we have

$$E\left[\left(\mathrm{Im}\left(W_n(s)\right)\right)^2\right] = \sum_{k,j=0}^{[N/2]} r_k r_j E\left[\mathrm{Im}\left(\widehat{x}_k e^{i\eta_{n,k}}\right)\mathrm{Im}\left(\widehat{x}_j e^{i\eta_{n,j}}\right)\right]. \tag{88}$$

By Lemma 3,

$$E\left[\mathrm{Im}\left(\widehat{x}_k e^{i\eta_{n,k}}\right)\mathrm{Im}\left(\widehat{x}_j e^{i\eta_{n,j}}\right)\right] = E\left[\mathrm{Re}\left(\widehat{x}_k\right)\mathrm{Re}\left(\widehat{x}_j\right)\right]\sin\eta_{n,k}\sin\eta_{n,j} + E\left[\mathrm{Im}\left(\widehat{x}_k\right)\mathrm{Im}\left(\widehat{x}_j\right)\right]\cos\eta_{n,k}\cos\eta_{n,j}. \tag{89}$$

This implies that

$$E\left[\left(\mathrm{Im}\left(W_n(s)\right)\right)^2\right] = \sum_{k=0}^{N/2-1} r_k^2\left(E\left[\left(\mathrm{Re}\left(\widehat{x}_k\right)\right)^2\right]\sin^2\eta_{n,k} + E\left[\left(\mathrm{Im}\left(\widehat{x}_k\right)\right)^2\right]\cos^2\eta_{n,k}\right) = \sum_{k=0}^{(N/2)-1} r_k^2 E\left[\left(\mathrm{Re}\left(\widehat{x}_k\right)\right)^2\right]. \tag{90}$$

Therefore, we have

$$\mathrm{Var}\left(\mathrm{Re}\left(W_n(s)\right)\right) = \mathrm{Var}\left(\mathrm{Im}\left(W_n(s)\right)\right) = \sum_{k=0}^{[N/2]} r_k^2 E\left[\left(\mathrm{Re}\left(\widehat{x}_k\right)\right)^2\right] = \frac{\sigma^2}{2N\left(1-\lambda^2\right)}\sum_{k=0}^{[N/2]} P_k(\lambda)\left|\widehat{\psi}\left(s\omega_k\right)\right|^2. \tag{91}$$

Now, we prove that $\mathrm{Re}(W_n(s))$ and $\mathrm{Im}(W_n(s))$ are independent.

By Lemmas 1–3,

$$\begin{aligned} &E\left[\mathrm{Re}\left(W_n(s)\right)\mathrm{Im}\left(W_n(s)\right)\right] \\ &= \sum_{k,j=0}^{[N/2]} r_k r_j\left(E\left[\mathrm{Re}\left(\widehat{x}_k\right)\mathrm{Re}\left(\widehat{x}_j\right)\right]\cos\eta_{n,k}\sin\eta_{n,j} - E\left[\mathrm{Im}\left(\widehat{x}_k\right)\mathrm{Im}\left(\widehat{x}_j\right)\right]\sin\eta_{n,k}\cos\eta_{n,j}\right) \\ &= \frac{1}{2}\sum_{k=0}^{[N/2]} r_k^2\left(E\left[\left(\mathrm{Re}\left(\widehat{x}_k\right)\right)^2\right]\sin\left(2\eta_{n,k}\right) - E\left[\left(\mathrm{Im}\left(\widehat{x}_k\right)\right)^2\right]\sin\left(2\eta_{n,k}\right)\right) = 0. \end{aligned} \tag{92}$$

Since both $\mathrm{Re}(W_n(s))$ and $\mathrm{Im}(W_n(s))$ are Gaussian random variables with mean 0 and

$$\mathrm{Var}\left(\mathrm{Re}\left(W_n(s)\right)\right) = \mathrm{Var}\left(\mathrm{Im}\left(W_n(s)\right)\right) =: \sigma^2(s), \tag{93}$$

where

$$\sigma^2(s) = \frac{\sigma^2}{2N\left(1-\lambda^2\right)}\left(\sum_{k=0}^{[N/2]} P_k(\lambda)\left|\widehat{\psi}\left(s\omega_k\right)\right|^2\right), \tag{94}$$

we obtain Theorem 2.

Consider the phase $\Phi = \mathrm{Arg}(W_n(s))$. Notice that the p.d.f.s of $\mathrm{Re}(W_n(s))$ and $\mathrm{Im}(W_n(s))$ are, respectively,

$$p_R(x) = \frac{1}{\sqrt{2\pi}\sigma(s)} e^{-\left(x^2/2\sigma^2(s)\right)},$$
$$p_I(x) = \frac{1}{\sqrt{2\pi}\sigma(s)} e^{-\left(y^2/2\sigma^2(s)\right)}, \tag{95}$$

and $\mathrm{Re}(W_n(s))$ and $\mathrm{Im}(W_n(s))$ are independent, the joint p.d.f. of $\mathrm{Re}(W_n(s))$ and $\mathrm{Im}(W_n(s))$ is

$$p(x, y) = \frac{1}{2\pi\sigma^2(s)} e^{-\left(\left(x^2+y^2\right)/2\sigma^2(s)\right)}. \tag{96}$$

The probability

$$P(\beta_1 < \Phi < \beta_2) = \frac{1}{2\pi\sigma^2(s)} \iint_{\Omega} e^{-\left(\left(x^2+y^2\right)/2\sigma^2(s)\right)} \mathrm{d}x\mathrm{d}y, \tag{97}$$

where the domain $\Omega: = \{0 < r < \infty, 0 \le \beta_1 < \varphi < \beta_2 < 2\pi\}$. Hence,

$$P(\beta_1 < \Phi < \beta_2) = \frac{1}{2\pi\sigma^2(s)} \int_{\beta_1}^{\beta_2} \mathrm{d}\varphi \int_0^{\infty} r e^{-\left(r^2/2\sigma^2(s)\right)} \mathrm{d}r = \frac{1}{2\pi}(\beta_2 - \beta_1), \tag{98}$$

i.e., Theorem 3 holds.

5. Climate Diagnosis

Climatic background noises are often modeled as red noise [4–9]. In order to extract instinct features of climatic time series, we can use Theorems 1 and 2 to compare the wavelet power spectrum of climatic time series with that of red noise. If the values of the wavelet power spectrum of climate time series at some regions are all outside the 95% confidence interval for the distribution for the wavelet power spectrum of the red noise, then the wavelet power spectrum at this region contain instinct features of climatic time series. Moreover, we can use Theorem 3 to test the synchronization between the two climatic time series. If the difference of the wavelet phase of the two climatic time series does not change in some significant regions of the wavelet power spectrum, noticing that Theorem 3 indicates that this cannot be caused by climatic background noise effects, these two climatic time series demonstrate synchronization.

Data Availability

No data were used to support this research.

Conflicts of Interest

The author declares no conflicts of interest.

Acknowledgments

This research was partially supported by the European Commissions Horizon 2020 Framework Program under No. 861584 and Taishan Distinguished Professor Fund.

References

[1] R. N. McDonough and A. D. Whalen, *Detection of Signals in Noise*, Academic Press, Cambridge, MA, USA, 1995.
[2] T. Li, *Time Series with Mixed Spectra*, Chapman and Hall/CRC, Boca Raton, FL, USA, 2019.
[3] L. Abualigah and A. Diabat, "Advances in sine cosine algorithm: a comprehensive survey," *Artificial Intelligence Review*, vol. 54, no. 4, pp. 2567–2608, 2021.
[4] Z. Zhang, *Multivariate Time Series Analysis in Climate and Environmental Research*, Springer, Berlin, Germany, 2018.
[5] Z. Zhang, *Big Data Mining for Climate Change*, Elsevier, Amsterdam, Netherlands, 2020.
[6] M. E. Mann and J. M. Lees, "Robust estimation of background noise and signal detection in climatic time series," *Climatic Change*, vol. 33, no. 3, pp. 409–445, 1996.
[7] M. R. Allen and L. A. Smith, "Investigating the origins and significance of low-frequency modes of climate variability," *Geophysical Research Letters*, vol. 21, no. 10, pp. 883–886, 1994.
[8] J. E. Kutzbach and R. A. Bryson, "Variance spectrum of holocene climatic fluctuations in the north atlantic sector," *Journal of the Atmospheric Sciences*, vol. 31, no. 8, pp. 1958–1963, 1974.
[9] D. L. Gilman, F. J. Fuglister, and J. M. Mitchell, "On the power spectrum of "red noise"," *Journal of the Atmospheric Sciences*, vol. 20, no. 2, pp. 182–184, 1963.
[10] L. Abualigah and M. Alkhrabsheh, "Amended hybrid multiverse optimizer with genetic algorithm for solving task scheduling problem in cloud computing," *The Journal of Supercomputing*, 2021.
[11] L. Abualigaha, A. Diabat, S. Mirjalili, M. A. Elaziz, and A. H. Gandomi, "The arithmetic optimization algorithm," *Computer Methods in Applied Mechanics and Engineering*, vol. 376, Article ID 113609, 2021.
[12] L. Abualigah, D. Yousri, M. A. Elaziz, A. A. Ewees, M. A. A. Al-qaness, and A. H. Gandomi, "Aquila optimizer: a novel meta-heuristic optimization algorithm," *Computers & Industrial Engineering*, vol. 157, Article ID 107250, 2021.
[13] L. Abualigah, A. Diabat, and M. A. Elaziz, "Intelligent workflow scheduling for big data applications in IoT cloud computing environments," *Cluster Computing*, 2021.
[14] C. K. Chui, *An Introduction to Wavelet*, Academic Press, Cambridge, MA, USA, 1992.
[15] C. Torrence and G. P. Compo, "A practical guide to wavelet analysis," *Bulletin of the American Meteorological Society*, vol. 79, no. 1, pp. 61–78, 1998.
[16] M. Jansen, *Noise Reduction by Wavelet Thresholding*, Vol. 161, Springer-Verlag, New York, NY, USA, 1 edition, 2001.
[17] D. L. Donoho, "De-noising by soft thresholding," *IEEE Transactions on Information Theory*, vol. 41, no. 3, Article ID 613C627, 1995.
[18] G. P. Nason and D. Savchev, "White noise testing using wavelets," *Stat*, vol. 3, no. 1, pp. 351–362, 2014.
[19] G. Ferrante and D. Persano Adorno, "A wavelet analysis of 1/f and white noise in microwave transistors," *Microelectronics Reliability*, vol. 41, no. 1, pp. 99–104, 2001.
[20] Z. Zhang and P. Jorgensen, "Modulated haar wavelet analysis of climatic background noise," *Acta Applicandae Mathematica*, vol. 140, pp. 71–93, 2015.

Hindawi
Mathematical Problems in Engineering
Volume 2021, Article ID 2321042, 7 pages
https://doi.org/10.1155/2021/2321042

Research Article

Drivers of Stock Prices in Ghana: An Empirical Mode Decomposition Approach

Emmanuel. N. Gyamfi,[1] **Frederick A. A. Sarpong**,[1] **and Anokye M. Adam**[2]

[1]*School of Business, Ghana Institute of Management and Public Administration, Accra, Ghana*
[2]*School of Business, University of Cape Coast, Cape Coast, Ghana*

Correspondence should be addressed to Emmanuel. N. Gyamfi; engyamfi@gimpa.edu.gh

Received 22 July 2021; Accepted 28 August 2021; Published 26 September 2021

Academic Editor: Yuxing Li

This study utilized the empirical mode decomposition (EMD) technique and examined which group of investors based on their trading frequencies influence stock prices in Ghana. We applied this technique to a dataset of daily closing prices of GSE Financial Stock Index for the period 04/01/2011 to 28/08/2015. The daily closing prices were decomposed into six intrinsic mode functions (IMFs) and a residue. We used the hierarchical clustering method to reconstruct the IMFs into high frequency, low frequency, and trend components. Using statistical measures such as Pearson product moment correlation coefficient and the Kendall rank correlation, we found that the low frequency and trend components of stock prices are the main drivers of the GSE stock index. These low-frequency traders are the institutional investors. Therefore, stock prices on the GSE are affected by real economic growth but not short-lived market fluctuations.

1. Introduction

The analysis of financial time series remains a challenging task because of its extremely complex nonlinear and nonstationarity dynamic behaviour [1]. For stock market prices, several factors such as business cycle, government policies, types of investors, and firm-specific factors deepen its complexity [2]. The behaviour of stock prices to quickly discover market imperfections, exploited and corrected by market participant, makes use of conventional time-domain tools inappropriate in analyzing stock markets [3]. For example, the dynamic low-frequency traders like institutional and central banks bringing to the market price formation differ from high-frequency traders like speculators and market makers. This shows that price formation in the stock market is determined by the diverse traders with different trading frequencies. Consequently, some attractive characteristics may not be uncovered if stock prices are analyzed within the time-domain framework. Owing to these, a number of methods have been used in the analysis of stock prices, in general, ranging from linear and nonlinear methods in the frequency-domain [4, 5].

In an attempt to solve the problem of nonlinearity and nonstationary in time series data, Huang et al. [6] proposed a time-frequency method named Hilbert–Huang transform (HHT) which is popular in signal analysis [7, 8]. The technique works through performing a time adaptive decomposition operation named empirical mode decomposition (EMD) on the signal, and then the signal will be decomposed into a set of complete and almost orthogonal components named intrinsic mode function (IMF), which is almost monocomponent. It has been increasingly recognized as an effective analysis model in financial time series. The application of EMD has already been explored in the analysis of economic and financial data. For instance, it has been applied in modelling crude oil price [9–11], exchange rate [12–15], electricity price [16, 17], gold price [18, 19], and carbon price [20].

In contrast to previous methods such as wavelet analysis and spectrum analysis, EMD is intuitive, direct, posterior, and adaptive [21]. The EMD can be used to decompose a series into a finite and often small number of intrinsic mode functions (IMFs) [6].

Similar to EMD, wavelet has been used to study nonstationary signal analysis. Studies such as Tiwari et al. [22, 23]; Jammazi et al. [24]; Jiang et al. [25]; Ferrer et al. [26]; Yang et al. [27]; Wang et al. [28]; Boubaker and Raza [29]; and Frimpong et al. [30] used wavelet-based methods to study the behaviour of financial variables such as oil prices, exchange rates, inflation, and stock prices at different frequencies. However, wavelet has certain drawbacks which EMDs can easily overcome. For instance, wavelet analysis restricts one from selecting an objective wavelet function from a set of wavelet functions. In a wavelet, choosing the basis function and decomposition levels is subjective, and this may lead to the extraction of false cycles forming the time series [31, 32]. EMD nevertheless does not require a subjective test since the decomposition is based on the local characteristic time scale of the data. However, EMD has not been widely used in the analysis of stock prices. Some of the recent studies which have used EMDs in analyzing stock prices are [21, 33–35].

In this paper, we apply EMD in time-frequency analysis for GSE index for the period from 04/01/2011 to 28/08/2015. The main objective of this study is to determine which group of investors based on their trading frequencies influence stock prices in Ghana.

It remains imperative to detect the frequencies that have a significant impact on stock prices. Generally, the stock market reflects the economic conditions of an economy. In a growing economy, there is an increase in output leading to firms experiencing high profitability. These higher profits make shares of companies more attractive because they are able to pay higher dividends to shareholders. A long period of economic growth tends to benefit shareholders.

This study is innovative in the sense that it investigates the group of investors that drive stock prices on the Ghana stock exchange using the empirical mode decomposition (EMD). The following contributions are also made to the literature. First, it provides a detailed analysis of the use of EMD to decompose the stock price into several IMFs and one residue.

Second, these IMFs and the residue are reconstructed into high frequency, low frequency, and trend components using the hierarchical clustering method. Different measures were then used to assess the importance of each frequency for the overall stock price series.

Finally, the economic significance of these components is identified as short-term fluctuations and long-term trend. If the effect of the low frequency or trend components of stock prices on the aggregate stock prices is dominant, it can be concluded that stock prices are driven by the real growth of the economy.

The remainder of the paper is structured as follows. Section 2 provides a brief description of the data. Section 3 describes the methodology. Section 4 contains the results of our analysis, and Section 5 concludes the paper.

2. Data

The data which were obtained from DataStream are the daily closing prices of the GSE Financial Stock (GSE-FSI) index coded in DataStream as GSEFSII (Price Index). The data period is between January 4, 2011, and August 28, 2015. The period of study was chosen because of data availability. The closing prices were transformed into returns which were calculated by taking the natural log first difference of prices.

3. Methodology

We follow Zhu et al. [20] in presenting the EMD algorithm. The EMD technique assumes that the stock prices of GSEFSII have many IMFs of different oscillations and that an IMF must satisfy two conditions according to Huang et al. [6] as follows:

(i) An IMF has the same number of extremum and zero crossing or differs by one at the most

(ii) An IMF is symmetric with the local zero mean

(iii) To extract IMFs, EMD uses the following sifting process:

(a) All the maxima and minima of the time series (stock prices of GSEFSII) denoted $x(t)$ were identified

(b) Next, we generated upper and lower envelopes $e_{\max}(t)$ and $e_{\min}(t)$ using cubic spline interpolation

(c) The point-by-point mean denoted $m(t)$ were calculated from the upper and lower envelopes as

$$m(t) = \frac{e_{\max}(t) + e_{\min}(t)}{2}. \tag{1}$$

(d) The mean was extracted from $x(t)$ and we defined the difference between $x(t)$ and $m(t)$ as $d(t)$. Thus $d(t) = x(t) - m(t)$.

(e) The properties of $d(t)$ were checked. If $d(t)$ was found to be an IMF, we denoted $d(t)$ as the ith IMF and replaced $x(t)$ with the residue; $r(t) = x(t) - d(t)$. The ith IMF is often denoted as $c_i(t)$ where i is its index. However, if $d(t)$ was not an IMF, $x(t)$ was replaced with $d(t)$.

Steps (a)–(e) were repeated until the residue satisfied some stopping criteria. See Zhu et al. [20] for more on the stopping criteria.

Therefore, the stock price $x(t)$ can be expressed as the sum of IMFs and a residue. This can be mathematically represented as

$$x(t) = \sum_{i=1}^{m} c_i(t) + r_m(t), \tag{2}$$

where m is the number of IMFs, $r_m(t)$ is the final residue, and $c_i(t)$ is the ith IMF.

4. Results and Discussion

A plot of the natural logarithmic values of the daily closing prices of GSEFSII for the period from 04/1/2011 to 28/08/2015 is shown in Figure 1. Using the empirical mode decomposition (EMD) method, the natural logarithmic values of the prices were decomposed into six different frequencies called the intrinsic mode functions (IMFs) and one residue. The IMFs as plotted in Figure 2 are arranged from high to low frequencies.

Next, the IMFs are analyzed using the following measures: first, we recorded the mean period of each IMF. The mean period is measured as the length of an IMF divided by the number of peaks.

Subsequently, the Pearson product moment correlation coefficient and the Kendall rank correlation coefficient were used to measure correlations between each IMF (residue) and the observed stock prices.

Finally, in order to explain the movement of each IMF (residue) to the total movement of stock prices, we computed the variance and variance percentage of each IMF (residue). The results obtained for each of these measures are presented in Table 1.

We observed from Table 1 that, the residue which is known as the deterministic long-term trend by Huang et al. [6] was the dominant mode. It had the highest correlation coefficient with the observed prices of 0.9764 and 0.7769 for Pearson and Kendall correlation coefficients, respectively. The next was IMF6 with a mean period of 121.4. The residue contributed 94.9% of the total variation. For IMF1, IMF2, IMF3, IMF4, and IMF5, the values of the correlation coefficients were very low. These IMFs (IMF1–IMF5) only accounted for 1.39% of the total variation. This shows that the effect of (IMF1–IMF5) on stock prices was very low.

Next, following Zhu et al. [20], we used the hierarchical clustering and the Euclidean distance between pairs of any two IMFs or between an IMF and the residue to group the IMFs into three components. The clustering results are shown in Figure 3. When the Euclidean distance was less than 10, an IMF was classified as a high-frequency component, when the Euclidean distance was between 10 and 20, an IMF was classified as a low-frequency component, and an IMF with a Euclidean distance of more than 20 was classified as the trend component. Therefore, IMF1–IMF5 were grouped as high-frequency component, IMF6 as the low-frequency component, and the residue served as the trend component. A plot of the extracted components and their statistical measures are presented in Figure 4 and Table 2, respectively.

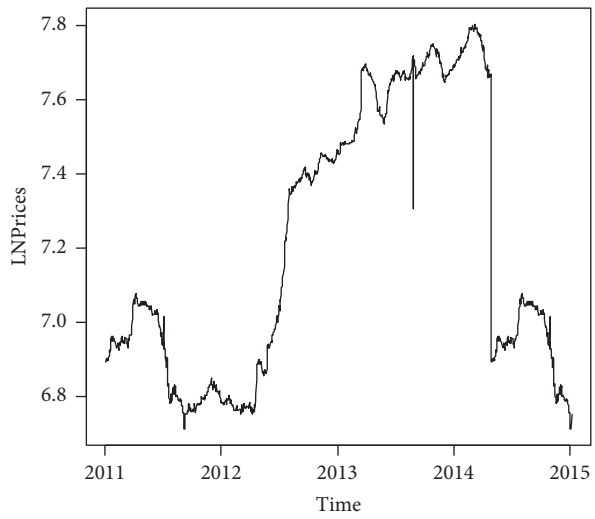

Figure 1: Plot of natural logarithmic values of GSEFSII from 04/01/2011 to 28/08/2015.

Each of the 3 components in Figure 4 had distinct features. The residue varied around the long-term trend slowly. The residue was as thus considered as the long-term trend of stock prices. The correlation between the trend and stock prices contributed to about 96% of the total variation of the stock prices. The trend affected the long-term movement of stock prices in the long-run.

The high-frequency component reflected the effect of short-term market fluctuations such as speculation. Market fluctuations were short-lived and had little effect on stock prices as observed from the mean periods and variance values from Table 1.

The low-frequency component such as excessive government spending and the global financial crisis affected stock prices. An upward or downward movement indicated the effects of significant trend break on stock prices. The effect lasted longer than investors anticipated as evidenced by the mean period and variance values in Table 2.

The low frequency and trend components contributed to about 99.7% of the total variation and hence were considered as the most important components of the stock prices. Thus, the Nigerian stock exchange has driven real growth of the economy but not short-lived market fluctuations. Our results confirm the findings obtained in studies by Tiwari et al. [23] and Heaton and Lucas [36].

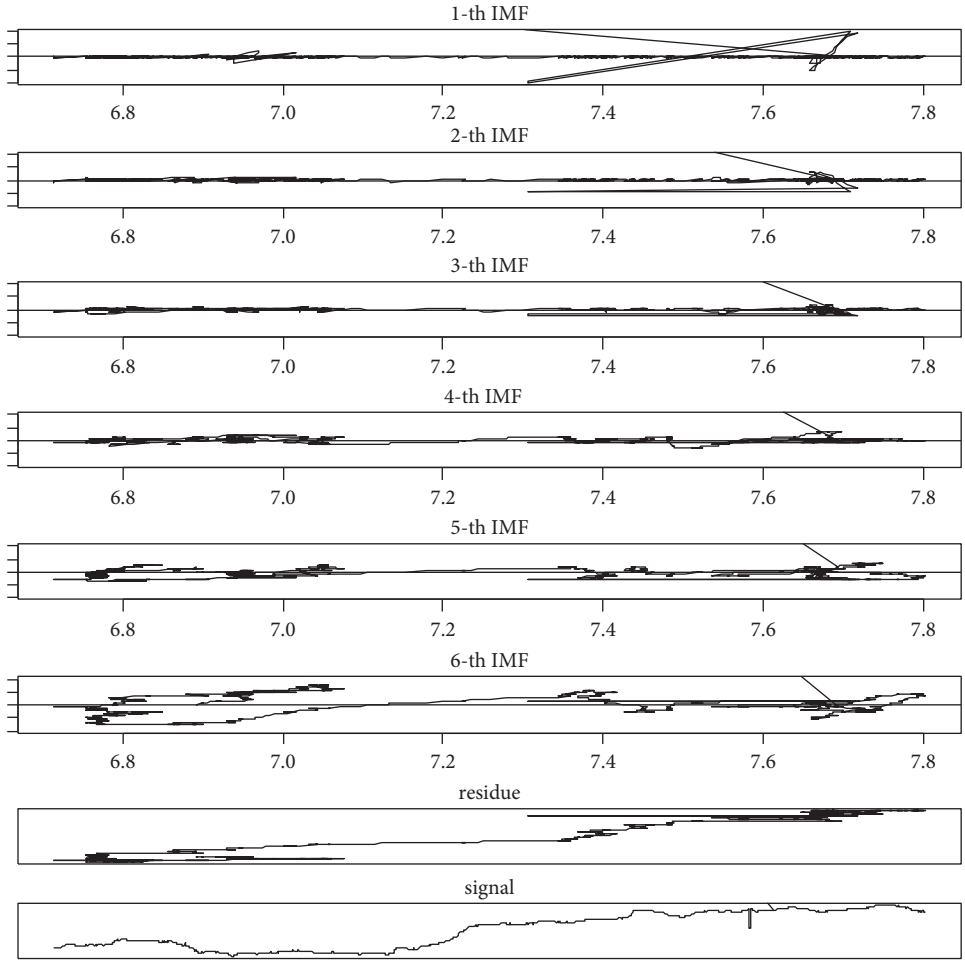

Figure 2: IMFs and residue of GSEFSI obtained using EMD.

Table 1: Measures of IMFs and residue of GSEFSII.

	Mean period	Pearson correlation	Kendall correlation	Variance	Variance as % of observed	Variance as % of $\sum$ IMFs + residue
Observed series	2.3124			0.1404		
IMF1	1.63	0.0288	0.0116	0.0003	0.20	0.20
IMF2	3.67	0.0211	0.0252	0.0001	0.07	0.07
IMF3	9.06	0.0133	0.0039	0.0001	0.07	0.07
IMF4	23.35	0.0937*	0.0711*	0.0004	0.28	0.28
IMF5	60.70	0.0471	0.0295	0.0011	0.77	0.77
IMF6	121.4	0.1824**	0.1636**	0.0052	3.70	3.71
Residue	607	0.9764**	0.7769**	0.1330	94.73	94.90
		Sum			99.82	100

Note. * and **: correlation is significant at the level of 0.05 and 0.01 (2-tailed) respectively.

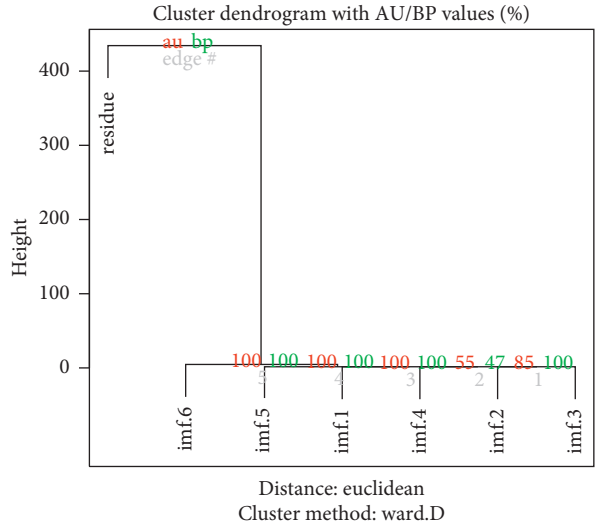

Figure 3: Hierarchical clustering tree obtained for the IMFs and residue.

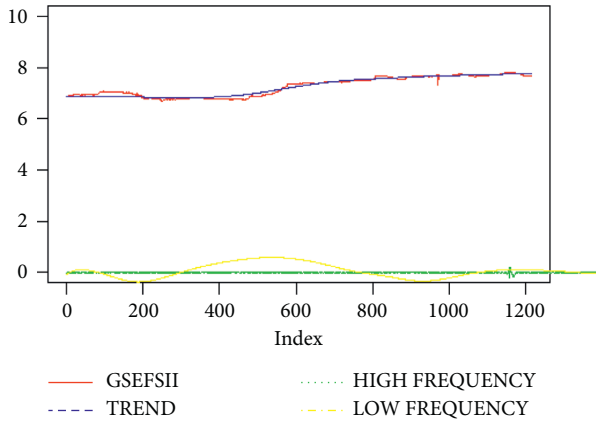

Figure 4: Three components of GSEFSII.

Table 2: Correlation and variance of components for GSEFII.

	Mean period	Pearson correlation	Kendall correlation	Variance	Variance as % of observed	Variance as % of ∑ IMFs + residue
Observed series	2.3124			0.1401		
High Frequency	4.7201	0.0421	0.0276	0.0004	0.2849	0.2886
Low Frequency	121.4	0.1824	0.1636	0.0052	3.7037	3.7518
Residue	607	0.9764**	0.7769**	0.1330	94.73	95.9596
		Sum			98.7186	100

**Correlation is significant at the level of 0.05 (2-tailed).

5. Conclusion

The empirical mode decomposition (EMD) was used to decompose the natural logarithmic values of the daily closing prices of the GSE Financial Stock (GSE-FSI) index between 04/01/2011 and 28/08/2015 into six IMFs and a residue. Statistical measures such as the mean period, Pearson product moment correlation coefficient, and the Kendall rank correlation coefficient were used in assessing the effects of the IMFs and the residue on stock prices. The use of hierarchical clustering and Euclidean distance techniques helped us group IMFs and residue into high frequency, low frequency, and trend components. The trend and low-frequency components constituted about 99.7% of the total variation of the stock prices and were thus considered to affect stock prices than the high-frequency components.

We, therefore, conclude that stock prices on the Ghana stock exchange are affected by real economic growth but not short-lived market fluctuations.

Data Availability

The data used were obtained from Thomson Reuters DataStream.

Conflicts of Interest

The authors declare that they have no conflicts of interest.

References

[1] T. Jin, H. Ding, B. Li, H. Xia, and C. Xue, "Valuation of interest rate ceiling and floor based on the uncertain fractional differential equation in Caputo sense," *Journal of Intelligent & Fuzzy Systems*, vol. 40, no. 3, pp. 5197–5206, 2021.

[2] K. He, R. Zha, J. Wu, and K. Lai, "Multivariate EMD-based modeling and forecasting of crude oil price," *Sustainability*, vol. 8, no. 4, p. 387, 2016.

[3] N. Nava, T. Matteo, and T. Aste, "Financial time series forecasting using empirical mode decomposition and support vector regression," *Risks*, vol. 6, no. 7, pp. 1–21, 2018.

[4] X. Qiu, H. Zhu, P. N. Suganthan, and G. A. J. Amaratunga, "Stock price forecasting with empirical mode decomposition based ensemble ν-support vector regression model," in *Computational Intelligence, Communications, and Business Analytics. CICBA 2017. Communications in Computer and Information Science*, J. Mandal, P. Dutta, and S. Mukhopadhyay, Eds., Springer, Singapore, 2017.

[5] A. M. Adam and P. Owusu Junior, *Financial Econometrics: An Example-Based Handbook*, Nova Science Publishers, New York, NY, USA, 2017.

[6] N. E. Huang, Z. Shen, S. R. Long et al., "The empirical mode decomposition and the Hilbert spectrum for nonlinear and non-stationary time series analysis," *Proceedings of the Royal Society of London. Series A: Mathematical, Physical and Engineering Sciences*, vol. 454, no. 1971, pp. 903–995, 1998.

[7] L. Zhao, J. Gong, and H. Chong, "The extraction method of gearbox compound fault features based on EEMD and cloud model," *Mathematical Problems in Engineering*, vol. 2020, Article ID 6661975, 8 pages, 2020.

[8] H. Zhao, H. Liu, Y. Jin, X. Dang, and W. Deng, "Feature extraction for data-driven remaining useful life prediction of rolling bearings," *IEEE Transactions on Instrumentation and Measurement*, vol. 70, pp. 1–10, 2021.

[9] L. Yu, S. Wang, and K. K. Lai, "Forecasting crude oil price with an EMD-based neural network ensemble learning paradigm," *Energy Economics*, vol. 30, no. 5, pp. 2623–2635, 2008.

[10] X. Zhang, K. K. Lai, and S.-Y. Wang, "A new approach for crude oil price analysis based on empirical mode decomposition," *Energy Economics*, vol. 30, no. 3, pp. 905–918, 2008.

[11] X. Zhang, L. Yu, S. Wang, and K. K. Lai, "Estimating the impact of extreme events on crude oil price: an EMD-based event analysis method," *Energy Economics*, vol. 31, no. 5, pp. 768–778, 2009.

[12] C.-S. Lin, S.-H. Chiu, and T.-Y. Lin, "Empirical mode decomposition-based least squares support vector regression for foreign exchange rate forecasting," *Economic Modelling*, vol. 29, no. 6, pp. 2583–2590, 2012.

[13] B. Premanode and C. Toumazou, "Improving prediction of exchange rates using Differential EMD," *Expert Systems with Applications*, vol. 40, no. 1, pp. 377–384, 2013.

[14] V. Plakandaras, T. Papadimitriou, and P. Gogas, "Forecasting daily and monthly exchange rates with machine learning techniques," *Journal of Forecasting*, vol. 34, no. 7, pp. 560–573, 2015.

[15] A. M. Adam, K. Kyei, S. Moyo, R. Gill, and E. N. Gyamfi, "Similarities in Southern African Development Community (SADC) exchange rate markets structure: evidence from the ensemble empirical mode decomposition," *Journal of African Business*, pp. 1–16, 2021.

[16] N. An, W. Zhao, J. Wang, D. Shang, and E. Zhao, "Using multi-output feedforward neural network with empirical mode decomposition based signal filtering for electricity demand forecasting," *Energy*, vol. 49, pp. 279–288, 2013.

[17] F. Lisi and F. Nan, "Component estimation for electricity prices: procedures and comparisons," *Energy Economics*, vol. 44, pp. 143–159, 2014.

[18] Q. Hua and T. Jiang, "The prediction for London gold price: improved empirical mode decomposition," *Applied Economics Letters*, vol. 22, no. 17, pp. 1404–1408, 2015.

[19] P. Owusu Junior, A. M. Adam, and G. Tweneboah, "Connectedness of cryptocurrencies and gold returns: evidence from frequency-dependent quantile regressions," *Cogent Economics & Finance*, vol. 8, no. 1, Article ID 1804037, 2020.

[20] B. Zhu, P. Wang, J. Chevallier, and Y. Wei, "Carbon price analysis using empirical mode decomposition," *Computational Economics*, vol. 45, no. 2, pp. 195–206, 2015.

[21] M. Xu, P. Shang, and A. Lin, "Cross-correlation analysis of stock markets using EMD and EEMD," *Physica A: Statistical Mechanics and Its Applications*, vol. 442, pp. 82–90, 2016.

[22] A. K. Tiwari, A. B. Dar, and N. Bhanja, "Oil price and exchange rates: a wavelet based analysis for India," *Economic Modelling*, vol. 31, no. 1, pp. 414–422, 2013a.

[23] A. Kumar Tiwari, A. Billah Dar, and N. Bhanja, "Stock market integration in Asian countries: evidence from wavelet multiple correlations," *Journal of Economic Integration*, vol. 28, no. 3, pp. 441–456, 2013b.

[24] R. Jammazi, A. Lahiani, and D. Khuong, "Nguyen A wavelet-based nonlinear ARDL model for assessing the exchange rate pass-through to crude oil prices," *Journal of International Financial Markets, Institutions and Money*, vol. 34, pp. 173–187, 2015.

[25] C. Jiang, T. Chang, and X. L. Li, "Money growth and inflation in China: new evidence from a wavelet analysis," *International Review of Economics & Finance*, vol. 35, pp. 249–261, 2015.

[26] R. Ferrer, V. J. Bolós, and R. Benítez, "Interest rate changes and stock returns: a European multi-country study with wavelets," *International Review of Economics & Finance*, vol. 44, pp. 1–12, 2016.

[27] L. Yang, X. J. Cai, H. Zhang, and S. Hamori, "Interdependence of foreign exchange markets: a wavelet coherence analysis," *Economic Modelling*, vol. 55, pp. 6–14, 2016.

[28] G. J. Wang, X. Chi, and S. Chen, "Multiscale correlation networks analysis of the US stock market: a wavelet analysis," *Journal of Economic Interaction and Coordination*, vol. 12, no. 3, pp. 561–594, 2017.

[29] H. Boubaker and S. A. Raza, "A wavelet analysis of mean and volatility spillovers between oil and BRICS stock markets," *Energy Economics*, vol. 64, pp. 105–117, 2017.

[30] S. Frimpong, E. N. Gyamfi, Z. Ishaq, S. K. Agyei, D. Agyapong, and A. M. Adam, "Can global economic policy uncertainty drive the interdependence of agricultural commodity prices?

Evidence from partial wavelet coherence analysis," *Complexity*, vol. 2021, Article ID 8848424, 13 pages, 2021.

[31] D. B. Percival and A. T. Walden, *Wavelet Methods for Time Series Analysis*, Volume 4 of Cambridge Series in Statistical and Probabilistic Mathematics, Cambridge University Press, Cambridge, UK, 2000.

[32] B. Wang, Y. M. Hu, Y. D. Du, Z. H. Zhai, and X. Y. Wu, "Study on the difference between wavelet analysis and EEMD in multi-scale decomposition of temperature and precipitation of Guangzhou," *Journal of Tropical Meteorology*, vol. 30, no. 4, pp. 769–776, 2014.

[33] J. Sun and H. Sheng, "Applications of ensemble empirical mode decomposition to stock-futures basis analysis," in *Proceedings of the Information and Financial Engineering (ICIFE), 2010 2nd IEEE International Conference on*, pp. 396–399, Chongqing, September 2010.

[34] H. Yu and H. Liu, "Improved stock market prediction by combining support vector machine and empirical mode decomposition," in *Proceedings of the Computational Intelligence and Design (ISCID), 2012 Fifth International Symposium on*, pp. 531–534, Hangzhou, October 2012.

[35] C. H. Cheng and L. Y. Wei, "A novel time-series model based on empirical mode decomposition for forecasting TAIEX," *Economic Modelling*, vol. 36, pp. 136–141, 2014.

[36] D. Lucas and J. Heaton, "Portfolio choice in the presence of background risk," *Economic Journal*, vol. 110, pp. 1–26, 2000.

Hindawi
Mathematical Problems in Engineering
Volume 2021, Article ID 8258778, 19 pages
https://doi.org/10.1155/2021/8258778

Research Article

COVID-19 as Information Transmitter to Global Equity Markets: Evidence from CEEMDAN-Based Transfer Entropy Approach

Peterson Owusu Junior,[1] **Siaw Frimpong**,[1] **Anokye M. Adam**,[1] **Samuel K. Agyei**,[1] **Emmanuel N. Gyamfi**,[2] **Daniel Agyapong**,[1] **and George Tweneboah**[3]

[1]*Department of Finance, School of Business, University of Cape Coast, Cape Coast, Ghana*
[2]*GIMPA Business School, Ghana Institute of Management and Public Administration, Accra, Ghana*
[3]*Wits Business School, University of the Witwatersrand, Johannesburg, Parktown, South Africa*

Correspondence should be addressed to Anokye M. Adam; aadam@ucc.edu.gh

Received 14 July 2021; Revised 1 August 2021; Accepted 13 August 2021; Published 27 August 2021

Academic Editor: Yuxing Li

This study provides an analysis of chaotic information transmission from the COVID-19 pandemic to global equity markets in a novel denoised frequency domain entropy framework. The current length of the pandemic data offers the opportunity to examine its role in the asymmetric behaviour patterns of investors according to time horizons and the diversification potentials available to them. We employ the total daily global confirmed cases of COVID-19 and 27 equity indices from December 31, 2019, to April 18, 2021. Our results corroborate the idea that diversification potentials are stronger in the short to medium term. The Global Index (higher risk) and Canada and New Zealand (lower risk) remain at both ends to pair some other equities to offer diversification prospects because of the transmission of information from COVID-19 to the selected equity markets. In addition, we provide the source of these diversification prospects as information flow rather than transmission of shocks, which is common in the literature. Furthermore, our results suggest detailed levels of risk (lower vis-à-vis higher) in the situation where they have been stripped of the noise in the market. The findings allow both investors and policymakers to make informed decisions based on the time horizons since the pandemic communicates different chaotic information with the lapse of time. This is imperative to avoid the negative consequences of the increasing infection rate on global stock markets.

1. Introduction

The outbreak of coronavirus disease 2019 (COVID-19) as an epidemic in Wuhan, China, took the world by surprise to become a global pandemic on March 11, 2020 (WHO, 2020). On April 18, 2020, the global confirmed cases of the pandemic had reached 141,404,998 with more than 387,352 deaths per million [1]. While there are ongoing mass vaccinations in different parts of the world, the spread of the virus has not come to a stop (https://covid19.who.int/). Different variants keep popping up in different places. However, the rate of spread has changed from an increasing rate to a decreasing rate. This suggests hopes of containing and finally providing a cure in the long term. However, the pandemic is still here and the economic, social, and financial havoc it has wreaked so far is yet to be fully quantified. This has led to major disruptions in personal lives, businesses, and economic activities, with more than half of the world's population currently under restrictions of movement and partial lockdown [2, 3]. The impact that "pausing" the economy may have on supply chains, household demand, and the financial stability of the economy is largely unknown [3].

Many governments across the globe have resorted to drastic measures such as enhanced quarantine processes, lockdown (total or partial), limiting human contacts through social distancing, and contact tracking and tracing through their cell phones to curb the rate of infection of COVID-19. As a panic result, a phenomenon due to COVID-19 fear erupted in all markets that have caused a shortage of food

and everyday goods in supermarkets and a drop in share prices [2, 4]. In the US, the stock market plunged by 12% amid COVID-19 fears against all 11 groups in the S&P 500 falling on March 16, 2020. Share prices in Asia and Europe also fell, and the yield of bonds declined in most parts of Europe, where a measure of market stress hit levels not experienced since the euro crisis in 2011-2012. On April 6, 2020, most stocks soared following a reduction in daily new cases over the previous weekend. The COVID-19 pandemic has proven its potency to be contagious with financial assets. This evidence corroborates the tenets of the efficient market theory, as it is known to its adherents. The hypothesis holds that the market prices of most stocks are correctly priced based on the information available at that time [5, 6]. The theory posits that when markets are efficient, all available relevant information about a financial asset is utilised in fixing current prices to reflect the fact that the optimal forecast return is equivalent to the market equilibrium return. Impliedly, information that suggests future economic activity is a key conditioning factor in determining the current prices of financial assets. Thus, this paper argues that global financial markets are likely to respond to communications on "pausing" the economy and its implications, such as a reduction in productive activities, an increase in unemployment, a gradual reduction in market participants, and the general uncertainty primarily caused by COVID-19. Based on the prediction of the efficient market theory, market prices are expected to dip under the current global conditions created by COVID-19. But the evidence against the theory such as the January effect, market overreaction, excessive volatility, mean reversion, and delayed effect of price responses to information [7, 8] and the fact that global financial market efficiency levels are not homogeneous place the empirical investigation in perspective.

Nonetheless, the behavioural patterns of investors tend to differ across time, especially under turbulent times such as those we are experiencing now. This asymmetric and time-based behaviour of investors is what reflect in the market prices because the market does not operate in a vacuum. Two theories that support this phenomenon are the adaptive market hypothesis (AMH) [9] and the heterogeneous market hypothesis (HMH) [10]. While the EMH assumes that the rationality of investors depends on neither time nor circumstances [11], Cornell [11] argues that rationality (and irrationality) is state-dependent over time and between investors. Thus, in "What is the Alternative to Market Efficiency" (AHME), Cornell [11] captures both AMH and HMH in the sense that the AMH enjoins the study of investor behaviour over small subsamples against the full sample. The latter reveal different levels of efficiency unlike the stationary and perpetually equilibrium notion of the EMH. Furthermore, the HMH advance that different economic agent takes their investment decisions on different time horizons in line with their risk and return preferences by analysing past and current news. To account for time horizon, the authors redefine time as intrinsic time which corresponds to time scales of short, medium, and long term. It becomes obvious that these behavioural dynamics introduce asymmetry, nonlinearity, nonstationary, and noise in the price-generating process of asset returns. Hence, empirical studies require methods that can account for all these complexities.

Theoretically and empirically, it is believed that these investor-generated complexities span across different markets that offer different levels, returns, and risks, in line with the generic idea of portfolio diversification. These markets are not only different, but their distinguishing feature is the competitive risks and returns they provide. Again, the market can be in the same asset class or not. Notably, competing risks and rewards seem to come from nontraditional asset classes such as cryptocurrencies, where traditional investors diversify into. Particularly, in turbulent market times, the assets and/or asset classes that competitively satisfy the investor's wishes are called safe havens [12]. Since the emergence of cryptocurrency as a nontraditional asset class, recent episodes of financial crises, and currently the COVID-19 pandemic, a plethora of studies have revisited the basic premise of portfolio diversification in search of competitive returns and risk levels [13–27]. The underlying thread in these and many studies is the idea that investors are always scouring competing risks and rewards and this search intensifies under stressed market conditions. Also, while information flows between markets precedents on investors' search, the flow deepens as well under difficult market periods. From the foregoing discourse, we sum this up and refer to it as the *competitive market hypothesis (CMH)*, which implies that, in part, the intensity of information flows and spillover between markets of the same and differing asset classes are exacerbated by rational, albeit irrational investors' relentless search of competing rewards and risks to satisfy the portfolio goals.

Generally, there is a paucity of literature on the relationship between pandemics and financial market behaviour. The tumbling of the various stock markets around the world offers the opportunity to understand their relationship with COVID-19. The relationship between pandemics and financial market prices could be direct through the related information dissemination channel and indirect through the pandemic-led weakened economic activity in the market because of a general reduction in income levels of market participants. Generally, empirical evidence suggests that the health conditions of economies help explain differences in wealth of nations [28–30] probably due to the loss of adequate and sufficient labour force. Barret et al. [31] argue that the cost of a pandemic goes beyond the loss of productivity due to sickness to include the cost of disease avoidance, caring for dependents, closure of schools, and the cost of dealing with behavioural changes that are likely to have economic outcomes.

The cost of COVID-19 is likely to also include loss of tax revenue, idle labour costs, increased social welfare cost, security cost, financial bailouts, damaged international relations, political mistrust, and hampering global efforts towards the achievement of sustainable development goals. Sander et al. [32] argue that pandemics such as influenza reduce per capita growth, but the extent of economic shrinkage depends on the mitigation measures put in place. Schwartz [33] corroborates this finding by predicting that a

deep coronavirus-induced recession in the US is virtually inevitable. Notwithstanding, governments are likely to reduce operating costs by functioning at close to half capacity, even though this is not likely to be significant. Projected reductions in per capita income can influence financial market activity through the indirect channel of reducing the economic well-being of market participants. Unfortunately, however, there are few existing empirical studies on the economic implications of COVID-19, whose end is shrouded in uncertainty. Policy decisions are likely to be less informed because according to Reinhart [34], historical episodes are nonexisting. The consequence may be the creation of another global problem because of the desperate measures to solve one. The thrust of this paper is to provide a baseline study to support the formulation of global policies in these extraordinary times. The paper extends the scope of Schoenfeld [35] who evaluated the effect of COVID-19 on markets in the United States to paint a global picture of the effect of the pandemic on global equity markets.

Since COVID-19 was declared a pandemic, many studies have trickled in what one may call a "mad rush" to publish. These early studies have attempted to examine the impact of the pandemic on many aspects of our lives. Nonetheless, given the span of data during those earlier stages, it was not feasible to tell a good story which naturally evolved over time. The news and reality of the pandemic triggered panic in the early stages but had abated with time with the reduced infection rates and vaccinations. For more than a year, different investors have had ample time to rebalance their portfolios as they monitor the markets in their decision-making processes. This is enough time for the adaptive and heterogeneous behaviour of investors to become evident. This allows us to adequately track the dynamic relations resulting from the pandemic through the time horizons as evidenced by frequency decomposition (also referred to as frequency domain). Many early studies bear the limitation of not being able to show these dynamics. Furthermore, others attempted to examine the relationship between COVID-19 and equities using wavelet coherence [36], between COVID-19 and energy commodities [37], and between financial and nonfinancial firms in China and G7 countries [38] with dynamic conditional correlation (DCC). Given the data-intensive nature of these techniques, the results from these studies can be perceived with caution. We opine that data-intensive studies with data spanning less than a year since the World Health Organisation (WHO) declared that the COVID-19 global pandemic may be a too small a sample. This is informed by a minimum forecasting length of one year as prescribed by the Bank for International Settlements (BIS) (https://www.bis.org/statistics/gli.htm?m=6%7C333%7C690).

On the other hand, many studies on the impact of COVID-19 on equities have focused mainly on the quantum of spillover between markets (see, e.g., [18, 39–45]). However, it is evident that, under the circumstances, the driving force of these transmissions is panic or fear from the pandemic. Thus, it is more prudent to quantify the information flow between the markets using the right technique. For two or more variables evolving in time, a theoretic information measure can be quantified in terms of the driving and responding transfer. This is the transfer entropy as predicted by Schreiber [46]. Rightfully, a growing number of studies have employed the transfer entropy in investigating the impact of COVID-19. Notable among these is the study by Lahmiri and Bekiros [47] who used the largest Lyapunov exponent (LLE) based on the Rosenstein method and approximate entropy. This study is motivated, in part, by the robustness of the method to small samples. However, the sample at this stage is no longer small. Regarding studies that have looked at the frequency domain impact of COVID-19 on equity markets under information transfer, the literature is booming. Lahmiri and Bekiros [47] examined the impact of COVID-19 on the randomness of global equity volatilities based on the Shannon entropy wavelet transform domain. Wang and Wang [48] also used multiscale transfer entropy to examine the effect of COVID-19 on major global equity, currencies, and Bitcoin. These studies suffer from small sample bias, on the one hand, and the use of Shannon entropy, on the other hand. As it will be clear soon, the Shannon entropy is weak in assigning equal weights to different portions during the distribution of the data (see also [49, 50]).

Our study is one of the few which fills these gaps identified in the literature. To do this, we employ the Complete Ensemble Empirical Mode Decomposition with Adaptive Noise- (CEEMDAN-) based entropy to quantify the information flow from COVID-19 to major global equities. In so doing, we use a longer sample period, which is needed to better understand the dynamics of investor behaviour. The CEEMDAN technique decomposes the time series into intramode decomposition (IMF) which represents different time horizons. This addresses the asymmetric, nonlinearity, and nonstationarity dynamics as espoused by the AMH and HMH. Another strong feature of the CEEMDAN is that it can strip the noise that is embedded in the data due to the behaviour of irrational investors. This is also supported by the AHME as it encompasses both AMH and HMH. Further, we employ a unique variant of entropy called Rényi entropy which can differentiate between the tails of the distribution by assigning appropriate weights. While it is well established that financial assets exhibit heavy tails, the Shannon entropy does not capture this. Particularly in a pandemic such as COVID-19, these fat tails are stronger and should be taken into account accordingly [51]. However, we provide results from the Shannon entropy for comparison purposes (see Figure 1 and Table 1).

Our study makes significant contributions to the nascent COVID-19 equity nexus. First, this is the first to employ noise-assisted techniques on equities to provide a clearer picture of the effect of the pandemic. It is shown that noise in signals (time series) can impact the results of the analysis to some extent that the noise can be more pronounced than the signal's effect [52]. The CEEMDAN reduces noise to its barest minimum. Second, the frequency decomposition itself offers a way to analyse the seemingly unwanted impact of the pandemic across time horizons. This allows investors and policymakers to tailor future decisions in line with the adaptive and heterogeneous nature of the market

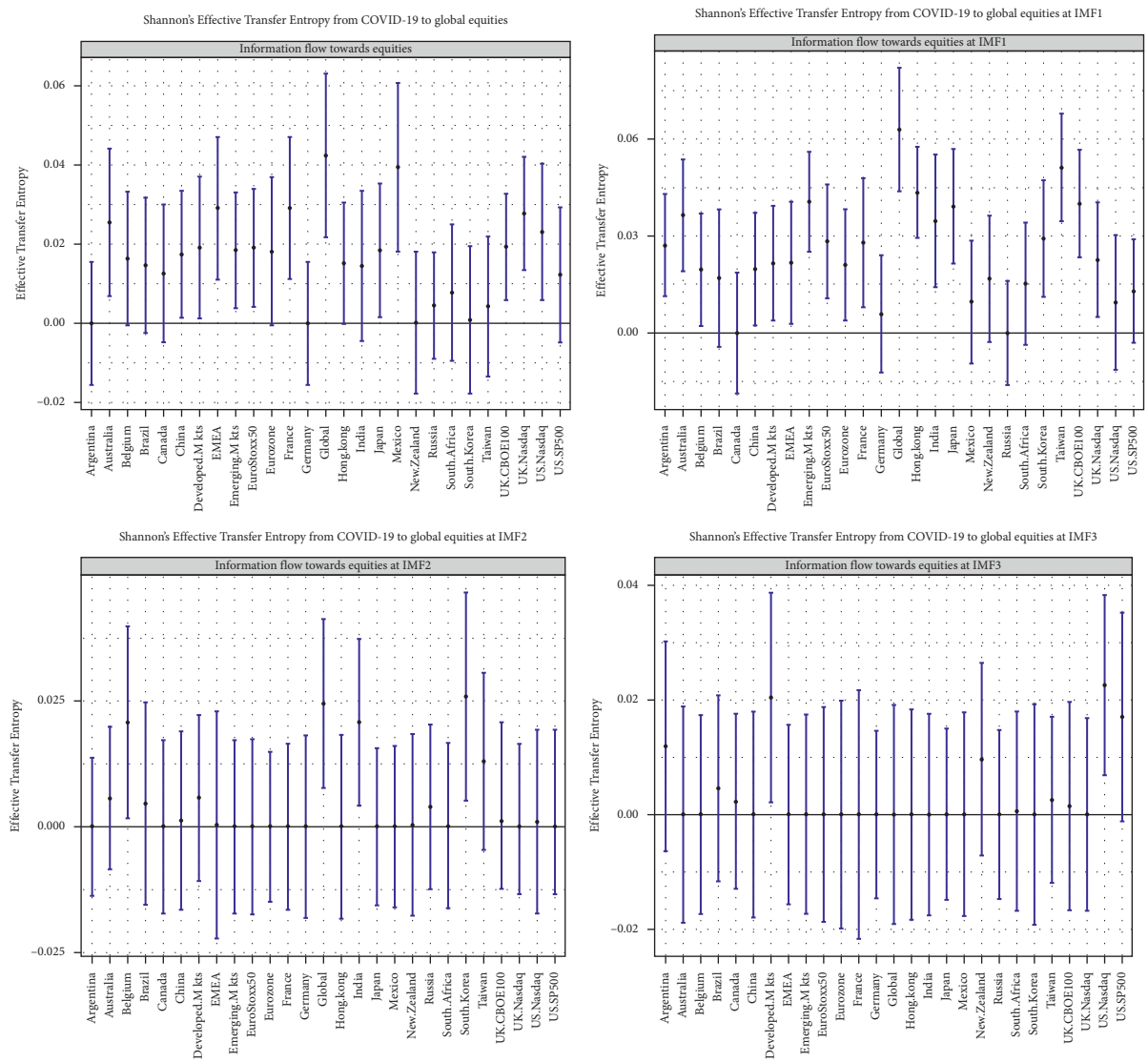

(a)

Figure 1: Continued.

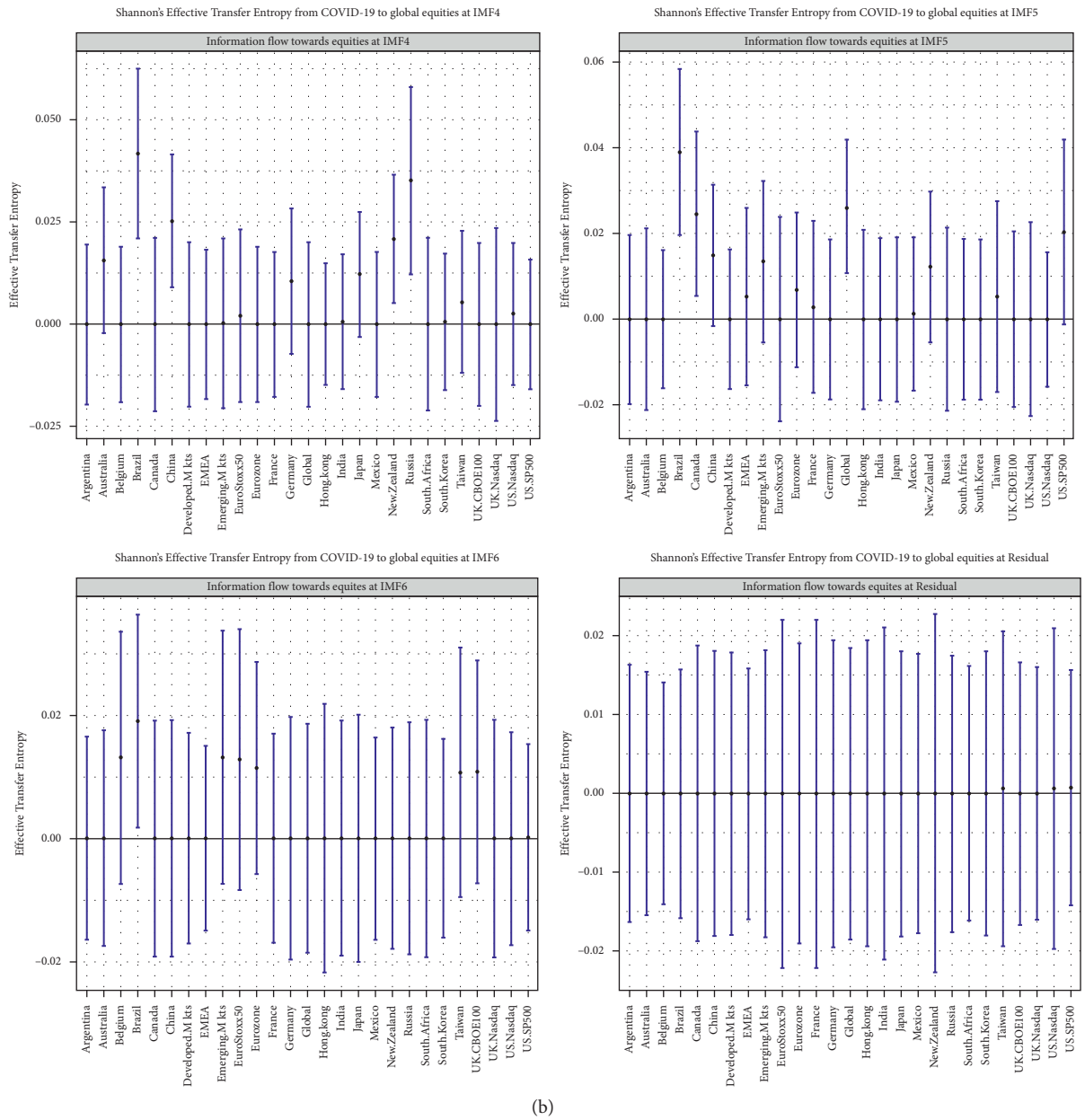

(b)

Figure 1: Shannon ETE from COVID-19 to global equity markets in composite and frequency domain.

Table 1: Summary effective transfer entropy from COVID-19 to global equities.

Series	Time horizon	Rényi		Shannon	
		Diversification potential	Equities involved		
Composite	—	Yes	Global versus Australia, Belgium, Canada, EMEA, France, Mexico, UK (CBOE100), and UK (Nasdaq)	No	—
IMF1	Short term	Yes	Global versus Argentina, China, UK (CBOE100), and UK (Nasdaq)	No	—
IMF2	Short term	No	—	No	—
IMF3	Short term	No	—	No	—
IMF4	Medium term	No	—	No	—
IMF5	Medium term	Yes	(Canada and New Zealand) versus Argentina, Belgium, EuroStoxx50, Germany, India, and Taiwan	No	—
IMF6	Medium term	No	—	No	—
Residual	Long term	No	—	No	—

participants. In the same vein, we provide an asymmetric, nonlinear, nonstationary, and nonparametric lens to view the effect of the pandemic on equity. These circumvent a myriad of estimation limitations which otherwise are difficult to deal with. Third, we use the transfer entropy technique to provide evidence quantifying the information flow between the markets. This is in contravention to spillover indices such as Diebold and Yilmaz [53] and Baruník and Křehlík [54], which ignore the intrinsic information driving the market. Transfer entropy methods also implicitly advance causality. In this case, we provide knowledge of the causality levels of COVID-19 to the global equity market. Thus, our study offers a result on asymmetric, nonlinear, and nonparametric causality. The use of this rich causality information is important for both policy and investment.

Fourth, since we employ the Rényi transfer entropy [55], we provide COVID-19 impact results that are consistent with stylised financial returns. In this regard, readers are confident that the fat-tail and leverage effect of asset returns have been accounted for. This knowledge is indispensable to make the right investment decision on asset allocation and risk analysis. Furthermore, we use the Rényi entropy to estimate the effective transfer entropy (ETE) which delineates lower-risk assets from higher-risk assets. The ETE provides negative and positive estimates for higher risk and lower-risk assets, respectively. With this information, investors are confident in the combination of assets in their portfolio, which can help minimize risk and achieve high returns during this pandemic. One novel contribution of this study is that we can diversify based on quantified negative and positive transfer of information rather than just spillover, as is commonplace in the diversification literature. This is a new lens through which to view diversification in a distribution-free asymmetric nonlinear frequency domain framework.

Overall, our results show that negative recipients increase with time horizon (IMFs) while positive recipients reduce. At the composite level, the Global Index (higher risk) can be paired with Australia, Belgium, Canada, EMEA, France, Mexico, UK CBOE100, and UK (Nasdaq), which are lower-risk assets. We find more diversification potential in the short term for the Global Index (higher risk) paired with Argentina, China, the UK, CBOE100, and the UK (Nasdaq) (lower risk) indices. In the medium term, Canada and New Zealand (lower risk) can be combined with Argentina, Belgium, EuroStoxx50, Germany, India, and Taiwan (higher risk) equities.

The remainder of the paper is structured as follows. In Section 2, the methodologies and CEEMDAN-based Rényi transfer entropy are presented. In Section 3, information on the data used and preliminary outputs is presented. Analysis of the main results is contained in Section 4, and Section 5 concludes the study.

2. Methodology

Our methodology involves a two-stage approach. First, we decompose the equity indices into intrinsic mode functions (IMFs) using the CEEMDAN technique. The IMFs denote intrinsic time that correspond to short, medium, and long terms. This allows us to determine the effects of COVID-19 in different decision-making time frames. Second, we estimate the effective transfer entropy using the Rényi entropy (RE) specification. The RE quantifies the information flow from COVID-19 to the equity markets by assigning much weight to the tail of the distributions in line with the extant literature. Together, these combined methods address asymmetry, nonlinearity, and nonstationarity in the series [56] in a nonparametric way. In this study, we have elected to examine the unidirectional flow of information from COVID-19 to the equity markets. It is logical to assume that there is no transfer of information in the reverse direction. We also decide to keep the COVID-19 series in its composite form without decomposition. This choice is premised on the fact that the COVID-19 pandemic is not economic agent that updates its decision across time horizons. However, investors adjust their decisions based on the trend exhibited by the pandemic in the number of confirmed cases.

2.1. Complete Ensemble Empirical Mode Decomposition. Ramsey and Lampart [57] correctly put it that economists have long known that the relationships between variables in terms of form, degree, and direction differ across time horizons. However, the tools to decompose economic time series into all orthogonal time-scale components have been lacking until now. Further, tools for dealing with noise that usually dominates financial time series in the short term are currently available [57, 58]. A typical example is the CEEMDAN which is the latest of the empirical mode decomposition (EMD) sequel started by Huang [59]. The strength of mode decomposition is its efficiency, reconstruction accuracy, and minimization of the noise-to-signal ratio (SNR) in unstable state signals [60]. The CEEMDAN proposed by Torres et al. [61] comes out on top in these qualities compared to their predecessors. For instance, while the EEMD does a relatively good job in removing noise, it fails to fully recover the original signal with the sum of IMFs. This limitation does not allow the EEMD to determine the SNR. However, CEEMDAN has mechanisms to obtain the SNR by appending the white noise to the residual of previous iterations instead of to the original signal [62]. We use the CEEMDAN mainly due to its noise-removal strength, especially for this study period of panic in the financial markets caused by the COVID-19. We implement this with the *libeemd* package (in the R environment for statistical computing and graphics).

The CEEMDAN algorithm is summarised as follows, adapted from Liu et al. [63]:

(1) Add a Gaussian white noise $\omega_k(t)$ of different amplitudes to a signal $x(t) = s(t) + n(t)$, where $s(t)$ is the actual signal and $n(t)$ is the noise. This results in many new signals:

$$x_k(t) = x(t) + \omega_k(t). \tag{1}$$

(2) Employ EMD technique to decompose (1) to obtain the first IMF.

(3) Estimate the average of this first IMF as

$$\overline{\mathrm{IMF}_1(n)} = \frac{1}{K}\sum_{k=1}^{K}\mathrm{IMF}_{1k}(t). \tag{2}$$

(4) Calculate the remainder of signal components C_n of the original signal as

$$C_n = \begin{cases} x(t) - \mathrm{IMF}_1(n), & n = 1, \\ C_{n-1} - \mathrm{IMF}_1(n), & n > 1. \end{cases} \tag{3}$$

(5) The ρ-th component post-EMD of the signal is denoted by E_ρ. Subsequent components ($L + 1$ IMFs) can be obtained by

$$\mathrm{IMF}_{(L+1)}(n) = \frac{1}{K}\sum_{k=1}^{K} E_L\{C_L(t) + \sigma_L E_L(\omega_k(t))\}. \tag{4}$$

(6) Last, the n steady-state IMFs are reconstructed to produce the original signal as

$$x(t) = C(t) + \sum_{m=1}^{M}\overline{\mathrm{IMF}_m}(t). \tag{5}$$

The total number of IMFs (and one residual) of a time series signal is given as $\log_2 N$, where $N = T$ (number of observations). For further reading on the empirical mode decomposition sequel; see [64–66].

2.2. Rényi Transfer Entropy. Transfer entropy finds its root in the general information theory of Hartley [67]. Hartley's [67] theory measures information via an algorithm on all possible number of symbolic sequences that can occur in a specific probability distribution [68, 69]. The current literature on transfer entropy is based on the mathematical theory of communication by Shannon [70] as a measure of uncertainty, a derivation of information theory.

For a probability distribution with diverse symbols of a given experiment P_j, each symbol's average information is specified as

$$H = \sum_{j=1}^{n} P_j \log_2\left(\frac{1}{P_j}\right)\text{bits}, \tag{6}$$

where n denotes the number of distinct symbols with respect to the probabilities p_j [67]. In the Shannon's [70] framework (hereafter referred to as Shannon entropy), for a discrete random variable J with probability distribution $p(j)$, the average number of bits needed to optimally encode independent draws can be given as [68]

$$H_J = -\sum_{j=1}^{n} p(j)\log_2\, p(j). \tag{7}$$

Under the assumption that two time series processes are Markov, Shannon entropy's measure of information flow between these processes is borrowed from the Kullback and Leibler [71] distance model. We present I and J as two discrete random variables with corresponding marginal probabilities of $p(i)$ and $p(j)$, joint probability $p(i, j)$, with dynamic stationary Markov process of order k (process I) and I (process J). The Markov property implies that the probability to observe I at time $t + 1$ in the state i conditional on the k previous observations is $p(i_{t+1}|i_t, \ldots, i_{t-k+1}) = p(i_{t+1}|i_t, \ldots, i_{t-k})$. To encode the observation at $t + 1$, the average bits number needed before k values is known, which can be illustrated as

$$h_j(k) = -\sum_{i} p\left(i_{t+1}, i_t^{(k)}\right)\log_2\, p\left(i_{t+1}|i_t^{(k)}\right), \tag{8}$$

where $i_t^{(k)} = (i_t, \ldots, i_{t-k+1})$ (analogously for process J). In a bivariate case, relying on the Kullback–Leibler distance, the information flow from process J to process I is measured by quantifying the deviation from the generalised Markov property $p(i_{t+1}|i_t^{(k)}) = p(i_{t+1}|i_t^{(k)}, j_t^{(I)})$. The Shannon transfer entropy is then given as

$$T_{J\longrightarrow I}(k, l) = \sum P\left(i_{t+1}, i_t^{(k)}, j_t^{(I)}\right)\log\frac{P\left(i_{t+1}|i_t^{(k)}, j_t^{(I)}\right)}{P\left(i_{t+1}|i_t^{(k)}\right)}, \tag{9}$$

where $T_{J\longrightarrow I}$ calculates the information flow from J to I. Conversely, the information flow from I to J, $T_{I\longrightarrow J}$, can be derived. The dominant direction of the information flow can be referred to as the net information flow calculated as the difference between $T_{J\longrightarrow I}$ and $T_{I\longrightarrow J}$.

While the Shannon entropy is useful, in the financial setting, it is lacking in assigning equal weights to all possible realisation in the specified probability distribution. This assumption does not account for heavy tails which are rife in asset prices and returns. However, the Rényi [55] transfer entropy (RE) solves this problem through a weighting parameter q. The RE can be calculated as

$$H_J^q = \frac{1}{1-q}\log_2\sum_j P^q(j), \tag{10}$$

with $q > 0$. For $q \longrightarrow 1$, RE converges to Shannon entropy. For $0 < q < 1$, thus, low probability events receive more weight, while for $q > 1$, the weights benefit outcomes j with a higher initial probability. As a result, Rényi entropy allows for emphasis to be placed on different portions of the distribution, depending on parameter q [13, 68]. This is the desirable feature of the RE financial applications, as against the Shannon entropy.

Further, with the escort distribution, $\varnothing_q(j) = p^q(j)/\sum_j p^q(j)$ for $q > 0$ to normalise the weighted distributions [72], RE is derived as

$$\mathrm{RE}_{J\longrightarrow I}(k,l) = \frac{1}{1-q}\, p\left(i_{t+1}, i_t^{(k)}, j_t^{(I)}\right)\log_2 \frac{\sum_i \varnothing_q\left(i_t^{(k)}\right) P^q\left(i_{t+1}|i_t^{(k)}\right)}{\sum_{i,j} \varnothing_q\left(i_t^{(k)}, j_t^{(I)}\right) P^q\left(i_{t+1}|i_t^{(k)}, j_t^{(I)}\right)}. \tag{11}$$

Note that the calculation of the Rényi transfer entropy can result in negative values. In such a situation, knowing the history of J depicts even greater uncertainty than would otherwise be indicated by only knowing the history of I alone. In the application of our study, negative values depict higher risk while positive values indicate lower risks.

In small samples, transfer entropy estimates tend to be biased [73]. This can be corrected by calculating the effective transfer entropy (ETE) as

$$\mathrm{ETE}_{J\longrightarrow I}(k,l) = T_{J\longrightarrow I}(k,l) - T_{J\mathrm{shuffled}\longrightarrow I}(k,l), \tag{12}$$

where $T_{J\mathrm{shuffled}\longrightarrow I}(k,l)$ denote the transfer entropy using shuffled versions of the time series J. By repeated random drawings of the observed time series J and realigning them to generate a new time series, the process destroys the time series serial dependencies of J, while keeping any statistical dependencies between J and I. This directs $T_{J\mathrm{shuffled}\longrightarrow I}(k,l)$ to converge to zero with an increasing sample size, and any nonzero value of $T_{J\mathrm{shuffled}\longrightarrow I}(k,l)$ is due to small sample effects. Thus, repeated shuffling and the average of the resulting shuffled transfer entropy estimates across all replications serve as an estimator for the small sample bias. These are subtracted from the RE estimate to obtain bias-corrected effective transfer entropy estimates.

The statistical significance of the transfer entropy estimates can be determined using the Markov block bootstrap technique. This preserves the dependencies within the variables J and I but eliminates the statistical dependencies between them unlike shuffling. Thus, bootstrapping provides a distribution of transfer entropy estimates to be tested under the null hypothesis of no information flow. The associated p – value is given by $1 - \widehat{q}\mathrm{T}$, where $\widehat{q}\mathrm{T}$ denotes the quantile of the simulated distribution that is determined by the respective transfer entropy estimate [68].

Last, since transfer entropy algorithms are originally based on discrete data, continuous data used in the framework need to be discretised. This can be done by partitioning the data into a finite set of bins; the process is known as symbolic encoding [68]. For a number of bins n, with bounds $q_1, q_2, q_3, \ldots, q_{n-1}$ $(q_1 < q_2 < q_3 < \cdots < q_{n-1})$ and continuous observed time series data y_t, the symbolically encoded time series (i.e., discrete) can be given as

$$S_t = \begin{cases} 1, & y_t \le q_1, \\ 2, & q_1 < y_t < q_2, \\ \vdots & \\ n-1, & q_{n-2} < y_t < q_{n-1}, \\ n, & y_t \ge q_{n-1}. \end{cases} \tag{13}$$

The choice of the number of bins must be informed by the size and distribution of the observed time series. Since tail observations are of importance, binning is usually based on the empirical quantiles of the left and right tails. This is easily achieved by choosing the 5% and 95% empirical quantiles as lower and upper bounds of the bins. This results in three symbolic encodings where the first bin (5%) comprises negative extreme returns (i.e., lower tail), the third bin (95%) captures positive extreme returns (upper tail), and the second bin (middle 90%) contains the normal returns. By making use of the chain rule on the symbolic encoding, conditional probabilities can be written as fractions of joint probability. In that case, the probabilities in equations (9) and (11) can be computed by the relative frequencies of all possible realisation. See Behrendt et al. [68] for a complete description.

3. Data and Preliminary Analysis

We used daily closing prices of the 27 world equity indices from 20 countries, 4 economic blocs (Developed Markets, Emerging Markets, Europe, Middle East, Africa (EMEA), and Eurozone), and the Nasdaq Global Equity Index. We track the information transfer from the daily global confirmed cases of COVID-19 from December 31, 2019, to April 18, 2021. The data on equity indices and COVID-19 (see Table 2) were retrieved from the *EquityRT* and *Our World in Data* (https://ourworldindata.org/coronavirus) platforms, respectively. Some of the selected indices are overlapping in the sense that some are subsets of others. This is helpful to ascertain both aggregate and disaggregated impact of COVID-19. It is obvious that all the indices are subsets of the Global Index. The descriptive statistics of the returns of all equity indices and confirmed COVID-19 cases are presented in Table 2. The returns were calculated as the difference of logarithms for consecutive closing indices as $r_t = \log(P_{t+1}) - \log(P_t)$, where r_t is the return from period t to $t+1$ and P_t and P_{t+1} are observations at periods t and $t+1$, respectively. To facilitate comparison, all the series have been matched by date to balance.

Table 2: Descriptive statistics of equity return and COVID-19 confirmed cases.

Country (equity index)	Min.	Max.	Mean.	Std. dev.	Skewness	Kurtosis these are excess kurtosis values
Argentina (Merval)	−0.1587	0.0962	−0.0030	0.0303	−0.5499	4.0402
Australia (ASX 200)	−0.1122	0.0755	0.0003	0.0193	−1.3039	9.3884
Belgium (BL20)	−0.1618	0.0629	0.0010	0.0194	−2.6899	23.4941
Brazil (Ibovespa)	−0.2038	0.1608	−0.0009	0.0322	−1.0793	10.7386
Canada (TSX Comp. Index)	−0.1372	0.0863	0.0011	0.0189	−2.3079	18.9526
China (SSE Comp. Index)	−0.0472	0.0621	0.0007	0.0116	0.5450	4.4084
Eurozone (EuroStoxx50)	−0.1409	0.0628	0.0011	0.0182	−2.3791	18.0107
France (CAC 40)	−0.1395	0.0740	0.0011	0.0185	−2.0936	16.9682
Germany (DAX)	−0.1391	0.0493	0.0011	0.0181	−2.4053	17.3262
Hong Kong (Heng Seng Index)	−0.0574	0.0377	−0.0002	0.0132	−0.5067	2.2285
India (BSE SENSEX)	−0.0932	0.0947	0.0018	0.0190	−0.2215	6.2844
Japan (Nasdaq Index)	−0.0668	0.0684	0.0005	0.0137	−0.1635	6.1673
Mexico (Nasdaq Index)	−0.1532	0.1106	−0.0001	0.0322	−0.8090	4.3852
New Zealand (Nasdaq Index)	−0.0866	0.0652	0.0016	0.0162	−0.6615	5.9766
Russia (Moex Russia Index)	−0.0909	0.0504	0.0005	0.0197	−0.5886	2.2965
South Africa (FTSE/JSE Index)	−0.1264	0.0721	0.0016	0.0215	−1.0916	7.1083
South Korea (KOSPI)	−0.1147	0.0861	0.0009	0.0198	−1.1480	7.1550
Taiwan (TAIEX Index)	−0.0676	0.0376	0.0008	0.0124	−1.1693	4.9676
UK 1 (CBOE 100)	−0.1290	0.0558	0.0003	0.0180	−1.7788	12.8458
US 1 (S&P 500)	−0.0999	0.0888	0.0011	0.0179	−0.4174	8.2283
UK 2 (Nasdaq)	−0.1404	0.0551	0.0005	0.0180	−2.3834	18.0158
US 2 (Nasdaq)	−0.0991	0.0893	0.0012	0.0196	−0.4722	5.2161
Nasdaq Dev. Mkts	−0.1034	0.0514	0.0011	0.0149	−1.8690	13.3438
Nasdaq EM	−0.0790	0.0472	0.0008	0.0136	−1.1082	6.7668
Nasdaq EMEA	−0.1385	0.0431	0.0010	0.0166	−3.2909	24.8351
Nasdaq Eurozone	−0.1507	0.0486	0.0012	0.0179	−3.2665	25.4667
Nasdaq Global	−0.1219	0.0777	0.0015	0.0249	−0.9766	4.0239
COVID-19	0.0026	0.2890	0.0215	0.0330	4.3780	24.7706

Before we delve into the statistical distribution of returns, it is appropriate to have a quick look at the behavioural trajectories of the indices under consideration and COVID-19 confirmed cases. Figure 2 shows the graphical representation of the trend of the time series of the indices of the 27 stock markets and COVID-19 confirmed cases over the study period. A glance shows that all the indices saw a sharp downward trend in the early days of the pandemic which was rising quickly. While the COVID-19 confirmed cases have kept rising until now, more calm returned to the markets as we see upward trends as many countries embarked on lockdown from early February of 2020. However, the markets started to dip again when most countries came out of lockdown, and international travels resumed gradually beginning October 2020. This resulted in a second wave of the virus leading up to the Chistmas festivities. [74] Conversely, there has been an upward trend in the markets after the Christmas season as fears of the second wave abated. The downward trend of the indices reflects the investors and economic reaction to catastrophic events such as pandemics [32]. It is natural to see the inverse relationship between pandemic and financial markets.

A cursory glance at the descriptive statistics of the returns presented in Table 2 reveals interesting features of the return rates of the included stock markets. All 27 indices had positive means in the period considered, except for Argentina, Brazil, Hong Kong, and Mexico. Thus, on average only a few countries have had losses on their equity markets due to COVID-19. In terms of skewness, all countries record higher losses more frequently than higher gains, which is indicated by negative skewness, except for China. This not surprising because China is one of a few countries which have managed the pandemic effectively despite being its origin.

Currently, China ranks 98 out of 221 countries in confirmed cases (https://www.worldometers.info/coronavirus/countries-where-coronavirus-has-spread/). Many countries have recorded only a few hundred cases after the 196th rank and many bottom countries have single-digit confirmed cases. These explain why China's equity market could record higher returns than lower returns. The returns of all assets showed excess kurtosis. This implies that the returns are heavy-tailed relative to the normal distribution. This is not surprising, as it is a well-known stylised fact about financial assets [75].

4. Analysis of Rényi Entropy Results

At this stage, we address the main objective of this study. We analyse the information transfer from COVID-19 to the selected global equities. We only examine unidirectional transmission from COVID-19 to the equity markets since the equities do not have the potential to influence COVID-19 confirmed cases. Effective transfer entropies (ETEs) from the Rényian entropy framework result in both negative (high risk) and positive (low risk) values. This allows for diversification potential by pairing negative receiving ETEs equities with positive recipients. In line with the stylised facts

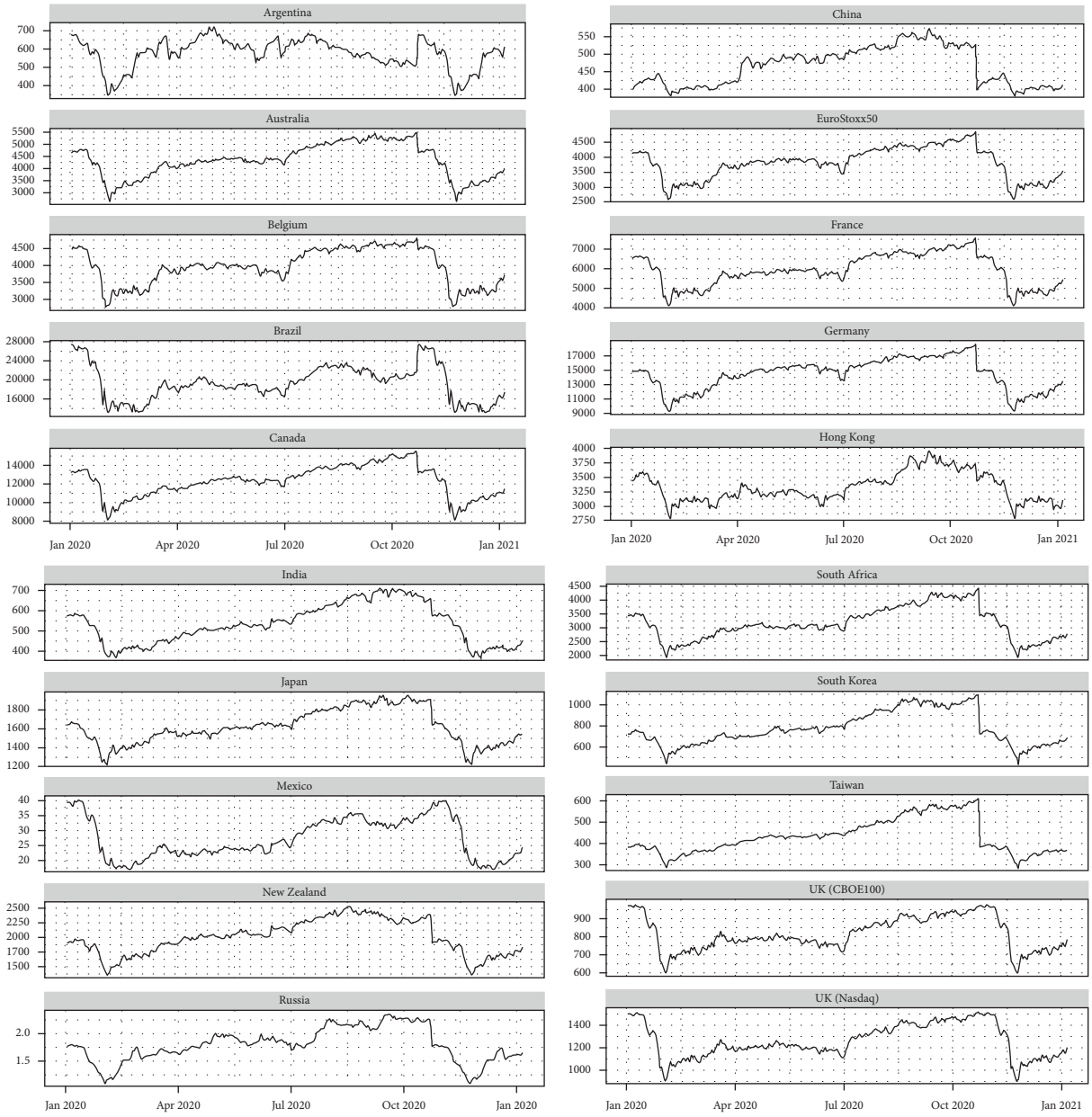

(a)

Figure 2: Continued.

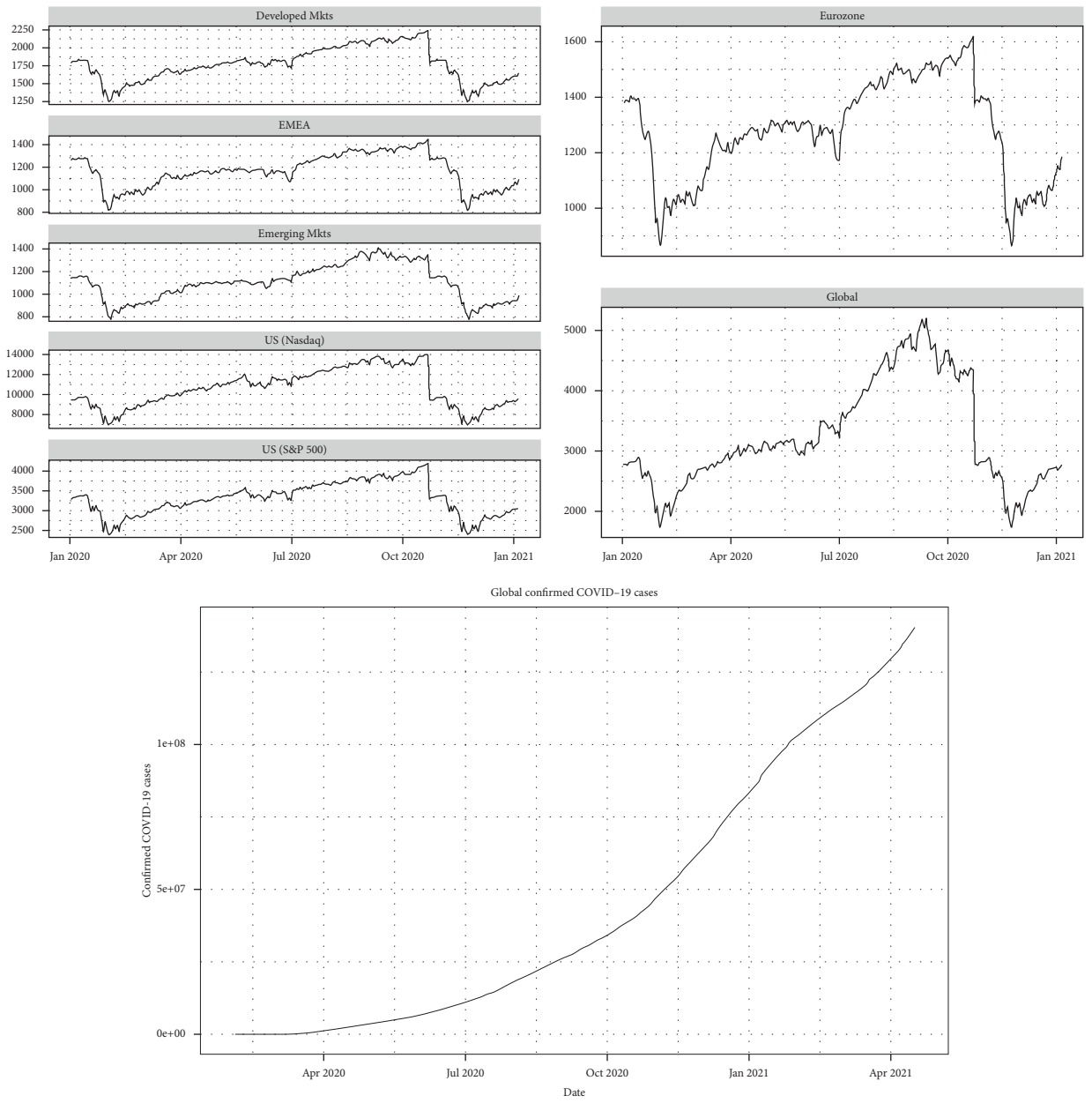

(b)

Figure 2: Time series plot of COVID-19 and global equities.

of financial returns, we choose the fault weight of 0.30 to account for heavy tails in the equity returns. We also present results for both the composite level and frequency domain. In the latter, intrinsic times are indicated by IMF1 through to IMF6 and Residual. These are representative of short-, medium-, and long-term dynamics, where the residuals denote the long-term trend, which implies the fundamental behaviour of the respective series. These time horizons enable us to analyse the evolving response of the markets to the pandemic.

In Figures 2 (composite level) and 3 (frequency domain), ETEs are indicated by black points inside blue bars. The ends of the blue bars indicate 95% confidence bounds. For this reason, these confidence bounds should be in either the positive or negative regions for us to fail to accept the null hypothesis of no information flow. Any overlap at the origin shows an insignificant information flow. From Figure 3, we find mostly positive information transfer (ETE) from COVID-19 to the equities, except for Argentina, Brazil, Germany, and Global Index which are negative. Therefore, COVID-19 creates a high risk for Argentina, Brazil, Germany, and the Global Index, but a low risk for the rest.

However, all these ETEs are not statistically significant. Only the Global Index receives a statistically significant negative information flow from COVID-19. However, there are significant positive information flows only to Australia,

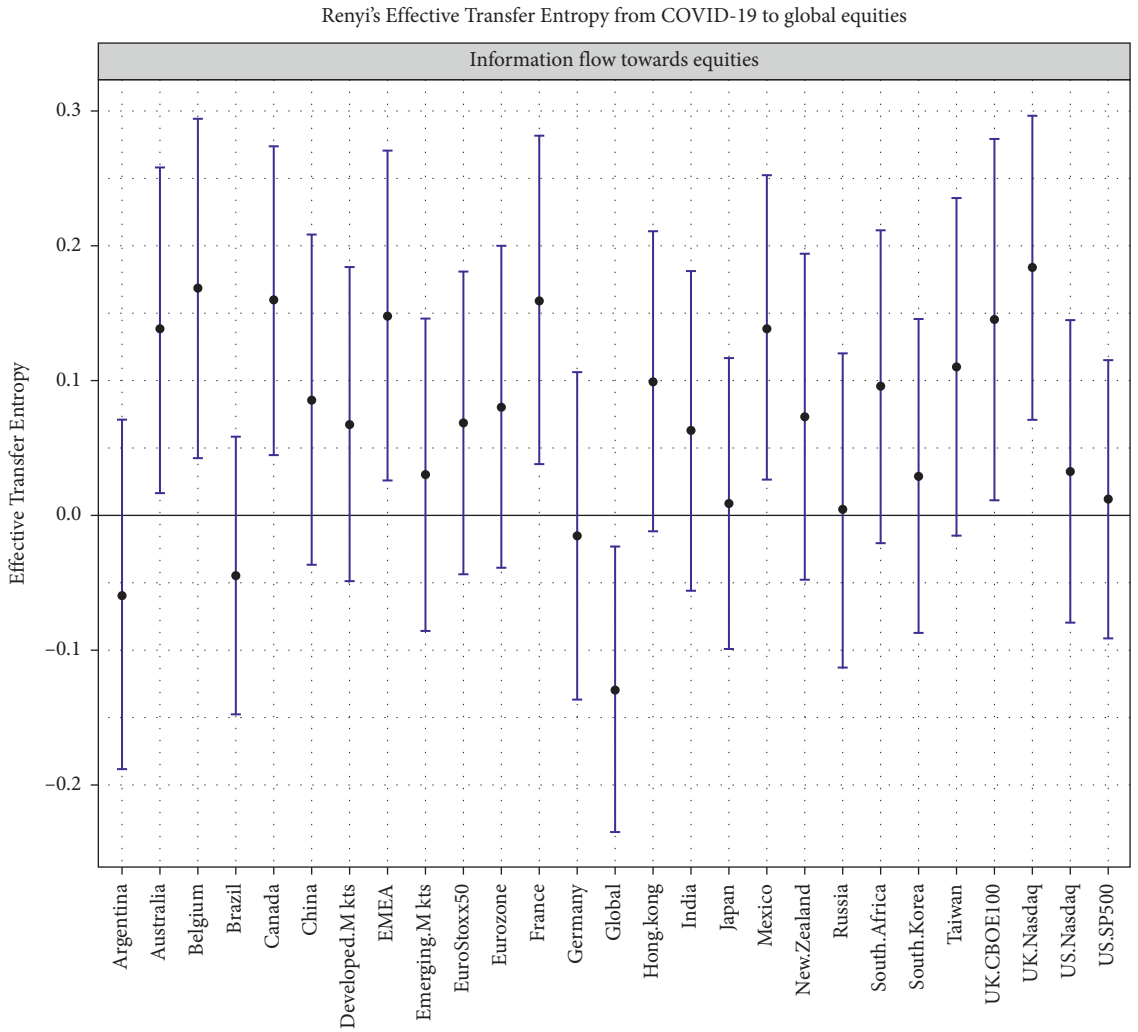

Figure 3: Rényian ETE from COVID-19 to global equity markets at the composite level.

Belgium, Canada, EMEA, France, Mexico, UK (CBOE100), and UK (Nasdaq) (recording the highest). The pandemic that fosters high risks in the global equity market is not a surprise. This is a pandemic that has never been seen in modern history and panic associated with it somehow can surpass the real havoc it is inflicting. However, for countries that have managed this well and have stronger financial systems, the composite effect of the pandemic should not be so devastating. This is true as investors tend to take refuge by investing in more advanced and stable economies during crises [76]. We also assume that the impact of COVID-19 is not all doom and gloom, but an avenue to diversify portfolios to reduce risk. Given the negative and positive ETEs, international investors are presented with the opportunity to combine the Global Index as a high-risk asset with any of the equities of Australia, Belgium, Canada, EMEA, France, Mexico, UK (CBOE100), and UK (Nasdaq) to mitigate their risk exposure.

From Figure 4, in the short term of IMF1, there is an increase in the number of equities that receive negative information flow (7: Brazil, Canada, Germany, Global, India, Russia, South Korea, and Taiwan) compared to the composite series (4: Argentina, Brazil, Germany, and Global). Among these, on the ETE to Global Index, Argentina, China (highest), UK (CBOE100), and UK (Nasdaq) are significant. Hence, the Global Index could be bundled with the positive recipients to mitigate risks. At IMF2, negative receiving equities increased to 18 out of 27, but only 3 (Global, Hong Kong (highest), and Mexico) are significant. Given that there are no significant lower-risk assets, no diversification avenue exists at this scale. The pattern holds for IMF3 and IMF4 as well. Negative ETE recipients increase, some significant, while all positive flows are insignificant. These do not offer diversification prospects, as COVID-19 information transmission produces only high-risk assets.

There is a change in the pattern at the medium term of IMF5 where significant positive transmissions are recorded by Canada and New Zealand as negative receipts again by Argentina, Belgium, EuroStoxx50, Germany, India, and Taiwan. It is clear that combinations can help reduce portfolio risk. However, at the long-term scales of IMF6 and Residual diversification potential vanish [77]. In IMF6, all markets receive negative information flows from the

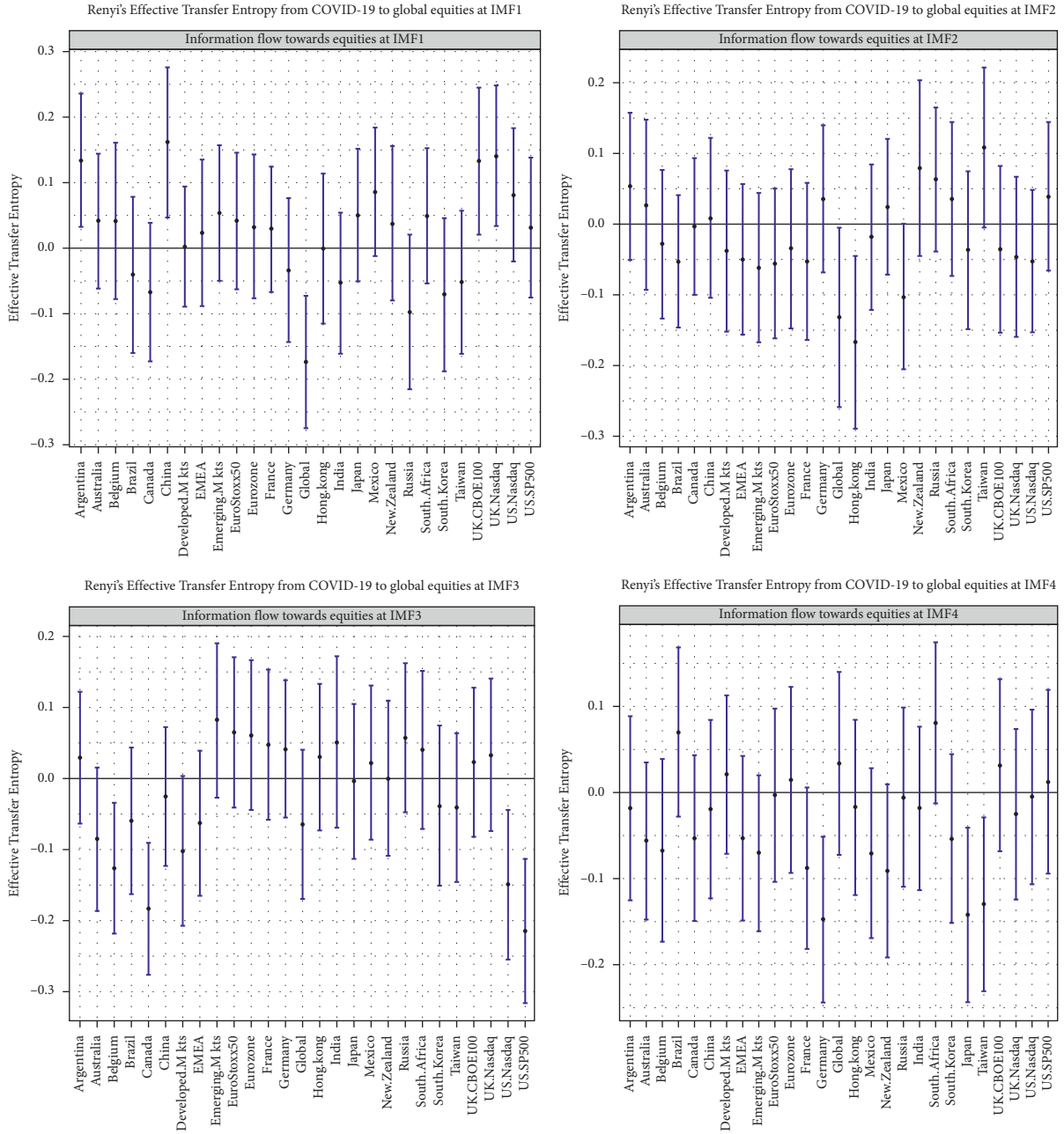

(a)

Figure 4: Continued.

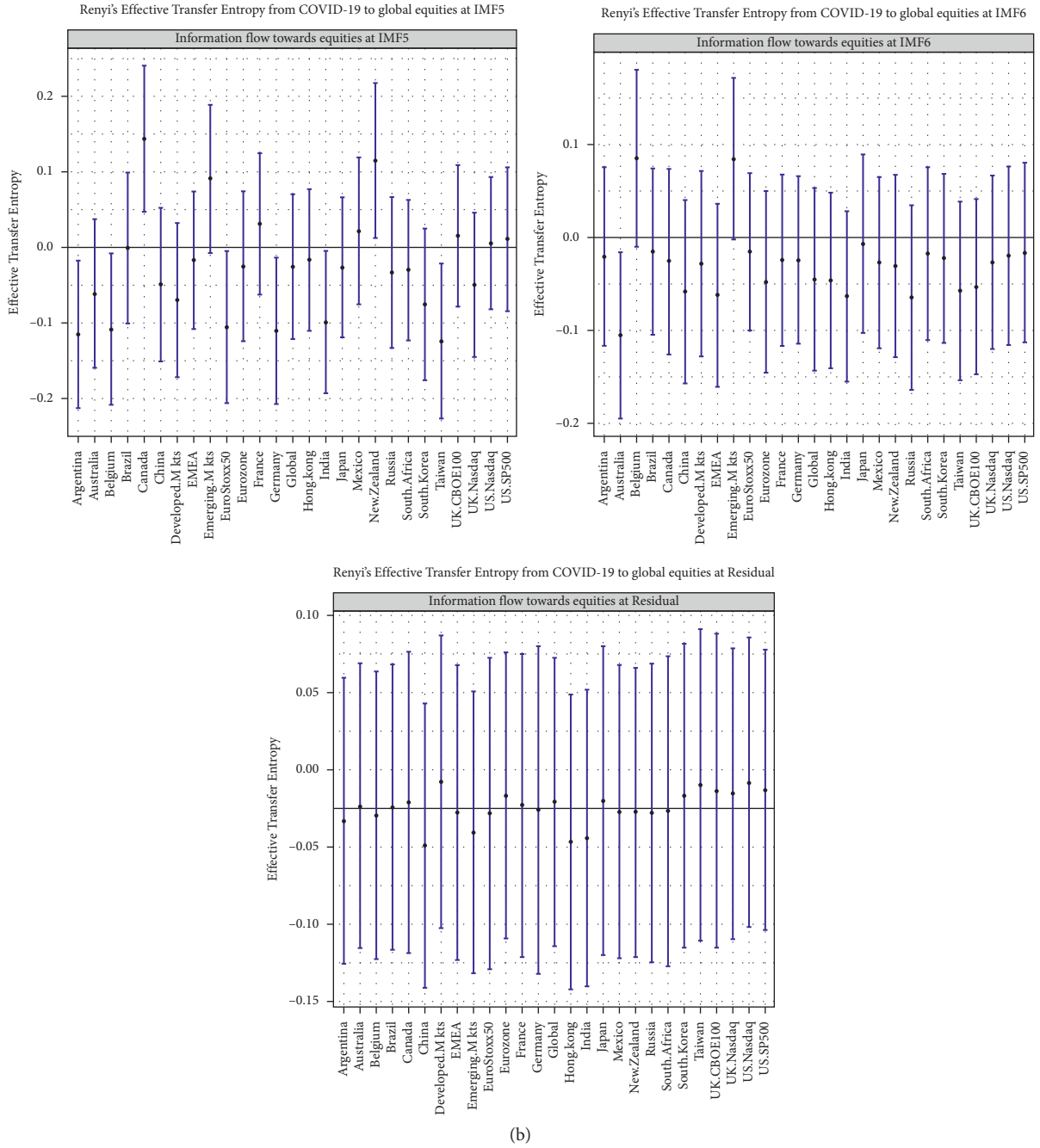

(b)

Figure 4: Rényian ETE from COVID-19 to global equity markets in frequency domain.

COVID-19 pandemic, except for Belgium and emerging markets, but only Australia's is statistically significant. Contrary to EMH, the differing transfer entropies of positive and negative across different time scales confirm the adaptive market hypothesis (AMH) of Lo [9], heterogeneous market hypothesis (HMH) of Müller et al. [10], and alternative hypothesis to market efficiency by Cornell [11]. In addition, the results confirm the *competitive market hypothesis (CMH)* proposed in this study. In all, the results suggest that investors adapt to market dynamics-based sentiment, risk, and reward preferences across time and assets in search for competition compensations to satisfy their goals.

When the fundamental structure of the equity markets is revealed at the Residual scale, all COVID-19 transmits only negative information to all the COVID-19 pandemic but none of them is statistically significant. While the negative flows do not come as surprise, their insignificance communicates an important message to all stakeholders in the financial market. Fundamentally, the pandemic (the number of global infections and the fear associated with it) does not affect the equity markets. We can consider short-term and

medium-term transmissions as the products of irrational investor behaviour which many see as noise [11, 52]. We purport that in the long term investors may have allayed their fears and rebalanced their portfolios only marginally incorporating the news about the pandemic. For prospective investors and policymakers, the pandemic may not be used as an important variable in arriving at investment and policy decisions concerning global equities. The reason is that the pandemic does not communicate any risks attributes (neither positive nor negative) of the equities to be used in investment and allocation of resources across assets as well as COVID-19 relief packages to the financial or equity markets. In many aspects, this paradigm reflects the efficient market hypothesis (EMH) by Fama [5, 6] in the sense that the rationality of the market participants is revealed in spite of the ensuing pandemic. This also confirms the long-term market efficiency [6].

In the spirit of the existing literature, we consider IMF1, IMF2, and IMF3 to represent the short term, IMF4 and IMF5 to capture the medium term, and IMF6 and Residual to denote long-term dynamics, respectively [25, 58, 78, 79]. Yang et al. [58] interpret the short term as a period driven by investor sentiments and market microstructure, the medium term as representing the effect of significant events, and the long term as representative of fundamental values. These demarcations imply that our results are mixed in terms of diversification potentials, being present and absent simultaneously in the short and medium term, as well as at the composite scale. The summary of the results is presented in Table 1. We also note that, although they vary in magnitude, equity markets receiving both positive and negative significant ETEs are from a mixture of countries and regions that are hard vis-à-vis soft hit by COVID-19 with respect to confirmed cases and fatalities https://www.worldometers.info/coronavirus/countries-where-coronavirus-has-spread/. Hence, it may suggest that while we are in the midst of a global pandemic, COVID-19 is not the only force driving the equity markets. Countries and economic blocs already have underlying fundamentals which determine their performance to a large extent. It is also natural to assume that the extent of the impact of COVID-19 on an equity market is a function of the economic, financial, social, health, technological, and environmental fabric of its host economy. We find empirical support for this analogy in [80] that economies with strong institutions and macroeconomic fundamentals are less impacted by the pandemic.

In the empirical literature, our frequency domain findings corroborate and contradict several studies. The asymmetry in the flow of information in the equity markets is consistent with the sentiment and the connectivity of return and volatility among global equities [49, 50]. The insignificant ETEs in the long term contradict the findings of [81] that connectedness across financial markets is largely driven by the COVID-19 pandemic. However, the relatively limited diversification prospects and pronounced insignificant entropies for this study confirm the evidence from Lahmiri and Bekiros [49] that international equity markets have not changed in the level of stability but have only become more irregular. Further, pertaining to alternating significant and insignificant transfer entropies between the composite series and the IMFs, we corroborate the weak fleeing impact of the COVID-19 pandemic on global equities as shown in Ahundjanov et al. [82]. They find that a unit increase in COVID-19 popularity of COVID-19 (as measured by related Google search queries) is accompanied by a cumulative decline of 0.038 to 0.069% in global financial indices after one day and a decline of 0.054 to 0.150% after one week, after controlling for confirmed cases of COVID-19. Nonetheless, Lahmiri and Bekiros [47] find a stronger effect of COVID-19 on equity markets than on energy markets using the GARCH-based Shannon entropy approach. The disparity can be ascribed to the methodological paradigms used.

4.1. Analysis of Shannon Entropy Results. The results of the Shannon ETE in totality confirm the desirability of the Rényi ETE. It is important to note that since the Shannon entropy assigns equal weights to the tails of the return distribution. Hence, we are not surprised that the results do not corroborate the stylised facts of asset returns. The outputs in Figure 1 indicate that there are no significant negative transfer entropies from COVID-19 to the global equities. Where they are significant, only positive information flows are recorded. These imply only high risks in assets regardless of investment horizon. They are also suggesting no diversification potential within the set of global assets.

Furthermore, we find that, at the composite level, the highest number of equity markets receive significant ETEs. The number of significant ETEs tends to reduce with increasing frequency. In the long term, there is not significant ETE to any market at all. In general, these results contradict the AME, HMH, and CMH. However, they align with the EMH in that all the markets are responding in the same way to the COVID-19 pandemic across all investment horizons. Furthermore, we find that, in the long term, there is a convergence between the Rényi and Shannon entropies, and both confirm the EMH. These indicate that the markets cease to react to the COVID-19 pandemic and revert their fundamental dynamics. The summary of the Shannon entropy results is also presented in Table 1.

5. Conclusions and Recommendations

This study examined the possible connection between the COVID-19 infection rate and global equity markets to allow further inferences on how the COVID-19 pandemic could affect global stock markets. First, we decomposed the returns of 27 global stock market indices using the CEEMDAN technique into intrinsic time of short-, medium-, and long-term scales. This helps to understand the dynamic behaviour of the investors' response to the pandemic while removing the noise from the series. This approach appeals to the AMH, HMH, and AHME, all in opposition to the EMH. The EMH has also been confirmed to decline sharply and persists for the S&P 500 index in the early stages of the pandemic, as shown in Wang and Wang [48]. Second, we employ the Rényi transfer entropy on both composite series and their

frequency domain counterparts to quantify the flow of information from COVID-19 to the equity markets. This method accounts for heavy tails in the asset returns while distinguishing between high-risk (negative ETEs) and low-risk (positive ETEs) assets because of the COVID-19 pandemic. For the purposes of comparison and confirmation we also employed the Shannon transfer entropy to the data. Our data span December 31, 2019, through April 18, 2021.

With Rényi transfer entropy, our results confirm EMH in the long term, but in the short and medium term, they confirm the AMH, HMH, and AHME which disagree with the EMH. The summary of our empirical results is that, in the long run, both the Rényi and Shannon transfer entropies fail to reject the null hypothesis of no information flow from COVID-19 to the selected global equity markets. At the time horizon, the fundamental dynamics of the markets are at play. Thus, there exists no potential for diversification across the equity markets. This corroborates the existing empirical literature but for a different reason. The common reason for no diversification avenue in the long term is a high level of integration among markets; however, in this, it is for the fact that the market is saturated with the needed information to make rational decisions. Therefore, the information transmitted by the COVID-19 pandemic does not influence investors' choices. Nevertheless, in terms of the Shannon entropy, there are no diversification potentials because all significant entropies are positive across the board.

However, the Rényian entropies show a different outlook. In the short and medium terms, there is a mixed result of significant and insignificant information flows (both positive and negative) for several equities. Except in the long term, all information flows to the Global Index were significant and negative. This indicates an overall high-risk perception of the global equity market due to the COVID-19 pandemic. On the bright side, this pattern offers diversification potential to low-risk equities during the period, notable among them are those from Canada, New Zealand, China, Argentina, and the UK, EMEA, France, Belgium, and Mexico, at different scales. We note that only significant negative flows were recorded for the US. The response of the US to the pandemic, especially at the early stages, was not optimal mainly due to political differences [83]. They may still be hanging over them, as seen in the negative flows.

In the composite series, we find a wider array of low-risk equities (9) to diversify across the Global Index compared to only 4 at IMF1 and 6 at IMF5 (refer to Table 1). It is clear that diversification prospects are generally limited as they occur at only 2-time scales (IMF1 and IMF5) out of a total of 6-time scales. These confirm, to some extent, that investor expectations have not been strongly influenced by the pandemic.

Our study has made a significant contribution to the fledgling empirical literature on the impact of COVID-19 in the finance ecosystem. We provide both corroborative and contradictive evidence. In the former, the results conform to stronger and slim (to none) diversification prospects in the short term and long term, respectively. However, in the latter, the reasons are not due to weak versus strong comovements or spillovers but due to quantifiable, significant, or insignificant asymmetric (positive or negative) information flows from COVID-19 to the respective equity markets. Specifically, our CEEMDAN-based transfer entropy methodology sheds new light on diversification potential in the frequency domain. In a noise-free environment, the direction of diversification is further informed by low-risk vis-à-vis high risk as suggested by positive and negative effective transfer entropies, respectively. In the end, investors are equipped with the knowledge to make decisions by taking cognisance of time horizon, the type of information flow, and the reason for the existence of diversification prospects. Similarly, policymakers can formulate and implement actions with respect to these tenets. This suggestion reiterates [84] that both investors and policymakers need to be careful against sentimental shocks and decisions. The findings have implications for the world stock markets in the sense that the propensity of COVID-19 to escalate and cause irreversible damage to global financial markets is relatively small. In contrast to Akhtaruzzaman et al. [38] and Yu et al. [85], our results do not make any attributions to financial contagion emanating from the COVID-19 pandemic. However, a long lifespan of the pandemic may have lasting effects on the global financial markets [86].

Data Availability

The data used in this paper are publicly available. Since this study used secondary data publicly available, the authors, therefore, decided not to reshare.

Conflicts of Interest

The authors declare no conflicts of interest.

References

[1] M. Roser, H. Ritchie, E. Ortiz-Ospina, and J. Hasell, "Coronavirus Pandemic (COVID-19): our world data," 2020, https://ourworldindata.org/coronavirus.

[2] N. J. Gormsen and R. Koijen, "Coronavirus: impact on stock prices and growth expectations," 2020, https://voxeu.org/article/coronavirus-impact-stock-prices-and-growth-expectations.

[3] S. Ramelli and A. F. Wagner, *Feverish Stock Price Reactions to COVID-19*, https://ideas.repec.org/p/chf/rpseri/rp2012.html, Swiss Finance Institute, Zürich, Switzerland, 2020, https://ideas.repec.org/p/chf/rpseri/rp2012.html.

[4] H. Herron and V. Hajric, "'The Market's in Panic Mode.' Stock Markets Plunge 12% Amid Coronavirus Fears (Time)," 2020, https://time.com/5803847/coronavirus-stocks-fall/.

[5] E. F. Fama, "Efficient capital markets: a review of theory and empirical work," *The Journal of Finance*, vol. 25, no. 2, pp. 383–417, 1970.

[6] E. F. Fama, "Market efficiency, long-term returns, and behavioral finance," *Journal of Financial Economics*, vol. 49, no. 3, pp. 283–306, 1998.

[7] M. Jensen, "Some anomalous evidence regarding market efficiency," *Journal of Financial Economics*, vol. 6, no. 2-3, pp. 95–101, 1978.

[8] F. S. Mishkin and S. Eakins, *Financial Markets and Institutions*, Pearson, New York, NY, USA, 9th edition, 2017.

[9] A. W. Lo, "The adaptive markets hypothesis," *Journal of Portfolio Management*, vol. 30, no. 5, pp. 15–29, 2004.

[10] U. A. Müller, M. M. Dacorogna, R. D. Davé, O. V. Pictet, R. B. Olsen, and J. R. Ward, "Fractals and intrinsic time: a challenge to econometricians," Unpublished Manuscript, Olsen Associates, Zürich, Switzerland, 1993.

[11] B. Cornell, "What is the alternative hypothesis to market efficiency?" *Journal of Portfolio Management*, vol. 44, no. 7, pp. 3–6, 2018.

[12] D. G. Baur and B. M. Lucey, "Is gold a hedge or a safe haven? An analysis of stocks, bonds and gold," *Financial Review*, vol. 45, no. 2, pp. 217–229, 2010.

[13] A. M. Adam, "Susceptibility of stock market returns to international economic policy: evidence from effective transfer entropy of Africa with the implication for open innovation," *Journal of Open Innovation: Technology, Market, and Complexity*, vol. 6, no. 3, p. 71, 2020.

[14] A. M. Adam, K. Kyei, S. Moyo, R. Gill, and E. N. Gyamfi, "Similarities in southern african development community (SADC) exchange rate markets structure: evidence from the ensemble empirical mode decomposition," *Journal of African Business*, pp. 1–16, 2021.

[15] D. G. Baur and T. K. McDermott, "Is gold a safe haven? International evidence," *Journal of Banking & Finance*, vol. 34, no. 8, pp. 1886–1898, 2010.

[16] D. G. Baur and T. K. J. McDermott, "Why is gold a safe haven?" *Journal of Behavioral and Experimental Finance*, vol. 10, pp. 63–71, 2016.

[17] S. Bekiros, S. Boubaker, D. K. Nguyen, and G. S. Uddin, "Black swan events and safe havens: the role of gold in globally integrated emerging markets," *Journal of International Money and Finance*, vol. 73, pp. 317–334, 2017.

[18] A. Dutta, D. Das, R. K. Jana, and X. V. Vo, "COVID-19 and oil market crash: revisiting the safe haven property of gold and Bitcoin," *Resources Policy*, vol. 69, Article ID 101816, 2020.

[19] M. M. Habib and L. Stracca, "Getting beyond carry trade: what makes a safe haven currency?" *Journal of International Economics*, vol. 87, no. 1, pp. 50–64, 2012.

[20] Y. Huang, K. Duan, and T. Mishra, "Is Bitcoin really more than a diversifier? A pre- and post-COVID-19 analysis," *Finance Research Letters*, Article ID 102016, 2021.

[21] Y. Jiang, J. Lie, J. Wang, and J. Mu, "Revisiting the roles of cryptocurrencies in stock markets: a quantile coherency perspective," *Economic Modelling*, vol. 95, pp. 21–34, 2021.

[22] A. Kliber, P. Marszałek, I. Musiałkowska, and K. Świerczyńska, "Bitcoin: safe haven, hedge or diversifier? Perception of Bitcoin in the context of a country's economic situation—a stochastic volatility approach," *Physica A: Statistical Mechanics and Its Applications*, vol. 524, pp. 246–257, 2019.

[23] W. Mensi, R. Nekhili, X. V. Vo, and S. H. Kang, "Oil and precious metals: volatility transmission, hedging, and safe haven analysis from the Asian crisis to the COVID-19 crisis," *Economic Analysis and Policy*, vol. 71, pp. 73–96, 2021.

[24] P. Owusu Junior, A. M. Adam, and G. Tweneboah, "Connectedness of cryptocurrencies and gold returns: evidence from frequency-dependent quantile regressions," *Cogent Economics & Finance*, vol. 8, no. 1, Article ID 1804037, 2020.

[25] P. O. Junior, A. K. Tiwari, H. Padhan, and I. Alagidede, "Analysis of EEMD-based quantile-in-quantile approach on spot- futures prices of energy and precious metals in India," *Resources Policy*, vol. 68, Article ID 101731, 2020.

[26] P. Owusu Junior and G. Tweneboah, "Are there asymmetric linkages between African stocks and exchange rates?" *Research in International Business and Finance*, vol. 54, Article ID 101245, 2020.

[27] L. Yarovaya, R. Matkovskyy, and A. Jalan, "The effects of a "black swan" event (COVID-19) on herding behavior in cryptocurrency markets," *Journal of International Financial Markets, Institutions and Money*, Article ID 101321, 2021.

[28] D. Acemoglu, S. Johnson, and J. Robinson, "Disease and development in historical perspective," *Journal of the European Economic Association*, vol. 1, no. 2-3, pp. 397–405, 2003.

[29] D. E. Bloom, J. D. Sachs, P. Collier, and C. Udry, "Geography, demography, and economic growth in Africa," *Brookings Papers on Economic Activity*, vol. 1998, no. 2, pp. 207–295, 1998.

[30] S. Gallup and D. Mellinger, *Geography and Economic Development*, Harvard University Press, Cambridge, MA, USA, 1999, https://www.hks.harvard.edu/centers/cid/publications/faculty-working-papers/geography-and-economic-development.

[31] C. Barrett, K. Bisset, J. Leidig, A. Marathe, and M. Marathe, "Economic and social impact of influenza mitigation strategies by demographic class," *Epidemics*, vol. 3, no. 1, pp. 19–31, 2011.

[32] B. Sander, A. Nizam, L. P. Garrison, M. J. Postma, M. E. Halloran, and I. M. Longini, "Economic evaluation of influenza pandemic mitigation strategies in the United States using a stochastic microsimulation transmission model," *Value in Health*, vol. 12, no. 2, pp. 226–233, 2009.

[33] N. D. Schwartz, "Coronavirus recession looms, its course 'unrecognizable'—the New York Times," 2020, https://www.nytimes.com/2020/03/21/business/economy/coronavirus-recession.html.

[34] C. M. Reinhart, "This time truly is different by Carmen M. Reinhart (Project Syndicate)," 2020, https://www.project-syndicate.org/commentary/covid19-crisis-has-no-economic-precedent-by-carmen-reinhart-2020-03.

[35] J. Schoenfeld, "The invisible risk: pandemics and the financial markets," *SSRN Electronic Journal*, 2020.

[36] J. W. Goodell and S. Goutte, "Diversifying with cryptocurrencies during COVID-19," *SSRN Electronic Journal*, 2020.

[37] K. P. Prabheesh, "Dynamics of foreign portfolio investment and stock market returns during the COVID-19 pandemic: evidence from India," *Asian Economics Letters*, vol. 1, no. 2, Article ID 17658, 2020.

[38] M. Akhtaruzzaman, S. Boubaker, and A. Sensoy, "Financial contagion during COVID-19 crisis," *Finance Research Letters*, vol. 38, Article ID 101604, 2021.

[39] T. Conlon, S. Corbet, and R. J. McGee, "Are cryptocurrencies a safe haven for equity markets? An international perspective from the COVID-19 pandemic," *Research in International Business and Finance*, vol. 54, Article ID 101248, 2020.

[40] B. Garg and K. P. Prabheesh, "The nexus between the exchange rates and interest rates: evidence from BRIICS economies during the COVID-19 pandemic," *Studies in Economics and Finance*, vol. 38, no. 2, pp. 469–486, 2021.

[41] W. Hanif, W. Mensi, and X. V. Vo, "Impacts of COVID-19 outbreak on the spillovers between US and Chinese stock sectors," *Finance Research Letters*, vol. 40, Article ID 101922, 2021.

[42] M. M. Karim, M. A. F. Chowdhury, and M. Masih, "Re-examining oil and BRICS' stock markets: new evidence from wavelet and MGARCH-DCC," *Macroeconomics and Finance in Emerging Market Economies*, pp. 1–19, 2021.

[43] K. Malik, S. Sharma, and M. Kaur, "Measuring contagion during COVID-19 through volatility spillovers of BRIC countries using diagonal BEKK approach," *Journal of Economics Studies*, 2021.

[44] P. K. Narayan, N. Devpura, and H. Wang, "Japanese currency and stock market-What happened during the COVID-19 pandemic?" *Economic Analysis and Policy*, vol. 68, pp. 191–198, 2020.

[45] L. Yarovaya, A. H. Elsayed, and S. Hammoudeh, "Determinants of spillovers between islamic and conventional financial markets: exploring the safe haven assets during the COVID-19 pandemic," *Finance Research Letters*, vol. 79, Article ID 101979, 2021.

[46] T. Schreiber, "Measuring information transfer," *Physical Review Letters*, vol. 85, no. 2, pp. 461–464, 2000.

[47] S. Lahmiri and S. Bekiros, "Randomness, informational entropy, and volatility interdependencies among the major world markets: the role of the COVID-19 pandemic," *Entropy*, vol. 22, no. 8, p. 833, 2020.

[48] J. Wang and X. Wang, "COVID-19 and financial market efficiency: evidence from an entropy-based analysis," *Finance Research Letters*, Article ID 101888, 2021.

[49] S. Lahmiri and S. Bekiros, "The impact of COVID-19 pandemic upon stability and sequential irregularity of equity and cryptocurrency markets," *Chaos, Solitons & Fractals*, vol. 138, Article ID 109936, 2020.

[50] S. Lahmiri and S. Bekiros, "Renyi entropy and mutual information measurement of market expectations and investor fear during the COVID-19 pandemic," *Chaos, Solitons & Fractals*, vol. 139, Article ID 110084, 2020.

[51] T. Dimpfl and F. J. Peter, "The impact of the financial crisis on transatlantic information flows: an intraday analysis," *Journal of International Financial Markets, Institutions and Money*, vol. 31, pp. 1–13, 2014.

[52] H. Hassani, A. Dionisio, and M. Ghodsi, "The effect of noise reduction in measuring the linear and nonlinear dependency of financial markets," *Nonlinear Analysis: Real World Applications*, vol. 11, no. 1, pp. 492–502, 2010.

[53] F. X. Diebold and K. Yilmaz, "Better to give than to receive: predictive directional measurement of volatility spillovers," *International Journal of Forecasting*, vol. 28, no. 1, pp. 57–66, 2012.

[54] J. Baruník and T. Křehlík, "Measuring the frequency dynamics of financial connectedness and systemic risk," *Journal of Financial Econometrics*, vol. 16, no. 2, pp. 271–296, 2018.

[55] A. Rényi, "On measures of information and entropy," in *Proceedings of the 4th Berkeley Symposium on Mathematics, Statistics and Probability*, vol. 1, p. 547, Berkeley, CA, USA, 1961.

[56] S. I. Ivanov, "The influence of ETFs on the price discovery of gold, silver and oil," *Journal of Economics and Finance*, vol. 37, no. 3, pp. 453–462, 2013.

[57] J. B. Ramsey and C. Lampart, "The decomposition of economic relationships by time scale using wavelets: expenditure and income," *Studies in Nonlinear Dynamics and Econometrics*, vol. 3, no. 1, pp. 23–42, 1998.

[58] B. Yang, Y. Sun, and S. Wang, "A novel two-stage approach for cryptocurrency analysis," *International Review of Financial Analysis*, vol. 72, Article ID 101567, 2020.

[59] Z. Huang, "Extensions to the k-means algorithm for clustering large data sets with categorical values," *Data Mining and Knowledge Discovery*, vol. 2, no. 3, pp. 283–304, 1998.

[60] P. J. J. Luukko, J. Helske, and E. Räsänen, "Introducing libeemd: a program package for performing the ensemble empirical mode decomposition," *Computational Statistics*, vol. 31, no. 2, pp. 545–557, 2016.

[61] M. E. Torres, M. A. Colominas, G. Schlotthauer, and P. Flandrin, "A complete ensemble empirical mode decomposition with adaptive noise," in *Proceedings of the 2011 IEEE International Conference on Acoustics, Speech and Signal Processing (ICASSP)*, pp. 4144–4147, Prague, Czech Republic, May 2011.

[62] Q. Peng, F. Wen, and X. Gong, "Time-dependent intrinsic correlation analysis of crude oil and the US dollar based on CEEMDAN," *International Journal of Finance & Economics*, vol. 26, no. 1, pp. 834–848, 2021.

[63] Y. Liu, L. Wang, L. Yang, X. Liu, and L. Wang, "Runoff prediction and analysis based on improved CEEMDAN-OS-QR-ELM," *IEEE Access*, vol. 9, p. 1, 2021.

[64] Z. Wu and N. E. Huang, "Ensemble empirical mode decomposition: a noise-assisted data analysis method," *Advances in Adaptive Data Analysis*, vol. 1, no. 1, pp. 1–41, 2009.

[65] P. Flandrin, G. Rilling, and P. Goncalves, "Empirical mode decomposition as a filter bank," *IEEE Signal Processing Letters*, vol. 11, no. 2, pp. 112–114, 2004.

[66] R. J. Gledhill, *Methods for Investigating Conformational Change in Biomolecular Simulations*, A Dissertation for the Degree of Doctor of Philosophy at the Department of Chemistry, University of Southampton, Southampton, UK, 2003.

[67] R. V. L. Hartley, "Transmission of Information1," *Bell System Technical Journal*, vol. 7, no. 3, pp. 535–563, 1928.

[68] S. Behrendt, T. Dimpfl, F. J. Peter, and D. J. Zimmermann, "RTransferEntropy-quantifying information flow between different time series using effective transfer entropy," *Software*, vol. 10, Article ID 100265, 2019.

[69] T. Dimpfl and F. J. Peter, "Using transfer entropy to measure information flows between financial markets," *Studies in Nonlinear Dynamics and Econometrics*, vol. 17, no. 1, pp. 85–102, 2013.

[70] C. E. Shannon, "A mathematical theory of communication," *Bell System Technical Journal*, vol. 27, no. 3, pp. 379–423, 1948.

[71] S. Kullback and R. A. Leibler, "On information and sufficiency," *The Annals of Mathematical Statistics*, vol. 22, no. 1, pp. 79–86, 1951.

[72] C. Beck and F. Schögl, *Thermodynamics of Chaotic Systems: An Introduction*, Cambridge University Press, Cambridge, UK, 1993.

[73] R. Marschinski and H. Kantz, "Analysing the information flow between financial time series," *The European Physical Journal B*, vol. 30, no. 2, pp. 275–281, 2002.

[74] S. J. Salyer, J. Maeda, S. Sembuche et al., "The first and second waves of the COVID-19 pandemic in Africa: a cross-sectional study," *The Lancet*, vol. 397, no. 10281, pp. 1265–1275, 2021.

[75] E. J. d. A. L. Pereira, P. J. S. Ferreira, M. F. da Silva, J. G. V. Miranda, and H. B. B. Pereira, "Multiscale network for 20 stock markets using DCCA," *Physica A: Statistical Mechanics and its Applications*, vol. 529, 2019.

[76] K. J. Forbes and F. E. Warnock, "Capital flow waves: surges, stops, flight, and retrenchment," *Journal of International Economics*, vol. 88, no. 2, pp. 235–251, 2012.

[77] X. Zhao, Y. Sun, X. Li, and P. Shang, "Multiscale transfer entropy: measuring information transfer on multiple time scales," *Communications in Nonlinear Science and Numerical Simulation*, vol. 62, pp. 202–212, 2018.

[78] J. Bouoiyour, R. Selmi, and M. E. Wohar, "Safe havens in the face of Presidential election uncertainty: a comparison between Bitcoin, oil and precious metals," *Applied Economics*, vol. 51, no. 57, pp. 6076–6088, 2019.

[79] J. Bouoiyour, R. Selmi, A. K. Tiwari, and O. R. Olayeni, "What drives Bitcoin price," *Economic Bulletin*, vol. 36, no. 2, pp. 843–850, 2016.
[80] K. Chahuán-Jiménez, R. Rubilar, H. de la Fuente-Mella, and V. Leiva, "Breakpoint Analysis for the COVID-19 pandemic and its effect on the stock markets," *Entropy*, vol. 23, no. 1, p. 100, 2021.
[81] O. B. Adekoya and J. A. Oliyide, "How COVID-19 drives connectedness among commodity and financial markets: evidence from TVP-VAR and causality-in-quantiles techniques," *Resources Policy*, vol. 70, 2021.
[82] B. B. Ahundjanov, S. B. Akhundjanov, and B. B. Okhunjanov, "Information search and financial markets under COVID-19," *Entropy*, vol. 22, no. 7, p. 791.
[83] M. Andersen, "Early evidence on social distancing in response to COVID-19 in the United States," *SSRN Electronic Journal*, 2020.
[84] E. Bouri, R. Demirer, D. Gabauer, and R. Gupta, "Financial market connectedness: the role of investors' happiness," *Finance Research Letters*, Article ID 102075, 2021.
[85] H. Yu, W. Chu, Y. Ding, and X. Zhao, "Risk contagion of global stock markets under COVID-19: A network connectedness method," *Accounting and Finance*, Article ID 12775, 2021.
[86] N. T. Vo and N. T. Hung, "Directional spillover effects and time-frequency nexus between oil, gold and stock markets: evidence from pre and during COVID-19 outbreak," *International Review of Financial Analysis*, vol. 76, Article ID 101730, 2021.

Hindawi
Mathematical Problems in Engineering
Volume 2021, Article ID 3351074, 9 pages
https://doi.org/10.1155/2021/3351074

Research Article

FLS-Based Nonuniform Trajectory Tracking AILC for Uncertain Nonlinear Systems with Nonsymmetric Dead-Zone Input and Initial State Error

Chunli Zhang, Xu Tian, and Lei Yan

Xi'an University of Technology, Shannxi Key Laboratory of Complex System Control and Intelligent Information Processing, Xi'an, China

Correspondence should be addressed to Chunli Zhang; gaozhangchunli@163.com

Received 22 June 2021; Accepted 9 August 2021; Published 19 August 2021

Academic Editor: Xiao Chen

This paper proposes an AILC method for uncertain nonlinear system to solve different target tracking problems. The method uses fuzzy logic systems (FLS) to approximate every uncertain term in systems. All closed-loop signals are bounded on $[0, T]$ according to the Lyapunov theory. A time-varying boundary layer and a typical convergent series are introduced to handle initial state error, unknown bounds of errors, and nonuniform target tracking, respectively. The result is that the tracking error's norm can converge to a small neighborhood along iteration increasing asymptotically. Finally, the simulation results of mass-spring mechanical system show the correctness of the theory and validity of the method.

1. Introduction

The research of the nonuniform trajectory is an interesting problem. The paper [1] proposed a new ILC law for first-order hybrid parametric system and the paper [2] proposed a novel AILC method for nonlinear hybrid parameter systems. Recently, AILC is presented; a nonuniform target tracking AILC method was proposed in the paper [3]. The paper [4] proposed a fault-tolerant ILC technique for mobile robots' nonrepetitive target tracking with output constraints. From the above literature analysis, solving the nonuniform target tracking problem for uncertain mechanical nonlinear system is an important problem.

Adaptive control is used to handle system's control problem about uncertainties which is a challenging problem. Adaptive control schemes learn uncertainties by adaptive laws. NN and FLS are used in the method as function approximators, such as the papers [5–8]. The literature [9] could complete the varying control tasks by designing an adaptive fuzzy ILC for uncertain nonlinear system. Based on RBF neural network approximation, the literature [10] proposed AILC for nonlinear pure-feedback systems to solve the nonuniform target tracking problem. The uniform AILC frame for uncertain nonlinear system was proposed in the paper [11]; by Lyapunov theory, it can prove the convergence. It should be noted that Lyapunov function-based AILC plays an important role in dealing with the time-varying parameter in the literatures [9, 11, 12]. But initial state error is a challenging one as they need to converge to zero for keeping stability. Only the papers [9, 10, 13] considered this problem recently it is an important problem for AILC.

Due to the physical limitations of actuators, in real systems, control inputs are often constrained, such as dead-zone inputs. However, these constraints may damage the performance of the system. In the papers [14–23], control performance could be changed by using different techniques recently. The question of adaptive stabilization for time-delay system had been solved in the literature [16]. The paper [17] developed an adaptive backstepping method of uncertain nonlinear systems about nonsymmetric dead-zone. As yet, there is no report from the literature for the AILC of nonlinear systems with nonsymmetric dead-zone input and initial state error. This is a problem that needs to be solved urgently.

In this paper, the nonuniform trajectory tracking issue is discussed for the uncertain nonlinear systems with nonsymmetric dead-zone input and initial state error. The contributions of the proposed control method are presented as follows:

(i) The nonuniform trajectory tracking issue is studied for uncertain nonlinear systems under nonsymmetric dead-zone input and initial state error issues.

(ii) The AILC method is used to uncertain nonlinear systems. FLS is introduced to learn unknown dynamic. A convergence order is introduced to solve the unknown bound and nonuniform target tracking problem.

Finally, simulation results of mass-spring mechanical system are given to verify the validity of the designed controller.

The remainder of this paper is organized as follows: in Section 2, the system description and related concepts are given in detail. The controller design process and main results are presented in Section 3. A simulation is shown in Section 4. Section 5 is the conclusion.

2. System Description

2.1. System Model. The following nonlinear systems are considered:

$$\begin{aligned} \dot{x}_{1,k} &= x_{2,k} + f_1\left(\overline{x}_{1,k}\right), \\ \dot{x}_{j,k} &= x_{j+1,k} + f_j\left(\overline{x}_{j,k}\right), \\ \dot{x}_{n,k} &= \Gamma\left(u_k\right) + f_n\left(\overline{x}_{n,k}\right), \\ y_k &= x_{1,k}, \end{aligned} \tag{1}$$

where $\overline{x}_{j,k} = [x_{1,k}, \ldots, x_{j,k}]^T \in R^j$, $x = \overline{x}_n$ is the state that is measured; $\Gamma(u_k) \in R$ represents the actuator characteristics and $y_k \in R$ is the system output; $f_j(\overline{x}_{j,k})$, $j = 1, 2, \ldots, n$, are smooth unknown nonlinear functions.

Here, the function $\Gamma(u_k)$ represents actuator output with nonsymmetric dead-zone and can be expressed as

$$\Gamma\left(u_k\right) = \begin{cases} m_r\left(u_k - b_r\right), & \text{if } u_k \geq b_r, \\ 0, & \text{if } -b_l < u_k < b_r, \\ m_l\left(u_k + b_l\right), & \text{if } u_k \leq -b_l, \end{cases} \tag{2}$$

where m_r and m_l present the right and left slopes, respectively; b_r and b_l present the breakpoint of dead-zone. The nonsymmetric dead-zone can be rewritten as a combination of a line and a disturbance-like term [18].

$$\Gamma\left(u_k\right) = m(t)u_k + d(t), \tag{3}$$

where

$$m(t) = \begin{cases} m, & \text{if } u_k \leq 0, \\ m_r, & \text{if } u_k > 0, \end{cases} \quad d(t) = \begin{cases} -m_r b_r, & \text{if } u_k \geq b_r, \\ -m(t)u_k, & \text{if } -b_l < u_k < b_r, \\ m_l b_l, & \text{if } u_k \leq -b_l. \end{cases} \tag{4}$$

Assumption 1. Parameters m_l, m_r, b_l, and b_r are uncertain constants. There exists an unknown ν satisfing $0 < \nu \leq \min\{m_l, m_r\}$, which is small enough. The unknown constant $\overline{d}$ is the upper bound of $d(t)$.

Designing an AILC law $u_k(t)$ on $[0, T]$ to make the output $y_k(t)$ following the target trajectory $y_{r,k}(t)$ is our control objective, that is to say, $\lim_{k\longrightarrow\infty}\|y_k(t) - y_{r,k}(t)\| \leq \varrho$, where ϱ is the small positive error. Guarantee that the closed-loop signals are bounded. $y_{r,k}(t)$ is the smooth desired target. k is the iteration index.

2.2. Convergent Series Sequence. The following definition and lemma can be used in the design process.

Definition 1 (see [20]). $\{\Delta_k\}$ is a series convergent sequence which is shown as

$$\Delta_k = \frac{a}{k^l}, \tag{5}$$

where $k = 1, 2, \ldots$; a and l are the needed parameters, satisfing $a > 0 \in R$, $l \geq 2 \in N$.

Lemma 1 (see [20]). *For $\{1/k^l\}$, where $k = 1, 2, \ldots, l \geq 2$, the inequality as follows holds:*

$$\lim_{k\longrightarrow\infty} \sum_{j=1}^{k} \frac{1}{j^l} \leq 2. \tag{6}$$

2.3. Description of Fuzzy Logic System (FLS). The FLS has a good approximation property [24]. For a smooth $f(x) \in R$ can be approximated by

$$f(x) = \left(W^*\right)^T S(x) + \delta(x), \tag{7}$$

where $\delta(x)$ is the fuzzy approximated error, $(W^*)^T$ is the optimal weight vector satisfing

$$\left(W^*\right)^T = \arg\min_{W^* \in \Omega_{W^*}} \left\{ \sup_{x \in D_x} \left|\widehat{f}(x|W) - f(x)\right| \right\}, \tag{8}$$

where D_x represents the set of x and $\widehat{f}(x|W)$ that is estimated f, shown by

$$\widehat{f}(x|W) = W^T S(x), \tag{9}$$

with an adjustable W, and Ω_{W^*} is given as follows:

$$\Omega_{W^*} = \left\{ W^* \middle| \left\|W^*\right\| \leq W_M^* \right\}, \tag{10}$$

with W_M^* being a positive constant.

Assumption 2. In this paper, the following inherent approximation error $\delta_j(\overline{x}_{j,k})$ is assumed to be bounded with $|\delta_j(\overline{x}_{j,k})| \leq \theta_j$, where the unknown parameters $\theta_j (1 \leq j \leq n)$ denote the smallest upper bounds of $|\delta_j(\overline{x}_{j,k})|$ with $\theta_j \geq 0$.

2.4. Time-Varying Boundary Layer. Introduce the function $z_{j\phi,k}$ as follows to deal with initial state errors:

$$z_{j\phi,k} = z_{j,k} - \phi_{j,k}(t)\mathrm{sat}\left(\frac{z_{j,k}}{\phi_{j,k}(t)}\right),$$
$$\phi_{j,k}(t) = \varepsilon_{j,k}e^{-\eta t}, \tag{11}$$

where $z_{j,k}$ and $z_{j\phi,k}$ are variables of t; $\varepsilon_{j,k}$ is a series convergence sequence; the saturation function sat is given as

$$\mathrm{sat}\left(\frac{z_{j,k}}{\phi_{j,k}(t)}\right) = \begin{cases} 1, & \text{if } z_{j,k} > \phi_{j,k}(t), \\ \dfrac{z_{j,k}}{\phi_{j,k}(t)}, & \text{if } -\phi_{j,k}(t) \le z_{j,k} \le \phi_{j,k}(t), \\ -1, & \text{if } z_{j,k} < -\phi_{j,k}(t), \end{cases} \tag{12}$$

where $\phi_{j,k}(t)$ is the time-varying boundary layer. The control objective can be achieved by this. See the literature [9] for specific analysis.

Assumption 3. The initial state errors must satisfy $|z_{j,k}(0)| = \varepsilon_{j,k}$ for some positive parameters $\varepsilon_{j,k}$ which are known; $j = 1, \ldots, m$, $z_{j,k}(0)$ are given later in this paper.

3. AILC Design and Convergence Analysis

The specific process about designing controller is given as follows.

Step 1. Let $z_{1,k} = x_{1,k} - y_{r,k}$, $z_{2,k} = x_{2,k} - \alpha_{1,k}$, $F_1(\overline{x}_{1,k}) = f_1(\overline{x}_{1,k})$, and $\alpha_{1,k}$ is a virtual controller. Introduce the error function $z_{1\phi,k}$ and $z_{2\phi,k}$ from Section 2.4 to deal with initial state errors as

$$z_{1\phi,k} = z_{1,k} - \phi_{1,k}(t)\mathrm{sat}\left(\frac{z_{1,k}}{\phi_{1,k}(t)}\right),$$
$$\phi_{1,k}(t) = \varepsilon_{1,k}e^{-\eta_1 t},$$
$$z_{2\phi,k} = z_{2,k} - \phi_{2,k}(t)\mathrm{sat}\left(\frac{z_{2,k}}{\phi_{2,k}(t)}\right),$$
$$\phi_{2,k}(t) = \varepsilon_{2,k}e^{-\eta_2 t}. \tag{13}$$

Recall that

$$\dot{x}_{1,k} = x_{2,k} + F_1\left(\overline{x}_{1,k}\right). \tag{14}$$

Derivate $z_{1\phi,k}$ as follows:

$$\dot{z}_{1\phi,k} = z_{2,k} + \alpha_{1,k} + F_1\left(\overline{x}_{1,k}\right) - \dot{y}_{r,k} - \mathrm{sgn}\left(z_{1\phi,k}\right)\dot{\phi}_{1,k}. \tag{15}$$

According to Section 2.3, by FLS, $F_1(\overline{x}_{1,k})$ is approximated as follows:

$$F_1\left(\overline{x}_{1,k}\right) = W_1^T S_1\left(\overline{x}_{1,k}\right) + \delta_1\left(\overline{x}_{1,k}\right), \tag{16}$$

where $\delta_1(\overline{x}_{1,k})$ is the approximation error and W_1 is the optimal weight vector.

Define $N_1 = \omega_{M1}^2$, which is needed later; $\Delta_k = (a/k^l)$, $a > 0$, and $l \ge 2$. The virtual controller is taken as

$$\alpha_{1,k} = -\widehat{W}_{1,k}^T S_1\left(\overline{x}_{1,k}\right) - \widehat{N}_{1,k}\frac{1}{\Delta_k}z_{1\phi,k} + \dot{y}_{r,k} - \eta_1 z_{1,k}. \tag{17}$$

Substitute equations (16) and (17) into equation (15), then

$$\begin{aligned}\dot{z}_{1\phi,k} &= z_{2,k} - \widehat{N}_{1,k}\frac{1}{\Delta_k}z_{1\phi,k} \\ &\quad + W_1^T S_1\left(\overline{x}_{1,k}\right) + \delta_1\left(\overline{x}_{1,k}\right) - \widehat{W}_{1,k}^T S_1\left(\overline{x}_{1,k}\right) \\ &\quad - \eta_1 z_{1,k} - \mathrm{sgn}\left(z_{1\phi,k}\right)\dot{\phi}_{1,k}(t) \\ &= z_{2\phi,k} - \widehat{N}_{1,k}\frac{1}{\Delta_k}z_{1\phi,k} - \widetilde{W}_{1,k}^T S_1\left(\overline{x}_{1,k}\right) + \delta_1\left(\overline{x}_{1,k}\right) \\ &\quad + \phi_{2,k}(t)\mathrm{sat}\left(\frac{z_{2,k}}{\phi_{2,k}(t)}\right) - \eta_1 z_{1,k} - \mathrm{sgn}\left(z_{1\phi,k}\right)\dot{\phi}_{1,k}(t),\end{aligned} \tag{18}$$

where the estimated W_1 and N_1 are $\widehat{W}_{1,k}$ and $\widehat{N}_{1,k}$, respectively. $\widetilde{W}_{1,k} = \widehat{W}_{1,k} - W_1$ and $\widetilde{N}_{1,k} = \widehat{N}_{1,k} - N_1$ are the errors of estimated parameters. The last two terms of equation (18) can be changed as

$$\begin{aligned}-\eta_1 z_{1,k} - \mathrm{sgn}\left(z_{1\phi,k}\right)\dot{\phi}_{1,k}(t) &= -\eta_1 z_{1\phi,k} \\ &\quad - \eta_1\phi_{1,k}(t)\mathrm{sat}\left(\frac{z_{1,k}}{\phi_{1,k}(t)}\right) - \mathrm{sgn}\left(z_{1\phi,k}\right)\dot{\phi}_{1,k}(t) \\ &= -\eta_1 z_{1\phi,k}.\end{aligned} \tag{19}$$

Equations (18) and (19) can be rewritten as

$$\begin{aligned}\dot{z}_{1\phi,k} &= z_{2\phi,k} - \widehat{N}_{1,k}\frac{1}{\Delta_k}z_{1\phi,k} - \eta_1 z_{1\phi,k} + \widetilde{W}_1^T S_1\left(\overline{x}_{1,k}\right) \\ &\quad + \delta_1\left(\overline{x}_{1,k}\right) + \phi_{2,k}(t)\mathrm{sat}\left(\frac{z_{2,k}}{\phi_{2,k}(t)}\right).\end{aligned} \tag{20}$$

Let $\omega_1 = \delta_1(\overline{x}_{1,k}) + \phi_{2,k}(t)\mathrm{sat}(z_{2,k}(t)/\phi_{2,k}(t))$, then equation (20) becomes

$$\dot{z}_{1\phi,k} = z_{2\phi,k} - \widehat{N}_{1,k}\frac{1}{\Delta_k}z_{1\phi,k} - \eta_1 z_{1\phi,k} + \widetilde{W}_1^T S_1\left(\overline{x}_{1,k}\right) + \omega_1. \tag{21}$$

Assumption 4. The bounded term ω_1 satisfies $|\omega_1| \le \omega_{M1}$, where ω_{M1} is a positive parameter.

Take the following nonnegative function:

$$V_{1,k} = \frac{1}{2}z_{1\phi,k}^2 + \frac{1}{2}\widetilde{W}_{1,k}^T\Gamma_{11}^{-1}\widetilde{W}_{1,k} + \frac{1}{2}\Gamma_{21}^{-1}\widetilde{N}_{1,k}^2, \tag{22}$$

where Γ_{11} and Γ_{21} are symmetric matrices and are positive. Derivate $V_{1,k}$ according to equation (21), then

$$\begin{aligned}\dot{V}_{1,k} &= z_{1\phi,k}z_{2\phi,k} - \eta_1 z_{1\phi,k}^2 \\ &\quad - \widetilde{W}_{1,k}^T\Gamma_{11}^{-1}\left(\Gamma_{11}S_1\left(\overline{x}_{1,k}\right)z_{1\phi,k} - \dot{\widehat{W}}_{1,k}\right) \\ &\quad - \widehat{N}_{1,k}\frac{1}{\Delta_k}z_{1\phi,k}^2 + \omega_{1,k}z_{1\phi,k} + \Gamma_{21}^{-1}\widetilde{N}_{1,k}\dot{\widehat{N}}_{1,k} \\ &\le z_{1\phi,k}z_{2\phi,k} - \eta_1 z_{1\phi,k}^2 \\ &\quad - \widetilde{W}_{1,k}^T\Gamma_{11}^{-1}\left(\Gamma_{11}S_1\left(\overline{x}_{1,k}\right)z_{1\phi,k} - \dot{\widehat{W}}_{1,k}\right) \\ &\quad - \widehat{N}_{1,k}\frac{1}{\Delta_k}z_{1\phi,k}^2 + \frac{1}{\Delta_k}\omega_{M1}^2 z_{1\phi,k}^2 + \frac{1}{4}\Delta_k + \Gamma_{21}^{-1}\widetilde{N}_{1,k}\dot{\widehat{N}}_{1,k} \\ &= z_{1\phi,k}z_{2\phi,k} - \eta_1 z_{1\phi,k}^2 \\ &\quad - \widetilde{W}_{1,k}^T\Gamma_{11}^{-1}\left(\Gamma_{11}S_1\left(\overline{x}_{1,k}\right)z_{1\phi,k} - \dot{\widehat{W}}_{1,k}\right) \\ &\quad - \widetilde{N}_{1,k}\Gamma_{21}^{-1}\left(\Gamma_{21}\frac{1}{\Delta_k}z_{1\phi,k}^2 - \dot{\widehat{N}}_{1,k}\right) + \frac{1}{4}\Delta_k.\end{aligned} \tag{23}$$

In the previous equation, $mn \le (1/r)m^2 + (1/4)n^2 r$ is used, where $r = \Delta_k$.

Step j. $(2 \le j \le n-1)$. Denote $F_j(\overline{x}_{j,k}) = f_j(\overline{x}_{j,k}) - \sum_{l=1}^{j-1}(\partial\alpha_{j-1,k}/\partial x_{l,k})\dot{x}_{l,k}(\overline{x}_{l,k})$, $N_j = \omega_{Mj}^2$, which is given later. $z_{j+1,k} = x_{j+1,k} - \alpha_{j,k}$, the same to Step 1; $z_{j\phi,k}$ and $z_{(j+1)\phi,k}$ from Section 2.4 are introduced as

$$\begin{aligned}z_{j\phi,k} &= z_{j,k} - \phi_{j,k}(t)\mathrm{sat}\left(\frac{z_{j,k}}{\phi_{j,k}(t)}\right), \\ \phi_{j,k}(t) &= \varepsilon_{j,k}e^{-\eta_j t}, \\ z_{(j+1)\phi,k} &= z_{(j+1),k} - \phi_{(j+1),k}(t)\mathrm{sat}\left(\frac{z_{(j+1),k}}{\phi_{(j+1),k}(t)}\right), \\ \phi_{(j+1),k}(t) &= \varepsilon_{(j+1),k}e^{-\eta_{(j+1)}t}.\end{aligned} \tag{24}$$

Derivate $z_{j\phi,k}$ as follows:

$$\dot{z}_{j\phi,k} = z_{j+1,k} + \alpha_{j,k} + f_j\left(\overline{x}_{j,k}\right) - \dot{\alpha}_{j-1,k} - \mathrm{sgn}\left(z_{j\phi,k}(t)\right)\dot{\phi}_{j,k}, \tag{25}$$

where $\dot{\alpha}_{j-1,k} = \sum_{l=1}^{j-1}(\partial\alpha_{j-1,k}/\partial x_{l,k})(x_{l+1,k} + f_l(\overline{x}_{l,k})) + (\partial\alpha_{j-1,k}/\partial\widehat{W}_{j-1,k})\dot{\widehat{W}}_{j-1,k} + (\partial\alpha_{j-1,k}/\partial\widehat{N}_{j-1,k})\dot{\widehat{N}}_{j-1,k} + (\alpha_{j-1,k}/\partial t)$. Denote $F_j(\overline{x}_{j,k}) = f_j(\overline{x}_{j,k}) - \sum_{l=1}^{j}(\partial\alpha_{j-1,k}/\partial x_{j,k})(x_{j+1,k} + f_j(\overline{x}_{j,k}))$, $P_{j-1,k} = (\partial\alpha_{j-1,k}/\partial\widehat{W}_{j-1,k})\dot{\widehat{W}}_{j-1,k} + (\partial\alpha_{j-1,k}/\partial\widehat{N}_{j-1,k})\dot{\widehat{N}}_{j-1,k} + (\alpha_{j-1,k}/\partial t)$, then equation (25) can be rewritten as

$$\dot{z}_{j\phi,k} = z_{j+1,k} + \alpha_{j,k} + F_j\left(\overline{x}_{j,k}\right) - P_{j-1,k} - \mathrm{sgn}\left(z_{j\phi,k}(t)\right)\dot{\phi}_{j,k}. \tag{26}$$

According to Section 2.3, $F_j(\overline{x}_{j,k})$ by FLS can become

$$F_j\left(\overline{x}_{j,k}\right) = W_j^T S_j\left(\overline{x}_{j,k}\right) + \delta_j\left(\overline{x}_{j,k}\right), \tag{27}$$

where $\delta_j(\overline{x}_{j,k})$ is the approximation error and W_j is the optimal weight vector.

The virtual controller is taken as

$$\alpha_{j,k} = -z_{(j-1)\phi,k} - \widehat{W}_{j,k}^T S_j\left(\overline{x}_{j,k}\right) - \widehat{N}_{j,k}\frac{1}{\Delta_k}z_{j\phi,k} + P_{j-1,k} - \eta_j z_{j,k}. \tag{28}$$

Equations (27) and (28) are substituted into equation (26), then we have

$$\begin{aligned}\dot{z}_{j\phi,k} &= z_{j+1,k} - z_{(j-1)\phi,k} - \widehat{N}_{j,k}\frac{1}{\Delta_k}z_{j\phi,k} - \eta_j z_{j,k} - \mathrm{sgn}\left(z_{j\phi,k}(t)\right)\dot{\phi}_{j,k} \\ &\quad + W_j^T S_j\left(\overline{x}_{j,k}\right) + \delta_j\left(\overline{x}_{j,k}\right) - \widehat{W}_{j,k}^T S_j\left(\overline{x}_{j,k}\right) \\ &= z_{j+1,k} - z_{(j-1)\phi,k} - \widehat{N}_{j,k}\frac{1}{\Delta_k}z_{j\phi,k} - \widetilde{W}_{j,k}^T S_j\left(\overline{x}_{j,k}\right) \\ &\quad + \delta_j\left(\overline{x}_{j,k}\right) - \eta_j z_{j,k} - \mathrm{sgn}\left(z_{j\phi,k}\right)\dot{\phi}_{j,k} \\ &= z_{(j+1)\phi,k} - z_{(j-1)\phi,k} - \widehat{N}_{j,k}\frac{1}{\Delta_k}z_{j\phi,k} - \widetilde{W}_{j,k}^T S_j\left(\overline{x}_{j,k}\right) \\ &\quad + \delta_j\left(\overline{x}_{j,k}\right) + \phi_{(j+1)\phi,k}(t)\mathrm{sat}\left(\frac{z_{(j+1)\phi,k}}{\phi_{(j+1),k}(t)}\right) \\ &\quad - \eta_j z_{j,k} - \mathrm{sgn}\left(z_{j\phi,k}(t)\right)\dot{\phi}_{j,k},\end{aligned} \tag{29}$$

where $\widehat{W}_{j,k}$ and $\widehat{N}_{j,k}$ are the estimated parameters of W_j and N_j, respectively. $\widetilde{W}_{j,k} = \widehat{W}_{j,k} - W_j$ and $\widetilde{N}_{j,k} = \widehat{N}_{j,k} - N_j$ are estimated parameter errors. The last two terms of equation (30) can be changed as

$$\begin{aligned}-\eta_j z_{j,k} - \mathrm{sgn}\left(z_{j\phi,k}\right)\dot{\phi}_{j,k}(t) &= -\eta_j z_{j\phi,k} - \eta_j\phi_{j,k}(t)\mathrm{sat}\left(\frac{z_{j,k}}{\phi_{j,k}(t)}\right) \\ &\quad - \mathrm{sgn}\left(z_{j\phi,k}\right)\dot{\phi}_{j,k}(t) \\ &= -\eta_j z_{j\phi,k}.\end{aligned} \tag{30}$$

Let $\omega_j = \delta_j(\overline{x}_{j,k}) + \phi_{(j+1)\phi,k}(t)\mathrm{sat}(z_{(j+1)\phi,k}/\phi_{(j+1),k}(t))$, then equation (29) becomes

$$\begin{aligned}\dot{z}_{j\phi,k} &= z_{(j+1)\phi,k} - z_{(j-1)\phi,k} - \eta_j z_{j\phi,k} \\ &\quad - \widehat{N}_{j,k}\frac{1}{\Delta_k}z_{j\phi,k} + \widetilde{W}_{j,k}^T S_j\left(\overline{x}_{j,k}\right) + \omega_j.\end{aligned} \tag{31}$$

Assumption j. ω_j satisfies $|\omega_j| \le \omega_{Mj}$; here, ω_{Mj} is unknown.

Positive definite function is chosen:

$$V_{j,k} = V_{j-1,k} + \frac{1}{2}z_{j\phi,k}^2 + \frac{1}{2}\widetilde{W}_{j,k}^T\Gamma_{1j}^{-1}\widetilde{W}_{j,k} + \frac{1}{2}\Gamma_{2j}^{-1}\widetilde{N}_{j,k}^2. \quad (32)$$

Derive $V_{j,k}$ according to equation (31),

$$\dot{V}_{j,k} \le z_{j\phi,k}z_{(j+1)\phi,k} - \sum_{l=1}^{j}\eta_l z_{l,k}^2 - \sum_{l=1}^{j}\widetilde{W}_{l,k}^T\Gamma_{1l}^{-1}\left(\Gamma_{1l}S_j\left(\overline{x}_{l,k}\right)z_{l\phi,k} - \dot{\widehat{W}}_{l,k}\right) - \sum_{l=1}^{j}\widetilde{N}_{l,k}\Gamma_{2l}^{-1}\left(\Gamma_{2l}\frac{1}{\Delta_k}z_{l\phi,k}^2 - \dot{\widehat{N}}_{l,k}\right) + j\frac{1}{4}\Delta_k. \quad (33)$$

Step n. Define $z_{n,k} = x_{n,k} - \alpha_{n-1,k}$; $z_{n\phi,k}$ from Section 2.4 is introduced as

$$z_{n\phi,k} = z_{n,k} - \phi_{n,k}(t)\mathrm{sat}\left(\frac{z_{n,k}}{\phi_{n,k}(t)}\right), \qquad \phi_{n,k}(t) = \varepsilon_{n,k}e^{-\eta_n t}. \quad (34)$$

Derive $z_{n\phi,k}$ as follows:

$$\dot{z}_{n\phi,k} = \Gamma(u_k) + f\left(\overline{x}_{n,k}\right) - \dot{\alpha}_{n-1,k} - \mathrm{sgn}\left(z_{n\phi,k}\right)\dot{\phi}_{n,k}(t), \quad (35)$$

where $\dot{\alpha}_{n-1,k} = \sum_{l=1}^{n-1}(\partial\alpha_{n-1,\ k}/\partial x_{l,k})(x_{l+1,k} + f_l(\overline{x}_{l,k})) + (\partial\alpha_{n-1,k}/\partial\widehat{W}_{n-1,k})\dot{\widehat{W}}_{n-1,k} + (\partial\alpha_{n-1,k}/\partial\widehat{N}_{n-1,k})\ \dot{\widehat{N}}_{n-1,k} + (\alpha_{n-1,k}/\partial t)$. Denote $F_n(\overline{x}_{n,k}) = f_n(\overline{x}_{n,k}) - \sum_{l=1}^{n}(\partial\alpha_{n-1,k}/\partial x_{l,k})(x_{l+1,k} + f_l(\overline{x}_{l,k}))$, $P_{n-1,k} = (\partial\alpha_{n-1,k}/\partial\widehat{W}_{n-1,k})\dot{\widehat{W}}_{n-1,k} + (\partial\alpha_{n-1,k}\ /\partial\widehat{N}_{n-1,k})\dot{\widehat{N}}_{n-1,k} + (\alpha_{n-1,k}/\partial t)$, and by equation (3), then equation (35) can be rewritten as

$$\dot{z}_{n\phi,k} = m(t)u_k + F\left(\overline{x}_{n,k}\right) - P_{n-1,k} - \mathrm{sgn}\left(z_{n\phi,k}\right)\dot{\phi}_{n,k}(t) + d(t), \quad (36)$$

from which $F_n(\overline{x}_{n,k})$ can be rewritten as follows:

$$F_n\left(\overline{x}_{n,k}\right) = W_n^T S_n\left(\overline{x}_{n,k}\right) + \delta_n\left(\overline{x}_{n,k}\right), \quad (37)$$

where $\delta_n(\overline{x}_{n,k})$ is the approximation error and W_n is an optimal weight vector.

Let $u_{1,k} = -z_{(n-1)\phi,k} - \widehat{W}_{n,k}^T\ S_n(\overline{x}_{n,k}) - \widehat{N}_{n,k}(1/\Delta_k)z_{n,k} + P_{n-1,k} - \eta_n z_{n,k}$. Take the actual controller as

$$u_k = u_{1,k} + u_{2,k}, \quad (38)$$

where $u_{2,k}$ is designed to compensate for unknown input gain $m(t)$.

Then, according to equations (37) and (38), equation (36) can be rewritten as

$$\begin{aligned}\dot{z}_{n\phi,k} &= u_k + (m(t)-1)u_k + W_n^T S_n\left(\overline{x}_{n,k}\right) + \delta_n\left(\overline{x}_{n,k}\right) - P_{n-1,k} - \mathrm{sgn}\left(z_{n\phi,k}\right)\dot{\phi}_{n,k}(t) + d(t)\\ &= -z_{(n-1)\phi,k} - \widetilde{W}_{n,k}^T S_n\left(\overline{x}_{n,k}\right) - \widehat{N}_{n,k}\frac{1}{\Delta_k}z_{n,k} + m(t)u_{2,k} + (m(t)-1)u_{1,k}\\ &\quad + \delta_n\left(\overline{x}_{n,k}\right) + d(t) - \eta_n z_{n,k} - \mathrm{sgn}\left(z_{n\phi,k}\right)\dot{\phi}_{n,k}(t),\end{aligned} \quad (39)$$

where $\widehat{W}_{n,k}$ and $\widehat{N}_{n,k}$ are the estimated parameters of W_n and N_n, respectively. $\widetilde{W}_{n,k} = \widehat{W}_{n,k} - W_n$ and $\widetilde{N}_{n,k} = \widehat{N}_{n,k} - N_n$ are the estimated parameter errors.

The last two terms of equation (39) can be changed as

$$\begin{aligned}-\eta_n z_{n,k} - \mathrm{sgn}\left(z_{n\phi,k}\right)\dot{\phi}_{n,k}(t) &= -\eta_n z_{n\phi,k} - \eta_n\phi_{n,k}(t)\mathrm{sat}\left(\frac{z_{n,k}}{\phi_{n,k}(t)}\right) - \mathrm{sgn}\left(z_{n\phi,k}\right)\dot{\phi}_{n,k}(t)\\ &= -\eta_n z_{n\phi,k}.\end{aligned} \quad (40)$$

Then,

$$\dot{z}_{n\phi,k} = -z_{(n-1)\phi,k} - \eta_n z_{n\phi,k} - \widetilde{W}_{n,k}^T S_n\left(\overline{x}_{n,k}\right) - \widehat{N}_{n,k}\frac{1}{\Delta_k}z_{n,k} + m(t)u_{2,k} + (m(t)-1)u_{1,k} + \delta_n\left(\overline{x}_{n,k}\right) + d(t). \quad (41)$$

Take $u_{2,k} = -\mathrm{sat}(z_{n,k}/\phi_{n,k}(t))(\widehat{\rho}_k(t)+1)|u_{1,k}|$, where $\widehat{\rho}_k(t)$ is the estimation of uncertain parameter $\rho = 1/m(t)$ and let $\omega_n = \delta_n(\overline{x}_{n,k}) + d(t)$, then equation (41) becomes

$$\dot{z}_{n\phi,k} = -z_{(n-1)\phi,k} - \eta_n z_{n\phi,k} - \widetilde{W}_{n,k}^T S_n\left(\overline{x}_{n,k}\right) - \widehat{N}_{n,k}\frac{1}{\Delta_k}z_{n\phi,k} - m(t)\mathrm{sat}\left(\frac{z_{n,k}}{\phi_{n,k}(t)}\right)(\widehat{\rho}_k(t)+1)\left|u_{1,k}\right| + (m(t)-1)u_{1,k} + \omega_n. \quad (42)$$

Assumption n. Because of assumptions 1 and 2, ω_n is bounded such that $|\omega_n| \le \omega_{Mn}$ with ω_{Mn} being unknown.

Adaptive learning laws are taken as follows:

$$\dot{\widehat{W}}_{j,k} = \Gamma_{1j}S_j\left(\overline{x}_{j,k}\right)z_{j\phi,k}, \quad j = 1,\ldots,m, \quad (43)$$

$$\dot{\widehat{N}}_{j,k} = \Gamma_{2j}\frac{1}{\Delta_k}z_{j\phi,k}^2, \quad j = 1,\ldots,m, \quad (44)$$

$$\dot{\widehat{\rho}}_k(t) = \Gamma_3\left|u_{1,k}\right|\left|z_{n\phi,k}\right|, \quad (45)$$

where Γ_3 is the learning gain to be designed.

Positive definite function is chosen:

$$V_{n,k} = V_{n-1,k} + \frac{1}{2}z_{n\phi,k}^2 + \frac{1}{2}\widetilde{W}_{n,k}^T\Gamma_{1n}^{-1}\widetilde{W}_{n,k} + \frac{1}{2}\Gamma_{2n}^{-1}\widetilde{N}_{n,k}^2 + \frac{1}{2}\Gamma_3^{-1}m(t)\widetilde{\rho}_k^2. \quad (46)$$

Derive $V_{n,k}$ according to equation (42) and substitute equations (43)–(45) into it, then

$$\dot{V}_{n,k} \le z_{(n-1)\phi,k}z_{n\phi,k} - \sum_{l=1}^{n-1}\eta_l z_{l\phi,k}^2 - \sum_{l=1}^{n-1}\widetilde{W}_{l,k}^T\Gamma_{1l}^{-1}\left(\Gamma_{1l}S_l\left(\overline{x}_{l,k}\right)z_{l\phi,k} - \dot{\widehat{W}}_{l,k}\right)$$

$$
\begin{aligned}
&- \sum_{l=1}^{n-1} \widetilde{N}_{l,k}\Gamma_{2l}^{-1}\left(\Gamma_{2l}\frac{1}{\Delta_k}z_{l\phi,k}^2 - \dot{\widehat{N}}_{l,k}\right) + (n-1)\frac{1}{4}\Delta_k \\
&+ z_{n\phi,k}\dot{z}_{n\phi,k} + \widetilde{W}_{n,k}^T\Gamma_{1n}^{-1}\dot{\widehat{W}}_{n,k} \\
&+ \Gamma_{2n}^{-1}\widetilde{N}_{n,k}\dot{\widehat{N}}_{n,k} + \Gamma_3^{-1}m(t)\widetilde{\rho}_k\dot{\widehat{\rho}}_k \\
\le & - \sum_{l=1}^{n}\eta_l z_{l\phi,k}^2 - \sum_{l=1}^{n}\widetilde{W}_{l,k}^T\Gamma_{1l}^{-1}\left(\Gamma_{1l}S_l\left(\overline{x}_{l,k}\right)z_{l\phi,k} - \dot{\widehat{W}}_{l,k}\right) \\
&- \sum_{l=1}^{n-1} \widetilde{N}_{l,k}\Gamma_{2l}^{-1}\left(\Gamma_{2l}\frac{1}{\Delta_k}z_{l\phi,k}^2 - \dot{\widehat{N}}_{l,k}\right) + (n-1)\frac{1}{4}\Delta_k \\
&- \widehat{N}_{n,k}\frac{1}{\Delta_k}z_{n\phi,k}^2 - m(t)\widehat{\rho}_k(t)\left|u_{1,k}\right|\left|z_{n\phi,k}\right| + \left|u_{1,k}\right|\left|z_{n\phi,k}\right| \\
&+ \frac{1}{\Delta_k}\omega_{Nn}^2 z_{n\phi,k}^2 + \frac{1}{4}\Delta_k + \Gamma_{2n}^{-1}\widetilde{N}_{n,k}\dot{\widehat{N}}_{n,k} + \Gamma_3^{-1}m(t)\widetilde{\rho}_k\dot{\widehat{\rho}}_k \\
= & - \sum_{l=1}^{n}\eta_l z_{l\phi,k}^2 - \sum_{l=1}^{n}\widetilde{W}_{l,k}^T\Gamma_{1l}^{-1}\left(\Gamma_{1l}S_l\left(\overline{x}_{l,k}\right)z_{l\phi,k} - \dot{\widehat{W}}_{l,k}\right) \\
&- \sum_{l=1}^{n} \widetilde{N}_{l,k}\Gamma_{2l}^{-1}\left(\Gamma_{2l}\frac{1}{\Delta_k}z_{l\phi,k}^2 - \dot{\widehat{N}}_{l,k}\right) + n\frac{1}{4}\Delta_k \\
&- \Gamma_3^{-1}m(t)\widetilde{\rho}_k\left(\left|\Gamma_3\right|\left|u_{1,k}\right|\left|z_{n\phi,k}\right| - \dot{\widehat{\rho}}_k\right) \\
= & - \sum_{l=1}^{n}\eta_l z_{l,k}^2 + n\frac{1}{4}\Delta_k.
\end{aligned}
\tag{47}
$$

The assumption below is needed.

Assumption 5. For any k, as $t = 0, \widehat{N}_{j,k}(0) = \widehat{N}_{j,k-1}(T)$, $\widehat{W}_{j,k}(0) = \widehat{W}_{j,k-1}(T)$; $j = 1, \ldots, m$, $\widehat{\rho}_k(0) = \widehat{\rho}_{k-1}(T)$.

Theorem 1. *Under assumptions 1, 2, 3, 4–n, and 5, design controller equation (38), and adaptive parameter estimation laws (43)–(45) for system (1), we get all signals bounded, and*

$$\lim_{k\longrightarrow\infty} z_{l\phi,k}(t) = 0, \quad l = 1, 2, \ldots, n, \tag{48}$$

i.e., $\lim_{k\longrightarrow\infty} z_{1\phi,k}(t) = 0$, $\|z_{1,k}(t)\| < \phi_{1,\infty}(t) + \varsigma$ *as* $k \longrightarrow \infty$, *where* ς *is a small positive parameter.*

Proof. From Section 2.4, $\|z_{\phi,k}(0)\|^2 = 0 \le \|z_{\phi,k}(T)\|^2$, where $z_{\phi,k} = [z_{1\phi,k}, z_{2\phi,k}, \ldots, z_{n\phi,k}]^T$. By (46), we get

$$V_{n,k}\left(z_{\phi,k}(0), \widehat{W}_k(T), \widehat{N}_k(T), \widehat{\rho}_k(T)\right) \le V_{n,k}(0) + \int_0^T \dot{V}_{n,k}\mathrm{d}t, \tag{49}$$

where $\widehat{W}_k = [\widehat{W}_{1,k}, \widehat{W}_{2,k}, \ldots, \widehat{N}_{n,k}]^T$, $\widehat{N}_k = [\widehat{N}_{1,k}, \widehat{N}_{2,k}, \ldots, \widehat{N}_{n,k}]^T$.

Substituting equation (47) into equation (49), we get

$$
\begin{aligned}
V_{n,k}\left(z_{\phi,k}(0), \widehat{W}_k(T), \widehat{N}_k(T), \widehat{\rho}_k(T)\right) &\le V_{n,1}(0) \\
&- \sum_{j=1}^{k}\sum_{l=1}^{m}\int_0^T \eta_l\left(z_{l\phi,j}\right)^2\mathrm{d}t + n\left(\frac{1}{4}\right)T\left(\sum_{j=1}^{k}\Delta_j\right).
\end{aligned}
\tag{50}
$$

Denote $V_{0,k} = V_{n,1}(0) + n(1/4)T(\sum_{j=1}^{k}\Delta_j)$, then equation (50) can be rewritten as

$$\sum_{l=1}^{k}\sum_{l=1}^{n}\int_0^T \eta_l\left(z_{l\phi,j}\right)^2\mathrm{d}t \le V_{0,k} - V_{n,k}\left(z_{\phi,k}(0), \widehat{W}_k(T), \widehat{N}_k(T), \widehat{\rho}_k(T)\right). \tag{51}$$

By equation (6), $\lim_{k\longrightarrow\infty} V_{0,k} \le V_{n,1}(0) + 2\mathrm{an}(1/4)T$, then $V_{0,k}$ is bounded; by assumption 5 and equation (50), $V_{n,k}(0)$ can be bounded. $V_{n,k}(z_k(0), \widehat{W}_k(T), \widehat{N}_k(T), \widehat{\rho}_k(T)) \ge 0$, so

$$\lim_{k\longrightarrow\infty}\sum_{l=1}^{n}\int_0^T \eta_l\left(z_{l\phi,k}\right)^2\mathrm{d}t = 0. \tag{52}$$

By equation (46), for any k, $V_{n,k}(t) = V_{n,k}(0) + \int_0^t \dot{V}_{n,k}(\tau)\mathrm{d}\tau$, by (47), then

$$V_{n,k}(t) \le V_{n,k}(0) - \sum_{l=1}^{n}\int_0^t \eta_l\left(z_{l\phi,k}(\tau)\right)^2\mathrm{d}\tau + \mathrm{tn}\left(\frac{1}{4}\right)\Delta_k. \tag{53}$$

By equation (52), $\sum_{l=1}^{n}\int_0^t \eta_l(z_{l\phi,k}(\tau))^2\mathrm{d}\tau$ is bounded. By Definition 1, Δ_k is bounded, and $t \in [0, T]$, so $\mathrm{tn}(1/4)\Delta_k$ is also bounded. From above all, for any k, $V_{n,k}(t)$ is bounded, then we have $x_{j,k}$; $\widehat{W}_k(t)$ and $\widehat{N}_k(t)$ are bounded. By equation (38), u_k is bounded. By equation (31), $\dot{z}_{j\phi,k}$ is bounded; $z_{j\phi,k}$ is continuous uniformly; according to Barbalat lemma, $z_{j\phi,k} \longrightarrow 0$ when $k \longrightarrow \infty$, i.e., $k \longrightarrow \infty$, $z_{1\phi,k} \longrightarrow 0$, then $\|z_{1\phi,k}\| < \varsigma$. $\|z_{1,k}\| = \|z_{1\phi,k} + \mathrm{sgn}(z_{1\phi,k})\phi_{1,k}(t)\| \le \|z_{1\phi,k}\| + \|\phi_{1,k}(t)\| < \|\phi_{1,k}(t)\| + \varsigma$, so $k \longrightarrow \infty$, $\|z_{1,k}\| < \phi_{1,\infty}(t) + \varsigma$, finished. □

4. Simulation

In this section, a mass-spring mechanical system is considered to show the effectiveness of the proposed controller. $\overline{m}$ is a mass; assume that resistive force caused by friction is zero. The external force u_k drives the mass, which is a control variable. y_k is the displacement from a reference position; the motion equation of the system with nonsymmetric deadzone input is as follows:

$$\overline{m}\ddot{y}_k + F_{ms}(y_k) = \Gamma(u_k), \tag{54}$$

where $t \in [0, \pi]$, $F_{ms}(\cdot)$ is the spring's restoring force; k denotes the iteration index.

We define $x_{1,k} = y_k$, $x_{2,k} = \dot{y}_k$, and $\overline{m} = 1$, so equation (54) can be transformed into the state-space form

$$
\begin{aligned}
\dot{x}_{1,k} &= x_{2,k}, \\
\dot{x}_{2,k} &= \Gamma(u_k) - F_{ms}\left(x_{1,k}\right).
\end{aligned}
\tag{55}
$$

The spring's restoring force can be modeled as

$$F_{ms}\left(x_{1,k}\right) = kx_{1,k}\left(\sum_{i=0}^{q} a_i x_{1,k}^i\right). \tag{56}$$

In the system, we have $k = 1$, $a_0 = 0$, $a_1 = a_2 = a_3 = a_4 = 1$, and $q = 4$.

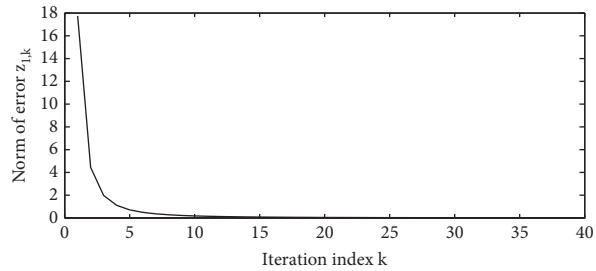

Figure 1: Curve graph of $\|z_{1,k}\|$ along k.

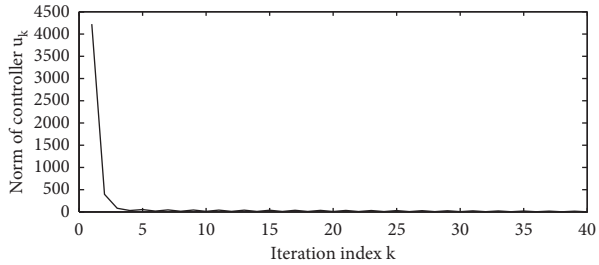

Figure 2: Curve graph of $\|u_k\|$ along k.

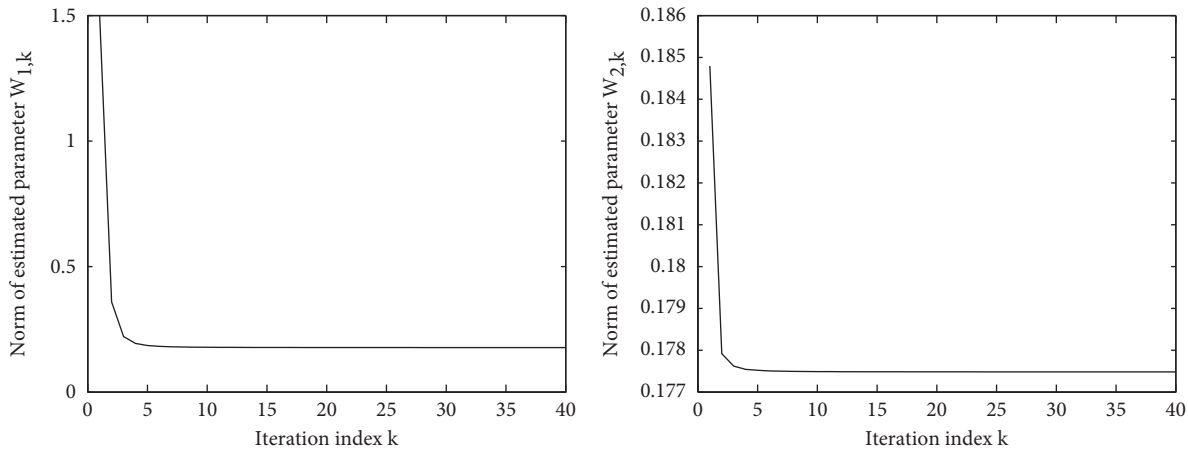

Figure 3: Curve graph of $\|\widehat{W}_{1,k}\|$, $\|\widehat{W}_{2,k}\|$ along k.

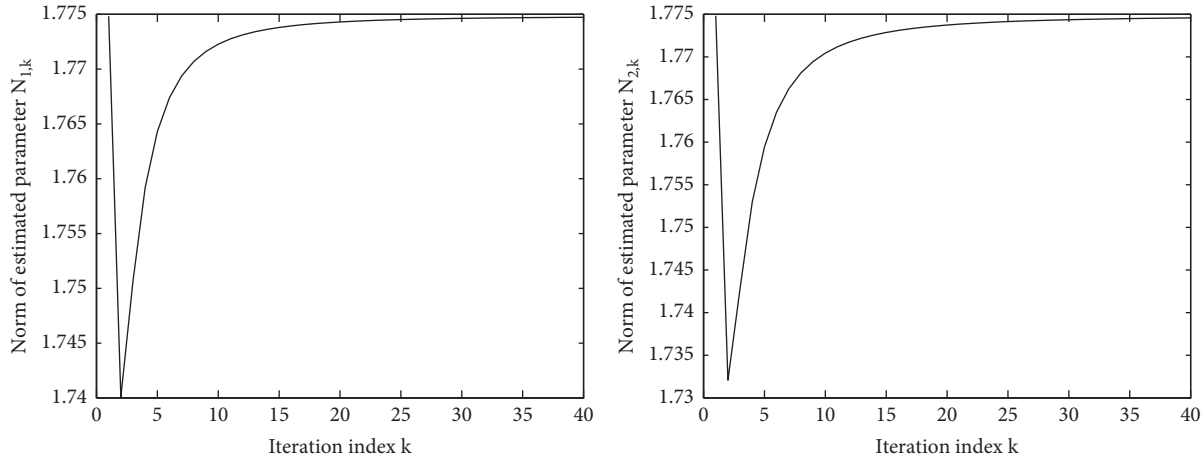

Figure 4: Curve graph of $\|\widehat{N}_{1,k}\|$, $\|\widehat{N}_{2,k}\|$ along k.

The nonsymmetric dead-zone is shown as

$$\Gamma(u_k) = \begin{cases} u_k - 1, & \text{if } u_k \geq 1, \\ 0, & \text{if } -3 < u_k < 1, \\ u_k + 3, & \text{if } u_k \leq -3. \end{cases} \tag{57}$$

System objective is that the output of system (54) can follow the reference trajectory $y_{r,k}$ on $[0, \pi]$ when $k \longrightarrow \infty$. In the different target case, $y_{r,k} = g_k \sin(2t)$ as k is even, and $y_{r,k} = g_k \cos(t)$ as k is odd, where $g_k = \text{rand}(0, 1)$.

By Theorem 1, the AILC is chosen as

$$\begin{aligned} \alpha_{1,k} &= -\widehat{W}_{1,k}^T S_1(\overline{x}_{1,k}) - \widehat{N}_{1,k} \frac{1}{\Delta_k} z_{1\phi,k} + \dot{y}_{r,k} - \eta_1 z_{1,k}, \\ u_k &= u_{1,k} + u_{2,k}, \\ u_{1,k} &= -z_{1\phi,k} - \widehat{W}_{2,k}^T S_2(\overline{x}_{2,k}) - \widehat{N}_{2,k} \frac{1}{\Delta_k} z_{2,k} + P_{1,k} - \eta_2 z_{2,k}, \\ u_{2,k} &= -\text{sat}\left(\frac{z_{2,k}}{\phi_{2,k}(t)} \right) (\widehat{\rho}_k(t) + 1) |u_{1,k}|, \end{aligned} \tag{58}$$

where $P_{1,k} = (\partial \alpha_{1,k} / \partial \widehat{W}_{1,k}) \dot{\widehat{W}}_{1,k} + (\partial \alpha_{1,k} / \partial \widehat{N}_{1,k}) \dot{\widehat{N}}_{1,k} + (\alpha_{1,k} / \partial y_r) \dot{y}_r + (\alpha_{1,k} / \partial \dot{y}_r) \ddot{y}_r$ and the estimation laws are represented by equations (43)–(45), where $\eta_1 = 10$, $\eta_2 = 1$, $\Delta_k = a/k^2$, $a = 100/3$, $\Gamma_{11} = \text{diag}\{0.1, 0.1, 0.1, 0.1, 0.1\}$, $\Gamma_{21} = 1$, $\Gamma_{12} = \text{diag}\{0.1, 0.1, 0.1, 0.1, 0.1\}$, $\Gamma_{22} = 1$, and $\Gamma_3 = 1$. The inputs of the FLS are $x_{1,k}$, $x_{2,k}$; the membership function of every variable is given as follows:

$$\begin{aligned} \mu_{A_i^1} &= \exp\left(-\left(\frac{y_i + a_i}{b_i} \right)^2 \right), \\ \mu_{A_i^2} &= \exp\left(-\left(\frac{y_i + 0.5 \times a_i}{b_i} \right)^2 \right), \\ \mu_{A_i^3} &= \exp\left(-\left(\frac{y_i}{b_i} \right)^2 \right), \\ \mu_{A_i^4} &= \exp\left(-\left(\frac{y_i - 0.5 \times a_i}{b_i} \right)^2 \right), \\ \mu_{A_i^5} &= \exp\left(-\left(\frac{y_i - a_i}{b_i} \right)^2 \right), \end{aligned} \tag{59}$$

where $i = 1, \ldots, 4$, $y_1 = x_{1,k}$, $y_2 = x_{2,k}$, $a_1 = a_2 = 2$, and $b_1 = b_2 = 2$, and the fuzzy rules are given as

$$R_t^j: \text{ if } y_t \text{ is } A_t^j, f_s(\overline{x}_s) \text{ is } B_s^j, \tag{60}$$

where $s = 1, 2$: as $s = 1$, $t = 1, 2, 3$, as $s = 2$, $t = 1, 2, 4$. The period of sampling is 0.01 s.

Here, choose the parameters and initial values as follows: $z_{1,k}(0) = 1/k^2$, $z_{2,k}(0) = 1/k^2$, $\widehat{W}_{1,1}(0) = [0.01, 0, 0, 0, 0]^T$, $\widehat{W}_{2,1}(0) = [0.01, 0, 0, 0, 0]^T$, $\widehat{N}_{1,1}(0) = -0.1$, $\widehat{N}_{2,1}(0) = -0.1$, and $\widehat{\rho}_1(0) = 0.1$. Taking $k = 40$, Figures 1–5 are the simulation figures.

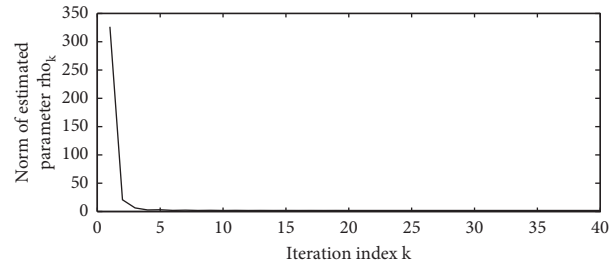

Figure 5: Curve graph of $\|\widehat{\rho}_k\|$ along k.

Figure 1 shows the convergence of error. Moreover, on the interval $[0, \pi]$, Figures 2–5 give that $\|u_k\|$, $\|\widehat{W}_{1,k}\|$, $\|\widehat{W}_{2,k}\|$, $\|\widehat{N}_{1,k}\|$, $\|\widehat{N}_{2,k}\|$, and $\|\widehat{\rho}_k\|$ are bounded. Figures 1–5 confirm the validity of control scheme which is developed in this article from the simulation results.

5. Conclusions

The different target tracking problem for unknown nonlinear systems with nonsymmetric dead-zone input is solved. Introduce FLS to deal with the uncertain dynamics, and the problem of approximation error and initial state error can be efficiently solved by suitable means. This paper can keep all signals being bounded on $[0, T]$; errors can converge to a small set along iteration increasing. Simulation study proves the correctness of AILC method of this paper.

Data Availability

No data were used to support this study.

Conflicts of Interest

The authors declare that they have no conflicts of interest.

Acknowledgments

This work was supported by the National Natural Science Foundation of China under Grant no. 61603296 and Natural Science Foundation Project of Shaanxi Provincial Education Department under Grant no. 16JK1541.

References

[1] J.-X. Xu and J. Xu, "On iterative learning from different tracking tasks in the presence of time-varying uncertainties," *IEEE Transactions on Systems, Man and Cybernetics, Part B (Cybernetics)*, vol. 34, no. 1, pp. 589–597, 2004.

[2] J. M. Li, Y. P. Sun, and Y. Liu, "Hybrid adaptive iterative learning control of non-uniform trajectory tracking," *Control Theory & Applications*, vol. 25, no. 1, pp. 100–104, 2008.

[3] C.-L. Zhang and J.-M. Li, "Adaptive iterative learning control of non-uniform trajectory tracking for strict feedback nonlinear time-varying systems with unknown control direction," *Applied Mathematical Modelling*, vol. 39, no. 10-11, pp. 2942–2950, 2015.

[4] J. Xu, "Fault-tolerant iterative learning control for mobile robots non-repetitive trajectory tracking with output constraints," *Automatica*, vol. 94, pp. 63–71, 2018.

[5] H. Yue and S. Yu, "Adaptive fuzzy tracking control for a class of stochastic nonlinearly parameterized systems with distributed input delay," *Journal of the Franklin Institute*, vol. 353, no. 3, pp. 713–734, 2016.

[6] H. Y. Yue, J. R. Shi, L. Y. Du et al., "Adaptive fuzzy tracking control for a class of perturbed nonlinearly parameterized systems using minimal learning parameters algorithm," *Iranian Journal of Fuzzy Systems*, vol. 15, no. 3, pp. 99–116, 2018.

[7] H. Y. Yue et al., "Fuzzy adaptive tracking control for a class of nonlinearly parameterized systems with unknown control directions, Iran," *Journal of Fuzzy Systems*, vol. 16, no. 5, pp. 97–112, 2019.

[8] H. Yue, Z. Wei, Q. Chen, and X. Zhang, "Dynamic surface control for a class of nonlinearly parameterized systems with input time delay using neural network," *Journal of the Franklin Institute*, vol. 357, no. 4, pp. 1961–1986, 2020.

[9] C. J. Chiang-Ju Chien, "A combined adaptive law for fuzzy iterative learning control of nonlinear systems with varying control tasks," *IEEE Transactions on Fuzzy Systems*, vol. 16, no. 1, pp. 40–51, 2008.

[10] C. L. Zhang and X. Tian, "Non-uniform trajectory tracking adaptive iterative learning control for nonlinear pure-feedback systems with initial state error based on RBF-neural network," in *Proceedings of the 40th Chinese Control Conference*, Shanghai, China, July 2021.

[11] A. Taybi and C. J. Chien, "A unified adaptive iterative learning control framework for uncertain nonlinear systems," *IEEE Transactions on Automatic Control*, vol. 52, no. 10, pp. 1907–1913, 2007.

[12] J. X. Jian-Xin Xu and R. Rui Yan, "Adaptive learning control for finite interval tracking based on constructive function approximation and wavelet," *IEEE Transactions on Neural Networks*, vol. 22, no. 6, pp. 893–905, 2011.

[13] C. Zhang and J. Li, "Adaptive iterative learning control for nonlinear pure-feedback systems with initial state error based on fuzzy approximation," *Journal of the Franklin Institute*, vol. 351, no. 3, pp. 1483–1500, 2014.

[14] J.-X. Xu and R. Yan, "Iterative learning control design without a priori knowledge of the control direction," *Automatica*, vol. 40, no. 10, pp. 1803–1809, 2004.

[15] Y. Tan, H.-H. Dai, D. Huang, and J.-X. Xu, "Unified iterative learning control schemes for nonlinear dynamic systems with nonlinear input uncertainties," *Automatica*, vol. 48, no. 12, pp. 3173–3182, 2012.

[16] X. J. Wu, X. L. Wu, R. Zhen, X. y. Luo, and Q. M. Zhu, "Adaptive control for time-delay non-linear systems with non-symmetric input non-linearity," *International Journal of Modelling, Identification and Control*, vol. 13, no. 3, pp. 152–160, 2011.

[17] X. Luo, X. Guan, and X. Wu, "Adaptive backstepping fault-tolerant control for unmatched non-linear systems against actuator dead-zone," *IET Control Theory and Applications*, vol. 4, no. 5, pp. 879–888, 2010.

[18] X. Wu, X. Wu, X. Luo, Q. Zhu, and X. Guan, "Neural network-based adaptive tracking control for nonlinearly parameterized systems with unknown input nonlinearities," *Neurocomputing*, vol. 82, pp. 127–142, 2012.

[19] W. S. Chen, "Adaptive backstepping dynamic surface control for systems with periodic disturbances using neural networks," *IET Control Theory and Applications*, vol. 3, no. 10, pp. 1383–1394, 2009.

[20] S. Zhu, M.-X. Sun, and X.-X. He, "Iterative learning control of strict-feedback nonlinear time-varying systems," *Acta Automatica Sinica*, vol. 36, no. 3, pp. 454–458, 2010.

[21] J. Li and J. Li, "Adaptive iterative learning control for coordination of second-order multi-agent systems," *International Journal of Robust and Nonlinear Control*, vol. 24, no. 18, pp. 3282–3299, 2014.

[22] Y. Chen, Z. Liu, C. L. P. Chen, and Y. Zhang, "Adaptive fuzzy control of switched nonlinear systems with uncertain dead-zone: a mode-dependent fuzzy dead-zone model," *Neurocomputing*, vol. 432, pp. 133–144, 2021.

[23] D. Meng and K. L. Moore, "Learning to cooperate: networks of formation agents with switching topologies," *Automatica*, vol. 64, pp. 278–293, 2016.

[24] L. X. Wang, "Fuzzy systems are universal approximators," in *Proceedings of the IEEE International Conference on Fuzzy Systems*, pp. 1163–1170, San Diego, CA, USA, March 1992.

Hindawi
Mathematical Problems in Engineering
Volume 2021, Article ID 6858023, 10 pages
https://doi.org/10.1155/2021/6858023

Research Article

RBFNN-Based Nonuniform Trajectory Tracking Adaptive Iterative Learning Control for Uncertain Nonlinear System with Continuous Nonlinearly Input

Chunli Zhang, Xu Tian, and Lei Yan

Xi'an University of Technology, Shannxi Key Laboratory of Complex System Control and Intelligent Information Processing, Xi'an, China

Correspondence should be addressed to Chunli Zhang; gaozhangchunli@163.com

Received 12 July 2021; Revised 23 July 2021; Accepted 27 July 2021; Published 9 August 2021

Academic Editor: Ali Ahmadian

This paper proposes an adaptive iterative learning control (AILC) method for uncertain nonlinear system with continuous nonlinearly input to solve different target tracking problem. The method uses the radial basis function neural network (RBFNN) to approximate every uncertain term in systems. A time-varying boundary layer, a typical convergent series are introduced to deal with initial state error and unknown bounds of errors, respectively. The conclusion is that the tracking error can converge to a very small area with the number of iterations increasing. All closed-loop signals are bounded on finite-time interval $[0, T]$. Finally, the simulation result of mass-spring mechanical system shows the correctness of the theory and validity of the method.

1. Introduction

The research of the nonuniform trajectory is an interesting problem. Two new AILC methods for first-order hybrid parametric systems and high-order nonlinear hybrid parameter systems were proposed in the literature studies [1, 2], respectively. Recently, AILC was presented, the literature [3] proposed a nonuniform target tracking AILC method, and the literature [4] proposed a fault-tolerant ILC technique for mobile robot nonrepetitive target tracking with output constraints. An ILC for a flapping wing micro aerial vehicle under distributed disturbances was proposed in the literature [5]. It can be seen from the above literature studies that solving the nonuniform target tracking problem for uncertain nonlinear systems is an important problem.

Adaptive control is used to handle system control problem about uncertainties. Adaptive control schemes learn uncertainties by adaptive laws. NN and FLS are used in the method as function approximators, for example, the paper [6, 7]. The literature [8] could complete the varying control tasks by designing an adaptive fuzzy ILC for the uncertain nonlinear system. Based on RBF neural network approximation, the paper [9] proposed AILC for nonlinear pure-feedback systems to solve the nonuniform target tracking problem. The uniform AILC frame for uncertain nonlinear system was proposed in the literature [10], by Lyapunov theory, and it could prove the convergence. It should be noted that Lyapunov function-based AILC played an important role in dealing with the time-varying parameter [8, 10, 11]. However, initial state error problem is a challenging one as they need to converge to zero for keeping stability. The literature studies [8, 9, 12] considered this problem recently. It is an important problem for AILC.

Because the actuator's physical is limited, the control input widely exists continuous nonlinearly such that system performance can be deteriorated. In the literature studies [13–22], control performance could change by using different technique recently. The literature [15] solved the question of adaptive stabilization for the time-delay system. The literature [16] developed an adaptive backstepping method of uncertain nonlinear systems about nonsymmetric

dead-zone. As yet, there is no report from the literature for the AILC of nonlinear systems with continuous nonlinearly input and initial state error. This is a problem that needs to be solved urgently.

In this paper, the nonuniform trajectory tracking issue is discussed for the uncertain nonlinear systems with continuous nonlinearly input and initial state error. The contributions of the proposed control method are presented as follows:

(i) The nonuniform trajectory tracking issue is studied for uncertain nonlinear systems under continuous nonlinearly input and initial state error issues.

(ii) The AILC method is used to uncertain nonlinear systems. The RNFNN is introduced to learn unknown dynamic. A convergence order is introduced to solve the unknown bound and nonuniform target tracking problem.

Finally, simulation results of the mass-spring mechanical system are given to verify the validity of the designed controller.

This paper is organized as follows: in Section 2, the system description and related concepts are given in detail. The main results are presented in Section 3. A simulation is shown in Section 4. Section 5 is the conclusion.

2. System Description and Related Concepts

2.1. System Model. The following nonlinear systems are considered:

$$\begin{aligned} \dot{x}_{1,k} &= x_{2,k} + f_1\left(\overline{x}_{1,k}\right), \\ \dot{x}_{j,k} &= x_{j+1,k} + f_j\left(\overline{x}_{j,k}\right), \\ \dot{x}_{n,k} &= N\left(u_k\right) + f_n\left(\overline{x}_{n,k}\right), \\ y_k &= x_{1,k}, \end{aligned} \tag{1}$$

where $\overline{x}_{j,k} = [x_{1,k}, \ldots, x_{j,k}]^T \in R^j$, and $x = \overline{x}_n$ is the state that is measured. $N(u_k) \in R$ represents the actuator characteristics, and $y_k \in R$ is the system output. $f_j(\overline{x}_{j,k})$, $j = 1, 2, \ldots, n$, are smooth unknown nonlinear functions.

$N(u_k)$ represents continuous nonlinearly input with $N(0) = 0$ which belongs to $[g_1, g_2]$, i.e.,

$$\begin{cases} g_1 u_k \le N\left(u_k\right) \le g_2 u_k, & \text{if } u_k \ge 0, \\ g_1 u_k \ge N\left(u_k\right) \ge g_2 u_k, & \text{if } u_k \le 0. \end{cases} \tag{2}$$

Assumption 1. g_1 and g_2 are unknown nonzero positive parameters.

Remark 1. This is a reasonable assumption, because many system constraints can satisfy this condition.

Designing an AILC law $u_k(t)$ on $[0, T]$ to make the output $y_k(t)$ following the target trajectory $y_{r,k}(t)$ is the control objective of this paper; that is to say, $\lim_{k\longrightarrow\infty}\|y_k(t) - y_{r,k}(t)\| \le \varrho$, where ϱ is a very small positive number. All closed-loop signals are guaranteed to be bounded. $y_{r,k}(t)$ is the smooth desired target. k is the iteration index.

2.2. Convergent Series Sequence. The following definition and lemma are used in the controller design process.

Definition 1 (see [19]). $\{\Delta_k\}$ is a series convergent sequence which is shown as

$$\Delta_k = \frac{a}{k^l}, \tag{3}$$

where $k = 1, 2, \ldots$, a and l satisfies $a > 0 \in R$, $l \ge 2 \in N$.

Lemma 1 (see [19]). *For $\{1/k^l\}$, where $k = 1, 2, \ldots, l \ge 2$, the following inequality holds:*

$$\lim_{k\longrightarrow\infty} \sum_{j=1}^{k} \frac{1}{j^l} \le 2. \tag{4}$$

2.3. Description of RBFNN Approximation (see [23])

$$F_j\left(\overline{x}_{j,k}\right) = W^T \zeta_j\left(\overline{x}_{j,k}\right) + \delta_j\left(\overline{x}_{j,k}\right), \tag{5}$$

where $\zeta_j(\overline{x}_{j,k}) = [s_1(\overline{x}_{j,k}), \ldots, s_l(\overline{x}_{j,k})]^T \colon \Omega \longrightarrow R^m$ are known, and $l > 1$ is the number of NN node. $s_j(\overline{x}_{j,k})(1 \le j \le l)$ are Gaussian basis functions, $s_j(\overline{x}_{j,k}) = \exp[-\|\overline{x}_{j,k} - \mu_j\|^2/\eta^2]$, $\mu_j \in \Omega$, and $\eta > 0$ are the center and the width of $s_j(\overline{x}_{j,k})$, respectively. The truth weight $W = [w_1, \ldots, w_l]^T$ is given as follows:

$$W = \operatorname{argmin}_{\widehat{W}\in R^l}\left\{\sup_{\overline{x}_{j,k}\in\Omega}\left|F_j\left(\overline{x}_{j,k}\right) - \widehat{W}^T\zeta\left(\overline{x}_{j,k}\right)\right|\right\}, \tag{6}$$

and $\delta(\overline{x}_{j,k})$ are the NN approximation errors. The following assumption holds.

Assumption 2. On a compact set Ω, $\delta_j(\overline{x}_{j,k})$ are bounded and $|\delta_j(\overline{x}_{j,k})| \le \theta_j$, where $\theta_j (1 \le j \le n)$ are unknown and $\theta_j \ge 0$.

Remark 2. This is a general assumption for the approximation error of the neural network. The approximation error can be arbitrarily decreased by increased NN node number. So, this assumption is reasonable. The following assumptions $(4 - j)$, $j = 1, 2, \ldots, n$ are also reasonable.

2.4. Time-Varying Boundary Layer. The following functions $z_{j\phi,k}$ are introduced to deal with initial state errors:

$$\begin{aligned} z_{j\phi,k} &= z_{j,k} - \phi_{j,k}(t)\operatorname{sat}\left(\frac{z_{j,k}}{\phi_{j,k}(t)}\right), \\ \phi_{j,k}(t) &= \varepsilon_{j,k} e^{-\eta t}, \end{aligned} \tag{7}$$

where $z_{j,k}$ and $z_{j\phi,k}$ are variables of t, $\varepsilon_{j,k}$ are sequences of convergent series, and the saturation function sat is given as follows:

$$\operatorname{sat}\left(\frac{z_{j,k}}{\phi_{j,k}(t)}\right)=\begin{cases}1, & \text{if } z_{j,k}>\phi_{j,k}(t),\\ \dfrac{z_{j,k}}{\phi_{j,k}(t)}, & \text{if } \left\|z_{j,k}\right\|\le\phi_{j,k}(t),\\ -1, & \text{if } z_{j,k}<-\phi_{j,k}(t),\end{cases}\tag{8}$$

where $\phi_{j,k}(t)$ are the time-varying boundary layers. The control objective can be achieved by this. See the literature [8] for specific analysis.

Assumption 3. The initial state errors must satisfy $|z_{j,k}(0)| = \varepsilon_{j,k}$ for some known positive parameters $\varepsilon_{j,k}$, $j = 1, \ldots, n$, where $z_{j,k}(0)$ are initial state errors at each iteration of state errors which are given later in this paper.

Remark 3. Under normal circumstances, the initial state errors at each iteration are zero, small, or fixed. Compared with the assumptions of the initial state in other articles, the assumptions in this paper are more relaxed and easy to be satisfied.

3. Adaptive Iterative Learning Controller Design and Convergence Analysis

In this section, we will discuss the detailed controller design process, main conclusion, and specific proof process.

3.1. Adaptive Iterative Learning Controller Design. The following Lemma 2 is used in the controller design process.

Lemma 2. *For the controller u_k and the error $z_{n\phi,k}$, the following inequality holds:*

$$z_{n\phi,k}N(u_k)\le g z_{n\phi,k}u_k,\quad g\in\{g_1, g_2\}.\tag{9}$$

Proof. If both sides of equation (2) multiply u_k, we obtain

$$g_1u_k^2\le u_kN(u_k)\le g_2u_k^2.\tag{10}$$

If both sides of equation (10) multiply $z_{n\phi,k}^2$, we obtain

$$g_1u_k^2z_{n\phi,k}^2\le u_kN(u_k)z_{n\phi,k}^2\le g_2u_k^2z_{n\phi,k}^2,\tag{11}$$

i.e.,

$$g_1\left(z_{n\phi,k}u_k\right)^2\le z_{n\phi,k}\left(z_{n\phi,k}u_k\right)N(u_k)\le g_2\left(z_{n\phi,k}u_k\right)^2.\tag{12}$$

If u_k satisfies $z_{n\phi,k}u_k\le 0$, then

$$z_{n\phi,k}N(u_k)\le g_1z_{n\phi,k}u_k.\tag{13}$$

If u_k satisfies $z_{n\phi,k}u_k\ge 0$, then

$$z_{n\phi,k}N(u_k)\le g_2z_{n\phi,k}u_k.\tag{14}$$

So, the result is obtained.

The specific process about designing controller is given as follows. □

Step 1. Let $z_{1,k}=x_{1,k}-y_{r,k}$, $z_{2,k}=x_{2,k}-\alpha_{1,k}$, $F_1(\overline{x}_{1,k})=f_1(\overline{x}_{1,k})$, $\alpha_{1,k}$ is the virtual controller. Introduce error function $z_{1\phi,k}$ and $z_{2\phi,k}$ by Section 2.4 to deal with initial state error as

$$\begin{aligned}z_{1\phi,k}&=z_{1,k}-\phi_{1,k}(t)\operatorname{sat}\left(\frac{z_{1,k}}{\phi_{1,k}(t)}\right),\\ \phi_{1,k}(t)&=\epsilon_{1,k}e^{-\eta_1t};\\ z_{2\phi,k}&=z_{2,k}-\phi_{2,k}(t)\operatorname{sat}\left(\frac{z_{2,k}}{\phi_{2,k}(t)}\right),\\ \phi_{2,k}(t)&=\epsilon_{2,k}e^{-\eta_2t}.\end{aligned}\tag{15}$$

Recall that

$$\dot{x}_{1,k}=x_{2,k}+F_1\left(\overline{x}_{1,k}\right).\tag{16}$$

The derivative of $z_{1\phi,k}$ is as follows:

$$\begin{aligned}\dot{z}_{1\phi,k}=&\,z_{2,k}+\alpha_{1,k}+F_1\left(\overline{x}_{1,k}\right)\\ &-\dot{y}_{r,k}-\operatorname{sgn}\left(z_{1\phi,k}\right)\dot{\phi}_{1,k}.\end{aligned}\tag{17}$$

According to Section 2.3, by RBFNN, $F_1(\overline{x}_{1,k})$ is approximated and approximate error $\delta_1(\overline{x}_{1,k})$ is as follows:

$$F_1\left(\overline{x}_{1,k}\right)=W_1^T\zeta_1\left(\overline{x}_{1,k}\right)+\delta_1\left(\overline{x}_{1,k}\right),\tag{18}$$

where W_1 is optimal weight vector.

Denote $N_1=\omega_{M1}^2$, which is needed later, $\Delta_k=a/k^l$, $a>0$, and $l\ge 2$. The virtual controller is taken as

$$\begin{aligned}\alpha_{1,k}=&-\widehat{W}_{1,k}^T\zeta_1\left(\overline{x}_{1,k}\right)-\widehat{N}_{1,k}\frac{1}{\Delta_k}z_{1\phi,k}\\ &+\dot{y}_{r,k}-\eta_1z_{1,k}.\end{aligned}\tag{19}$$

When (18) and (19) are substituted into (17), we have

$$\begin{aligned}\dot{z}_{1\phi,k}=&\,z_{2,k}-\widehat{N}_{1,k}\frac{1}{\Delta_k}z_{1\phi,k}\\ &+W_1^T\zeta_1\left(\overline{x}_{1,k}\right)+\delta_1\left(\overline{x}_{1,k}\right)-\widehat{W}_{1,k}^T\zeta_1\left(\overline{x}_{1,k}\right)\\ &-\eta_1z_{1,k}-\operatorname{sgn}\left(z_{1\phi,k}\right)\dot{\phi}_{1,k}(t)\\ =&\,z_{2\phi,k}-\widehat{N}_{1,k}\frac{1}{\Delta_k}z_{1\phi,k}-\widetilde{W}_{1,k}^T\zeta_1\left(\overline{x}_{1,k}\right)\\ &+\delta_1\left(\overline{x}_{1,k}\right)+\phi_{2,k}(t)\operatorname{sat}\left(\frac{z_{2,k}}{\phi_{2,k}(t)}\right)\\ &-\eta_1z_{1,k}-\operatorname{sgn}\left(z_{1\phi,k}\right)\dot{\phi}_{1,k}(t),\end{aligned}\tag{20}$$

where estimated W_1 and N_1 are $\widehat{W}_{1,k}$ and $\widehat{N}_{1,k}$, respectively. $\widetilde{W}_{1,k}=\widehat{W}_{1,k}-W_1$ and $\widetilde{N}_{1,k}=\widehat{N}_{1,k}-N_1$ are the errors of estimated parameters. The last two terms of (20) can be changed to

$$
\begin{aligned}
&- \eta_1 z_{1,k} - \operatorname{sgn}\left(z_{1\phi,k}\right)\dot{\phi}_{1,k}(t) \\
&= -\eta_1 z_{1\phi,k} - \eta_1 \phi_{1,k}(t)\operatorname{sat}\left(\frac{z_{1,k}}{\phi_{1,k}(t)}\right) - \operatorname{sgn}\left(z_{1\phi,k}\right)\dot{\phi}_{1,k}(t) \\
&= -\eta_1 z_{1\phi,k}.
\end{aligned} \tag{21}
$$

By (20), (21) can be rewritten as

$$
\begin{aligned}
\dot{z}_{1\phi,k} &= z_{2\phi,k} - \widehat{N}_{1,k}\frac{1}{\Delta_k} z_{1\phi,k} - \eta_1 z_{1\phi,k} \\
&\quad + \widetilde{W}_1^T \zeta_1\left(\overline{x}_{1,k}\right) + \delta_1\left(\overline{x}_{1,k}\right) \\
&\quad + \phi_{2,k}(t)\operatorname{sat}\left(\frac{z_{2,k}}{\phi_{2,k}(t)}\right).
\end{aligned} \tag{22}
$$

Let $\omega_1 = \delta_1(\overline{x}_{1,k}) + \phi_{2,k}(t)\operatorname{sat}(z_{2,k}(t)/\phi_{2,k}(t))$, then (22) becomes

$$
\begin{aligned}
\dot{z}_{1\phi,k} &= z_{2\phi,k} - \widehat{N}_{1,k}\frac{1}{\Delta_k} z_{1\phi,k} - \eta_1 z_{1\phi,k} \\
&\quad + \widetilde{W}_1^T \zeta_1\left(\overline{x}_{1,k}\right) + \omega_1.
\end{aligned} \tag{23}
$$

Assumption 4. 1: the bounded term ω_1 satisfies $|\omega_1| \le \omega_{M1}$, where ω_{M1} is a positive parameter.

Take the following nonnegative function:

$$
V_{1,k} = \frac{1}{2} z_{1\phi,k}^2 + \frac{1}{2}\widetilde{W}_{1,k}^T \Gamma_{11}^{-1} \widetilde{W}_{1,k} + \frac{1}{2}\Gamma_{21}^{-1}\widetilde{N}_{1,k}^2, \tag{24}
$$

where Γ_{11} and Γ_{21} are the symmetric positive definite matrixes. The derivative of $V_{1,k}$ along (23) is as follows:

$$
\begin{aligned}
\dot{V}_{1,k} &= z_{1\phi,k} z_{2\phi,k} - \eta_1 z_{1\phi,k}^2 \\
&\quad - \widetilde{W}_{1,k}^T \Gamma_{11}^{-1}\left(\Gamma_{11}\zeta_1\left(\overline{x}_{1,k}\right) z_{1\phi,k} - \dot{\widehat{W}}_{1,k}\right) \\
&\quad - \widehat{N}_{1,k}\frac{1}{\Delta_k} z_{1\phi,k}^2 + \omega_{1,k} z_{1\phi,k} + \Gamma_{21}^{-1}\widetilde{N}_{1,k}\dot{\widehat{N}}_{1,k} \\
&\le z_{1\phi,k} z_{2\phi,k} - \eta_1 z_{1\phi,k}^2 \\
&\quad - \widetilde{W}_{1,k}^T \Gamma_{11}^{-1}\left(\Gamma_{11}\zeta_1\left(\overline{x}_{1,k}\right) z_{1\phi,k} - \dot{\widehat{W}}_{1,k}\right) \\
&\quad - \widehat{N}_{1,k}\frac{1}{\Delta_k} z_{1\phi,k}^2 + \frac{1}{\Delta_k}\omega_{M1}^2 z_{1\phi,k}^2 \\
&\quad + \frac{1}{4}\Delta_k + \Gamma_{21}^{-1}\widetilde{N}_{1,k}\dot{\widehat{N}}_{1,k} \\
&= z_{1\phi,k} z_{2\phi,k} - \eta_1 z_{1\phi,k}^2 \\
&\quad - \widetilde{W}_{1,k}^T \Gamma_{11}^{-1}\left(\Gamma_{11}\zeta_1\left(\overline{x}_{1,k}\right) z_{1\phi,k} - \dot{\widehat{W}}_{1,k}\right) \\
&\quad - \widetilde{N}_{1,k}\Gamma_{21}^{-1}\left(\Gamma_{21}\frac{1}{\Delta_k} z_{1\phi,k}^2 - \dot{\widehat{N}}_{1,k}\right) + \frac{1}{4}\Delta_k.
\end{aligned} \tag{25}
$$

In previous equation, $mn \le (1/r)m^2 + (1/4)n^2 r$ is used, where $r = \Delta_k$.

Step 2. j: $(2 \le j \le n-1)$. Denote $F_j(\overline{x}_{j,k}) = f_j(\overline{x}_{j,k}) - \sum_{l=1}^{j-1}(\partial\alpha_{j-1,k}/\partial x_{l,k})\dot{x}_{l,k}(\overline{x}_{l,k})$, $N_j = \omega_{Mj}^2$, which is given later. $z_{j+1,k} = x_{j+1,k} - \alpha_{j,k}$, similar to Step 1, and $z_{j\phi,k}$ and $z_{(j+1)\phi,k}$ by Section 2.4 are introduced as follows:

$$
\begin{aligned}
z_{j\phi,k} &= z_{j,k} - \phi_{j,k}(t)\operatorname{sat}\left(\frac{z_{j,k}}{\phi_{j,k}(t)}\right), \\
\phi_{j,k}(t) &= \varepsilon_{j,k} e^{-\eta_j t}, \\
z_{(j+1)\phi,k} &= z_{(j+1),k} - \phi_{(j+1),k}(t)\operatorname{sat}\left(\frac{z_{(j+1),k}}{\phi_{(j+1),k}(t)}\right), \\
\phi_{(j+1),k}(t) &= \varepsilon_{(j+1),k} e^{-\eta_{(j+1)} t}.
\end{aligned} \tag{26}
$$

The derivative of $z_{j\phi,k}$ is as follows:

$$
\begin{aligned}
\dot{z}_{j\phi,k} &= z_{j+1,k} + \alpha_{j,k} + f_j\left(\overline{x}_{j,k}\right) \\
&\quad - \dot{\alpha}_{j-1,k} - \operatorname{sgn}\left(z_{j\phi,k}(t)\right)\dot{\phi}_{j,k},
\end{aligned} \tag{27}
$$

where $\dot{\alpha}_{j-1,k} = \sum_{l=1}^{j} -1\partial\alpha_{j-1,k}/\partial x_{l,k}(x_{l+1,k} + f_l(\overline{x}_{l,k})) + (\partial\alpha_{j-1,k}/\partial\widehat{W}_{j-1,k})\dot{\widehat{W}}_{j-1,k} + (\partial\alpha_{j-1,k}/\partial\widehat{N}_{j-1,k})\dot{\widehat{N}}_{j-1,k} + \alpha_{j-1,k}/\partial t$. Denote $F_j(\overline{x}_{j,k}) = f_j(\overline{x}_{j,k}) - \sum_{l=1}^{j}\partial\alpha_{j-1,k}/\partial x_{j,k}(x_{j+1,k} + f_j(\overline{x}_{j,k}))$, $P_{j-1,k} = (\partial\alpha_{j-1,k}/\partial\widehat{W}_{j-1,k})\dot{\widehat{W}}_{j-1,k} + (\partial\alpha_{j-1,k}/\partial\widehat{N}_{j-1,k})\dot{\widehat{N}}_{j-1,k} + \alpha_{j-1,k}/\partial t$, then (27) can be rewritten as

$$
\begin{aligned}
\dot{z}_{j\phi,k} &= z_{j+1,k} + \alpha_{j,k} + F_j\left(\overline{x}_{j,k}\right) \\
&\quad - P_{j-1,k} - \operatorname{sgn}\left(z_{j\phi,k}(t)\right)\dot{\phi}_{j,k}.
\end{aligned} \tag{28}
$$

According to Section 2.3, $F_j(\overline{x}_{j,k})$ can become by the RBFNN

$$
F_j\left(\overline{x}_{j,k}\right) = W_j^T \zeta_j\left(\overline{x}_{j,k}\right) + \delta_j\left(\overline{x}_{j,k}\right), \tag{29}
$$

where $\delta_j(\overline{x}_{j,k})$ are the approximation errors and W_j are optimal weight vectors.

The virtual controller is chosen as follows:

$$
\begin{aligned}
\alpha_{j,k} &= -z_{(j-1)\phi,k} - \widehat{W}_{j,k}^T \zeta_j\left(\overline{x}_{j,k}\right) - \widehat{N}_{j,k}\frac{1}{\Delta_k} z_{j\phi,k} \\
&\quad + P_{j-1,k} - \eta_j z_{j,k}.
\end{aligned} \tag{30}
$$

When (29) and (30) are substituted into (28), we have

$$
\begin{aligned}
\dot{z}_{j\phi,k} &= z_{j+1,k} - z_{(j-1)\phi,k} - \widehat{N}_{j,k}\frac{1}{\Delta_k} z_{j\phi,k} - \eta_j z_{j,k} - \operatorname{sgn}\left(z_{j\phi,k}(t)\right)\dot{\phi}_{j,k} \\
&\quad + W_j^T \zeta_j\left(\overline{x}_{j,k}\right) + \delta_j\left(\overline{x}_{j,k}\right) - \widehat{W}_{j,k}^T \zeta_j\left(\overline{x}_{j,k}\right) \\
&= z_{j+1,k} - z_{(j-1)\phi,k} - \widehat{N}_{j,k}\frac{1}{\Delta_k} z_{j\phi,k} - \widetilde{W}_{j,k}^T \zeta_j\left(\overline{x}_{j,k}\right) + \delta_j\left(\overline{x}_{j,k}\right) \\
&\quad - \eta_j z_{j,k} - \operatorname{sgn}\left(z_{j\phi,k}\right)\dot{\phi}_{j,k} \\
&= z_{(j+1)\phi,k} - z_{(j-1)\phi,k} - \widehat{N}_{j,k}\frac{1}{\Delta_k} z_{j\phi,k} - \widetilde{W}_{j,k}^T \zeta_j\left(\overline{x}_{j,k}\right) \\
&\quad + \delta_j\left(\overline{x}_{j,k}\right) + \phi_{(j+1)\phi,k}(t)\operatorname{sat}\left(\frac{z_{(j+1)\phi,k}}{\phi_{(j+1),k}(t)}\right) \\
&\quad - \eta_j z_{j,k} - \operatorname{sgn}\left(z_{j\phi,k}(t)\right)\dot{\phi}_{j,k},
\end{aligned} \tag{31}
$$

where $\widehat{W}_{j,k}$ and $\widehat{N}_{j,k}$ are the estimated parameters of W_j and N_j, respectively. $\widetilde{W}_{j,k} = \widehat{W}_{j,k} - W_j$ and $\widetilde{N}_{j,k} = \widehat{N}_{j,k} - N_j$ are estimated parameter errors. The last two terms of (31) can be changed as

$$\begin{aligned} &-\eta_j z_{j,k} - \operatorname{sgn}\left(z_{j\phi,k}\right)\dot{\phi}_{j,k}(t) \\ &= -\eta_j z_{j\phi,k} - \eta_j \phi_{j,k}(t)\operatorname{sat}\left(\frac{z_{j,k}}{\phi_{j,k}(t)}\right) - \operatorname{sgn}\left(z_{j\phi,k}\right)\dot{\phi}_{j,k}(t) \\ &= -\eta_j z_{j\phi,k}. \end{aligned} \tag{32}$$

Let $\omega_j = \delta_j(\overline{x}_{j,k}) + \phi_{(j+1)\phi,k}(t)\operatorname{sat}(z_{(j+1)\phi,k}/\phi_{(j+1),k}(t))$, then (31) becomes

$$\begin{aligned} \dot{z}_{j\phi,k} &= z_{(j+1)\phi,k} - z_{(j-1)\phi,k} - \eta_j z_{j\phi,k} - \widehat{N}_{j,k}\frac{1}{\Delta_k} z_{j\phi,k} \\ &\quad + \widetilde{W}_{j,k}^T \zeta_j\left(\overline{x}_{j,k}\right) + \omega_j. \end{aligned} \tag{33}$$

Assumption 5. j: ω_j satify $|\omega_j| \le \omega_{Mj}$, here ω_{Mj} is unknown.

The following positive definite function is chosen:

$$V_{j,k} = V_{j-1,k} + \frac{1}{2}z_{j\phi,k}^2 + \frac{1}{2}\widetilde{W}_{j,k}^T \Gamma_{1j}^{-1}\widetilde{W}_{j,k} + \frac{1}{2}\Gamma_{2j}^{-1}\widetilde{N}_{j,k}^2. \tag{34}$$

The derivative of $V_{j,k}$ is as follows by substituting (33):

$$\begin{aligned} \dot{V}_{j,k} &\le z_{j\phi,k} z_{(j+1)\phi,k} - \sum_{l=1}^{j} \eta_l z_{l,k}^2 \\ &\quad - \sum_{l=1}^{j} \widetilde{W}_{l,k}^T \Gamma_{1l}^{-1}\left(\Gamma_{1l}\zeta_j\left(\overline{x}_{l,k}\right) z_{l\phi,k} - \dot{\widehat{W}}_{l,k}\right) \\ &\quad - \sum_{l=1}^{j} \widetilde{N}_{l,k}\Gamma_{2l}^{-1}\left(\Gamma_{2l}\frac{1}{\Delta_k} z_{l\phi,k}^2 - \dot{\widehat{N}}_{l,k}\right) + j\frac{1}{4}\Delta_k. \end{aligned} \tag{35}$$

Step 3. n, define $z_{n,k} = x_{n,k} - \alpha_{n-1,k}$, $z_{n\phi,k}$ by Section 2.4 is introduced as follows:

$$\begin{aligned} z_{n\phi,k} &= z_{n,k} - \phi_{n,k}(t)\operatorname{sat}\left(\frac{z_{n,k}}{\phi_{n,k}(t)}\right), \\ \phi_{n,k}(t) &= \varepsilon_{n,k} e^{-\eta_n t}. \end{aligned} \tag{36}$$

The derivative of $z_{n\phi,k}$ is as follows:

$$\begin{aligned} \dot{z}_{n\phi,k} &= N(u_k) + f\left(\overline{x}_{n,k}\right) - \dot{\alpha}_{n-1,k} \\ &\quad - \operatorname{sgn}\left(z_{n\phi,k}\right)\dot{\phi}_{n,k}(t), \end{aligned} \tag{37}$$

where $\dot{\alpha}_{n-1,k} = \sum_{l=1}^{n-1} \partial\alpha_{n-1,k}/\partial x_{l,k}\,(x_{l+1,k} + f_l(\overline{x}_{l,k})) + (\partial\alpha_{n-1,k}/\partial\widehat{W}_{n-1,k})\dot{\widehat{W}}_{n-1,k} + (\partial\alpha_{n-1,k}/\partial\widehat{N}_{n-1,k})\dot{\widehat{N}}_{n-1,k} + \partial\alpha_{n-1,k}/\partial t$. Denote $F_n(\overline{x}_{n,k}) = f_n(\overline{x}_{n,k}) - \sum_{l=1}^{n} \partial\alpha_{n-1,k}/\partial x_{l,k}\,(x_{l+1,k} + f_l(\overline{x}_{l,k}))$, $P_{n-1,k} = (\partial\alpha_{n-1,k}/\partial\widehat{W}_n \quad -1,k)\dot{\widehat{W}}_{n-1,k} + (\partial\alpha_{n-1,k}/\partial\widehat{N}_{n-1,k})\dot{\widehat{N}}_{n-1,k} + (\partial\alpha_{n-1,k}/\partial t)$, and then (37) can be rewritten as follows:

$$\begin{aligned} \dot{z}_{n\phi,k} &= N(u_k) + F\left(\overline{x}_{n,k}\right) - P_{n-1,k} \\ &\quad - \operatorname{sgn}\left(z_{n\phi,k}\right)\dot{\phi}_{n,k}(t). \end{aligned} \tag{38}$$

$F_n(\overline{x}_{n,k})$ can be rewritten by RBFNN approximation as follows:

$$F_n\left(\overline{x}_{n,k}\right) = W_n^T \zeta_n\left(\overline{x}_{n,k}\right) + \delta_n\left(\overline{x}_{n,k}\right), \tag{39}$$

where $\delta_n(\overline{x}_{n,k})$ is the approximation error and W_n is an optimal weight vector.

Then, (38) can be rewritten by substituting (39):

$$\begin{aligned} \dot{z}_{n\phi,k} &= N(u_k) + W_n^T \zeta_n\left(\overline{x}_{n,k}\right) + \delta_n\left(\overline{x}_{n,k}\right) \\ &\quad - P_{n-1,k} - \operatorname{sgn}\left(z_{n\phi,k}\right)\dot{\phi}_{n,k}(t). \end{aligned} \tag{40}$$

Lyapunov function is chosen as follows:

$$\begin{aligned} V_{n,k} &= V_{n-1,k} + \frac{1}{2}z_{n\phi,k}^2 + \frac{1}{2}\widetilde{W}_{n,k}^T \Gamma_{1n}^{-1}\widetilde{W}_{n,k} \\ &\quad + \frac{1}{2}\Gamma_{2n}^{-1}\widetilde{N}_{n,k}^2 + \frac{1}{2}\Gamma_4^{-1} g\widetilde{\varrho}_k^2, \end{aligned} \tag{41}$$

where estimated W_n, N_n and $\varrho = 1/g$ are $\widehat{W}_{n,k}$, $\widehat{N}_{n,k}$ and $\widehat{\varrho}_k(t)$, respectively. $\widetilde{W}_{n,k} = \widehat{W}_{n,k} - W_n$, $\widetilde{N}_{n,k} = \widehat{N}_{n,k} - N_n$, and $\widetilde{\varrho}_k(t) = \widehat{\varrho}_k(t) - \varrho$ are parameter estimation errors. And Γ_4 is learning gain to be designed.

Using the derivative of $V_{n,k}$ along (40), then we have

$$\begin{aligned} \dot{V}_{n,k} &\le z_{(n-1)\phi,k} z_{n\phi,k} - \sum_{l=1}^{n-1} \eta_l z_{l\phi,k}^2 \\ &\quad - \sum_{l=1}^{n-1} \widetilde{W}_{l,k}^T \Gamma_{1l}^{-1}\left(\Gamma_{1l}\zeta_l\left(\overline{x}_{l,k}\right) z_{l\phi,k} - \dot{\widehat{W}}_{l,k}\right) \\ &\quad - \sum_{l=1}^{n-1} \widetilde{N}_{l,k}\Gamma_{2l}^{-1}\left(\Gamma_{2l}\frac{1}{\Delta_k} z_{l\phi,k}^2 - \dot{\widehat{N}}_{l,k}\right) \\ &\quad + (n-1)\frac{1}{4}\Delta_k + z_{n\phi,k}\dot{z}_{n\phi,k} + \widetilde{W}_{n,k}^T \Gamma_{1n}^{-1}\dot{\widehat{W}}_{n,k} \\ &\quad + \Gamma_{2n}^{-1}\widetilde{N}_{n,k}\dot{\widehat{N}}_{n,k} + \Gamma_4^{-1} g\widetilde{\varrho}_k\dot{\widehat{\varrho}}_k \\ &\le z_{(n-1)\phi,k} z_{n\phi,k} - \sum_{l=1}^{n-1} \eta_j z_{l\phi,k}^2 \\ &\quad - \sum_{l=1}^{n-1} \widetilde{W}_{l,k}^T \Gamma_{1l}^{-1}\left(\Gamma_{1l}\zeta_l\left(\overline{x}_{l,k}\right) z_{l\phi,k} - \dot{\widehat{W}}_{l,k}\right) \\ &\quad - \sum_{l=1}^{n-1} \widetilde{N}_{l,k}\Gamma_{2l}^{-1}\left(\Gamma_{2l}\frac{1}{\Delta_k} z_{l\phi,k}^2 - \dot{\widehat{N}}_{l,k}\right) \\ &\quad + (n-1)\frac{1}{4}\Delta_k + \left(u_k + (g-1)u_k\right. \\ &\quad + W_n^T \zeta_n\left(\overline{x}_{n,k}\right) + \delta_n\left(\overline{x}_{n,k}\right) - P_{n-1,k} \\ &\quad \left. -\operatorname{sgn}\left(z_{n\phi,k}\right)\dot{\phi}_{n,k}(t)\right) z_{n\phi,k} + \widetilde{W}_{n,k}^T \Gamma_{1n}^{-1}\dot{\widehat{W}}_{n,k} \\ &\quad + \Gamma_{2n}^{-1}\widetilde{N}_{n,k}\dot{\widehat{N}}_{n,k} + \Gamma_4^{-1} g\widetilde{\varrho}_k\dot{\widehat{\varrho}}_k. \end{aligned} \tag{42}$$

Choose $u_{1,k} = -z_{(n-1)\phi,k} - \widehat{W}_{n,k}^T \zeta_n(\overline{x}_{n,k}) - \widehat{N}_{n,k}(1/\Delta_k) z_{n,k} + P_{n-1,k} - \eta_n z_{n,k}$.

Take the actual controller as follows:

$$u_k = u_{1,k} + u_{2,k}, \tag{43}$$

where $u_{2,k}$ is needed to design for dealing with g.

Then, (42) becomes

$$\begin{aligned}
\dot{V}_{n,k} \le\ & z_{(n-1)\phi,k} z_{n\phi,k} - \sum_{l=1}^{n-1} \eta_l z_{l\phi,k}^2 \\
& - \sum_{l=1}^{n-1} \widetilde{W}_{l,k}^T \Gamma_{1l}^{-1} \left(\Gamma_{1l} \zeta_l\left(\overline{x}_{l,k}\right) z_{l\phi,k} - \dot{\widehat{W}}_{l,k} \right) \\
& - \sum_{l=1}^{n-1} \widetilde{N}_{l,k} \Gamma_{2l}^{-1} \left(\Gamma_{2l} \frac{1}{\Delta_k} z_{l\phi,k}^2 - \dot{\widehat{N}}_{l,k} \right) \\
& + (n-1)\frac{1}{4}\Delta_k + \Big(-z_{(n-1)\phi,k} - \widetilde{W}_{n,k}^T \zeta_n\left(\overline{x}_{n,k}\right) \\
& - \widehat{N}_{n,k} \frac{1}{\Delta_k} z_{n,k} - \eta_n z_{n,k} + (g-1)\left(u_{1,k} + u_{2,k}\right) \\
& + u_{2,k} + \delta_n\left(\overline{x}_{n,k}\right) - \operatorname{sgn}\left(z_{n\phi,k}\right) \dot{\phi}_{n,k}(t) \Big) z_{n\phi,k} \\
& + \widetilde{W}_{n,k}^T \Gamma_{1n}^{-1} \dot{\widehat{W}}_{n,k} + \Gamma_{2n}^{-1} \widetilde{N}_{n,k} \dot{\widehat{N}}_{n,k} + \Gamma_4^{-1} g \widetilde{\varrho}_k \dot{\widehat{\varrho}}_k.
\end{aligned} \tag{44}$$

When $\omega_n = \delta_n(\overline{x}_{n,k})$, the following equation holds:

$$\begin{aligned}
& - \eta_n z_{n,k} - \operatorname{sgn}\left(z_{n\phi,k}\right) \dot{\phi}_{n,k}(t) \\
& = -\eta_n z_{n\phi,k} - \eta_n \phi_{n,k}(t) \operatorname{sat}\left(\frac{z_{n,k}}{\phi_{n,k}(t)} \right) - \operatorname{sgn}\left(z_{n\phi,k}\right) \dot{\phi}_{n,k}(t) \\
& = -\eta_n z_{n\phi,k},
\end{aligned} \tag{45}$$

and then we have

$$\begin{aligned}
\dot{V}_{n,k} \le\ & - \sum_{l=1}^{n} \eta_l z_{l\phi,k}^2 \\
& - \sum_{l=1}^{n-1} \widetilde{W}_{l,k}^T \Gamma_{1l}^{-1} \left(\Gamma_{1l} \zeta_l\left(\overline{x}_{l,k}\right) z_{l\phi,k} - \dot{\widehat{W}}_{l,k} \right) \\
& - \sum_{l=1}^{n-1} \widetilde{N}_{l,k} \Gamma_{2l}^{-1} \left(\Gamma_{2l} \frac{1}{\Delta_k} z_{l\phi,k}^2 - \dot{\widehat{N}}_{l,k} \right) \\
& + (n-1)\frac{1}{4}\Delta_k + \Big(-\widetilde{W}_{n,k}^T \zeta_n\left(\overline{x}_{n,k}\right) \\
& - \widehat{N}_{n,k} \frac{1}{\Delta_k} z_{n\phi,k} + g u_{2,k} + (g-1) u_{1,k} \\
& + \omega_n \Big) z_{n\phi,k} + \widetilde{W}_{n,k}^T \Gamma_{1n}^{-1} \dot{\widehat{W}}_{n,k} + \Gamma_{2n}^{-1} \widetilde{N}_{n,k} \dot{\widehat{N}}_{n,k} + \Gamma_4^{-1} g \widetilde{\varrho}_k \dot{\widehat{\varrho}}_k.
\end{aligned} \tag{46}$$

Take $u_{2,k} = -\operatorname{sat}(z_{n,k}/\phi_{n,k}(t))(\widehat{\varrho}_k(t) + 1)|u_{1,k}|$, and then (46) becomes

$$\begin{aligned}
\dot{V}_{n,k} \le\ & - \sum_{l=1}^{n} \eta_l z_{l\phi,k}^2 \\
& - \sum_{l=1}^{n-1} \widetilde{W}_{l,k}^T \Gamma_{1l}^{-1} \left(\Gamma_{1l} \zeta_l\left(\overline{x}_{l,k}\right) z_{l\phi,k} - \dot{\widehat{W}}_{l,k} \right) \\
& - \sum_{l=1}^{n-1} \widetilde{N}_{l,k} \Gamma_{2l}^{-1} \left(\Gamma_{2l} \frac{1}{\Delta_k} z_{l\phi,k}^2 - \dot{\widehat{N}}_{l,k} \right) \\
& + (n-1)\frac{1}{4}\Delta_k + \Big(-\widetilde{W}_{n,k}^T \zeta_n\left(\overline{x}_{n,k}\right) \\
& - \widehat{N}_{n,k} \frac{1}{\Delta_k} z_{n\phi,k} + \omega_n \\
& - g \operatorname{sat}\left(\frac{z_{n,k}}{\phi_{n,k}(t)} \right) \left(\widehat{\varrho}_k(t) + 1\right) \left| u_{1,k} \right| + (g-1) u_{1,k} \\
& + \widetilde{W}_{n,k}^T \Gamma_{1n}^{-1} \dot{\widehat{W}}_{n,k} + \Gamma_{2n}^{-1} \widetilde{N}_{n,k} \dot{\widehat{N}}_{n,k} + \Gamma_4^{-1} g \widetilde{\varrho}_k \dot{\widehat{\varrho}}_k.
\end{aligned} \tag{47}$$

Assumption 6. n: bounded ω_n satisfies $|\omega_n| \le \omega_{Mn}$, here ω_{Mn} is an unknown parameter.

Choose the AILC laws as follows:

$$\dot{\widehat{W}}_{j,k} = \Gamma_{1j} \zeta_j\left(\overline{x}_{j,k}\right) z_{i\phi,k}, \quad j = 1, \ \ldots, m, \tag{48}$$

$$\dot{\widehat{N}}_{j,k} = \Gamma_{2j} \frac{1}{\Delta_k} z_{j\phi,k}^2, \quad j = 1, \ldots, m, \tag{49}$$

$$\dot{\widehat{\varrho}}_k(t) = \Gamma_4 \left| u_{1,k} \right\| z_{n\phi,k} \Big|, \tag{50}$$

and then we obtain

$$\begin{aligned}
\dot{V}_{n,k} \le\ & - \sum_{l=1}^{n} \eta_l z_{l\phi,k}^2 \\
& - \sum_{l=1}^{n} \widetilde{W}_{l,k}^T \Gamma_{1l}^{-1} \left(\Gamma_{1l} \zeta_l\left(\overline{x}_{l,k}\right) z_{l\phi,k} - \dot{\widehat{W}}_{l,k} \right) \\
& - \sum_{l=1}^{n} \widetilde{N}_{l,k} \Gamma_{2l}^{-1} \left(\Gamma_{2l} \frac{1}{\Delta_k} z_{l\phi,k}^2 - \dot{\widehat{N}}_{l,k} \right) + n\frac{1}{4}\Delta_k \\
& - \Gamma_4^{-1} g \widetilde{\varrho}_k \left(\Gamma_4 \left| u_{1,k} \right\| z_{n\phi,k} \right| - \dot{\widehat{\varrho}}_k \Big) \\
= & - \sum_{l=1}^{n} \eta_l z_{l,k}^2 + n\frac{1}{4}\Delta_k.
\end{aligned} \tag{51}$$

3.2. Convergence Analysis. According to the above design process, we can get the following conclusion expressed by Theorem 1. The following assumption is needed.

Assumption 7. For any k, as $t = 0$, $\widehat{W}_{j,k}(0) = \widehat{W}_{j,k-1}(T)$; $\widehat{N}_{j,k}(0) = \widehat{N}_{j,k-1}(T)$, $j = 1, \ldots, m$, $\widehat{\varrho}_k(0) = \widehat{\varrho}_{k-1}(T)$.

Remark 4. This is the general setting of initial state in ILC.

Theorem 1. *Under Assumptions 1–7, by controller (43) and adaptive parameter estimation laws (48)–(50) for system (1), we get all signals are bounded, and*

$$\lim_{k\longrightarrow\infty} z_{l\phi,k}(t) = 0, \quad l = 1, 2, \ldots, n, \tag{52}$$

i.e., $\lim_{k\longrightarrow\infty} z_{1\phi,k}(t) = 0$, $\|z_{1,k}(t)\| < \phi_{1,\infty}(t) + \varsigma$ *as* $k \longrightarrow \infty$, *where* ς *is a small positive parameter.*

Proof. By Section 2.4, $\|z_{\phi,k}(0)\|^2 = 0 \le \|z_{\phi,k}(T)\|^2$, where $z_{\phi,k} = [z_{1\phi,k}, z_{2\phi,k}, \ldots, z_{n\phi,k}]^T$. By (41), we get

$$\begin{aligned} &V_{n,k}\left(z_{\phi,k}(0), \widehat{W}_k(T), \widehat{N}_k(T), \widehat{\varrho}_k(T)\right) \\ &\le V_{n,k}(0) + \int_0^T \dot{V}_{n,k}\mathrm{d}t, \end{aligned} \tag{53}$$

where $\widehat{W}_k = [\widehat{W}_{1,k}, \widehat{W}_{2,k}, \ldots, \widehat{N}_{n,k}]^T$ and $\widehat{N}_k = [\widehat{N}_{1,k}, \widehat{N}_{2,k}, \ldots, \widehat{N}_{n,k}]^T$.

(51) is substituted into (53), and we get

$$\begin{aligned} &V_{n,k}\left(z_{\phi,k}(0), \widehat{W}_k(T), \widehat{N}_k(T), \widehat{\varrho}_k(T)\right) \\ &\le V_{n,1}(0) - \sum_{j=1}^{k}\sum_{l=1}^{m}\int_0^T \eta_l\left(z_{l\phi,j}\right)^2\mathrm{d}t \\ &\quad + n\left(\frac{1}{4}\right)T\left(\sum_{j=1}^{k}\Delta_j\right). \end{aligned} \tag{54}$$

Denote $V_{0,k} = V_{n,1}(0) + n(1/4)T(\sum_{j=1}^{k}\Delta_j)$, and then (54) can be rewritten as

$$\begin{aligned} &\sum_{l=1}^{k}\sum_{l=1}^{n}\int_0^T \eta_l\left(z_{l\phi,j}\right)^2\mathrm{d}t \\ &\le V_{0,k} - V_{n,k}\left(z_{\phi,k}(0), \widehat{W}_k(T), \widehat{N}_k(T), \widehat{\varrho}_k(T)\right). \end{aligned} \tag{55}$$

By (4), $\lim_{k\longrightarrow\infty} V_{0,k} \le V_{n,1}(0) + 2an(1/4)T$, then $V_{0,k}$ is bounded, and by Assumption 7 and (54), $V_{n,k}(0)$ is bounded. $V_{n,k}(z_k(0), \widehat{W}_k(T), \widehat{N}_k(T), \widehat{\varrho}_k(T)) \ge 0$, so

$$\lim_{k\longrightarrow\infty}\sum_{l=1}^{n}\int_0^T \eta_l\left(z_{l\phi,k}\right)^2\mathrm{d}t = 0. \tag{56}$$

By (41), for any k, $V_{n,k}(t) = V_{n,k}(0) + \int_0^t \dot{V}_{n,k}(\tau)\mathrm{d}\tau$, by (51), then

$$V_{n,k}(t) \le V_{n,k}(0) - \sum_{l=1}^{n}\int_0^t \eta_l\left(z_{l\phi,k}(\tau)\right)^2\mathrm{d}\tau + tn\left(\frac{1}{4}\right)\Delta_k. \tag{57}$$

By (56), $\sum_{l=1}^{n}\int_0^t \eta_l(z_{l\phi,k}(\tau))^2\mathrm{d}\tau$ is bounded. By Definition 1, Δ_k is bounded, and $t \in [0, T]$, $tn(1/4)\Delta_k$ is also bounded. From above all, for any k, $V_{n,k}(t)$ is bounded, then we have $x_{j,k}$, and $\widehat{W}_k(t)$ and $\widehat{N}_k(t)$ are bounded. By (43), u_k is bounded. By (33), $\dot{z}_{j\phi,k}$ is bounded, $z_{j\phi,k}$ is continuous uniformly, according to Barbalat lemma, $z_{j\phi,k} \longrightarrow 0$, when $k \longrightarrow \infty$, i.e., $k \longrightarrow \infty$, $z_{1\phi,k} \longrightarrow 0$, then $\|z_{1\phi,k}\| < \varsigma$. $\|z_{1,k}\| = \|z_{1\phi,k} + \mathrm{sgn}(z_{1\phi,k})\phi_{1,k}(t)\| \le \|z_{1\phi,k}\| + \|\phi_{1,k}(t)\| < \|\phi_{1,k}(t)\| + \varsigma$, so $k \longrightarrow \infty$, $\|z_{1,k}\| < \phi_{1,\infty}(t) + \varsigma$, and the proof is finished. □

4. Simulation

In this section, a mass-spring mechanical system is considered to show the effectiveness of the proposed controller. $\overline{m}$ is a mass, and assume that resistive force caused by friction is zero. The external force u_k drives the mass, which is a control variable. y_k is the displacement from a reference position, and the motion equation of the system with continuous nonlinearly input is as follows:

$$\overline{m}\ddot{y}_k + F_{ms}(y_k) = N(u_k), \tag{58}$$

where $t \in [0, \pi]$ and $F_{ms}(\cdot)$ is the restoring force of the spring. k denotes the iteration index.

We define $x_{1,k} = y_k$, $x_{2,k} = \dot{y}_k$, and $\overline{m} = 1$ which transform (58) into the state-space form

$$\begin{aligned} \dot{x}_{1,k} &= x_{2,k}, \\ \dot{x}_{2,k} &= N(u_k) - F_{ms}\left(x_{1,k}\right). \end{aligned} \tag{59}$$

The restoring force of the spring can be modeled as

$$F_{ms}\left(x_{1,k}\right) = kx_{1,k}\left(\sum_{i=0}^{q} a_i x_{1,k}^i\right). \tag{60}$$

In the system, we have $k = 1$, $a_0 = 0$, $a_1 = a_2 = a_3 = a_4 = 1$, and $q = 4$.

Continuous nonlinearly input $N(u)$ is shown as $N(u) = (0.5 + 0.1\sin(u))u$. System objective is that the output of (59) can follow the reference trajectory $y_{r,k}$ on $[0, \pi]$ when $k \longrightarrow \infty$. In the different target case, $y_{r,k} = g_k \sin(2t)$ as k is even, and $y_{r,k} = g_k \cos(t)$ as k is odd, where $g_k = \mathrm{rand}(0, 1)$.

By Theorem 2, the AILC is chosen as

$$\begin{aligned} \alpha_{1,k} &= -\widehat{W}_{1,k}^T\zeta_1\left(\overline{x}_{1,k}\right) - \widehat{N}_{1,k}\frac{1}{\Delta_k}z_{1\phi,k} + \dot{y}_r - \eta_1 z_{1,k}, \\ u_k &= u_{1,k} + u_{2,k}, \\ u_{1,k} &= -z_{1\phi,k} - \widehat{W}_{2,k}^T\zeta_2\left(\overline{x}_{2,k}\right) - \widehat{N}_{2,k}\frac{1}{\Delta_k}z_{2,k} + P_{1,k} - \eta_2 z_{2,k}, \\ u_{2,k} &= -\mathrm{sat}\left(\frac{z_{n,k}}{\phi_{n,k}(t)}\right)\left(\widehat{\varrho}_k(t) + 1\right)\left|u_{1,k}\right|. \end{aligned} \tag{61}$$

where $P_{1,k} = (\partial\alpha_{1,k}/\partial\widehat{W}_{1,k})\dot{\widehat{W}}_{1,k} + (\partial\alpha_{1,k}/\partial\widehat{N}_{1,k})\dot{\widehat{N}}_{1,k} + (\alpha_{1,k}/\partial y_r)\dot{y}_r + (\alpha_{1,k}/\partial\dot{y}_r)\ddot{y}_r$ and the parameter estimation laws are represent by (48)–(50), where $\eta_1 = 10$, $\eta_2 = 5$, $\Delta_k = a/k^2$, $a = 100/3$, $\Gamma_{11} = \mathrm{diag}\left\{1, \underbrace{0.1, \ldots, 0.1}_{30}\right\}$, $\Gamma_{21} = 1$,

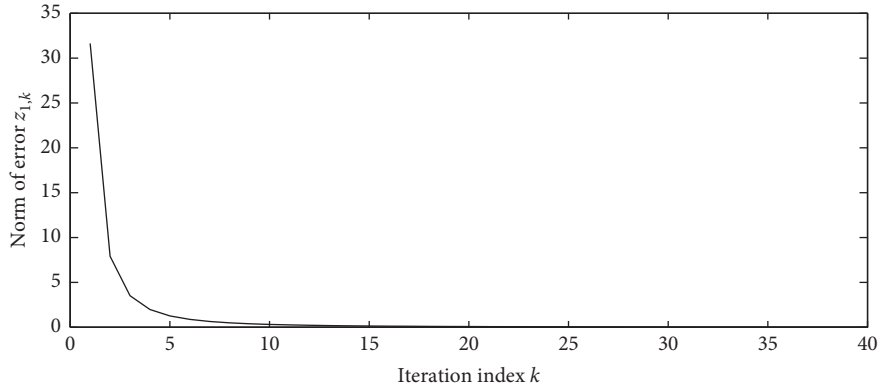

Figure 1: Curve graph of $\|z_{1,k}\|$ along k.

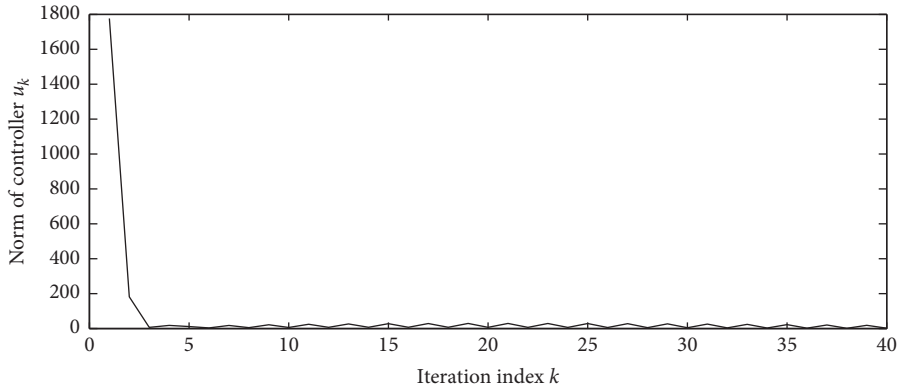

Figure 2: Curve graph of $\|u_k\|$ along k.

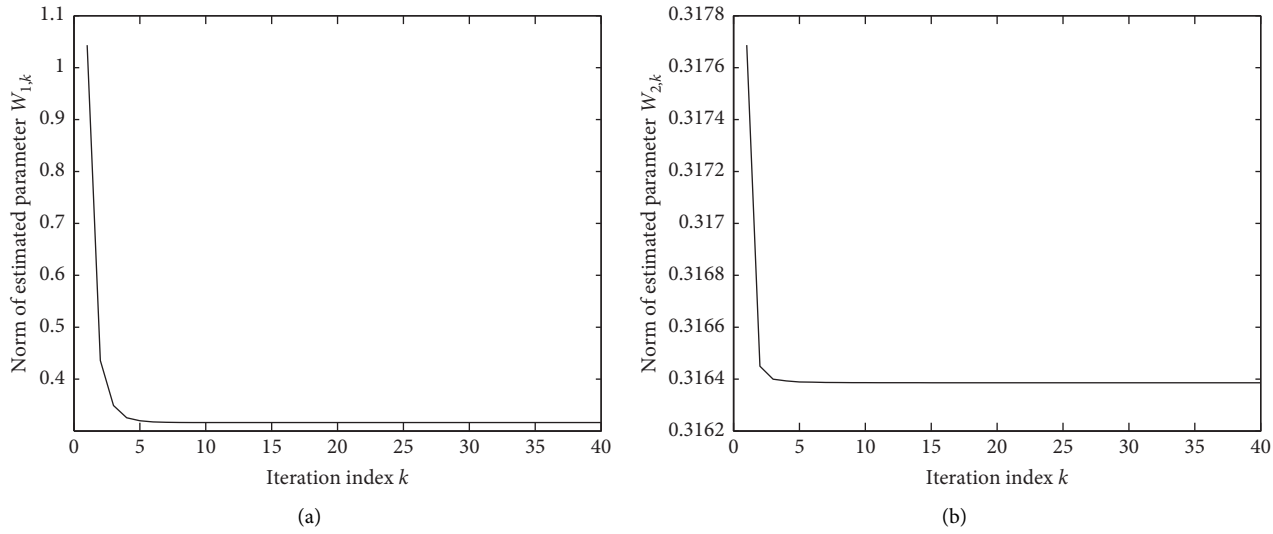

Figure 3: Curve graph of $\|\widehat{W}_{1,k}\|$, $\|\widehat{W}_{2,k}\|$ along k.

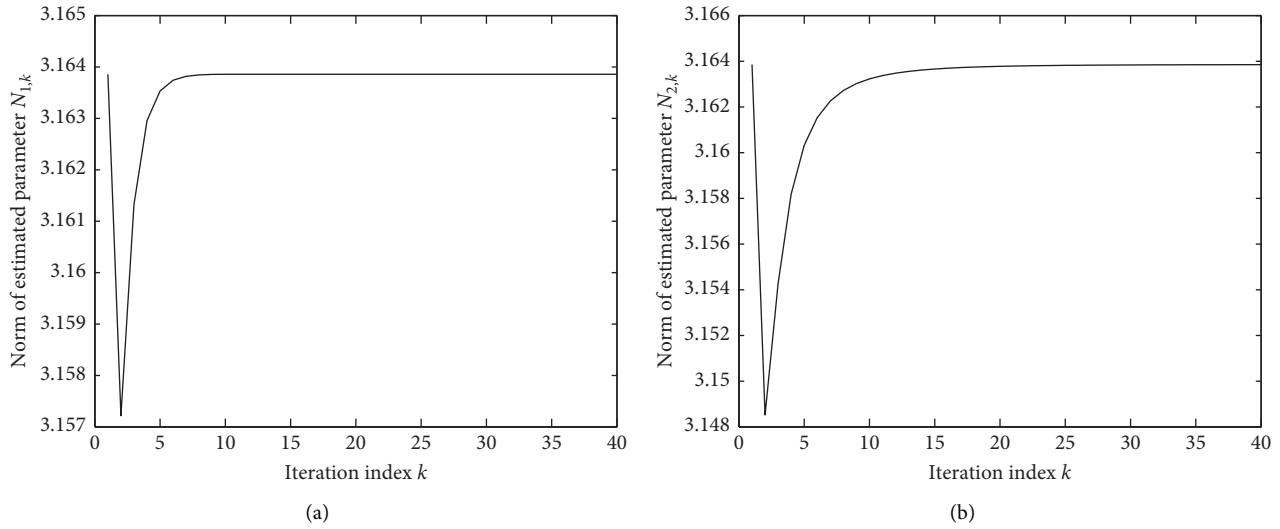

FIGURE 4: Curve graph of $\|\widehat{N}_{1,k}\|$, $\|\widehat{N}_{2,k}\|$ along k.

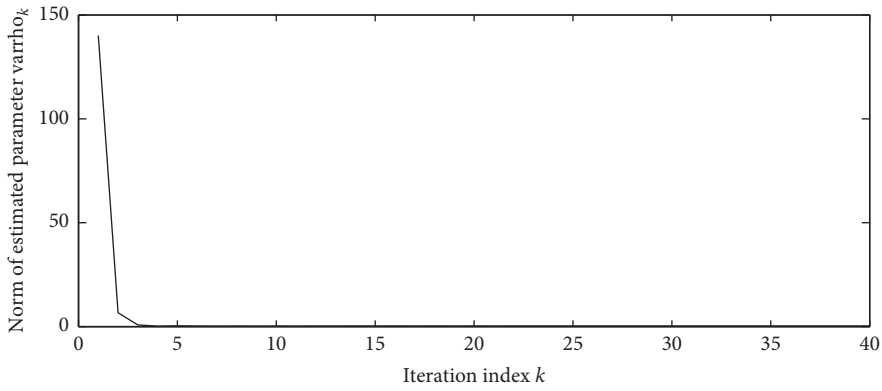

FIGURE 5: Curve graph of $\|\widehat{\varrho}_k\|$ along k.

$\Gamma_{12} = \text{diag}\left\{0.1, 1, \underbrace{0.1, \ldots, 0.1}_{29}\right\}$, $\Gamma_{22} = 1$, $\Gamma_3 = 1$. The variables $x_{1,k}$, $x_{2,k}$ are used as the inputs of the RBFNNS; the neural network consists of 31 neurons, the center of basis function uniform coverage of $[-1, 1]$, and the width of basis function is set to 1.

Here, choose the parameters and initial value as follows: $z_{1,k}(0) = 1/k^2$, $z_{2,k}(0) = 1/k^2$, $\widehat{W}_{1,1}(0) = [0.01, \underbrace{0, \ldots, 0}_{30}]^T$, $\widehat{W}_{2,1}(0) = [0.01, \underbrace{0, \ldots, 0}_{30}]^T$, $\widehat{N}_{1,1}(0) = -0.1$, $\widehat{N}_{2,1}(0) = -0.1$, $\widehat{\varrho}_1(0) = 0.1$. Taking $k = 40$, Figures 1–5 are the simulation figures.

Figure 1 shows the convergence of error. Moreover, on the interval $[0, \pi]$, Figures 2–5 give that $\|u_k\|$, $\|\widehat{W}_{1,k}\|$, $\|\widehat{W}_{2,k}\|$, $\|\widehat{N}_{1,k}\|$, $\|\widehat{N}_{2,k}\|$, $\|\varrho_k\|$ are bounded. Figures 1–5 confirm the validity of control scheme which is developed in this article from the simulation results.

5. Conclusions

The different target tracking problem for unknown nonlinear systems with continuous nonlinearly input is solved in this paper. We introduce the RBFNN to deal with the uncertain dynamics. The problems of approximation error and initial state error can be efficiently solved by suitable means. This paper can keep all signals being bounded on $[0, T]$, and errors can converge with the number of iterations increasing. Finally, the effectiveness of the proposed control method is verified via a simulation example.

Data Availability

No data were used to support this study.

Conflicts of Interest

The authors declare that they have no conflicts of interest.

Acknowledgments

This work was supported by the National Natural Science Foundation of China under grant no. 61603296 and Natural Science Foundation Project of Shaanxi Provincial Education Department under grant no. 16JK1541.

References

[1] J. X. Xu and J. Xu, "On iterative learning from different tracking tasks in the presence of time-varying uncertainties," *IEEE Transactions on Systems, Man, and Cybernetics-Part B: Cybernetics*, vol. 34, no. 1, pp. 589–597, 2004.

[2] J. M. Li, Y. P. Sun, and Y. Liu, "Hybrid adaptive iterative learning control of non-uniform trajectory tracking," *Control Theory and Applications*, vol. 25, no. 1, pp. 100–104, 2008.

[3] C.-L. Zhang and J.-M. Li, "Adaptive iterative learning control of non-uniform trajectory tracking for strict feedback nonlinear time-varying systems with unknown control direction," *Applied Mathematical Modelling*, vol. 39, no. 10-11, pp. 2942–2950, 2015.

[4] J. Xu, "Fault-tolerant iterative learning control for mobile robots non-repetitive trajectory tracking with output constraints," *Automatica*, vol. 94, pp. 63–71, 2018.

[5] W. He, T. Meng, X. He, and C. Sun, "Iterative learning control for a flapping wing micro aerial vehicle under distributed disturbances," *IEEE Transactions on Cybernetics*, vol. 49, no. 4, pp. 1524–1535, 2019.

[6] W. He, Y. Chen, and Z. Yin, "Adaptive neural network control of an uncertain robot with full-state constraints," *IEEE Transactions on Cybernetics*, vol. 46, 2016.

[7] L. Kong, W. He, Y. Dong, L. Cheng, C. Yang, and Z. Li, "Asymmetric bounded neural control for an uncertain robot by state feedback and output feedback," *IEEE Transactions on Systems, Man, and Cybernetics: Systems*, vol. 51, 2019.

[8] C. J. Chien, "A combined adaptive law for fuzzy iterative learning control of nonlinear systems with varying control tasks," *IEEE Transactions on Fuzzy Systems*, vol. 16, no. 1, pp. 40–51, 2008.

[9] C. L. Zhang and X. Tian, "Non-uniform trajectory tracking adaptive iterative learning control for nonlinear pure-feedback systems with initial state error based on RBF-neural network," in *Proceedings of the 40th Chinese Control Conference*, Shanghai, China, July 2021.

[10] A. Taybi and C. J. Chien, "A unified adaptive iterative learning control framework for uncertain nonlinear systems," *IEEE Transactions on Automatic Control*, vol. 52, no. 10, pp. 1907–1913, 2007.

[11] J. X. Xu and R. Yan, "Adaptive learning control for finite interval tracking based on constructive function approximation and wavelet," *IEEE Transactions on Neural Networks*, vol. 22, no. 6, pp. 893–905, 2011.

[12] C. L. Zhang and J. M. Li, "Adaptive iterative learning control for nonlinear pure-feedback systems with initial state error based on fuzzy approximation," *Journal of the Franklin Institute*, vol. 351, no. 3, pp. 1483–1500, 2014.

[13] J.-X. Xu and R. Yan, "Iterative learning control design without a priori knowledge of the control direction," *Automatica*, vol. 40, no. 10, pp. 1803–1809, 2004.

[14] Y. Tan, H.-H. Dai, D. Huang, and J.-X. Xu, "Unified iterative learning control schemes for nonlinear dynamic systems with nonlinear input uncertainties," *Automatica*, vol. 48, no. 12, pp. 3173–3182, 2012.

[15] X. J. Wu, X. L. Wu, X. Y. Ran, Z. Luo, and Q. M. Zhu, "Adaptive control for time-delay non-linear systems with non-symmetric input non-linearity," *International Journal of Modelling, Identification and Control*, vol. 13, no. 3, pp. 152–160, 2011.

[16] X. Y. Luo, X. J. Wu, and X. P. Guan, "Adaptive backstepping fault-tolerant controlfor unmatched non-linear systems against actuator dead-zone," *IET Control Theory and Applications*, vol. 4, no. 5, pp. 879–888, 2010.

[17] X. Wu, X. Wu, X. Luo, Q. Zhu, and X. Guan, "Neural network-based adaptive tracking control for nonlinearly parameterized systems with unknown input nonlinearities," *Neurocomputing*, vol. 82, pp. 127–142, 2012.

[18] W. S. Chen, "Adaptive backstepping dynamic surface control for systems with periodic disturbances using neural networks," *IET Control Theory and Applications*, vol. 3, no. 10, pp. 1383–1394, 2009.

[19] S. Zhu, M. X. Sun, and X. X. He, "Iterative learning control of strict-feedback nonlinear time-varying systems," *Acta Automatica Sinica*, vol. 36, no. 3, pp. 454–458, 2010.

[20] J. S. Li and J. M. Li, "Adaptive iterative learning control for coordination of second-order multi-agent systems," *International Journal of Robust and Nonlinear Control*, vol. 24, no. 18, pp. 3282–3299, 2014.

[21] Y. Chen, Z. Liu, C. L. P. Chen, and Y. Zhang, "Adaptive fuzzy control of switched nonlinear systems with uncertain dead-zone: a mode-dependent fuzzy dead-zone model," *Neurocomputing*, vol. 432, pp. 133–144, 2021.

[22] D. Meng and K. L. Moore, "Learning to cooperate: networks of formation agents with switching topologies," *Automatica*, vol. 64, pp. 278–293, 2016.

[23] L. X. Wang, "Fuzzy systems are universal approximators," in *Proceeding of IEEE International Conference on Fuzzy Systems*, pp. 1163–1170, San Diego, CA, USA, March 1992.

Hindawi
Mathematical Problems in Engineering
Volume 2021, Article ID 6362660, 17 pages
https://doi.org/10.1155/2021/6362660

Research Article

Development of Hybrid Methods for Prediction of Principal Mineral Resources

Maria Qurban,[1] Xiang Zhang,[2] Hafiza Mamona Nazir,[1] Ijaz Hussain,[1] Muhammad Faisal,[3] Elsayed Elsherbini Elashkar,[4] Jameel Ahmad Khader,[5] Sadaf Shamshoddin Soudagar,[6] Alaa Mohamd Shoukry,[7,8] and Fares Fawzi Al-Deek[9]

[1]*Department of Statistics, Quaid-i-Azam University, Islamabad, Pakistan*
[2]*National Engineering Research Center of Geographic Information System, School of Geography and Information Engineering, China University of Geosciences (Wuhan), Wuhan 430074, China*
[3]*Faculty of Health Studies, University of Bradford, Bradford, BD7 1DP, UK*
[4]*Administrative Sciences Department, Community College, King Saud University, Riyadh, Saudi Arabia*
[5]*College of Business Administration, King Saud University Muzahimiyah, Al-Muzahmiya, Saudi Arabia*
[6]*College of Business Administration, King Saud University Riyadh, Riyadh, Saudi Arabia*
[7]*Arriyadh Community College, King Saud University, Riyadh, Saudi Arabia*
[8]*KSA Workers University, Nsar, Egypt*
[9]*Administrative Sciences Department, Arriyadh Community College, King Saud University, Riyadh, Saudi Arabia*

Correspondence should be addressed to Xiang Zhang; zhangxiang76@cug.edu.cn and
Alaa Mohamd Shoukry; aabdulhamid@ksu.edu.sa

Received 10 June 2021; Revised 24 July 2021; Accepted 26 July 2021; Published 9 August 2021

Academic Editor: Yuxing Li

Accurate estimation of the mining process is vital for the optimal allocation of mineral resources. The development of any country is precisely connected with the management of mineral resources. Therefore, the forecasting of mineral resources contributed much to management, planning, and a maximum allocation of mineral resources. However, it is challenging because of its multiscale variability, nonlinearity, nonstationarity, and high irregularity. In this paper, we proposed two revised hybrid methods to address these issues to predict mineral resources. Our methods are based on denoising, decomposition, prediction, and ensemble principles that are applied to the production of mineral resource time-series data. The performance of the proposed methods is compared with the existing traditional one-stage model (without denoised and decomposition strategies) and two-stage hybrid models (based on denoised strategy), and three-stage hybrid models (with denoised and decomposition strategies). The performance of these methods is evaluated using mean relative error (MRE), mean absolute error (MAE), and mean square error (MSE) as evaluation measures for the production of four principle mineral resources of Pakistan. It is concluded that the proposed framework for the prediction of mineral resources indicated better performance as compared to other existing one-stage, two-stage, and three-stage models. Furthermore, the prediction accuracy of the revised hybrid model is improved by reducing the complexity of the production of mineral resource time-series data.

1. Introduction

In the development of the national economy of any country, there is a significant contribution of minerals. The development of effective policies is necessary for mining industries. The income obtained by the mineral sector can be optimized, and the industry can alleviate the shortage of metals through accurate prediction of the mining process, as minerals have a massive impact on the economy of Pakistan. Since the mineral production data are nonstationary and have multiscale stochastic attributes, the mining process is affected by climate change and other projects related to socioeconomic developments that result in a challenging task for predicting the production of minerals resources.

Two models are commonly used to predict such types of data: a process-based model and a data-driven model. The process-based model needs an extensive calibration and validation dataset [1]. The data-driven model considered the physical mechanism and scientific knowledge of stochastic geologic processes [2]. Huang et al. [2] used the process-based models for the prediction of hydrological data that were also nonlinear and having complex characteristics. They concluded that the lack of scientific knowledge and unavailability of sufficient data make it difficult to predict. Data-driven models were efficiently used to overcome the drawback of process-based models [3].

The data-driven models are further categorized as traditional statistical and machine learning (ML) models. The traditional statistical methods, i.e., autoregressive integrated moving average (ARIMA), only consider the stationary and linear data. The ARIMA model is successfully applied to predict the production of mineral resources [4]. However, the problem with this traditional model is that it needed data to be stationary. Furthermore, since the production data of mineral resources are nonstationary and have nonlinearity in them, they also contain complex time-varying characteristics. Therefore traditional statistical models are not enough to capture the nonlinearity and time-varying characteristics of the nonlinear data. However, ML techniques can be used to deal with the drawbacks and instability of the traditional statistical models, as ML methods are used to deal with nonstationary and nonlinear time-series data [5]. Therefore, ML methods also are suitable for capturing the nonstationary and nonlinear behavior of mineral production data.

Commonly used ML techniques are artificial neural network (ANN) and support vector machine (SVM), which also suffered from the problem of parameter selection and overfitting, and do not consider time-varying characteristics of nonstationary time-series data. Moreover, the production data of mineral resources contain noises that forbid the researcher to predict them accurately. Therefore, hybrid techniques are needed to model the noise corrupted and time-varying characteristics of the production of mineral resources data. Bokde et al. [6] proposed a hybrid model (EMD-ANN) for the nonstationary wind speed prediction and concluded that its performance was highly satisfactory and robust for jumping samplings than ANN and ARIMA models.

To deal with the limitations of simple existing models, some of the preprocessing strategies are utilized with different data-driven models to increase the prediction accuracy of a different kind of nonlinear and nonstationary time series. The hybris models are developed to get the time-varying characteristics through noise reduction. The different hybrid models with preprocessing strategies have already been applied for complex and nonlinear data, having time-varying characteristics [7]. The strategy of the hybrid technique is based on decomposition and denoising, prediction, and ensemble stages [1, 8, 9]. Several algorithms are developed, such as spectral analysis, wavelet analysis (WA), Fourier analysis, and empirical mode decomposition (EMD), to reduce these noises or stochastic volatiles from the data [10, 11]. Fourier analysis and spectral analysis are used for those kinds of data that are stationary or linear. However, EMD and WA are the most commonly used preprocessing algorithms for nonlinear or nonstationary data and provide better results. The algorithms of WA decompose the nonlinear and nonstationary data of mineral resources into multiscale components [12]. These components are used as inputs at the prediction stage, and then these predicted components are ensemble for final prediction. The authors in [5] proposed a hybrid model for forecasting streamflow by using wavelet transform to decompose streamflows and use ANN for forecasting purposes. They concluded that their hybrid model was efficient than simple existing models. In the present paper, EMD- and WA-based thresholds are used to reduce noises from the mineral production data. The WA is considered as a powerful tool for converting a signal into a stationary signal with specific effectiveness. In the literature, different hybrid models with wavelet decomposition are used for the prediction of different kinds of nonlinear and nonstationary time-series data [13]. Wu et al. [14] proposed a hybrid forecasting model in combination with the particle swarm optimization algorithm and wavelet neural network (PSO-WNN) to predict China's natural gas consumption. They used the PSO algorithm to optimize the initial weights, and the parameters of wavelet are updated through dynamic learning to have improvement in forecasting precision and reduce fluctuation of the WNN. They concluded that the proposed model is superior as compared to ANN- and WNN-based models. Some improvements have been made in hybrid modes consisting WA decomposition to get more accurate results of the prediction of daily flows which is also nonlinear time-series data [13]. However, the performance of the WA depends upon the selection of the type of mother wavelet. Prior knowledge about the signal, which is to be analyzed, and prior knowledge about its frequency content are needed for a suitable choice of the mother wavelet. Wu et al. [15] proposed an EMD method to overcome the shortcomings of WA for scrutinizing the nonlinear data and nonstationary datasets. Complex time-series data can be decomposed into a small and finite number of IMFs by using EMD. The EMD strategy has the advantage of converting the nonstationary series into stationary series. There exist different studies in the literature that used EMD with different data-driven models such as EMD-artificial neural network (EMD-ANN), EMD-radial basis function (EMD-RBF), EMD-support vector machines (EMD-SVMs), EMD-relevant vector machine (EMD-RVM), and EMD-ARIMA, and these hybrid models improve the prediction accuracy [16–18]. The EMD is combined with the ANN in many past studies, especially in hydrology [19], and also a novel model based on EMD and deep learning is used by Mi et al. [20] to reduce the noises and extract the information of trend of the original data of wind speed. However, EMD suffers from the problem of mode mixing between the IMFs [13]. To overcome the mode mixing problem, the authors in [13] proposed a new technique of decomposition called ensemble empirical mode decomposition (EEMD), in which they used white Gauss noise. The EEMD method can separate the

signals without inappropriate mode mixing. It uses white noise that helps to establish the dyadic reference frame on time-scale space. They concluded that removing the problem of mode mixing EEMD produced a set of IMFs that carry the full physical meanings. Many hybrid techniques based on EEMD are used for streamflow and wind speed prediction and in hydrology [21, 22]. Di et al. [1] proposed a four-stage hybrid model based on EEMD decomposition to bring improvement in the prediction accuracy by minimizing the noises. They concluded that EEMD in combination with data-driven models could improve the prediction accuracy compared to EMD-based hybrid models. Liu [23] proposed a hybrid model by combining EEMD with the grey SVM model (GSVM) to forecast high-speed rail passenger flow. They concluded that their two-stage hybrid model is more suitable for short-term predictions than other single and hybrid models.

Ghumman et al. [24] proposed two hybrid models based on preprocessing techniques EEMD, called EEMD pattern sequence-based forecasting (EEMD-PSF) and EEMD difference pattern sequence-based forecasting (EEMD-DPSF) models. The first model decomposes the series into number of IMFs and improves the prediction performance using the PSF model, and the second model reduced the effects of seasonality, trend, and irregularity from the wind speed data. They compared their performances with simple PSF, ARIMA, and LSSVM models for wind speed and concluded that EEMD-PSF and EEMD-DPSF models outperformed than simple models. Jaitly and Hinton [25] presented a comprehensive review of decomposition-based methods to improve the wind forecasting accuracy. They used and discussed wavelet analysis, EMD, seasonal adjusted, intrinsic time-scale decomposition, variational mode decomposition, and Bernaola-Galvan algorithm for decomposition of wind speed time-series data as an alternative forecasting algorithm. Through comparative analysis of various decomposition-based models, they concluded that the decomposition-based model provided the accuracy in prediction as compared to other forecasting algorithms.

Although EEMD proved helpful in solving mode mixing issues, it created one other problem: some residual noise during signal reconstruction. As a result, there may be different modes because of the various realizations of signal and noise. To solve this problem, Mehrsai et al. [26] proposed the complete ensemble empirical mode decomposition with adaptive noise (CEEMDAN) technique. A specific noise is added in their proposed model at each decomposition stage, and a residue is calculated to get each mode. The final complete results of decomposition are obtained numerically with the negligible error term.

This paper proposed a revised hybrid model to decompose the time-varying characteristics of the production data of mineral resources built upon CEEMDAN based on a 48-step ahead of the direct recursive prediction strategy. The study focuses on the preprocessing techniques (denoising and decomposing) and their effect on the prediction of mineral resources. An important point to note from the past studies is that they used a one-step-ahead prediction strategy rather than a multistep-ahead prediction [27]. In one-step-ahead prediction, all the observations are used by the predictor to estimate the parameter for the time step, and we used 48-month-ahead prediction to predict the mineral resources. For improved and better performance of the revised hybrid model, the long-term behavior of mineral resource production is observed by considering the 48-step-ahead direct recursive prediction strategy.

In the current study, we aimed to make a revised hybrid model using the preprocessing techniques to decompose the production data of mineral resources using the WA-CEEMDAN technique, which follows the steps of EEMD by adding white noise at each level of decomposition. Therefore, the purpose of using the CEEMDAN algorithm in the current study is to find an efficient way to decompose the time-series data of mineral resources, which increased its prediction accuracy. Furthermore, the current study explores its prediction performance using 48-step-ahead prediction, especially for nonlinear data, by considering this emerging hybrid modeling technique.

Based on the details outlined above, this paper is focused on developing a modified model to predict the production of mineral resources, improving the EMD/WA-CEEMDAN-based multimodels (EMD/WA-CEEMDAN). In this paper, the prediction performance of CEEMDAN-based hybrid models used for long-term to review the prediction of mineral resources is observed. Section 2 is focused on the motivations behind the production data of mineral resource prediction. A short review of models used for prediction of mineral's data and an introduction to EMD, EEMD, CEEMDAN, and their modified versions are discussed in Section 3. Additionally, a short review of various approaches used in hybrid CEEMDAN models to select the appropriate prediction methods with the consideration of the characteristics of respective IMFs is also discussed in Section 3. Section 4 describes details of the study area and data. Section 5 presents and discusses the results of the case study, while conclusions are made for this research in Section 6.

2. Motivation behind the Prediction of the Mineral Resources

In recent years, prediction of mineral resource prediction has become a challenging task for researchers. Although there is abundance of coal reserves in Pakistan, still share of gas and oil is about 65% in the energy mix. Pakistan, despite being a mineral-enriched country, is facing an alarming situation as its power generation is based on foreign exchange. The mineral sector of Pakistan is dominated by four principal minerals which are gas, oil, gypsum, and coal. There is a need to analyze and accurate prediction of the production of these four major minerals to deal with emerging challenges. The main purpose towards accurate prediction of mineral production data is to get the efficient and optimum utilization of natural resources in the development of the economy.

Prediction of the mineral resources is considered to be an important study because of nonlinear, nonstationary, and having time-varying characteristics of datasets. Many researchers are working towards accurate prediction of

nonlinear datasets, having complex time-varying characteristics. Although these researchers have the same goal, most of them have varieties in their motivations.

Saadat et al. [28] used the CEEMDAN algorithm in their proposed model to predict the daily peak load. The proposed three-stage hybrid model comprised the CEEMDAN technique, which showed a robust decomposed ability of reliable prediction. Nazir et al. [29] developed a robust hybrid model by utilizing the CEEMDAN algorithm to decompose hydrological time-series data, which showed the robust decomposition ability to forecast the nonlinear and complex time-series data. The purpose of including such article is that those inferred the practicability and serviceability of the hybrid models for the decomposition of nonlinear datasets.

3. Proposed Methodology

In the current study, we proposed two hybrid methods to enhance the prediction accuracy of the time-series data. Both methods have the same map and formation except in the denoising stage, where the approaches for eliminating the noises from the data are different. At the decomposition stage of both methods, CEEMDAN (an improved form of EEMD) [25] is used to identify the oscillation. At the prediction stage, the multimodels are used after considering the nature of IMFs to predict the obtained IMFs accurately. There are two main objectives of using the multimodels: predicting the IMF by looking up their nature accurately. The second objective is to determine the attainments of the complex and straightforward models after the reduction of the complexity of mineral resource time-series data by using decomposition strategies. Finally, all the IMFs obtained through prediction are combined to predict the time-series data. The proposed hybrid models consist of denoising, denoted as D-step, decomposition, and prediction, denoted as Decompose-step and P-step, respectively [29]. A short description of these steps is given as follows:

(1) In D-step, the WA and EMD methods are presented to remove the noise from the production of mineral resource time-series data.

(2) In Decompose-step, CEEMDAN is used to decompose the denoised series into the k IMF components and one residual term.

(3) In P-step, the series obtained after denoising is decomposed into IMF components and one residual term, which is predicted by using linear stochastic and nonlinear machine learning methods. The model, which has a lower rate of error for prediction than other models, is utilized for further consideration based on three performance evaluation criteria. At last, the predicted results are combined to get the final prediction.

Compared with the earlier review papers, the main contribution of the current study is to review the prediction literature from the perspective of decomposition-based hybrid methods. More precisely, we compile the decomposition-based models and discuss their algorithms and structures. Furthermore, we examine that how decomposition-based hybrid models improve prediction accuracy. Finally, existing techniques adopted in recent years to improve the performance of decomposition-based models are also compiled and discussed.

To better understand and ease the reader, by combining all the steps mentioned above, the proposed strategy can be named as EMD (denoising)-CEEMDAN (decomposing)-MM (multimodels), and WA (denoising)-CEEMDAN (decomposing)-MM (multimodels) shortly named as EMD-CEEMDA-MM and WA-CEEMDAN-MM models. Both models are exhibited in Figure 1.

3.1. Denoising Step (D-Step). In many time-series data, noises are certain components that sometimes reduce the prediction accuracy. Many algorithms exist in the literature, such as spectral analysis, WA, Fourier analysis, and EMD, to reduce these noises or stochastic volatiles from the data [30]. Fourier analysis and spectral analysis are used for those kinds of data that are stationary or linear. However, EMD and WA can also deal with nonlinear or nonstationary data and provide better results. In this study, EMD- and WA-based thresholds are used to reduce noises from the mineral production data.

3.1.1. Wavelet Analysis (WA). WA has developed as an efficient tool for converting a signal into a stationary signal with specific effectiveness. The wavelet with finite energy (small wave) is established in time, or frequency for analysis of temporal phenomena serves as a basis function. One of the favorite uses of the discrete wavelet transformation (DWT) is to eliminate the noises from the signal. This idea contains a strategy of applying the threshold wavelet on the coefficients of the signal contains the noises called the wavelet technique for denoising. The wavelet threshold is recognized as a powerful method for removing the noises from the signal. For using the wavelet basis soft and hard threshold, it is necessary to decide about the choice of the mother wavelet function. Using the Symlet 8 mother wavelet [31], the mineral production data are decomposed into the following coefficients [26, 30]:

$$b_{k,l} = \sum_{l=0}^{2^{N-k}-1} 2^{-k/2} \phi\left(2^{-k} p - l\right), \tag{1}$$

$$c_{k,l} = \sum_{k=1}^{K} \sum_{l=0}^{2^{N-k}-1} 2^{-k/2} \theta\left(2^{-k} p - l\right), \tag{2}$$

where $b_{k,l}$ is the approximation coefficient and $c_{k,l}$ is the detail coefficient.

Signal's energy can be divided over some of the wavelet coefficients with high magnitude by using this technique. On the other side, noise energy can be divided into many wavelet coefficients that have a low magnitude. The denoised signal can be obtained by removing wavelet coefficient noise and by reconstructing the coefficients. Wavelet denoising has three steps: (1) decomposition of the signal into

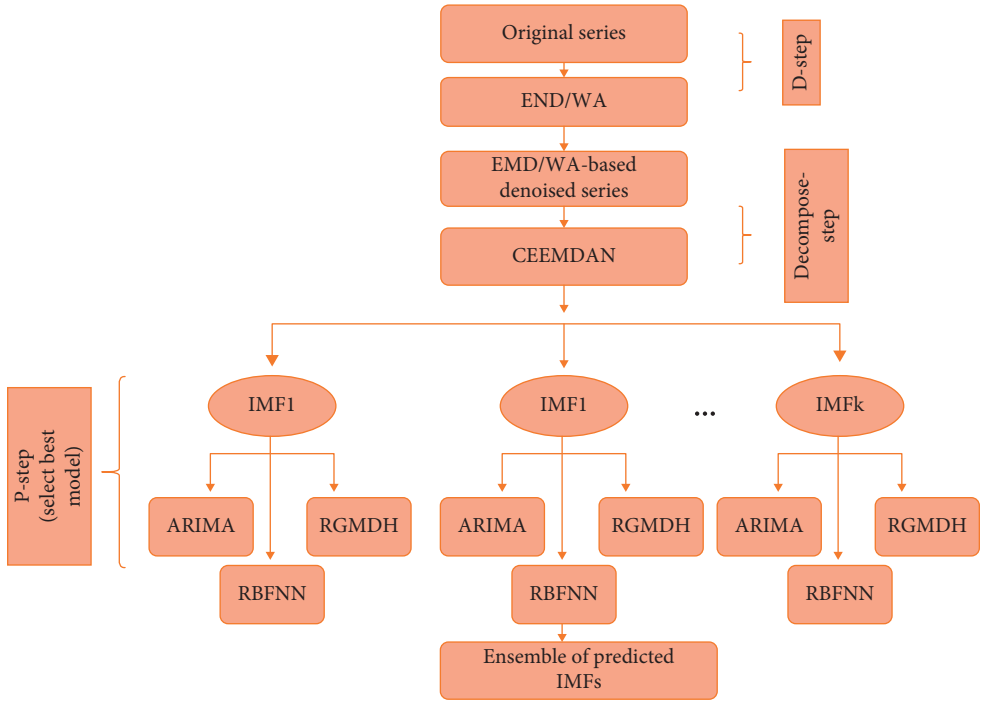

Figure 1: The suggested structure of EMD/WA-CEEMDAN-MM for the prediction of production data of mineral resources.

coefficients of wavelet, (2) applying thresholds on the coefficients obtained in step 1 [32], and (3) reconstruction of the wavelet coefficients.

3.1.2. Hard and Soft Thresholds. The assignment of the actual threshold is necessary for the elimination of the noises during denoising. As in wavelet transformation, the efficiency of the denoising technique depends on the value of the threshold. Several selection procedures are most likely for deciding about the thresholding rule, but two symbolic ones are hard thresholding and soft thresholding [33]. In the current study, for calculating the wavelet coefficients, soft and hard thresholding are applied to implement the wavelet denoising technique, which is listed below [26]. The soft thresholding is

$$c'_{k,l} = \begin{cases} c_{k,l}, & |c_{k,l}| \geq \mathrm{Th}_k, \\ 0, & |c_{k,l}| < \mathrm{Th}_k, \end{cases} \tag{3}$$

and the hard thresholding is

$$c'_{k,l} = \begin{cases} \mathrm{sgn}\left(c_{k,l}\right)\left(|c_{k,l}| - \mathrm{Th}_k\right), & |c_{k,l}| \geq \mathrm{Th}_k, \\ 0, & |c_{k,l}| < \mathrm{Th}_k, \end{cases} \tag{4}$$

where Th_k is the threshold which is calculated as $\mathrm{Th}_k = a\sqrt{2E_k \ln(N)}, k = 1, 2, 3, \ldots, K$, a is the constant which considers the values in the interval of 0.4 and 1.4 with the jump of 0.1, and $\widehat{\mathrm{Md}}_k$ is the median deviation, i.e.,

$$\widehat{\mathrm{Md}}_k = \frac{\mathrm{median}\left(\left\{c_{k-1,l} | k = 1, 2, 3, \ldots, 2^{k-1} - 1\right\}\right)}{0.6745}. \tag{5}$$

By utilizing the following equation, the decomposed signal is reconstructed using the approximations and noise-free details:

$$x(p) = \sum_{k=0}^{2^{N-K}-1} a'_{k,l} 2^{-k/2} \phi\left(2^{-k}p - l\right) + \sum_{k=1}^{k} \sum_{k=0}^{2^{N-k}-1} c'_{k,l} 2^{-k/2} \theta\left(2^{-k}p - l\right), \tag{6}$$

where $a'_{k,l}$ and $c'_{k,l}$ are the threshold approximation and detailed coefficients, respectively.

3.1.3. Empirical Mode Decomposition (EMD). The EMD is a flexible kind of decomposition technique and a purely data-driven technique to decompose the sophisticated signals into the series of components of the nonlinear and nonstationary data. After decomposition, by combining all the components for reconstructing, the original signal without any loss of the information can be obtained. The primary purpose of EMD is to get the IMFs from the complex signals. The following two conditions should be satisfied by the extracted IMFs [34]: (a) from all the data, the total of zero-crossings and the extrema should either be equal or differ by at most one; (b) at any point, the value of the envelope should be zero.

The main steps of the EMD for an original time series $x(p)$, $(p = 1, 2, 3, \ldots, N)$ are as follows [33]:

(1) Identification of all the local extrema of original time series $x(p)$.

(2) Create the upper and lower envelope as $U(p)$ and $G(p)$ by using a cubic spline.

(3) Estimate the mean value of the upper envelope and the lower envelope$m(p) = (U(p) + G(p))/2$.

(4) Find the difference in the mean of the envelope from the original series $x(p)$. The difference $d(p)$ is calculated as $d(p) = x(p) - m(p)$. Then, examine the properties of $d(p)$.

(5) Repeat 1–4 steps before the number of extrema is less than or equal to one so that no more IMF can be extracted or residue $e(p)$ becomes a monotonic function.

At last, the signal can be shown as the sum of all the IMFs and residue $e(p)$, where n is the number of IMFs, $C_i(p)$, $(i = 1, 2, 3, \ldots, n)$ is the i^{th} IMF, and $e(p)$is the residue. The way to denoise the IMF is the same as described in steps (1)–(4), except for the last two because of the low-frequency IMFs, which are used without denoising them [26, 35]:

$$x(p) = \sum_{i}^{n} d_i + e(p), \tag{7}$$

where n shows the number of sifted IMFs, as $(i = 1, 2, 3, \ldots, n)$ $e(p)$ is the trend of the signal and $d_i(p)$ is the i^{th} IMF. Except for the last two IMFs, which are used without applying denoising techniques on them because of the low magnitude in their frequencies, the rest of the procedure of denoising process is the same as in wavelet-based denoising by using (3), (4), and (7) equations. In equations (3), (4), and (7), according to the number of IMFs, the subscript is replaced by i. Before reconstructing the signal, a smooth signal for input can be obtained by applying the thresholds on IMFs. The rebuilding of the denoised signal is generalized as

$$x(p) = \sum_{i=1}^{n_1-2} h_i(p) + \sum_{i=n_1-2}^{n} h_i(p) + e(p), \tag{8}$$

where the parameter n_1 is the number of IMFs which provides us with the easiness of the elimination of the low-order IMF which are noisy and also of higher-order IMFs, which are a little bit noisy in Gaussian noise conditions as $(i = 1, 2, 3, \ldots, n)$ $h_i(p)$, and $e(p)$ is the i^{th} IMF and trend of the signal, respectively.

3.2. Decomposition Step (Decompose-Step). In the decomposition step, we need to apply a helpful tool to reduce the noises, providing accurate results. EEMD technique is applied in the decomposition step to handle the trouble of mode mixing.

3.2.1. Ensemble Empirical Mode Decomposition (EEMD). To improve the EMD and mitigate the mode mixing, EEMD is developed. In this technique, the white noise added by EEMD is distributed equally among all the time-frequency space, which helps in the separation of the frequency scales and decreases the occurrence of mode mixing. The procedure is presented as follows [36, 37]:

(i) Initialization of the ensemble number Q.

(ii) Set the amplitude of the added white noise $i = 1$.

(iii) Add the random white noise signal $\text{wn}_i(p)$ in the original signal $x(p)$:

$$x_i(p) = x(p) + \text{wn}_i(p), \tag{9}$$

where $\text{wn}_i(p)$ is the i^{th} included series of white noise and $x_i(p)$ denotes the i^{th} included noise signal $i = 1 \sim Q, Q > 1$.

(iv) By using EMD, decompose the noise signal $x_i(p)$ into N IMFs$C_{j,i}(p)$, $(j = 1, 2, 3, \ldots, P)$, where $C_{j,i}(p)$ shows the j^{th} IMF of the i^{th} noise signal and P is the total number of IMFs.

(a) To obtain the pro-IMF $s_1(p)$, subtract the mean envelope $m_1(p)$ from the original $x_1(p)$, i.e., $s_1(p) = x_1(p) - m_1(p)$, where $m_1(p) = (U(p) + G(p))/2$.

(b) Consider $s_1(p)$ as a new signal if the average of the lower and upper envelope becomes zero and if the number of zero-crossing and the number of extrema are equal or almost one.

(c) Consider the points (a)–(c) of 4$^{\text{th}}$ step as far as the resulting signal as proper IMF $C_1(p)$.

(d) From the original signal, $x_1(p)$, subtract the resulting IMF $C_1(p)$. Consider the residue $e_1(p)$ as the new data and go back to step 1:

$$x_1(p) = C_1(p) + e_1(p). \tag{10}$$

(e) In the substep, if the residue becomes the monotonic function, then complete the algorithm, and if $i < Q$, then go back to step 3. The last residual is treated as the trend:

(v) Estimate the ensemble mean $\text{IMF}_j(p)$ of all trials of each IMF:

$$\text{IMF}_j(p) = \frac{1}{P} \sum_{j=1}^{P} C_{j,i}(p), \quad j = 1, 2, 3, \ldots, P, i = 1, 2, 3, \ldots, Q. \tag{12}$$

(vi) Consider the mean $\text{IMF}_j(p)$ as the final mean of all the P IMFs.

3.2.2. Complete Ensemble Empirical Mode Decomposition with Added Noise (CEEMDAN). Although EEMD can bring down the problem of mode mixing to a certain degree with included white noise sequence, the error cannot be eliminated after the computation of the averaging to a finite number. It affects the sequence of reconstruction. For the elimination of the mode mixing, CEEMDAN adds the adaptive white noise smoothing pulse interference in decomposition, and for making the decomposition of the data more complete, it uses the properties of the mean Gaussian white noise whose mean is zero. The detailed procedure of the CEEMDAN is as follows.

Persistent with EEMD, in the calculation of CEEMDAN, P times decompose the original signal $x(p)$, i.e., $x(p) + r_i wn_i(p)$, where r_i is the parameter which deals the signal to noise ratio. The first component of the IMF is

$$\mathrm{IMF}_1(p) = \frac{1}{P}\sum_{i=1}^{P} c_{j,1}(p). \tag{13}$$

The residual of the signal is

$$e_1(p) = x(p) - \mathrm{IMF}_1(p). \tag{14}$$

The $d(p)$ is defined as the l^{th} IMF component obtained from EMD. The sequence $v_1(p) + r_1 d_1(p)(n_j(p))$ is decomposed as follows to get the second IMF component:

$$\mathrm{IMF}_2(p) = \frac{1}{P}\sum_{j=1}^{P} d_1\Big(e_1(p) + r_1 d_1\big(n_j(p)\big)\Big). \tag{15}$$

The second residual signal is

$$e_2(p) = e_1(p) - \mathrm{IMF}_2(p). \tag{16}$$

Similarly, by following the above procedure, the expression of the l^{th} residual signal will be as follows:

$$e_l(p) = e_{l-1}(p) - \mathrm{IMF}_l(p). \tag{17}$$

The expression of the $l + 1^{\text{th}}$ residual signal is

$$\mathrm{IMF}_{l+1}(p) = \frac{1}{P}\sum_{j=1}^{P} d_l\Big(e_l(p) + r_l d_l\big(n_j(p)\big)\Big). \tag{18}$$

The above procedure is repeated until the criterion is met. The expression of the original sequence, if the number of IMF components is M, is as follows:

$$x(p) = \sum_{i=1}^{M} \mathrm{IMF}_i(p) + e(p), \tag{19}$$

where $\mathrm{IMF}_i(p)$ is the i^{th} IMF, $e(p)$ is the overall residual signal, and $x(p)$ is the signal obtained after decomposition. The decomposed IMFs are further used in the prediction stage.

3.3. Prediction Step (P-Step). Multistep-ahead prediction is used to predict a sequence of values in time-series data. This approach is applied to predict a model step-by-step and use the predicted value of the current time step to determine its value in the next time step. We split the data into training and testing datasets. For the training dataset, 70% of the observations are used, and 30% are used for the testing dataset.

In the prediction stage, by using machine learning time series and stochastic methods, the denoised IMFs are used as input to predict the production data of mineral resources. For this, we used multistep-ahead forecasting strategy. The reason for using two different types of models in prediction is that the IMFs with high frequencies are predicted accurately through ML methods and do not provide accurate results for the IMFs having low frequencies. Stochastic models provide better outcomes for the prediction of the IMFs with low frequencies. These two types of models are used for the direct forecast of IMFs having high and low frequencies.

The models used for the prediction purpose are briefly described as follows.

3.3.1. Autoregressive Integrated Moving Average (ARIMA) Model. For the prediction of the IMF, the autoregressive moving average model is used as follows:

$$\begin{aligned}\mathrm{IMF}_k^i = {} & \psi_1 \mathrm{IMF}_{k-1}^i + \cdots + \psi_p \mathrm{IMF}_{k-p}^i + \varepsilon_k^i + \varphi_1 \varepsilon_{k-1}^i \\ & + \cdots + \varphi_q \varepsilon_{k-q}^i,\end{aligned} \tag{20}$$

where IMF_k^i shows the i^{th} IMF and ε_p^i shows i^{th} residual obtained through CEEMDAN, and p and q are the lag values of autoregressive and moving average term. Sometimes the time-series data are nonstationary; in such a situation, the series can be made stationary by differencing to an appropriate degree. Then, in the case of differencing the series, the model is called ARIMA(p, d, q), where d is a degree of difference that makes the series stationary.

3.3.2. Group Method of Data Handling (GMDH)-Type NN Model. GMDH is a type of unexplored neural network. The GMDH-NN models are established by considering the evolutionary method of modeling (GEvoM), which is a program that generates a polynomial type neural network for modeling the data. The input variables, hidden layers containing neurons, best model structure, and the number of layers are determined automatically in these networks. By considering the evaluation criteria, some of the neurons are chosen then the output of these selected neurons turns into the input of the next layer. For the selection of the neurons, the prediction means square criterion is considered using some transfer functions shown in Table 1.

The procedure is repeated until the final layer. In the last segment, only one predicted neuron is considered. However, GMDH-NN selects the relation of only two variables and ignores the effect of an individual variable. The relationship between input and output variables is generally expressed through the Volterra functional series called Kolmogorov–Gabor polynomial [38]:

$$v = b_0 + \sum_{k=1}^{n} b_k u_k + \sum_{k=1}^{n}\sum_{l=1}^{n} b_{kl} u_k u_l + \sum_{k=1}^{n}\sum_{l=1}^{n}\sum_{m=1}^{n} b_{klm} u_k u_l u_m + \cdots. \tag{21}$$

A refined form of GMDN-NN is the architecture group method of data handling (RGMDH-NN), which not only considers two variables but also considers them individually; the remaining procedure of RGMDH is the same as GMDH.

3.3.3. Radial Basis Function Neural Network (RBFNN). As an ANN technique, RBFNN is used to predict the decomposed IMFs and components of residual. The reason for the selection of RBFNN is the simplicity of its structure and flexibility in selecting the number of neurons [39]. On the contrary to other feedforward neural networks, that RBFNN consists of one layer. Moreover, the RBFNN has a

Table 1: Transfer functions for GMDH-NN algorithms.

Transfer functions	
Sigmoid function	$v = (1/(1 + \exp^{-u}))$
Tangent function	$v = \tan u$
Radial basis function	$v = \exp^{-u^2}$
Polynomial function	$v = u$

sound capability of approximation and fast convergence speed [40].

The structure of the RBFNN consists of two sections, one section is the nonlinear conversion of input (the first layer in Figure 2) to the hidden layer (the second layer in Figure 2), and the other part is the linear conversion of the hidden layer to the output layer which is the third layer described in Figure 2. Some of the expressions of RBF are shown in Table 2.

3.3.4. Mutistep-Ahead Prediction. Time-series prediction can be used for both single (one-step-ahead prediction) and multiple periods (multistep-ahead prediction). Multistep-ahead prediction has to deal with problems, such as accumulation error, uncertainty, and accuracy, unlike one-step-ahead prediction. However, accurate time-series prediction for long horizon has become challenging. A multistep-ahead time-series prediction consists of predicting the next H values of a time series consists of N observations, where the forecasting horizon is denoted by $H > 1$.

The DirREC strategy [41] combines the steps and the principles of direct and iterated strategies. The recursive strategy is used for the prediction of all IMFs using three different models, and at last, all the predicted IMFs are ensembled and predicted by direct approach. DirREC makes the prediction with different models for each horizon, and also, as the recursive approach, it increases the set of inputs by adding more variables related to the predictions of the previous step. However, the embedding size is different for all horizons.

4. Study Area and Experimental Design

4.1. Selection of Area for Study. Pakistan is blessed with numerous geological potential and has numerous reserves of minerals such as coal, copper, gold, and limestone, which are much useful for industrial development. However, we have not yet promoted growth and eliminated poverty in the country by utilizing our natural resources to the maximum level. The wealthiest province of Pakistan is Baluchistan, with approximately 80 to 85% minerals. The rest of the minerals, 10 to 15%, are present in KPK, Sindh, and Punjab. Despite Pakistan's precious mineral resources and two continuous mineral policies, this sector contributes poorly to the country's GDP. The reason may be insufficient assessments and monitoring, political instability, problems related to weather, shortage of foreign investments, and insecurity in the mineral-rich areas (https://www.pc.gov.pk/uploads/pub/FIRST_05_PAGES_STRATEGY_FOR_MINERAL_SECTOR_DEVELOPMENT_IN_PAKISTAN.pdf).

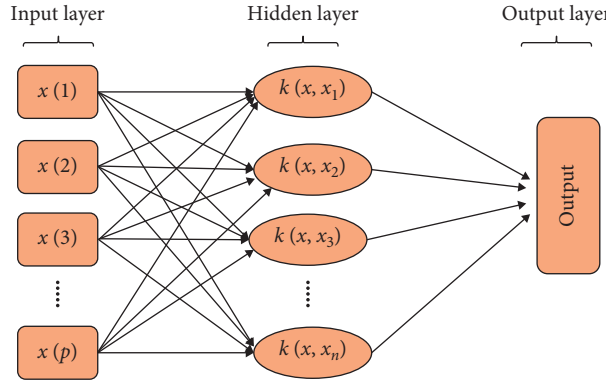

Figure 2: Structure of the radial basis function neural network.

4.2. Description of Data. The observed data consist of the production of principle minerals resources of Pakistan, which are named natural gas, oil, coal, and gypsum measured in terms of metric tons. It consists of 168 monthly observations recorded from July 2005 to June 2019. The data are divided into the training dataset and testing data for observing the model performance. The dataset of data contains 118 observations from the month of July 2005 to April 2015, and the testing dataset contains 50 observations from May 2015 to June 2019. The training dataset consists of 80% observations of the observed series, and the testing dataset includes 20% observations of the observed series.

4.3. Comparison of the Proposed Hybrid Model with Other Models. Both suggested models are compared with other models used for prediction, with and without decomposed and denoised techniques. We named them 1-stage, 2-stage, and 3-stage models for our convenience, which we used for comparison purposes:

(i) 1-stage model: models without having denoising and decomposition techniques are selected in this stage, i.e., ARIMA. We called them 1-stage as used in [29].

(ii) 2-stage model: in 2-stage models, denoised techniques (EMD/WA) are selected for comparison, having noise removal capacity, i.e., EMD/WA-ARIMA, EMD/WA-RGMDH, and EMD/WA-RBFNN. For prediction purposes, different models are selected to compare the statistical model with the models based on artificial intelligence, i.e., RGMDH and RBFNN models. These 2-stage models are selected from [42] for comparison purpose.

(iii) 3-stage model: in these models, both denoised and decomposed strategies are accessed; that is, EMD-EEMD-MM is selected from [15] for the purpose of comparison. Multiple models are selected under 3-stage models for the prediction by keeping the same strategy as in the proposed model. A direct 48-step-ahead forecasting strategy is used in the prediction step. We used a multistep-ahead forecasting methodology. Three methods for prediction are used: one traditional statistical model, i.e., ARIMA

Table 2: Transfer functions for RBFN algorithms.

Radial basis functions for RBFN algorithms	
Power function	$\psi(w) = w^c, c = \text{odd}, w \in R$
Gaussian function	$\psi(w) = \exp(-w^2/2c^2), c > 0, w \in R$
Square root function	$\psi(w) = \sqrt{w^2 + c^2}, c > 0, w \in R$
Hyperbolic tangent function	$\psi(w) = ((1 - e^{-2w})/(1 + e^{-2w})), w \in R$
Sigmoid function	$\psi(w) = (1 + e^{-w})^{-1}, w \in R$
Thin plate spline function	$\psi(w) = w^2 \log(w), w \in R$
Reciprocal square root function	$\psi(w) = (w^2 + c^2)^{-1/2}, c > 0, w \in R$

(p, d, and q), and two machine learning methods, i.e., GMDH and RBFNN.

4.4. Accuracy Measure Techniques. The performance of the model can be achieved by measuring the closeness of the predicted values and the observed values for the test dataset. By using three evaluation measures, i.e., signal-to-noise ratio (SNR), mean relative error (MRE), mean absolute error (MAE), mean square error (MSE), and mean absolute percentage error (MAPE) [43], the prediction accuracy of the selected and proposed models is obtained. The following are their mathematical expressions:

$$\begin{aligned}
\text{MRE} &= \frac{1}{N}\frac{\sum_{p=1}^{n}\left|g(p)_0 - g(p)_{\text{pred}}\right|}{g(p)_0},\\
\text{MAE} &= \frac{1}{N}\sum_{p=1}^{n}\left|g(p)_0 - g(p)_{\text{pred}}\right|,\\
\text{MSE} &= \frac{1}{N}\sum_{p=1}^{n}\left(g(p)_0 - g(p)_{\text{pred}}\right)^2,\\
\text{MAPE} &= \frac{\left|g(p)_{m0} - g(p)_{m(\text{pred})}\right|}{\left|g(p)_{m0}\right|} * 100,
\end{aligned} \tag{22}$$

where $g(p)_{\text{pred}}$ and $g(p)_0$ are the predicted and real data, respectively, and n is the data size; also, $g(p)_{m0}$ is the mean of the observed data, and $g(p)_{m(\text{pred})}$ is the mean of the predicted values. MRE, MAE, and MSE measures the departure between the original values and predicted values. The neurons of neural networks (GMDH and RGMDH) are selected according to their MSEs.

5. Results and Discussion

In Figure 1, step-by-step procedure of the proposed method is described. In which firstly, in D-step, the original series is decomposed using EMD or WA. In the second step (Decompose-step), the denoised series is decomposed using the CEEMDAN technique. In the third step of Figure 1, the IMFs which are obtained through CEEMDAN are predicted using ARIMA, RGMDH, and RBFNN models. At the final stage, all the predicted IMFs are ensembled :

D-stage results: according to Figure 1, the original series of data is decomposed in the first step by using two noise removal filters; the results of denoising are described as follows:

Wavelet-based denoising: by following the ELT process shown in Figure 1 and using equations (1) and (2), the approximations are calculated on the data of mineral resources of Pakistan, and soft and hard thresholding are used to remove the noises from the coefficients of mineral production time-series data. Rules of soft and hard thresholding are calculated by using equations (3) and (4), respectively. Then, based on the lower value of MSE, denoised series, hard thresholds are reconstructed for wavelet analysis.

EMD-based denoising: for removing the noises from the production of mineral resource data using EMD, IMFs are calculated using equation (7). For denoising, these calculated IMFs except for the last two IMFs, soft and hard thresholding rules, are used as in WA by using equations (3) and (4), respectively. Since the last two IMFs are smooth and have low-frequency characteristics, that is why there is no need for denoising the last two IMFs. The denoised IMFs based on hard thresholding reconstruct noise-free mineral resource time-series data from equation (8). The WA- and EMD-based denoising are combined in Figure 3 for gas and oil. The statistical measures of the original series and denoised series of all four minerals, i.e., mean, standard deviation, MRE, MAE, and MSE for EMD and wavelet noise removal techniques, are shown in Table 3. According to these findings, it can be observed that EMD behaves better than WA.

According to statistical measures, the results show that WA and EMD behave differently for all four minerals. The mean and standard deviation of the original series, denoised series by EMD, and denoised by WA are almost the same in all minerals. However, for gas and coal production, the standard deviation becomes less by using WA. According to other statistical measures, i.e., MRE, MAE, and MSE, EMD performs better than WA, as, in all minerals, these measures have lower values than WA. Therefore, it is concluded that EMD and WA performed equally to denoise the mineral resources in the long run. In the decomposition stage, EMD and WA, both denoising techniques are used separately as input to get those characteristics that change in terms of varying frequencies, i.e., high frequencies and low frequencies.

Decompose-stage results: to get the local changing features for the time from denoised time-series data of

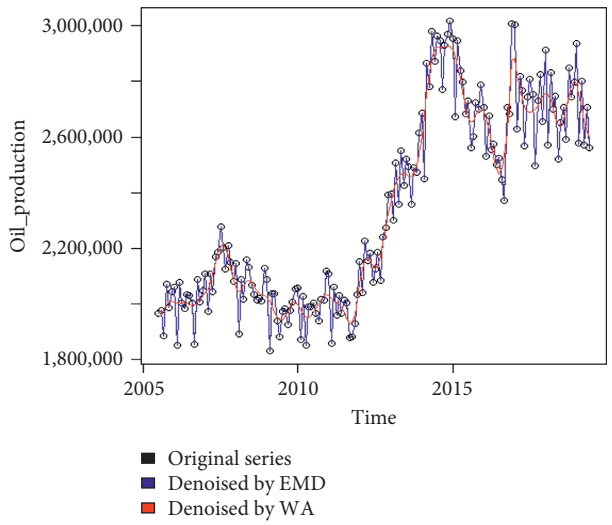

Figure 3: The denoised series for the production of gas and oil. The denoised series are obtained by EMD-threshold (in blue color) and wavelet threshold (in red color).

Table 3: Statistical measures of WA- and EMD-based denoised production of four-mineral time-series datasets.

Mineral resources	Mode	μ	σ	MRE	MAE	MSE
Gas production	Original series	122355	5477.39			
	EMD	122352.4	5452.545	64.56	0.00	5849.80
	WA	122355	3757.383	3258.05	0.03	14792170
Oil production	Original series	2341219	353450.2			
	EMD	2341179	353338.3	441.92	0.00	266404.30
	WA	2341219	343459.1	62569.99	0.03	6181270027
Gypsum production	Original series	109677.6	56078.37			
	EMD	109673.2	56031.31	178.88	0.00	43509.52
	WA	109675.9	54138.90	9578.65	0.10	143169479
Coal production	Original series	297596.6	73584.54			
	EMD	297615.9	73382.25	315.16	0.00	144581.50
	WA	297596.6	58222.67	30897.95	0.12	1552598008

mineral resources by WA/EMD, which are decomposed further into six IMF components and one residual term. The EMD and CEEMDAN decomposition methods are used for the extraction of IMFs from four minerals. The decomposition results of EMD-CEEMDAN techniques of gas and oil are presented in Figure 4, where all four minerals are decomposed into six IMF components, and one residual term is presented. The drawn-out IMFs represent mineral production time-series data characteristics where the starting IMFs show the higher frequency. In contrast, the last three IMFs represent lower frequency and residual shown as a trend.

The results of WA-CEEMDAN decomposition are shown in Figure 5. The extracted IMFs represent the attributes of production of mineral resource time-series data, where at the beginning, some IMFs have a higher frequency and then slowly frequency reduces till sixth IMF and residual shown as the trend in Figures 4 and 5. The amplitude's value of the white noise is chosen as 0.2, and a maximum number of the ensemble members (1000) are selected. Almost all IMFs and residuals for all minerals show identical characteristics for EMD-CEEMDAN and WA-CEEMDAN decomposition methods.

P-step results: three methods are adopted to predict all extracted IMFs and for residuals to get precise results. For this purpose, one traditional and two other nonlinear methods are used, i.e., ARIMA (p, d, and q) as traditional statistical method and GMDH-NN and RBFNN as nonlinear methods, which are used for the prediction of IMFs and residual for all four-mineral production. The mineral resource data of four minerals are partitioned into 70% and 30% for the training dataset and testing dataset, respectively. The parameters of the model and its structure are estimated using 118 observations of mineral resources. Then, the suggested model and other models used for comparison purposes are tested in terms of their validity using 30% mineral resource data. After estimating multimodels for every

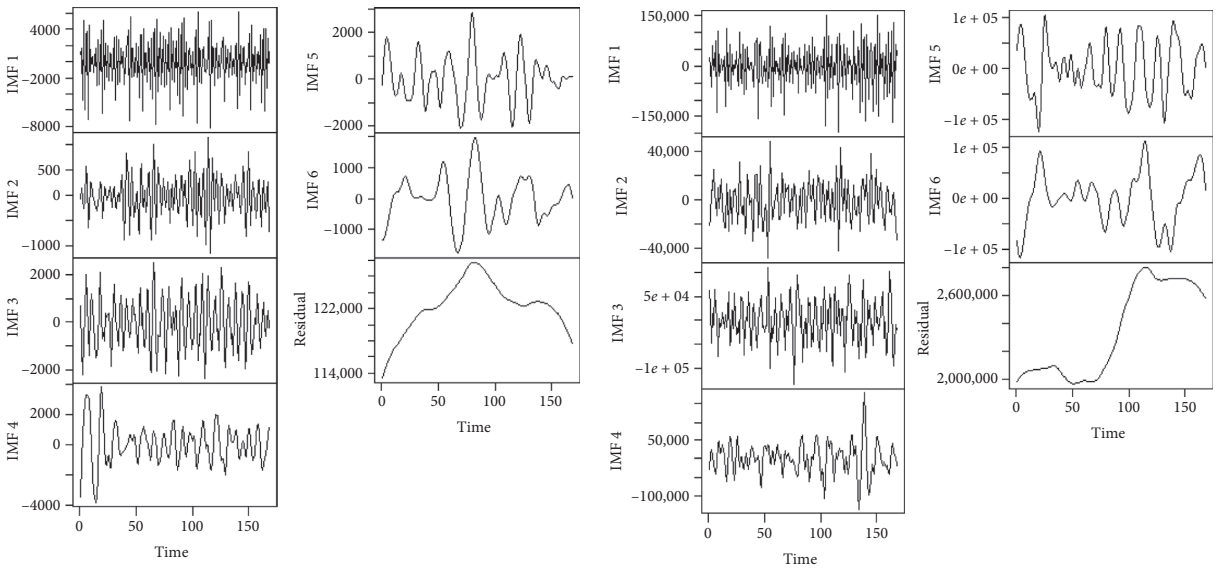

Figure 4: The EMD-CEEMDAN decomposition of gas (a) and oil (b) production. The four series are decomposed into six IMF components and one residual.

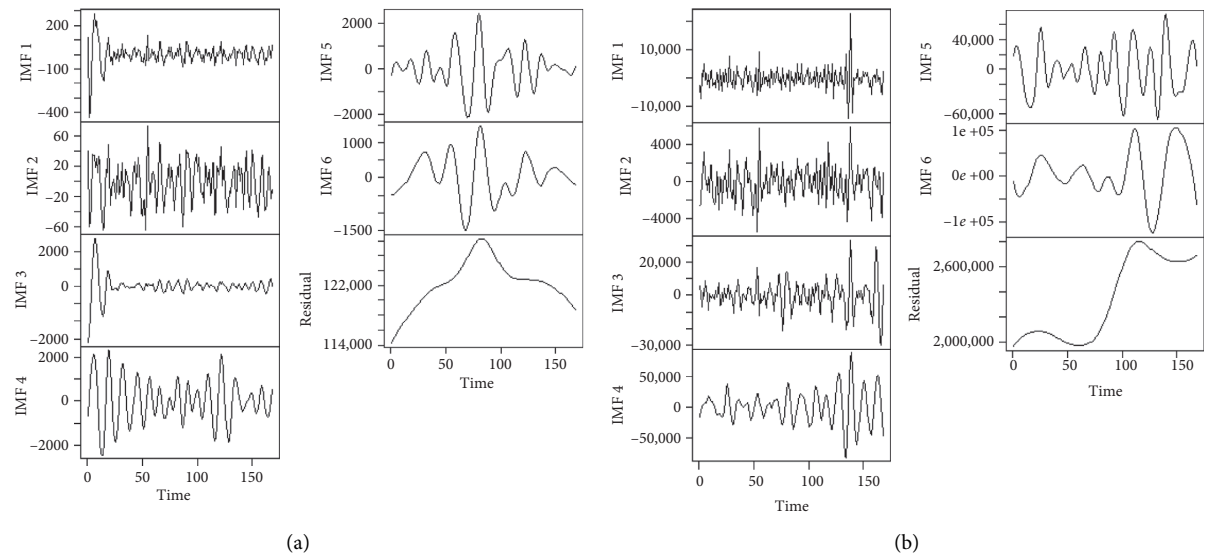

Figure 5: The WA-CEEMDAN decomposition of gas (a) and oil (b) production. The four series are decomposed into six IMF components and one residual.

IMF component and residual, the model with the least value of MRE, MAE, and MSE is considered as the most appropriate and selected for the prediction of each IMF. The findings for the training dataset of the suggested model and all other models in comparison to gas, oil, coal, and gypsum production are given in Table 4. The prediction results of suggested models EMD-CEEMDAN-MM and WA-CEEMDAN-MM illustrated the effectiveness of all four minerals with a minimum value of MRE, MAE, and MSE compared with 1-stage, 2-stage, and 3-stage evaluation models. However, the suggested model WA-CEEMDAN-MM acquires the lowest value of MSE than another proposed EMD-CEEMDAN-MM model. The model with the worst prediction is a 1-stage model, as shown in Table 4, with the maximum value of MRE, MAE, and MSE.

Here, the 1-stage model, i.e., the ARIMA model, attains the maximum value of MSE without applying the techniques of denoising and decomposition on the mineral production time-series data. The predicted graph of the suggested model EMD-CEEMDAN-MM in comparison with 2-stage, i.e., EMD-ARIMA and

Table 4: The evaluation of the prediction error of the suggested model (EMD-CEEMDAN-MM and WA-CEEMDAN-MM) in comparison with other existing models for gas, oil, coal, and gypsum production.

Mineral production	Model name	Models	MRE	MAE	MSE
Gas production	1-S	ARIMA	5562.08	0.05	34688672
	2-S	WA-ARIMA	564.79	0.00	500307.2
		WA-RGMDH	1041.51	0.01	1621799
		WA-RBFN	22919.26	0.19	545273283
		EMD-ARIMA	3750.39	0.03	23240715
		EMD-RGMDH	3753.87	0.03	23340680
		EMD-RBFN	22916.16	0.19	556913324
		EMD-EEMD-MM	2020.75	0.02	7766789
	3-S	**WA-CEEMDAN-MM**	**158.46**	**0.00**	**38472.38**
		EMD-CEEMDAN-MM	1195.00	0.01	2336537
Oil production	1-S	ARIMA	86924.62	0.04	12933064462
	2-S	WA-ARIMA	32680.16	0.01	1778236730
		WA-RGMDH	24693.97	0.01	981106280
		WA-RBFN	441208.80	0.17	313742347809
		EMD-ARIMA	86826.35	0.04	12907664665
		EMD-RGMDH	84082.76	0.04	11935015062
		EMD-RBFN	445083.30	0.17	318704000000
		EMD-EEMD-MM	34349.94	0.01	2014443387
	3-S	**WA-CEEMDAN-MM**	**5676.63**	**0.00**	**54755189**
		EMD-CEEMDAN-MM	26569.21	0.01	1213733733
Coal production	1-S	ARIMA	47665.83	0.19	3554183458
	2-S	WA-ARIMA	4919.99	0.02	63677954
		WA-RGMDH	7587.04	0.03	109980128
		WA-RBFN	65501.76	0.20	6500657737
		EMD-ARIMA	47592.77	0.19	3543414179
		EMD-RGMDH	46715.48	0.19	3480224927
		EMD-RBFN	74976.31	0.25	8461474651
		EMD-EEMD-MM	14999.79	0.06	365101582
	3-S	**WA-CEEMDAN-MM**	**2384.12**	**0.01**	**10215110**
		EMD-CEEMDAN-MM	13761.37	0.05	328725693
Gypsum production	1-S	ARIMA	16095.92	0.16	494553674
	2-S	WA-ARIMA	10218.46	0.09	239738995
		WA-RGMDH	9318.04	0.08	217996433
		WA-RBFN	44669.82	0.42	3399773324
		EMD-ARIMA	16040.73	0.16	492041414
		EMD-RGMDH	16495.23	0.16	501503414
		EMD-RBFN	45538.21	0.43	3549328950
		EMD-EEMD-MM	6876.55	0.08	77558497
	3-S	**WA-CEEMDAN-MM**	**2569.18**	**0.02**	**25152289**
		EMD-CEEMDAN-MM	21073.19	0.22	773453648

EMD-RGMDH models, is presented in Figure 6, and also, the predicted graph of WA-CEEMDAN-MM in comparison with 2-stage, i.e., WA-ARIMA and WA-RGMDH models, is presented in Figure 7. Here, in Table 4, the MSE of the RBFNN model is greater than all the MSEs of other models, so for comparison, we skip RBFNN in the graphical presentation of predicted results. Denoising, decomposition, and ensemble principles can be used to predict the mineral resources' production. In Table 4, 2-stage, i.e., ARIMA and RGMDH models, performs better than the single-stage model, and from the 2-stage model, the WA-based model performs better than EMD-based models.

However, it is concluded from Table 4 that the suggested models perform well to predict the production of mineral resources by decreasing its intricacy and increasing the performance of prediction over 1-stage, 2-stage, and 3-stage models.

The prediction errors for the testing dataset are presented in Table 5. It can be concluded that our suggested model performed better than all other benchmark models, i.e., the error obtained through prediction using the testing dataset in comparison with the error of prediction using the training dataset. From Table 5, it can be examined that the performance of the WA-CEEMDAN-MM model with minimum values of MAD, MAPE, and MSE is better than all other models. The graphical presentation of suggested models by considering the testing dataset for only gas production is exhibited in Figure 8, based on the EMD technique. Figure 9 is based on the WA technique. From these figures, it can be observed that our

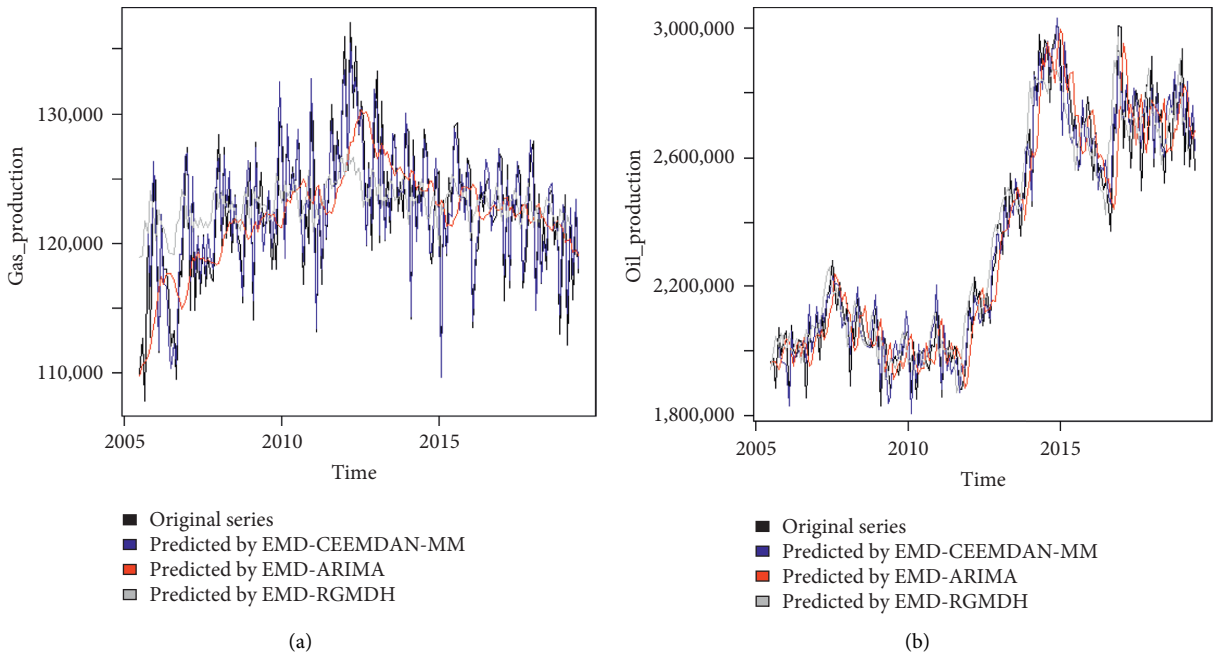

Figure 6: Prediction results of gas and oil production using suggested EMD-CEEMDAN-MM in comparison with EMD-ARIMA and EMD-RGMDH predicted models.

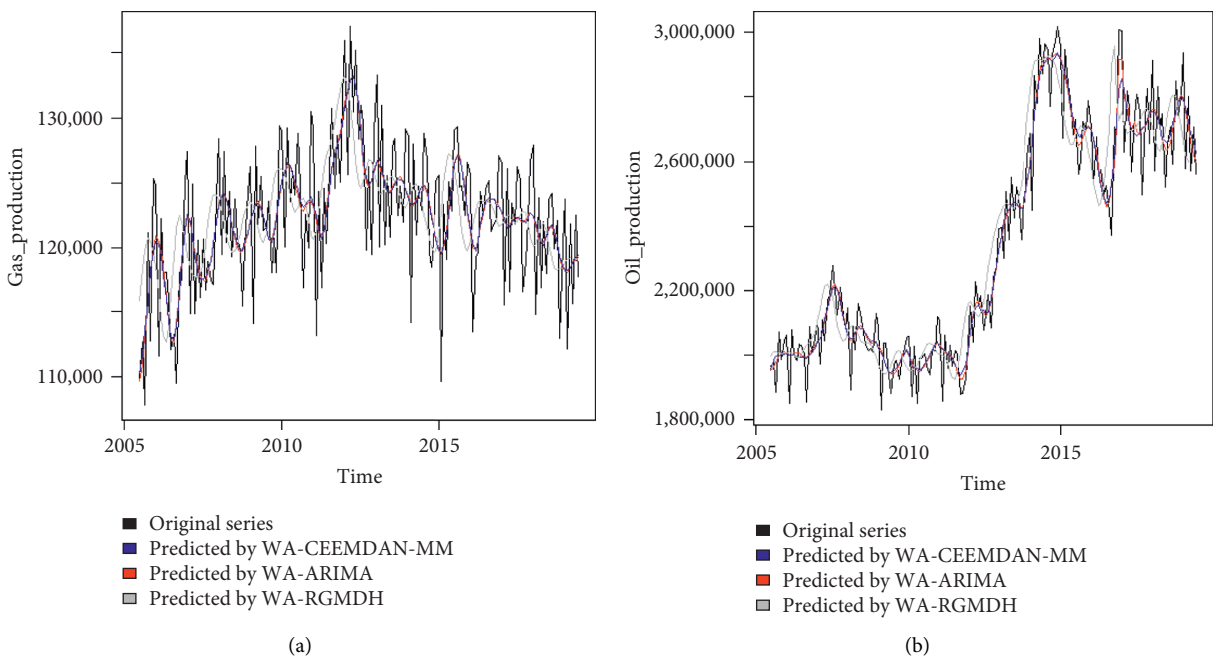

Figure 7: Prediction results of oil production using suggested WA-CEEMDAN-MM in association with WA-ARIMA and WA-RGMDH models.

suggested model performed better than all other existing models.

Overall comparison of the proposed model with denoised and decomposed models: in general, from Tables 4 and 5, it can be observed that removing the noises from the production data of mineral resources by using EMD and WA techniques provides better results as compared to single or model without denoising and decomposing. It can be observed that the value of MAE, MRE, and MSE from Tables 4 and 5 of all four minerals performs well for 2-stage models as compared to 1-stage models. It is noticed that the 1-

Table 5: The evaluation of the prediction error of the suggested model (EMD-CEEMDAN-MM and WA-CEEMDAN-MM) in comparison with other models for all four minerals having the testing dataset.

Mineral production	Model name	Models	MRE	MAE	MSE
Gas production	1-S	ARIMA	3253.46	0.03	16505715
	2-S	WA-ARIMA	3357.08	0.03	14297822
		WA-RGMDH	85.12	0.00	10700.46
		WA-RBFN	85178.71	0.70	7484485277
		EMD-ARIMA	3243.62	0.03	16313393
		EMD-RGMDH	3564.16	0.03	17443358
		EMD-RBFN	85223.53	0.70	7507698054
		EMD-EEMD-MM	120692.20	1.00	14573026239
	3-S	**WA-CEEMDAN-MM**	**55.78**	**0.00**	**4528.72**
		EMD-CEEMDAN-MM	1121.05	0.01	1835955
Oil production	1-S	ARIMA	104425.90	0.04	16912634727
	2-S	WA-ARIMA	92291.30	0.03	11294925595
		WA-RGMDH	5925.51	0.00	64583522
		WA-RBFN	1919080.00	0.70	3802014000000
		EMD-ARIMA	104445.20	0.04	16895725118
		EMD-RGMDH	100369.30	0.04	15464333281
		EMD-RBFN	1919040.00	0.70	3814679000000
		EMD-EEMD-MM	2722506.00	1.00	7416098000000
	3-S	**WA-CEEMDAN-MM**	**7888.74**	**0.00**	**147703705**
		EMD-CEEMDAN-MM	34261.48	0.01	1730054305
Coal production	1-S	ARIMA	52706.14	0.17	3986455945
	2-S	WA-ARIMA	34790.81	0.11	1834667964
		WA-RGMDH	3399.37	0.01	17296854
		WA-RBFN	234617.90	0.69	61083423522
		EMD-ARIMA	52689.36	0.17	3984927942
		EMD-RGMDH	47981.98	0.16	3413398302
		EMD-RBFN	234083.70	0.68	63318268986
		EMD-EEMD-MM	332627.70	1.06	111602246835
	3-S	**WA-CEEMDAN-MM**	**2207.27**	**0.01**	**9144544**
		EMD-CEEMDAN-MM	20414.31	0.07	20414.31
Gypsum production	1-S	ARIMA	26046.03	0.14	1164947275
	2-S	WA-ARIMA	29409.92	0.16	1482365241
		WA-RGMDH	1007.13	0.00	1651773
		WA-RBFN	135000.60	0.70	19562632811
		EMD-ARIMA	26005.65	0.14	11618477
		EMD-RGMDH	27240.40	0.14	1228486486
		EMD-RBFN	134601.00	0.69	20165977385
		EMD-EEMD-MM	193557.50	1.02	38076758501
	3-S	**WA-CEEMDAN-MM**	**1023.04**	**0.01**	**2727448**
		EMD-CEEMDAN-MM	11205.51	0.06	213535838

stage ARIMA model predicted some of the IMFs having low frequencies, precisely but not for the IMFs having high frequencies as they contained more time-varying characteristics. Moreover, different statistical and machine learning models are used with these denoised series to predict mineral production and explore the performances of simple and complex models. These statistical and machine learning models can be seen from Tables 4 and 5, where RBFNN with EMD and WA performs worst than EMD- and WA-based ARIMA and RGMDH. This shows that one can use simple models for predicting mineral production compared to complex models such as RBFNN.

It is observed that the two-stage model performed on average 6.7% better than the 1-stage model, and the 3-stage existing model performed 76.3% better than the 1-stage model on average and 87.3% on average better than the two-stage model.

Our proposed model 3-stage EMD/WA-CEEMDAN-MM attained 29.4% on average less value of MSE compared to the 1-stage model, 49.2% less value compared to 2-stage, and 68.75% less value of MSE as compared to the existing 3-stage model, similarly, on average 10.87% less value of MRE as compared to 1-stage, 2.0% on average less value of MRE than the 2-stage model, and 75.5% on average than the 3-stage model. Also, on average, there is a 22.49%, 52.38%, and −46.63% decrease in MAE by using the proposed model as compared with 1-stage, 2-stage, and existing 3-stage models.

However, the performance of 3-stage models, i.e., EMD–CEEMDAN-MM and WA-CEEMDAN-MM, is

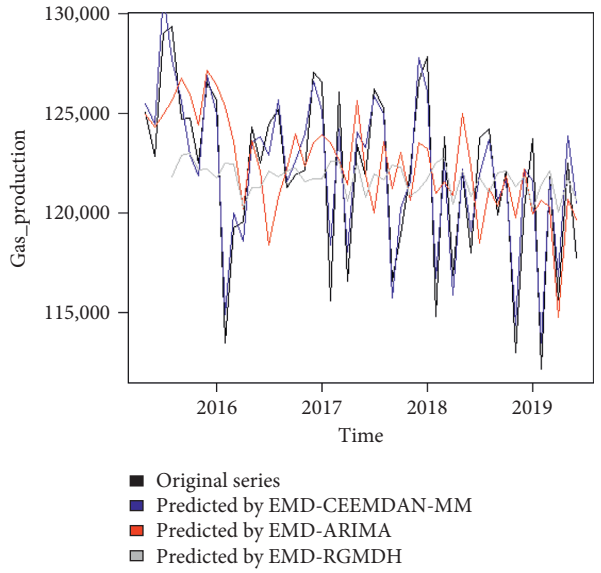

Figure 8: The prediction of gas production using the hybrid model (EMD-CEEMDAN-MM) in comparison with EMD-ARIMA and EMD-RGMDH models.

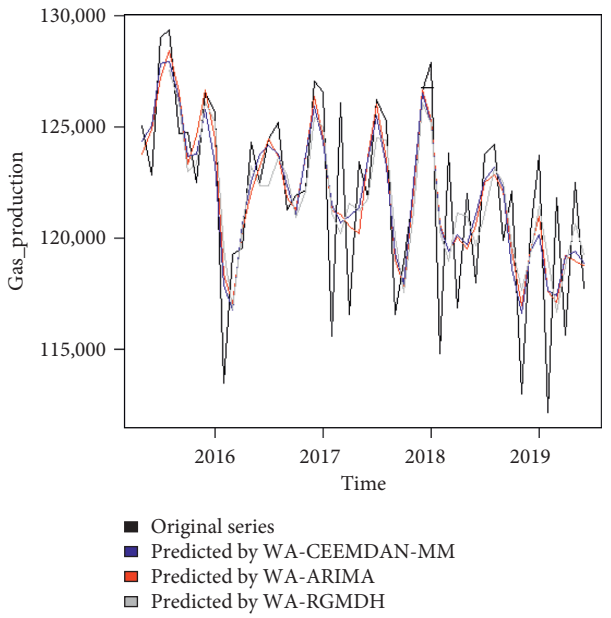

Figure 9: The prediction of gas production using the hybrid model (WA-CEEMDAN-MM) in comparison with WA-ARIMA and WA-RGMDH models.

better than 1-stage and 2-stage models as it reduces the complexity of mineral production data in many ways by combining denoising and decomposing techniques. The integrated features of denoising and decomposing of 3-stage models enhance the prediction accuracy of mineral production, as shown in Tables 4 and 5. Moreover, the WA-based hybrid models provided better accuracy of prediction as compared to EMD-based models.

6. Conclusion

For the optimal mineral supply and the purposes of mineral resources, an accurate prediction of mineral resources is necessary. Here, some of the data processing methods are utilized to increase the prediction accuracy of such stochastic type data by efficiently using decomposition techniques. By using the three strategies, denoising, decomposing, and ensemble, two hybrid models with 3-stages are suggested, EMD-CEEMDAN-MM and WA-CEEMDAN-MM, from which WA-CEEMDAN-MM performed better than the EMD-CEEMDAN-MM model for the decomposition of the nonstationary and nonlinear data of minerals. For evaluating the performance of both models, the production data of four minerals are used. In general, our suggested model performed well for all four minerals than the other 1-stage, 2-stage, and existing 3-stage models. For evaluation measures, three techniques are utilized, i.e., MAE, MSE, and MAPE. These 3-stage hybrid models can be used for the decomposition of any nonlinear and nonstationary data for prediction [44–47].

Data Availability

The dataset used in the manuscript is available on the following website: http://www.pbs.gov.pk/content/energy-mining-statistics. R-GUI codes: the codes to perform proposed methods are available on a public repository whose link is provided as follows: https://github.com/ihussain13/hybrid-methods-for-prediction.

Conflicts of Interest

The authors declare that they have no conflicts of interest.

Acknowledgments

This work was supported by grants from the National Natural Science Foundation of China program (41801339). The authors are also thankful to the Deanship of Scientific Research at King Saud University, through research group no. RG-1437-027.

References

[1] C. Di, X. Yang, and X. Wang, "A four-stage hybrid model for hydrological time series forecasting," *PLoS One*, vol. 9, no. 8, Article ID e104663, 2014.

[2] N. E. Huang, Z. Shen, S. R. Long et al., "The empirical mode decomposition and the Hubert spectrum for nonlinear and non-stationary time series analysis," *Proceedings of the Royal Society A: Mathematical, Physical and Engineering Sciences*, vol. 454, no. 1971, pp. 903–995, 1998.

[3] J. Dybała and R. Zimroz, "Rolling bearing diagnosing method based on empirical mode decomposition of machine vibration signal," *Applied Acoustics*, vol. 77, pp. 195–203, 2014.

[4] Y. Kopsinis and S. McLaughlin, "Development of EMD-based denoising methods inspired by wavelet thresholding," *IEEE Transactions on Signal Processing*, vol. 57, no. 4, pp. 1351–1362, 2009.

[5] S. Forecasting, U. Empirical, and A. N. Networks, "Streamflow forecasting using empirical wavelet transform and artificial neural networks," *Water*, vol. 9, no. 6, p. 406, 2017.

[6] N. Bokde, A. Feijóo, and K. Kulat, "Analysis of differencing and decomposition preprocessing methods for wind speed prediction," *Applied Soft Computing*, vol. 71, pp. 926–938, 2018.

[7] M. Yang, Y. F. Sang, C. Liu, and Z. Wang, "Discussion on the choice of decomposition level for wavelet based hydrological time series modeling," *Water (Switzerland)*, vol. 8, no. 5, 2016.

[8] T. Peng, J. Zhou, C. Zhang, and W. Fu, "Streamflow forecasting using empirical wavelet transform and artificial neural networks," *Water*, vol. 9, no. 6, p. 406, 2017.

[9] W. Chen, D. Zhang, and Y. Chen, "Random noise reduction using a hybrid method based on ensemble empirical mode decomposition," *Journal of Seismic Exploration*, vol. 26, no. 3, pp. 227–249, 2017.

[10] Z. Islam, "Literature review on physically based hydrological modeling," Ph. D. thesis, University of Alberta, Edmonton, Canada, 2011.

[11] H. Liu, C. Chen, H. Q. Tian, and Y. F. Li, "A hybrid model for wind speed prediction using empirical mode decomposition and artificial neural networks," *Renewable Energy*, vol. 48, pp. 545–556, 2012.

[12] D. Srinivasan, "Energy demand prediction using GMDH networks," *Neurocomputing*, vol. 72, no. 1–3, pp. 625–629, 2008.

[13] S. Kim and H. Kim, "A new metric of absolute percentage error for intermittent demand forecasts," *International Journal of Forecasting*, vol. 32, no. 3, pp. 669–679, 2016.

[14] X. J. Wu, G. C. Jiang, X. J. Wang, N. Fang, L. Zhao, and Y. M. Ma, "Prediction of reservoir sensitivity using RBF neural network with trainable radial basis function," *Neural Computing and Applications*, vol. 22, pp. 947–953, 2013.

[15] C. L. Wu, K. W. Chau, and Y. S. Li, "Methods to improve neural network performance in daily flows prediction," *Journal of Hydrology*, vol. 372, no. 1–4, pp. 80–93, 2009.

[16] D. Wang, Y. Liu, Z. Wu, H. Fu, Y. Shi, and H. Guo, "Scenario analysis of natural gas consumption in China based on wavelet neural network optimized by particle swarm optimization algorithm," *Energies*, vol. 11, no. 4.

[17] T. Xiong, Y. Bao, and Z. Hu, "Beyond one-step-ahead forecasting: evaluation of alternative multi-step-ahead forecasting models for crude oil prices," *Energy Economics*, vol. 40, pp. 405–415, 2013.

[18] A. Sorjamaa, J. Hao, N. Reyhani, Y. Ji, and A. Lendasse, "Methodology for long-term prediction of time series," *Neurocomputing*, vol. 70, no. 16–18, pp. 2861–2869, 2007.

[19] M. E. Torres, M. A. Colominas, G. Schlotthauer, and P. Flandrin, "A complete ensemble empirical mode decomposition with adaptive noise," in *Proceedings of the 2011 IEEE International Conference on Acoustics, Speech and Signal Processing (ICASSP)*, Prague, Czech Republic, May 2011.

[20] X. Mi, H. Liu, and Y. Li, "Wind speed prediction model using singular spectrum analysis, empirical mode decomposition and convolutional support vector machine," *Energy Conversion and Management*, vol. 180, pp. 196–205, 2019.

[21] W. Niu, Z. Feng, M. Zeng et al., "Forecasting reservoir monthly runoff via ensemble empirical mode decomposition and extreme learning machine optimized by an improved gravitational search algorithm," *Applied Soft Computing*, vol. 82, p. 105589, 2019.

[22] M. A. Farahani, M. T. V. Wylie, E. Castillo-Guerra, and B. G. Colpitts, "Reduction in the number of averages required in BOTDA sensors using wavelet denoising techniques," *Journal of Lightwave Technology*, vol. 30, no. 8, 2012.

[23] W. Liu, K. He, Q. Gao, and C. Liu, "Application of EMD-based SVD and SVM to coal-gangue interface detection," *Journal of Applied Mathematics*, vol. 2014, Article ID 283606, 6 pages, 2014.

[24] A. R. Ghumman, Y. M. Ghazaw, A. R. Sohail, and K. Watanabe, "Runoff forecasting by artificial neural network and conventional model," *Alexandria Engineering Journal*, vol. 50, no. 4, pp. 345–350, 2011.

[25] N. Jaitly and G. Hinton, "Learning a better representation of speech soundwaves using restricted Boltzmann machines," in *Proceedings of the ICASSP, IEEE International Conference on Acoustics, Speech and Signal Processing*, Prague, Czech Republic, May 2011.

[26] A. Mehrsai, H. R. Karimi, K. D. Thoben, and B. Scholz-Reiter, "Application of learning pallets for real-time scheduling by the use of radial basis function network," *Neurocomputing*, vol. 101, pp. 82–93, 2013.

[27] J. Kim, C. Y. Chun, and B. H. Cho, "Comparative analysis of the DWT-based denoising technique selection in noise-riding DCV of the Li-Ion battery pack," in *Proceedings of the 9th International Conference on Power Electronics-ECCE Asia: "Green World with Power Electronics", ICPE 2015-ECCE Asia*, Seoul, Korea, June 2015.

[28] S. Saadat, I. Hussain, and M. Faisal, "Modeling and forecasting of principal minerals production," *Arabian Journal of Geosciences*, vol. 14, no. 9, pp. 1–16, 2021.

[29] H. M. Nazir, I. Hussain, M. Faisal, A. M. Shoukry, S. Gani, and I. Ahmad, "Development of multidecomposition hybrid model for hydrological time series analysis," *Complexity*, vol. 2019, Article ID 2782715, 14 pages, 2019.

[30] S. Huang, J. Chang, Q. Huang, and Y. Chen, "Monthly streamflow prediction using modified EMD-based support vector machine," *Journal of Hydrology*, vol. 511, pp. 764–775, 2014.

[31] Y. Lei, Z. He, and Y. Zi, "Application of the EEMD method to rotor fault diagnosis of rotating machinery," *Mechanical Systems and Signal Processing*, vol. 23, no. 4, pp. 1327–1338, 2009.

[32] M. Santhosh, C. Venkaiah, and D. M. Vinod Kumar, "Ensemble empirical mode decomposition based adaptive wavelet neural network method for wind speed prediction," *Energy Conversion and Management*, vol. 168, no. May, pp. 482–493, 2018.

[33] Z. Qu, K. Zhang, J. Wang, W. Zhang, and W. Leng, "A hybrid model based on ensemble empirical mode decomposition and fruit fly optimization algorithm for wind speed forecasting," *Advances in Meteorology*, vol. 2016, Article ID 3768242, 14 pages, 2016.

[34] K. L. Chong, S. H. Lai, and A. El-Shafie, "Wavelet transform based method for river stream flow time series frequency analysis and assessment in tropical environment," *Water Resources Management*, vol. 33, no. 6, pp. 2015–2032, 2019.

[35] S. Xu and R. Niu, "Computers and geosciences displacement prediction of Baijiabao landslide based on empirical mode decomposition and long short-term memory neural network in Three Gorges area, China," *Computers and Geosciences*, vol. 111, pp. 87–96, 2018.

[36] J. Zhang, R. Jiang, B. Li, and N. Xu, "Computers and geosciences an automatic recognition method of microseismic signals based on EEMD-SVD and ELM," *Computers and Geosciences*, vol. 133, p. 104318, 2019.

[37] H. Liu, C. Chen, H. Q. Tian, and Y. F. Li, "A hybrid model for wind speed prediction using empirical mode decomposition and artificial neural networks," *Renewable Energy*, vol. 48, pp. 545–556, 2012b.
[38] X. Wei, R. Lin, S. Liu, and C. Zhang, "Improved EEMD denoising method based on singular value decomposition for the chaotic signal," *Shock and Vibration*, vol. 2016, Article ID 7641027, 14 pages, 2016.
[39] S. Dai, D. Niu, and Y. Li, "Daily peak load forecasting based on complete adaptive noise and support vector machine optimized by modified grey wolf," *Energies*, vol. 11, no. 1, 2018.
[40] Z. Guo, W. Zhao, H. Lu, and J. Wang, "Multi-step forecasting for wind speed using a modified EMD-based artificial neural network model," *Renewable Energy*, vol. 37, no. 1, 2012.
[41] A. Grossmann and J. Morlet, "Decomposmon of hardy functions into square integrable wavelets of constant shape," in *Fundamental Papers in Wavelet Theory*, pp. 126–139, Princeton University Press, Princeton, NJ, USA, 2009.
[42] Z. Qian, Y. Pei, H. Zareipour, and N. Chen, "A review and discussion of decomposition-based hybrid models for wind energy forecasting applications," *Applied Energy*, vol. 235, no. November 2018, pp. 939–953, 2019.
[43] H. Liu, H. Q. Tian, C. Chen, and Y. Fei, "A hybrid statistical method to predict wind speed and wind power," *Renewable Energy*, vol. 35, no. 8, pp. 1857–1861, 2010.
[44] A. K. Tiwari, Z. Mukherjee, R. Gupta, and M. Balcilar, "A wavelet analysis of the relationship between oil and natural gas prices," *Resources Policy*, vol. 60, no. December 2018, pp. 118–124, 2019.
[45] Z. Y. Wang, J. Qiu, and F. F. Li, "Hybrid models combining EMD/EEMD and ARIMA for long-term streamflow forecasting," *Water (Switzerland)*, vol. 10, no. 7, pp. 1–14, 2018.
[46] X. Jiang, L. Zhang, and X. Chen, "Short-term forecasting of high-speed rail demand: a hybrid approach combining ensemble empirical mode decomposition and gray support vector machine with real-world applications in China," *Transportation Research Part C: Emerging Technologies*, vol. 44, pp. 110–127, 2014.
[47] S. Yannis Kopsinis, "Empirical mode decomposition based denoising techniques," in *Proceedings of the IAPR Workshop on Cognitive Information Processing*, Santorini, Greece, 2008.

Hindawi
Mathematical Problems in Engineering
Volume 2021, Article ID 1951456, 7 pages
https://doi.org/10.1155/2021/1951456

Research Article

Fitting of Atomic Force Microscopy Force Curves with a Sparse Representation Model

Qing Wang,[1] Nan Hu,[2] and Junbo Duan[3]

[1]*School of Electronic Engineering, Xidian University, Xi'an 710071, China*
[2]*First Affiliated Hospital, Xi'an Jiaotong University, Xi'an 710049, China*
[3]*Key Laboratory of Biomedical Information Engineering of Ministry of Education and Department of Biomedical Engineering, School of Life Science and Technology, Xi'an Jiaotong University, Xi'an 710049, China*

Correspondence should be addressed to Junbo Duan; junbo.duan@mail.xjtu.edu.cn

Received 15 June 2021; Accepted 21 July 2021; Published 29 July 2021

Academic Editor: Yuxing Li

Atomic force microscopy (AFM) is a high-resolution scanning technology, and the measured data are a set of force curves, which can be fitted with a piecewise curve model and be analyzed further. Most methods usually follow a two-step strategy: first, the discontinuities (or breakpoints) are detected as the boundaries of two consecutive pieces; second, each piece separated by the discontinuities is fitted with a parametric model, such as the well-known worm-like chain (WLC) model. The disadvantage of this method is that the fitting (the second step) accuracy depends largely on the discontinuity detection (the first step) accuracy. In this study, a sparse representation model is proposed to jointly detect discontinuities and fit curves. The proposed model fits the curve with a linear combination of parametric functions, and the estimation of the parameters in the model can be formulated as an optimization problem with ℓ_0-norm constraint. The performance of the proposed model is demonstrated by the fitting of AFM retraction force curves with the WLC model. Results shows that the proposed method can segment the force curve and estimate the parameter jointly with better accuracy, and hence, it is promising for automatic AFM force curve processing.

1. Introduction

The atomic force microscopy (AFM) is a high-resolution scanning probe microscopy [1–3], which is widely used in life science [4], chemistry [5], and nanotechnology [6]. A typical AFM instrument consists of five components: laser generator, probe, cantilever, piezoelectric scanner, and photodiode detector. The testing sample is mounted above the piezoelectric scanner, which can move in an approaching manner toward the probe or a retracting manner away from the probe. When the sample surface and the probe are close enough, the interaction force between them yields the cantilever deflecting toward (attractive force) or away (repulsive force) from the probe. The deflection can be calculated from the output of the photodiode detector, which measures the laser reflected by the cantilever. The characteristics (e.g., the Hooke constant) of the cantilever are usually known in advance, so the interaction force can be calculated from the deflection of the cantilever. As a result, the measurement of AFM is the interaction force f versus piezoelectric scanner indentation z.

There are several parametric models describing the relationship between the interaction force and indentation. For the approaching force curve, there are models such as the Hertz model, Johnson–Kendall–Roberts model, and Derjaguin–Müller–Toporov model [3]. For the retracting force curve, the worm-like chain (WLC) model and freely jointed chain (FJC) received a wide range of interests [3], which describe the elastic behavior of polymers. As mentioned in the previous study [7], the low-load, moderate-load, and high-load regions of an approaching force curve can be modeled as the exponential model, Hertz model, and Hooke model, respectively; each piece between the two neighboring jumps of a retracting force curve can be modeled as either WLC or FJC.

The processing of AFM data is a typical curve fitting problem, which aims to estimate the parameters of the given models that can best fit the curve. Those parameters can help investigators better understand the biochemical and biophysical properties of the biochemical samples or nanomaterials. There are lots of methods to estimate parameters specific to different models. When the model is linear with respect to its parameters, the noisy data can be transformed into the parametric space, in which the parameters are estimated, e.g., the classical Fourier analysis. When the model is nonlinear with respect to its parameters, one can minimize the difference between the noisy output and the ideal model, which is known as regression analysis.

Since the AFM force curves usually consist of piecewise segments, we focus on the piecewise curve fitting with given parametric models. One well-known technique is the spline fitting [8, 9] for piecewise smoothing. However, spline is constrained to polynomial functions and needs to have the prior knowledge of discontinuities (or break points, change points, and knots in spline terminology), which is often unknown. Polyakov et al. [7] proposed a two-step strategy. In the first step, discontinuities were detected from noisy curves. To detect the discontinuities, a set of functions consisting of piecewise polynomials were used to fit the force curve. The piecewise polynomials are the ensemble of Heaviside step functions, the first, the second, . . ., and the r^{th} degree integration of Heaviside step functions, where r is the highest degree of the polynomial. In the second step, the noisy curve was segmented into pieces by the detected discontinuities, and then, each piece was fitted with a parametric model by nonlinear optimization.

Another way of parameter estimation is clustering in the space of model parameters directly, and hence, curve fitting can be avoided. A method of such kind was proposed by Maity et al. [10], in which the contour length of the WLC model is estimated for each data point on a force curve by solving a third-order polynomial equation, and then, the force versus contour length scatter plot is obtained, and the contour lengths are finally estimated by clustering. Since the segmentation procedure in the curve fitting is replaced by clustering, the performance of such method highly depends on that of clustering, which is still an open question.

This study is organized as follows: in Section 2, the curve fitting problem is formulated as a sparse representation model, and then, propose a systematic method to find the best fitting. In Section 3, the proposed method is applied to process a retracting force curve from AFM, which can be fitted with the WLC model. The study is concluded in Section 4.

2. Methodology

2.1. Worm-Like Chain (WLC). In stretching experiments, several jumps may present in the retracting force curve. This phenomenon is caused by the bound between macromolecule and the probe (similar to that of Velcro). Each jump represents a detachment from the surface.

There are several models describing this phenomenon, among which the WLC and FJC models received wide interests. Since the FJC model was intensively studied [7], this study only focuses on the WLC model. However, the method can be applied to the FJC model straightforward. The WLC model considers a polymer as an elastic cylinder with a constant bending elasticity and of constant length. The relationship between the interaction force f and extension z reads

$$f\left(z; L_c, l_p\right) = \frac{k_B T}{l_p}\left(\frac{z}{L_c} - \frac{1}{4} + \frac{1}{4\left(1 - \left(z/L_c\right)\right)^2}\right), \tag{1}$$

where k_B is the Boltzmann constant, T is the absolute temperature, L_c is the contour length, and l_p is the persistence length. In the stretching experiments, one would like to estimate the persistence length l_p and contour length L_c from experimental data f and z. Figure 1(a) shows the WLC model, which shows that the WLC model exhibits an asymptotic behavior, with asymptote $z = L_c$. Figure 1(b) shows a typical AFM retracting force curve. Each piece between two jumps can be fitted with a WLC model. Because of this asymptotic behavior, two-step methods suffer from modeling error, since the polynomial function set was used to detect the discontinuities. Instead, in this study, the set of WLC signals is proposed to detect discontinuities and to fit curves jointly.

2.2. From 2D to 1D Estimation. It is noticeable that, for a given L_c, the term in the parenthesis is fixed. So from experimental data f and z, the coefficient $k_B T/l_p$ can be easily estimated by solving a least square problem, yielding estimate $\widehat{l}_p(L_c)$. Thus, the 2D (two parameters L_c and l_p) problem (1) can be simplified to a 1D function $f(z; L_c, \widehat{l}_p(L_c))$. Based on this, the principle of the proposed method is as follows: first, a signal set (or dictionary) $\mathscr{F}$ is built by sampling contour length L_c within the feasible region $[L_c^{\min}, L_c^{\max}]$ with high intensity (large n), i.e.,

$$\mathscr{F} = \left\{\overline{f}\left(z; L_c^i\right) \mid L_c^{\min} \le L_c^i \le L_c^{\max}, i = 1, \ldots, n\right\}, \tag{2}$$

where

$$\overline{f}\left(z; L_c\right) = \left(\frac{z}{L_c} - \frac{1}{4} + \frac{1}{4\left(1 - \left(z/L_c\right)\right)^2}\right) \tag{3}$$

is the term in the parenthesis in function (1). Then, the force curve $f(z)$ can be fitted with a linear combination of $\overline{f}(z; L_c^i)$: $f(z) \approx \sum_{i=1}^{n} x_i \overline{f}(z; L_c^i)$, where x_i is the coefficient and can be formulated as the problem in equation (5), where each scalar x_i is an entry of the vector x.

Once the estimate of x_i, i.e.,$\widehat{x}_i$ is known, for those $\widehat{x}_i$ who are nonzeros, the corresponding estimate of contour length is L_c^i, and the corresponding persistence length l_p can be estimated as

$$\widehat{l}_p = \frac{k_B T}{\widehat{x}_i}. \tag{4}$$

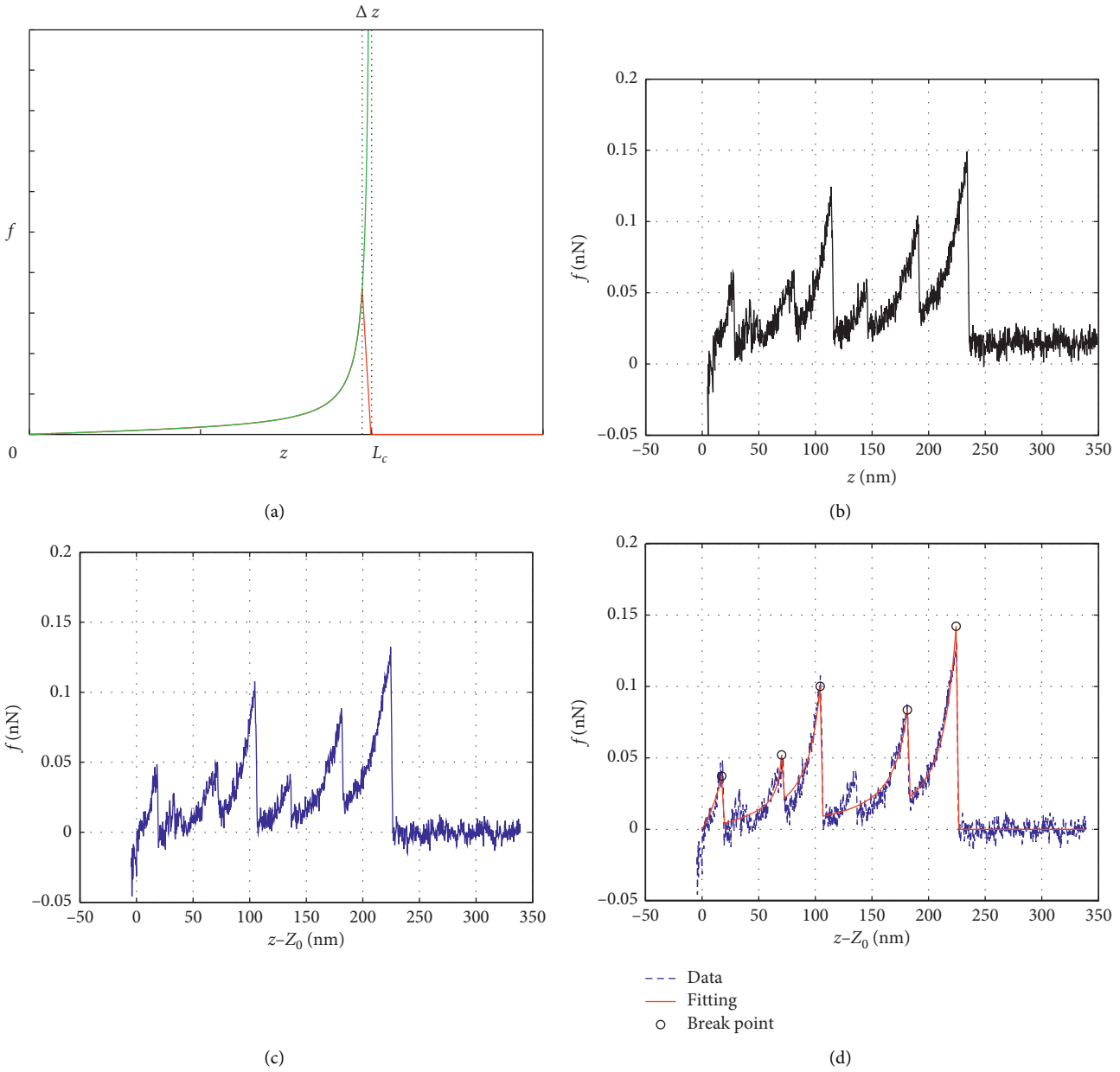

Figure 1: Continued.

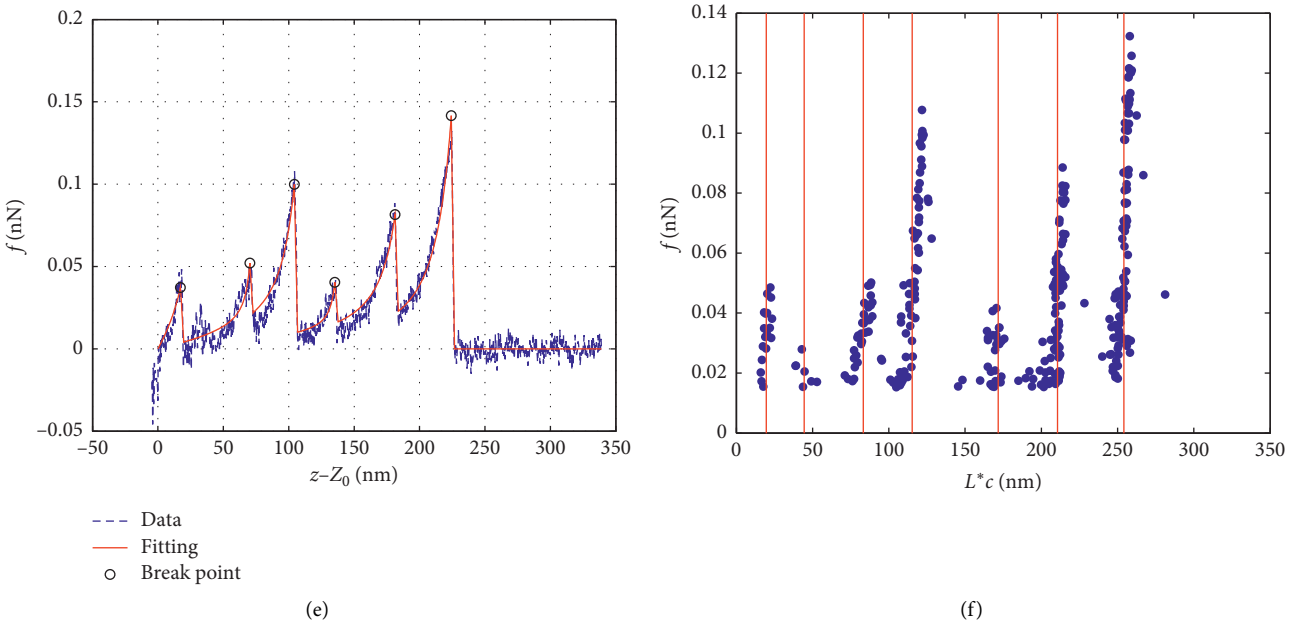

Figure 1: (a) The schematic illustration of the WLC model (only the term in the parenthesis, without the coefficient term). The green thin curve represents the whole theoretical WLC model, which exhibits an asymptotic behavior with asymptote $z = L_c$ (the right dotted vertical line). The red bold curve represents the truncated version, which constitutes the matrix F. (b) A typical force curve sample from CNGA1 data. (c) The force curve after preprocessing. (d), (e) The fitting results with five and six WLC pieces, respectively. (f) The fitting results with Maity et al.'s method [10], each blue point is a solution (L_c^*, f), and red vertical lines represent centers/means of each cluster.

2.3. Sparse Representation Model. In a sparse representation model, one would like to approximate a given signal $f \in \mathbb{R}^m$ using a limited number of functions from a dictionary $F \in \mathbb{R}^{m\times n}$. Here, signal f and dictionary F are the vectorized version of f and by discretization z. This approximation problem is usually formulated as an $\ell - 0$ constrained least square optimization problem:

$$x_k^* = \arg\min_{\|x\|_0 \le k} \|f - Fx\|^2, \tag{5}$$

where $x \in \mathbb{R}^n$ is the vector which gathers the fitting coefficients, and $\|x\|_0$ denotes the number of nonzero entries in vector x, i.e., the ℓ–0 norm of x; k is the sparsity level (or model degree), which controls the tradeoff between the model complexity and fitting quality. It is easy to see that larger k yields better fitting quality, while smaller k yields less complexity of the model (use less columns in matrix F). For discrete Fourier transform (DFT) and discrete cosine transform (DCT) [11], the columns of F are complex exponential and cosinusoids functions with different frequencies, respectively; for deconvolution problems, F is a Toeplitz matrix formed from the impulse response function [12]; and in compressed sensing, F is a random sampling matrix [13, 14]. In our WLC fitting problem mentioned above, each column in dictionary F is generated by sampling the parametric model given by equation (2).

2.4. Model Solver. The optimization problem (5) was proved to be NP-hard [15], and the optimal solution can only be found by performing an exhaustive search of all the combination of the columns in F. The exhaustive search is time-consuming even when the dimension of the solution vector is moderate (in the magnitude of hundreds). In real applications, the dimension is often more than thousands, so exhaustive search is unrealistic. Instead, heuristical methods, such as matching pursuit (MP) [16], orthogonal matching pursuit (OMP) [17], and orthogonal least square (OLS) [18], were proposed to get the suboptimal solutions. However, when the correlation between the columns in the matrix F (or mutual coherence [19]) is high ($1 - 5.5e - 6$ for F), the performance of these methods are not satisfactory.

Therefore, single best replacement (SBR) [12] and continuation of SBR [20] were developed to tackle the problem (5). SBR is a forward-backward algorithm. In each iteration, one column in the matrix F is included into or excluded from the so-called active set. Only the columns in the active set are used to fit the signal f by least squares, yielding nonzero coefficients in x. The coefficients corresponding to columns excluded from the active set are assigned to be zeros. The criterion to determine which column shall be included into or excluded from the active set is the deepest-descent of the cost function.

The highlight of continuation of SBR is an efficient way to explore the solution set by increasing the model degree k, which controls the tradeoff between the model complexity and the fitting quality. The output of the continuation algorithm is a set of solutions $\{\widehat{x}_k\}$ with respect to model degree k, and each solution is a tradeoff profile, which obeys $\|\widehat{x}_k\|_0 = k$. For the WLC fitting problem, k actually represents the number of segments. For more details of SBR and continuation SBR, readers are referred to our previous publications.

Once the solution set $\{\widehat{x}_k\}$ is ready, the following issue is to select a proper solution or to determine the best model degree k.

2.5. Model Degree Determination. The choice of the model degree k, which is usually unknown in advance, is an important issue. A relative high model degree yields overfitting, while a low model degree yields underfitting. For the curve fitting problem is this study, k represents the number of pieces in an AFM force curve.

There are several ways to determine k; most notable one is the information criteria such as Akaike information criterion (AIC) [21], Bayesian/Schwarz information criterion (SIC) [22] (also known as minimal description length (MDL)), Hannan and Quinn criterion (HQC) [23], Draper information criterion (DIC) [24], and others [25]. All these criteria are essentially penalized logarithm likelihood estimates with the following formulation [26, 27]:

$$\min_k \ln L(k) + \lambda k, \tag{6}$$

where $\ln L(k)$ is the logarithm likelihood estimate and is equal to $m \ln \|f - \widehat{f}_k\|^2$, and $\widehat{f}_k = F\widehat{x}_k$ is the fitted curve. λ is equal to 2, $\ln m$, and $2 \ln \ln m$, for AIC, BIC, and HQC, respectively. The best model degree k is achieved where an information criterion reaches its minimum. Since the results of previous subsection is a set of solutions $\{\widehat{x}_k\}$, problem (6) can be solved straightforward.

3. Real Data Processing

AFM is widely used in molecular and cell biology [28]. In this section, the proposed method described above is shown to process a real AFM force curve (Figure 1(b)) sampled on *Xenopus laevis* oocytes with single-molecule force spectroscopy (SMFS) at room temperature (20 ~ 24°C, so average $T = 295$ K), which aims to study the cyclic nucleotide-gated channel subunit alpha 1 (CNGA1) [10, 29]. CNGA1 consists of several secondary structures, and its conformation changes by the stretching force, yielding several jumps in the force curve. Each piece between the two neighboring jumps can be described with the worm-like chain model.

3.1. Raw Data Preprocessing. The raw data were first preprocessed with the following steps: (1) reorder the data points (z, f) with respect to z, such that they arrange in an ascent manner; (2) resample the force curve at an uniform grid of z (four samples per nanometer since the raw force curve's sample step is 0.24 ± 0.08 nanometer) using linear interpolation; (3) align the "contact point" Z_0 to origin; (4) remove the baseline by subtracting a linear function, such that the null interaction force region (right part of the force curve) is horizontal, and the mean of this region is zero; and (5) keep only the right part of the force curve whose adjusted position $(z - Z_0)$ is nonnegative. A force curve f of length $m = 1357$ after preprocessing is shown in Figure 1(b).

3.2. Worm-Like Chain Dictionary Building. In a real situation, the force curve cannot reach the asymptote $z = L_c$, where $f = +\infty$. In order to avoid numerical instability, when building the dictionary F, an additional parameter Δz is introduced, such that function $\overline{f}(z; L_c)$ in (3) is evaluated only at the interval $[0, L_c - \Delta z]$ and linearly declines to zero at the interval $(L_c - \Delta z, L_c]$. In our real data, Δz is 1 ~ 25 nm with a step of 1 nm. For contour length L_c, the feasible region $[L_c^{\min}, L_c^{\max}]$ is 25 ~ 300 nm and is sampled with a step of 1 nm. Following these settings, for each given Δz and L_c, a vector of length m is sampled and appended to the matrix F as a column. Each vector is sampled as follows (Figure 1(a), the red bold line): at the interval $[0, L_c - \Delta z]$, function $\overline{f}(z; L_c)$ in (3) is sampled; at the interval $[L_c, z_{\max}]$, the samples are set to be zero; and in between, i.e., at the interval $(L_c - \Delta z, L_c)$, the samples are linearly sampled, where $z_{\max}$ is the maximum of z in the force curves ($z_{\max} \approx 340$ nm in our experiment). All the data points are sampled at the uniform grid with a step of four points each nanometer, yielding a vector of length $m = 1357$. Above all, after exploring all the n configurations of L_c and Δz, a WLC dictionary F of size 1357×6900 is built.

3.3. Curve Fitting and Parameter Estimation. Once the force curve f and the dictionary F are given, the continuation of SBR [12, 20] was used to solve the sparse representation problem (5), yielding a set of solutions $\{\widehat{x}_k\}$. For each solution $\widehat{x}_k$, the fitted curve can be calculated as $\widehat{f}_k = F\widehat{x}_k$. Note that the sparsity level k equals to the number of discontinuities in the fitted force curve $\widehat{f}_k$ in our WLC fitting problem. Since each column in F contains a discontinuity, the total number of discontinuities in $\widehat{f}_k$ equals to the number of selected columns in F, i.e., $\|\widehat{x}_k\|_0$, or k. Information criteria aforementioned were employed, but neither provide a meaningful fitting results; hence, $\lambda = 200$ was used; equivalently, $k = 6$. Figures 1(d) and 1(e) show the fitted curves with $k = 5$ and 6, respectively.

The contour length L_c of each piece can be retrieved from the corresponding column in F, and the persistence length l_p can be estimated following equation (4). Table 1 provides the estimates of contour length and persistence length of six WLC pieces in Figure 1(e).

The fitting results show that the proposed method successfully detects the discontinuities with good fitting quality. Comparing Figures 1(d) and 1(e), one can see that with the increase of k, one more discontinuity was detected, yielding an improved fitting which consists of six WLC pieces.

The proposed method was also compared with the method proposed by Maity et al. [10], which is introduced briefly in the Appendix, and whose result is shown in Figure 1(f). In this panel, six clusters are shown, indicating the six WLC pieces with contour lengths as the red vertical lines. A t-test shows that the estimates of contour length with both methods are consistent. However, Maity et al.'s method cannot estimate persistence length, and hence, it assumes a constant.

Table 1: The estimate of contour length L_c and persistence length l_p of six WLC pieces in Figure 1(f).

Piece	1	2	3	4	5	6
L_c(nm)	39	77	125	142	197	249
l_p(nm)	0.12	3.94	0.42	15.36	2.06	0.73
L_c^*(nm)	22	84	118	170	211	254

The six WLC pieces are located left of the six discontinuities. L_c^* is the estimate with Maity et al.'s method.

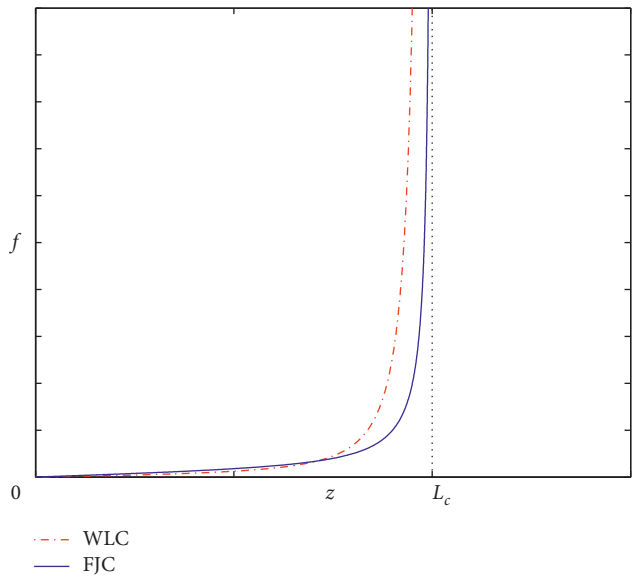

Figure 2: Demonstration of WLC and FJC models.

4. Conclusion and Discussion

This study proposed a method to fit a piecewise curve with parametric models. Different from many existing methods, a linear combination of several model functions (with parameters to be determined) from the dictionary was used to fit the curve, which was formulated as a sparse representation problem. By employing the continuation of the SBR algorithm, a set of solutions with different sparsity levels was obtained. The proposed method was applied to process the retracting force curve from AFM and was compared with a state-of-art method.

One advantage of the proposed method is that it can perform both the discontinuity detection and curve fitting at the same time. Most common methods use two separate steps, i.e., discontinuity detecting followed by curve fitting, and hence, the fitting result largely depends on the detection of discontinuities. For example, when using the piecewise polynomial functions to detect the discontinuities in a retracting force curve (which could be fitted with the WLC model), false detection of discontinuity is inevitable because of the presence of modeling error. However, this problem is solved by our proposed method.

Another advantage of our proposed method is its flexibility. If one wants to use other parametric models, e.g., freely jointed chain (FJC), which reads [3, 7]

$$z(f; L_c, l_k) = L_c\left(\coth\left(\frac{fl_k}{k_bT}\right) - \frac{k_bT}{fl_k}\right), \tag{7}$$

where l_k is the Kuhn length; other notations are the same as in the WLC model (equation (2)). By comparing the FJC with WLC model and following the method in Section 3.2, one can simply build a dictionary F with FJC functions. And by replacing the dictionary in optimization problem (5), one can finally fit the data with the FJC model. Figure 2 demonstrates both WLC and FJC models.

The disadvantage of the proposed method is the large storage space of the matrix F and the corresponding computational cost introduced by fine sampling of model parameters. In our experiment, L_c is sampled 25 ~ 300 nm with a step of 1 nm (276 configurations), and Δz is sampled 1 ~ 25 nm with a step of 1 nm (25 configurations). So the total number of columns in F is $276 \times 25 = 6900$. f is of size 1357. Then, the size of F is 1357×6900. If one would like to improve the resolution, e.g., L_c, the step has to be reduced, e.g., 0.5 nm, which doubles the size of F. Hopefully, with the rapid developing of computing resources in recent years, better performance is expected.

The fitting at the boundary region of the force curve can be further improved. Note that there seems a WLC segment between 20 and 40 nm, but neither Maity's method nor ours discovered it. The reason might be that the right slope is not steep, which is the characteristic of the WLC model, and hence, this segment was treated as inference.

As a perspective, at the beginning of the force curve, it can be modeled as a truncated linear function, while at the end of the force curve, it can be modeled as a step function. By appending more columns to matrix F and each newly added column representing the model at the boundary region, better fitting results can be expected to achieve.

Appendix

Maity et al.'s Method

Maity et al. [10] proposed a method to estimate contour length L_c of the WLC model by solving equations. However, their description has a minor error (ω should not depend on L_c), so here is a short summary of their method with correction.

For each data point on a force curve (z, f), a third order polynomial equation of λ is solved, which reads

$$4\lambda^3 + \omega\lambda^2 - 1 = 0, \tag{A.1}$$

where $\omega = (4f/\alpha) - 3$, $\alpha = (k_BT/l_p)$, and $l_p = 0.4$ nm.

This equation has three roots, and the real one is denoted as λ^*, which is between 0 and 1. Finally, the estimate of contour length reads $L_c^* = (z/1 - \lambda^*)$.

For all the data points on a curve, force versus contour length (L_c^*, f) scatter plot is obtained, and the contour lengths are estimated as the means of scatters, which is shown in Figure 1(f) as red vertical lines.

Data Availability

The dataset used to support the findings of this study is available at https://github.com/galvanetto/Fodis/blob/master/Datasets/TXT%20universal%20import%20files/104_CNGA1_selected.txt.

Conflicts of Interest

The authors declare that there are no conflicts of interest.

Acknowledgments

This study was partially supported by Provincial Science Foundation of Shaanxi (2021JM-128).

References

[1] G. R. Heath, E. Kots, J. L. Robertson et al., "Localization atomic force microscopy," *Nature*, vol. 594, no. 7863, pp. 385–390, 2021.

[2] B. Voigtländer, *Atomic Force Microscopy, NanoScience and Technology*, Springer, Berlin, Germany, 2019.

[3] H.-J. Butt, B. Cappella, and M. Kappl, "Force measurements with the atomic force microscope: technique, interpretation and applications," *Surface Science Reports*, vol. 59, no. 1–6, pp. 1–152, 2005.

[4] S. Lyonnais, M. Hénaut, A. Neyret et al., "Atomic force microscopy analysis of native infectious and inactivated sars-cov-2 virions," *Scientific Reports*, vol. 11, no. 1, Article ID 11885, 2021.

[5] C. Geary, G. Grossi, E. K. S. McRae, P. W. K. Rothemund, and E. S. Andersen, "RNA origami design tools enable cotranscriptional folding of kilobase-sized nanoscaffolds," *Nature Chemistry*, vol. 13, no. 6, pp. 549–558, 2021.

[6] R. Zhang, W. S. Fall, K. W. Hall, G. A. Gehring, X. Zeng, and G. Ungar, "Quasi-continuous melting of model polymer monolayers prompts reinterpretation of polymer melting," *Nature Communications*, vol. 12, no. 1, p. 1710, 2021.

[7] P. Polyakov, C. Soussen, J. Duan, J. F. Duval, D. Brie, and G. Francius, "Automated force volume image processing for biological samples," *PLoS One*, vol. 6, no. 4, Article ID e18887, 2011.

[8] C. H. Reinsch, "Smoothing by spline functions," *Numerische Mathematik*, vol. 10, no. 3, pp. 177–183, 1967.

[9] M. Unser, "Splines: a perfect fit for signal and image processing," *IEEE Signal Processing Magazine*, vol. 16, no. 6, pp. 22–38, 1999.

[10] S. Maity, M. Mazzolini, M. Arcangeletti et al., "Conformational rearrangements in the transmembrane domain of CNGA1 channels revealed by single-molecule force spectroscopy," *Nature Communications*, vol. 6, no. 7093, pp. 1–15, 2015.

[11] A. Oppenheim and W. Schafer, *Discrete-Time Signal Processing*, Prentice-Hall, New York, NY, USA, 3rd edition, 2009.

[12] C. Soussen, J. Idier, D. Brie, and J. Duan, "From Bernoulli-Gaussian deconvolution to sparse signal restoration," *IEEE Transactions on Signal Processing*, vol. 59, no. 10, pp. 4572–4584, 2011.

[13] R. Baraniuk, "Compressive sensing," *IEEE Signal Processing Magazine*, vol. 24, no. 4, pp. 118–121, 2007.

[14] E. J. Candès and M. B. Wakin, "An introduction to compressive sampling," *IEEE Signal Processing Magazine*, vol. 25, no. 2, pp. 21–30, 2008.

[15] B. K. Natarajan, "Sparse approximate solutions to linear systems," *SIAM Journal on Computing*, vol. 24, no. 2, pp. 227–234, 1995.

[16] S. G. Mallat and Z. Zhang, "Matching pursuits with time-frequency dictionaries," *IEEE Transactions on Signal Processing*, vol. 41, no. 12, pp. 3397–3415, 1993.

[17] Y. Pati, R. Rezaiifar, and P. Krishnaprasad, "Orthogonal matching pursuit: recursive function approximation with applications to wavelet decomposition," in *Proceedings of 27th Asilomar Conference on Signals, Systems and Computers*, pp. 40–44, Pacific Grove, CA, USA, November 1993.

[18] S. Chen, S. A. Billings, and W. Luo, "Orthogonal least squares methods and their application to non-linear system identification," *International Journal of Control*, vol. 50, no. 5, pp. 1873–1896, 1989.

[19] D. L. Donoho and Y. Tsaig, "Fast solution of $l1$ -norm minimization problems when the solution may be sparse," *IEEE Transactions on Information Theory*, vol. 54, no. 11, pp. 4789–4812, 2008.

[20] J. Duan, C. Soussen, D. Brie, and J. Idier, "A continuation approach to estimate a solution path of mixed L2-L0 minimization problems," in *Proccedings of the Signal Processing with Adaptive Sparse Structured Representations (SPARS workshop)*, pp. 1–6, Saint-Malo, France, April 2009.

[21] H. Akaike, "A new look at the statistical model identification," *IEEE Transactions on Automatic Control*, vol. 19, no. 6, pp. 716–723, 1974.

[22] G. Schwarz, "Estimating the dimension of a model," *Annals of Statistics*, vol. 6, pp. 461–464, 1978.

[23] E. J. Hannan and B. G. Quinn, "The determination of the order of an autoregression," *Journal of the Royal Statistical Society: Series B (Methodological)*, vol. 41, no. 2, pp. 190–195, 1979.

[24] D. Draper, "Assessment and propagation of model uncertainty," *Journal of the Royal Statistical Society: Series B (Methodological)*, vol. 57, no. 1, pp. 45–70, 1995.

[25] K. E. Markon and R. F. Krueger, "An empirical comparison of information-theoretic selection criteria for multivariate behavior genetic models," *Behavior Genetics*, vol. 34, no. 6, pp. 593–610, 2004.

[26] Y. Yang, "Can the strengths of AIC and BIC be shared? a conflict between model indentification and regression estimation," *Biometrika*, vol. 92, no. 4, pp. 937–950, 2005.

[27] H. De and G. Acquah, "Comparison of Akaike information criterion (AIC) and Bayesian information criterion (BIC) in selection of an asymmetric price relationship," *Journal of Development and Agricultural Economics*, vol. 2, no. 1, pp. 1–6, 2010.

[28] Y. F. Dufrêne, T. Ando, R. Garcia et al., "Imaging modes of atomic force microscopy for application in molecular and cell biology," *Nature Nanotechnology*, vol. 12, no. 4, pp. 295–307, 2017.

[29] N. Galvanetto, A. Perissinotto, A. Pedroni, and V. Torre, "Fodis: software for protein unfolding analysis," *Biophysical Journal*, vol. 114, no. 6, pp. 1264–1266, 2018.

Hindawi
Mathematical Problems in Engineering
Volume 2021, Article ID 8357981, 11 pages
https://doi.org/10.1155/2021/8357981

Research Article

Localization of Alternating Magnetic Dipole in the Near-Field Zone with Single-Component Magnetometers

Gao Xiang,[1] **Du Bo-cheng**,[2] **and Wang Qi-long**[3]

[1]*School of Electrical Engineering, Xi'an University of Technology, Xi'an 710077, China*
[2]*Xi'an Modern Control Technology Research Institute, Xi'an 710065, China*
[3]*School of Mechanical and Precision Instrument Engineering, Xi'an University of Technology, Xi'an 710077, China*

Correspondence should be addressed to Gao Xiang; 646653296@qq.com

Received 21 May 2021; Accepted 27 June 2021; Published 7 July 2021

Academic Editor: Xiao Chen

Tri-axis magnetometers are widely used to measure magnetic field in engineering of the magnetic localization technology. However, the magnetic field measurement precision is influenced by the nonorthogonal error of tri-axis magnetometers. A locating model of the alternating magnetic dipole in the near-field zone with single-component magnetometers was proposed in this paper. Using the vertical component of the low-frequency magnetic field acquired by at least six single-component magnetometers, the localization of an alternating magnetic dipole could be attributed to the solution for a class of nonlinear unconstrained optimization problem. In order to calculate the locating information of alternating magnetic dipole, a hybrid algorithm combining the Gauss–Newton algorithm and genetic algorithm was applied. The theoretical simulation and field experiment for the localization of alternating magnetic dipole source were carried out, respectively. The positioning result is stable and reliable, indicating that the locating model has better performance and could meet the requirements of actual positioning.

1. Introduction

Magnetic positioning technology, with characteristics of all-weather, low power consumption, and simple signal processing, has gradually drawn people's attention. Due to the lower noise level of the magnetic sensor and the higher measurement accuracy, it would be easier to detect weak magnetic signals. Using the magnetic field signal of the target detected by a magnetic sensor or magnetic sensor array, the position information and motion state of the target were obtained by data inversion, which could be widely used in identification of vehicles [1], monitoring of magnetic field [2, 3], prediction of earthquake [4], diagnosis of pipeline failure [5], and exploration of crude oil [6].

Because the positioning algorithm of the magnetic target based on the static magnetic field is greatly influenced by the interference of the geomagnetic environment and other magnetic sources, some researchers have studied the localization of alternating magnetic dipole sources. In 2001, Paperno et al. proposed a method for magnetic position and orientation tracking. Based on two-axis generation of a quasi-static rotating magnetic field and three-axis sensing, two mutually orthogonal coils fed with phase-quadrature currents comprise the excitation source could be equivalent to a mechanically rotating magnetic dipole [7]. In 2006, Nara et al. presented a simple reconstruction formula for localization of a magnetic dipole. In order to calculate the locating information, the dipole position is expressed in terms of the magnetic field and its spatial gradients at a single place [8]. In 2010, Plotkin et al. developed a new scleral search coil (SSC) to track the target. The theoretical deduction and numerous simulations have shown that the proposed method could obtain the orientation and location information of SSC [9]. In 2013, Sheinker et al. proposed a locating method in 3D using beacons of low-frequency magnetic field. The method could be used in many applications, such as the navigation of indoor robot and the mapping of underground cavity [10]. Using beacons of low-frequency magnetic field, the authors proposed a method of remote tracking a year later [11]. In 2016, Pasku et al.

described a positioning system based on low-frequency magnetic field. The system could accommodate an arbitrary number of users without any additional infrastructure [12]. In 2015, Li et al. proposed an approach based on the genetic algorithm to search the location of the dipole. Only an electric field sensor in seawater is needed to measure the modulus of electric field intensity at the corresponding positions. Then, the position of the dipole could be determined accurately [13]. In 2017, the author proposed a positioning method for moving objectives with alternating magnetic fields using coherent demodulation. However, the magnetic fields were measured by using a tri-axis magnetometer. The magnetic field measurement precision is influenced by the nonorthogonal error of tri-axis magnetometers [14, 15]. In 2018, Dai et al. proposed a new 6D tracking method using the 3D linear motion, 2D rotational motion, and 3D orientation tracking. The hybrid method of magnetic tracking and inertial sensing verified that the full 6D pose could be used to track the target accurately [16]. In 2020, Song et al. proposed a positioning method of low-frequency magnetic beacons based on the genetic algorithm. In a wide-range measurement, the theoretical simulation and field experiment had been tested to show the accuracy of localization for the target [17].

A positioning method of alternating magnetic dipole in the near-field zone with single-component magnetometers was introduced in this paper. A measuring array consisting of at least six single-component magnetic sensors was used to collect the magnetic field emitted by the alternating magnetic dipole. Through the process of coherent demodulation, the varying curve of alternating magnetic field could be obtained. A hybrid algorithm combining the Gauss–Newton algorithm and genetic algorithm was applied to obtain the track of a moving target, which showed a good agreement with the actual motion information [18–22].

2. Materials and Methods

2.1. The Vertical Component of Alternating Magnetic Dipole. The alternating magnetic dipole source is a transmitting coil that radiates a low-frequency sinusoidal electromagnetic signal, and the working frequency of the signal is set as a fixed frequency. For example, the working frequency of the signal ranges from 100 Hz to 1000 Hz, and the corresponding wave length is between 3×10^5 meters and 3×10^6 meters correspondingly. The geometry of the radiation coil is much smaller than its working wavelength so that the radiation coil could be equivalent to a magnetic dipole. The schematic diagram of magnetic dipole in the cylindrical coordinate system is shown in Figure 1.

The radiation magnetic moment of the magnetic dipole is expressed by the formula as follows:

$$M = \mu_0 IS. \tag{1}$$

In formula (1),

μ_0 is the magnetic permeability of the medium

I is the current intensity in the coil

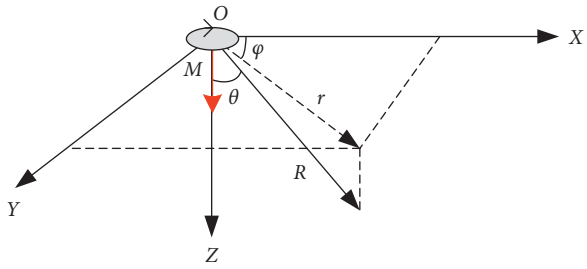

Figure 1: Schematic diagram of magnetic dipole in the cylindrical coordinate system.

S is the cross-sectional area of the coil, whose direction is the normal direction of the right-handed spiral

Using Maxwell's equations and boundary conditions, the electromagnetic field expression of magnetic dipole radiation could be expressed as

$$\begin{cases} H_R = \dfrac{2M}{4\pi\mu_0 R^3}\cos\theta(1 + jKR)e^{-jKR}, \\ H_\theta = \dfrac{M\sin\theta}{4\pi\mu_0 R^3}\left[1 + jKR + (jKR)^2\right]e^{-jKR}, \\ E_\varphi = \dfrac{\omega M}{4\pi R^2}\sin\theta(KR - j)e^{-jKR}. \end{cases} \tag{2}$$

In formula (2),

ω is the angular frequency of the alternating electromagnetic field

R is the distance from the magnetic dipole source to the observation point

K is the number of complex waves, which is plural in the conductive medium

Formula (2) contains the item labelled as KR. According to the distance labelled as R between the magnetic dipole source and the receiving point, the wavelength of the radiated electromagnetic wave in the propagation medium is labeled as λ.The electromagnetic field magnetic transmitted by the magnetic dipole could be divided into three regions.

(1) When $KR \ll 1$, it is called the near zone, also known as the quasi-stationary zone or the zone of stability

(2) When $KR \gg 1$, it is called the far zone

(3) The region between the near zone and the far zone is called intermediate zone

Usually, $R \ll 0.1\lambda$. Considering of the target's working frequency, the positioning region of the target is the near-field zone of the magnetic dipole source.

The distribution of the electromagnetic field in the near zone of the alternating magnetic dipole approximates that of the static magnetic dipole ($\omega = 0$, promptly, $K = 0$), which is similar to the constant stability field. It is assumed that the magnetic moment of an alternating magnetic dipole source located at the point labelled as $P_0(x_0, y_0, z_0)$ could be recorded as

$$\overrightarrow{M} = M_{x0}\cos(2\pi ft+\rho)\overrightarrow{i} + M_{y0}\cos(2\pi ft+\rho)\overrightarrow{j} + M_{z0}\cos(2\pi ft+\rho)\overrightarrow{k}. \tag{3}$$

The magnetic vector potential and magnetic fields at the receiving point labelled as $P(x, y, z)$ are as follows:

$$\begin{aligned} &\min_{\overrightarrow{x}\in R^n} S(x), \\ &(t_i, B_{0i}), \quad i = 1, 2, \ldots, N, \end{aligned} \tag{4}$$

where $r = \sqrt{(x-x_0)^2 + (y-y_0)^2 + (z-z_0)^2}$.

The three component magnetic fields acquired by a tri-axis magnetometer could be described as follows:

$$\begin{bmatrix} H_{x2} \\ H_{y2} \\ H_{z2} \end{bmatrix} = \frac{1}{4\pi r^5} \begin{bmatrix} \left[3(x-x_0)^2 - r^2\right] & 3(x-x_0)(y-y_0) & 3(x-x_0)(z-z_0) \\ 3(x-x_0)(y-y_0) & \left[3(y-y_0)^2 - r^2\right] & 3(y-y_0)(z-z_0) \\ 3(x-x_0)(z-z_0) & 3(y-y_0)(z-z_0) & \left[3(z-z_0)^2 - r^2\right] \end{bmatrix} \begin{bmatrix} M_{x0}\cos(2\pi ft+\rho) \\ M_{y0}\cos(2\pi ft+\rho) \\ M_{z0}\cos(2\pi ft+\rho) \end{bmatrix}. \tag{5}$$

From a strictly mathematical point of view, at least six single-component sensors are required since there are six unknown quantities: the three position coordinates labelled as $P_0(x_0, y_0, z_0)$ and the three moment components labelled as $M_0(M_{x0}, M_{y0}, M_{z0})$, and each sensor provides only one equation.

2.2. The Static Locating Method Based on Single-Component of Magnetic Field. Assume that the measuring array consisting of six single-component magnetic field sensors is shown in Figure 2, and their coordinates are labelled as $P_n(x_n, y_n, z_n)$ where $1 \le n \le 6$. The alternating magnetic dipole source is at the point labelled as $P_0(x_0, y_0, z_0)$.

The vertical component of the magnetic field generated by the alternating magnetic dipole at the point labelled as $P_0(x_0, y_0, z_0)$ was recorded as

$$H_n = H_{zn}\cos(2\pi ft+\rho). \tag{6}$$

Using the coherent demodulation, the alternating magnetic field labelled as H_n could be transformed to the varying curve signed as H_{zn} [14]. Then, the formula could be described as follows:

$$\begin{bmatrix} H_{z1} \\ H_{z2} \\ H_{z3} \\ H_{z4} \\ H_{z5} \\ H_{z6} \end{bmatrix} = \begin{bmatrix} \frac{3(x_1-x_0)(z_1-z_0)}{4\pi r_1^5} & \frac{3(y_1-y_0)(z_1-z_0)}{4\pi r_1^5} & \frac{\left[3(z_1-z_0)^2 - r_1^2\right]}{4\pi r_1^5} \\ \frac{3(x_2-x_0)(z_2-z_0)}{4\pi r_2^5} & \frac{3(y_2-y_0)(z_2-z_0)}{4\pi r_2^5} & \frac{\left[3(z_2-z_0)^2 - r_2^2\right]}{4\pi r_2^5} \\ \frac{3(x_3-x_0)(z_3-z_0)}{4\pi r_3^5} & \frac{3(y_3-y_0)(z_3-z_0)}{4\pi r_3^5} & \frac{\left[3(z_3-z_0)^2 - r_3^2\right]}{4\pi r_3^5} \\ \frac{3(x_4-x_0)(z_4-z_0)}{4\pi r_4^5} & \frac{3(y_4-y_0)(z_4-z_0)}{4\pi r_4^5} & \frac{\left[3(z_4-z_0)^2 - r_4^2\right]}{4\pi r_4^5} \\ \frac{3(x_5-x_0)(z_5-z_0)}{4\pi r_5^5} & \frac{3(y_5-y_0)(z_5-z_0)}{4\pi r_5^5} & \frac{\left[3(z_5-z_0)^2 - r_5^2\right]}{4\pi r_5^5} \\ \frac{3(x_6-x_0)(z_6-z_0)}{4\pi r_6^5} & \frac{3(y_6-y_0)(z_6-z_0)}{4\pi r_6^5} & \frac{\left[3(z_6-z_0)^2 - r_6^2\right]}{4\pi r_6^5} \end{bmatrix} \begin{bmatrix} M_{x0} \\ M_{y0} \\ M_{z0} \end{bmatrix}. \tag{7}$$

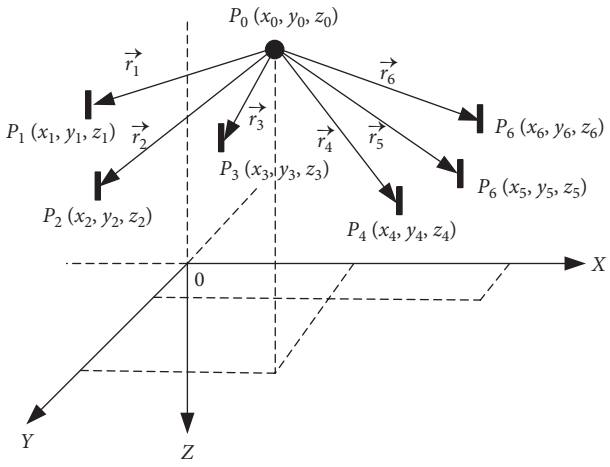

Figure 2: Coordinate of alternating magnetic dipole and measurement array consisting of six single-component magnetometers.

2.3. The Positioning Model of Alternating Magnetic Dipole. The positioning model of alternating magnetic dipole in the near-field zone with a measuring array consisting of six single-component magnetometers could be attributed to the solution for a class of nonlinear unconstrained optimization problem.

$$\mathbf{E}_0 = \min\left\{\left(\mathbf{F}_0\mathbf{M}_0 - \mathbf{H}_0\right)^T\left(\mathbf{F}_0\mathbf{M}_0 - \mathbf{H}_0\right)\right\}, \tag{8}$$

where $\mathbf{E}_0$ is the objective function of the nonlinear unconstrained optimization problem.

$$\mathbf{M}_0 = \left(\mathbf{F}_0^T\mathbf{F}_0\right)^{-1}\mathbf{F}_0^T\mathbf{H}_0, \tag{9}$$

which is called the coefficient matrix of magnetic moment parameters.

$$\mathbf{H}_0 = \begin{bmatrix} H_{z1} \\ H_{z2} \\ H_{z3} \\ H_{z4} \\ H_{z5} \\ H_{z6} \end{bmatrix}, \tag{10}$$

which is the varying curve of the vertical component for the alternating magnetic dipole in the near-field using the coherent demodulation [14, 15].

$$\mathbf{F}_0 = \begin{bmatrix} \frac{3(x_1-x_0)(z_1-z_0)}{4\pi r_1^5} & \frac{3(y_1-y_0)(z_1-z_0)}{4\pi r_1^5} & \frac{\left[3(z_1-z_0)^2-r_1^2\right]}{4\pi r_1^5} \\ \frac{3(x_2-x_0)(z_2-z_0)}{4\pi r_2^5} & \frac{3(y_2-y_0)(z_2-z_0)}{4\pi r_2^5} & \frac{\left[3(z_2-z_0)^2-r_2^2\right]}{4\pi r_2^5} \\ \frac{3(x_3-x_0)(z_3-z_0)}{4\pi r_3^5} & \frac{3(y_3-y_0)(z_3-z_0)}{4\pi r_3^5} & \frac{\left[3(z_3-z_0)^2-r_3^2\right]}{4\pi r_3^5} \\ \frac{3(x_4-x_0)(z_4-z_0)}{4\pi r_4^5} & \frac{3(y_4-y_0)(z_4-z_0)}{4\pi r_4^5} & \frac{\left[3(z_4-z_0)^2-r_4^2\right]}{4\pi r_4^5} \\ \frac{3(x_5-x_0)(z_5-z_0)}{4\pi r_5^5} & \frac{3(y_5-y_0)(z_5-z_0)}{4\pi r_5^5} & \frac{\left[3(z_5-z_0)^2-r_5^2\right]}{4\pi r_5^5} \\ \frac{3(x_6-x_0)(z_6-z_0)}{4\pi r_6^5} & \frac{3(y_6-y_0)(z_6-z_0)}{4\pi r_6^5} & \frac{\left[3(z_6-z_0)^2-r_6^2\right]}{4\pi r_6^5} \end{bmatrix}, \tag{11}$$

which is the coefficient matrix of positions for the target.

3. Simulations

The measuring array consisting of six single-component magnetic field sensors is in the plane labelled as xOy of the Cartesian coordinate system and is shown in Figure 3, and the origin is signed as O. The magnetic target at the point P moves along a straight line from the point $P(-20, -20, 2)$ to the point $Q(20, 20, 2)$. The velocity is a constant of 10 m/s in the x-axis and 10 m/s in the y-axis. The coordinates of the six sensors are labelled as $P_1(-2, 1, 0)$, $P_2(0, 1, 0)$, $P_3(2, 1, 0)$, $P_4(-2, -1, 0)$, $P_5(0, -1, 0)$, and $P_6(2, -1, 0)$. The vertical component of the alternating magnetic fields is acquired by a measuring array consisting of six single-component magnetic field sensors.

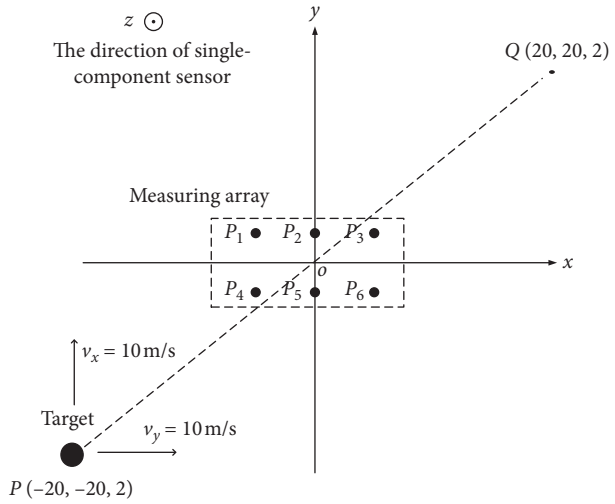

Figure 3: Overhead view of the target and measuring consisting of six single-component magnetometers.

In the whole movement, the source of alternating magnetic dipole moves from −20 m to 20 m in the x-axis and −20 m to 20 m in the y-axis. The height is set as 2 m in the z-axis. The magnetic moment of an alternating magnetic dipole source is $\mathbf{M} = 40\cos(400\pi t + (\pi/3))\vec{i} + 30\cos(400\pi t + (\pi/3))\vec{j} + 20\cos(400\pi t + (\pi/3))\vec{k}$ Am^2. The alternating magnetic field data acquired by six single-component magnetometers are shown in Figure 4.

The varying curve of alternating magnetic field data acquired by six single-component magnetometers during the target's whole movement was obtained by the coherent demodulation (see Figure 5). Then, the localization for moving target with the alternating magnetic field could be transformed to the problem of that with the static magnetic field.

As shown in Figure 6, the locating results show a good agreement with the actual values as predetermined in the simulation. It could also be seen that the target moved from −20 m to 20 m in the X-axis, and the average velocity is 10 m/s. The result in the Y-axis is the same as that in the X-axis. The result in the Z-axis is a constant value of 2 m at the time from 1 s to 5 s.

From the results of above simulation, the position information calculated by the model is completely consistent with the predetermined position information of the moving target. These verify the feasibility of localization for alternating magnetic dipole source using the single-component magnetic field.

4. Experiment

The field experiment was operated in Xi'an, China. An experimenter pushed the trolley carrying the transmitting equipment through the measuring array at the speed of about 0.2 m/s. The height of the solenoid as an alternating magnetic dipole source is about 1.2 m from the ground (see Figure 7(a)). The magnetic field is acquired by a measuring array consisting of eight single-component magnetometers (see Figure 7(b)).

The relationship between the movement of the solenoid and the position of the measuring array is shown in Figure 8. The target moved from the starting point $P(-3, -5, 1.2)$ to the ending point $Q(-3, 5, 1.2)$ along a straight line. The horizontal pitch of the measuring array is 0.5 m, and the vertical pitch is also 0.5 m.

The frequency of the sinusoidal signal emitted by the solenoid is set as 500 Hz. The measuring array consisting of eight single-component magnetometers collected the vertical component of the magnetic field, which is transferred to a PC via a data acquisition card. The sampling rate is set as 5000 Hz. Because the experimental environment is not ideal, there is strong interference of power frequency and other frequencies. It is impossible to directly use the signals collected by the single-component inductive magnetic field sensors.

The signals collected by the single-component inductive magnetic field sensors were passed through a band-pass filter with a cut-off frequency from 480 Hz to 520 Hz. Taking the signal collected by sensor #2 as an example, Figure 9 shows the time domain signals before and after filtering. It also showed that the signals emitted by the signal source collected by sensor #2 were well extracted.

Figure 10 shows the magnetic signals collected by the induction magnetic field sensor #1 to #4 processed after filtering.

Figure 11 shows the magnetic signals collected by the induction magnetic field sensor #5 to #8 processed after filtering.

As shown in Figure 12, the varying curves of alternating magnetic fields collected by the induction magnetic field sensor labelled from #1 to #4 were obtained by coherent demodulation [14, 15].

As shown in Figure 13, the varying curves of alternating magnetic fields collected by the induction magnetic field sensor labelled from #5 to #8 were obtained by coherent demodulation [14, 15].

Since the radiating rod inevitably has the problem of swaying during the movement, the curves obtained by

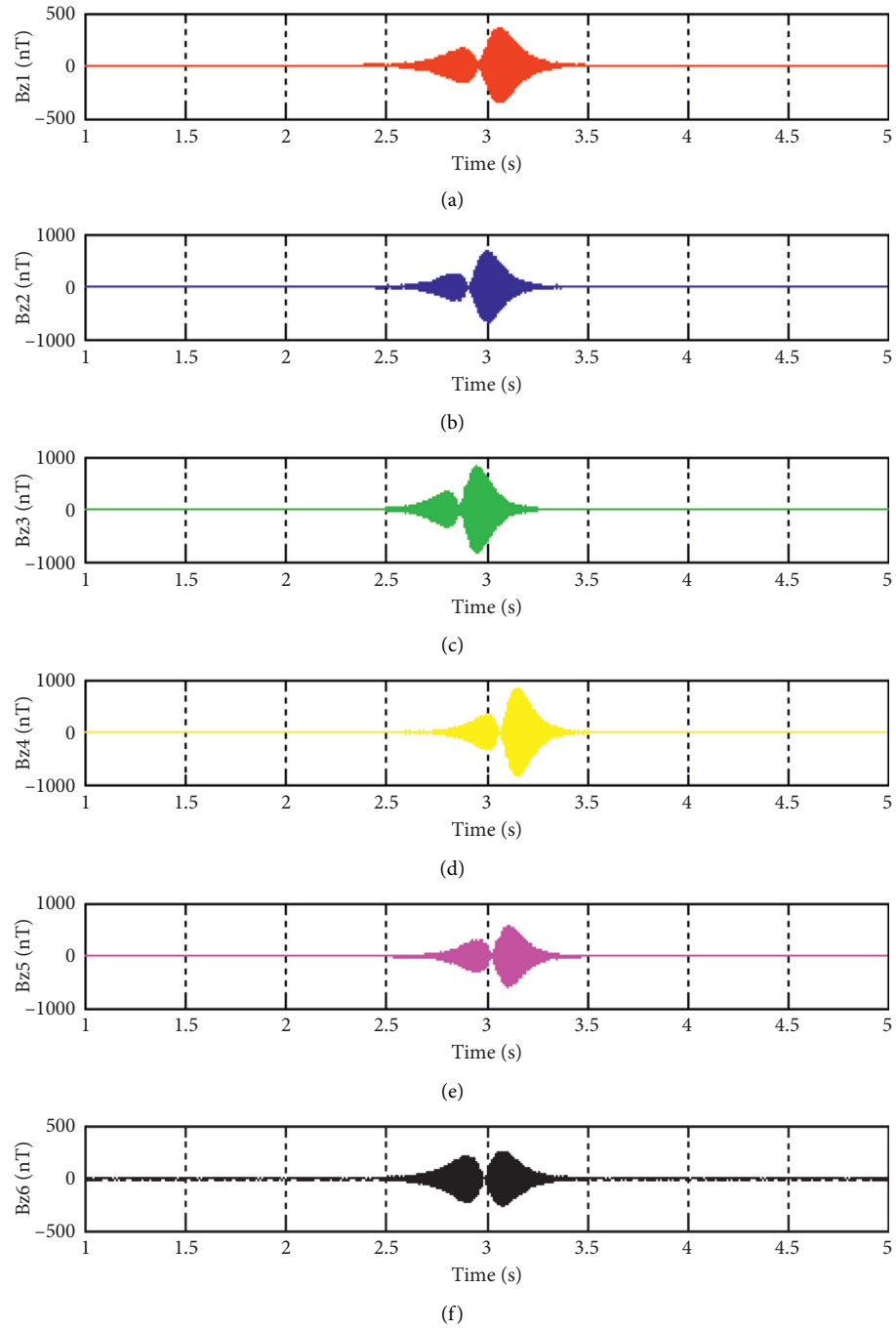

Figure 4: The vertical component of alternating magnetic fields acquired by six single-component magnetic sensors.

coherent demodulation have a certain amount of shaking compared with the smooth curves in the simulation. The peak values of sensor #1 in Figure 12 are significantly greater than those of sensor #2, sensor #3, and sensor #4 located in the same line. At the same time, it could be found that the peak values of sensor #7 in Figure 13 are significantly smaller than those of sensor #5, sensor #6, and sensor #8 located in the same line. These were caused by the different sensitivities of each sensor. In order to reduce the impact of different sensitivities of the sensor, the signals collected by sensor #7 and sensor #1 were excluded in the final positioning solution.

Using the hybrid algorithm combining the Gauss–Newton algorithm and genetic algorithm, the positioning results of the target in the X direction are shown in Figure 14. The location result is about −3 m in the X direction from the time of 20 s to 55 s. These show a good agreement with the actual value. This is the reason that the magnetic field signal gradually increases as the distance between the target and the sensor becomes close.

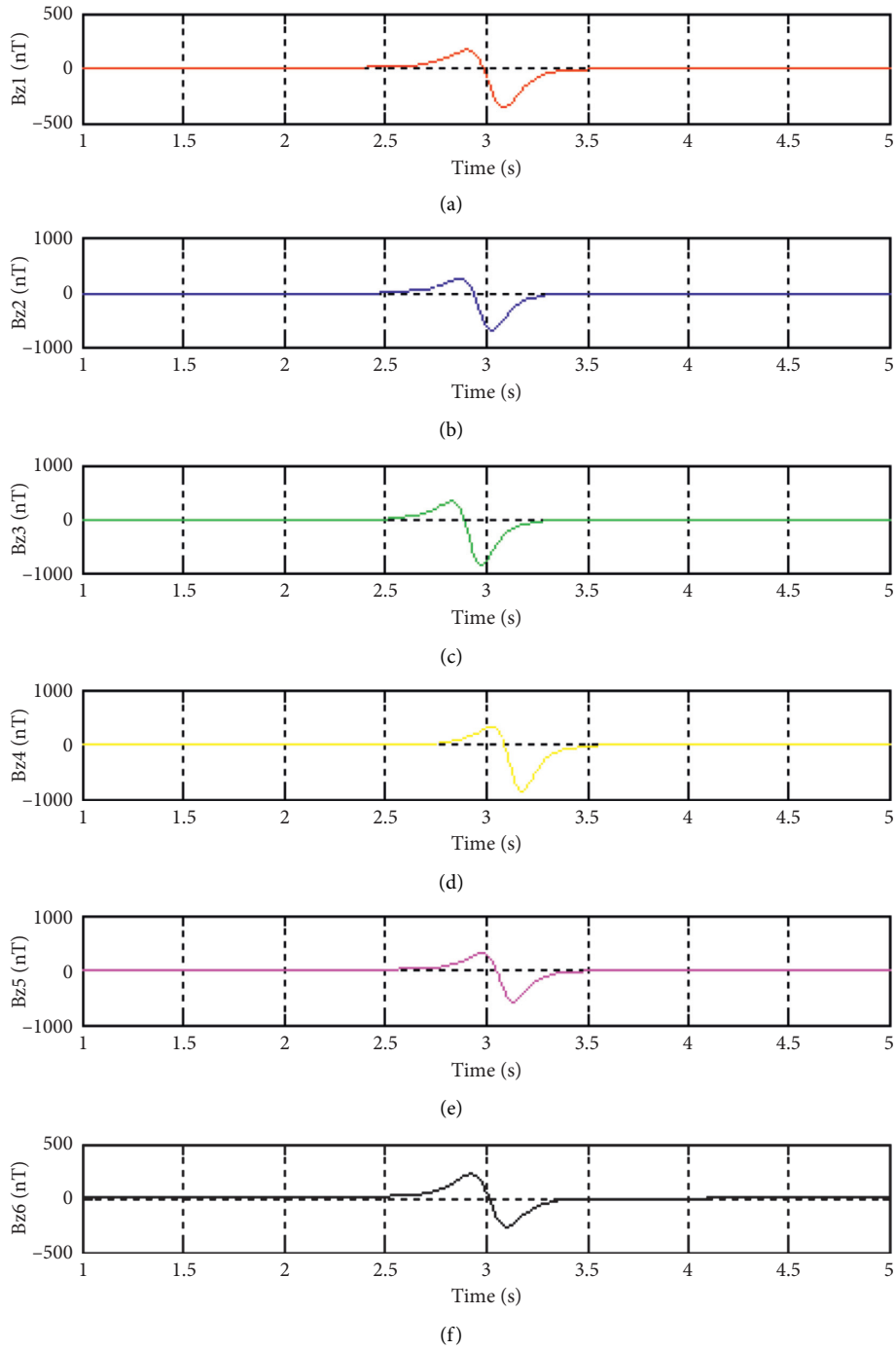

Figure 5: Varying curve of alternating magnetic field data acquired by six single-component magnetometers.

The error curve between the positioning result and the actual movement trajectory of the target in the x direction is shown in Figure 15. It could be found that when the target passed through the array, the positioning error was very small and the positioning effect was very good. The average error of positioning is 0.17 m from the time of 20 s to 55 s. However, as the target moved away from the array, the positioning error became larger and the positioning effect became poorer.

As shown in Figure 16, the average velocity was about 0.2 m/s in the Y direction from the time of 20 s to 55 s. These also showed a good agreement with the actual value and a disagreement in the other times.

The error curve between the positioning result and the actual movement trajectory of the target in the Y direction is shown in Figure 17. It could be found that when the target passed through the array, the positioning error was very small and the positioning effect was very good. The average

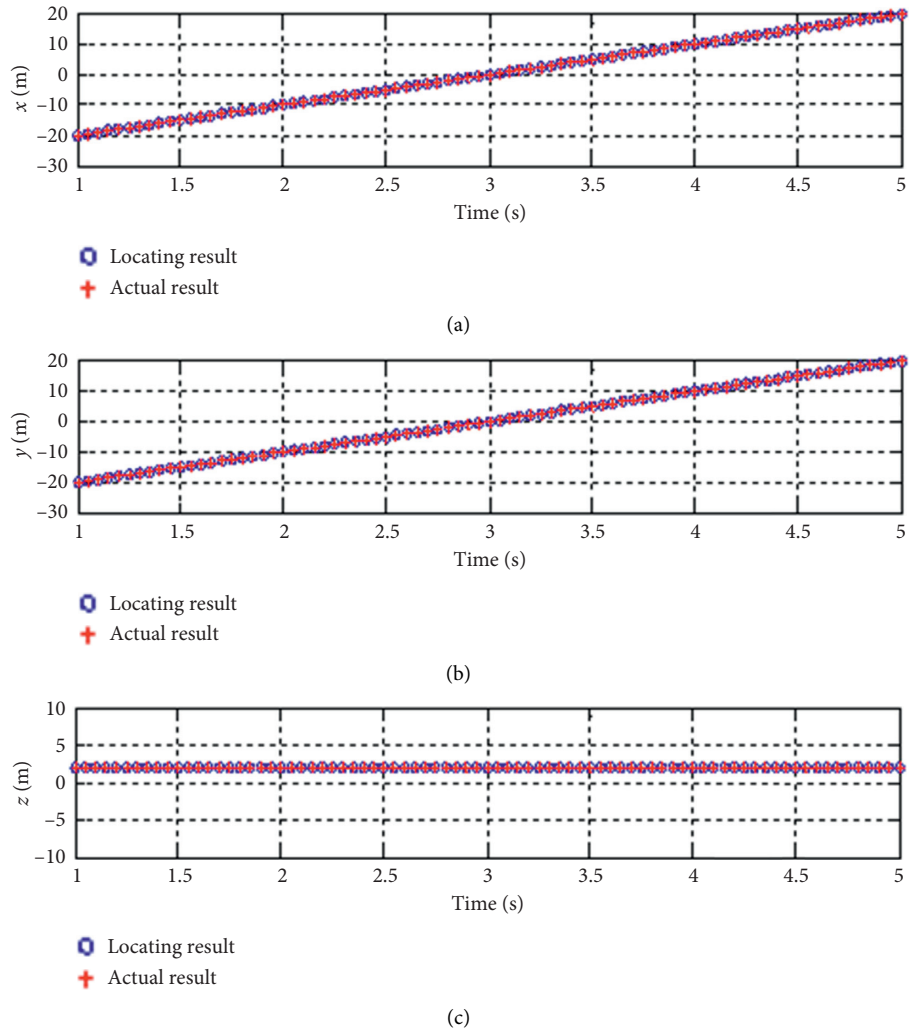

Figure 6: Contrast of location result and actual values for the moving target.

(a) (b)

Figure 7: (a) Radiation source and (b) single-component magnetometers.

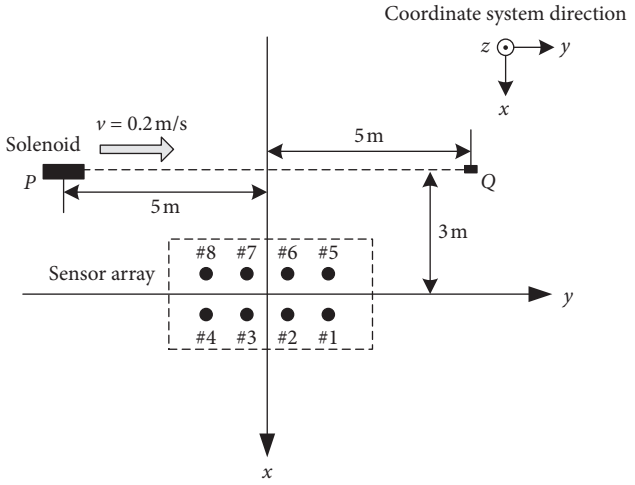

Figure 8: Overhead view of experimental tests.

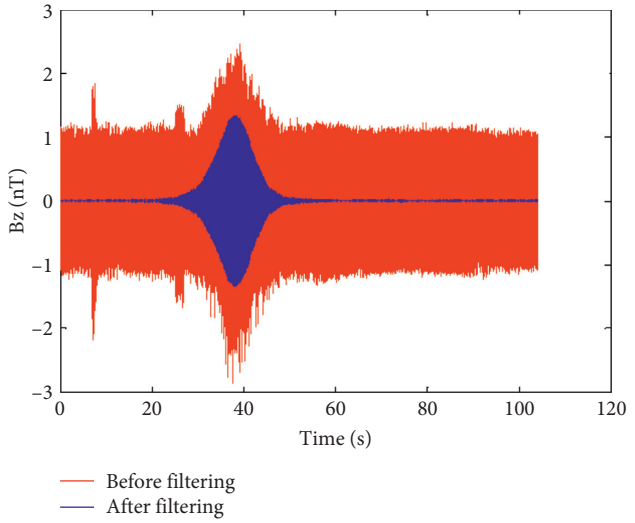

Figure 9: Alternating magnetic field collected by sensor #2 before and after filtering.

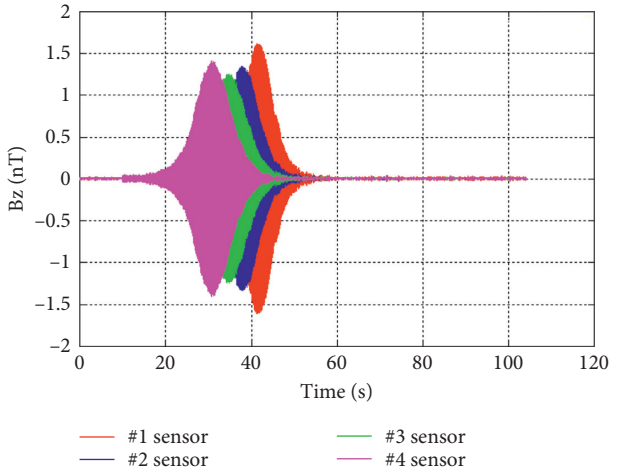

Figure 10: The signals collected by the induction magnetic field sensor #1 to #4 processed after filtering.

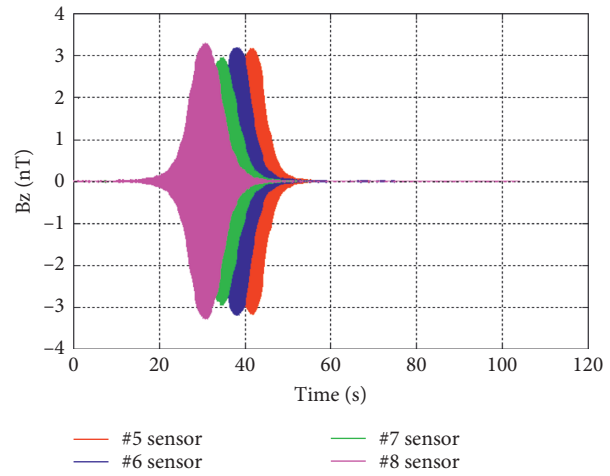

Figure 11: The signals collected by the induction magnetic field sensor #5 to #8 processed after filtering.

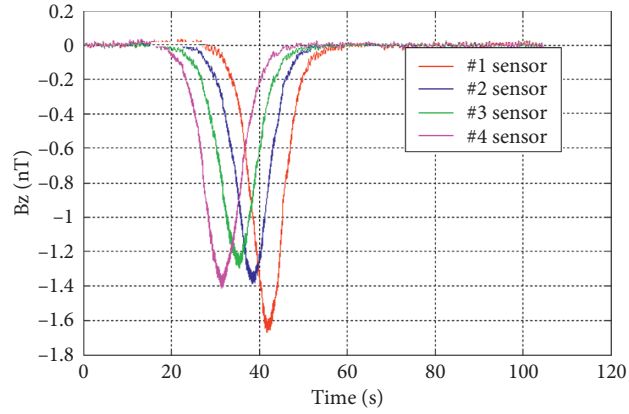

Figure 12: The varying curves of alternating magnetic field data collected by the sensor labelled as from #1 to #4.

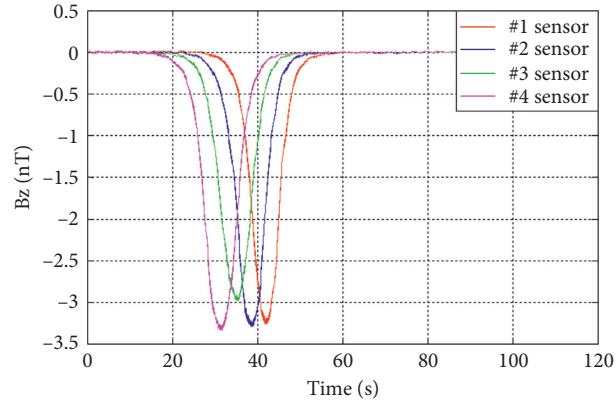

Figure 13: The varying curves of alternating magnetic fields collected by the sensor labelled as from #5 to #8.

error of positioning is 0.12 m from the time of 20 s to 55 s. However, as the target moved away from the array, the positioning error also became larger and the positioning effect became poorer.

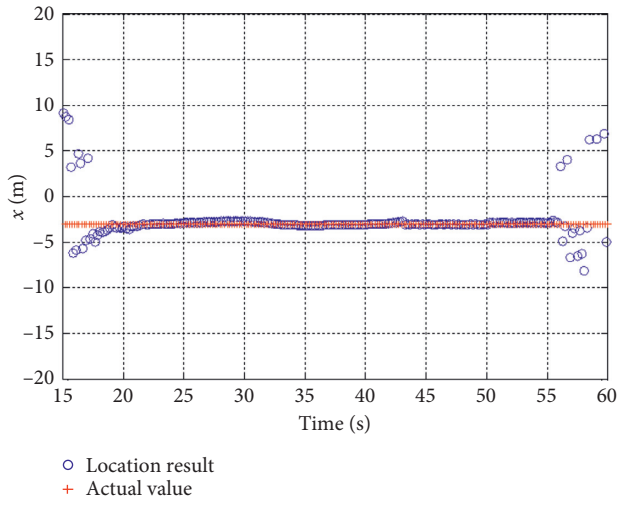

Figure 14: Contrast of location result and actual value in the X direction.

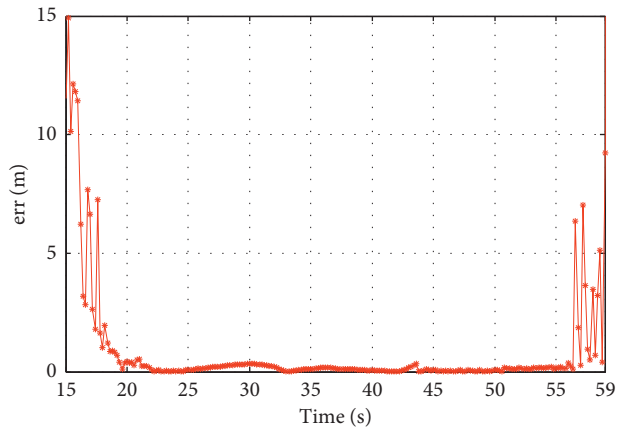

Figure 15: Error curve between the positioning result and the actual movement trajectory of the target in the X direction.

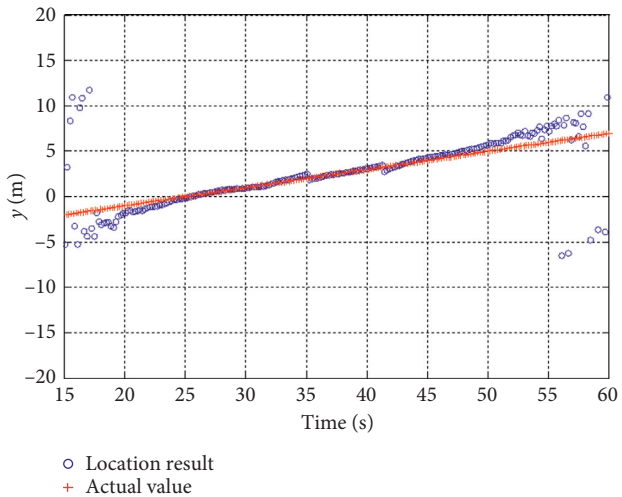

Figure 16: Contrast of location result and actual value in the Y direction.

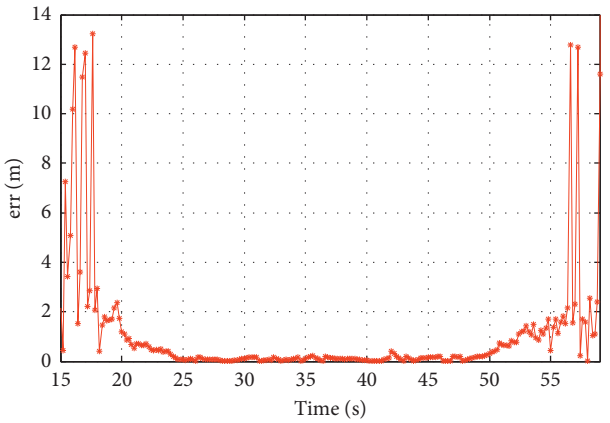

Figure 17: Error curve between the positioning result and the actual movement trajectory of the target in the Y direction.

As the simulation result in the Z direction was the same as that in the X direction, the analysis would not be repeated in this paper.

5. Conclusions

Most of the traditional research studies on magnetic positioning technology are based on the magnetic target location of static magnetic anomalies, and the positioning effect is easily affected by geomagnetic anomalies and other magnetic interference noise. The magnetic field positioning methods of the alternating magnetic dipole model are studied, which have strong anti-interference ability. The methods could overcome the interference of geomagnetic environmental interference and reduce the influence of other frequency interference signals on the positioning through some signal processing methods. Using single-component magnetometers could reduce costs and avoid the steering differential calibration of tri-axis magnetometers. The theoretical analysis of simulation and experimental results showed that the position information agreed well with the actual moving state of the target, which verified the feasibility and practicability of the localization algorithm. It is of great significance in the application of engineering.

Data Availability

The data used to support the findings of this study are available from the corresponding author upon request.

Conflicts of Interest

The authors declare that they have no conflicts of interest.

References

[1] L. Merlat and P. Naz, "Magnetic localization and identification of vehicles," in *Proceedings of SPIE: Unattended Ground Sensor Technologies and Applications V*, vol. 5090, pp. 174–185, Orlando, FL, USA, 2003.

[2] C. Coillot, J. Moutoussamy, R. Lebourgeois, S. Ruocco, and G. Chanteur, "Principle and performance of a dual-band

search coil magnetometer: a new instrument to investigate fluctuating magnetic fields in space," *IEEE Sensors Journal*, vol. 10, no. 2, pp. 255–260, 2009.

[3] P. Palangio, F. Masci, M. Di Persio, and C. Di Lorenzo, "Electromagnetic field measurements in ULF-ELF-VLF [0.001 Hz–100 kHz] bands," *Advances in Geosciences*, vol. 14, pp. 69–73, 2008.

[4] S. Bhattacharya, S. Sarkar, A. K. Gwal, and M. Parrot, "Satellite and ground-based ULF/ELF emissions observed before Gujarat earthquake in March 2006," *Current Science*, vol. 93, pp. 41–46, 2007.

[5] Z. Zhi Sun and I. F. Akyildiz, "Magnetic induction communications for wireless underground sensor networks," *IEEE Transactions on Antennas and Propagation*, vol. 58, no. 7, pp. 2426–2435, 2010.

[6] G. Wang, L. Yang, and B. Liu, "Study on the testing method of oil-gas pipeline stress damage based on magnetic memory," *Chinese Journal of Scientific Instrument*, vol. 38, no. 2, pp. 271–278, 2017.

[7] E. Paperno, I. Sasada, and E. Leonovich, "A new method for magnetic position and orientation tracking," *IEEE Transactions on Magnetics*, vol. 37, no. 4, pp. 1938–1940, 2001.

[8] T. Nara, S. Suzuki, and S. Ando, "A closed-form formula for magnetic dipole localization by measurement of its magnetic field and spatial gradients," *IEEE Transactions on Magnetics*, vol. 42, no. 10, pp. 3291–3293, 2006.

[9] A. Plotkin, O. Shafrir, E. Paperno, and D. M. Kaplan, "Magnetic eye tracking: a new approach employing a planar transmitter," *IEEE Transactions on Biomedical Engineering*, vol. 57, no. 5, pp. 1209–1215, 2010.

[10] A. Sheinker, B. Ginzburg, N. Salomonski, L. Frumkis, and B.-Z. Kaplan, "Localization in 3-D using beacons of low frequency magnetic field," *IEEE Transactions on Instrumentation and Measurement*, vol. 62, no. 12, pp. 3194–3201, 2013.

[11] A. Sheinker, B. Ginzburg, N. Salomonski, L. Frumkis, and B.-Z. Kaplan, "Remote tracking of a magnetic receiver using low frequency beacons," *Measurement Science and Technology*, vol. 25, no. 10, Article ID 105101, 2014.

[12] V. Pasku, A. De Angelis, M. Dionigi, G. De Angelis, A. Moschitta, and P. Carbone, "A positioning system based on low-frequency magnetic fields," *IEEE Transactions on Industrial Electronics*, vol. 63, no. 4, pp. 2457–2468, 2016.

[13] T. Li, X. Wang, and J. Dou, "Time-harmonic horizontal dipole in coastal," *Ship Electronic Engineering*, vol. 35, no. 5, pp. 142–146, 2015.

[14] X. Gao, S. Yan, and B. Li, "A novel method of localization for moving objects with an alternating magnetic field," *Sensors*, vol. 17, no. 4, pp. 923–934, 2017.

[15] X. Gao, S. Yan, and B. Li, "Localization of moving object under the interference of ferromagnetic platform with the alternating magnetic field," in *Proceedings of the 2017 5th International Conference on Mechanical, Automotive and Materials Engineering*, Guangzhou, China, August 2017.

[16] H. Dai, S. Song, C. Hu, B. Sun, and Z. Lin, "A novel 6-D tracking method by fusion of 5-D magnetic tracking and 3-D inertial sensing," *IEEE Sensors Journal*, vol. 18, no. 23, pp. 9640–9648, 2018.

[17] J. Song, D. Sun, Z. Zhao, H. Zhou, H. Xia, and G. Ma, "Localization of low-frequency magnetic beacons based on genetic algorithm," in *Proceedings of the 39th Chinese Control Conference*, Shenyang, China, September 2020.

[18] X. Pi, S. Zhao, H. Liu, B. Xia, X. Shi, and X. Zheng, "Localization of site-specific delivery capsule in vivo with alternating electromagnetic field," in *Proceedings of the 2008 World Automation Congress*, Waikoloa, HI, USA, 2008.

[19] S. Song, H. Ren, W. Liu, and C. Hu, "An analytic algorithm based electromagnetic localization method," in *Proceedings of the International Conference on Information and Automation*, Yinchuan, China, August 2013.

[20] J. Ge, S. Wang, H. Dong et al., "Real-time detection of moving magnetic target using distributed scalar sensor based on hybrid algorithm of particle swarm optimization and Gauss-Newton method," *IEEE Sensors Journal*, vol. 20, no. 18, pp. 10717–10723, 2020.

[21] W. Gong and Y. Lin, "The study on the application of BP neural network based on genetic algorithm optimization in magnetic flux leakage (MFL) of rail top surface stripping defects," in *Proceedings of the 2020 39th Chinese Control Conference*, Shenyang, China, July 2020.

[22] H. Ghorbaninejad and R. Heydarian, "New design of waveguide directional coupler using genetic algorithm," *IEEE Microwave and Wireless Components Letters*, vol. 26, no. 2, pp. 86–88, 2016.